UNIVERSITÉ DE MONTRÉAL

OPTIMIZATION AND CALCULATION OF THERMODYNAMIC PROPERTIES AND PHASE DIAGRAMS OF MULTI-COMPONENT OXIDE SYSTEMS

Par

Ping WU

DÉPARTEMENT DE MÉTALLURGIE ET DE GÉNIE DES MATÉRIAUX

ÉCOLE POLYTECHNIQUE

THÈSE PRÉSENTÉE EN VUE DE L'OBTENTION

DU GRADE DE PHILOSOPHIAE DOCTOR (Ph.D.)

(GÉNIE MÉTALLURGIQUE)

JANVIER 1992

© droits réservés de Ping WU 1992.

UNIVERSITÉ DE MONTRÉAL

ÉCOLE POLYTECHNIQUE

Cette thèse: Optimization and calculation of thermodynamic properties and phase diagrams of multicomponent oxide systems

présenté par: Ping Wu

en vue de l'obtention du grade de: PHILOSOPHIAE DOCTOR (PH.D)

a été dûment accepté par le jury d'examen constitué de:

M. Christopher W. Bale, Ph.D, président

M. Arthur D. Pelton, Ph.D, membre et directeur de recherche

M. Milton Blander, Ph.D, examinateur externe

M. Gunnar Eriksson, Ph.D, membre

To my dear wife,

Pei-lin Mao

SOMMAIRE

Une banque de données thermodynamiques pour les systèmes d'oxydes a été développée avec succès. Ainsi toutes les données thermodynamiques et tous les points du diagramme de phases d'un système d'oxydes sont représentés et entreposés à l'aide d'une petite série de coefficients. Cette méthode réduit grandement la quantité d'information nécessaire pour définir complètement un système. De plus, étant donné la cohérence thermodynamique de tout le procédé, l'interpolation et l'extrapolation des résultats à partir de ces coefficients peuvent être faites avec confiance. L'équation de l'énergie de Gibbs d'un système multi-composants peut être élaborée à partir des sous-systèmes binaires et ternaires. Ainsi, les équilibres multi-phases multi-composants d'oxydes avec d'autres phases tel que gaz, métaux, etc. peuvent être prédits par des programmes de minimisation de l'énergie de Gibbs (comme le programme EQUILIB du système F*A*I*T qui a été développé à l'École Polytechnique) en utilisant la présente banque de données. Ceci constitue les motifs originaux de cette recherche.

Pour bâtir une banque de données, il faut d'abord choisir des modèles thermodynamiques adéquats qui permettent de trouver des expressions pour l'énergie de Gibbs de toutes les phases. Des modèles simples comme les modèles pour les

solutions Raoultiennes, régulières et polynomiales ont été utilisés pour les solutions solides d'oxydes. Pour les laitiers par contre, de grands écarts à l'idéalité sont observés. Ainsi, un modèle général pouvant être utilisé tant pour les systèmes ordonnés que pour les systèmes non ordonnés a été préféré pour la phase liquide. Comme il est discuté au Chapitre 1, quoique les modèles pour les solutions polynomiales soient les plus simples, ils ne peuvent, ni représenter correctement les phénomènes d'ordonnance qui existent couramment dans les laitiers à base de silicates, ni interpoler de façon adéquate les propriétés thermodynamiques des systèmes d'ordre supérieur à partir des systèmes d'ordre inférieur. Parmi les autres modèles, il y a les modèles structuraux pour silicates qui sont utilisés avec succès aux laitiers à base de silicates malgré leur complexité. Si la banque de données doit être construite à partir d'un seul modèle, la plupart des modèles structuraux pour silicates doivent être écartés à cause justement de leur complexité et de leur incapacité à représenter les propriétés des laitiers qui ne sont pas à base de silicates. Le modèle de cellule et celui de deux sous-réseaux ont aussi été utilisés avec succès sur les laitiers, tant ceux à base de silicates que les autres systèmes d'oxydes. Le modèle de cellule est attrayant théoriquement parce qu'il suppose que seuls les paramètres binaires sont nécessaires pour approximer les propriétés

thermodynamiques des solutions d'oxydes multi-composants. Cependant, en pratique, il s'avère très difficile de reproduire précisément les diagrammes de phases ternaires à partir du modèle de cellule. Quant au modèle des deux sous-réseaux, même si plusieurs études sur les systèmes d'oxydes ont été faites en l'utilisant, le modèle est toujours en développement pour corriger la supposition de lacunes chargées dans la phase liquide et il n'a pas encore été démontré que le modèle s'applique aux systèmes multi-composants. C'est pourquoi le modèle quasi-chimique modifié a été choisi pour bâtir la présente banque de données thermodynamiques sur les oxydes.

Conformément au modèle quasi-chimique modifié, les propriétés thermodynamiques (telles ΔH et ΔG) sont des fonctions non-linéaires des paramètres du modèle ω_i et η_i (i=0, 1,...,7). Ainsi, des techniques non-linéaires d'optimisation par moindres carrés ont été développées. Pour l'optimisation des binaires, le premier terme d'une série de Taylor centrée autour d'un point estimé ($\omega^* - \eta^* T$) qui est une fonction linéaire de ($\omega - \eta T$) a été accepté pour le formalisme de cette fonction. Par une régression linéaire des moindres carrés, ($\omega - \eta T$) a été calculé et a été pris comme nouvel estimé pour la prochaine itération. A mesure que les itérations progressent, la valeur de ($\omega - \eta T$) converge vers la

valeur exacte. Dans certains systèmes d'oxydes, une connaissance de l'entropie ou de l'enthalpie des solutions est disponible. Un programme d'optimisation binaire appelé FITQUAS a été écrit avec lequel toutes les donnés thermodynamiques et tous les points du diagramme de phases pour la phase liquide peuvent être évalués. Les propriétés thermodynamiques des composés intermédiaires, tel que l'enthalpie de formation peuvent être évaluées indirectement aussi. Les détails d'une évaluation de 25 systèmes binaires d'oxydes sont discutés dans la Section 2.3. A partir des paramètres quasi-chimiques calculés et du modélé quasi-chimique, on peut calculer, soit les propriétés thermodynamiques, soit le diagramme de phases du système. Les valeurs d'activité calculées et les diagrammes de phases sont bien reproduits à l'intérieur des marges d'incertitude expérimentales. De cette façon, le diagramme de phases et les propriétés thermodynamiques des phases liquides et solides sont cohérents les uns avec les autres. Les propriétés thermodynamiques peuvent être extrapolées et interpolées avec confiance. Elles peuvent être utilisées pour la construction de diagrammes de phases d'ordre supérieur.

La cohérence thermodynamique est démontrée au Chapitre 3 en évaluant la série des systèmes d'oxydes des terres rares avec Al_2O_3: les tendances que l'on l'observe pour les propriétés à mesure qu'on avance dans la série peuvent être

exploitées afin d'améliorer les évaluations et/ou de prédire les propriétés s'il y a un manque de données dans une région ou sur tous le diagramme. Une évaluation critique des 15 systèmes d'oxydes de terres rares avec Al_2O_3 a été effectuée. Les propriétés thermodynamiques de tous les composés et de toutes les solutions liquides ont été prédites, même si pour 3 des 15 systèmes aucun diagramme de phases n'avait été rapporté.

Le modèle quasi-chimique modifié a été extrapolé avec succès aux systèmes ternaires et multi-composants par Pelton. L'optimisation non-linéaire ternaire peut être effectuée par une simple méthode de gradient. Dans la présente étude, deux améliorations ont été ajoutées au programme d'optimisation ternaire de sorte que les points d'une lacune de miscibilité ternaire peuvent être optimisés simultanément avec les autres données thermodynamiques et le reste du diagramme de phases. L'optimisation ternaire reste valide même pour des termes très larges. Dans la Section 4.2, les détails des évaluations de 8 systèmes d'oxydes ternaires sont discutés. La phase liquide a été optimisée en utilisant le programme d'optimisation ternaire qui est basé sur le modèle quasi-chimique modifié. Dans l'optimisation, seulement de petits termes ternaires ont normalement été requis pour reproduire le diagramme de phases. Même pour quelques systèmes ternaires complexes où des écarts

extrêmement négatifs (indiqués par la formation d'un composé ternaire) coexistaient dans la phase liquide avec d'autres largement positifs (une lacune de miscibilité est formée), les diagrammes de phases ont pu être évalués par le modèle quasi-chimique. Ainsi, le modèle quasi-chimique et le programme d'optimisation ternaire sont très efficaces pour les calculs thermodynamiques ternaires.

Les données thermodynamiques évaluées pour tous les solides stoechiométriques sont citées en annexe.

Dans la Section 4.3, pour montrer un exemple de calculs d'équilibres multi-composants multi-phases en utilisant la présente banque de données, l'équilibre des phases dans le système ZrO_2-Al_2O_3-TiO_2-SiO_2 a été prédit. L'accord avec les données expérimentales est bon.

Dans le Chapitre 5, en optimisant tous les résultats disponibles, i.e. toutes les donnés thermodynamiques et tous les points sur les diagrammes de phases, pour tous les systèmes du laitier formé de PbO-ZnO-SiO_2-FeO-Fe_2O_3-CaO, une banque de données thermodynamiques a été construite en utilisant le modèle quasi-chimique modifié. Ainsi des équations donnant l'activité des espèces présentes dans le laitier en fonction des compositions d'équilibre ont été

générées. Cette banque de données peut être utilisée par le système informatique F*A*I*T pour calculer la composition d'équilibre d'un laitier lors du smeltage du plomb, si P_{O2} et la composition de la phase métallique sont connues. Ainsi, quelqu'un peut prédire le contenu en PbO et le ratio $Fe^{+3}/(Fe^{+2}+Fe^{+3})$ du laitier. L'accord de nos prédictions avec les résultats expérimentaux est bon sur une grande gamme de compositions et de températures. La banque de données peut donc fournir un moyen utile d'améliorer les techniques industrielles actuelles pour le smeltage du plomb.

Présentement, toutes les phases liquides et les composés solides (à l'exception des composés solides contenant PbO) de 84 systèmes binaires énumérés dans le Tableau 2-1 ainsi que les 28 laitiers ternaires montrés aux Tableaux 4-7 et 4-8 ont été évalués. De plus, 3 systèmes quaternaires ZrO_2-TiO_2-SiO_2-Al_2O_3, FeO-Fe_2O_3-CaO-SiO_2 et FeO-CaO-ZnO-SiO_2, et un système quinaire PbO-SiO_2-CaO-FeO-Fe_2O_3 ont été prédits avec succès.

Les calculs d'équilibre multi-phases multi-composants utilisant la présente banque de données peuvent être classés en se basant sur la précision attendue lors de l'estimation:

1) Les calculs pour les systèmes multi-composants contenant seulement des oxydes pour lesquels tous les sous-systèmes binaires et ternaires ont été optimisés (tel

qu'énuméré dans les Tableaux 2-1, 4-7 et 4-8) sont de grande précision.

2) Les calculs pour les systèmes contenant seulement des oxydes pour lesquels tous les sous-système binaires ont été optimisés (tel qu'énuméré dans le Tableau 2-1) et pour lesquels tous les sous-systèmes ternaires sont, soit optimisés, soit marqués d'un "O" dans le Tableau 4-7 sont de précision moyenne.

3) Les calculs pour les systèmes contenant des oxydes pour lesquels les sous-systèmes binaires ont été optimisés mais pour lesquels les sous-systèmes ternaires sont marqués d'un "N" dans le Tableau 4-7 sont de précision faible.

4) Les calculs pour les systèmes pour lesquels certains sous-systèmes binaires n'ont pas été optimisés sont de précision minimale.

Dans un système multi-composants multi-phases, tel que montré dans le Chapitre 5, la présente banque de données peut être utilisée pour fournir l'expression de l'énergie de Gibbs d'un laitier multi-composant, tandis que les autres banques de donnés (gaz, alliages, etc.) du système F*A*I*T peuvent former les expressions de l'énergie de Gibbs pour les autres phases. Ainsi, en minimisant l'énergie de Gibbs totale du système multi-composants multi-phases (par l'emploi d'un programme de minimisation de l'énergie libre du système F*A*I*T) des

équilibres complexes impliquant des laitiers contenant SiO_2, TiO_2, Al_2O_3, FeO, Fe_2O_3, CaO, MgO. MnO, PbO, ZnO, Na_2O, K_2O, ZrO_2, NiO, Ti_2O_3 et les oxydes des terres rares peuvent être calculés. Les équilibres multi-composants et multi-phases peuvent donc être raisonnablement prédits par la présente banque de données conjointement avec les autres banques de donnés.

Nous croyons qu'il s'agit de la banque de données sur les oxydes la plus complète qui soit disponible actuellement.

ABSTRACT

A thermodynamic database for oxide systems has been successfully developed. As a result, all thermodynamic as well as phase diagram data of an oxide system are represented and stored by means of a small set of coefficients. Consequently, multi-component multiphase equilibria involving oxides with other phases such as gas, metals etc. can be predicted by a Gibbs energy minimization program using the present database.

To build a database, simple models such as the Raoultian etc. have been employed for solid oxide solutions. For liquid oxide solutions, as discussed in Chapter 1 (where some practical solution models are reviewed), the modified quasi-chemical model has been chosen to build the present thermodynamic oxide database.

According to the modified quasi-chemical model, thermodynamic properties are non-linear functions of the model coefficients. Hence, non-linear least squares techniques have been developed and a binary optimization program has been written accordingly. All the evaluated liquid and solid thermodynamic properties and the phase diagram are internally consistent with each other. This thermodynamic internal consistency has been demonstrated in Chapter 3 when evaluating a series of rare earth oxide-Al_2O_3 binary systems. Therefore, the thermodynamic properties may be extrapolated or

interpolated with confidence to predict unknown phase diagrams (shown in Chapter 3), and may be used for reasonable construction of phase diagrams of higher order systems.

The modified quasi-chemical model has been successfully extrapolated in ternary and multi-component systems. In Chapter 4, two improvements have been made to the ternary optimization program developed previously.

In Section 4.2 and Chapter 5, successful examples of predicting multi-component and multiphase equilibria are provided.

The components considered in the present study are SiO_2, Al_2O_3, TiO_2, FeO, CaO, MgO, MnO, Na_2O, K_2O, ZrO_2, Fe_2O_3, Ti_2O_3, NiO, PbO, ZnO and rare earth oxides. Optimizations of 26 binaries and 8 ternaries are discussed. In total, the database contains 84 binaries and 28 ternaries. In addition, 3 quaternaries ZrO_2-TiO_2-SiO_2-Al_2O_3, FeO-Fe_2O_3-CaO-SiO_2 and FeO-CaO-ZnO-SiO_2, and 1 quinary PbO-SiO_2-CaO-Fe_2O_3-FeO have been successfully predicted. Optimized phase diagrams are all reproduced precisely. At present this is believed to be the most extensive oxide solution database available.

ACKNOWLEDGEMENTS

I would like to express my deep appreciation to Dr. A.D. Pelton, whose guidance and enthusiastic support were of immeasurable help to me at all stages of this project. His earlier work with slag systems provided the starting point of this thesis, and his solid financial assistance allowed me to concentrate on my research work.

I am also grateful to my co-director, Dr. G. Eriksson, for his continual helpful advice and collaboration in my study. I enjoyed all the time we worked together.

I also thank Dr. C. Bale for his critical review and good suggestions. As well, I express my gratitude to Dr. J. Sangster who corrected the grammar of this thesis.

I am indebted to all the members of the CRCT, Jhoaan, Jame, Paul, Ling, Romero, Jianzhong, Yves et al., for their assistance and friendship during my study in Canada.

TABLE OF CONTENTS

PAGE

DEDICATION iv

SOMMAIRE v

ABSTRACT xiv

ACKNOWLEDGEMENTS xvi

TABLE OF CONTENTS xvii

LIST OF FIGURES xxii

LIST OF TABLES xxxiii

INTRODUCTION 1

CHAPTER 1 - SOLUTION MODELS FOR OXIDE SYSTEMS 14

1.1 INTRODUCTION 14

1.2 POLYNOMIAL SOLUTION MODELS 16

1.3 STRUCTURE BASED SILICATE MODELS 20

1.3.1 Introduction 20

1.3.2 Toop and Samis [62Too] 22

1.3.3 Whiteway, Smith and Masson [70Whi] . . 26

1.3.4 Lin and Pelton [86Lin] 30

1.3.5 The cell model of Kapoor and Frohberg [71Kap] 34

1.3.6 Sub-lattice model of Hillert et al. [90Hil1] 40

1.3.7 Conclusions 44

1.4 QUASI-CHEMICAL MODEL 46

1.4.1 Quasi-chemical model 46
1.4.2 Modification of the quasi-chemical model 55
1.4.2.1 Fixing the composition of maximum ordering 56
1.4.2.2 Composition dependence of ω and η 59
1.5 CONCLUSIONS 60
CHAPTER 2 - OPTIMIZATION AND CALCULATION OF BINARY SYSTEMS 74
2.1 INTRODUCTION 74
2.1.1 Linear optimization 76
2.1.2 The non-linear optimization 81
2.1.3 Non-linear optimization of the quasi-chemical model 83
2.1.3.1 Introduction 83
2.1.3.2 The simultaneous optimization of ω and η 88
2.1.3.3 The optimization of ω while η possesses a fixed value 88
2.1.3.4 The optimization of η while ω possesses a fixed value 89
2.1.3.5 The weighting of experimental data in the optimization procedure 89
2.1.3.6 Optimization of the liquidus line of an intermediate compound 90

2.1.3.7 Miscibility gaps 94
2.1.4 Conclusions 95
2.2 THERMODYNAMIC PROPERTIES OF THE COMPONENT OXIDES 97
2.3 BINARY SYSTEM EVALUATIONS 106
2.3.1 The MgO-MnO system 106
2.3.2 The $MnO-SiO_2$ system 109
2.3.3 The $MgO-SiO_2$ system 113
2.3.4 The $CaO-SiO_2$ system 116
2.3.5 The $FeO-SiO_2$ system 120
2.3.6 The Na_2O-SiO_2 system 124
2.3.7 The K_2O-SiO_2 system 129
2.3.8 The SiO_2-TiO_2 system 132
2.3.9 The ZrO_2-SiO_2 system 134
2.3.10 The $Al_2O_3-TiO_2$ system 136
2.3.11 The $Na_2O-Al_2O_3$ system 139
2.3.12 The $K_2O-Al_2O_3$ system 143
2.3.13 The $Al_2O_3-ZrO_2$ system 147
2.3.14 The $CaO-TiO_2$ system 149
2.3.15 The $MnO-TiO_2$ system 152
2.3.16 The $MgO-TiO_2$ system 156
2.3.17 The Na_2O-TiO_2 system 160
2.3.18 The K_2O-TiO_2 system 164
2.3.19 The TiO_2-ZrO_2 system 166
2.3.20 The CaO-MnO system 169
2.3.21 The CaO-FeO system 171

2.3.22 The $CaO-ZrO_2$ system 174
2.3.23 The FeO-MnO system 177
2.3.24 The MgO-CaO system 180
2.3.25 The FeO-MgO system 182
2.3.26 The $FeO-ZrO_2$ system 184
2.4 CONCLUSIONS 186
CHAPTER 3 - THERMODYNAMIC AND PHASE DIAGRAM CALCULATION OF BINARY RARE EARTH OXIDE-Al_2O_3 SYSTEMS 230
3.1 INTRODUCTION 230
3.2 COUPLED THERMODYNAMIC/PHASE DIAGRAM ASSESSMENT OF THE RARE EARTH OXIDE-ALUMINUM OXIDE BINARY SYSTEMS 231
CHAPTER 4 - OPTIMIZATION AND CALCULATION OF TERNARY AND MULTI-COMPONENT SYSTEMS 288
4.1 INTRODUCTION 288
4.1.1 Quasi-chemical model for ternary and multi-component systems 288
4.1.2 Optimization and Calculation of ternary systems 294
4.1.3 Calculation of multi-component oxide systems 302
4.2 TERNARY SYSTEM EVALUATIONS 303
4.2.1 The $CaO-MgO-TiO_2$ system 303
4.2.2 The TiO_2-SiO_2-CaO system 307
4.2.3 The $MgO-SiO_2-TiO_2$ System 313
4.2.4 The $MnO-SiO_2-TiO_2$ system 315

4.2.5 The SiO_2-TiO_2-ZrO_2 system 316

4.2.6 The TiO_2-ZrO_2-Al_2O_3 system 318

4.2.7 The SiO_2-ZrO_2-Al_2O_3 system 320

4.2.8 The TiO_2-SiO_2-Al_2O_3 system 321

4.3 THE Al_2O_3-SiO_2-TiO_2-ZrO_2 SYSTEM 323

4.4 CONCLUSIONS 325

CHAPTER 5 - PREDICTION OF PbO CONTENT AND $Fe^{+3}/(Fe^{+2}+Fe^{+3})$ RATIO IN LEAD SLAGS 348

5.1 INTRODUCTION 348

5.2 OPTIMIZATION OF SLAG SUB-SYSTEMS 351

5.3 COMPARISON OF MODEL PREDICTIONS WITH DATA ON LEAD SLAGS 360

5.4 CONCLUSIONS 365

CONCLUSIONS 395

REFERENCES 401

APPENDIX - THERMODYNAMIC DATA OF PURE SUBSTANCES IN THE PRESENT DATABASE 430

LIST OF FIGURES

PAGE

Fig. 0-1 Schematic phase diagram of an R_2O_3-Al_2O_3 system and the corresponding Gibbs energy-composition diagram at a temperature T' 13

Fig. 1-1 Distribution of oxygen species (according to the Toop and Samis model [62Too]). 62

Fig. 1-2 Calculated binary free energy of mixing curves for various values of K according to the Toop and Samis model [62Too]. The open circles are from [54Ric] and the closed circles are from [55Ell, 53Dar]. . . . 63

Fig. 1-3 The variations of a_{MO} with composition in the PbO-SiO_2 system, given by the modified Toop and Samis model for hypothetical melts of $\Delta G^{\circ}/RT$ = 0, -1.88 and -3 (which is presented by the dashed line A, B and C, respectively) in comparison with the experiment of [54Ric] (solid line). 64

Fig. 1-4 Curve-fitting of equation (1-3-13) (dashed line) with the experimental a_{PbO} in PbO-SiO_2 melts at 1100°C [54Ric] (solid line). 65

Fig. 1-5 Comparison of experiment activities (solid lines) [81Gay] with the calculation using the cell model (dashed lines) [84Gay] at T=1550°C. 66

Fig. 1-6 Experimental phase diagram of the CaO-Al_2O_3-SiO_2 system in weight percent [60Osb]. 67

Fig. 1-7 Calculated phase diagram of the CaO-Al_2O_3-SiO_2 system using the cell model [85Gay]. 68

Fig. 1-8 Comparison of the CaO activity, as calculated at 1500° (solid line) from the sub-lattice model [90Hil1, 90Hil4] (with the assumption of SiO_3^{2-} anions) and from measurements at 1600° [82Zou], 1500° [62Sha] and 1500°C [57Car] (which is presented by +). 69

Fig. 1-9 Comparison of the SiO_2 activity, as calculated at 1550° (solid line) from the sub-lattice model [90Hil1, 90Hil4] (with the assumption of SiO_3^{2-} anions) and from measurements at 1600° [82Zou], 1550° [60Kay], 1550° [31Rei] (which is presented by +) and 1550°C [58Bai] (which is presented by *). 70

Fig. 1-10 Calculated phase diagram of the CaO-SiO_2

system using the sub-lattice model [90Hil1, 90Hil4] (with the assumption of SiO_3^{2-} anions). Numbers in parentheses are experimental values and without parentheses are calculated values. 71

Fig. 1-11 Enthalpy and entropy of mixing of a binary system for different degrees of ordering with maximum ordering at the equimolar composition. Curves are calculated from the extended quasi-chemical theory at T= 1000°C with z=2 for the constant values of ω (KJ) shown with $n=0$. 72

Fig. 2-1 Optimized MgO-MnO Phase Diagram. 188

Fig. 2-2 Optimized activities of MgO in solid MgO-MnO solutions. 189

Fig. 2-3 Optimized MnO-SiO_2 Phase Diagram 190

Fig. 2-4 Optimized Activities of MnO in Liquid MnO-SiO_2 Solutions 191

Fig. 2-5 Optimized MgO-SiO_2 Phase Diagram 192

Fig. 2-6 Calculated activities of SiO_2 in liquid MgO-SiO_2 solutions at 1600° and 1700°C 193

Fig. 2-7 Optimized CaO-SiO_2 Phase Diagram 194

Fig. 2-8 Calculated SiO_2 activities in liquid CaO-SiO_2 solutions at 1550°C (upper curve) and 1600°C (lower curve) 195

Fig. 2-9 Calculated CaO activities in liquid CaO-SiO_2 solutions at 1500°C 196
Fig. 2-10 Optimized FeO-SiO_2 Phase Diagram for equilibrium with metallic Fe (total iron expressed as "FeO") 197
Fig. 2-11 Calculated activity of FeO in liquid FeO-SiO_2 solutions at 1325°C and 1880°C . . . 198
Fig. 2-12 Calculated enthalpy of mixing of liquid FeO and solid SiO_2 at 1420°C compared to data of Ban-ya et al [82Ban1]. 199
Fig. 2-13 Assessed Na_2O-SiO_2 Phase Diagram Compositions in terms of components $NaO_{0.5}$-SiO_2 200
Fig. 2-14 Calculated $NaO_{0.5}$ Activities in Liquid Na_2O-SiO_2 Solutions 201
Fig. 2-15 Optimized K_2O-SiO_2 Phase Diagram Compositions in terms of components $KO_{0.5}$-SiO_2 202
Fig. 2-16 Activity of $KO_{0.5}$ in liquid $KO_{0.5}$-SiO_2 solutions calculated at 1100°C, 1300°, 1400° and 1500°C. 203
Fig. 2-17 Optimized SiO_2-TiO_2 Phase Diagram 204
Fig. 2-18 Optimized ZrO_2-SiO_2 phase diagram showing data of [56Tor, 67But, 53Cur]. 205
Fig. 2-19 Optimized Al_2O_3-TiO_2 Phase Diagram Compositions are in Terms of the

Components $AlO_{1.5}$-TiO_2 206
Fig. 2-20 Assessed Na_2O-Al_2O_3 Phase Diagram 207
Fig. 2-21 Assessed K_2O-Al_2O_3 Phase Diagram 208
Fig. 2-22 Optimized $AlO_{1.5}$-ZrO_2 phase diagram with selected experimental points [70Alp, 61McN]. Values in parentheses are experimental from [81Fis, 64Alp]. 209
Fig. 2-23 Optimized CaO-TiO_2 Phase Diagram 210
Fig. 2-24 Optimized MnO-TiO_2 Phase Diagram 211
Fig. 2-25 Optimized activities of MnO in liquid MnO-TiO_2 solutions at 1500°C 212
Fig. 2-26 Optimized MgO-TiO_2 Phase Diagram 213
Fig. 2-27 Assessed Na_2O-TiO_2 Phase Diagram Compositions in terms of components $NaO_{0.5}$-TiO_2 214
Fig. 2-28 Assessed K_2O-TiO_2 Phase Diagram Compositions in terms of components $KO_{0.5}$-TiO_2 215
Fig. 2-29 Optimized TiO_2-ZrO_2 phase diagram with selected experimental points [54Bro, 54Cou, 65Coc, 80She, 86Ban, 86McH]. Values in parentheses are experimental (from [80She] except for 1200° peritectoid from [86McH]). 216
Fig. 2-30 Optimized CaO-MnO Phase Diagram 217
Fig. 2-31 Optimized activities of CaO in CaO-MnO

solid solutions 218
Fig. 2-32 Optimized CaO-FeO Phase Diagram for Equilibrium with Fe. 219
Fig. 2-33 Optimized FeO activities at 1100°C for CaO-FeO solid solutions in equilibrium with Fe. 220
Fig. 2-34 Optimized CaO-ZrO_2 phase diagram with selected experimental points [89Bar, 77Stu, 67Nog]. Values in parentheses are experimental from [67Nog, 77Stu, 89Bar]. 221
Fig. 2-35 Experimental ZrO_2-CaO phase diagram reported by [77Stu]. 222
Fig. 2-36 Optimized FeO-MnO Phase Diagram for Equilibrium with Fe. 223
Fig. 2-37 Optimized activities of FeO in FeO-MnO solid solutions in equilibrium with Fe at 1150°C 224
Fig. 2-38 Assessed MgO-CaO Phase Diagram. 225
Fig. 2-39 Optimized FeO-MgO phase diagram for equilibrium with Fe 226
Fig. 2-40 Optimized FeO activities in FeO-MgO solid solutions at 1127°C in equilibrium with Fe 227
Fig. 2-41 Optimized FeO-ZrO_2 phase diagram with experimental points from [57Fis]. Values

in parentheses are experimental from [57Fis]. 228

Fig. 3-1 Melting points of the rare earth metals (1) 265

Fig. 3-2 Schematic phase diagram of an R_2O_3-Al_2O_3 system and the corresponding Gibbs energy-composition diagram at a temperature T' 266

Fig. 3-3 Assessed La_2O_3-Al_2O_3 phase diagram calculated thermodynamically 267

Fig. 3-4 Assessed Ce_2O_3-Al_2O_3 phase diagram calculated thermodynamically 268

Fig. 3-5 Assessed Pr_2O_3-Al_2O_3 phase diagram calculated thermodynamically 269

Fig. 3-6 Assessed Nd_2O_3-Al_2O_3 phase diagram calculated thermodynamically 270

Fig. 3-7 Assessed Pm_2O_3-Al_2O_3 phase diagram calculated thermodynamically 271

Fig. 3-8 Assessed Sm_2O_3-Al_2O_3 phase diagram calculated thermodynamically 272

Fig. 3-9 Assessed Eu_2O_3-Al_2O_3 phase diagram calculated thermodynamically 273

Fig. 3-10 Assessed Gd_2O_3-Al_2O_3 phase diagram calculated thermodynamically 274

Fig. 3-11 Assessed Tb_2O_3-Al_2O_3 phase diagram calculated thermodynamically 275

Fig. 3-12 Assessed Dy_2O_3-Al_2O_3 phase diagram calculated thermodynamically 276
Fig. 3-13 Assessed Ho_2O_3-Al_2O_3 phase diagram calculated thermodynamically 277
Fig. 3-14 Assessed Er_2O_3-Al_2O_3 phase diagram calculated thermodynamically 278
Fig. 3-15 Assessed Tm_2O_3-Al_2O_3 phase diagram calculated thermodynamically 279
Fig. 3-16 Assessed Yb_2O_3-Al_2O_3 phase diagram calculated thermodynamically 280
Fig. 3-17 Assessed Lu_2O_3-Al_2O_3 phase diagram calculated thermodynamically 281
Fig. 3-18 Calculated R_2O_3-Al_2O_3 phase diagrams at lower temperatures. Tentative only. 282
Fig. 3-19 Assessed congruent melting points of oxides (congruent melting may be metastable). 283
Fig. 4-1 The geometrical relationships involved in the symmetric (Kohler-like) and asymmetric (Toop-like) equations. 327
Fig. 4-2 A ternary miscibility gap. 328
Fig. 4-3 Reported [69Rou] CaO-MgO-TiO_2 phase diagram (wt. %). 329
Fig. 4-4 Calculated CaO-MgO-TiO_2 phase diagram (wt. %). 330
Fig. 4-5 Reported [55Dev] CaO-SiO_2-TiO_2 phase

diagram (wt. %). 331
Fig. 4-6 Calculated $CaO-SiO_2-TiO_2$ phase diagram (wt. %). 332
Fig. 4-7 Calculated $MgO-SiO_2-TiO_2$ phase diagram (wt. %). 333
Fig. 4-8 Calculated $MnO-SiO_2-TiO_2$ phase diagram (wt. %). 334
Fig. 4-9 Reported [76Pen, 57McT] $SiO_2-TiO_2-ZrO_2$ phase diagram (wt. %). 335
Fig. 4-10 Calculated $SiO_2-TiO_2-ZrO_2$ phase diagram (weight %, T in °C). 336
Fig. 4-11 $TiO_2-ZrO_2-Al_2O_3$ phase diagram as estimated by [55Ber]. 337
Fig. 4-12 $SiO_2-ZrO_2-Al_2O_3$ phase diagram reported by [56Bud]. 338
Fig. 4-13 $TiO_2-SiO_2-Al_2O_3$ phase diagram reported by [52Aga, 58Gal]. 339
Fig. 5-1 PbO(liq) activities in $PbO-SiO_2$ slags at 1000°C as reported by several authors. Diagram taken from [82Tas]. Line is calculated from model. 367
Fig. 5-2 SiO_2-ZnO phase diagram [30Bun] 368
Fig. 5-3 PbO-CaO phase diagram [74Kux] 369
Fig. 5-4 PbO-ZnO phase diagram [63Bau] 370
Fig. 5-5 $PbO-Fe_2O_3$ phase diagram [86Nev] 371
Fig. 5-6 $PbO-Fe_2O_3$ phase diagram [62Mou] 372

Fig. 5-7 $CaO-Fe_2O_3$ phase diagram in air [76Sch]. . . . 373

Fig. 5-8 $FeO-Fe_2O_3$ phase diagram showing oxygen isobars from work of [45Dar, 60Phi, 58Mua]. Calculated isobars in the liquid are shown as solid lines. 374

Fig. 5-9 $FeO-Fe_2O_3-SiO_2$ phase diagram [60Osb] showing oxygen isobars in the liquid region. 375

Fig. 5-10 $CaO-FeO-Fe_2O_3$ phase diagram at 1200° and 1300°C [80Tak] showing oxygen isobars. (In the article of [80Tak], the labels for 1200° and 1300°C were inverted). 376

Fig. 5-11 $SiO_2-CaO-FeO-Fe_2O_3$ system at 1450°C showing oxygen isobars in the liquid region [70Tim] . 377

Fig. 5-12 Experimental [84Tas] and calculated PbO(liq) activity coefficients in $PbO-FeO-CaO-SiO_2-Fe_2O_3$ slags in equilibrium with liquid Pb. 378

Fig. 5-13 Experimental [84Tas] and calculated PbO(liq) activity coefficients in $PbO-FeO-CaO-SiO_2-Fe_2O_3$ slags in equilibrium with liquid Pb. 379

Fig. 5-14 Experimental [84Tas] and calculated PbO(liq) activity coefficients in $PbO-FeO-CaO-SiO_2-Fe_2O_3$ slags in equilibrium with liquid Pb. 380

Fig. 5-15 Experimental [84Tas] and calculated $Fe^{3+}/(Fe^{2+}+Fe^{3+})$ ratios in $PbO-FeO-CaO-SiO_2-Fe_2O_3$ slags in equilibrium with liquid Pb. 381

Fig. 5-16 Experimental [84Tas] and calculated

$Fe^{3+}/(Fe^{2+}+Fe^{3+})$ ratios in PbO-FeO-CaO-SiO_2-Fe_2O_3 slags in equilibrium with liquid Pb. 382

Fig. 5-17 Pb content versus oxygen pressure for lead blast furnace type slags "normalized" to 1150°C and a CaO/SiO_2 weight ratio of 0.6 as reported by [85Fon] and as calculated by assuming a typical slag composition. 383

Fig. 5-18 Reported PbO activity coefficient data [66Mey, 80Gra, 89Wri] at low PbO content. 384

Fig. 5-19 Fe^{3+}/Fe^{2+} ratio versus Pb content of quenched blast furnace slags as reported by [79Ril]. Line shown is calculated dissolved Pb content calculated at 1225°C for the average slag composition given by [79Ril]. The experimental lead contents comprise from 50 to 100% entrained bullion. 385

LIST OF TABLES

PAGE

Table 1-1 Comparison of Experimental [84Bjo] and Calculated a_{FeO} in the solid phase 73

Table 2-1 List of optimized binary systems 229

Table 3-1 Optimized parameters of quasichemical model for liquid oxides 284

Table 3-2 Calculated thermodynamic properties of compounds 285

Table 4-1 Comparison of calculated and reported invariant points in the TiO_2-CaO-MgO system 340

Table 4-2 Comparison of calculated and reported invariant points in the TiO_2-CaO-SiO_2 system 341

Table 4-3 Invariant Points in the MgO-TiO_2-SiO_2 System 342

Table 4-4 Calculated invariant points in the MnO-SiO_2-TiO_2 system 343

Table 4-5 Comparison of calculated and reported [52Aga] invariant points in the TiO_2-SiO_2-Al_2O_3 system (Fig. 4-13) 344

Table 4-6 Comparison of Calculated and Experimental [77Pen1, 77Pen2, 79Pen, 84Pen] Invariant Points in the Al_2O_3-SiO_2-TiO_2-ZrO_2 System . . 345

Table 4-7 List of optimized ternary systems containing SiO_2. 346

Table 4-8 List of optimized non-silicate ternary systems 347

TABLE 5-1 Typical compositions of lead blast furnace slags and bullion wt.% [91CAN] 386

TABLE 5-2 Optimized binary parameters ω_{AB}^{j0} and ternary parameters $\omega_{AB(C)}^{jk}$ of the quasichemical model for molten PbO-ZnO-SiO_2-FeO-Fe_2O_3-CaO slags in cal/equivalent. 387

TABLE 5-3 Comparison of measured [83Rey] and calculated activities of ZnO (relative to the solid standard state) in molten ZnO-SiO_2 slags at 1560°C 389

TABLE 5-4 Comparison of calculated and reported [60Osb] oxygen isobars at the eight points shown on Fig. 5-17 for the FeO-Fe_2O_3-SiO_2 system . . . 390

TABLE 5-5 Comparison of measured [84Toi] and calculated activities of PbO(liq) in PbO-SiO_2-ZnO slags at 1000°C 391

TABLE 5-6 Comparison of measured [82Tas] and calculated activities of PbO(liq) in PbO-SiO_2-CaO slags at 1000°C 392

TABLE 5-7 Comparison of experimental [78Fil] and calculated activities of FeO (liq. standard state) and ZnO (solid standard state) in FeO-CaO-ZnO-SiO_2 slags at 1250°C. 393

TABLE 5-8 Comparison of calculated activity coefficients of PbO(liq) in slags with those reported by Willis [80Wil, 66Mey]. 394

INTRODUCTION

Slags containing Al_2O_3, CaO, FeO, Fe_2O_3, K_2O, MgO, MnO, Na_2O, NiO, rare earth oxides, SiO_2, TiO_2, Ti_2O_3, PbO, ZnO and ZrO_2 are essential components in the fields of metallurgy, geology and ceramics. Their properties, together with those of other phases (such as of gas or of alloy), determine principally the whole chemical process in the above industrial practices. Therefore, in order to improve or create new techniques either for use in industrial processes, or for laboratory research, a fundamental requirement is to understand the chemical equilibria relations in these systems. Experimental measurements of these multi-component and multiphase equilibria turn out to be very difficult and tedious. Therefore, new methods of phase equilibrium calculation have been developed.

A fundamental principle of phase equilibrium is that the stable phases or mixtures have a lower Gibbs energy than the metastable or unstable. Thus phase diagram data such as equilibrium compositions and temperatures become related with the thermodynamic properties of the system. This leads to a new approach (which has been advanced significantly by the international CALPHAD group) for predicting phase equilibria by thermodynamic calculations.

To qualitatively demonstrate the relations between

thermodynamic properties and phase diagrams, an R_2O_3-Al_2O_3 (R represents a rare earth metal) binary phase diagram is shown schematically in Fig. 0-1 along with a Gibbs-energy composition diagram at a constant temperature T'. A completely miscible liquid phase and three stoichiometric solids (R_2O_3, $RAlO_3$ and Al_2O_3) are shown. $G_i^{o(l)}$ and $G_i^{o(s)}$ are the standard Gibbs energies of the pure liquid and solid compounds. The Gibbs energy of fusion of R_2O_3 is shown on Fig. 0-1:

$$\Delta G^o_{fus(R_2O_3)} = \Delta H^o_{fus(R_2O_3)} - T\Delta S^o_{fus(R_2O_3)} \qquad (1)$$

Similarly for Al_2O_3:

$$\Delta G^o_{fus(Al_2O_3)} = \Delta H^o_{fus(Al_2O_3)} - T\Delta S^o_{fus(Al_2O_3)} \qquad (2)$$

The Gibbs energy of formation of $RAlO_3$ from solid R_2O_3 and Al_2O_3 and the Gibbs energy of fusion of $RAlO_3$ are also indicated on Fig. 0-1:

$$\Delta G^o_{f(RAlO_3)} = \Delta H^o_{f(RAlO_3)} - T\Delta S^o_{f(RAlO_3)} \qquad (3)$$

$$\Delta G^o_{fus(RAlO_3)} = \Delta H^o_{fus(RAlO_3)} - T\Delta S^o_{f(RAlO_3)} \qquad (4)$$

The tangent intercepts at points **a**, **b** and **c** determine the liquidus compositions at T', because in this way the stable phases or two phase mixtures have the lowest Gibbs energy.

The Gibbs energy of liquid mixing is also indicated on Fig. 0-1:

$$\Delta G_m = \Delta H_m - T\Delta S_m \qquad (5)$$

Therefore, one can construct a phase diagram as in Fig. 0-1 if the Gibbs energy curves for all the phases at all temperatures are determined.

To predict multi-component and multiphase equilibria by thermodynamic calculations, all available thermodynamic and phase equilibrium data for a system are evaluated simultaneously with a view to obtaining one set of consistent "optimized" equations for the Gibbs energies of all phases as functions of temperature and composition. The data are thus smoothed and evaluated in a thermodynamically correct manner in accordance with principles of solution behaviour. The thermodynamic data can aid in the phase diagram assessment which lead to the prediction of multi-component multiphase equilibria, and the phase diagram assessment permits the calculation of thermodynamic properties as well.

Being one of the most active CALPHAD groups, the CRCT (Centre de Recherche en Calcul Thermochimique) contributes research in the field of predicting multi-component multiphase equilibria involving salt, alloy, aqueous, gas, slag etc. phases. Several computer programs such as POTCOMP, TERNFIG and EQUILIB have been developed in the CRCT respectively to calculate binary, ternary and higher-order phase diagrams from the thermodynamic properties of the phases expressed in analytical form. F*A*C*T, a computing system which contains a number of the above thermodynamic calculation programs, has been generated and operated by the CRCT. Through an on-line computer network the F*A*C*T system is providing thermodynamic calculation service for many industrial and university research groups. A large thermodynamic database which provides the optimized Gibbs energies equations for all phases as functions of temperature and composition is being built under the F*A*C*T computing system [85Tho]. Thus, it is possible to predict multi-component multiphase equilibria by the F*A*C*T computing system.

As an example, in a lead blast furnace, the PbO content in the slag phase regulates the lead loss in the bullion. Hence it is very important to predict the PbO content in the slag to control the lead loss in industrial practice. This prediction can be carried out by EQUILIB (a Gibbs energy minimization program in the F*A*C*T system) combined with a

database. Suppose a slag which has the initial components as 50.5 gram FeO, 33.7 gram SiO_2, 15.7 gram CaO and 10.5 gram PbO is in equilibrium with liquid lead at 1300°C, the equilibrium composition of the slag can, thus, be predicted by the following EQUILIB calculation:

ENTER REACTION

50.5 FeO + 33.7 SiO_2 + 15.7 CaO + 10.5 PbO + Pb =

ENTER FINAL STATE

****

T PROD P PROD V PROD

(°C) (ATM) (L)

****

1300 1.0

LIST OF SPECIES IN THE DATABASE

1 - 14 GASES

15 - 40 LIQUIDS

41 - 111 SOLIDS

112 - 116 SOLN-SLAG LIQUID OXIDE DATABASE

ENTER THE SELECTION (enter "LIST" to list species)

(enter the species to participate in to the reaction)

/1,5,9,11,12/SOLN-SLAG/24,37

PRESS <RETURN> WHEN READY FOR OUTPUT

(gram) 50.5 FeO + 33.7 SiO_2 + 15.7 CaO + 10.5 PbO + Pb

=

0.00000E+00 mol (0.46711E-01 Pb
+ 0.14758E-06 Fe
+ 0.13615E-09 O_2
+ 0.34573E-13 Ca
+ 0.15635E-18 Si)
(1300.00 C, 1.0000 atm, gas, a=0.46711E-01)

+ 103.75 gram (44.046 wt.% FeO
+ 32.718 wt.% SiO_2
+ 15.268 wt.% CaO
+ 5.5903 wt.% Fe_2O_3
+ 2.3781 wt.% PbO)
(1300.00 C, 1.0000 atm, slag)

+ 8.4729 gram Pb
(1300.00 C, 1.0000 atm, L1, a=1.0000)

+ 0.0000E+00 gram PbO
(1300.00 C, 1.0000 atm, L1, a=0.33507E-02)

This is a multi-component multiphase (gas, slag and liquid lead) equilibrium calculation, which predicts the PbO content in the slag is 2.38 wt%, the activity of liquid PbO in the slag is 0.00335, the oxygen partial pressure is 1.36×10^{-10}

atm and the FeO/Fe_2O_3 weight ratio is 7.88. Based on these results, engineers can better control the lead loss.

To perform the above prediction there are two requirements; a Gibbs energy minimization program such as EQUILIB and a database which provides the "optimized" Gibbs energies equations for all phases (such as gas, slag and liquid lead in the above example) as functions of temperature and composition. The present study is a part of the continuing research program in the CRCT to build such a thermodynamic database for oxide systems so that multi-component multiphase equilibria involving oxides may be predicted by the F*A*C*T computing system.

The general procedures in developing a thermodynamic database in the CRCT can be stated as:

1. Optimize all available binary thermodynamic and phase equilibrium data to obtain best equations (based on certain models) for Gibbs energies as function of composition and temperature for all phases. These equations are then stored in the database.

2. Obtain ternary parameters by optimizing ternary data where available (if necessary). Store the ternary parameters in the database.

3. Use binary and ternary coefficients in database with model to predict Gibbs energies of multi-component solutions.

To build an oxide database, these three steps are to be respected too. But first of all proper thermodynamic models which provide formulas for the Gibbs energy equations for all phases have to be chosen. To this end, Chapter 1 contributes to a general review of thermodynamic models such as the polynomial, structure based silicate, cell, sub-lattice and the modified quasi-chemical models. Since the experimental enthalpy of mixing of the oxide liquid phase often indicates the presence of a strong ordering which cannot be represented efficiently by the polynomial models, while most of the structure based silicate models are valid only for silicate melts, the modified quasi-chemical model will be employed for the liquid phase to build the present slag database. Simple models such as Raoultian, regular or polynomial solution models will be applied for solid phases.

In step one (the first of the three procedures in building a database), coefficients of all the Gibbs energy equations for all phases in the binary system have to be found by least squares regression to best reproduce the reported thermodynamic and phase diagram data. However, in the quasi-chemical model, thermodynamic properties (such as ΔH and ΔG) are non-linear functions of the quasi-chemical coefficients. To obtain these coefficients non-linear least squares analysis, which normally cannot directly be solved analytically except by successive approximation, has to be

developed. This is the main topic of Chapter 2 where general linear and non-linear least squares regressions will be introduced. A binary optimization program called FITQUAS, by which all thermodynamic and phase diagram data of binary slags (including the compound liquidus surface) can be evaluated by means of the quasi-chemical model, was written by the present author based on a non-linear least squares technique.

Before optimizing any binary system using FITQUAS, thermodynamics of the components Al_2O_3, CaO, FeO, Fe_2O_3, K_2O, MgO, MnO, Na_2O, NiO, rare earth oxides, SiO_2, TiO_2, Ti_2O_3, PbO, ZnO and ZrO_2 will be evaluated in Section 2.2. Since the thermodynamic database for solid oxides developed by Berman and Brown [85Ber] is thermodynamically consistent, we accept their data if they are available. The compilation of Barin [90Bar] is another main source for the unary data.

In Chapter 2, details of evaluations of 26 binary oxide systems will be performed. A list of all optimized binary systems in the database will be shown.

The above optimization technique is particularly significant when evaluating a series of systems such as the R_2O_3-Al_2O_3 (R=rare earth) binary systems, because trends in the properties as one proceeds along the series can be exploited in order to refine the assessments and to predict

properties by interpolation or extrapolation. In Chapter 3, a critical assessment of the 15 R_2O_3-Al_2O_3 systems where R=rare earth will be performed and thermodynamic properties of all compounds will be predicted along with the thermodynamic properties of the liquid solutions, although for 3 of the 15 systems no phase diagrams have ever been reported. This chapter is composed mainly of a paper accepted for publication in The Journal of Alloys and Compounds [92Wu].

After binary optimization in Chapter 2 and 3, ternary parameters are to be determined (this procedure is known as step two in building a database). Since the quasi-chemical model was originally developed for binary solutions, in Chapter 4 the extrapolation of the modified quasi-chemical model to ternary and multi-component solutions [86Pel1] will be introduced. Chapter 4 also introduces a ternary optimization program which was written by Professor Pelton based on a modified gradient method. As expected, ternary thermodynamic properties in the quasi-chemical model are also non-linear functions with respect to the ternary parameters, and so a non-linear least squares method was employed to this end. The ternary optimization program was later improved by the present author in order to simultaneously evaluate the ternary immiscibility gap with all the other ternary thermodynamic and phase diagram data, and to enhance the convergence of the program so that the program can accept very

large ternary parameters (see Chapter 4 for details). Details of evaluations of 8 ternary systems are shown to test both the ternary quasi-chemical model and the ternary optimization program.

When both binary and ternary optimizations are established, the Gibbs energy equation of a multi-component liquid phase can be constructed based on the multi-component system quasi-chemical model [86Pel1] (This procedure is known as step three in building a database). To demonstrate the reliability of this approximation, phase equilibria in the ZrO_2-Al_2O_3-TiO_2-SiO_2 system will be calculated in Chapter 4 using EQUILIB based on the Gibbs energy equation of the liquid phase constructed from those of its 6 sub-binary and 4 sub-ternary systems. The predicted multi-component and multi-phase equilibria agree well with the reported values [77Pen1, 77Pen2, 79Pen and 84Pen]. Therefore, multi-component multiphase equilibria may be predicted with confidence by the present database. A list of all available ternary evaluations stored in the database is shown at the end of Chapter 4.

As a direct industrial application, in Chapter 5, the present database will be used to predict multi-component multiphase equilibria in lead smelting, especially to predict the PbO content and Fe^{+3}/Fe^{+2} ratio in the slag phase. Agreement with experiment is very good. Therefore, the

database can be used to help control the lead loss in lead blast furnace practice. In fact, this database is being used by CANMET.

Lists of all binary, ternary, quaternary and quinary systems evaluated in the present study is given at the end of the thesis. This is believed to be the most extensive molten oxide solution database presently available. It may be employed to credibly predict multi-component and multi-phase equilibria involving oxides.

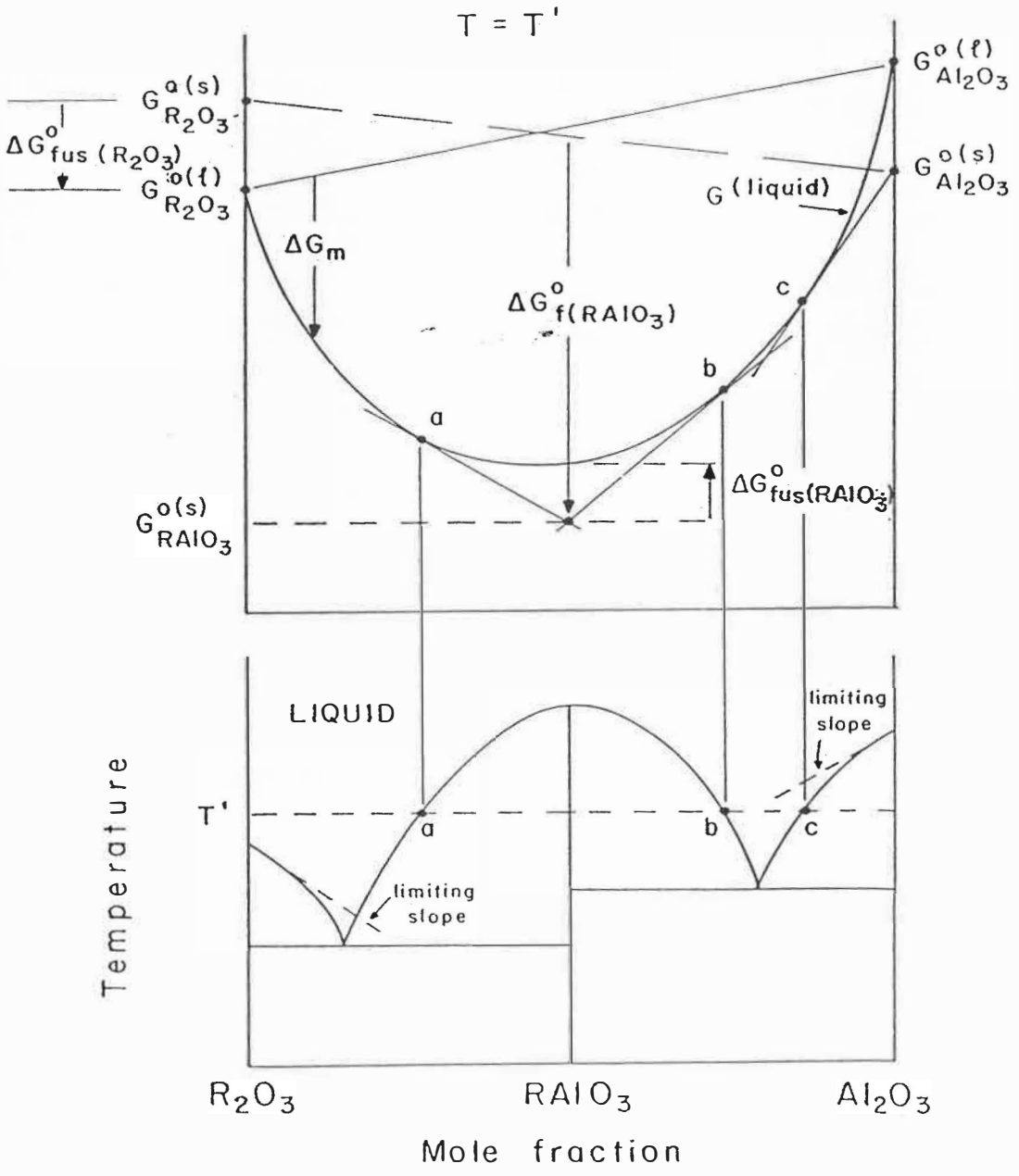


Fig. 0-1 Schematic phase diagram of an R_2O_3-Al_2O_3 system and the corresponding Gibbs energy-composition diagram at a temperature T'

CHAPTER 1

SOLUTION MODELS FOR OXIDE SYSTEMS

1.1 INTRODUCTION

A solution model relates the Gibbs energy of one phase to some measurable properties such as the equilibrium compositions and temperature of the same phase. It provides the means of constructing the Gibbs energy curves of a phase. Therefore, a review of solution models will be presented in this chapter.

A good understanding of the atomic nature of the system under consideration is usually very helpful in proposing a proper solution model. For example, when a solution exhibits strong ordering (as a result, the component activities may vary dramatically in a narrow composition range), the so-called association solution models are recommended [50Hil, 54Pri, 74Bha], in which it is assumed that in addition to the component species some association between the component species takes place during the mixing procedure. In this way, successful mathematical descriptions of the Gibbs energy curves of the solution are reported [50Hil, 54Pri, 74Bha].

In addition, some structurally-based solution models have been formulated to reduce the number of parameters in optimizations and to describe the thermodynamic properties of

ternary or higher order solutions from their binary sub-systems.

Normally, most of the structure-based silicate models are too complicated and are restricted to certain specific systems. Hence, the quasi-chemical model [86Pel1] was developed as a general solution model which can be applied to both ordering and non-ordering solutions and to calculate their thermodynamic properties from their subsystems. The present liquid oxide database is based on the so-called modified quasi-chemical model.

A general description of the polynomial, structure based silicate and quasi-chemical models is given in the following sections.

1.2 POLYNOMIAL SOLUTION MODELS

Polynomial solution models are successfully used in the thermodynamic calculation of solutions in which the interaction between species is rather weak. In this section, the regular and polynomial solution models will be discussed. Application of the polynomial solution model will also be presented.

Consider an A-B regular solution. The excess molar Gibbs energy of mixing is:

$$g^E = \phi X_A X_B \qquad (1\text{-}2\text{-}1)$$

where X_A and X_B are the mole fractions of components A and B, respectively. The parameter ϕ is called the regular solution constant, which is characteristic of the solution.

The molar Gibbs energy of mixing is:

$$\Delta G = RT(X_A ln X_A + X_B ln X_B) + \phi X_A X_B \qquad (1\text{-}2\text{-}2)$$

where R is the universal gas constant and T is the thermodynamic temperature in kelvins.

It may happen that the "regular solution constant" in equation (1-2-1) is not a constant for a real solution. Polynomial solution models shown below have been proposed to

represent the thermodynamic properties of the solution.

$$G^E = (1-X)X\Sigma A_i X^i \qquad [1895Mar](1\text{-}2\text{-}3)$$

$$G^E = (1-X)X\Sigma B_i (1-2X)^i \qquad [48Red](1\text{-}2\text{-}4)$$

$$G^E = (1-X)X\Sigma C_i (1-X)^{n-i} X^i \qquad [34Bor](1\text{-}2\text{-}5)$$

$$G^E = (1-X)X\Sigma D_i P_i (1-2X) \qquad [74Bal](1\text{-}2\text{-}6)$$

where $X=X_B$, $P_i(1-2X)$ is the ith Legendre polynomial. If the excess entropy of the solution is not zero, A_i, B_i, C_i and D_i are temperature dependent.

The above polynomial models are all equivalent and interconvertible. Williams and Brynestad [82Wil] suggested the use of a Redlich-Kister expansion. They noted that the first term of the Redlich-Kister [48Red] expression (1-2-4) represents the regular parameter of a symmetric effect, the second term represents the sub-regular parameter of an asymmetric effect. As an example, the Redlich-Kister model is employed in the thermodynamic calculation in the CaO-FeO solid solution as discussed below.

Example of the FeO-CaO system:

The activity of FeO in the FeO-CaO solid solution, in equilibrium with solid iron, was obtained by EMF measurements

[84Bjo]. The solid miscibility gap in the system was determined by heating and quenching techniques [75Abb]. In order to fit simultaneously the activity and phase diagram data, three parameters of the Redlich Kister model were obtained,

$$G^E = X_{FeO}X_{CaO}[25083.2 - 6191.1(1-2X_{CaO}) + 3880.6(1-2X_{CaO})^2] \quad J/mol \qquad (1\text{-}2\text{-}7)$$

where X_{FeO} and X_{CaO} are mole fractions of FeO and CaO in the solution.

Details of the optimization procedure are shown in Chapter 2. The calculated activities (with respect to solid FeO) and the phase diagram are shown in Table 1-1 and Fig. 2-32. Agreements are very good.

This example shows that polynomial solution models are very simple and easy to employ.

However, if the interactions between the species in the solution are so strong that the solution exhibits ordering effects (which can cause a rapid change of activity data in a narrow composition range), the polynomial solution models are then no longer preferable. For example, Berman and Brown [86Ber] used six Margules parameters in optimizing the liquid SiO_2-CaO solution. The calculated phase boundaries are up to

40K from the experimental values, which is beyond experimental uncertainties. This is not surprising because at the composition corresponding to Ca_2SiO_4 the liquid phase exhibits very strong ordering which is not accounted for by the polynomial models. Moreover, with the 6 Margules parameters one cannot interpolate or extrapolate into higher order systems.

In this section, polynomial solution models have been developed based on the regular solution theory. Normally polynomial models are employed as a first approximation when there are few experimental data, and are used when the interaction between species is not too strong.

1.3 STRUCTURE BASED SILICATE MODELS

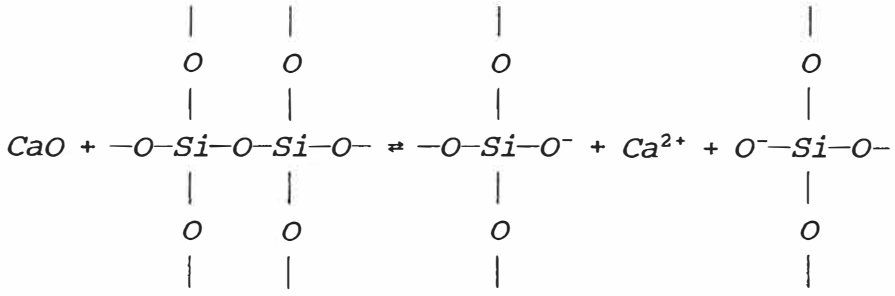
1.3.1 Introduction

The structure of molten SiO_2 is a three-dimensional network of SiO_4^{4-} tetrahedra [84Phi] where the average Si-O distance and Si-O-Si angle (inter-tetrahedral angle) are 1.60Å and 144° [80Gas], respectively.

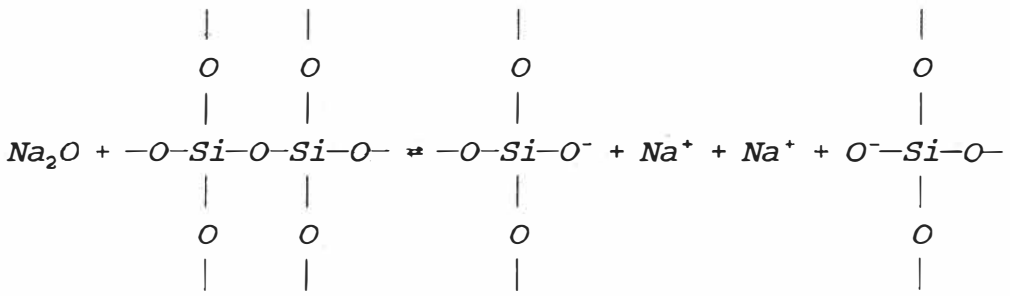
When, in a basic oxide-silicate system the basic oxide is added to the network of silica, it will form two simple ions. In the case of CaO:

$$CaO \rightleftharpoons Ca^{2+} + O^{2-}$$

it will introduce O^{2-} into the three-dimensional Si-O network, breaking it according to the following scheme:



with an alkaline base:



When breaking of the network continues, some sheet-like, as well as chain-like or ring clusters (which have the approximate stoichiometry of $Si_2O_5^{2-}$ or SiO_3^{2-}) may form in the melt. As the process continues, the above clusters may reduce their sizes to dimers $Si_2O_7^{6-}$ and monomers SiO_4^{4-}.

This assumption is supported by some Raman spectroscopy studies [82Mys]. The reported properties of metal oxide-silica melts [68Bab, 69Rob] show systematic relationships with bulk composition such as rapid changes over a narrow composition range in the functions describing the properties. They may suggest the structure of the melt also shows rapid changes over the same composition ranges. Hence different clusters (of the stoichiometries of SiO_2, $Si_2O_5^{2-}$, SiO_3^{2-}, $Si_2O_7^{6-}$ or SiO_4^{4-}) may become dominant in certain composition ranges.

When the melt composition reaches approximately that of an ortho-silicate melt, units of SiO_4^{4-} will dominate the melt structure. Furthermore, when more metal oxide is to be added to the ortho-silicate melt, a new unit O^{2-} will be introduced

into the anion structure of the melt. Therefore, the anionic species of the melt are principally O^{2-} and SiO_4^{4-} units in this range.

Based on the above schemes, there are numerous thermodynamic models of a binary silicate liquid. In this section, the models of Toop and Samis [62Too], of Whiteway et al. [70Whi], of Lin and Pelton [86Lin], of Hillert et al. [90Hil1], of Kapoor and Frohberg [71Kap] and of Gaye [84Gay] are introduced.

1.3.2 Toop and Samis [62Too]

Since the formation of a silicate melt is viewed as a chemical interaction between metal oxide (e.g., MO) and silica, Toop and Samis [62Too] regarded the result of the process as a homogeneous equilibrium of the form

$$Si\text{-}O\text{-}Si + M\text{-}O\text{-}M \rightleftharpoons 2Si\text{-}O\text{-}M, \qquad (1\text{-}3\text{-}1)$$

where the oxygen in Si-O-Si is bridging (O°), in Si-O-M it is non-bridging (O^{-}) and in M-O-M it is considered a free oxygen (O^{2-}). Thus, they wrote the equilibrium (1-3-1) in shorthand;

$$O^{\circ} + O^{2-} = 2O^{-} \qquad (1\text{-}3\text{-}2)$$

The equilibrium constant, K, for reaction (1-3-2) is expressed

as:

$$K = \frac{n_-^2}{n_o n_{2-}} \qquad (1\text{-}3\text{-}3)$$

where n_o, n_- and n_{2-} are respectively, the numbers of moles of O^o, O^- and O^{2-} present per mole of binary silicate $MO\text{-}SiO_2$. Here K is characteristic of the cationic species and is assumed independent of the composition of the melt [62Too].

When X moles of SiO_2 and (1-X) moles of basic oxide, MO, react to form one mole of binary silicate melt, charge and mass balance considerations, respectively, require that:

$$2X = n_o + \frac{n_-}{2} \qquad (1\text{-}3\text{-}4)$$

$$1 - X = n_{2-} + \frac{n_-}{2} \qquad (1\text{-}3\text{-}5)$$

Combining equation (1-3-3), (1-3-4) and (1-3-5) they obtained;

$$(4K^{-1}-1)n_-^2 + (2X+2)n_- + 8X(X-1) = 0 \qquad (1\text{-}3\text{-}6)$$

which shows that n_- is a function of K and composition. To demonstrate such a function, we discuss a simple case as below.

If K=∞, equation (1-3-6) reduces to;

$$n_-^2 - (2X+2)n_- + 8X(1-X) = 0 \qquad (1\text{-}3\text{-}7)$$

and this is shown as Fig. 1-1. According to equations (1-3-4), (1-3-5) and (1-3-7), free and non-bridging oxygens coexist (mixtures of O^{2-}, M^{2+} and SiO_4^{4-}) in the composition range from 0 mol% SiO_2 to 33.3 mol%, non-bridging and bridging oxygens coexist at higher SiO_2 content, and only non-bridging oxygens (neither bridging nor free oxygens) exist at 33.3 mol% SiO_2, where n_- reaches its maximum value, 1.33. Because the composition of 33.3 mol% SiO_2 corresponds to that of ortho-silicate stoichiometry, ortho-silicate melts consist only of SiO_4^{4-} tetrahedra in association with metal cations. Furthermore, as expected, this composition also closely matches that of the reported minimum Gibbs energy of mixing [50Dar] (Fig. 1-2). The thermodynamic stability of the melt is thus directly explained by its structure. The liquid solution in the MO-SiO_2 system exhibits minimum entropy of mixing (ie. maximum ordering) near this composition.

To derive the free energy of formation of a binary silicate melt, Toop and Samis suggested that the free energy could be calculated as the product of n_- and the free energy change per mole of O^- formed by reaction (1-3-2). The free energy of mixing was calculated as

$$\Delta G^{mix} = -\frac{n_-}{2} RT \ln K \qquad (1\text{-}3\text{-}8)$$

where R is the gas constant and T is temperature in Kelvin.

Toop and Samis noted that the curves generated by equation (1-3-8) are remarkably similar to those of the free energy of mixing of binary silicates (see Fig. 1-2) and, by curve-fitting equation (1-3-8) to experimental data, they proposed values of K for several systems.

After an examination of structure and equilibria in silicate melts, Toop and Samis [62Too] found that polymerization in basic and acid slags may be expressed in terms of an equilibrium constant involving bridging oxygens, non-bridging oxygens and free oxygens in the melt. For appropriate values of the equilibrium constant, they found that integral molar free energy of mixing curves may be calculated that are close to, or equal to those of various binary silicate melts (see Fig. 1-2). This indicated that the integral free energy of mixing of a binary silicate melt may arise solely from the interaction of anions (oxygen ions and silica). On the other hand the cations in the melts are considered to affect the equilibrium constant of reaction (1-3-2). This is the crux of their model.

As noted by Gaskell [81Gas], equation (1-3-3) indicates random mixing of the three type of oxygens on (1 + X) equivalent oxygen "sites" since activities of the species were replaced by molar fractions. Thus the theoretical free energy of mixing must contain a contribution due to the random mixing of the O^{o}, O^{-} and O^{2-} in addition to the free energy change due to chemical reaction (1-3-2). Therefore, equation (1-3-8) is wrong. Gaskell [81Gas] modified the model of Toop and Samis by considering this random contribution, but he still could not represent the experimental activity of PbO in the $PbO-SiO_2$ melts (see Fig. 1-3). New models were expected to solve the above problems. To this end we will introduce the model of Whiteway et al. [70Whi].

1.3.3 Whiteway, Smith and Masson [70Whi]

A major advance in the theoretical treatment of basic binary silicate melts was made by Masson [65Mas], who considered that these melts contain M^{2+} cations, O^{2-} anions and an array of linear chain silicate anions of the general formula $Si_x O_{3x+1}^{2(x+1)-}$. Linear chain silicate anions are formed by polymerization of pseudo-bifunctional SiO_4^{4-} monomers, i.e. SiO_4^{4-} ions of which only two of the four O^{-} oxygens may react in accordance with equation (1-3-2). In this approach the equilibrium size distribution of the linear chain silicate anions is determined by assuming that the equilibrium constant, $K_{1,x}$, for the reaction

$$SiO_4^{4-} + Si_xO_{3x+1}^{2(x+1)-} = Si_{x+1}O_{3x+3}^{2(x+2)-} + O^{2-} \qquad (1\text{-}3\text{-}9)$$

is independent of x. This assumption is similar to that of Toop and Samis [62Too], namely, that the free energy change for the reaction given by equation (1-3-2) is independent of the composition and degree of polymerization of the melt. Since polymerization and depolymerization of linear chain silicate anions can occur at only two sites, namely the ends of the chain, $K_{1,x}$ may be reasonably assumed to be independent of the chain length.

Whiteway et al. [70Whi] extended the linear chain polymerization model to include consideration of branching chains, which are formed by polymerization of four-functional SiO_4^{4-} monomers, i.e. SiO_4^{4-} ions of which all four O^- oxygens may react in accordance with equation (1-3-2). In this case the number of sites available for growth and degradation by reaction (1-3-2) varies with x. Hence $K_{1,x}$ depends on the chain length.

The fraction of x-mer anions (or the chain length distribution), N_x, was derived by Whiteway et al. [70Whi] through a probability calculation

$$N_x = \frac{3x!}{(2x+1)!x!}\left(\frac{2\sigma}{3}\right)^{x-1}\left(1-\frac{2\sigma}{3}\right)^{2x+1}(1-N_{2^-}) \qquad (1\text{-}3\text{-}10)$$

where N_{2^-} is the fraction of free oxygens in the system at

equilibrium and σ is the fraction of initial O^- oxygens which have reacted to form O°. Therefore, N_x is a function of σ and composition.

By assuming Temkin mixing of the anions, the equilibrium constant, K_{11}, for the reaction (1-3-9) at x=1 is

$$K_{11} = \frac{N_2 N_{2-}}{N_1^2} = \frac{6\sigma(1-3N_o+2\sigma N_o)}{N_o(3-2\sigma)(1-2\sigma)} \qquad (1\text{-}3\text{-}11)$$

where N_o is the number of Si atoms in the system. K_{11} is a function of σ and composition.

From mass balance considerations and the Temkin equation

$$a_{MO} = N_{2-} \qquad (1\text{-}3\text{-}12)$$

as well as equation (1-3-11), they obtained;

$$\frac{1}{N_o} = \frac{1-\dfrac{1}{\dfrac{1}{3}+\dfrac{a_{MO}}{K_{11}(1-a_{MO})}}}{1-a_{MO}} + 2 \qquad (1\text{-}3\text{-}13)$$

from which they calculated the activity of PbO in the $PbO-SiO_2$ system at 1000°C with K_{11} = 0.196. Their calculation agrees well with the experimental results as shown in Fig. 1-4.

At high SiO_2 content, polymers are expected to exist in the binary silicate melts, so it is not surprising that the activity calculation, using the model of Whiteway et al.,

agrees better with the experiment (Fig. 1-4) than it does when the modified model of Toop and Samis is used (Fig. 1-3) in which all polymers and monomers are equally considered through equation (1-3-2). The former model is therefore more powerful than the latter one.

As in conventional polymer theory, the following assumptions were made in deriving the present model:

(a) the ring and network polymers may be neglected.

(b) all functional groups of the same kind are chemically equivalent. This means that at every stage of the polymerization process an equal opportunity for reaction is available to each functional group of a given chemical type, irrespective of the size of the molecule to which it is attached.

In a real melt, at high SiO_2 contents, ring and network polymers may no longer be ignored. And at low SiO_2 contents, the chain of the silicate anion may be so short as to allow the specific effect of one end O^- on the reactivity of the other to be appreciable. The model is valid therefore only in a limited composition range. Furthermore, a specific structure (branching chain) is proposed in the present model, that makes the model very complicated and physically unclear. To solve those problems, Lin and Pelton [86Lin] proposed a thermodynamic model which did not restrict the configuration

of chain silicate anions.

1.3.4 Lin and Pelton [86Lin]

Like Toop and Samis [62Too], the formation of a silicate melt is considered as reaction (1-3-2) by Lin and Pelton, who suggested that one mole of melt can be constructed in two steps, namely,

(a) N Si and n_{2-} O^{2-} atoms are randomly located among N + n_{2-} "sites", while each Si atom is associated with 4 oxygen atoms and the number of neighbouring Si-Si pairs, N_{Si-Si}, is

$$N_{Si-Si} = \frac{4N}{2}\frac{N}{N+n_{2-}} \qquad (1\text{-}3\text{-}14)$$

(b) n_o O^o atoms are distributed randomly between N_{Si-Si} neighbouring Si-Si pairs.

Let Ω_1, Ω_2 and Ω be the ways of mixing for step (a), (b) and (a) + (b), respectively. According to probability theory

$$\Omega_1 = C^{N}_{N+n_{2-}} = \frac{(N+n_{2-})!}{N!\,n_{2-}!} \qquad (1\text{-}3\text{-}15)$$

$$\Omega_2 = C^{n_o}_{N_{Si-Si}} = \frac{(N_{Si-Si})!}{(N_{Si-Si}-n_o)!\,n_o!} \qquad (1\text{-}3\text{-}16)$$

Since step (a) and (b) are independent,
The configurational entropy of mixing is given by

$$\Omega = \Omega_1 \Omega_2 \qquad (1\text{-}3\text{-}17)$$

$$\Delta S^M = k \ln \Omega = k \ln (\Omega_1 \Omega_2) \qquad (1\text{-}3\text{-}18)$$

where k is Boltzmann's constant. From the mass and charge balance, ΔS^M can be written as a function of N and n_- in a manner similar to equation (1-3-4) and (1-3-5).

The enthalpy of mixing can be calculated as

$$\Delta H^M = \frac{n_-}{2 N_A} \Delta e \qquad (1\text{-}3\text{-}19)$$

where N_A is Avogadro's number and Δe is the molar energy change for equation (1-3-2). This was adopted as

$$\Delta e = A(1 - \frac{N}{N_A}) + B\frac{N}{N_A} + C\frac{N(1-N)}{N_A^2} \qquad (1\text{-}3\text{-}20)$$

From equation (1-3-18) and (1-3-19), the free energy of mixing

$$\Delta G^M = \Delta H^M - T\Delta S^M \qquad (1\text{-}3\text{-}21)$$

is a function of N, n_-, A, B and C.

Now n_- can be calculated as a function of composition from the condition

$$\left[\frac{\partial \Delta G^m}{\partial n_-}\right]_N = 0 \qquad (1\text{-}3\text{-}22)$$

The values of A, B and C can be determined from curve-fitting the experimental thermodynamic properties of the melts.

Instead of equation (1-3-20), Romero and Pelton [92Rom] considered Δe as a polynomial function of composition. Δe values can be determined from curve-fitting the experimental thermodynamic properties of the liquid solutions. In this way they successfully calculated several binary phase diagrams such as for the $MgO\text{-}SiO_2$, $CaO\text{-}SiO_2$ and $Na_2O\text{-}SiO_2$ systems.

Lin and Pelton also derived the chain length distributions of polymers in their theoretical melts. Since the average number of oxygen bridges per silicon, $\bar{n}$, is $2n_o/N$, the probability p that an oxygen, bonded to a silicon, is a bridging oxygen is

$$p = \frac{n_o}{2N}$$

Let ω_n (n = 0 to 4) be the probability that a given Si is bridged to exactly n other silicons. ω_n can be written as

$$\omega_n = \frac{4!}{(4-n)!\,n!} p^n (1-p)^{4-n} \qquad (1\text{-}3\text{-}23)$$

Let P_n (n=0 to 4) be the probability that, given a bridge, a given end of this bridge will be joined to a silicon which has exactly n bridges. It can be seen that

$$P_n = \frac{n\omega_n}{\omega_1 + 2\omega_2 + 3\omega_3 + 4\omega_4} = \frac{n\omega_n}{n^-} \qquad (1\text{-}3\text{-}24)$$

Thus N_1, the number of monomers per mole of solution is

$$N_1 = N\omega_o$$

The number of dimers, N_2, is the number of bridges, n_o times the probability that each end of a bridge is bonded to a silicon which possesses only one bridging oxygen:

$$N_2 = n_o P_1 P_1$$

Similarly

$$\begin{aligned} N_3 &= n_o P_1 P_2 P_1 \\ N_4(linear) &= n_o P_1 P_2 P_2 P_1 \\ N_4(branched) &= \frac{1}{3}(n_o P_1 P_3 P_1 P_1 + n_o P_3 P_1 P_1 P_1) \end{aligned}$$

Following Whiteway et al., Lin and Pelton derived the chain-length distribution of the melts.

Unlike the model of Whiteway et al., the Lin and Pelton model applies over the entire composition range from pure MO to SiO_2. The calculated chain length distributions [79Lin]

from the curve-fitted parameters are in very good agreement with those calculated from the model of Whiteway et al. [70Whi]. Romero and Pelton [91Rom] modified the above model recently. They made Δe a polynomial function of the composition, and successfully studied several binary silicate systems [92Rom]. So far, this is the most acceptable among all the structure-based silicate models.

Besides the above models, the so-called "cell model" as well as the "sub-lattice" silicate models are very important in the field of thermodynamic calculation of silicate melts. Therefore, a brief review of these models will be given below.

1.3.5 The cell model of Kapoor and Frohberg [71Kap]

By using a concept of oxygen and cation sub-lattices, Yokokawa and Niwa [69Yok] presented a statistical approach to calculate the thermodynamic properties of silicate melts. They considered a melt containing n "molecules" of MO and m "molecules" of SiO_2 in which the 2m+n oxygens are arranged such that they tetrahedrally coordinate m+n/2 sites available for the m silicons. Thus n/2 of the sites available for the silicons are vacant. The distribution of the silicons on the available sites is considered in terms of pairs of sites. Therefore, the configurational integral of such a system, Ω, is evaluated [69Yok] to predict thermodynamic properties of the system.

In a similar way, Kapoor and Frohberg [71Kap] proposed the so called cell model for binary or ternary silicate melts, which was extended to multi-component systems later by Gaye and Welfringer [84Gay]. The cell model, which claimed that only binary parameters were needed to represent the thermodynamic properties of multi-component systems, is very important in the thermodynamic study of silicate melts, thus, details of the model as well as its applications will be discussed below.

Since the mixing of metal oxides and silicates can be regarded as the transfer of oxygen ions from one state of polarization to another (like equation: $O^{o} + O^{2-} = 2O^{-}$) and furthermore, the state of polarization of the oxygen ions is determined by their surrounding cations, the pure oxides, silica and their mixtures can thus be divided [71Kap, 84Gay] into cells in such a way that each oxygen ion is surrounded by cations. In this way, an oxide $M_i O$ or silica can be regarded as mixtures of symmetric cells of the type $M_i OM_i$ or SiOSi, respectively. A $M_i O$-SiO_2 melt can be regarded as a mixture of the above two types of symmetric cells ($M_i OM_i$ and SiOSi) and of asymmetric cells of the type $M_i OSi$. To predict the equilibrium properties of the melt by a statistical treatment, its configurational integral:

$$\Omega = \Sigma g(E_i) \exp \frac{-E_i}{NkT} \qquad (1\text{-}3\text{-}25)$$

has been evaluated by Kapoor and Frohberg [71Kap], where E_i and $g(E_i)$ are the total energy of the (i)th configuration and the number of combinations for the energy E_i, respectively, N, k, and T are Avogadro's number, Boltzmann's constant and temperature in kelvins, respectively.

Consider a mixture of n_I, n_{II}, and $2n_S$ moles of M_IO, $M_{II}O$, and SiO_2 respectively containing $2r_{I\,II}$, $2r_{IS}$, and $2r_{IIS}$ moles of cells of the types M_IOM_{II}, M_IOSi, and $M_{II}OSi$, respectively. Kapoor and Frohberg [71Kap] proposed the following equilibrium reactions for the melt:

$$M_IOM_I + M_{II}OM_{II} = 2M_IOM_{II} \qquad (1\text{-}3\text{-}26)$$

$$\Delta G_1^o = 2W_{I\,II} \qquad (1\text{-}3\text{-}27)$$

$$M_IOM_I + SiOSi = 2M_IOSi \qquad (1\text{-}3\text{-}28)$$

$$\Delta G_2^o = 2W_{IS} \qquad (1\text{-}3\text{-}29)$$

$$M_{II}OM_{II} + SiOSi = 2M_{II}OSi \qquad (1\text{-}3\text{-}30)$$

$$\Delta G_3^o = 2W_{II\,S} \qquad (1\text{-}3\text{-}31)$$

where $W_{I\,II}$, W_{IS} and W_{IIS} are the cell formation energies of the asymmetric cells M_IOM_{II}, M_IOSi and $M_{II}OSi$ from the respective symmetric cells. Further assumptions were needed in

order to evaluate the Ω expression:

1. Compared to the cell formation energies, the interaction energies among the cells of the types $M_I OM_I$, $M_I OM_{II}$, $M_{II} OM_{II}$, $M_{II} OSi$, and $M_I OSi$ are negligible.

2. Let $\epsilon_{is,ss}$ be the interaction energy between the cells of the type $M_i OSi$ and SiOSi. The interaction energies $\epsilon_{ii,ss}$ and $\epsilon_{ij,ss}$ between the cells of the type $M_i OM_i$ and SiOSi, $M_i OM_j$ and SiOSi are assumed to be:

$$\begin{aligned} \epsilon_{ii,ss} &= 2\epsilon_{is,ss} \\ \epsilon_{ij,ss} &= \epsilon_{is,ss}+\epsilon_{js,ss} \end{aligned} \qquad (1\text{-}3\text{-}32)$$

These are the so-called additive rules.

3. The cell distribution is assumed to be random mixing which is the case when $\epsilon_{is,ss}/(kT)$ is small compared to unity.

Based on assumption 3, $g(E_i)$ can be derived as:

$$g(E_i) = f(n_I, n_{II}, n_S, r_{IS}, r_{II\,S}, r_{I\,II}) \qquad (1\text{-}3\text{-}33)$$

where f is a function defined as equation (10) in [71Kap].

The total energy E_i is the sum of the cell formation and cell interaction energies, E_i^F and E_i^I.

Further

$$E_i^F = 2r_{I\,II}W_{I\,II}+2r_{IS}W_{IS}+2r_{II\,S}W_{II\,S} \qquad (1\text{-}3\text{-}34)$$

and

$$E_i^I = V(\epsilon_{IS,SS}, \epsilon_{IIS,SS}, n_I, n_{II}, n_S, r_{IS}, r_{II\,S}, r_{I\,II}) \qquad (1\text{-}3\text{-}35)$$

where V is a function defined by equations (17)-(22) in [71Kap].

Inserting equations (1-3-33 to 1-3-35) into equation (1-3-25), Kapoor and Frohberg obtain the configuration sum:

$$\Omega = P(W_{I\,II}, W_{IS}, W_{II\,S}, \epsilon_{IS,SS}, \epsilon_{IIS,SS}, n_I, n_{II}, n_S, r_{IS}, r_{II\,S}, r_{I\,II}) \qquad (1\text{-}3\text{-}36)$$

where P is a function defined as equation (23) in [71Kap].

Values of r_{ij} (i,j=I,II or SS) can be determined by the equation

$$\left(\frac{\partial \ln\Omega}{\partial r_{ij}}\right) = 0 \qquad (1\text{-}3\text{-}37)$$

Therefore, thermodynamic properties of the melt such as the Gibbs energy of mixing (ΔG_m) and activities (a_{M_iO} and a_{SiO_2}) can be derived:

$$\frac{\Delta G_m}{RT} = -\frac{\ln\Omega}{n_I + n_{II} + 2n_s} \qquad (1\text{-}3\text{-}38)$$

$$\ln a_{M_iO} = -\left(\frac{\partial \ln\Omega}{\partial n_i}\right) \qquad (1\text{-}3\text{-}39)$$

$$\ln a_{SiO_2} = -\left(\frac{\partial \ln \Omega}{\partial n_s}\right) \qquad (1\text{-}3\text{-}40)$$

So by binary parameters only (W_{ij} and ϵ_{ij}), the Gibbs energy of mixing and component activities of the $M_I O$-$M_{II} O$-SiO_2 ternary system can be calculated. Kapoor and Frohberg [71Kap] calculated activities of FeO in the CaO-FeO-SiO_2 system by this model. Agreement of the results of their calculation with experiment [88Gay] is very good.

In addition to ternary systems, the cell model was later extended to multi-component systems by Gaye and Welfringer [84Gay]. They also assumed that both cell formation and cell interaction energies were linear functions of composition in order to get better reproduction of experimental thermodynamic properties. Applications of the cell model to the CaO-Al_2O_3-SiO_2 system [84Gay, 88Gay] are shown as Fig. 1-5 to Fig. 1-7. The activities rather than the phase diagram were better reproduced.

By considering an anion sub-lattice without vacancies filled with oxygen ions and a cation sub-lattice, a melt is regarded as a mixture of symmetric and asymmetric cells. After several assumptions, a statistical study led to an expression for the configurational integral, Ω, by which all thermodynamic properties of the melt can be calculated if all

the binary parameters are known. Thus, the cell model becomes very attractive. As shown in Fig. 1-5, the activities are indeed reproducible by means of the cell model. However, as shown in Fig. 1-6 and Fig. 1-7, although the main sketches are similar, the calculated phase diagram is obviously beyond experimental error limits. The calculation may be improved if ternary parameters are introduced. Nevertheless, the cell model is a very successful model in predicting thermodynamic properties of multi-component systems. Attempts to insert sulphur and P_2O_3 directly into the model were also reported [88Gay].

1.3.6 Sub-lattice model of Hillert et al. [90Hil1]

In a fused NaCl solution, as reported by Forland [64For], the transfer of a cation from a position where it is surrounded by anions to a position where it is surrounded by cations requires an energy of the order of magnitude of 200 kcal $mole^{-1}$, while the heat of fusion and the heat of vaporization of NaCl is merely 6.69 and 40.8 kcal $mole^{-1}$, respectively. Therefore, cations will virtually only have anions as closest neighbours, and vice versa. As a consequence, over a short range in the fused salt one can distinguish between two main kinds of positions, one for cations and one for anions. They were called sub-lattices. Based on the concept of sub-lattices several models have been proposed in the thermodynamic calculation of silicate melts.

Temkin [45Tem] estimated the configurational entropy of a salt mixture by assuming that all the cations mix at random with each other on one sub-lattice and so do all the anions on another sub-lattice. Furthermore, vacancies have been introduced into sub-lattices later by Hillert and Staffansson [75Hil] and Fernandez Guillermet et al. [81Fer] in describing thermodynamic properties of the Fe-S system. In another development, by introducing neutral species and charged vacancies into the anion sub-lattice, Hillert et al. [85Hil] extended the two-sublattice model to multi-component melts where the components may have different valencies. In particular, based on [85Hil], a model for silicate melts was developed by Hillert et al. [90Hil1] in which the cation sub-lattice contains only metal ions and the anion sub-lattice contains ions of O^{-2}, SiO_4^{4-} and SiO_3^{2-} and neutral species of SiO_2^0. Applications of the general two-sublattice model [85Hil], in which charged vacancies were introduced, can be found in [90Hil2, 90Hil3]. We will only discuss the silicate sub-lattice model [90Hil1] in detail and show an application of the model to the $CaO-SiO_2$ system at the end. As suggested by Flood and Knapp [63Flo], the entropy of mixing in a MO-rich melt of the $MO-SiO_2$ system could be estimated by assuming random mixing of O^{-2} and SiO_4^{4-} anions which actually exist in MO-rich melts. At higher SiO_2 contents, however, the above model [63Flo] does not hold because as predicted by Masson et al. [65Mas] a spectrum of silicate anions will be formed.

Therefore, Forland [64For] suggested that the silicate network can be broken by a pair of non-bridging oxygens so that the entropy of mixing can be calculated by assuming a random distribution of bridging and pairs of non-bridging oxygens. Forland's model works very well in predicting the limiting SiO_2 liquidus slopes of some alkali metal oxide-SiO_2 systems. Thus, the above two models are valid in MO-rich and SiO_2-rich side, respectively.

In an effort to combine the above two models, Hillert et al. [90Hil1] applied their two-sublattice model [85Hil] to describe silicate melts. Temkin's approximation [45Tem] of random mixing in both cation and anion sub-lattices was maintained. On the MO-rich side, they proposed a formula $(M^{+2})_P(O^{-2},SiO_4^{4-})_Q$ to present the system, where P and Q represent the number of ions on each sub-lattice; O^{-2} and SiO_4^{4-} are the species located in the anion sub-lattice. For the SiO_2-rich side, to be able to obtain the same entropy as Forland did, one neutral species $Si_{0.5}O^{\circ}$ (a bridging oxygen) and $Si_{0.5}O_2^{2-}$ (a pair of non-bridging oxygens) were proposed in the anion sub-lattice. However, the amount of O^{-2} according to the first model and $Si_{0.5}O^{\circ}$ according to the second model may both take low values when the composition of a silicate melt approaches $x_{MO}=1/3$ from one side or the other, the remaining anion is thus different in the two cases, SiO_4^{4-} and $Si_{0.5}O_2^{2-}$, respectively. So it would be difficult to combine the two

models. To solve this problem they modified the second formula to $(M^{+2})_P(SiO_2^0, SiO_4^{4-})_Q$. Unfortunately, the new formula will not give the same limiting slope of the SiO_2 liquidus as Forland's model does. Therefore, the SiO_3^{2-} species, which represents one bridging and two non-bridging oxygens, was introduced in the anion sub-lattice to obtain the same entropy as Forland's model. When the composition of a melt approaches $x_{MO}=1/3$, SiO_4^{4-} instead of SiO_3^{2-} species were expected to predominate. This can be accomplished by making the energy of formation much lower for SiO_4^{4-} than SiO_3^{2-} so that SiO_3^{2-} practically disappears at these compositions. In this way, they proposed the following formula over the complete silicate system:

$$(M^+)_P(O^{-2}, SiO_4^{4-}, SiO_3^{2-}, SiO_2^0)_Q$$

where M^+ represents metal ions of any valency.

By means of the above model, Hillert et al. have successfully evaluated the CaO-SiO_2 system [90Hil4]. As shown in Fig. 1-8 to Fig. 1-10, the liquidus surface and activities of CaO and SiO_2 in the liquid phase have been reproduced very well except the monotectic temperature which is determined mostly by the presence of SiO_3^{2-} and SiO_2^0 species.

Therefore, the two-sublattice model of Hillert et al.

[90Hil1] provides a suitable mathematical expression for the thermodynamic properties of silicate melts and is more or less physically reasonable at the MO-rich part of the system. With the introduction of one neutral species SiO_2^0, the presence of SiO_3^{2-} in the anion sub-lattice may not always be physically realistic (it is well known that pure silica does not contain any SiO_2^0 molecules but consists of a single network). Consequently the monotectic point in the above example [90Hil4] has caused considerable difficulties. Also, the ability of the model to give good prediction and representation of ternary and multi-component solutions has yet to be demonstrated. However, as to representing the thermodynamic properties of silicate melts with mathematical expressions, this is a very successful model.

1.3.7 Conclusions

Based on the structure of silicate melts, the formation of the melts is considered as the reaction of anions in the system, where the anions may be O^{2-}, O°, O^{-} or an array of silicates of the formula $Si_x O_{3x+1}^{2(x+1)-}$. By applying the principles of polymer theory, the ionic constitution and thermodynamic properties of the melts are linked directly. The models provide prediction of the thermodynamic solution properties of the melts and a better understanding of the behaviour of silicate melts. Classical polymer theory is, however, unable to evaluate the probability of ring ion

formation. The model of Toop and Samis and of Masson et al. are, then, restricted to some certain compositions. The model of Lin and Pelton is not restricted by ring ion formation and is the most recommended among the structure-based silicate models.

The cell model of Kapoor and Frohberg, which has been developed for multi-component systems by Gaye and Welfringer, is a very promising model since it claims that only binary parameters are needed to represent thermodynamic properties of multi-component system. As shown in Fig. 1-5 and 1-6, even though difficulties were reported when calculating the phase diagram, activities are indeed reproducible by means of the cell model. It is very interesting to compare the model of Toop and Samis to the cell model. In the former model a MO-SiO_2 melt is considered in terms of the equilibria between O^o, O^- and O^{2-} anions, while in the cell model, the melt is regarded as a mixture of the cells of SiOSi, MOSi and MOM types. Since the oxygens in the cells of SiOSi, MOSi and MOM are really an O^o, O^- and O^{2-}, respectively, the cell model is quite similar to the model of Toop and Samis.

The two-sublattice silicate model of Hillert et al. is very important since it provides a suitable mathematical expression for the thermodynamic properties of silicate melts. The model has been applied successfully in several silicate

systems though difficulties were reported in reproducing the limiting slopes of the silicate liquid surface.

Furthermore, Borgianni and Granati have used the lattice model of Yokokawa and Niwa [69Yok] as the basis for a Montecarlo calculation of the free energies [77Bor] and ionic structures [77Bor] in silicate melts.

For building an oxide thermodynamic database, most of the above models are not acceptable because they are specific only for silicate melts, and are very complex in calculation. The cell model as well as the general sub-lattice model of Hillert et al., however, are successfully applied in some oxide systems other than silicate melts. We do not feel comfortable with the assumption of charged vacancies in the liquid phase proposed by Hillert et al. nor believe that ternary phase diagrams such as that of $CaO-SiO_2-TiO_2$ system can be well reproduced without ternary parameters as expected by the cell model. Therefore, the so-called modified quasi-chemical model will be introduced in the next section.

1.4 QUASI-CHEMICAL MODEL

1.4.1 Quasi-chemical model

In building a thermodynamic database for molten oxides, it is preferable if highly ordered systems (including positive and negative deviations) as well as disordered systems can be described by the same model. This section will show that this goal is accomplished by the quasi-chemical model which was first proposed by Guggenheim [39Gug] and was modified by Blander and Pelton [86Bla].

According to the quasi-chemical theory, in a binary solution each component introduces one particle (such as M and Si in a $MO-SiO_2$ melt) and the solution consists substitutionally of particles "1" and "2" mixing on a quasi-lattice with a constant coordination number z. The relative amounts of the three types of nearest neighbour pairs (1-1, 2-2 and 1-2) are determined by the energy change associated with the formation of two 1-2 pairs from a 1-1 and 2-2 pair according to the relation

$$[1-1] + [2-2] = 2[1-2] \qquad (1\text{-}4\text{-}1)$$

If this energy change equals zero, then the solution is an ideal mixture. As this energy change becomes more negative, the formation of 1-2 pairs is favoured and the solution becomes more ordered. If this energy change becomes more positive, "1" particles prefer to be surrounded by "1", instead of "2" and "2" particles prefer "2" as neighbours rather than "1" and the solution shows a greater tendency to

be immiscible.

Let the enthalpy change for this process be $(2\epsilon_{12}-\epsilon_{11}-\epsilon_{22})$ where ϵ_{ij} (i,j=1,2) is the "pair bond energy". The total number of pairs per mole of solution is $N^{\circ}z/2$ where N° is Avogadro's number. The molar enthalpy change is defined as

$$\omega = \frac{N^{\circ}z}{2}(2\epsilon_{12}-\epsilon_{11}-\epsilon_{22}) \qquad (1\text{-}4\text{-}2)$$

and the molar non-configurational entropy change as

$$\eta = \frac{N^{\circ}z}{2}(2\sigma_{12}-\sigma_{11}-\sigma_{22}) \qquad (1\text{-}4\text{-}3)$$

where σ_{ij} (i,j=1,2) is the "non-configurational entropy of the pair bond".

Let n_1 and n_2 be the number of moles of "1" and "2" particles. For one mole of solution, $(n_1+n_2)=1$. The mole fractions of 1 and 2 are defined as $X_1=n_1/(n_1+n_2)=1-X_2$. Let n_{11}, n_{12} and n_{22} be the number of moles of each type of pair-bond in solution. The fraction of pair-bonds is defined as;

$$X_{ij} = \frac{n_{ij}}{n_{11}+n_{22}+n_{12}} \qquad (1\text{-}4\text{-}4)$$

Since the coordination number z is constant, particles "1" are bonded to zn_1 neighbours. From the mass balance it

follows that:

$$zn_1 = 2n_{11} + n_{12} \qquad (1\text{-}4\text{-}5)$$

$$zn_2 = 2n_{22} + n_{12} \qquad (1\text{-}4\text{-}6)$$

so,

$$2X_1 = 2X_{11} + X_{12} \qquad (1\text{-}4\text{-}7)$$

$$2X_2 = 2X_{22} + X_{12} \qquad (1\text{-}4\text{-}8)$$

The enthalpy of mixing, ΔH, is proportional to the number of "1-2" pairs;

$$\Delta H = \frac{X_{12}}{2}\omega \qquad (1\text{-}4\text{-}9)$$

The non-configurational entropy of mixing is similarly expressed:

$$\Delta S^{nonconfig} = \frac{X_{12}}{2}\eta \qquad (1\text{-}4\text{-}10)$$

To obtain an expression for the configurational entropy of mixing one must calculate the multiplicity of a solution containing n_{11}, n_{22} and n_{12} moles of 1-1, 2-2 and 1-2 pairs. This problem, which is equivalent to the Ising model, has not

been solved in three dimensions. In the approximate solution proposed by Guggenheim [39Gug], the pairs are distributed randomly over the $N^{\circ}z/2$ positions to give a molar entropy of mixing of

$$\Delta S = -\frac{1}{2}Rz(X_{11}lnX_{11} + X_{22}lnX_{22} + X_{12}lnX_{12}) \qquad (1\text{-}4\text{-}11)$$

This, however, over-counts the number of possible configurations. If the solution is completely random then, $X_{11}=X_1^2$, $X_{22}=X_2^2$ and $X_{12}=2X_1X_2$ giving

$$\Delta S = -\frac{1}{2}Rz(2X_1lnX_1 + 2X_2lnX_2 + 2X_1X_2ln2)$$

which is not identical to an ideal solution.

Blander and Pelton [86Bla] defined ΔS^{config} as

$$\begin{aligned}\Delta S^{config} = & -R(X_1lnX_1 + X_2lnX_2) \\ & -\frac{Rz}{2}(b_1X_1 + b_2X_2)\cdot \\ & (X_{11}\ln\frac{X_{11}}{X_1^2} + X_{22}\ln\frac{X_{22}}{X_2^2} + X_{12}\ln\frac{X_{12}}{2X_1X_2})\end{aligned} \qquad (1\text{-}4\text{-}12)$$

which satisfies the completely random mixing limiting condition.

If $(\omega-\eta T) \rightarrow -\infty$, perfect ordering will result at the composition $X_1=X_2=0.5$ with all "1" particles having only "2" particles as nearest neighbours and vice-versa. ΔS^{config}

should be zero at this composition, and thus

$$\Delta S^{config} = R(\frac{z}{2}-1)\ln\frac{1}{2} = 0 \qquad (1\text{-}4\text{-}13)$$

when z=2.

Consider a one-dimensional "necklace" of N_1 particles of type "1" and N_2 particles of type "2" with N_{11}, N_{22} and N_{12} being the number of 1-1, 2-2 and 1-2 pair-bonds. The "necklace" can be constructed as follows.

We first place the N_1 particles of type "1" in the ring and choose at random $(N_1 - N_{11})$ of the N_1 spaces between them. This choice can be make in $\Omega_1 = N_1!/(N_{11}!(N_1-N_{11})!)$ ways. We now place one particle of type "2" in each of these chosen spaces. This leaves $N_2 - (N_1 - N_{11}) = N_{22}$ particles of type "2". These are all placed into the $(N_1 - N_{11})$ chosen spaces with no restriction of the number in each space. This can be done in $\Omega_2 = N_2!/(N_{22}!(N_2-N_{22})!)$ ways since $(N_1 - N_{11}) = (N_2 - N_{22})$. The entropy is then given by:

$$\Omega = \Omega_1 \Omega_2 = \frac{N_1!\,N_2!}{(N_{11}!\,N_{22}!\,(N_1-N_{11})!\,(N_2-N_{22})!}$$

The statistical mechanical definition of entropy is

$$\Delta S = k ln \Omega$$

where k is Boltzmann's constant. Applying Stirling's approximation and

$$N_1 + N_2 = N^o$$
$$N_{11} + N_{22} + N_{12} = N^o$$
$$2X_1 = 2X_{11} + X_{12}$$
$$2X_2 = 2X_{22} + X_{12}$$

ΔS is written as;

$$\Delta S = k\ln\frac{N_1!N_2!}{N_{11}!N_{22}!(N_1-N_{11})!(N_2-N_{22})!}$$
$$= k[N_1 lnN_1 + N_2 lnN_2 - (N_1-N_{11})\ln(N_1-N_{11}) -$$
$$(N_2-N_{22})\ln(N_2-N_{22}) - N_{22}lnN_{22} - N_{11}lnN_{11}]$$
$$= R[X_1 lnN_1 + X_2 lnN_2 - (X_1-X_{11})\ln(N_1-N_{11})$$
$$-(X_2-X_{22})\ln(N_2-N_{22}) - X_{22}lnN_{22} - X_{11}lnN_{11}]$$
$$= -R(-X_1 lnX_1 - X_2 lnX_2 + \frac{X_{12}}{2}\ln\frac{X_{12}}{2} +$$
$$\frac{X_{12}}{2}\ln\frac{X_{12}}{2} + X_{22}lnX_{22} + X_{11}lnX_{11})$$
$$= -R(X_1 lnX_1 + X_2 lnX_2 - 2X_1 lnX_1 - 2X_2 lnX_2 +$$
$$X_{22}lnX_{22} + X_{11}lnX_{11} + X_{12}\ln\frac{X_{12}}{2})$$
$$= -R[X_1 lnX_1 + X_2 lnX_2$$
$$-(2X_{11}+X_{12})lnX_1 - (2X_{22}+X_{12})lnX_2$$
$$+X_{22}lnX_{22} + X_{11}lnX_{11} + X_{12}\ln\frac{X_{12}}{2}]$$
$$= -R(X_1 lnX_1 + X2 lnX_2) -$$
$$R(X_{11}\ln\frac{X_{11}}{X_1^2} + X_{22}\ln\frac{X_{22}}{X_2^2} + X_{12}\ln\frac{X_{12}}{2X_1X_2})$$

which is identical to equation (1-4-12) with z=2. This is the exact one-dimensional Ising model.

The equilibrium concentrations of the various pairs are given by minimizing the Gibbs energy at constant composition

$$\left(\frac{d(\Delta H - T\Delta S)}{dX_{12}}\right) = 0$$

Performing the derivation and solving gives

$$\frac{X_{12}^2}{X_{11}X_{22}} = 4\exp[\frac{-2(\omega-\eta T)}{zRT}] \qquad (1\text{-}4\text{-}14)$$

which resembles an equilibrium constant for reaction (1-4-1);

this is why the model is called "quasi-chemical". Using the mass balance equations we have

$$\frac{X_{12}}{2} = \frac{2X_1X_2}{1+\xi}$$

where

$$\xi = \sqrt{1+4X_1X_2\left(\exp\frac{2(\omega-\eta T)}{zRT}-1\right)}$$

For a given (ω-ηT) at a given composition X_1, X_{12} is determined through these last two equations.

If ω=0 and η=0, then $\Delta H = 0$ and $S^E = 0$, and the solution is ideal. When ω and η are small, $S^E \approx 0$, $X_{12} \approx 2X_1X_2$ and $\Delta H \approx X_1X_2\omega$, which defines a regular solution. As (ω-ηT) is made progressively more negative, the ΔH-X curve exhibits a gradually deeper peak at $X_1 = X_2 = 0.5$, the solution is ordered and ΔS goes through a minimum as shown in Fig. 1-11.

As mentioned earlier, the ordering phenomenon was not considered in polynomial solution models. These models could not be used to build an oxide thermodynamic database where ordering becomes quite evident. Though associated solution models were used successfully in some oxide system, their basic assumption of associations forming in the liquid is rather artificial and is poorly supported physically. Since we

seek a solution model that is as simple as possible, and also as general as possible so that, for instance, it can be used for disordered liquids as well as ordered ones, the entire multi-component system can be described by one simple set of equations. In addition to this, the self-consistent analytical representation of thermodynamic and phase diagram information permits the data to be interpolated and extrapolated. Finally, we decided to adopt the quasi-chemical model to this end.

When considering a MO-SiO_2 melt, the quasi-chemical model takes the melt as a mixture of M-M, Si-Si and Si-M cation pairs, the model of Toop and Samis regards the melt in terms of the equilibria between O^{2-}, O° and O^{-} anions, while the cell model considers the melt as a mixture of MOM, SiOSi and SiOM cells. Hence, the above three models are very similar since these three sets of entities can be considered as being formally equivalent.

1.4.2 Modification of the quasi-chemical model

The quasi-chemical model stipulates that the solution exhibits maximum ordering about the equimolar composition. This is not always the case with real oxide melts as shown in Fig. 1-2. At constant temperature and pressure the ΔH-X as well as ΔS-X and ΔG-X curves are often asymmetric with respect to the composition of maximum ordering. The following

modifications of Blander and Pelton make it possible to account for this behaviour.

1.4.2.1 Fixing the composition of maximum ordering

To make the model more general it must be possible to choose a composition of maximum ordering which corresponds to that observed.

The simplest means of accomplishing this is to replace the mole fractions X_1 and X_2 in the preceding equations by "equivalent fractions" y_1 and y_2, defined by

$$y_1 = \frac{b_1 X_1}{b_1 X_1 + b_2 X_2}, \quad y_2 = \frac{b_2 X_2}{b_1 X_1 + b_2 X_2} \qquad (1\text{-}4\text{-}15)$$

where b_1 and b_2 are numbers chosen so that $y_1 = y_2 = 0.5$ at the composition of maximum ordering. This is equivalent to setting the coordination numbers of pure "1" and pure "2" particles to be $z_1 = b_1 z$ and $z_2 = b_2 z$, respectively. The coordination number of a melt is, thus, $z = X_1 z_1 + X_2 z_2$. This gives physical meaning to the introduction of equivalent fractions and makes it less "arbitrary". The mass balance then becomes

$$z b_1 n_1 = 2n_{11} + n_{12}$$

$$z b_2 n_2 = 2n_{22} + n_{12}$$

$$2y_1 = 2X_{11} + X_{12}$$

$$2y_2 = 2X_{22} + X_{12}$$

The molar enthalpy of mixing and molar excess entropy are then

$$\Delta H = (b_1X_1 + b_2X_2)\frac{X_{12}}{2}\omega$$
$$\Delta S = -R(X_1 lnX_1 + X_2 lnX_2) - \frac{Rz}{2}(b_1X_1 + b_2X_2) \cdot (X_{11}\ln\frac{X_{11}}{y_1^2} + X_{22}\ln\frac{X_{22}}{y_2^2} + X_{12}\ln\frac{X_{12}}{2y_1y_2}) + (b_1X_1 + b_2X_2)\frac{X_{12}}{2}\eta \qquad (1\text{-}4\text{-}16)$$

It is important to note that in the ideal entropy term X_1 and X_2 are not replaced by y_1 and y_2 so that when $(\omega-\eta T)=0$ the equations still reduce to the ideal solution equation.

From equation (1-4-15), one can obtain

$$\frac{y_1}{y_2} = \frac{b_1X_1}{b_2X_2}$$

so in order to fix the composition of maximum ordering at $y_1/y_2=1$, only the ratio $b_1/b_2=X_2/X_1$ must be set. Furthermore, when $\omega=-\infty$, it is known that at the maximum ordering composition, $\Delta S=0$, $X_{11}=0$, $X_{22}=0$, $X_{12}=1$, $X_1=b_2/(b_1+b_2)$ and $X_2=b_1/(b_1+b_2)$.

Substituting into equation (1-4-16),

$$\Delta S = -R(X_1 lnX_1 + X_2 lnX_2) - \frac{Rz}{2}(b_1X_1 + b_2X_2)\,ln2 = 0$$

and upon rearranging the equation, one can obtain

$$b_2 z = -\frac{\ln r + (1-r)\, r^{-1} \ln(1-r)}{\ln 2} \qquad (1\text{-}4\text{-}17)$$

$$b_1 = \frac{b_2 r}{1-r} \qquad (1\text{-}4\text{-}18)$$

where $r=b_1/(b_1+b_2)$ is the ratio required to fix the composition of maximum ordering. For any given binary system it is possible to calculate b_1 and b_2 to satisfy equations (1-4-17) and (1-4-18), but this cannot always be carried over into multi-component systems. For example, consider the three components CaO, FeO and SiO_2. In the CaO-SiO_2 binary system (see Fig. 1-2), the maximum ordering in the liquid phase is located at 66.67 mol% CaO according to [62Too]. Thus $b_1/b_2=X_2/X_1=0.5$ where 1 and 2 are referred to component CaO and SiO_2 respectively. From equation (1-4-18) one can obtain r=1/3. In equation (1-4-17), if z=2, b_2 is calculated to be 1.3774, and $b_1=0.5b_2=0.6887=b_{CaO}$. However, in the CaO-FeO liquid phase, the maximum ordering composition is 50 mol% CaO; then $b_{CaO}/b_{FeO}=1$ and r=0.5. Similarly by substituting r=0.5 and z=2 into equations (1-4-17) and (1-4-18), one will obtain $b_{CaO}=b_{FeO}=1$ (no longer 0.6887). If one wishes to perform calculations in the CaO-FeO-SiO_2 ternary system b_{CaO} (and similarly b_{FeO}) must have only one constant value everywhere

in the ternary. A compromise is necessary. We have chosen always to set b_{SiO2}=1.3774. Equations (1-4-17) and (1-4-18) will then be satisfied for all binary systems containing SiO_2. For other binary oxide systems such as CaO-FeO, equations (1-4-17) and (1-4-18) will not be exactly satisfied. These systems are close to being ideal, so the compromise makes little difference in practice.

1.4.2.2 Composition dependence of ω and η

Constant values of ω and η are sufficient to represent the main features of the ΔH and ΔS curves for ordered systems, but for a quantitative representation of the thermodynamic properties of real systems it is necessary to introduce a composition dependence which empirically takes the configuration dependence of ω and η into account. In the present case simple polynomial expansions in the equivalent fraction y_2 were chosen

$$\omega = \omega_0 + \omega_1 y_1 + \omega_2 y_2 + \ldots\ldots$$
$$\eta = \eta_0 + \eta_1 y_1 + \eta_2 y_2 + \ldots\ldots$$

The temperature- and composition- independent coefficients ω_i and η_i can be optimized to give the best representation of the available thermodynamic and phase diagram data for a system. A detailed discussion on the procedure of optimization will be given in the next chapter.

It may be noted that when (ω-ηT) is small the excess configurational entropy is also small and $X_{12} \approx 2X_1X_2$ (assuming for simplicity that $b_1=b_2=1$ so that $X_1=y_1$ and $X_2=y_2$). In this case, from equations (1-4-9) and (1-4-10)

$$\Delta H \approx X_1X_2(\omega_0+\omega_1X_1+\omega_2X_{22}+.....) \qquad (1\text{-}4\text{-}19)$$

$$S^E \approx X_1X_2(\eta_0+\eta_1X_1+\eta_2X_{22}+.....) \qquad (1\text{-}4\text{-}20)$$

The quasi-chemical model then reduces to a polynomial expression, when (ω-ηT) is small and ω_i and η_i become numerically equal to the corresponding parameters in the polynomial expression. The modified quasi-chemical model is therefore a very general one which can represent efficiently both highly ordered and non-ordered solutions.

1.5 CONCLUSIONS

As a general introduction, polynomial, structure-based silicate and the modified quasi-chemical models have been discussed in this chapter. Since polynomial solution models are applied only when the interactions between species in the solution are rather weak, structure based silicate solution models are mostly limited to silicate slags, the modified

quasi-chemical model has, then, been established to build an oxide database.

It is very interesting to compare the quasi-chemical model with the cell and the Toop and Samis model:

$$(Si\text{-}Si) + (M\text{-}M) = 2(Si\text{-}M) \quad \text{(quasi-chemical model)}$$

$$[Si\text{-}O\text{-}Si] + [M\text{-}O\text{-}M] = 2[Si\text{-}O\text{-}M] \quad \text{(cell model)}$$

$$O^{\circ} + O^{2-} = 2O^{-} \quad \text{(Toop and Samis)}$$

where (Si-Si) is really [Si-O-SI] and O°, (M-M) is [M-O-M] and O^{2-}, (SI-M) is [Si-O-M] and O^{-}. The three models are very similar when describing a silicate melt.

In Chapters 2 and 4, the general principles of binary and ternary optimization respectively by means of the modified quasi-chemical model, will be presented.

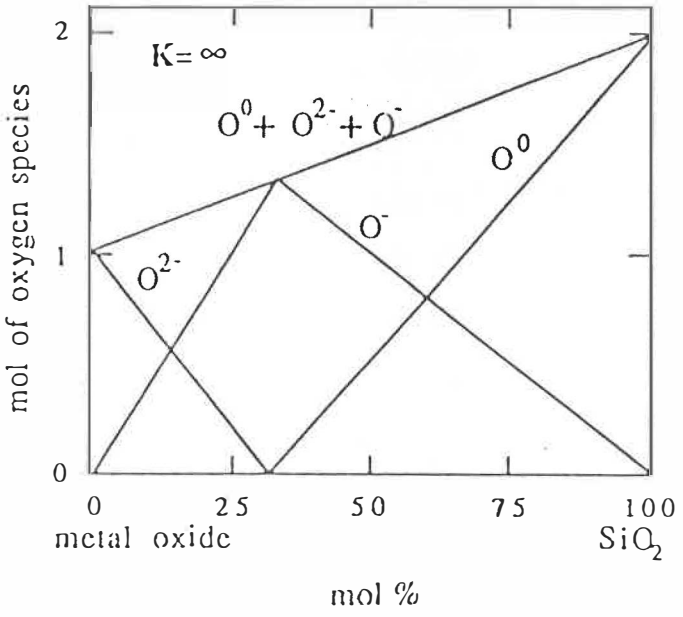


Fig. 1-1 Distribution of oxygen species (according to the Toop and Samis model [62Too]).

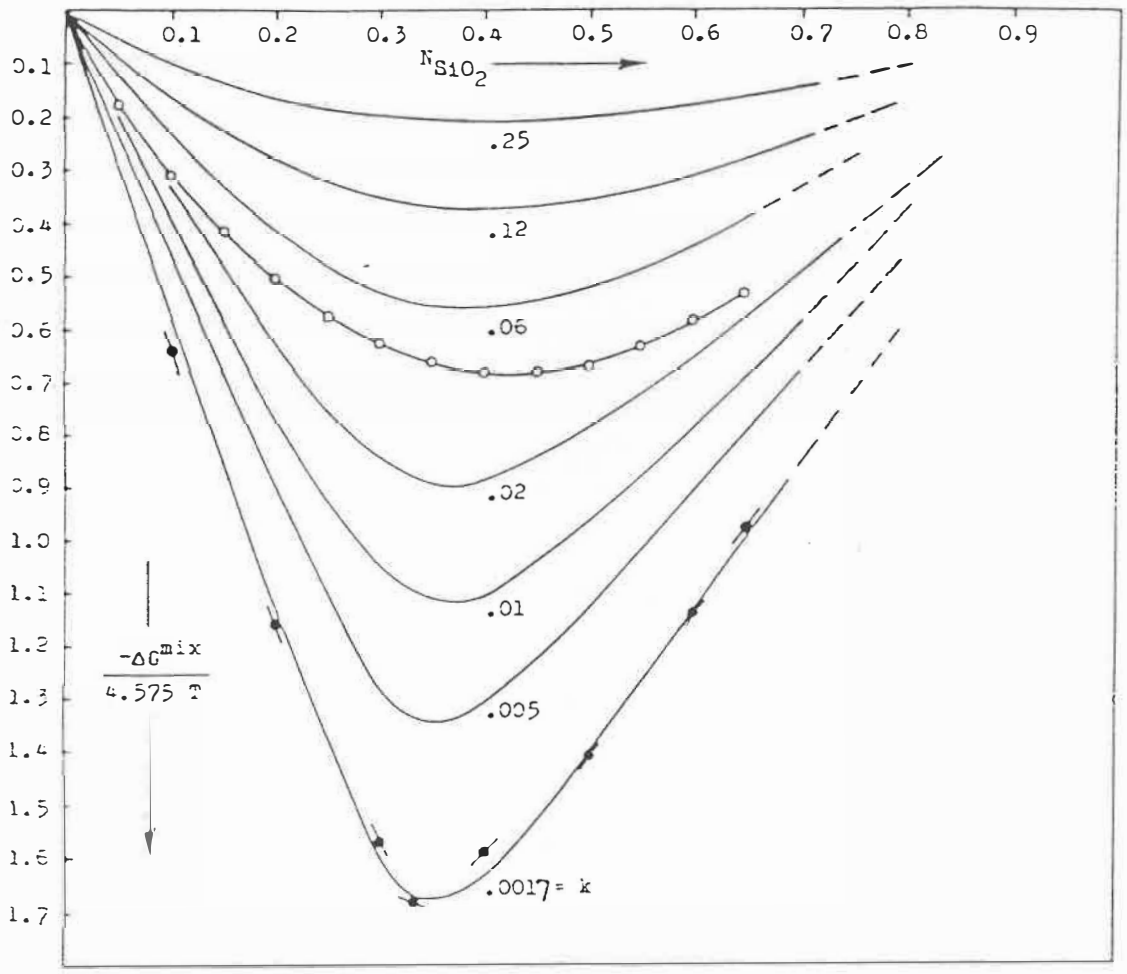


Fig. 1-2 Calculated binary free energy of mixing curves for various values of K according to the Toop and Samis model [62Too]. The open circles are from [54Ric] and the closed circles are from [55Ell, 53Dar].

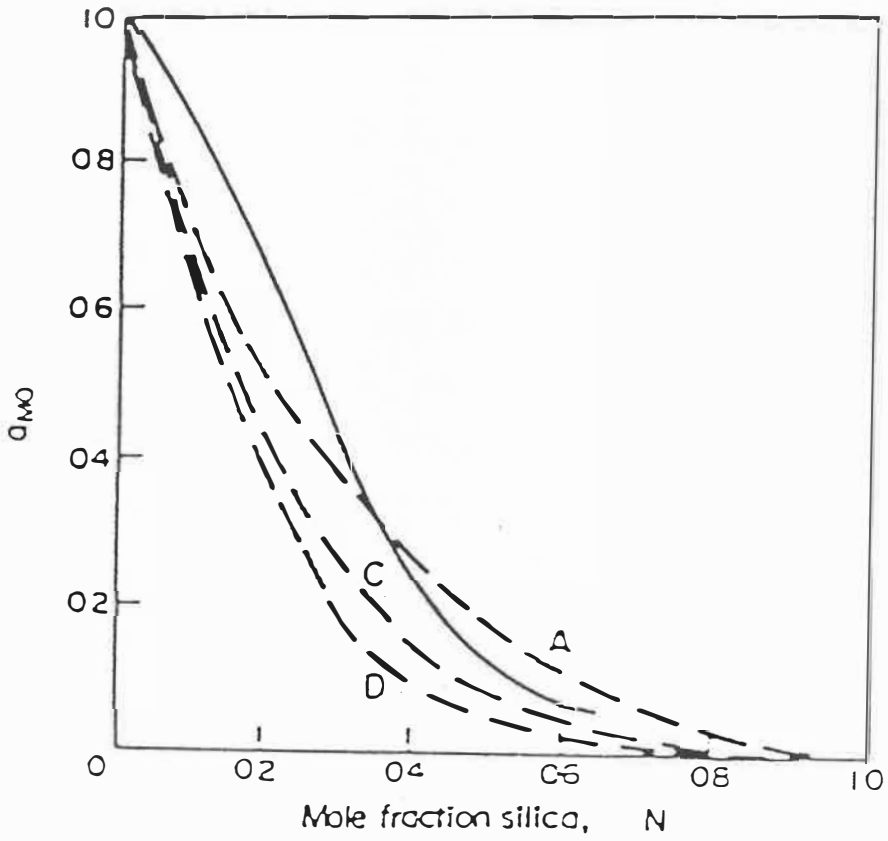


Fig. 1-3 The variations of a_{MO} with composition in the $PbO-SiO_2$ system, given by the modified Toop and Samis model for hypothetical melts of $\Delta G^{\circ}/RT$ = 0, -1.88 and -3 (which is presented by the dashed line A, B and C, respectively) in comparison with the experiment of [54Ric] (solid line).

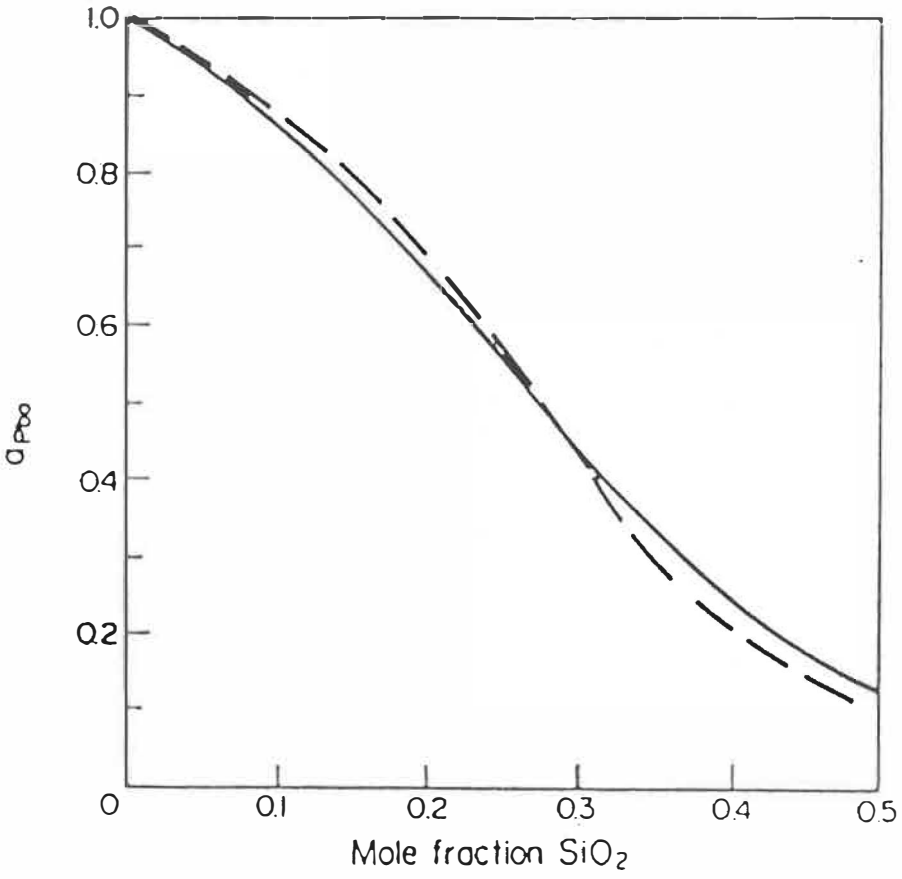


Fig. 1-4 Curve-fitting of equation (1-3-13) (dashed line) with the experimental a_{PbO} in $PbO-SiO_2$ melts at 1100°C [54Ric] (solid line).

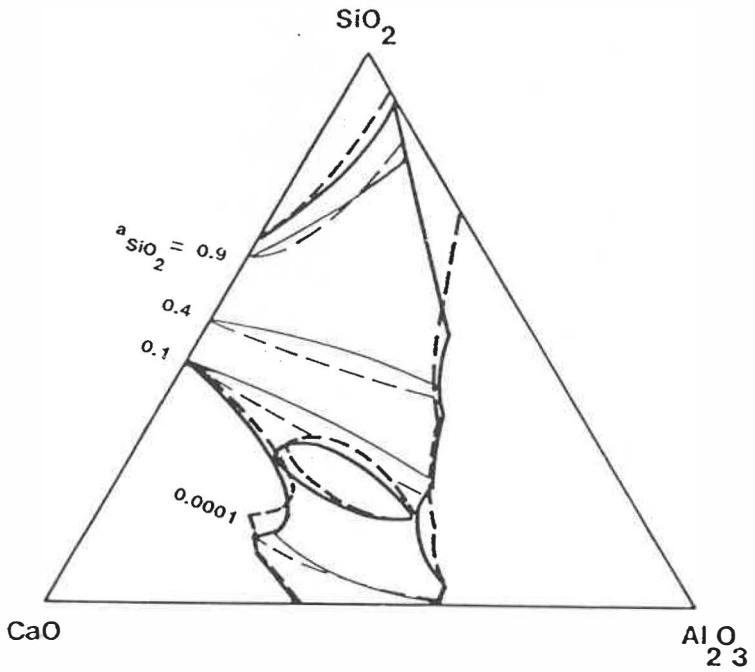


Fig. 1-5 Comparison of experiment activities (solid lines) [81Gay] with the calculation using the cell model (dashed lines) [84Gay] at T=1550°C.

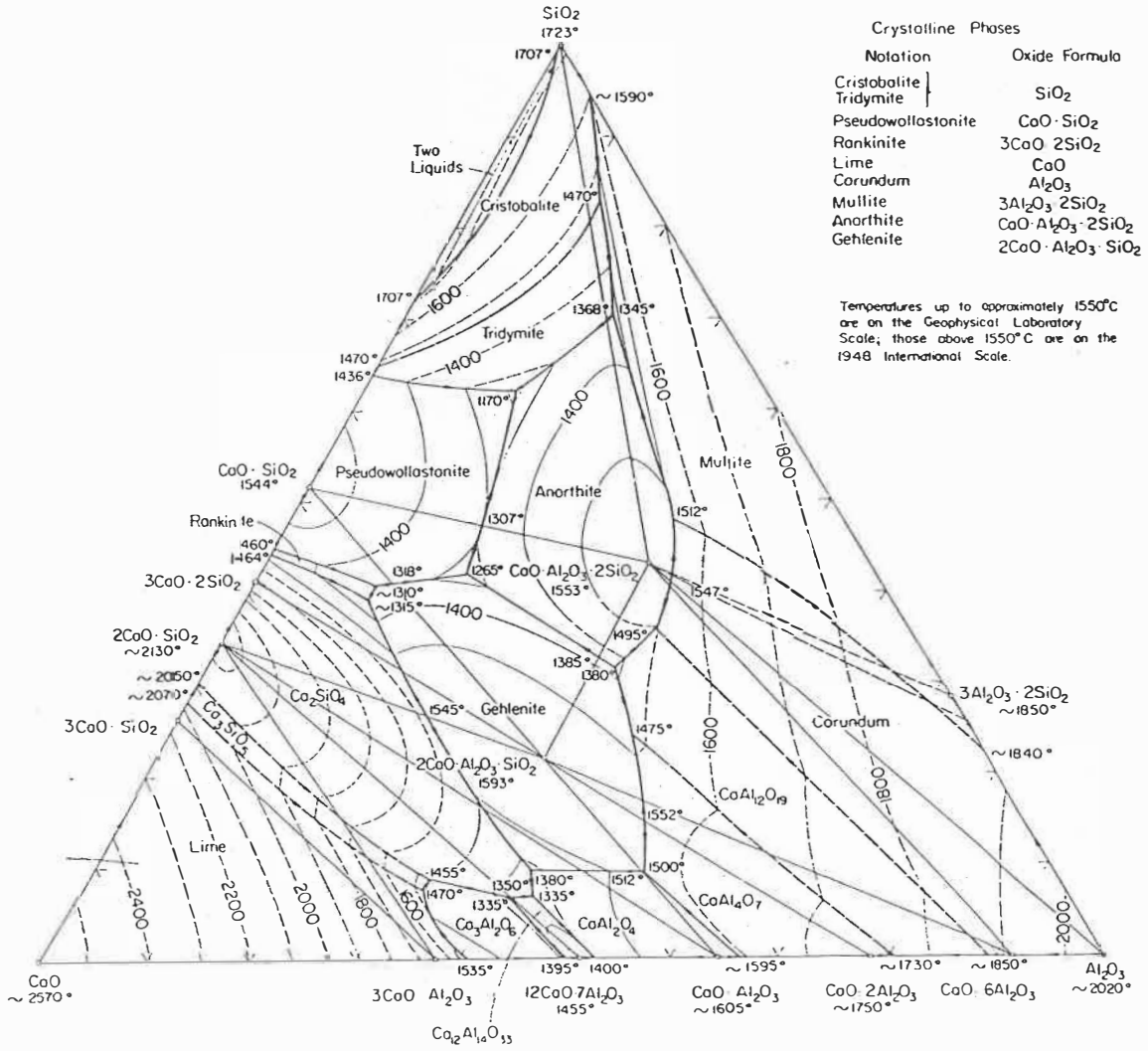


Fig. 1-6 Experimental phase diagram of the CaO-Al_2O_3-SiO_2 system in weight percent [600sb].

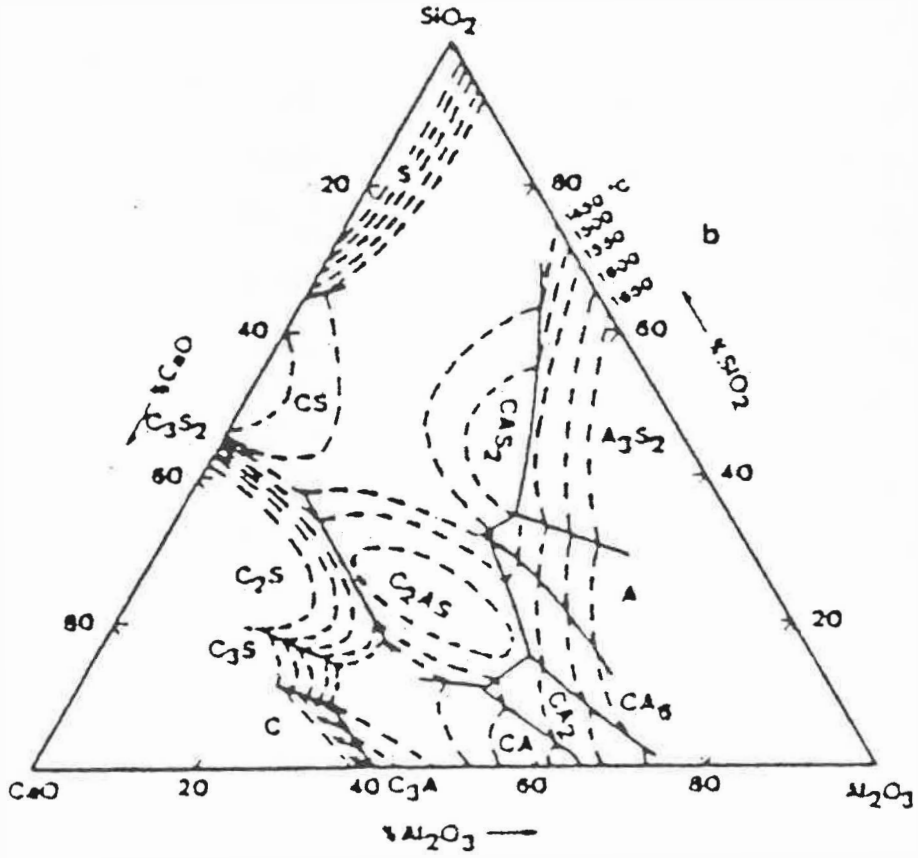


Fig. 1-7 Calculated phase diagram of the CaO-Al_2O_3-SiO_2 system using the cell model [85Gay].

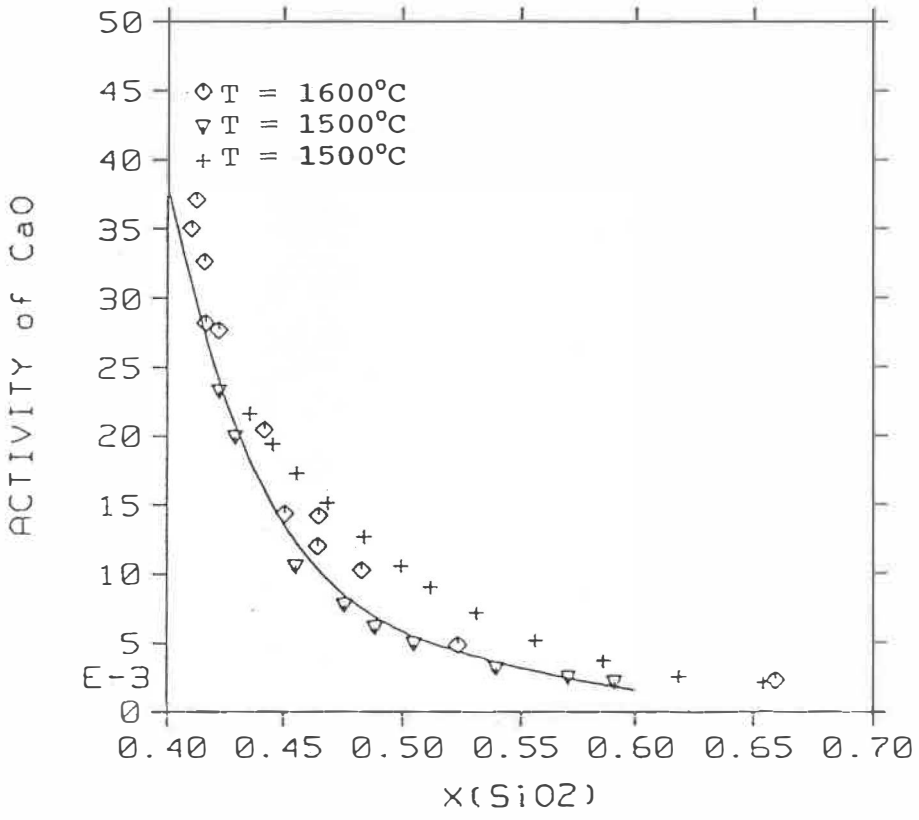


Fig. 1-8 Comparison of the CaO activity, as calculated at 1500° (solid line) from the sub-lattice model [90Hil1, 90Hil4] (with the assumption of SiO_3^{2-} anions) and from measurements at 1600° [82Zou], 1500° [62Sha] and 1500°C [57Car] (which is presented by +).

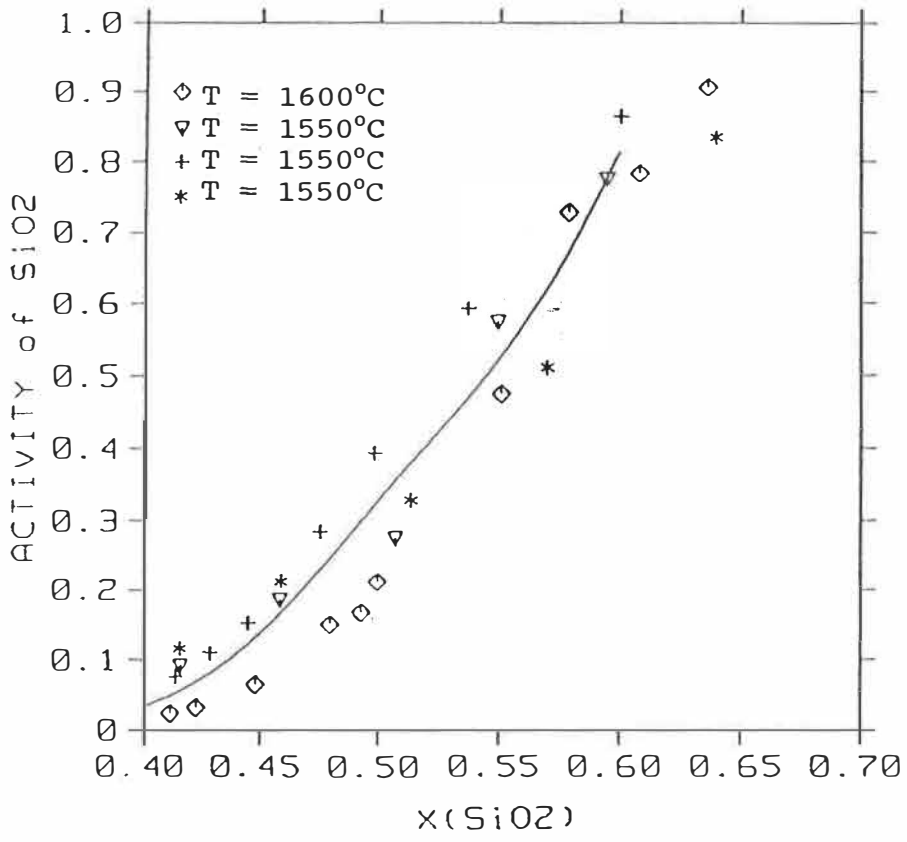


Fig. 1-9 Comparison of the SiO_2 activity, as calculated at 1550° (solid line) from the sub-lattice model [90Hil1, 90Hil4] (with the assumption of SiO_3^{2-} anions) and from measurements at 1600° [82Zou], 1550° [60Kay], 1550° [31Rei] (which is presented by +) and 1550°C [58Bai] (which is presented by *).

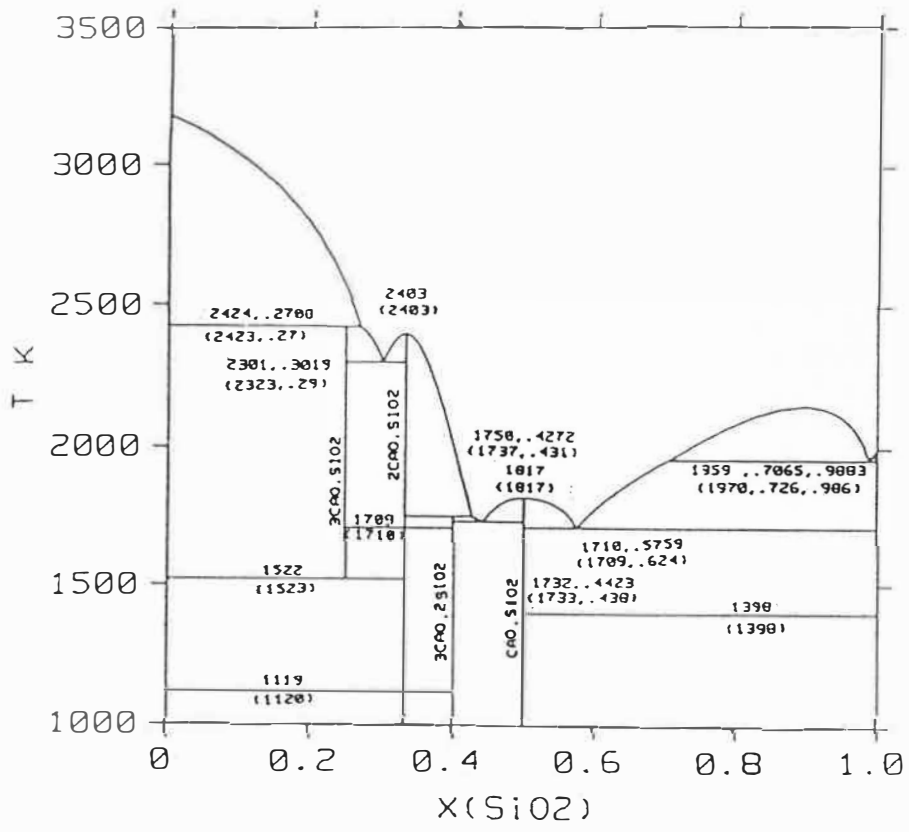


Fig. 1-10 Calculated phase diagram of the $CaO-SiO_2$ system using the sub-lattice model [90Hil1, 90Hil4] (with the assumption of SiO_3^{2-} anions). Numbers in parentheses are experimental values and without parentheses are calculated values.

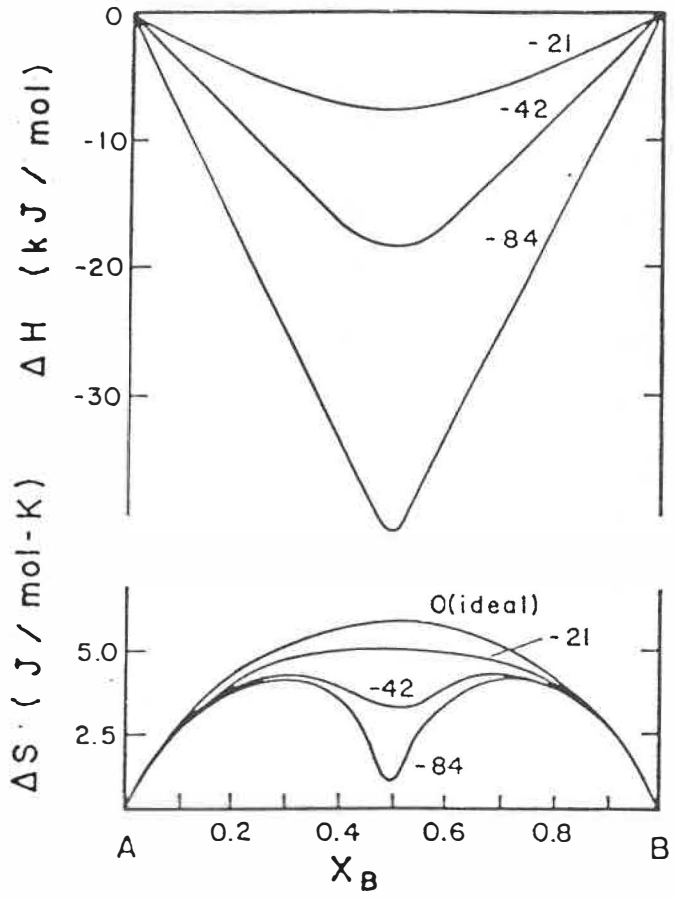


Fig. 1-11 Enthalpy and entropy of mixing of a binary system for different degrees of ordering with maximum ordering at the equimolar composition. Curves are calculated from the extended quasi-chemical theory at T= 1000°C with z=2 for the constant values of ω (KJ) shown with η=0.

Table 1-1 Comparison of Experimental [84Bjo] and Calculated a_{FeO} in the solid phase

x_{CaO}	T °C	a_{FeO} exp.	a_{FeO} cal.
0.098	927	0.934	0.922
0.098	1027	0.932	0.920
0.189	1027	0.874	0.870
0.243	1027	0.850	0.843
0.292	1077	0.807	0.818
0.348	1077	0.777	0.797
0.950	1077	0.692	0.681

CHAPTER 2

OPTIMIZATION AND CALCULATION OF BINARY SYSTEMS

2.1 INTRODUCTION

To build an oxide thermodynamic database, first of all, the Gibbs energy expression of the binary solutions must be determined, by which all reported thermodynamic and phase diagram data of the solutions can be reproduced within their stated error limits. In the present study, to begin with, the parameters (such as ω_0, ω_1, ..., ω_7, η_0, η_1, ..., η_7 of the quasi-chemical model) are to be found which best reproduce the measured experimental values. This procedure is known mathematically as regression or optimization. The most common principle of regression (or optimization) is the well-known least squares method, which could be applied directly for algebraic fitting of experimental data by means of a computer. According to the least squares method, the sum over all squared deviations has to be minimized:

$$S = \sum_j (f(X_j) - Y_j)^2 \dashrightarrow \min. \qquad (2\text{-}1\text{-}1)$$

where Y_j is the experimental value at $X=X_j$ and $f(X_j)$ is the calculated value at $X=X_j$ by its expression containing a certain set of parameters.

When the deviations e_j ($e_j = Y_j - f(X_j)$) are normally

distributed, that is, when only random errors appear in the measurements, the least squares method guarantees that the expectation of its estimation equals to the real value of the parameter. Thus the problem of optimization can be characterized as follows: Find by means of the least squares method a set of parameters of a certain function (or model) which fulfils the requirement of equation (2-1-1) for an actual set of experimental data. This procedure represents the core of the present study.

The problems of optimization are usually classified by the type of the functions $f(X;A^1,A^2,...A^n)$ with respect to the parameters A^j (j=1,...,n). If $f(X;A^1,A^2,...A^n)$ is a linear function of all parameters A^j [89Hil]:

$$f(X;A_1,A_2,...A_n) = \Sigma A_j Z_j(X)$$

where $Z_n(X)$ are arbitrary functions of the variable X, then the problem of optimization is called "linear". Otherwise, it is called non-linear optimization.

In this chapter, following a general discussion about linear and non-linear least squares methods, details of binary optimization by means of the modified quasi-chemical model are presented. Thermodynamics of the one component systems Al_2O_3, CaO, FeO, Fe_2O_3, K_2O, MgO, MnO, Na_2O, NiO, rare earth oxides, SiO_2, TiO_2, Ti_2O_3, PbO, ZnO and ZrO_2 will be evaluated in

Section 2.2. Details of evaluations of 26 binary oxide systems will also be discussed. A list of all optimized binary systems in the database will be shown at the end.

2.1.1 Linear optimization

For a binary solution of components A and B, the integral molar Gibbs energy of mixing relative to the pure components is expressed as;

$$\Delta g = RT(X_A lnX_A + X_B lnX_B) + {}^{\Delta}g^{E}$$

where X_A, X_B are the mole fractions and Δg^E is the excess integral molar Gibbs energy. According to the polynomial model, Δg^E can be expressed as a polynomial in the mole fraction X_B:

$$ {}^{\Delta}g^{E} = \Sigma D_{m_j,n_j} X_B^{m_j} (1-X_B)^{n_j} \qquad (2\text{-}1\text{-}2)$$

where $D_{mj,nj}$ are coefficients and m_j and n_j are positive integral powers. The coefficients $D_{mj,nj}$ may be written as linear functions of temperature, T:

$$D_{m_j,n_j} = h_{m_j,n_j} - Ts_{m_j,n_j} \qquad (2\text{-}1\text{-}3)$$

Hence, the integral molar enthalpy of mixing and excess entropy of mixing, assumed independent of T, are given in terms of the coefficients $h_{mj,nj}$ and $s_{mj,nj}$ as

$$\Delta h = \Sigma h_{m_j,n_j} X_B^{m_j} (1-X_B)^{n_j} \qquad (2\text{-}1\text{-}4)$$

$$s^E = \Sigma s_{m_j,n_j} X_B^{m_j} (1-X_B)^{n_j} \qquad (2\text{-}1\text{-}5)$$

Then, from differentiation, the partial excess properties can be obtained,

$$\Delta g_A^E = \Sigma (h_{m_j,n_j} - Ts_{m_j,n_j}) X_B^{m_j} (1-X_B)^{n_j} (1-n_j-m_j) + \Sigma n_j (h_{m_j,n_j} - Ts_{m_j,n_j}) X_B^{m_j} (1-X_B)^{n_j-1} \qquad (2\text{-}1\text{-}6)$$

$$\Delta g_B^E = \Sigma (h_{m_j,n_j} - Ts_{m_j,n_j}) X_B^{m_j} (1-X_B)^{n_j} (1-n_j-m_j) + \Sigma m_j (h_{m_j,n_j} - Ts_{m_j,n_j}) X_B^{m_j-1} (1-X_B)^{n_j} \qquad (2\text{-}1\text{-}7)$$

$$\Delta h_A = \Sigma h_{m_j,n_j} X_B^{m_j} (1-X_B)^{n_j} (1-n_j-m_j) + \Sigma n_j h_{m_j,n_j} X_B^{m_j} (1-X_B)^{n_j-1} \qquad (2\text{-}1\text{-}8)$$

$$\Delta h_B = \Sigma h_{m_j,n_j} X_B^{m_j} (1-X_B)^{n_j} (1-n_j-m_j) + \Sigma m_j h_{m_j,n_j} X_B^{m_j-1} (1-X_B)^{n_j} \qquad (2\text{-}1\text{-}9)$$

where Δg_A^E, Δg_B^E, Δh_A and Δh_B are partial excess Gibbs energy and enthalpy of components A and B, respectively.

When an immiscibility gap is shown on a phase diagram, let X_L and X_R be the X_B values of the left and right solutions in equilibrium at T_i, respectively. Another two equations can, thus, be set up:

$$RTln(1-X_L) + \Delta g^E_{A,L} = RTln(1-X_R) + \Delta g^E_{A,R} \qquad (2\text{-}1\text{-}10)$$

$$RTlnX_L + \Delta g^E_{B,L} = RTlnX_R + \Delta g^E_{B,R} \qquad (2\text{-}1\text{-}11)$$

where $\Delta g_{A,L}^{E}$, $\Delta g_{B,L}^{E}$, $\Delta g_{A,R}^{E}$ and $\Delta g_{B,R}^{E}$ are partial excess Gibbs energies defined as equations (2-1-6) and (2-1-7) while $X_B = X_L$ or X_R, respectively.

Hence, a set of coefficients $h_{mj,nj}$ and $s_{mj,nj}$ are sufficient to express all thermodynamic properties of the solution as well as phase diagram data (such as the immiscibility data) provided that (i) polynomial expansions yield adequate representations of the excess properties, (ii) Δh and s^E are independent of T.

Suppose that at a constant temperature, two immiscible solutions are in equilibrium and Δg^E has been measured at N_G different compositions, while, s^E, Δh, Δg_A^E (perhaps in the form of activity coefficient of component A) and Δh_A have been measured at N_s N_h, N_{GA} and N_{hA} different compositions, respectively. One wishes to obtain a set of coefficients $h_{mj,nj}$ and $S_{mj,nj}$ (j=1,M) in order to fit these data by least squares regression to equations (2-1-2), (2-1-4), (2-1-5), (2-1-6), (2-1-7), (2-1-8), (2-1-9), (2-1-10) and (2-11) simultaneously. This simultaneous fitting is made possible

through the fact that equations (2-1-2), (2-1-4), (2-1-5), (2-1-6), (2-1-7), (2-1-8), (2-1-9), (2-1-10) and (2-11) are written in terms of the same coefficients $h_{mj,nj}$, $S_{mj,nj}$. This is the crux of the present technique.

Let y_i be one of the above properties measured at $X_{B,i}$, and b_j (j=0,1,,...p-1) be one set of unknown parameters (like $h_{mj,nj}$, $S_{mj,nj}$ in the above equations). Suppose y_i can be expressed in the form

$$y_i = b_0 + b_1 x_{i1} + \ldots + b_{p-1} x_{i,p-1} + e_i \qquad (2\text{-}1\text{-}12)$$

where x_{i1}, x_{i2},...$x_{i,p-1}$ are linearly independent functions of X_B which are constants at $X_B = X_{B,i}$, and e_i is the error. For total n ($n = N_G + N_h + N_S + N_{SA} + N_{hA}$) measurements, we have a matrix form

$$\begin{pmatrix} y_1 \\ y_2 \\ \vdots \\ y_n \end{pmatrix} = \begin{pmatrix} x_{10} x_{11} x_{12} \ldots x_{1,p-1} \\ x_{20} x_{21} x_{22} \ldots x_{2,p-1} \\ \vdots \quad \vdots \quad \vdots \quad \vdots \quad \vdots \\ x_{n0} x_{n1} x_{n2} \cdots x_{n,p-1} \end{pmatrix} \begin{pmatrix} b_0 \\ b_1 \\ \vdots \\ b_{p-1} \end{pmatrix} + \begin{pmatrix} e_1 \\ e_2 \\ \vdots \\ e_n \end{pmatrix} \qquad (2\text{-}1\text{-}13)$$

or

$$\mathbf{Y = XB + e} \qquad (2\text{-}1\text{-}14)$$

where $x_{i0} = 1$ (i=1,...n). Definitions of matrices **Y, X, B** and **e** are quite obvious in equation (2-1-13). Since the columns of **X** are linearly independent, **X** has rank p. To estimate **B** by a least squares method, $\mathbf{e'e}=\Sigma_i e_i^2$ (**e'** is the transposed matrix of **e**) is to be minimized with respect to **B**.

Since

$$\mathbf{e'e} = (\mathbf{Y-XB})'(\mathbf{Y-XB})$$

$$= \mathbf{Y'Y} - 2\mathbf{B'X'Y} + \mathbf{B'X'XB}$$

differentiating $\mathbf{e'e}$ with respect to $\mathbf{B}$ and letting the derivative be zero, we have

$$-2\mathbf{X'Y} + 2\mathbf{X'XB} = 0$$

or

$$\mathbf{X'XB} = \mathbf{X'Y} \qquad (2\text{-}1\text{-}15)$$

where $\mathbf{X}$ has rank p. The inverse matrix of $\mathbf{X'X}$, $(\mathbf{X'X})^{-1}$, exists and we have

$$\mathbf{B} = (\mathbf{X'X})^{-1}\mathbf{X'Y}$$

The solution of $\mathbf{B}$ provides the least squares estimation of parameters in the above polynomial solution model. To solve equation (2-1-15), several computational techniques such as Gaussian elimination, Chilesky decomposition, triangular decomposition and the orthogonal-triangular decomposition method (among others) have been developed.

As an example, we will consider the solid solution of the CaO-FeO system. As mentioned in Chapter 1, Bjorkman [84Bjo] measured the activities of CaO in the CaO-FeO solid solution, Abbattista et. al. [75Abb] reported the phase diagram of this system which shows that the solid solution forms a miscibility gap before the liquid phase is reached. From the experimental miscibility data [75Abb1], a set of equations like equation (2-1-10) and (2-1-11) can be obtained. From the activity data,

which can be transformed to partial Gibbs energies, another set of equations like equation (2-1-7) are constructed. Therefore, following the above discussed procedure and the Gaussian elimination method, three parameters b_0, b_1 and b_2 are determined to be 2508.2, -6191.1 and 3880.6 J/mole. In return, by using the three parameters and the above equations, one can reproduce both the measured activities and the miscibility gap (see Table 1-1 and Fig. 2-32). We say the solid solution phase of the CaO-FeO system has been optimized or evaluated so that this phase may be inserted into the corresponding multi-component multi-phase equilibrium calculation. The CaO-FeO system is discussed in detail in Section 2.3.21.

2.1.2 The non-linear optimization

Unfortunately, for the quasi-chemical model, the thermodynamic properties are non-linear functions with respect to the parameters to be optimized, and the above linear optimization procedures are not valid. We have to develop a new method to optimize the parameters for the quasi-chemical model.

As we know, non-linear optimization can seldom be solved analytically and the optimal values of its parameters are to be located using a computer by either iterative techniques or non-iterative algorithms such as grid search and random

search. The iterative techniques are practically valuable and will be briefly reviewed.

Non-linear least squares regression is one of the most common iterative techniques and was employed in our binary optimization procedure. Suppose we have n observations (x_i, y_i), i=1,2,...,n, from a known function f which is non-linear with respect to **B**. Thus

$$y_i = f(x_i, \mathbf{B}) + e_i$$

where **B** is the parameter matrix and e_i is the normally distributed error. Let $\mathbf{B}^*$ be the optimal matrix of **B**. If a certain $\mathbf{B}^1$ is in the close neighbourhood of $\mathbf{B}^*$, the linear Taylor expansion is,

$$f_i(\boldsymbol{B}^*) \approx f_i(\boldsymbol{B}^1) + \sum_j \left(\frac{df_i}{db_j} \right)_{b_j = b_j^1} (b_j^* - b_j^1) \qquad (2\text{-}1\text{-}16)$$

where b_j are elements of **B**. Equation (2-1-16) is a linear function of $\mathbf{B}^*$ and so, by a linear least squares regression discussed earlier, $\mathbf{B}^*$ can be calculated. However, $\mathbf{B}^1$ may be far from $\mathbf{B}^*$ at the very beginning and $\mathbf{B}^*$ values obtained by linear least squares estimation through equation (2-1-16) may not be true. Therefore, iterations are needed to make the procedure converge. The non-linear least squares regression method can be stated as: Generate from an initial guess $\mathbf{B}^1$ by a certain algorithm, a sequence of points $\mathbf{B}^2$, $\mathbf{B}^3$,... to converge to minimize the sum of the least squares at $\mathbf{B}^*$. In

application, non-linear least squares regression is employed in determining parameters of the quasi-chemical model.

2.1.3 Non-linear optimization of the quasi-chemical model

2.1.3.1 Introduction

According to the quasi-chemical model, shown in Chapter 1, one can obtain

$$G^E = \frac{z}{2}RT(b_1X_1 + b_2X_2)$$
$$(y_1 \ln\frac{\xi - 1 + 2y_1}{y_1(\xi+1)} + y_2 \ln\frac{\xi - 1 + 2y_2}{y_2(\xi+1)})$$

$$G_1^E = RT\ln\gamma_1$$
$$= \frac{b_1 z}{2}RT\ln\frac{\xi - 1 + 2y_1}{y_1(\xi+1)} - \frac{2b_1 y_1 y_2^2}{1-\xi}\frac{d}{dy_2}(\omega - \eta T) \qquad (2\text{-}1\text{-}17)$$

$$G_2^E = RT\ln\gamma_2$$
$$= \frac{b_2 z}{2}RT\ln\frac{\xi - 1 + 2y_2}{y_2(\xi+1)} - \frac{2b_2 y_2 y_1^2}{1-\xi}\frac{d}{dy_2}(\omega - \eta T)$$

Based on equation (1-4-16), one can obtain:

$$\Delta H_1 = \frac{b_1}{2}x_{12}\omega + \frac{b_1\omega y_2(y_2 - y_1)}{\xi}$$
$$+ \frac{2b_1 y_2 \omega}{\xi(1+\xi)^2}(\xi^2 - 1 + 4y_1y_2)$$
$$\frac{y_1 y_2}{zRT}\frac{d}{dy_2}(\omega - \eta T) - \frac{b_1}{2}x_{12}y_2\frac{d\omega}{dy_2}$$

$$\Delta H_2 = \frac{b_2}{2} x_{12}\omega - \frac{b_2 \omega y_1 (y_2 - y_1)}{\xi} - \frac{2 b_2 y_1 \omega}{\xi (1+\xi)^2} (\xi^2 - 1 + 4 y_1 y_2) \frac{y_1 y_2}{zRT} \frac{d}{dy_2} (\omega - \eta T) + \frac{b_2}{2} x_{12} y_1 \frac{d\omega}{dy_2}$$

where

$$\xi = \sqrt{1 + 4 y_1 y_2 [\exp \frac{2(\omega - \eta T)}{zRT} - 1]} \qquad (2\text{-}1\text{-}18)$$

$$X_{12} = \frac{4 y_1 y_2}{1 + \xi} \qquad (2\text{-}1\text{-}19)$$

y_1 and y_2 are defined as equation (1-4-15), ω and η are defined in Section 1.4.2.2.

Because of the non-linear nature of the above equations [88Pel], the non-linear least square method will be applied here.

If one has an experimental point $G^E(y_{2i}, T_i)$, then by trial and error one can find the value of $(\omega - \eta T)$ at y_{2i} and T_i. The "experimental" values of $(\omega - \eta T)_i$, y_{2i} and T_i can then be directly optimized by the standard linear optimization procedure to give the parameters of equations (2-1-18) and (2-1-19). The same situation is the case for ΔH. For the partial molar properties the problem becomes more difficult. For the partial, one cannot convert experimental data points into $(\omega - \eta T)_i$, y_{2i}, T_i values because the partial depends not

only on $(\omega-\eta T)$ but also on $d(\omega-\eta T)/dy_2$.

Taking G_1^E as an example,

$$G_1^E = A(\omega-\eta T) - C(\omega-\eta T)\frac{d}{dy_2}(\omega-\eta T) \qquad (2\text{-}1\text{-}20)$$

where the definitions of the functions $A(\omega-\eta T)$ and $C(\omega-\eta T)$ are obvious from equation (2-1-17).

To apply the non-linear least squares regression, let ω^* and η^* be initial guesses for ω and η as function of y_2;

$$\omega^* = \sum_j \omega_j^* y_2^j$$
$$\eta^* = \sum_j \eta_j^* y_2^j$$

Pelton and Blander expanded $A(\omega-\eta T)$ as a Taylor expansion about $(\omega^*-\eta^* T)$ up to the first order term and by simply replacing $C(\omega-\eta T)$ by $C(\omega^*-\eta^* T)$, they obtained

$$G_1^E = A(\omega^*-\eta^* T) + A'(\omega^*-\eta^* T)[(\omega-\omega^*) - (\eta-\eta^*)T] - C(\omega^*-\eta^* T)\frac{d}{dy_2}(\omega-\eta T) \qquad (2\text{-}1\text{-}21)$$

Rearranging the equation,

$$[G_1^E - A(\omega^*-\eta^* T)]\frac{1+\xi^*}{2b_1 y_1 y_2^2} + (\xi^*-1+2y2)\frac{\omega^*-\eta^* T}{2\xi^* y_1 y_2} = \frac{\xi*-1+2y2}{2\xi^* y_1 y_2}\Sigma(\omega_j-\eta_j T)y_2^j - \Sigma j(\omega_j-\eta_j T)y_2^{j-1}$$

where $\xi^* = \xi^*(\omega^*-\eta^* T)$. Since ω^* and η^* are initial guesses for ω and η, the left side of the above equation is a constant for

a certain experimental point while the right side is a linear function of ω and η. Hence, by linear optimization as discussed earlier, the values of ω and η can be obtained. The initial estimates, ω^* and η^*, may be far from the correct values and the above equation may not be satisfied. So successive iterations must be made. The optimized ω and η values in the last iteration are taken as the estimated ω^* and η^* for the next one, until the procedure converges. In this way G_1^E, G_2^E and G^E can be simultaneously optimized.

Pelton and Blander reported that $(1+\xi)$ can vary only between the limits $1<(1+\xi)<2$, so that $C(\omega-\eta T)$ in equation (2-1-20) depends only weakly on $(\omega-\eta T)$. They decided to directly replace $C(\omega-\eta T)$ by $C(\omega^*-\eta^* T)$ in equation (2-1-21). However, according to equation (2-1-18), in a binary ideal solution (where $\omega=0$ and $\eta=0$), $\xi=1$, while in a binary positive solution (where $\omega-\eta T>0$), $\xi>1$. Therefore, the limits $1<(1+\xi)<2$ are not always correct. It is more reasonable to expand both $A(\omega-\eta T)$ and $C(\omega-\eta T)$ in equation (2-1-20) as a Taylor expansion about $(\omega^*-\eta^* T)$ up to the first order and ignore the higher order terms:

$$\begin{aligned} G_1^E \approx\ & A(\omega^*-\eta^*T) + A'(\omega^*-\eta^*T)\,[(\omega-\omega^*)-(\eta-\eta^*)\,T] \\ & -[C(\omega^*-\eta^*T) + C'(\omega^*-\eta^*T)\,(\omega-\eta T) \\ & -C'(\omega^*-\eta^*T)\,(\omega^*-\eta^*T)]\,\frac{d}{dy_2}(\omega-\eta T) \end{aligned}$$

Let,

$$(\omega-\eta T)\frac{d}{dy_2}(\omega-\eta T) \approx (\omega-\eta T)\frac{d}{dy_2}(\omega^*-\eta^* T)$$

Therefore,

$$\begin{aligned} G_1^E \approx\ & A(\omega^*-\eta^* T) + A'(\omega^*-\eta^* T)\,[(\omega-\omega^*)-(\eta-\eta^*)T] \\ & - C(\omega^*-\eta^* T)\frac{d}{dy_2}(\omega-\eta T) - C'(\omega^*-\eta^* T)\frac{d(\omega^*-\eta^* T)}{dy_2}(\omega-\eta T) \\ & + C'(\omega^*-\eta^* T)(\omega^*-\eta^* T)\frac{d}{dy_2}(\omega-\eta T) \end{aligned}$$

Then,

$$\begin{aligned} & \frac{G_1^E - A(\omega^*-\eta^* T)}{C(\omega^*-\eta^* T)} + \frac{A'(\omega^*-\eta^* T)(\omega^*-\eta^* T)}{C(\omega^*-\eta^* T)} \\ = & \left[\frac{A'(\omega^*-\eta^* T)}{C(\omega^*-\eta^* T)} - \frac{C'(\omega^*-\eta^* T)}{C(\omega^*-\eta^* T)}\frac{d}{dy_2}(\omega^*-\eta^* T)\right](\omega-\eta T) \\ & - \left(1-\frac{C'(\omega^*-\eta^* T)(\omega^*-\eta^* T)}{C(\omega^*-\eta^* T)}\right)\frac{d}{dy_2}(\omega-\eta T) \end{aligned}$$

(2-1-22)

We have linearized the non-linear least squares regression. Once more, iterations are needed in the optimization to make it converge. Similarly, the same procedure can be applied to linearize the non-linear least squares of ΔH_1 and ΔH_2.

In real applications, even before the optimization, sometimes one may already have an approximate value of the entropy (η) or enthalpy (ω) parameters of the solution through available experimental information. One may fix the entropy (η) or enthalpy (ω) parameters during the optimization

procedure. We will discuss three cases below.

2.1.3.2 The simultaneous optimization of ω and η

Here G_1^E is taken as an example, and the other partial properties can be treated by the same method.

From (2-1-22) we obtain

$$\frac{G_1^E - A(\omega^* - \eta^* T)}{C(\omega^* - \eta^* T)} + \frac{A'(\omega^* - \eta^* T)\,(\omega^* - \eta^* T)}{C(\omega^* - \eta^* T)}$$
$$= \left[\frac{A'(\omega^* - \eta^* T)}{C(\omega^* - \eta^* T)} - \frac{C'(\omega^* - \eta^* T)}{C(\omega^* - \eta^* T)} \frac{d}{dy_2}(\omega^* - \eta^* T)\right] \sum (\omega_j - \eta_j T)\, y_2^j$$
$$- \left(1 - \frac{C'(\omega^* - \eta^* T)\,(\omega^* - \eta^* T)}{C(\omega^* - \eta^* T)}\right) \sum j\,(\omega_j - \eta_j T)\, y_2^{j-1}$$

Note that the above equation is linear in $\omega_j - \eta_j T$. After some iterations, as discussed earlier, the experimental values of G_1^E can be successfully estimated as a linear function of ω_j and η_j. With a set of experimental values of G_1^E, G_2^E, G^E, ΔH, ΔH_1, ΔH_2, etc., by the linear least squares method, one can obtain a set of ω_j and η_j from which the thermodynamic properties and the phase diagram of this system can be reproduced. Thus the system is said to have been represented by a small number of parameters ω_j and η_j. This is referred to as the "optimization" of a system. Furthermore, these obtained parameters are stored in our database to perform multi-component and multiphase equilibria calculation.

2.1.3.3 The optimization of ω while η possesses a fixed value

In this case, η_j always equals η^*_j in the whole optimization procedure.

From equation (2-1-22) we see that,

$$\frac{G_1^E - A(\omega^* - \eta^* T)}{C(\omega^* - \eta^* T)} + \frac{A'(\omega^* - \eta^* T)\,\omega^*}{C(\omega^* - \eta^* T)}$$
$$= \left(\frac{A'(\omega^* - \eta^* T)}{C(\omega^* - \eta^* T)} - \frac{C'(\omega^* - \eta^* T)}{C(\omega^* - \eta^* T)} d\frac{\omega^*}{dy_2}\right)\sum \omega_j y_2^j$$
$$-\left(1 - \frac{C'(\omega^* - \eta^* T)\,\omega^*}{C(\omega^* - \eta^* T)}\right)\sum j\omega_j y_2^{j-1}$$

similar to Section 2.1.3.2, this is also a linear least squares problem.

2.1.3.4 The optimization of η while ω possesses a fixed value

In this case, ω_j always equals ω_j^* in the whole optimization procedure.

From equation (2-1-22) we see that,

$$\frac{G_1^E - A(\omega^* - \eta^* T)}{C(\omega^* - \eta^* T)} + \frac{A'(\omega^* - \eta^* T)\,(-\eta^*)}{C(\omega^* - \eta^* T)}$$
$$= \left(\frac{A'(\omega^* - \eta^* T)}{C(\omega^* - \eta^* T)} - \frac{C'(\omega^* - \eta^* T)}{C(\omega^* - \eta^* T)} d\frac{(-\eta^*)}{dy_2}\right)\sum (-\eta_j)\, y_2^j$$
$$-\left(1 - \frac{C'(\omega^* - \eta^* T)\,(-\eta^*)}{C(\omega^* - \eta^* T)}\right)\sum j\,(-\eta_j)\, y_2^{j-1}$$

once more it is reduced to the linear least squares problem.

2.1.3.5 The weighting of experimental data in the optimization procedure

As we know, the least squares method is designed to minimize the value of $\Sigma_i e_i^2$ (e_i is defined in equation (2-1-12)). Therefore, the greater is the absolute value of y_i (see equation (2-1-12)), the greater the value of e_i is expected to contribute to $\Sigma_i e_i^2$. Hence the least squares method gives higher weight to fit the experimental properties having higher absolute values rather than those with lower absolute values. Also, different measurements of different thermodynamic properties or of the phase diagram are of different accuracies, due to variable experimental conditions and methods. Some experimental data appear more reliable than others; often the phase diagram data are more easily obtained and more reliable than the thermodynamic properties. To control these facts in the least squares regression procedure, we set weighting factors W, in both sides of the above equations for every experimental point, the weighting being heavier if we believe that point has been more accurately measured or we are convinced that the absolute value of the function at this point is too small. Eutectic and peritectic points are usually weighted more heavily. Thus we can make some points more important than others in the optimization procedure.

2.1.3.6 Optimization of the liquidus line of an intermediate compound

If a binary system contains some compounds, the compound

liquidus lines can normally be measured well. Therefore, the compound liquidus lines are very important phase diagram data. In this section the compound liquidus line data will be included into the optimization of the binary system.

Consider an A-B binary system: if there is no solid solubility of B in A or the solid solubility is very small, one can calculate the activities of A in the liquid solution along the liquidus line (the same situation will hold for component B) from the ΔG_{fusion} of component A. Similarly, if the solid solubility in a compound $A_a B_b$ (let a+b=1) is very small (that is, if it is nearly a stoichiometric compound), one can directly use the $\Delta G_{formation}$ to calculate the activities of $A_a B_b$ in the liquid phase along the compound liquid lines. Even when the solid solubility is no longer negligible, simple solution models can be applied to describe the solid phase, and the activities of $A_a B_b$ in the liquid phase can be calculated too.

Let $\mu_A(l)$ and $\mu_B(l)$ be the chemical potentials of components A and B in the liquid phase;

$$\mu_A(l) = \mu_A^o(l) + RT\ln a_A = \mu_A^o(l) + \ln X_A \gamma_A$$
$$\mu_B(l) = \mu_B^o(l) + RT\ln a_B = \mu_B^o(l) + \ln X_B \gamma_B$$

where $\mu_A^{\circ}(l)$ and $\mu_B^{\circ}(l)$ are chemical potentials of A and B in pure A and pure B liquid phases, respectively. a_A, a_B, γ_A and

γ_B are activities and activity coefficients of A and B.

Taking liquid A and B, respectively, as the reference states of component A and B, $\mu_A^\circ(l)=\mu_B^\circ(l)=0$ and we have

$$\mu_A(l) = RTlnX_A + \ln\gamma_A$$
$$\mu_B(l) = RTlnX_B + \ln\gamma_B$$

Let (T_c, X_c) be a point on the equilibrium compound $(A_a B_b)$-liquidus line; then

$$\mu_{A_aB_b}(l, X_c) = \Delta G_c(T_c)$$

where $\mu_{A_aB_b}(l, X_c)$ is the chemical potential of $A_a B_b$ species in liquid phase at T_c and X_c, $\Delta G_c(T_c)$ is the Gibbs energy of formation of compound $A_a B_b$ from liquid A and B at T_c, which is a constant value at this temperature. Furthermore,

$$\mu_{A_aB_b}(l, X_c) = a\mu_A(l, X_c) + b\mu_B(l, X_c)$$

and,

$$\Delta G_c(T_c) - aRTln(1-X_c) - bRTlnX_c = aRTln\gamma_A + bRTln\gamma_B$$
$$= aG_1^E + bG_2^E$$

Note that the left side of the above equation is a constant at T_c and X_c and the right side is a function of ω and η through the quasi-chemical model. Thus from the compound-liquidus lines another set of experimental data were developed for the optimization.

This is again a non-linear least squares problem, and so

we expand both $G1^E$ and G_2^E as a Taylor expansion about $(\omega^* - \eta^* T)$ up to the first order and simply ignore the higher terms.

We obtain

$$\Delta G_c(T_c) - aRTln(1-X_c) - bRTlnX_c - aA_1(\omega^* - \eta^* T) - bA_2(\omega^* - \eta^* T) + [aA'_1(\omega^* - \eta^* T) - bA'_2(\omega^* - \eta^* T)](\omega^* - \eta^* T)$$
$$= [aA'_1(\omega^* - \eta^* T) - aC'_1(\omega^* - \eta^* T)\frac{d}{dy_2}(\omega^* - \eta^* T) + bA'_2(\omega^* - \eta^* T) + bC'_2(\omega^* - \eta^* T)\frac{d}{dy_2}(\omega^* - \eta^* T)]\Sigma(\omega_j - \eta_j T)y_2^j + [b - a - bC'_2(\omega^* - \eta^* T)(\omega^* - \eta^* T) + aC'_1(\omega^* - \eta^* T)(\omega^* - \eta^* T)]\Sigma j(\omega_j - \eta_j T)y_2^{j-1}$$

After some iterations as before, the above equation is satisfied. In summary, then, we can optimize compound-liquidus lines simultaneously with the other thermodynamic and phase diagram data such as G_1^E, G_2^E, G^E, ΔH, ΔH_1, ΔH_2, eutectic and peritectic points.

The liquidus line of the compound reflects not only the changes of the liquid entropy in that region but also the changes of the heat capacity and entropy of fusion of the compound. The greater the entropy of fusion of the compound, the flatter the liquidus line of the compound will be. Hence, by optimizing the liquidus line of the compound, the thermodynamic properties of the compound are also evaluated in that temperature range.

On the other hand, if the values of ω and η are determined by evaluating the system the $\Delta G_{formation}$ values of the compound can be calculated along the compound liquidus lines. And from these values, $\Delta G_{formation}$ can be fitted as a function of temperature.

2.1.3.7 Miscibility gaps

Another kind of important phase diagram data are those of miscibility gap which may be formed in the liquid phase. Based on the equilibrium conditions,

$$\mu_A(l, X_L) = \mu_A(l, X_R)$$
$$\mu_B(l, X_L) = \mu_B(l, X_R)$$

where X_L, X_R are mole fractions of B for an equilibrium tie-line in the miscibility gap region at a certain temperature and L and R represent left and right, respectively, one can obtain

$$RT\ln\frac{1-X_L}{1-X_R} = G_1^E(X_L) - G_1^E(X_R)$$
$$RT\ln\frac{X_L}{X_R} = G_2^E(X_L) - G_2^E(X_R)$$

By the same procedure as given for G_1^E, another two approximate equations linear with respect for ω_j and η_j are derived. Miscibility gaps can, then, be optimized simultaneously with the other available thermodynamic and

phase diagram data.

2.1.4 Conclusions

By means of the modified quasi-chemical model and the non-linear least squares regression, we can simultaneously optimize both thermodynamic and phase diagram information for all liquid and solid phases from room temperature up to the liquidus temperature. The thermodynamic properties and phase diagram evaluated in such a way are internally consistent with each other.

A program called FITQUAS was written, based on the above principles of linearizing the non-linear least squares regression. By means of FITQUAS all available thermodynamic and phase diagram data of a binary solution can be evaluated simultaneously. The optimized ω_j and η_j can be automatically transformed by FITQUAS to form a data file to calculate the phase diagram using the F*A*C*T computer system through POTCOMP (which is binary phase diagram calculation program).

In total, 84 binary oxide systems have been optimized with FITQUAS. All available thermodynamic and phase diagram data are evaluated and represented within reported experimental uncertainties by a small number of ω_j and η_j values. In Section 2.3, details of evaluations of 26 binary oxide systems will be discussed. 15 rare earth oxide-alumina

systems will be discussed in Chapter 3. All binary systems containing PbO and ZnO will be evaluated in Chapter 5. The remaining binary systems were optimized mainly by Professor Eriksson (except these containing NiO).

2.2 THERMODYNAMIC PROPERTIES OF THE COMPONENT OXIDES

Before the details of binary optimization using FITQUAS are presented, the thermodynamic properties of the pure component oxides: Al_2O_3, CaO, FeO, Fe_2O_3, K_2O, MgO, MnO, Na_2O, NiO, SiO_2, TiO_2, Ti_2O_3, PbO, ZnO and ZrO_2 will be evaluated. Rare earth oxides will be discussed in Chapter 3. Since the thermodynamic database for solid oxide developed by Berman and Brown [85Ber] is thermodynamically consistent, we will accept their data if available. The compilation of Barin [89Bar] is another principle source for the unary data.

Thermodynamic data for the above pure components as well as for intermediate compounds in the evaluated systems are listed in the Appendix. The thermodynamic properties of the intermediate compounds are discussed under the optimizations of binary (in Section 2.3) and ternary (in Chapter 4) systems.

THERMODYNAMIC PROPERTIES OF COMPONENT OXIDES

Al_2O_3:

Values of ΔH°_{298} and S°_{298} and C_p(sol) below the melting point were taken from Berman et al [85Ber2]. The melting temperature as well as ΔH°_{fus} and ΔS°_{fus} at the melting temperature were taken from Barin et al [77Bar], while C_p(liq) was obtained from the tabulated values of Barin [89Bar]. Above the melting point, C_p(sol) was set equal to C_p(liq). Below the melting point, C_p(liq) was obtained by adding to C_p(sol) the expression for $\Delta C_{p(fus)}$ from Barin et al [77Bar].

CaO:

Much controversy surrounds the equilibrium melting point of CaO. Earlier measurements by several authors gave a melting point of 2595 ±35°C. These data have been reviewed [69Tra, 85Jan, 86Yam]. The melting point was re-measured in a solar furnace by Traverse and Foex [69Tra] who obtained 2927 ±50°C. This value is preferred in the JANAF tables. Recently, a melting point of 2899°C was measured by digital pyrometry with an arc imaging furnace [86Yam]. Traverse and Foex suggest that tungsten contamination from the sample supports was responsible for the much lower melting points observed in the earlier studies. However, these earlier

studies were in good agreement with each other, and it seems unlikely that they would all suffer from exactly the same amount of contamination.

The solidus of the CaO-MnO system, which exhibits complete solid solubility, was measured by Schenck et al [64Sch] using an optical pyrometer over the composition range from 0 to 80 wt.% CaO and between 1900° and 2400°C. The solidus clearly extrapolates to a melting point of CaO between 2550° and 2650°C. Our thermodynamic assessment of this binary system, with an assumed melting point in this range, yielded a simple expression for the excess Gibbs energies of the solid and liquid solutions consistent with the measured solidus and with measured activities in the solid solution. The sample of Schenck et al was not in contact with any container or support material which could have caused contamination. Furthermore, their measurements were made at temperatures below 2400°C where there are fewer experimental difficulties. The melting point obtained from extrapolation of their liquidus agrees very closely with that obtained by direct measurement in the earlier studies.

Therefore, in the present assessments we have chosen a melting point in the temperature range of the early measurements. The chosen value of 2572°C is that given by Elliott and Gleiser [60Ell].

The enthalpy of fusion of 19 kcal/mol (79496 J/mol) was taken from Kubaschewski et al [67Kub]. All properties of the solid below the melting point were taken from Berman et al [85Ber2]. An expression for C_p(liq) was obtained from the tabulated data of Barin [89Bar]. Above the melting point, C_p(sol) was set equal to C_p(liq), and below the melting point C_p(liq) was set equal to C_p(sol).

FeO:

The thermodynamic properties of one mole of hypothetical solid stoichiometric FeO below the melting point were obtained by adding the values of the molar enthalpy, entropy and heat capacity of $Fe_{0.947}O$ given by Robie et al [78Rob] to those of 0.053 moles of Fe as given by Barin et al [77Bar]. (In the case of C_p, the expressions were obtained by curve-fitting the tabulated values.)

A melting point of 1371°C [67Kub] was adopted. The molar entropy of fusion of stoichiometric FeO was assumed equal to that of $Fe_{0.947}O$ as reported by Robie et al [78Rob] (since one mole of $Fe_{0.947}O$ contains one mole in total of cations and cation vacancies). The heat capacity of the liquid was taken from Coughlin et al [51Cou]. Above the melting point, C_p(sol) was set equal to C_p(liq), and below the melting point C_p(liq) was set equal to C_p(sol).

$\underline{K_2O}$:

The same procedure was followed as for Na_2O.

$\underline{MgO}$:

The same procudure was followed as for Al_2O_3.

$\underline{MnO}$:

Values of ΔH^{o}_{298} and S^{o}_{298} and C_p(sol) below the melting point were taken from [77Bar]. The melting point was taken from the recent compilation of Barin [89Bar], but the enthalpy of fusion at the melting point was taken from the earlier compilation of Barin et al [77Bar] since this value permitted easier optimizations of most binary phase diagrams. An expression for C_p(liq) was obtained by fitting the tabulated values of Barin et al [77Bar]. Above the melting point, C_p(sol) was set equal to C_p(liq), and below the melting point C_p(liq) was set equal to C_p(sol).

$\underline{Na_2O}$:

Values of ΔH^{o}_{298}, S^{o}_{298} and T^{o}_{fus} as well as ΔH^{o}_{fus} and ΔS^{o}_{fus} at the melting point were taken from Barin [89Bar]. Expressions for C_p were obtained by fitting the tabulated

values of Barin [89Bar]. Above the melting point, C_p(sol) was set equal to C_p(liq) and below the melting point, C_p(liq) was set equal to C_p(sol).

NiO:

Values of ΔH^o_{298}, S^o_{298}, ΔH^o_{fus}, ΔS^o_{fus} and T^o_{fus} were taken from Barin [89Bar]. Expressions for C_p were obtained by fitting the tabulated values of Barin [89Bar]. Above the melting point, C_p(sol) was set equal to C_p(liq). For C_p(liq), the expression obtained by fitting the data above the melting point was also used below the melting point.

PbO:

The same procedure was followed as for Na_2O.

SiO_2:

Enthalpy, entropy and heat capacity expressions for all solid phases were taken from Berman et al [85Ber2]. The melting point, and values of ΔH^o_{fus} and ΔS^o_{fus} at the melting point were taken from the JANAF Tables [85Jan]. An expression for C_p(liq) was obtained from the tabulated values in the JANAF Tables. Above the melting point, C_p(sol) was set equal to C_p(liq), while below the melting point C_p(liq) was set

equal to C_p of high cristobalite (the solid phase stable at the melting point).

$\underline{TiO_2}$:

Values of ΔH^o_{298}, S^o_{298} and C_p (sol) below the melting point were taken from Berman et al [85Ber2]. The melting point was taken from the JANAF Tables [85Jan], and an expression for C_p (liq) was obtained from the data in these tables. With the enthalpy of fusion of 16 ±4kcal/mol (66944 ±16700 J/mol) given in the JANAF Tables [85Jan], it was found to be very difficult to calculate the TiO_2-liquidus curves of the FeO-TiO_2, MnO-TiO_2 and MgO-TiO_2 systems unless very unlikely excess Gibbs energy expressions for the liquid solutions were invoked. Hence, we chose an optimized value of 11 kcal/mol (46024 J/mol) which reproduces well the liquidus curves in all these systems. Above the melting point, C_p (sol) was set equal to C_p (liq), and below the melting point C_p (liq) was set equal to C_p (sol).

$\underline{Ti_2O_3}$:

Values of ΔH^o_{298}, S^o_{298} and T^o_{fus} as well as ΔH^o_{fus} and ΔS^o_{fus} were taken from the JANAF Tables [85Jan]. Expressions for C_p were obtained by fitting the tabulated values in the JANAF Tables. Above the melting point, C_p (sol) was set equal to

C_p(liq), and below the melting point C_p(liq) was set equal to C_p(sol).

ZnO:

The same procedure was followed as for Na_2O.

ZrO_2:

The temperature of the transformation from the monoclinic to the tetragonal structure is given by Barin [89Bar] as 1205°C. A transformation from the tetragonal to a cubic structure has been reported at 2370°C [65Smi, 72Han, 72Nog] or at 2330°C [85She]. In the present assessment, a value of 2360°C was adopted.

Enthalpies, entropies and heat capacities of the monoclinic and tetragonal phases were taken from Barin [89Bar], the heat capacity expression being obtained by fitting the tabulated values. The entropy change of the tetragonal to cubic transformation was assumed to be the same as that for the transformation from monoclinic to tetragonal, and C_p of the cubic phase above 2360°C was taken from the tabulation of Barin [89Bar] even though Barin shows the tetragonal phase as being stable up to the melting point.

The melting temperature and the enthalpy and entropy of fusion at the melting temperature were taken from Barin [89Bar]. An expression for C_p(liq) was obtained by fitting the tabulated values of Barin above the melting point. This same expression was then used for C_p(liq) below the melting point. Above the melting point, C_p(sol) was set equal to C_p(liq).

2.3 BINARY SYSTEM EVALUATIONS

In this section, details of evaluations of 26 binary oxide systems will be discussed. The systems of $CaO-TiO_2$, $MnO-TiO_2$, $MgO-TiO_2$ were evaluated by Dr. N.G. Eriksson, using the program developed by the author. These are included here, because the binary evaluations are required for the later extension to ternary systems in Section 4. In addition, the optimizations of the $Al_2O_3-TiO_2$, Na_2O-TiO_2, K_2O-TiO_2 and $CaO-SiO_2$ systems were evaluated in large part by Dr. Eriksson with the author's assistance.

2.3.1 The MgO-MnO system

The solidus was measured by Schenck et al [64Sch] using a hot-stage microscope. Points shown in Fig. 2-1 are taken from the smoothed curve of these authors.

Activities of MgO in solid solutions in the range 890° to 1045°C were measured by Raghavan et al [85Rag] using galvanic cells with MgF_2 solid electrolytes. Their results are plotted in Fig. 2-2. Calculations of MgO activities were performed by Muan and co-workers [70Hah, 70Woe] based upon a study of the MgO-MnO-NiO ternary system at 1100°C. These calculations indicate larger positive deviations than those reported by Raghavan et al. In the present analysis, the data of Raghavan et al were used since these were directly measured for the

binary system and since they yield a very simple analysis for the system as discussed below.

The activities of MgO in the solid solution were represented by a regular solution model:

$$g^E(solid) = 9252\ X_{MgO}X_{MnO} \quad J/mol \qquad (2\text{-}3\text{-}1)$$

As can be seen in Fig. 2-2, this gives very good agreement with the measured activities, even as regards the temperature dependence.

Given the solidus and the thermodynamic properties of the solid phase, the liquidus and the thermodynamic properties of the liquid phase can be calculated thermodynamically if it assumed that s^E of the liquid is small [80Pel]. Such a calculation was performed, and the resulting liquid properties were then represented by the quasichemical model with:

$$\omega = 4184 \quad J/mol \qquad (2\text{-}3\text{-}2)$$

The calculated phase diagram is shown in Fig. 2-1. Positive deviations from ideality are greater in the solid solution than in the liquid solution. This is consistent with usual behaviour.

The enthalpy of mixing of solid solutions was measured at 40°C by Gripenberg et al [78Gri] who obtained h^E(sol) ≈ $20000X_{MgO}X_{MnO}$ J/mol. Combination of this with Eq (2-3-1) for g^E at ~950°C would give s^E(sol) ≈ 8.8 $X_{MgO}X_{MnO}$ J/mol.K. However, in view of the 1000° temperature difference between the measurements of Raghavan et al and Gripenberg et al and in view of the uncertainties in both these studies, it was assumed in the present analysis that g^E of Eq(1) is independent of temperature.

Probable maximum inaccuracy in assessed diagram:

± 50° for solidus,

± 100° for liquidus.

2.3.2 The $MnO-SiO_2$ system

Much of the early metallurgical and mineralogical work was reviewed by Doerinckel [11Doe] who also made a systematic investigation of the phase diagram at lower temperatures. Work up to 1962 has been reviewed [58Gla, 62Sin]. A congruent melting point of 1210°C for rhodonite ($MnSiO_3$) was reported by Lebedev [11Leb]. Kallenberg [14Kal] reported the congruent melting of tephroite (Mn_2SiO_4) at 1210°C. Smolenskii [12Smo] showed rhodonite melting congruently at 1220°C. Jaeger and van Klooster [16Jae] gave the melting point of artificial rhodonite as 1273°C, and claimed two transitions at 1208°C and 1120°C. They reported that a natural tephroite specimen melted at 1290°C. Three compounds were reported by Glaser [26Gla]. Tephroite and rhodonite were reported as melting congruently at 1310° and 1273°C respectively and an inversion in rhodonite was found at 1210°C. The third compound, $Mn_3Si_2O_7$, was described as a "manganese justite", melting incongruently at 1200°C. No other authors have reported this compound. Both Herty [30Her] and White et al [34Whi] showed rhodonite as melting incongruently, while Voos [35Voo] reported congruent melting at 1205°C. Greig [27Gre] determined that a mixture with 9 mol% MnO formed two immiscible liquids at 1725°C.

In most of these early experiments (except those of Voos [35Voo]) the partial pressure of O_2 was large enough to give

rise to significant amounts of Mn^{3+}. This could explain the low reported melting temperatures. To exclude Mn^{3+}, Glasser [58Gla] studied the system by a quenching technique in 5:1 CO_2/H_2 mixtures with p_{O_2} varying from 6×10^{-8} to 4×10^{-6} atm between 1400° and 1600°C. Rhodonite was found to melt incongruently at 1293°C, and tephroite to melt congruently at 1347°C. Eutectics were reported at 1319°C at 28.8 mol% SiO_2 and at 1253°C at 42.3 mol% SiO_2. A range of liquid immiscibility from 59 to 99 mol% SiO_2 at a monotectic temperature of 1708°C was reported.

In the experiments of Singleton et al [62Sin], samples were contained in Mo crucibles. Molybdenum contamination of up to 2% was noted. For firing above 1000°C, an atmosphere of He was used. Analysis was by X-ray and optical methods.

The diagrams of Glasser [58Gla] and Singleton et al [62Sin] are very similar. Several data points are shown in Fig. 2-3.

Points on the SiO_2-liquidus from Turkdogan and Hancock [58Tur] are also shown in Fig. 2-3. These were measured at carbon saturation at $p_{CO} = 1$ atm. Oxygen pressures varied from 7×10^{-17} atm at 1400°C to 4×10^{-16} atm at 1600°C. A SiO_2-liquidus point at 1650°C obtained by Davies [55Dav] at an unspecified oxygen pressure is also shown in Fig. 2-3.

MnO activities in the liquid were measured over the entire liquid range at 1400°, 1500° and 1600°C by Rao and Gaskell [81Rao1] by establishing equilibrium with an atmosphere of known p_{O_2} and a Pt-Mn foil in which the manganese activity was measured by the same authors. The data are reproduced in Fig. 2-4. MnO activities obtained at 1550°C by Schenck et al [61Sch1] by measuring the Mn distribution between slag and iron phases are in excellent agreement with those of Rao and Gaskell. However, in other studies [60Abr, 65Meh] activities up to 0.1 higher than those of Rao and Gaskell were reported. The reason for the difference is not evident. The measurements of Rao and Gaskell seem to be very carefully performed, and their data were used in the present optimization.

From discontinuities in the slope of a_{MnO} versus X_{MnO} in the curves of Rao and Gaskell, Fig. 2-4, compositions on the SiO_2-liquidus were determined at three temperatures. These are shown in Fig. 2-3. Since these points were obtained by an equilibrium technique (as opposed to a quenching technique), they have been given preference.

Gibbs energies of formation of tephroite and rhodonite were measured [87Rog] with galvanic cells with solid electrolytes. These results do not differ significantly from the data compiled by Robie et al [78Rob]. Data for ΔH°_{298},

S°_{298} and C_p were thus taken from Robie et al. In the optimization, ΔH°_{298} was changed by 3406 J/mol for Mn_2SiO_4 and -2141 J/mol for $MnSiO_3$. These changes are well within the uncertainties given by Robie et al.

The phase diagram and activity data were optimized simultaneously to give, for the liquid:

$$\omega = -79956 + 228819\ y^7_{SiO_2} \quad J/mol \qquad (2\text{-}3\text{-}3)$$

$$\eta = -20.920 + 62.760\ y^7_{SiO_2} \quad J/mol\ K \qquad (2\text{-}3\text{-}4)$$

Although the consolute temperature T_c of the liquid miscibility gap is unknown, the η_7 term in Eq (2-3-4) was added to give $T_c = 2200^{\circ}C$ which is close to the measured T_c in the $MgO\text{-}SiO_2$ and $CaO\text{-}SiO_2$ systems in which similar terms were required.

The phase diagram drawn in Fig. 2-3, and the activity curves in Fig. 2-4, are calculated from the optimized parameters.

Probable maximum inaccuracy in assessed diagram:
$\pm 5^{\circ}$ in central composition region, ±1 mol% for MnO- and SiO_2-liquidus curves.

2.3.3 The $MgO-SiO_2$ system

The calculated optimized phase diagram is shown in Fig. 2-5.

The system was studied by Bowen and Andersen [14Bow] by quenching and analysis. They reported a congruent melting point of forsterite, Mg_2SiO_4, of 1888°C and an incongruent melting of protoenstatite, $MgSiO_3$, at 1557°C, with a peritectic liquid composition of 51.0 mol% SiO_2. A eutectic involving $MgSiO_3$ and cristobalite, SiO_2, was reported at 1543°C with the eutectic liquid at 55.3 mol% SiO_2.

The eutectic involving Mg_2SiO_4 and periclase, MgO, was reported by Schlaudt and Roy [65Sch] to lie at 1863°C. These authors also reported an extensive solubility of SiO_2 in MgO (up to 10 mol% at 1863°C) and a solubility of MgO in forsterite of approximately 0.5 mol %. However, Henriksen and Kingery [79Hen], employing scanning electron microscopy and X-ray techniques, found a solubility of SiO_2 in MgO of less than 0.34 mol% at 1850°C. Considering the difference in crystal structure between these two compounds, appreciable solid solubility seems unlikely. In the present assessment all solid phases were assumed to be stoichiometric.

Greig [27Gre] reported a liquid-liquid miscibility gap extending over the range $0.60 < X_{SiO_2} < 0.985$ at the

monotectic temperature of 1694°C. Ol'shanskii [51Ols] and Hageman and Oonk [86Hag1] determined the miscibility gap boundaries by quenching experiments. The former reported a consolute temperature of 2200°C, whereas the latter gave 1990°C. The work of Hageman and Oonk, in this and other studies, appears to have been carefully performed, and so their data have been given precedence in the present analysis.

Activities of SiO_2 in the liquid phase were determined by Rein and Chipman [65Rei] at 1600°C by measuring the distribution of Si between the slag and an Fe-Si-C alloy saturated either with graphite or SiC. Kambayashi and Kato [83Kam, 84Kam] measured both SiO_2 and MgO activities by mass spectrometry at 1600° and 1700°C. The results of the two studies are in good agreement as can be seen in Fig. 2-6.

The optimization of the data yielded the following quasichemical parameters for the liquid:

$$\omega = -86090 - 48974 y_{SiO_2} + 328109 y_{SiO_2}^7 \quad J/mol \quad (2\text{-}3\text{-}5)$$

$$\eta = -37.656 y_{SiO_2} + 125.52 y_{SiO_2}^7 \quad J/mol.K \quad (2\text{-}3\text{-}6)$$

Data for S°_{298} and Cp of Mg_2SiO_4 and $MgSiO_3$ were taken from Berman et al [85Ber2]. ΔH°_{298} values from this reference were changed by -3206 and 453 J/mol for Mg_2SiO_4 and $MgSiO_3$ respectively in order to reproduce the measured melting points. These changes are within the stated [85Jan] uncertainties.

All data were reproduced very well by the optimization as can be seen in Figs. 2-5 and 2-6.

Probable maximum inaccuracy in assessed diagram:

$\pm 10^{\circ}$, $\pm 50^{\circ}$ for MgO-liquidus, $\pm 100^{\circ}$ for miscibility gap boundary.

2.3.4 The $CaO-SiO_2$ system

The optimized phase diagram is shown in Fig. 2-7.

In the first complete study of the phase diagram, Rankin and Wright [15Ran] determined the melting points of Ca_2SiO_4 and $CaSiO_3$ (pseudowollastonite) as 2126°C and 1540°C respectively. Rankinite ($Ca_3Si_2O_7$) was reported to melt peritectically at 1475°C. Eutectics were reported at 2061°C at 31.0 mol% SiO_2, 1455°C at 43.8 mol% SiO_2, and 1436°C at 61 mol% SiO_2. Greig [27Gre] reported points on the SiO_2-liquidus as shown in Fig. 2-7.

Osborn [43Osb], also using quenching techniques, reported that $Ca_3Si_2O_7$ melts peritectically at 1464°C, with the eutectic at 1460°C.

Troemel et al [69Tro2] employed DTA and high temperature X-ray techniques to measure the solubility of CaO in Ca_2SiO_4. Their reported solubility limits are shown in Fig. 2-7.

Rankin and Wright [15Ran] reported that Ca_3SiO_5 (hatrurite) decomposes to CaO and Ca_2SiO_4 at 1900°C. Troemel et al [69Tro2] found this compound to be stable only between 1300° and 1800°C. Meyers [30Mey] and Carlson [31Car] found that it is unstable below 1300°C. In contrast to these studies, others have reported Ca_3SiO_5 to melt congruently at

a temperature above 2000°C [48Zaw] or incongruently at 2073°C [59Wel].

The liquid-liquid miscibility gap has been studied by quenching techniques by several authors. The results of Greig [27Gre] show a gap extending from 71 to 99 mol% SiO_2 at a monotectic temperature of 1697°C. These results have been confirmed [51Ols, 56Tor]. Tewhey and Hess [79Tew] reported a gap from 72 to 98 mol% SiO_2 at a monotectic temperature of 1695°C, with a consolute point at 1871°C and 91 mol% SiO_2. The data points of these authors are shown on Fig. 2-7, as are those of Hageman et al [86Hag2] which are in close agreement. Earlier measurements [51Ols, 56Tor] indicated a much higher consolute temperature. In the present analysis, preference has been given to the later measurements which seem to have been carefully performed.

SiO_2 and CaO activities have been the subject of several studies which are reviewed by Rein and Chipman [65Rei]. These authors themselves measured silica activities by determining Si activities in slag/metal/graphite/gas systems at fixed p_{CO}. Other experimental methods involved gas/slag equilibria [57Car, 62Sha] and measurements of p_{CO} over slag/graphite/SiC systems [58Bai, 60Kay]. Selected data points from these studies are plotted on Figs 2-8 and 2-9.

C_p data for all intermediate compounds were taken from Berman and Brown [85Ber1, 86Ber]. Values of ΔH^o_{298} and S^o_{298} were taken from the literature for $CaSiO_3$ [85Ber2], $Ca_3Si_2O_7$ and Ca_3SiO_5 [89Bar], and Ca_2SiO_4 [78Rob]. The ΔH^o_{298} values were then adjusted in the optimization by -1079, -18155, -4123 and -66 J/mol respectively. The S^o_{298} value of Ca_3SiO_5 was adjusted by -0.803 J/mol.K. All these changes lie within reported uncertainties except for the case of $Ca_3Si_2O_7$ for which an uncertainty of 10500 J/mol is given [73Spe] for ΔH^o_{298}. On the other hand, ΔH^o_{298} of this compound differs by 21000 J/mol between older [77Bar] and more recent [89Bar] compilations.

For the liquid phase, the following quasichemical parameters were obtained in the optimization:

$$\omega = -158218 - 37932\, y_{SiO_2} - 90148\, y^5_{SiO_2} + 439893\, y^7_{SiO_2} \quad J/mol \qquad (2\text{-}3\text{-}7)$$

$$\eta = -19.456 + 133.888\, y^7_{SiO_2} \quad J/mol.K \qquad (2\text{-}3\text{-}8)$$

Calculated activities in the liquid are shown in Figs 2-8 and 2-9. Agreement with the measurements is within error limits.

For the non-stoichiometry of Ca_2SiO_4, a general defect model developed by Li and Pelton in this laboratory was used with energy parameters for the formation of both majority defects equal to 473378 + 31.38 T J/mol for α-Ca_2SiO_4 and 467254 + 31.38 T J/mol for a'-Ca_2SiO_4. This model will be discussed in future publications. The reported non-stoichiometry [69Tro2] is reproduced very closely. The invariant temperature for the three-phase (α-Ca_2SiO_4 + α'-Ca_2SiO_4 + $Ca_3Si_2O_7$) equilibrium is calculated as 1437°C which is the transformation temperature for the α' to α transformation of Ca_2SiO_4 given by Berman et al [85Ber2]. The three-phase (α-Ca_2SiO_4 + α'-Ca_2SiO_4 + Ca_3SiO_5) invariant temperature is calculated at 1447°C with the α and α' phases at this temperature containing 33.0 and 32.9 mol% SiO_2 respectively.

Probable maximum inaccuracy in assessed diagram:

±5° to 15°, ±1 mol %;

±50° for consolute T;

±50° for Ca_3SiO_5 range of stability.

2.3.5 The $FeO-SiO_2$ system

The calculated optimized phase diagram shown in Fig. 2-10 is for the system in equilibrium with metallic Fe with all Fe^{3+} converted to "FeO". That is, the composition axis is to be interpreted as $X_{SiO_2} = n_{Si} / (n_{Si} + n_{Fe^{2+}} + n_{Fe^{3+}})$ where n_i is the number of moles of species i, and the diagram is at unit Fe activity. The Fe^{3+} content of the liquid in equilibrium with Fe varies from approximately 10 mol% for pure "FeO" to about 3% at $X_{SiO_2} = 0.33$ [55All] depending upon the temperature.

Bowen and Schairer [32Bow] studied the equilibrium diagram using Fe crucibles under N_2 atmospheres. As pointed out by Allen and Snow [55All], Bowen and Schairer made an error in converting Fe^{3+} to "FeO". Their data points shown in Fig. 2-10 have been corrected. They reported fayalite, Fe_2SiO_4, melting at 1205°C with two eutectics at 1177°C and 27 mol% SiO_2 and at 1178°C and 42 mol% SiO_2. The system was later studied at compositions between FeO and Fe_2SiO_4 by Allen and Snow [55All] using Fe crucibles in $CO/CO_2/N_2$ atmospheres. They reported the eutectic at 1177°C and 24.7 mol% SiO_2. Measurements of Schuhmann and Ensio [51Sch], also shown in Fig. 2-10, are in good agreement with the other studies.

A liquid-liquid miscibility gap extending from 64 to 97.5 mol% SiO_2 at a monotectic temperature of 1690°C was reported by Greig [27Gre].

No solid solubilities were reported in any of the studies.

Activities of FeO in the liquid were first measured by Schuhmann and Ensio [51Sch] by equilibration of the melts, held in Fe crucibles, with CO/CO_2 mixtures in the range 1263° to 1364°C. No temperature dependence of the activities was found. Similar studies by Bodsworth [59Bod], using H_2/H_2O mixtures in the range 1265° to 1365°C, agreed very closely with those of Schuhmann and Ensio. Again, no temperature dependence of the activities was observed. Ban-ya et al [80Ban] performed measurements at 1400°C by the same technique. Their results also agree very closely with those of Schuhmann and Ensio. Dhima et al [86Dhi], using mass spectrometry at 1400°C, obtained results in reasonable agreement with those of the other studies. Activities at higher temperatures in the range 1785° to 1960°C were measured by Distin et al [71Dis] by levitation melting followed by sampling and analysis. They observed a temperature dependence, with a_{FeO} in slags at X_{SiO2} = 0.5 increasing by approximately 0.03 from 1785° to 1960°C. For the sake of

clarity, only the points of Schuhmann and Ensio at 1325°C and of Distin et al at 1880°C are shown in Fig. 2-11.

The enthalpy of mixing of liquid FeO and solid SiO_2 at 1420°C were measured calorimetrically by Ban-ya et al [82Ban1]. Their data points are shown in Fig. 2-12.

The data were optimized to yield the following quasichemical parameters for the liquid phase:

$$\omega = -17697 - 38528y_{SiO_2} + 842570y_{SiO_2}^5 - 1549201y_{SiO_2}^6 + 962015y_{SiO_2}^7 \ J/mol \qquad (2\text{-}3\text{-}9)$$

$$\eta = -16.736 + 62.76y_{SiO_2}^7 \ J/mol.K \qquad (2\text{-}3\text{-}10)$$

S^o_{298} and C_p of Fe_2SiO_4 were taken from Berman et al [85Ber2] while ΔH^o_{298} from this source was changed by -2213 J/mol in order to reproduce the melting point of 1205°C. This change is less than the stated [78Rob] uncertainty of 2410 J/mol.

All the data in Figs. 2-10, 2-11 and 2-12 are well reproduced. The temperature dependence of the activity of FeO

in the liquid as reported by Distin et al [71Dis] is also closely reproduced.

Although the consolute temperature of the liquid-liquid miscibility gap has not been reported, it is expected to be of the order of 2000°C as in the $CaO-SiO_2$ and $MgO-SiO_2$ systems. Accordingly, the η_7 term in Eq (2-3-10) was added. This gives a consolute temperature of 1996°C.

Probable maximum inaccuracy in assessed diagram: ± 10° for $X_{SiO_2} < 0.45$, ± 2 mol% for silica liquidus.

2.3.6 The Na_2O-SiO_2 system

The calculated optimized phase diagram is shown in Fig. 2-13. Compositions on Fig. 2-13 and in the following text are given in terms of the components $NaO_{0.5}$-SiO_2.

The assessment is based largely upon the phase diagram studies of Kracek [30Kra2, 39Kra] who used quenching techniques supplemented by heating curves. He reported that the compounds Na_2SiO_3 and $Na_2Si_2O_5$ melt congruently at 1090°C and 875°C respectively. Eutectics were reported at 847°C at 46 mol % SiO_2 and 794°C at 59 mol % SiO_2. D'Ans and Loeffler [30Dan], in excellent agreement with Kracek, reported congruent melting of Na_2SiO_3 at 1090°C and of $Na_2Si_2O_5$ at 875°C, with eutectics at 841°C at 44.4 mol % SiO_2 and 794°C at 59 mol % SiO_2.

The compound Na_4SiO_4 was reported by Kracek [30Kra2] to melt peritectically at 1119°C with a eutectic at 1023°C at 28 mol % SiO_2. Since the accepted melting point of Na_2O is 1132°C [85Jan], and since no compounds with compositions between Na_2O and Na_4SiO_4 have been reported, the peritectic melting of Na_4SiO_4 seems unlikely. In fact, D'Ans and Loeffler [30Dan] (see also [69Loe]) reported that Na_4SiO_4 melts congruently at 1085°C. They also reported another compound, $Na_6Si_2O_7$, with a congruent melting point of 1124°C

and eutectics at 1002°C and 22 mol % SiO_2 and at 1016°C at 29.5 mol % SiO_2.

Another compound, $Na_2Si_3O_7$ was reported by Matveev [56Mat]. Williamson and Glasser [65Wil], by XRD, showed the correct stoichiometry to be $Na_6Si_8O_{19}$. They reported that this compound melts incongruently at 809°C to quartz plus liquid and decomposes below 700°C to quartz plus $Na_2Si_2O_5$. However, both Kracek [30Kra2] and D'Ans and Loeffler [30Dan] reported a eutectic at 794°C at a SiO_2 concentration higher than that of $Na_6Si_8O_{19}$. This is inconsistent with the incongruent melting of $Na_6Si_8O_{19}$ to liquid plus quartz. In the present assessment, $Na_6Si_8O_{19}$ has been assumed to melt incongruently at 809°C as reported [65Wil], but to liquid plus $Na_2Si_2O_5$.

Wollast [61Wol] proposed extensive solubility of Na_2O in cristobalite and tridymite. Crystallographic considerations make this proposal doubtful and no solubility of Na_2O in solid silica was assumed in the present analysis.

Haller et al [74Hal] measured the boundary of the metastable two-liquid region by determining opalescence temperatures. Their experimental points are shown in Fig. 2-13.

Activities of Na_2O in the liquid have been reported by several researchers [73Fro, 75Rav, 79Koh, 80Neu, 80Sha, 82Yam, 85Tsu, 87Shu], generally with good agreement. Some results are plotted in Fig. 2-14. In the present assessment, most weight was accorded to the results of Yamaguchi et al [82Yam] who made measurements over a wide range of composition and temperature with a galvanic cell using a beta-alumina solid electrolyte.

For Na_2SiO_3 and $Na_2Si_2O_5$, ΔH°_{298} and S°_{298} were taken from the JANAF Tables [85Jan], while C_p was taken from Berman and Brown [85Ber1, 86Ber]. Above 678° C, in the case of $Na_2Si_2O_5$, C_p was taken from Barin et al [77Bar]. For Na_4SiO_4, all thermodynamic data were taken from Barin et al [77Bar]. In the optimization, these values of ΔH°_{298} of Na_2SiO_3, $Na_2Si_2O_5$ and Na_4SiO_4 were adjusted by 2826, -274, and 5347 J/mol respectively, the stated uncertainties being 4200 J/mol for Na_2SiO_3 and $Na_2Si_2O_5$ [85Jan] and 21000 J/mol for Na_4SiO_4 [77Bar]. For $Na_6Si_2O_7$ and $Na_6Si_8O_{19}$, C_p was estimated by the method of Berman and Brown [85Ber1, 86Ber]. Values of ΔH°_{298} and S°_{298} of $Na_6Si_8O_{19}$ were then chosen to reproduce the peritectic and eutectoid temperatures of 809° C and 700° C. For $Na_6Si_2O_7$, values of ΔH°_{298} and S°_{298} were chosen to reproduce the reported [30Dan] melting point and the two reported eutectic temperatures. The calculations then indicate that

$Na_6Si_2O_7$ decomposes eutectoidally below 782°C. This is shown only very tentatively in Fig. 2-13.

The following quasichemical parameters were obtained for the liquid phase:

$$\omega = -114344 - 381595\, y_{SiO_2} + 123010\, y^7_{SiO_2} \quad J/mol \qquad (2\text{-}3\text{-}11)$$

$$\eta = -43.932 - 20.920\, y^7_{SiO_2} \quad J/mol.K \qquad (2\text{-}3\text{-}12)$$

The measured phase diagram is reproduced very well, as are the activity measurements in Fig. 2-14. The calculated metastable liquid-liquid miscibility gap and spinodals are shown on Fig. 2-13. The consolute point agrees with the measured [74Hal], although the calculated gap is narrower than the reported gap.

Near the melting point of SiO_2, the calculated liquidus does not agree well with the points of Kracek [30Kra2]. The quasichemical model which was used for the liquid supposes that Na_2O in solution dissociates into two independent Na^+ ions. It can be argued that in solutions which are very rich in SiO_2, sodium ions actually form Na_2^{2+} groupings around "broken oxygen bridges" (Si-O$^-$ $^-$O-Si). This would give a

limiting liquidus slope at pure SiO_2 of one-half the calculated value shown in Fig. 2-13, thereby giving a liquidus closer to Kracek's points. On the other hand, measurements at very high temperatures in very viscous liquids are difficult. Evaporation of Na_2O during the experiments would shift the liquidus to higher temperatures.

One would expect that the same discrepancies, whatever their cause, would also appear in the optimized K_2O-SiO_2 phase diagram. However, at high SiO_2 contents the K_2O-SiO_2 liquidus, also measured by Kracek, was fitted very well by the quasichemical model. A very tentative explanation is that there is some solubility of Na_2O in solid SiO_2, although much less than proposed by Wollast [61Wol]. This would shift the liquidus to higher Na_2O contents. In the case of K_2O, this solubility would be expected to be smaller.

Probable maximum inaccuracy in assessed diagram:
$\pm 10^{\circ}$ for $X_{SiO_2} > 0.75$, $\pm 50^{\circ}$

2.3.7 The K_2O-SiO_2 system

The calculated equilibrium diagram is plotted in Fig. 2-15. Compositions are given relative to the components $KO_{0.5}$-SiO_2.

The equilibrium diagram in the composition range from K_2SiO_3 to SiO_2 was measured by Kracek et al [30Kra1, 37Kra] by quenching techniques. Liquidus data points are shown in Fig. 2-15. Melting points of K_2SiO_3, $K_2Si_2O_5$ and $K_2Si_4O_9$ were reported as 977°, 1046° and 771°C respectively. Three eutectics were reported at 781°, 743° and 770° at 39.6, 62.1 and 67.4 mol % SiO_2 respectively (relative to the components $KO_{0.5}$-SiO_2).

Wollast [61Wol] proposed that K_2O is soluble in solid SiO_2. However, this seems unlikely from structural considerations.

Activities of $KO_{0.5}$ in the liquid solutions have been measured [73Fro, 75Rav] by galvanic cell techniques in the temperature range 850° to 1100°C. Data points at 1100°C are plotted in Fig. 2-16. Steiler [82Ste] used a thermogravimetric method, monitoring the weight change during equilibration of slags with a gas of fixed oxygen potential at 1300°, 1400° and 1500°C. Data points are shown in Fig. 2-16. Defining a common reference and extrapolating his data to

1100°C, Steiler demonstrated that his results were in agreement with the previous studies as shown in Fig. 2-16.

For the compounds K_2SiO_3 and $K_2Si_2O_5$, heat capacities were taken from Berman and Brown [85Ber1, 86Ber] and values of ΔH^o_{298} and S^o_{298} were taken from the JANAF Tables [85Jan] and Spencer [73Spe] respectively. For $K_2Si_4O_9$, the data of Barin [89Bar], which are based mainly on estimations, were used. In order to reproduce the measured melting points of the compounds in the optimization, ΔH^o_{298} of K_2SiO_3, $K_2Si_2O_5$ and $K_2Si_4O_9$ were changed by -12282, -13397 and -22765 J/mol respectively which may be compared to the stated uncertainties of 8400 [85Jan], 12600 [73Spe] and 12600 [73Spe] J/mol.

For the liquid solution, the following quasichemical parameters were obtained:

$$\omega = -409986 - 1647688\, y^6_{SiO_2} + 1593677\, y^7_{SiO_2} \quad J/mol \qquad (2\text{-}3\text{-}13)$$

$$\eta = -58.576 + 33.472\, y^7_{SiO_2} \quad J/mol.K \qquad (2\text{-}3\text{-}14)$$

The calculated phase diagram, Fig. 2-15, is in good agreement with the measurements. The calculated liquid activities in Fig. 2-16 agree with the measurements within error limits.

The calculated metastable liquid (glass) spinodals are also plotted in Fig. 2-15. The calculated consolute temperature is 788°C.

Probable maximum inaccuracy in assessed diagram: ±15° and ±2 mol % for SiO_2-liquidus.

2.3.8 The SiO_2-TiO_2 system

The optimized diagram is shown in Fig. 2-17.

Most early investigations [08Rie, 33Bun, 36Bog, 51Ric] failed to report the liquid immiscibility, even though a two-liquid region was found by Umezu and Kakiuchi [30Ume]. In a study of the CaO-TiO_2-SiO_2 system, DeVries et al [55Dev] found a large region of liquid immiscibility in mixtures containing as little as 2 wt% CaO. Hence, they reinvestigated the SiO_2-TiO_2 binary system [54Dev2] by quenching techniques combined with polarizing microscopy and X-ray diffraction. A monotectic extending from 15 to 92 mol% TiO_2 at 1783 ± 10°C and a eutectic at 8 mol% TiO_2 at 1552 ±4°C were reported. Solid solubility in the system was said to be negligible.

The reported [54Dev2] melting point of TiO_2 of 1833°C differs by 24° from the assessed value [71Jan] of 1857°C. Hence, it was assumed that the reported monotectic temperature of 1783°C is also too low by 24°C, and in Fig. 2-17 a monotectic temperature of 1807°C was chosen.

The optimization yielded the following quasichemical liquid parameters:

$$\omega = 28847 + 52091 y_{TiO_2} - 44484 y_{TiO_2}^3 \quad J/mol \quad (2\text{-}3\text{-}15)$$

Probable maximum inaccuracy in assessed diagram: $\pm 30^{\circ}$, ± 4 mol% for monotectic, $\pm 10^{\circ}$, ± 1.5 mol% for eutectic.

2.3.9 The ZrO_2-SiO_2 system

The optimized phase diagram is shown in Fig. 2-18.

Liquid immiscibility was first reported by [32Bar]. In the work of [56Tor], a monotectic temperature of 2250°C with a gap extending from 41 to 62 wt. % ZrO_2 at this temperature was reported along with a consolute point at 2430°C at 53 wt. % SiO_2. Jones et al [67Jon] later confirmed the existence of this immiscibility gap in their study of the SiO_2-ZrO_2-FeO ternary system.

The eutectic was reported at 1687 $\pm$ 4°C and 97 wt.% SiO_2 [67But]; at 1675°C [49Gel]; and at 1677°C and 97 wt.% SiO_2 [53Cur].

The diagrams of [56Tor, 49Gel, 53Cur, 34Zhi] all show SiO_2 as soluble from 3 to 10 wt. % in solid ZrO_2. However, a later study [65Lan] by high temperature X-ray diffraction showed that the solid solubility does not exceed 0.1 wt.%.

A controversy surrounds the melting or dissociation temperature of zircon, $ZrSiO_4$, which has been reported to melt congruently at 2550°C [20Was] or 2430°C [34Zhi]; or to melt incongruently at 1775°C [49Gel] or 1720°C [58Coc]; or to decompose to SiO_2 and ZrO_2 at 1538°C [53Cur] or 1676°C [67But]. To attempt to resolve this controversy, [76Ans]

carried out tests on high purity (99.13%) Australian zircon. They observed solid state dissociation to begin between 1525°C and 1550°C, although the degree of dissociation remained small until the samples were heated above 1650°C. It thus appears that the kinetics of dissociation are slow, but that the equilibrium dissociation temperature is probably near that proposed by [53Cur], that is 1538°C.

C_p and S°_{298} for $ZrSiO_4$ were taken from [89Bar]. In order to reproduce the peritectoid at 1538°C, ΔH°_{298} was changed by -4338 J/mol from that given by [89Bar]. This is within the error limits of $\pm$ 6276 J (1500 cal) given by [89Bar]. If the higher dissociation temperature of 1676°C of [67But] is accepted, then a change of -6694 J is required which is outside the stated error limits. Hence, the thermodynamic data also tend to support the lower dissociation temperature.

Three parameters of the liquid quasichemical model were required to give a satisfactory optimization:

$$\omega = 4184 + 40585\, y_{SiO_2} - 11715\, y^7_{SiO_2} \quad Joules \quad (2\text{-}3\text{-}16)$$

Probable maximum inaccuracy in assessed diagram: ±30°, ±4 mol% for monotectic, ±10°, ±1.5 mol% for eutectic.

2.3.10 The Al_2O_3-TiO_2 system

The optimized phase diagram is plotted in Fig. 2-19 where the components have been chosen as $AlO_{1.5}$ and TiO_2.

The diagram was first studied by von Wartenberg and Reusch [32Von1] and by Bunting [33Bun]. The former gave the intermediate compound as $Al_2Ti_2O_7$, while the latter reported Al_2TiO_5 (tialite). The phase relationships reported by Lang et al [52Lan] from visual techniques combined with petrographic and X-ray studies suggest that tialite melts congruently at 1863°C, but due to extreme experimental difficulties due to the high temperatures and high melt viscosity, the possibility of incongruent melting could not be ruled out. These authors [52Lan] quote 1823°C as a transformation temperature of tialite. However, this finding is in doubt according to Azimov et al [84Azi].

Solid solubility of Al_2O_3 in tialite could not be ruled out [52Lan]. Solid solubility of TiO_2 in Al_2O_3 was reported [68Gol] as 0.6 mol %, while no solubility of Al_2O_3 in TiO_2 was detected. In the present assessment, no solid solubilities were assumed.

Goldberg [68Gol] reported a congruent melting point of tialite of 1850°C and, from micrographic studies, a eutectic at 1703°C and 67 mol % TiO_2 (calculated for the components

$AlO_{1.5}$-TiO_2). Lejus et al [66Lej] found two new compounds with compositions between 75 and 80 mol% $AlO_{1.5}$ which are stable in the approximate temperature range between 1800° and 1900°C. In the present analysis, these were both approximated by the one compound Al_4TiO_8.

No activity measurements have been reported for this system.

The temperature below which Al_2TiO_5 decomposes to Al_2O_3 and TiO_2 has been determined by Kato et al [80Kat] as 1280°C and by Woermann [90Woe] as 1264°C. Kato et al [80Kat] give a review of earlier work in which values for this temperature vary over the range from 1200° to 1300°C. The most recent value [90Woe] was adopted in the present assessment.

An optimization was performed in order to reproduce the eutectic temperature and composition and to have Al_2TiO_5 melting congruently near 1850°C and decomposing eutectoidally below 1264°C. The following two quasichemical parameters were obtained for the liquid:

$$\omega = 16023\ y_{TiO_2} + 3856\ y_{TiO_2}^2 \quad J/mol \qquad (2\text{-}3\text{-}17)$$

C_p of Al_2TiO_5 was taken from Berman and Brown [85Ber1, 86Ber] while S^o_{298} and ΔH^o_{298} were chosen to fit the diagram. No data for ΔH^o_{298} were found in the literature, but S^o_{298} is reported by Robie et al [78Rob]. The optimized value of S^o_{298} differs from this value by 18.8 J/mol.K which is far outside the stated [78Rob] uncertainty. In assessments of similar Al_2O_3- and TiO_2-containing systems, we have found that the liquid phase can generally be optimized with a few small terms as in Eq (2-3-17). Unless tialite is calculated as incongruently melting, the only way to achieve this in the present case is to change S^o_{298} as discussed above. However, this change is acceptable if the value of Robie et al is considered to apply to the low-temperature ordered compound while the present optimization is for the high-temperature disordered phase.

For Al_4TiO_8, C_p was predicted by the method of Berman and Brown [85Ber1, 86Ber] while ΔH^o_{298} and S^o_{298} were obtained from the phase diagram analysis in order to give a stability range between 1800° and 1900°C.

Probable maximum inaccuracy in assessed diagram: ±25° to ±75°C

2.3.11 The Na_2O-Al_2O_3 system

The optimized phase diagram is plotted in Fig. 2-20.

Earlier phase equilibrium studies were reviewed by DeVries and Roth [69Dev] who proposed a composite diagram. Rolin and Thanh [65Rol] used cooling curve techniques in argon atmospheres to obtain the liquidus points shown in Fig. 2-20. The compound $NaAlO_2$ was reported to melt at 1582°C. These authors also observed thermal arrests at 2003°, 1582° and 1412°C. These they attributed respectively to the incongruent melting of β-alumina (which they designated as $NaAl_{11}O_{17}$), the incongruent melting of β"-alumina (designated as $Na_2Al_{12}O_{19}$), and a eutectic involving β"-alumina and $NaAlO_2$. DeVries and Roth, on the other hand, attributed the thermal effect at 1412°C to a phase transformation of $NaAlO_2$, and proposed that a eutectic reaction occurs at 1582°C. Kay and Subbarao [75Kay] reported that β"-alumina decomposes at 1450°C. Dzieciuch and Weber [67Dzi] reported a eutectic temperature of 1595°C. Later, Weber and Venero [70Web] revised this temperature to 1585°C. They also reported some liquidus points which are shown on Fig. 2-20, and proposed a eutectic liquid composition of 65 mol% Al_2O_3.

These authors [70Web] reported a melting point of $NaAlO_2$ of 1867°C which is much higher that the values of 1582°C [65Rol] and 1650°C [23Mat] reported earlier, but in agreement

with a previously estimated value of 1850°C [56Sch]. Losses of Na_2O by volatilization may have been responsible for the lower reported values. In the assessed diagram, Fig. 2-20, the higher temperature has been adopted.

Early studies of β- and β"-alumina have been reviewed by Kummer [72Kum]. The homogeneity ranges of β-alumina (nominally $Na_2O.11Al_2O_3$ for a perfect crystal structure) and β"-alumina (nominally $Na_2O.6Al_2O_3$) were found by Jacob et al [91Jac], by electron probe microanalysis at 900°C, to range from $Na_2O.8.1Al_2O_3$ to $Na_2O.9.5Al_2O_3$ in the case of β-alumina and from $Na_2O.5.3Al_2O_3$ to $Na_2O.6.5Al_2O_3$ in the case of β"-alumina. In the present analysis, these were approximated as stoichiometric compounds with the formulae $Na_2O.9Al_2O_3$ and $Na_2O.6Al_2O_3$.

Many thermodynamic studies have been reported on the activity of Na_2O in two-phase (Al_2O_3 + β-alumina) mixtures [73Cho, 77Fra, 81Dub, 82Rog, 83Bri, 84Elr, 85Ito, 85Kum2, 91Jac] and in two-phase (β-alumina + β"-alumina) mixtures [82Rog, 84Elr, 85Ito, 86Cho, 91Jac] for the approximate temperature range from 500° to 1200° C. These studies are generally in fair agreement. The most recent values [91Jac] lie at approximately the mean of the other studies and so were adopted in the present analysis. Jacob et al [91Jac] also report activities of Na_2O in (β" alumina + $NaAlO_2$) mixtures.

From the measured Na_2O activities in the two-phase regions, Gibbs energies of formation of β-alumina, β"-alumina and $NaAlO_2$ from Na_2O and Al_2O_3 can be calculated. In the present analysis, C_p of $NaAlO_2$ was taken from Barin [89Bar], while C_p for β- and β"-alumina were obtained from the estimation technique of Berman and Brown [85Ber1, 86Ber]. Values of ΔH°_{298} and S°_{298} were then chosen so as to fit the values of the Gibbs energies of formation calculated from the data of Jacob et al [91Jac] at 727° and 1127°C. For $NaAlO_2$, the values of ΔH°_{298} and S°_{298} obtained in this way differ by 12326 J/mol and - 6.8313 J/mol.K from those reported by Barin [89Bar].

The thermodynamic properties of the solid phases were not changed further. The following optimized quasichemical parameters for the liquid solution (for the components $NaO_{0.5}$-$AlO_{1.5}$) were then obtained to reproduce the liquidus data including the melting point of $NaAlO_2$ and the eutectic reported by Weber and Venero [70Web]:

$$\omega = -483888 y_{AlO_{1.5}} - 447772 y^7_{AlO_{1.5}} \qquad J/mol \qquad (2\text{-}3\text{-}18)$$

$$\eta = -167.360 y_{AlO_{1.5}} - 221.752 y^7_{AlO_{1.5}} \quad J/mol.K \qquad (2\text{-}3\text{-}19)$$

As can be seen in Fig. 2-20, the liquidus data are fitted reasonably well. The $NaAlO_2$ liquidus of Weber and Venero [70Web], which starts off nearly horizontal and then drops rapidly near the eutectic, is extremely difficult to reproduce thermodynamically. The unusually large excess entropy terms in Eq (2-3-19) suggest that the liquidus data may be inaccurate.

From the thermodynamic data for the compounds, β"-alumina is calculated to dissociate at 1443°C which is very close to the temperature of 1412°C at which Rolin and Thanh [65Rol] observed a thermal effect and to the dissociation temperature of 1450°C reported by Kay and Subbarao [75Kay].

The thermodynamic data indicate that β-alumina remains stable down to 25°C in disagreement with reports [69Dev, 75Kay] that it decomposes to Al_2O_3 and β"-alumina at lower temperatures.

Probable maximum inaccuracy in assessed diagram: ± 50°.

2.3.12 The K_2O-Al_2O_3 system

The optimized phase diagram is shown in Fig. 2-21 for Al_2O_3 concentrations above 50 mol%.

A diagram was published by Roth [80Rot]. First melting of a sample held in an open crucible was found at 1910°C which was interpreted as the eutectic temperature. The eutectic composition was not determined, but was estimated at 73 mol% Al_2O_3. Samples of $KAlO_2$ heated in sealed Mo tubes were solid at 2250°C but internal pressure caused the tubes to rupture above 2260°C which was taken as an estimate of the melting point.

The β-alumina phase was reported, on the basis of thermogravimetric studies, to have a range of stoichiometry from about $K_2O.5.7Al_2O_3$ to $K_2O.9Al_2O_3$ over the temperature interval from 1200° to 1600°C [80Rot]. It was stated that β- and β"-alumina were never found below 1000°C, that the two phases were often found to coexist from 1000°C to 1200°C, that β"-alumina could be made almost single phase at about 1050° to 1100°C, but that β"-alumina is metastable.

In another study [82Moy] by DTA and X-ray diffraction, a eutectic at 1450°C was detected. This was not confirmed by Roth [80Rot] who observed no sign of melting below 1910°C although the fluid nature of the melts [80Rot] should have

made such detection relatively easy. These authors [82Moy] report the homogeneity range of β-alumina as extending from about $K_2O.4.8Al_2O_3$ to $K_2O.10Al_2O_3$ near 1500°C.

Eliezer and Howald [78Eli] calculated a phase diagram based upon estimated thermodynamic values [75Spe]. They showed β-alumina melting incongruently at 1900°C.

Early studies on β- and β"-alumina were reviewed by Kummer [72Kum]. The controversy over the range of homogeneity of potassium β-alumina and whether potassium β"-alumina is stable in the binary system is similar to the controversy regarding Na β- and β"-alumina which is discussed in the assessment of the Na_2O-Al_2O_3 system. Recent measurements [91Jac] have shown Na β- and β" alumina to have relatively narrow ranges of stoichiometry around the compositions $NaAl_9O_{14}$ and $Na_2Al_{12}O_{19}$. Hence, K β- and β"-alumina were approximated as the stoichiometric compounds KAl_9O_{14} and $K_2Al_{12}O_{19}$.

The activity of K_2O in two-phase (Al_2O_3 + β-alumina) mixtures has been reported from electrochemical studies [85Kum2, 88Ito, 89Kal] and ion exchange equilibria [61Kle, 65Her] over the approximate temperature interval from 325° to 800°C. These studies are in fair agreement apart from those of Kumar and Kay [85Kum2]. The most recent values [89Kal] lie

at approximately the mean of the other studies and so were adopted in the present analysis. From these measured K_2O activities in the two-phase region, the Gibbs energy of formation of β-alumina from K_2O and Al_2O_3 can be calculated. The estimation procedure of Berman and Brown [85Ber1, 86Ber] was used to calculate Cp. Then, ΔH°_{298} and S°_{298} were obtained in order to fit the Gibbs energies of formation at 327° and 727°C.

No measurements of K_2O activities in the two-phase (β-alumina + β"-alumina) or (β"-alumina + $KAlO_2$) regions have been reported. However, such measurements in the corresponding regions of the Na_2O-Al_2O_3 system were reported by Jacob et al [91Jac]. It was assumed that the ratio of the K_2O activity function to the Na_2O activity function in the corresponding region is the same in all three two-phase regions. This ratio can be calculated from data measured by the same authors in the (β-alumina + Al_2O_3) region [89Kal, 91Jac]. From the estimated K_2O activities, the Gibbs energies of formation of β"-alumina and $KAlO_2$ can be obtained. In the case of β"-alumina, the heat capacity was estimated by the method of Berman and Brown [85Ber1, 86Ber], and ΔH°_{298} and S°_{298} were then obtained in order to fit the Gibbs energies of formation at 327° and 727°C. In the case of $KAlO_2$, heat capacities measured [80Bey] in the range from -243° to 1127°C were used along with S°_{298} determined by the same authors by

the third law method. ΔH^{o}_{298} was then chosen so as to best reproduce the estimated Gibbs energy of formation in the range 327° to 727°C.

The melting point of $KAlO_2$ and the eutectic point were then reproduced by the following optimized quasichemical parameters for the liquid:

$$\omega = -531460 y_{AlO_{1.5}} + 160971 y^{7}_{AlO_{1.5}} \qquad J/mol \qquad (2\text{-}3\text{-}20)$$

$$\eta = -62.760 y_{AlO_{1.5}} \qquad J/mol.K \qquad (2\text{-}3\text{-}21)$$

A peritectic melting of β-alumina at 1920°C is predicted in good agreement with the earlier [78Eli] predicted value of 1900°C. β"-alumina is calculated to decompose to $KAlO_2$ and β-alumina above 1146°C.

Probable maximum inaccuracy in assessed diagram: ± 100°C.

2.3.13 The Al_2O_3-ZrO_2 system

The optimized phase diagram with selected experimental points is shown in Fig. 2-22.

Several early investigations [28War, 53Die, 61Suz, 65Kra, 68Cev, 70Sch] all agreed that the system is a simple eutectic with no compounds. However, the reported eutectic temperature ranged from 1710° to 1920°C and the eutectic composition ranged from 34 to 55 wt.% ZrO_2. A careful study reported by [70Alp] and [61McN] gave a eutectic at 40 wt.% Zro_2 at 1900°C. The most recent study by [81Fis] using a high temperature X-ray technique gave a eutectic at 1910 $\pm$ 20°C at 42.5 $\pm$ 1 wt.% ZrO_2.

The existence of a new high-temperature "ϵ-Al_2O_3" phase reported by [68Cev] was not confirmed in a later study [81Fis].

Solid solubility of 7 wt.% Al_2O_3 in tetragonal ZrO_2 and <1 wt.% ZrO_2 in Al_2O_3 was reported by [64Alp].

Two small parameters of the quasichemical model were required for the optimization of the liquid:

$$\omega = 6360 - 23221\, y_{ZrO_2}^2 \quad Joules \qquad (2\text{-}3\text{-}22)$$

The tetragonal and cubic ZrO_2 solutions were treated as Henrian with:

$$RT\ln\gamma_{AlO_{1.5}} = 30125 \quad J/mol \qquad (2\text{-}3\text{-}23)$$

relative to solid alumina as standard state.

Probable maximum inaccuracy in assessed diagram: ± 30°C, ±3 mol% for eutectic.

2.3.14 The $CaO-TiO_2$ system

The earliest study of the phase diagram [30Ume] gave $CaTiO_3$ as the only compound. Von Wartenberg et al [37Von] reported Ca_3TiO_5, Ca_2TiO_4 and $CaTiO_3$, while Coughanour et al [54Cou] and DeVries et al [54Dev1] included $Ca_3Ti_2O_7$ and $CaTiO_3$. Roth [58Rot] later revised his earlier [54Cou] work to include also $Ca_4Ti_3O_{10}$. Evidence for this phase was later obtained by liquidus measurements [70Jon]. However, Tulgar [76Tul] showed that the X-ray pattern for $Ca_4Ti_3O_{10}$ given by Roth [58Rot] corresponded to that of a mixture of $Ca_5Ti_4O_{13}$ and $Ca_3Ti_2O_7$.

The most recent study, chosen in the present assessment, is that of Tulgar [76Tul] who used cone softening and X-ray techniques. Three compounds were reported by Tulgar: $Ca_3Ti_2O_7$, $Ca_5Ti_4O_{13}$ and $CaTiO_3$, with only $CaTiO_3$ melting congruently, as shown in Fig. 2-23. $CaTiO_3$ was reported to melt at 1960°C. Peritectics were observed at 1840° and 1750°C with peritectic liquid compositions of 40 and 36 mol% TiO_2 respectively. Eutectics were observed at 1690°C at 32 mol% TiO_2 and at 1450°C at 76 mol% TiO_2. This latter eutectic was also reported by Rouf et al [69Rou] at 1475°C at 75 mol% TiO_2.

For $Ca_3Ti_2O_7$, S°_{298} and C_p were taken from the compilation of Barin [89Bar]. To reproduce the peritectic decomposition temperature of $Ca_3Ti_2O_7$, ΔH°_{298} was changed by 35587 J/mol from

the value given by Barin. This is much greater than the estimated [72Kub] uncertainty of 10500 J/mol. For $CaTiO_3$, ΔH^o_{298} and S^o_{298} were taken from Robie et al [78Rob], while C_p below the first order transition temperature of 1257°C was taken from Berman and Brown [85Ber1, 86Ber] and C_p above 1257°C was taken from Barin [89Bar]. No changes to these values were made in the optimization. No data are available for $Ca_5Ti_4O_{13}$. Hence, S^o_{298} was estimated by taking weighted averages of the values [89Bar] for $Ca_3Ti_2O_7$ and $CaTiO_3$, while C_p was estimated from the formula of Berman and Brown [85Ber1, 86Ber] and ΔH^o_{298} was chosen to reproduce the measured [76Tul] peritectic temperature.

Optimized parameters of the quasichemical model for the liquid are as follows:

$$\omega = -82797 - 126620\, y^2_{TiO_2} \quad J/mol \qquad (2\text{-}3\text{-}24)$$

The phase diagram in Fig. 2-23, calculated from the optimized parameters, agrees very closely with the diagram reported by Tulgar [76Tul]. The calculated eutectic composition of $X_{TiO_2} = 0.34$ is preferred to the reported value of 0.32 because the large change in experimental liquidus slope at the peritectic at 1750°C is unlikely and very difficult to reproduce thermodynamically.

Probable maximum inaccuracy in assessed diagram:
±20° for invariant temperatures and congruent melting point,
±2 mol % for liquidus

2.3.15 The $MnO-TiO_2$ system

Phase diagram points of Leusmann [79Leu], obtained by DTA with heating and cooling, are shown in Fig. 2-24. The compounds Mn_2TiO_4 and $MnTiO_3$ were reported to melt congruently at 1420° and 1410°C respectively, and eutectics were reported at 1410°C at 28 mol % TiO_2, 1385°C at 42 mol % TiO_2, and 1370°C at 57 mol % TiO_2. An earlier study [40Gri] employing thermal analysis and microscopic and X-ray techniques was rejected because of the very unlikely shape of the reported liquidus. These authors showed $MnTiO_3$ as melting peritectically.

A compound $Mn_2Ti_3O_8$ was prepared, characterized, and found to be stable up to 330°C [64Jou]. No thermodynamic data are available for this compound.

Evans and Muan [71Eva] give an estimated Gibbs energy of formation of the pseudobrookite phase $MnTi_2O_5$ at 1250°C. However, the precision of the estimation was not high enough for them to ascertain whether the phase is stable relative to the other compounds in the $MnO-TiO_2$ system. Navrotsky [75Nav] claims that it is unstable at all temperatures and suggests that this is due to the Mn^{2+} ion being somewhat too large for the sites in the pseudobrookite structure. Leusmann [70Leu] looked for the phase carefully but did not detect it.

Thermodynamic data for metastable $MnTi_2O_5$ are discussed in the assessment of the MnO-FeO-TiO_2 ternary system.

Activities in the liquid measured by Rao and Gaskell [81Rao2] are shown in Fig. 2-25. These were obtained by equilibration with Pt-Mn foil and oxygen atmospheres. From the observed discontinuities in the slopes of these activity data, points on the TiO_2-liquidus were obtained at 1500° and 1550°C as shown in Fig. 2-24. These lie at TiO_2 concentrations about 10% higher than those reported by Leusmann [79Leu]. Since the activity measurements are equilibrium measurements, whereas the DTA measurements [79Leu] are not, the former are preferred. Furthermore, the shape of the TiO_2-liquidus reported by Leusmann is improbable and very difficult to reproduce thermodynamically.

The enthalpy of fusion of TiO_2 is given in the JANAF Tables [85Jan] as 66944 ± 16700 J/mol. With this value it was very difficult to reproduce the TiO_2-liquidus curve of this system and of the MgO-TiO_2 and FeO-TiO_2 systems unless very unlikely excess Gibbs energies were invoked. Hence, an optimized value of 46024 J/mol was chosen which reproduces well the liquidus curves in all these systems.

Thermodynamic properties of Mn_2TiO_4 and $MnTiO_3$ were taken from Barin's compilation [89Bar]. In the optimization, ΔH°_{298}

was changed by 5898 and -5759 J/mol for Mn_2TiO_4 and $MnTiO_3$ respectively which may be compared with the estimated [72Kub] uncertainties of 12600 and 10500 J/mol. No changes were made to S°_{298} or C_p. A tetragonal to cubic transformation was observed [64Har] for Mn_2TiO_4 at 770°C. We have estimated the enthalpy of transformation as 1000 J/mol which is equal to that of Mg_2TiO_4 [84Wec]. C_p was taken to be the same below and above the transformation temperature.

The optimization gave the following quasichemical parameters for the liquid:

$$\omega = -33874 - 24986\ y^2_{TiO_2}\ J/mol \qquad (2\text{-}3\text{-}25)$$

The phase diagram calculated from the optimized parameters is shown in Fig. 2-24. Calculated liquid MnO activities are shown in Fig. 2-25. These are virtually constant over the temperature interval from 1500° to 1550°C. The TiO_2-liquidus in Fig. 2-24 passes through the liquidus points obtained from the activity data [81Rao2] within experimental error limits. Although the calculated eutectic composition of X_{TiO_2} = 0.63 is not close to the value of 0.57 reported by Leusmann [79Leu], this can be explained if two of his DTA points are re-interpreted as points on the $MnTiO_3$-

liquidus rather than on the TiO_2-liquidus. The composition of X_{TiO_2} = 0.28 reported by Leusmann for the other eutectic resulted from his interpretation of one DTA point at $X_{TiO_2} \approx$ 0.28 at 1420°C as a liquidus point. This however is very difficult to reproduce thermodynamically. In the optimization it was assumed that this single data point (shown on Fig. 2-24) actually resulted from the eutectic reaction.

Probable maximum inaccuracy in assessed diagram:

$\pm 20^\circ$ for $0.25 < X_{TiO_2} < 0.65$

$\pm 50^\circ$ for other compositions

2.3.16 The $MgO-TiO_2$ system

Woermann et al [69Woe], from quenching experiments, reported three compounds in this system: spinel (Mg_2TiO_4) which melts incongruently at 1756°C to form a liquid with 40 mol% TiO_2, geikielite ($MgTiO_3$) which melts incongruently at 1630°C to give a liquid with 52 mol% TiO_2 and karrooite which melts congruently at 1657°C. Two eutectics at 1620°C and 56 mol% TiO_2 and at 1632°C and 76 mol% TiO_2 were reported [69Woe]. Rouf et al [69Rou] obtained the same melting behaviour with peritectics at 1680°C and 52 mol% TiO_2 and at 1750°C and 43 mol% TiO_2, with a congruent melting point of $MgTi_2O_5$ of 1690°C, and with eutectics at 1620°C and 57 mol% TiO_2 and at 1636°C and 80 mol% TiO_2. The same melting behaviour was reported by Massazza and Sirchia [58Mas] and by Shindo [80Shi]. Earlier studies [32Von2, 53Cou] showed all compounds as congruently melting (the spinel phase was not detected by von Wartenberg and Prophet).

In the present optimization, the data of Woermann et al [69Woe] were preferred. The reported [80Shi] slight solubility of TiO_2 in $MgTiO_3$ was not taken into account in the analysis.

Wechsler and Navrotsky [84Wec] studied thermochemical and structural properties of the three compounds by high-temperature solution calorimetry and by transposed-temperature

drop calorimetry to characterize order-disorder phenomena. They suggest that Mg_2TiO_4 decomposes eutectoidally to MgO and $MgTiO_3$ below 1000°C and that $MgTi_2O_5$ decomposes eutectoidally to $MgTiO_3$ and TiO_2 below 130°C. The high-pressure results of Lindsley et al [74Lin] strongly suggest that the latter eutectoid temperature lies between room temperature and 700°C. The results of Wechsler and Navrotsky [84Wec] also indicate a first-order tetragonal to cubic transformation in the metastable spinel phase at 660°C with an enthalpy of transformation of approximately 1000 J/mol.

Heat capacities of the three compounds are given by Berman and Brown [85Berl, 86Ber]. The heat capacity of $MgTi_2O_5$ reported by Brown and Navrotsky [89Bro] was not used because good optimizations could not be obtained with this value. The heat capacities of tetragonal and cubic spinel were assumed equal. ΔH°_{298} and S°_{298} are reported for Mg_2TiO_4 [85Jan], $MgTiO_3$ [78Rob] and $MgTi_2O_5$ [85Jan].

Two other data used in the optimization are the equilibrium temperatures of 1325°C reported [88Win] for the 4-phase equilibrium:

$$MgSiO_3 + 2TiO_2 = MgTi_2O_5 + SiO_2 \qquad (2\text{-}3\text{-}26)$$

and of 996°C for the 4-phase equilibrium [69Mac]:

$$MgSiO_3 + MgTi_2O_5 = Mg_2SiO_4 + 2TiO_2 \qquad (2\text{-}3\text{-}27)$$

For the liquid, the optimization yielded the following quasichemical parameters:

$$\omega = -92199 y_{TiO_2} + 90500 y_{TiO_2}^2 \quad J/mol \qquad (2\text{-}3\text{-}28)$$

$$\eta = 30.543 y_{TiO_2} \quad J/mol.K \qquad (2\text{-}3\text{-}29)$$

Values of ΔH°_{298} of Mg_2TiO_4 and $MgTiO_3$ were altered by 7595 and 1213 J/mol respectively which may be compared to the stated uncertainties of 6300 [85Jan] and 1590 [78Rob] J/mol respectively. For $MgTi_2O_5$, ΔH°_{298} and S°_{298} were changed by 4467 J/mol and 1.740 J/mol.K in order to optimize simultaneously the interval of stability (<700°C to 1657°C) and the fixed point temperatures of reaction (2-3-26). These changes may be compared to the stated [85Jan] uncertainties of 10500 J/mol and 6.3 J/mol .K.

The calculated diagram in Fig. 2-26 agrees very closely with the data of Woermann et al [69Woe]. The calculated peritectic composition of 42 mol% TiO_2 at 1756°C is slightly

higher than the reported composition of 40 mol%, but no experimental points were presented in this region so that a peritectic composition of 42 mol% requires no experimental datum to be rejected.

The optimized lower eutectoid decomposition temperature of Mg_2TiO_4 is 1000°C in agreement with experiment [84Wec].

The calculated lower eutectoid decomposition temperature of $MgTi_2O_5$ is 700°C which is at the upper limit of the temperature range proposed by Lindsley et al [74Lin]. The reported equilibrium temperature of reaction (2-3-26) is reproduced exactly, but the calculated equilibrium temperature of reaction (2-3-27) is 1216°C which is not in good agreement with the reported value of 996°C. This however represents the best compromise when all data are simultaneously optimized.

Probable maximum inaccuracy in assessed diagram: ± 20° and ± 1 mol% for liquidus over the temperature range of Fig. 2-26.

2.3.17 The Na_2O-TiO_2 system

The assessed phase diagram is shown in Fig. 2-27. In the diagram, and in the following text, compositions are given in terms of the components $NaO_{0.5}$-TiO_2.

In an early study at TiO_2-rich compositions [36Jun], the compound $Na_2Ti_3O_7$ was identified. Budnikov and Tresvyats'kii [54Bud] later studied the system by thermal analysis for TiO_2 contents above 38 mol%. $Na_2Ti_3O_7$ was found to melt peritectically at 1132°C to a liquid of 58 mol% TiO_2. The compound $Na_8Ti_5O_{14}$ was reported to melt congruently at 1028°C, and a eutectic was found at 986° at 47 mol% TiO_2. No evidence was found of the compounds $Na_2Ti_2O_5$ or Na_2TiO_3. These results were confirmed by Bouaziz and Mayer [71Bou] and by Gicquel, Mayer and Bouaziz [72Gic] in thermal analysis experiments. These authors extended the composition range studied, reporting that Na_2TiO_3 melts peritectically at 965°C to a liquid of 29 mol% TiO_2 and that Na_4TiO_4 melts congruently at 1045°C. Eutectics were reported at 850°C and 862°C at 11 mol% and 24 mol% TiO_2 respectively. In addition, they observed the compound $Na_2Ti_6O_{13}$ with a peritectic at 1300°C and a peritectic liquid composition of 68 mol% TiO_2. The data points of these authors are reproduced in Fig. 2-27. Their measurements were performed under N_2 atmospheres, apparently in open crucibles. It would seem that compositions were not

checked after the experiments. Hence, some Na_2O losses many have occurred by volatilization.

Heat capacities for Na_2TiO_3 above 287°C and for $Na_2Ti_3O_7$ were taken from Berman and Brown [85Ber1, 86Ber], and their method of approximation was used to estimate Cp for Na_4TiO_4 and $Na_8Ti_5O_{14}$.

For Na_2TiO_3, all data (ΔH^o_{298}, S^o_{298}, C_p) below the first order transformation temperature of 287°C, and data for this transformation, were taken from Barin et al [77Bar]. The same source was used for ΔH^o_{298} and S^o_{298} of $Na_2Ti_3O_7$. In the optimization, these values of ΔH^o_{298} were changed by -11764 and -1018 J/mol respectively which are within the error limits [72Kub] of 16736 and 20920 J/mol respectively. Different data for Na_2TiO_3 and $Na_2Ti_3O_7$ are given in the more recent compilation of Barin [89Bar]. These are based upon the compilation of Medvedev et al [81Med]. However, when these data were used in the phase diagram optimization, much larger changes in ΔH^o_{298} were required. Hence, data from the older compilation were retained.

For $Na_2Ti_6O_{13}$ data were taken from the literature for ΔH^o_{298} [73Ben], S^o_{298} [82Stu] and C_p [86Fer]. ΔH^o_{298} was subsequently changed by -1269 J/mol which is well within the stated error limit of 7100 J/mol. For $Na_8Ti_5O_{14}$ and Na_4TiO_4,

no data for ΔH^{o}_{298} or S^{o}_{298} were found. These were obtained from the phase diagram optimization.

For the liquid solutions, the following quasichemical parameters were obtained:

$$\omega = -425965 - 416919\ y^{7}_{TiO_2} \qquad J/mol \qquad (2\text{-}3\text{-}30)$$

$$\eta = -79.496 - 188.280 y^{7}_{TiO_2} \qquad J/mol.K \qquad (2\text{-}3\text{-}31)$$

The very large entropy coefficients in Eq. (2-3-31) are necessary in order to reproduce the data. The unusual magnitude of these coefficients raises some concern about the accuracy of the data.

The very large negative value of ω in Eq (2-3-30) in the quasichemical model causes the Gibbs energy of mixing of the liquid to exhibit a very sharp and deep negative peak at 20 mol% TiO_2 which is the composition of the compound Na_4TiO_4. Consequently, the calculated liquidus of Na_4TiO_4 exhibits a very sharp peak at the congruent melting point as seen in Fig. 2-27. Gicquel et al [72Gic] interpreted their two liquidus points at 13 and 15 mol% TiO_2 as lying on the Na_4TiO_4-

liquidus, whereas in Fig. 2-27 these have been re-interpreted as lying on the $NaO_{0.5}$-liquidus. Since the quasichemical model for the liquid predicts maximum stability at the composition of Na_4TiO_4, it was necessary to make the optimized Gibbs energy of formation of the solid compound very negative in order to reproduce the melting point. The optimized value of ΔH^{o}_{298} of Na_4TiO_4 is thus probably too negative.

Thermodynamic data are given in the compilation of Barin et al [77Bar] for the compound $Na_2Ti_2O_5$. If these data are included in the calculations, the compound does not appear in the equilibrium phase diagram at any temperature, in accord with the observations [54Bud, 71Bou, 72Gic] at high temperatures. However, an increase in stability of only 1000 J/mol causes the compound to appear at lower temperatures. Therefore, it is concluded that the compound is not stable at high temperatures, but its stability at lower temperatures remains an open question.

Probable maximum inaccuracy in assessed diagram:
$\pm 30^{o}$ for $X_{TiO_2} > 0.3$, $\pm 100^{o}$ for $X_{TiO_2} < 0.3$.

2.3.18 The K_2O-TiO_2 system

The calculated optimized phase diagram is shown in Fig. 2-28. In the diagram, and in the following text, compositions are given in terms of the components $KO_{0.5}$-TiO_2.

The only published experimental phase diagram appears to be that of Schmitz-DuMont and Reckhard [59Sch] who used thermal and X-ray analysis techniques to study compositions above 50 mol% TiO_2. They reported a compound $K_2Ti_5O_{11}$ melting incongruently at 1302°C to a liquid of 65 mol% TiO_2, and the compound $K_2Ti_3O_7$ melting incongruently at 1051°C to a melt of 55 mol%TiO_2. The compound $K_2Ti_2O_5$ was also reported with a eutectic between $K_2Ti_2O_5$ and $K_2Ti_3O_7$ at 948°C and 50.5 mol% TiO_2.

Several other compounds have been synthesized and characterized. These include K_4TiO_4 [75Ola], $K_6Ti_2O_7$ [73Sch], K_2TiO_3 and $K_2Ti_4O_9$ [73Eas], $K_2Ti_6O_{13}$ [74Bel] and $K_2Ti_8O_{17}$ [80Mar].

Since the thermal stabilities of the compounds are largely unknown, we chose to assume that the compounds in the K_2O-TiO_2 system at high temperatures have the same stoichiometries as those in the Na_2O-TiO_2 system, viz: K_4TiO_4, K_2TiO_3, $K_8Ti_5O_{14}$, $K_2Ti_2O_5$, $K_2Ti_3O_4$, and $K_2Ti_6O_{13}$. The approximation equation of Berman and Brown [85Ber1, 86Ber] was

used to estimate heat capacities. Enthalpies and entropies of formation from the component oxides at 298K were assumed to be identical to those of the corresponding sodium compounds taken from the assessment of the Na_2O-TiO_2 system. The liquid quasichemical parameters were then optimized so as to fit the reported [59Sch] peritectic points and to obtain a liquidus surface at higher K_2O contents which approximately resembles that of the assessed Na_2O-TiO_2 phase diagram. The same terms (ω_o, ω_7, η_o, η_7) as in the Na_2O-TiO_2 system were used:

$$\omega = -364322 - 281374 y^7_{TiO_2} \qquad J/mol \qquad (2\text{-}3\text{-}32)$$

$$\eta = -41.840 - 83.680 y^7_{TiO_2} \qquad J/mol.K \qquad (2\text{-}3\text{-}33)$$

As was the case in the Na_2O-TiO_2 system, the compound $K_2Ti_2O_5$ was found to be unstable.

Probable maximum inaccuracy in assessed diagram: $\pm 25^{\circ}$ for $X_{TiO_2} > 0.5$.

2.3.19 The TiO_2-ZrO_2 system

The optimized phase diagram is shown in Fig. 2-29 along with selected experimental points from several authors [54Bro, 54Cou, 65Coc, 80She, 86Ban, 86McH].

The solid solubility of ZrO_2 in TiO_2 was shown by [54Bro] to vary from 18 mol % at the eutectic to 6 mol % at 980°C. This approximate solid solubility was confirmed by [65Coc]. The solid solubility of TiO_2 in ZrO_2 was reported by various authors [54Bro, 54Cou, 65Coc, 80She, 68Nog] as varying from less than 20 mol % to more than 40 mol %. The solubility was measured accurately by [86Ban] who took many precautions. These data points [86Ban] are shown on Fig. 2-29.

The compound $ZrTiO_4$ has been reported by several authors. It was reported to melt incongruently at 1820 $\pm$ 20° by [54Cou] and at 1830 $\pm$ 20° by [80She]. A range of homogeneity of 5 to 10 at. % for this compound has been reported [54Bro, 54Cou, 65Coc, 80She, 68Nog, 86McH] but is not well defined. In the present analysis, the compound was assumed stoichiometric.

The eutectic was reported as 1760°C at 20 mol % ZrO_2 by [54Cou] and 1720 $\pm$ 20° at 27 mol % ZrO_2 by [80She].

In a recent study, [86McH] report a new compound, Ti_2ZrO_6, decomposing to TiO_2 and $TiZrO_4$ at 1200°C. They also show $TiZrO_4$ as decomposing to ZrO_2 and Ti_2ZrO_6 below 1100°C.

No thermodynamic data are available for $TiZrO_4$ or Ti_2ZrO_6. It was assumed that ΔC_p of formation of these compounds from TiO_2 and ZrO_2 is zero. With ΔS° of formation of Ti_2ZrO_6 set to zero, ΔH°_{298} for this compound was chosen so as to reproduce the peritectoid temperature of 1200°C, while ΔS° and ΔH°_{298} of $TiZrO_4$ were adjusted so as to reproduce the peritectic temperature at 1830°C and the reported [86McH] eutectoid at 1100°C. This is only possible if ΔS° of formation of $TiZrO_4$ is unrealistically large. Hence, ΔS° of formation of $TiZrO_4$ from TiO_2 and ZrO_2 was set to be slightly positive (2.0 cal/mol K) and ΔH°_{298} was chosen so as to reproduce the peritectic only. Thus, in the optimized diagram, $TiZrO_4$ is stable down to room temperature. In any case, only one study [86McH] reports $TiZrO_4$ as decomposing eutectoidally. This point requires confirmation.

The optimized quasichemical parameters for the liquid are:

$$\omega = -17572 - 17004\, y^4_{ZrO_2} \quad Joules \qquad (2\text{-}3\text{-}34)$$

This is quite large in view of the fact that TiO_2 and ZrO_2 are members of the same group in the periodic table and in view of the high temperatures involved. On the other hand, the existence of the solid compound $TiZrO_4$ at very high temperature indicates that there are relatively strong interactions between TiO_2 and ZrO_2 even at these temperatures.

The TiO_2 solid solution was treated as Henrian with:

$$RT\ln\gamma_{ZrO_2} = 26586-5.7672T \ J/mol \qquad (2\text{-}3\text{-}35)$$

relative to cubic ZrO_2 as standard state.

Both the tetragonal and cubic ZrO_2 solid solutions were treated as Henrian solutions with:

$$RT\ln\gamma_{TiO_2} = 16945 \ J/mol \qquad (2\text{-}3\text{-}36)$$

relative to solid TiO_2 as standard state.

Probable maximum inaccuracy in assessed diagram: $\pm 50^{\circ}$ for solidus, $\pm 100^{\circ}$ for liquidus.

2.3.20 The CaO-MnO system

The solidus was measured by Schenck et al [64Sch] from visual observation of the beginning of melting. Points taken from their smoothed curve [64Sch] over the composition range of the measurements are shown in Fig. 2-30.

From measurements of FeO activities in the ternary CaO-MnO-FeO system at 1100°C, Tiberg and Muan [70Tib] showed that solid CaO-MnO solutions exhibit large positive deviations from ideality. CaO activities were measured by Raghavan et al [80Rag] using galvanic cells with CaF_2 solid electrolytes in the range from 940° to 1050°C. Their points are shown in Fig. 2-31.

The activities of Raghavan et al were fitted to a regular solution model with:

$$g^E(sol) = 15770\ X_{CaO}X_{MnO} \quad J/mol \qquad (2\text{-}3\text{-}37)$$

As can be seen in Fig. 2-31, the data are fitted quite well by this model, except at high X_{CaO}. However, the shape of the experimental activity curves in this composition range is inconsistent with Raoult's Law. Hence, these experimental points were ignored. It is noteworthy that the temperature

dependence of the activities is reproduced well by this model with only one temperature-independent parameter.

A solid-solid miscibility gap with a consolute temperature at approximately 675°C is predicted.

Given the solidus and the thermodynamic properties of the solid phase, the liquidus and the thermodynamic properties of the liquid phase can be calculated thermodynamically if it is assumed that s^E of the liquid is small [80Pel]. Such a calculation was performed, and the resultant liquid properties were then represented by the quasichemical model with:

$$\omega = 27006 \quad J/mol \qquad (2\text{-}3\text{-}38)$$

The calculated phase diagram in Fig. 2-30 reproduces the measured solidus points very closely.

Probable maximum inaccuracy in assessed diagram: ± 50° for solidus, ± 100° for liquidus.

2.3.21 The CaO-FeO system

Liquid CaO-FeO solutions in equilibrium with Fe can contain up to about 20 wt% Fe_2O_3 [55All]. Nevertheless, experimental results are often represented as binary diagrams as in Fig. 2-32. Compounds containing Fe^{3+} appear at lower temperatures. For example, $Ca_2Fe_2O_5$ + Fe transforms to two solid CaO-FeO solutions at 1045°C [75Abb2]. For this reason, Fig. 2-32 is not plotted below 1050°C.

Schuermann and Kraume [76Sch] reported a simple eutectic diagram with a maximum solubility of CaO in solid FeO of about 16 mol%. These findings were supported by Perrot [67Per] and by Aubry et al [70Aub]. However, Abbattista et al [75Abb2], from spectrographic measurements and microscopic observations on quenched specimens, reported a solubility of CaO in solid FeO of 37 mol% at 1100°C. In agreement with an older study by Allen and Snow [55All] and a recent study by Bergman and Song [88Ber], they suggest that the liquidus exhibits a minimum as in Fig. 2-32. According to Abbattista et al [75Abb2], the reason for this disagreement may be that, in quenching experiments, the rate of cooling must be higher than 700°C per second in order to conserve the high temperature state. Bergman and Song [88Ber] point out that the eutectic-like structure observed by Schuermann and Kraume [76Sch] probably resulted from a eutectoid decomposition of the wustite solution into $Ca_2Fe_2O_5$ and Fe. In the present analysis, the

liquidus and solidus points of Abbattista et al [75Abb2] in combination with studies of FeO solubility in CaO [55All, 62Zur, 65Joh, 67Per, 69Obs,74Sch] and of the CaO-liquidus at higher temperatures [41Oel, 55All, 58Bis, 61Fis2, 66Goe, 66Tro, 69Obs, 69Tro1, 71Sch, 74Sch] were used. Data points from several of these studies are reproduced in Fig. 2-32.

Activities of FeO at 1100°C in the solid solution in equilibrium with Fe were measured by several authors using gas equilibration [70Tib, 70Tim, 75Abb2] and galvanic cells with solid electrolytes [84Bjo]. As can be seen in Fig. 2-33, these results are in reasonable agreement, with the points of Abbattista et al [75Abb2] lying below the others. In the present analysis, preference was given to the electrochemical measurements of Bjoerkman [84Bjo].

The CaO- and FeO- rich solid solutions were treated as one phase with:

$$g^E = X_{Cao}X_{Feo}(22773 - 3140X_{Cao} + 15522X_{Cao}^2) \quad J/mol \qquad (2\text{-}3\text{-}39)$$

Good fits to the activity data (Fig. 2-33) and to the solvus data of Abbattista et al (Fig. 2-32) are obtained.

Three quasichemical coefficients were used to reproduce the liquidus and solidus:

$$\omega = -82362 - 40052 y^{7}_{FeO} \qquad J/mol \qquad (2\text{-}3\text{-}40)$$

$$\eta = -20.92 \quad J/mol.K \qquad (2\text{-}3\text{-}41)$$

The FeO-liquidus points of Allen and Snow [55All] shown in Fig. 2-32 are not well represented by the optimization. However, the shape of their experimental liquidus is inconsistent with the existence of a minimum which is almost always much broader, as in the optimized diagram and as suggested by the points of Abbattista et al. The liquidus points of Allen and Snow, measured by quenching techniques, could be in error because of a too low cooling rate.

Probable maximum inaccuracy in assessed diagram: ±2 mol% for $X_{FeO} < 0.80$, ±50° for $X_{FeO} > 0.80$.

2.3.22 The $CaO-ZrO_2$ system

The optimized phase diagram along with selected experimental points is shown in Fig. 2-34. The reported diagram from [77Stu] for the composition range from ZrO_2 to $CaZrO_3$ is shown in Fig. 2-35.

Earlier studies [52Duw, 63Fer, 68Gar, 68Car, 73Die, 75All] of the ZrO_2-$CaZrO_3$ composition range generally considered that the cubic phase did not exist for pure ZrO_2. The literature also contains a great deal of controversy over the existence of the nature of and the stability of the proposed compound $CaZr_4O_9$. The situation is complicated by the report by several authors of the existence of various ordered phases in this region. We were not able, with simple thermodynamic functions, to reproduce the phase diagram of [77Stu], Fig. 2-35, as regards the compound $CaZr_4O_9$. Since this region is still the subject of controversy, this compound has not been included in the optimization.

The liquidus over the entire range of composition was determined by [67Nog] using a solar furnace. They reported a eutectic between CaO and $CaZrO_3$ with a temperature given as 2112°C in their text, but at 2145°C on their diagram. These authors also reported a solid solubility of 6 mol % ZrO_2 in CaO at the eutectic temperature.

For $CaZrO_3$, the melting point of 2350°C of [89Bar] was used in the optimization. For this compound, S°_{298} and C_p as reported by [89Bar] were used, with the ΔH°_{298} value of [89Bar] adjusted by -842 J/mol in order to reproduce the congruent melting point exactly. This is well within the reported error limits.

The liquid phase was optimized with:

$$\omega = -27932 - 74867\, y_{ZrO_2} \quad Joules \qquad (2\text{-}3\text{-}42)$$

The solid solution of ZrO_2 in CaO was treated as Henrian with:

$$RT\ln\gamma_{ZrO_2} = -2092 \quad J/mol \qquad (2\text{-}3\text{-}43)$$

relative to cubic ZrO_2 as standard state.

The cubic ZrO_2 solid solution was treated as a regular solution with solid CaO as standard state:

$$G^E = X_{CaO}X_{ZrO_2}\,(-189159 + 57.873T) \quad J/mol \qquad (2\text{-}3\text{-}44)$$

The tetragonal ZrO_2 solution was treated as Henrian with:

$$RT\ln\gamma_{CaO} = -104600 + 33.472T \quad J/mol \qquad (2\text{-}3\text{-}45)$$

relative to solid CaO as standard state.

Probable maximum inaccuracy in assessed diagram: ± 50° for liquidus, ± 100° for solidus.

2.3.23 The FeO-MnO system

Liquidus points measured by Fischer and Fleischer [61Fis1], by thermal analysis, are shown in Fig. 2-36. These authors reported melting points of FeO and MnO of 1372° and 1878°C respectively. The latter is 36° higher than the presently assessed value. In the experiments, Fe crucibles were used for samples with less than 40 mol% MnO and MnO crucibles were used for samples with higher MnO contents. The reported liquidus exhibited a marked kink near 40 mol% MnO. Hence, in Fig. 2-36, all liquidus points obtained in MnO crucibles have been adjusted downwards by $36X_{MnO}$ degrees. The resultant curve is smooth. (For clarity, only a few of the 35 reported liquidus points are shown in Fig. 2-36. These span the reported composition range.)

The non-stoichiometry of FeO-MnO solid solutions has been studied by Engell and Kohl [62Eng1] at two selected oxygen pressures at 1250°C. The oxygen pressures of FeO-MnO solid solutions in equilibrium with Fe have been determined in several studies [29Sch, 56Fos, 62Eng2]. In the two former studies the condensed phases were equilibrated with CO/CO_2 mixtures, whereas in the latter study a galvanic cell with a calcia-stabilized zirconia solid electrolyte was used. The results of these studies are not in good agreement. The FeO activities of Foster and Welch [56Fos] are nearly ideal, those of Engell [62Eng2] show pronounced positive deviations, and

those of Schenck et al [29Sch] show moderate positive deviations.

More recently, oxygen pressures above FeO-MnO solid solutions in equilibrium with Fe were measured [67Sch] at 1000°, 1150° and 1300°C. No temperature dependence was observed. FeO activities taken from the smoothed curve of Schwerdtfeger and Muan [67Sch] are shown in Fig. 2-37. Small positive deviations were observed, in reasonable agreement with the results of Schenck et al [29Sch]. Activities of FeO-MnO solutions in equilibrium with Fe in the temperature range 800° to 1100°C were reported by Abbattista and Maja [75Abb1]. At 1100°C their results are in good agreement with those of Schwerdtfeger and Muan [67Sch]. However, a fairly large temperature dependence was reported. For a solution exhibiting nearly ideal behaviour, the nearly zero temperature dependence reported by Schwerdtfeger and Muan seems more likely. Accordingly, the activity measurements of these authors were fitted in the present analysis to a regular solution model (see Fig. 2-37) with:

$$g^{E}(sol) = 6126 X_{FeO} X_{MnO} \quad J/mol \qquad (2\text{-}3\text{-}46)$$

The liquid was assumed to be ideal. The calculated liquidus in Fig. 2-36 agrees very well with the measured [61Fis1] points.

The trivalent cation content of solid solutions equilibrated with Fe at high temperatures is of the order of 10% for pure FeO, 3% when $X_{MnO} = 0.5$, and <0.5% for pure MnO.

Probable maximum inaccuracy in assessed diagram: ± 25° for liquidus, ± 50° for solidus.

2.3.24 The MgO-CaO system

The optimized phase diagram is shown in Fig. 2-38.

Early reports of the eutectic temperature and eutectic liquid composition include 2300 ±50°C at 59 mol% CaO [16Ran], 2360°C at 55 mol% CaO [33Ruf], and 2250°C at 55 mol% CaO [37Von]. Based on considerations of lattice parameters and the observed solid solubilities in the ternary MgO-CaO-MnO system, Ford and White [49For] predicted a moderate solubility of MgO in CaO at 1650°C. Summarizing the work of several investigators, Troojer and Konopicky [49Tro] predicted solubilities at 1600°C of approximately 3 mol% MgO in CaO and 1 mol% CaO in MgO.

The liquidus, solidus and solvus lines were determined by Doman et al [63Dom] by a combination of visual and X-ray techniques. Their points are shown in Fig. 2-38. They reported a eutectic liquid composition of 59 mol% CaO at 2374°C. Their reported melting point of CaO of 2630°C is 58° higher than the present assessed value. Maximum solid solubilities at the eutectic temperature were reported as 22 mol% MgO in CaO and 5.7 mol% CaO in MgO.

The solubility of CaO in MgO between 1100°C and 1750°C was measured by Henney and Jones [69Hen] whose points are also shown in Fig. 2-38. Their solubilities are about twice those

of Doman et al. The solubilities reported by Doman et al were chosen in the present analysis.

The two terminal solid solutions, having the same crystal structure, were formally treated as one sub-regular solution with a miscibility gap with:

$$g^E(solid) = X_{MgO}X_{CaO}\,(118110 - 18.410\,T - 31380\,X_{CaO}) \qquad (2\text{-}3\text{-}47)$$

The liquid solution was optimized with the quasichemical model with:

$$\omega = 45329 - 30583\,y_{CaO} \quad J/mol \qquad (2\text{-}3\text{-}48)$$

As can be seen in Fig. 2-38, the diagram calculated from Eqs (2-3-37, 2-3-38) agrees very well with the measured points [63Dom] except for the liquidus at high X_{CaO} where the melting point of Doman et al is higher than the assessed value.

Probable maximum inaccuracy in assessed diagram: $\pm 50^{\circ}$ for liquidus, ±3 mol% for solidus and solidus.

2.3.25 The FeO-MgO system

It was shown by Bowen and Schairer [35Bow] that solid FeO and MgO are completely miscible at high temperatures. Solidus temperatures were determined by Schenck et al [61Sch2] up to 2400°C by a visual technique. Stoichiometric "FeO" was prepared by mixing Fe and Fe_2O_3. Since wustite is deficient in Fe, the solidus points shown in Fig. 2-39 were obtained in the presence of metallic Fe.

Several thermodynamic investigations of the solid solutions [61Sch3, 62Hah, 70Ber, 73Abb, 74Sah] have been reviewed [87Sre]. Results are in poor agreement. Furthermore, the non-linear variation of Fe^{3+} content with composition was often neglected in the derivation of FeO activities.

A reinvestigation of oxygen potentials of FeO-MgO solid solutions equilibrated with Fe was made by Srecec et al [87Sre] between 1060° and 1320°C. Fe^{3+} contents varied from ~10% of total Fe for pure FeO to ~2% at $X_{MgO} = 0.5$.

As shown in Fig. 2-40, the FeO activities of these authors are well represented by a regular solution model with:

$$g^E(sol) = 10175\ X_{FeO}X_{MgO} \quad J/mol \qquad (2\text{-}3\text{-}49)$$

Given the solidus and the thermodynamic properties of the solid phase, the liquidus and the thermodynamic properties of the liquid phase can be calculated thermodynamically if it is assumed that s^E of the liquid is small [80Pel]. Such a calculation was performed, and the resulting liquid properties were then represented by the quasichemical model with:

$$\omega = 3347 \quad J/mol \qquad (2\text{-}3\text{-}50)$$

The calculated solidus in Fig. 2-39 is in very good agreement with the measurements [61Sch2]. Positive deviations from ideality are smaller in the liquid than in the solid, as is consistent with normal behaviour. The calculated consolute temperature of the solid-solid miscibility gap is ~340°C.

Probable maximum inaccuracy in assessed diagram: ± 50° for solidus, ± 100° for liquidus.

2.3.26 The $FeO-ZrO_2$ system

The optimized phase diagram is shown in Fig. 2-41 along with the experimental points of [57Fis] who used X-ray techniques. No detectable solubility of ZrO_2 was found in solid FeO, but solubilities of 3 and 4 wt. % FeO in tetragonal ZrO_2 at 1800° and 1450°C respectively were reported [57Fis]. Although [69Bec] claimed the existence of Fe_2ZrO_4, Shultz and Muan [71Shu] later found no evidence for such a compound.

The reported eutectic composition and temperature of 3 wt. % ZrO_2 at 1330 ± 15°C [57Fis] are not consistent with the thermodynamic limiting liquidus slope law.

Two small parameters were used for the liquid phase in the optimization:

$$\omega = 23012 - 14.644T \quad Joules \qquad (2\text{-}3\text{-}51)$$

while the tetragonal and cubic ZrO_2 solutions were treated as Henrian with:

$$RT\ln\gamma_{FeO} = -11391 + 28.409T \quad J/mol \qquad (2\text{-}3\text{-}52)$$

relative to the solid standard state.

Parameters in equation (2-3-51) are small. Therefore, the liquid phase is slightly deviated from ideality.

Probable maximum inaccuracy in assessed diagram: ± 50° for solidus, ± 50° for liquidus.

2.4 CONCLUSIONS

In this chapter, linear as well as non-linear least squares regressions have been discussed.

Since thermodynamic properties such as partial Gibbs energy or partial enthalpy are non-linear functions with respect to the parameters of the modified quasi-chemical model, a non-linear least squares method has been developed based on a linear approximation of the Taylor expression. Therefore, phase diagram data such as the liquidus lines of pure components as well as the intermediate compounds and immiscibility gaps can be employed to optimize the quasi-chemical parameters simultaneously with those of thermodynamic measurements (such as the activity, Gibbs energy of formation or enthalpy of formation measurements). A binary optimization program called FITQUAS has been written based on the above non-linear least squares method. By FITQUAS all thermodynamic and phase diagram data of the liquid phase, such as activities and the entire liquidus surface, can be evaluated. Thermodynamic properties of intermediate compounds such as entropy or enthalpy of formation can be indirectly evaluated as well. On the other hand, by the calculated quasi-chemical parameters and the quasi-chemical model one can calculate both thermodynamic properties and the phase diagram of the system. The calculated activity data and phase diagram are well

reproduced within the reported experimental uncertainties. In this way, all liquid and solid thermodynamic properties and phase diagram data are internally consistent with each other.

Details of evaluation of 26 binary oxide systems have been discussed in Section 2.3. In the 26 binary systems, both thermodynamic and phase diagram data have been well reproduced within their reported experimental uncertainties. A list of all optimized binary oxide systems presently in the database is shown in Table 2-1. A discussion of 15 binary rare earth oxide-Al_2O_3 systems will be shown in Chapter 3, and evaluations of the binary systems containing PbO and ZnO will be introduced in Chapter 5.

Thermodynamic properties of pure components and intermediate compounds are listed in the Appendix.

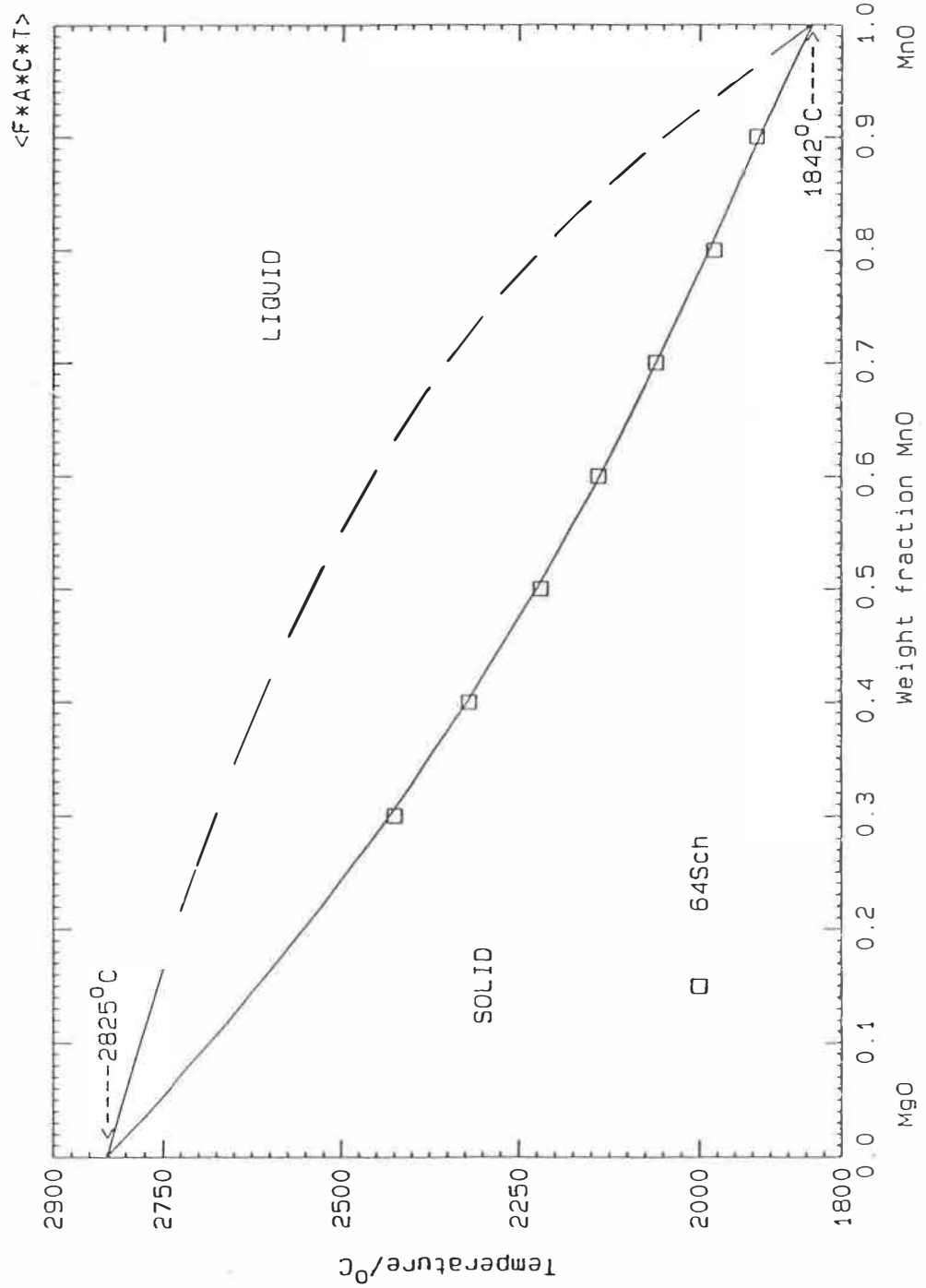


Fig. 2-1 Optimized MgO-MnO Phase Diagram.

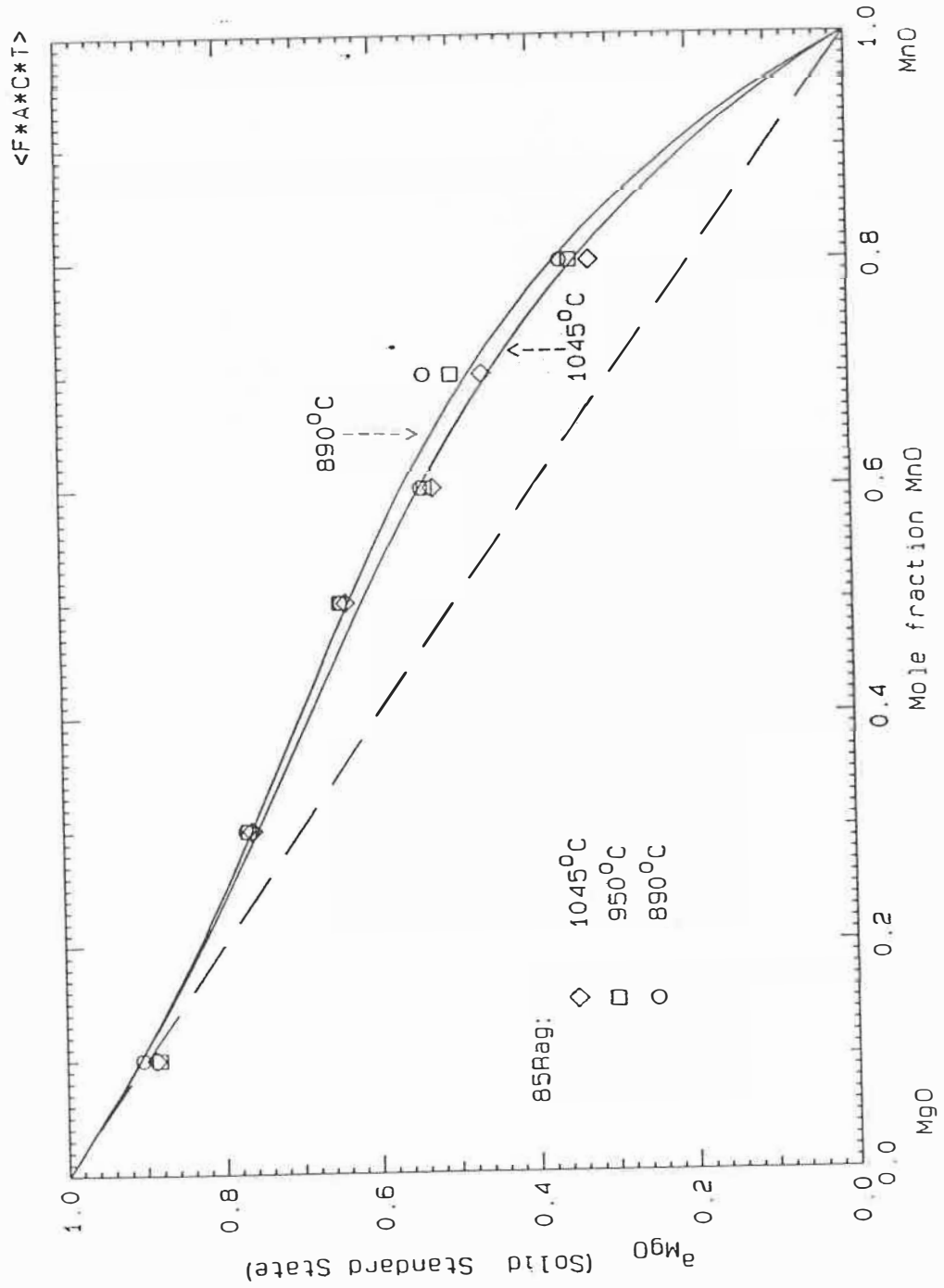


Fig. 2-2 Optimized activities of MgO in solid MgO-MnO solutions.

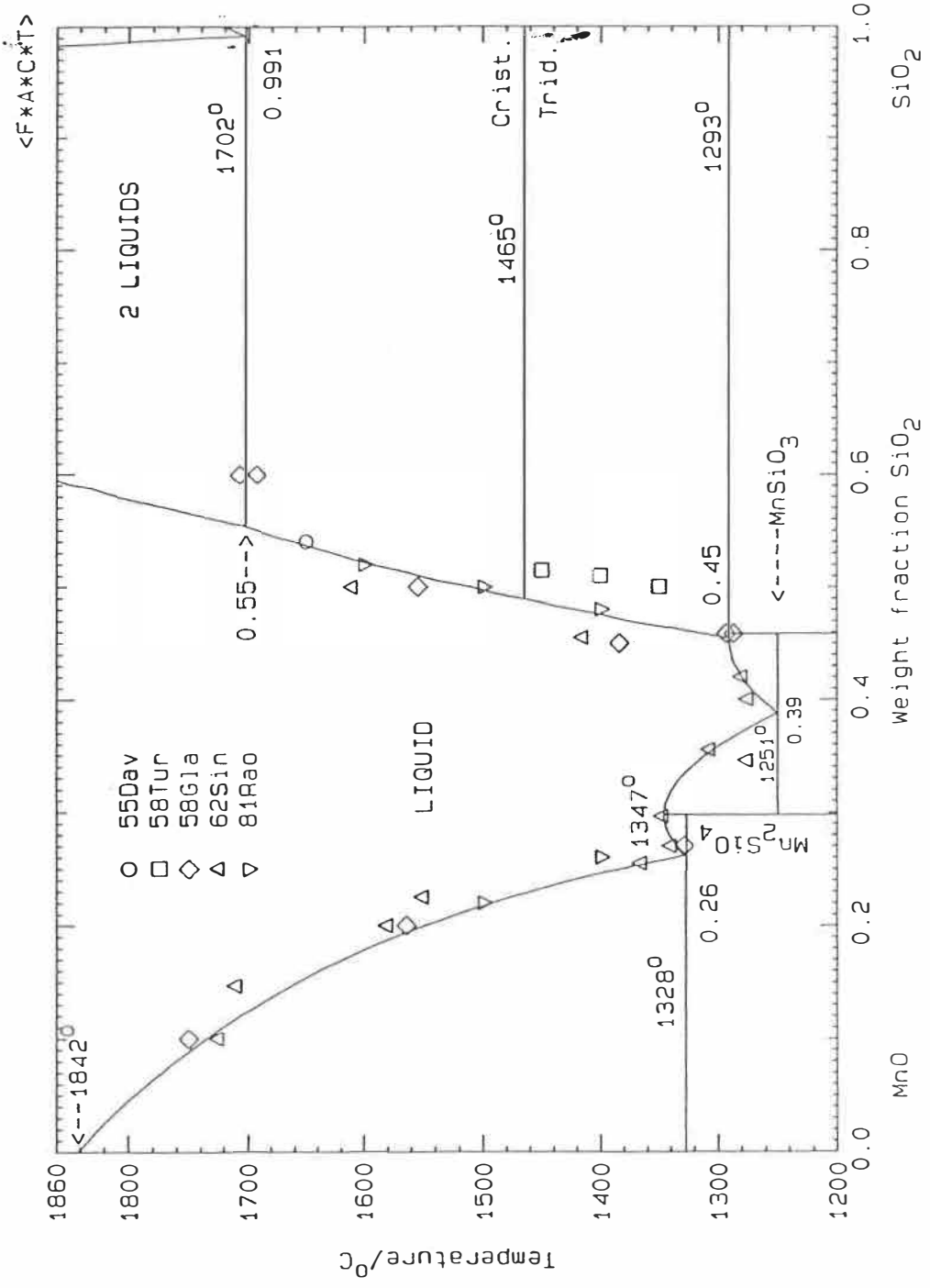


Fig. 2-3 Optimized $MnO-SiO_2$ Phase Diagram

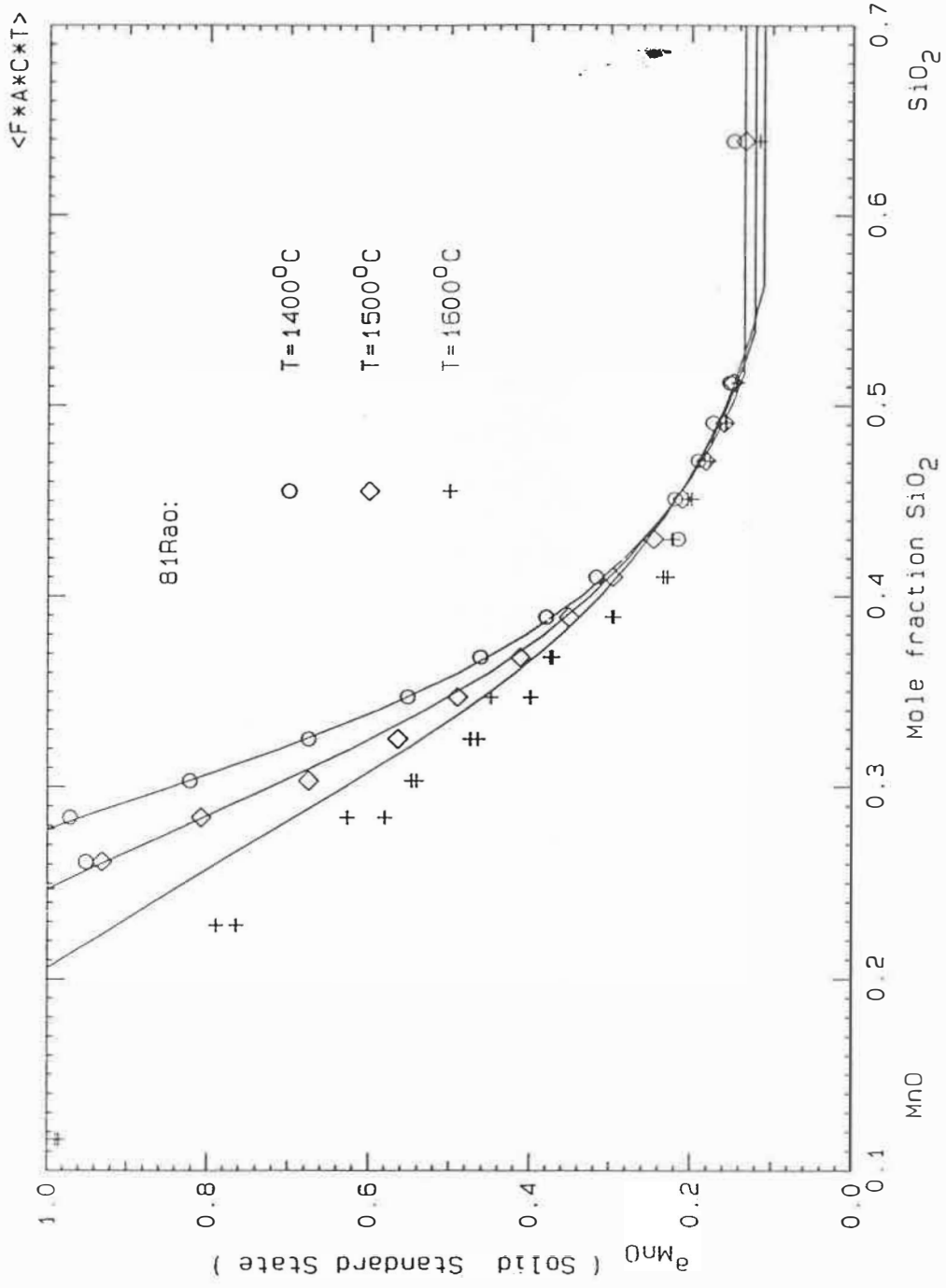


Fig. 2-4 Optimized Activities of MnO in Liquid $MnO-SiO_2$ Solutions

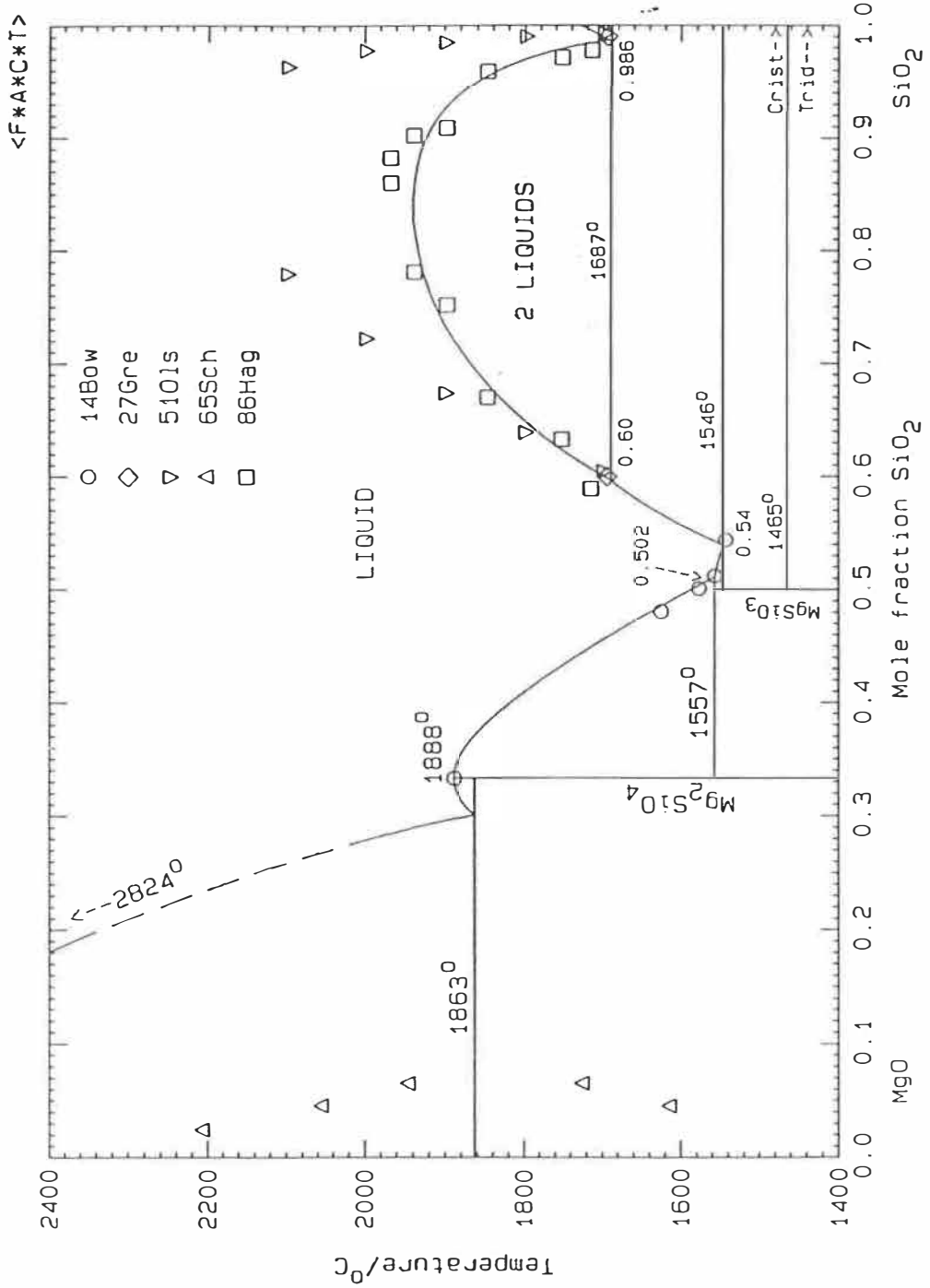


Fig. 2-5 Optimized MgO-SiO_2 Phase Diagram

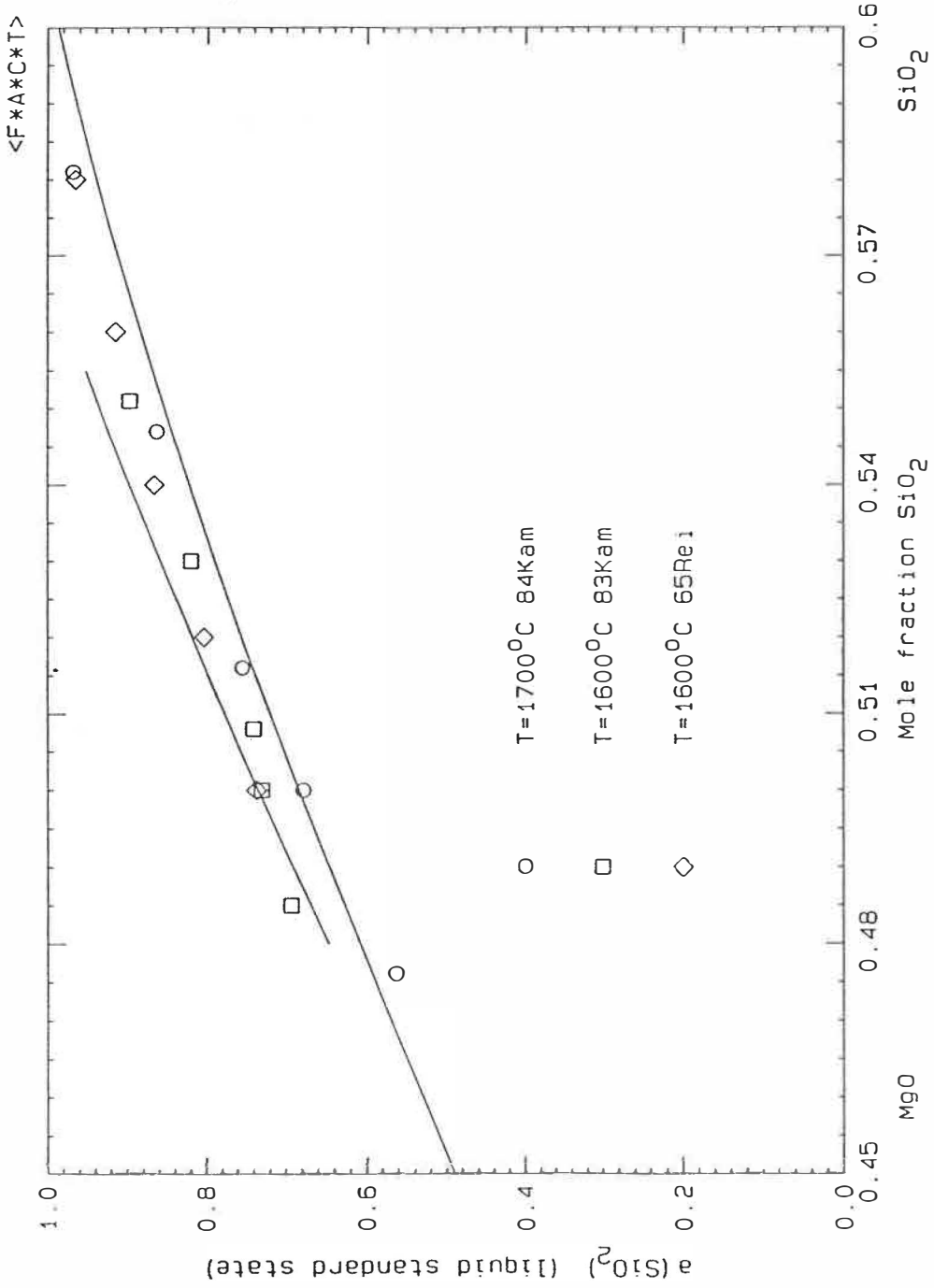


Fig. 2-6 Calculated activities of SiO_2 in liquid $MgO-SiO_2$ solutions at 1600° and 1700°C

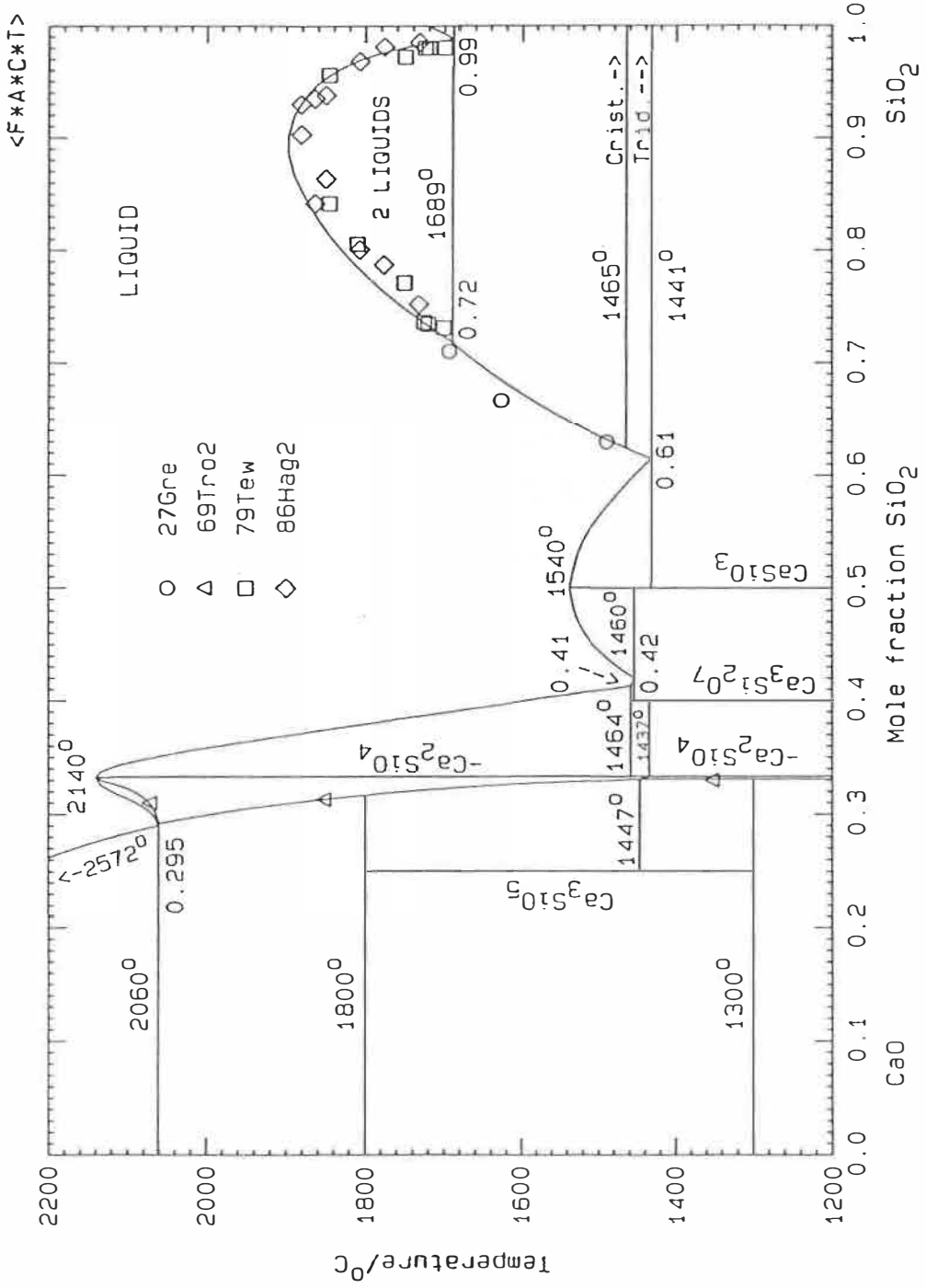


Fig. 2-7 Optimized CaO-SiO_2 Phase Diagram

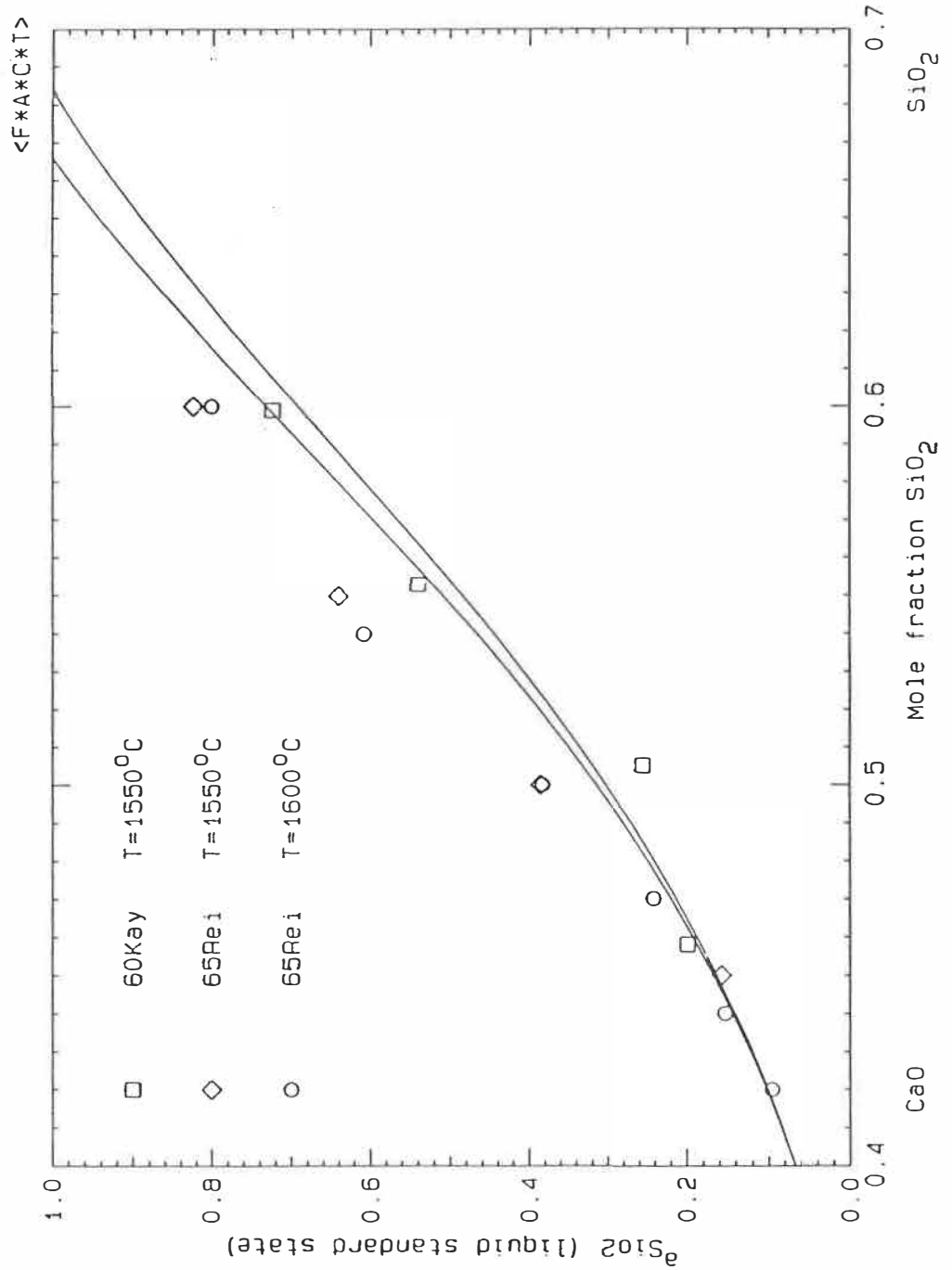


Fig. 2-8 Calculated SiO_2 activities in liquid CaO-SiO_2 solutions at 1550°C (upper curve) and 1600°C (lower curve)

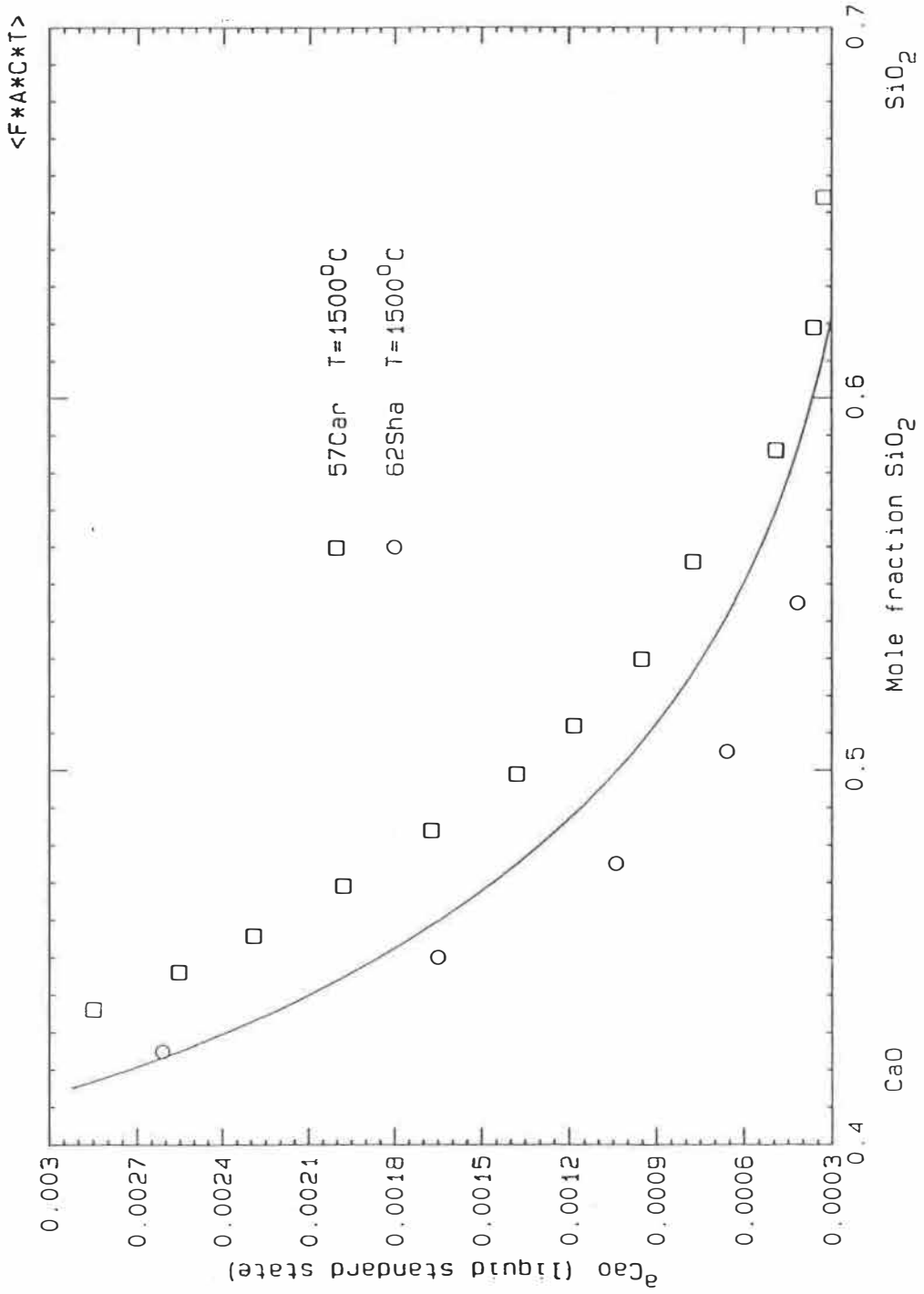


Fig. 2-9 Calculated CaO activities in liquid CaO-SiO_2 solutions at 1500°C

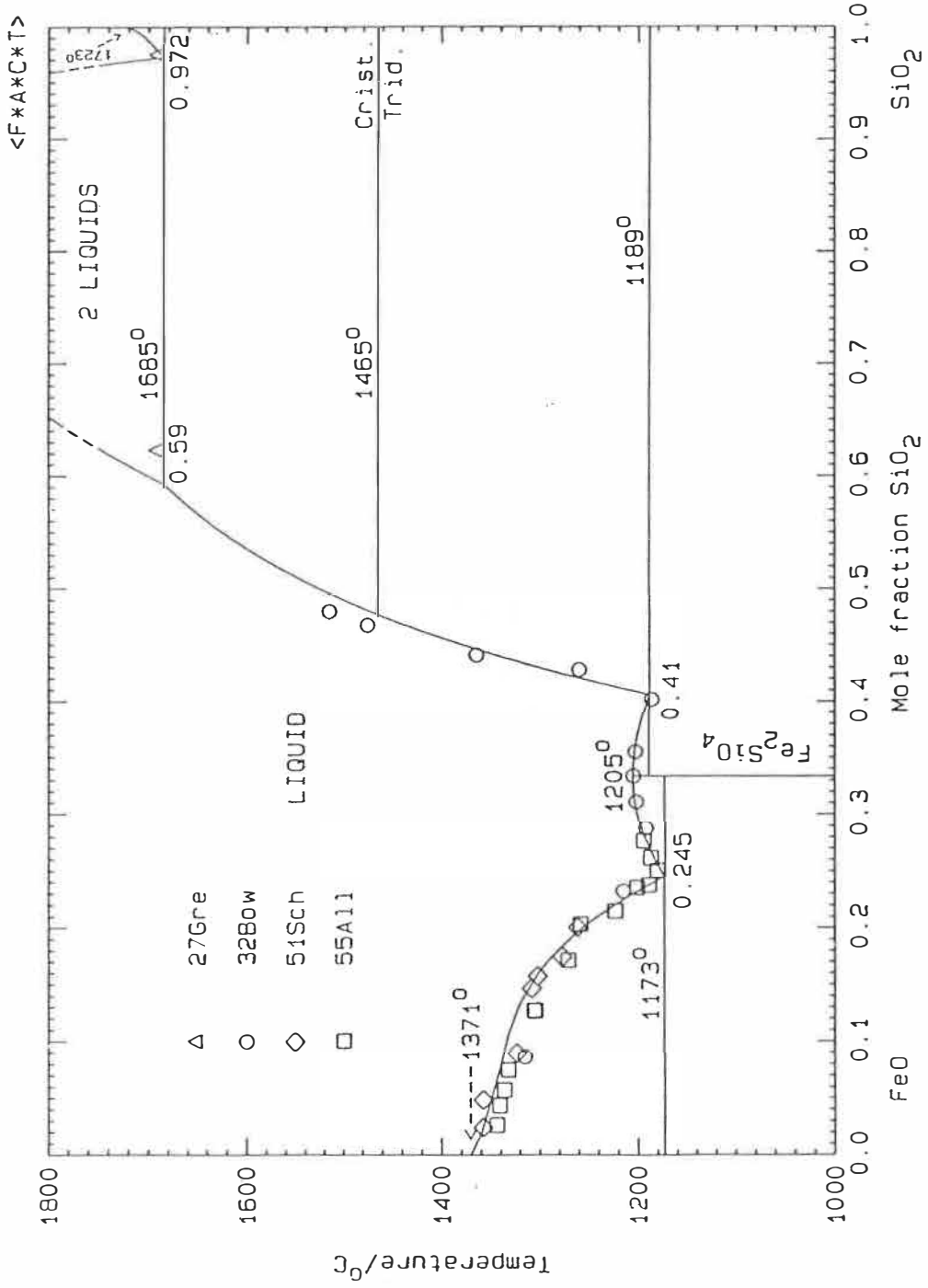


Fig. 2-10 Optimized FeO-SiO_2 Phase Diagram for equilibrium with metallic Fe (total iron expressed as "FeO")

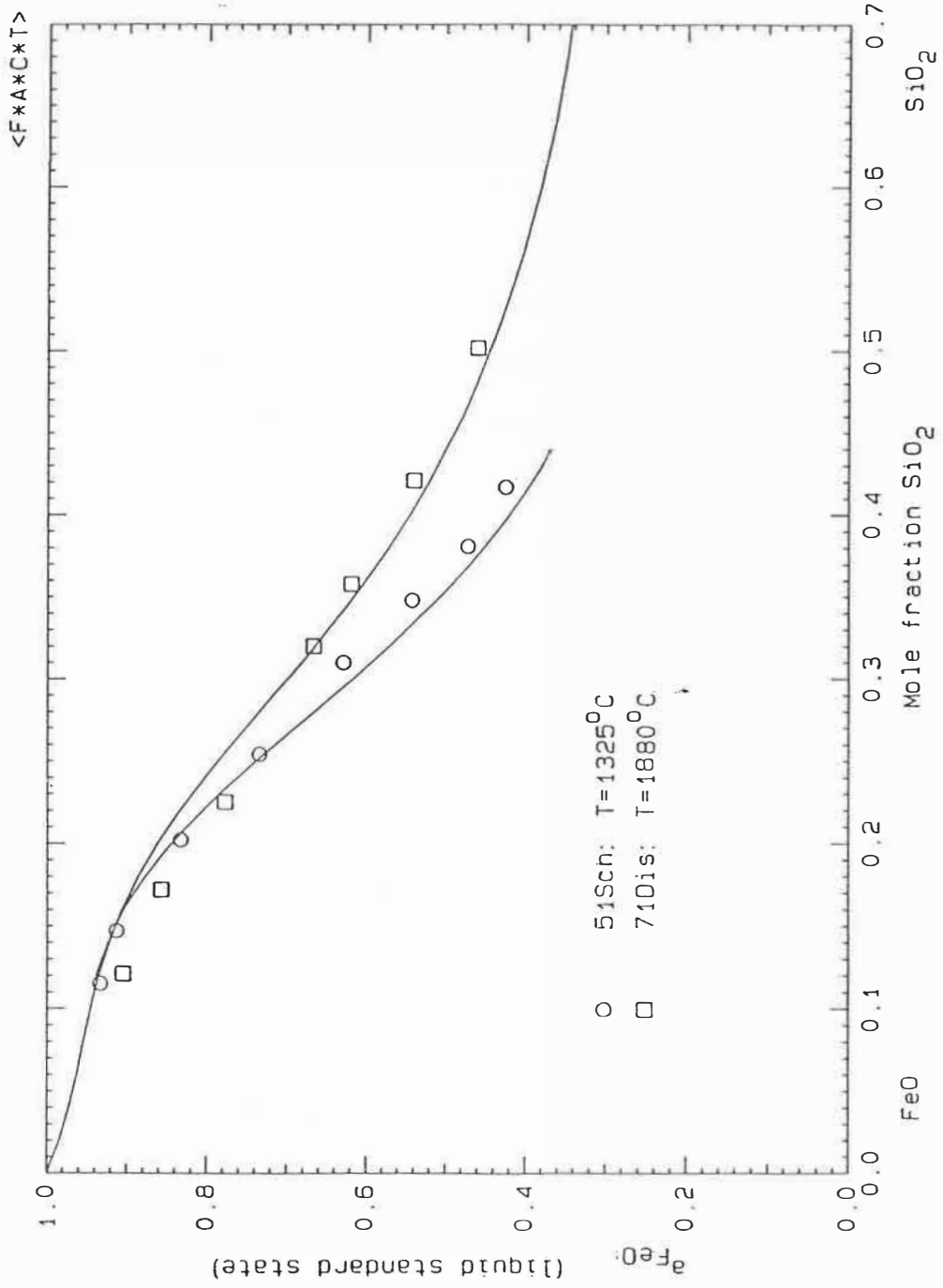


Fig. 2-11 Calculated activity of FeO in liquid $FeO-SiO_2$ solutions at 1325°C and 1880°C

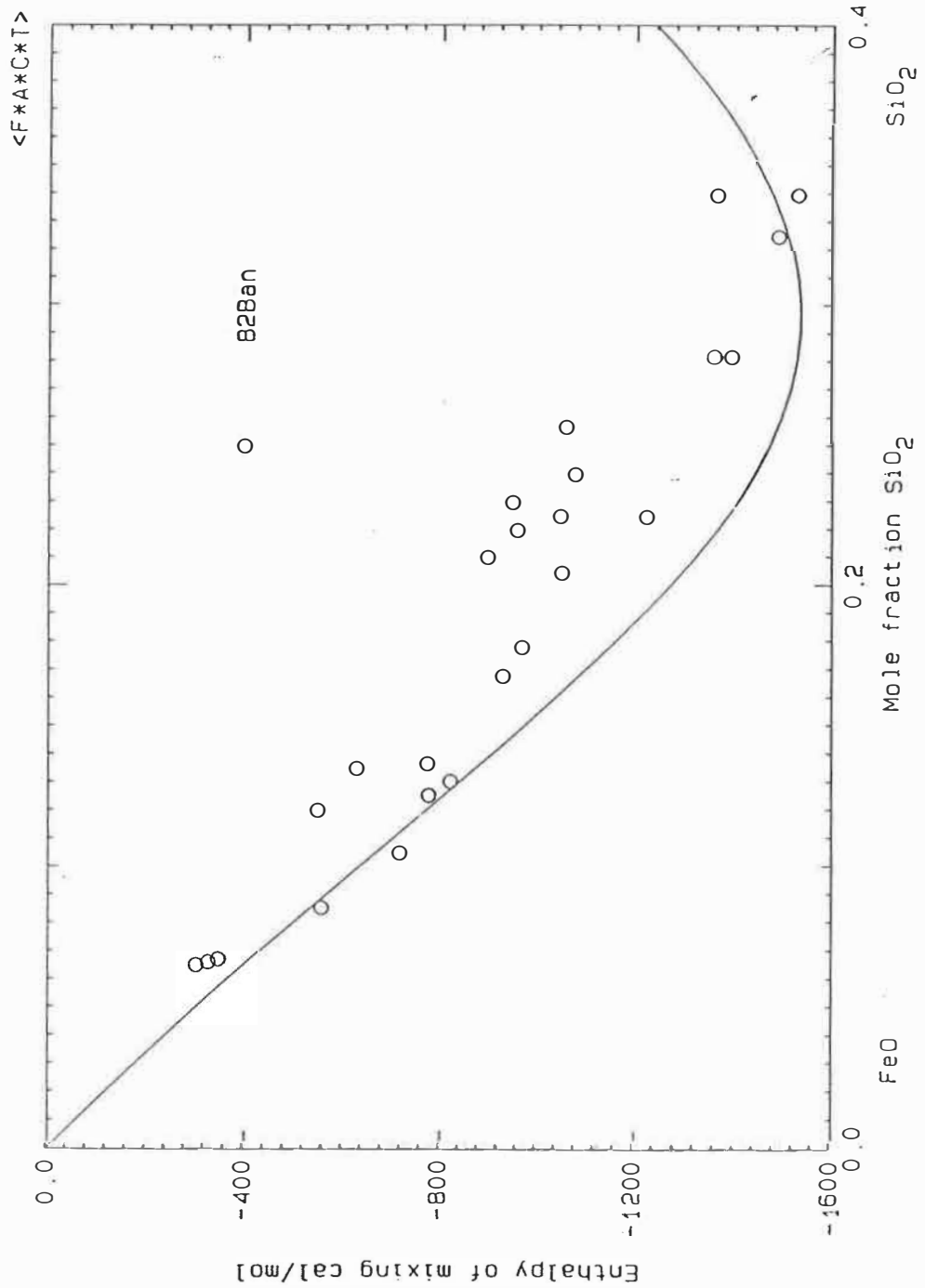


Fig. 2-12 Calculated enthalpy of mixing of liquid FeO and solid SiO_2 at 1420°C compared to data of Ban-ya et al [82Ban1].

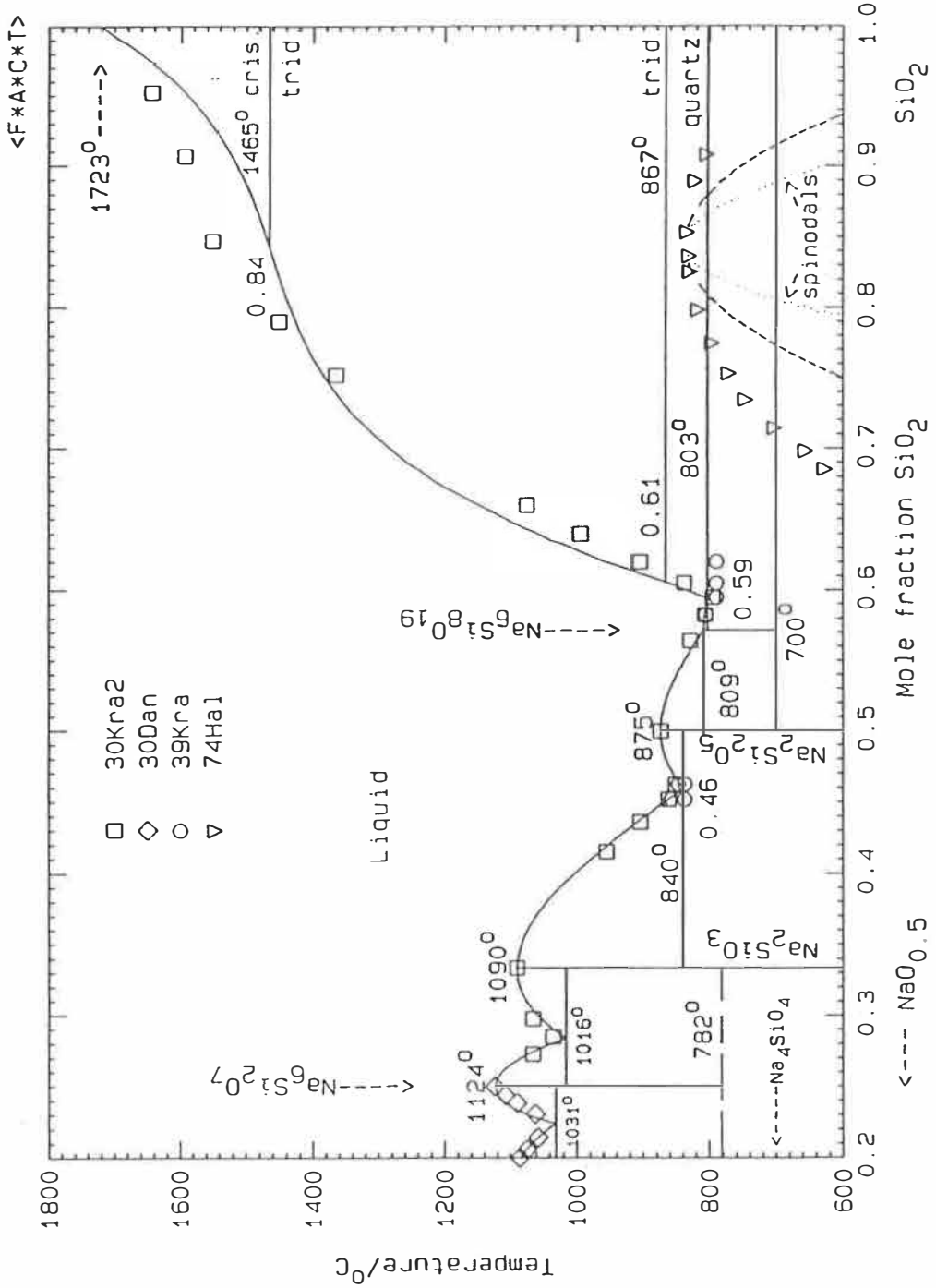


Fig. 2-13 Assessed Na_2O-SiO_2 Phase Diagram Compositions in terms of components $NaO_{0.5}$-SiO_2

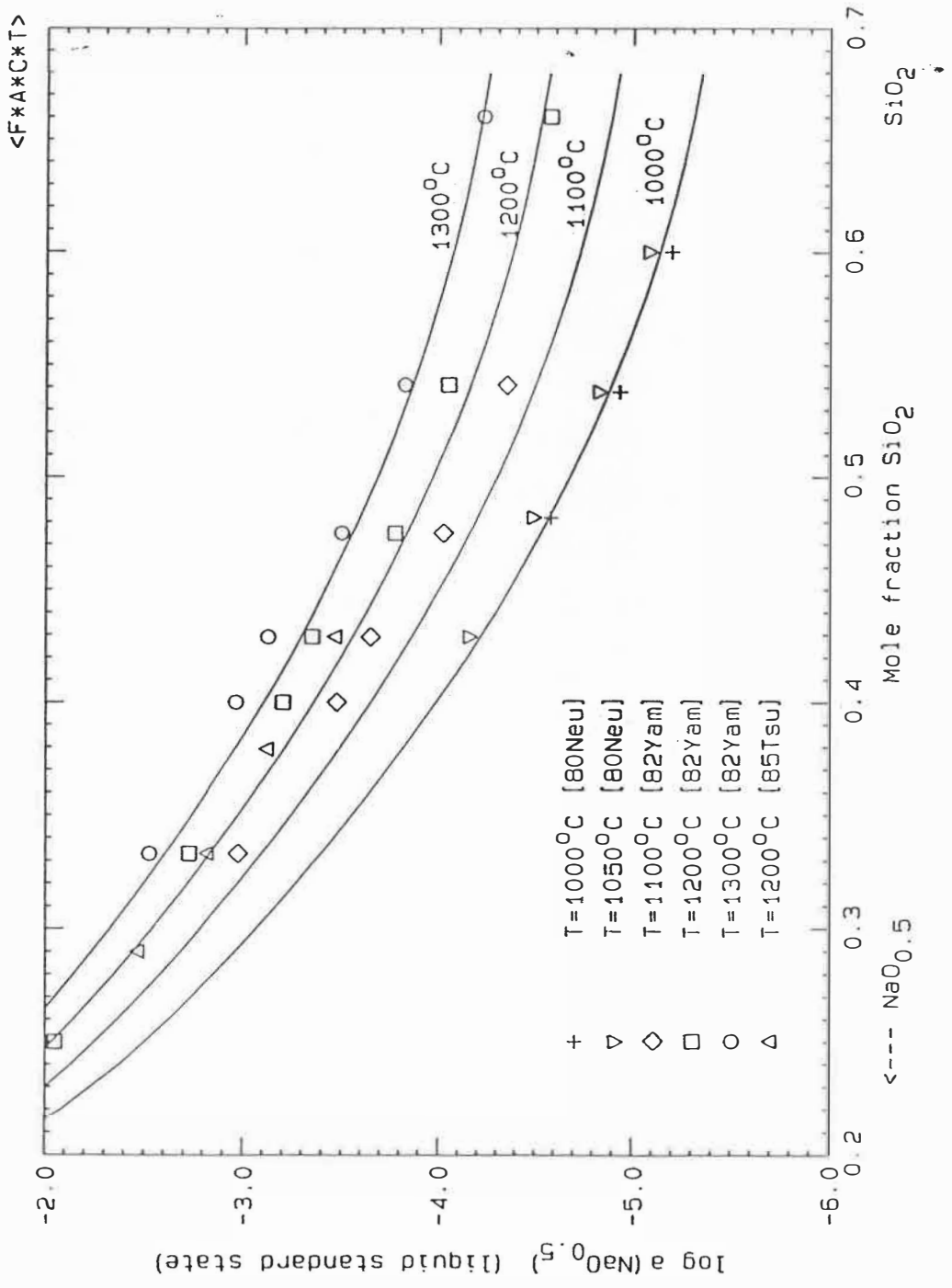


Fig. 2-14 Calculated $NaO_{0.5}$ Activities in Liquid Na_2O-SiO_2 Solutions

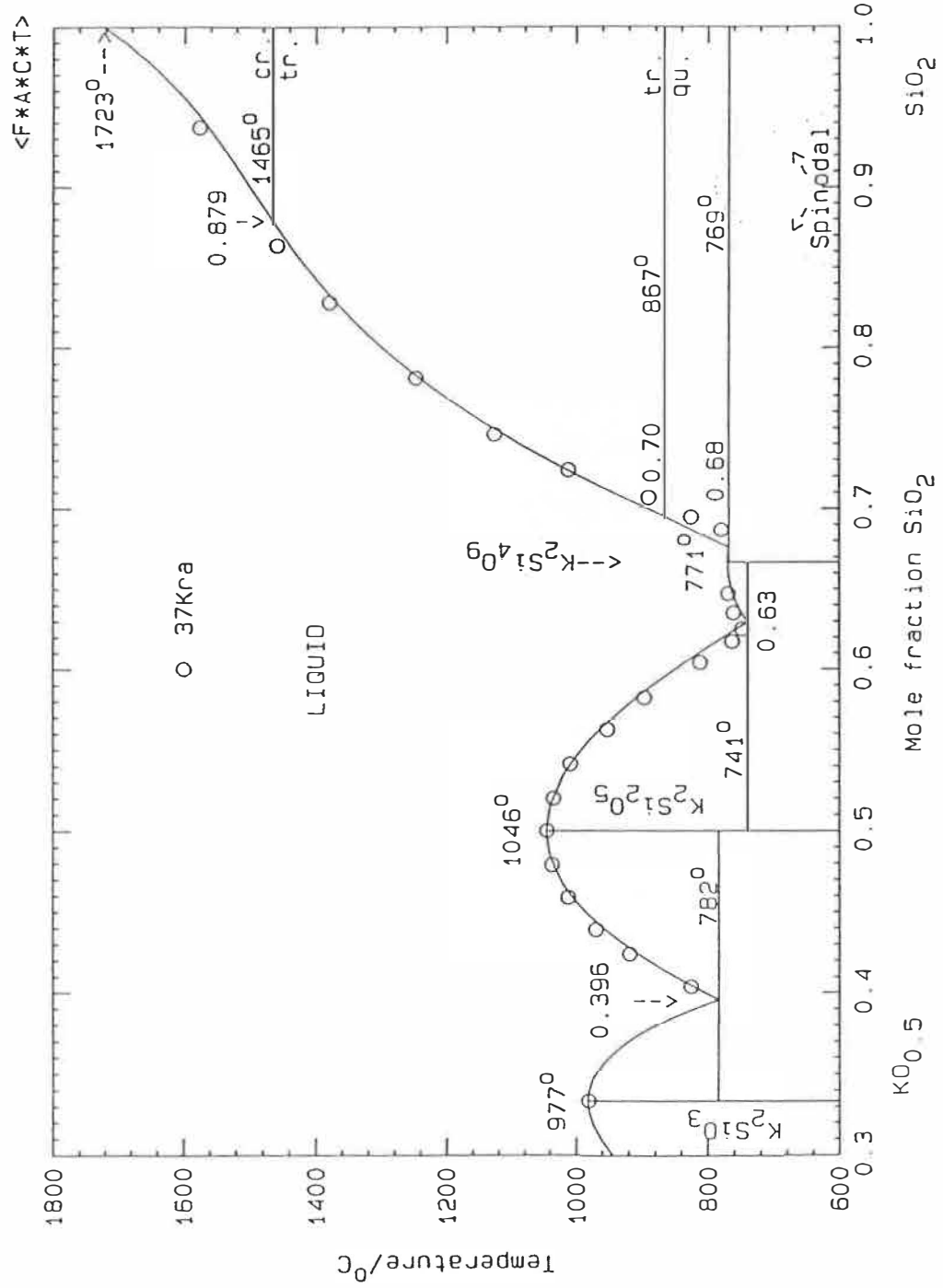


Fig. 2-15 Optimized K_2O-SiO_2 Phase Diagram Compositions in terms of components $KO_{0.5}$-SiO_2

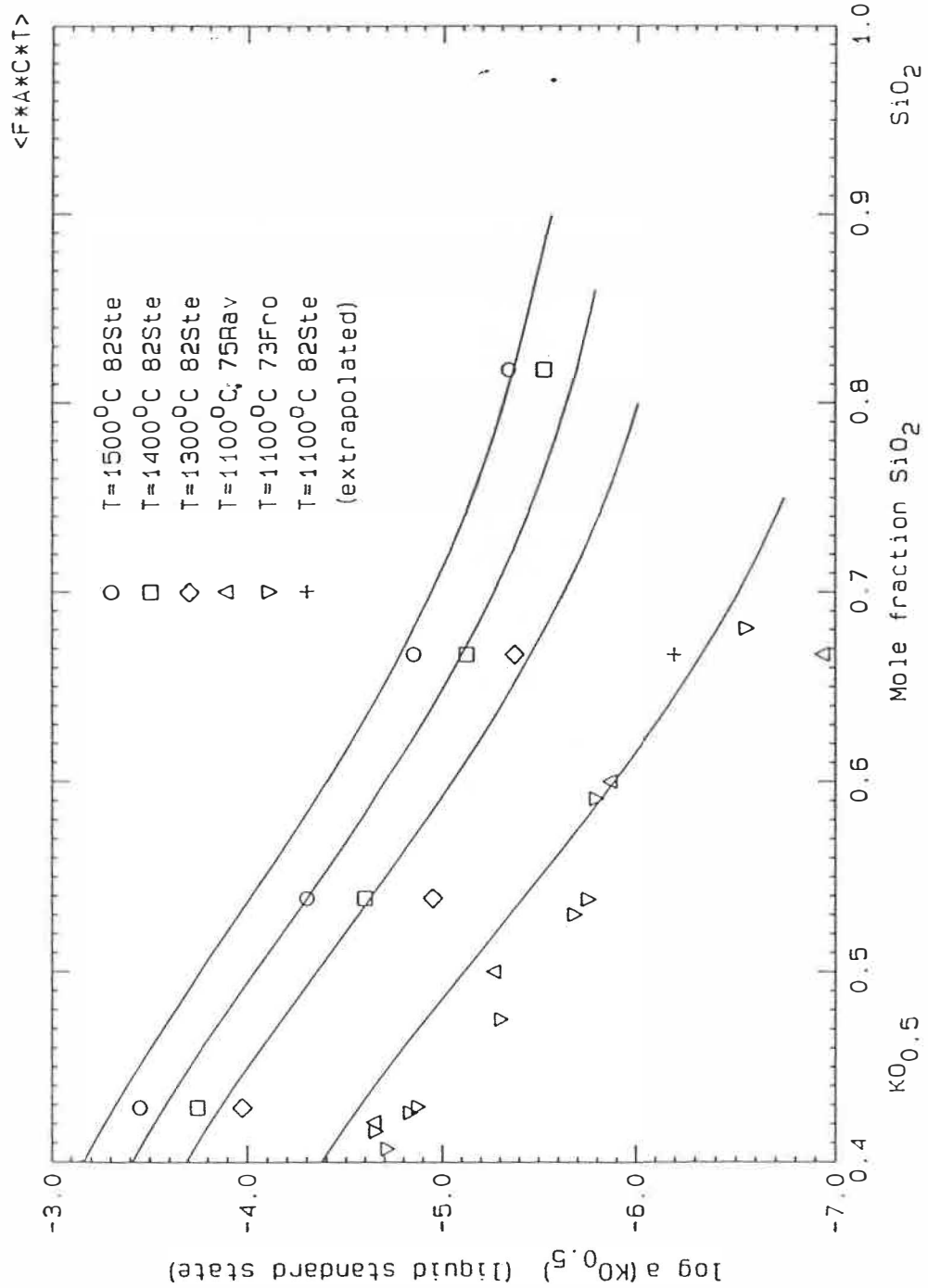


Fig. 2-16 Activity of $KO_{0.5}$ in liquid $KO_{0.5}$-SiO_2 solutions calculated at 1100°C, 1300°, 1400° and 1500°C.

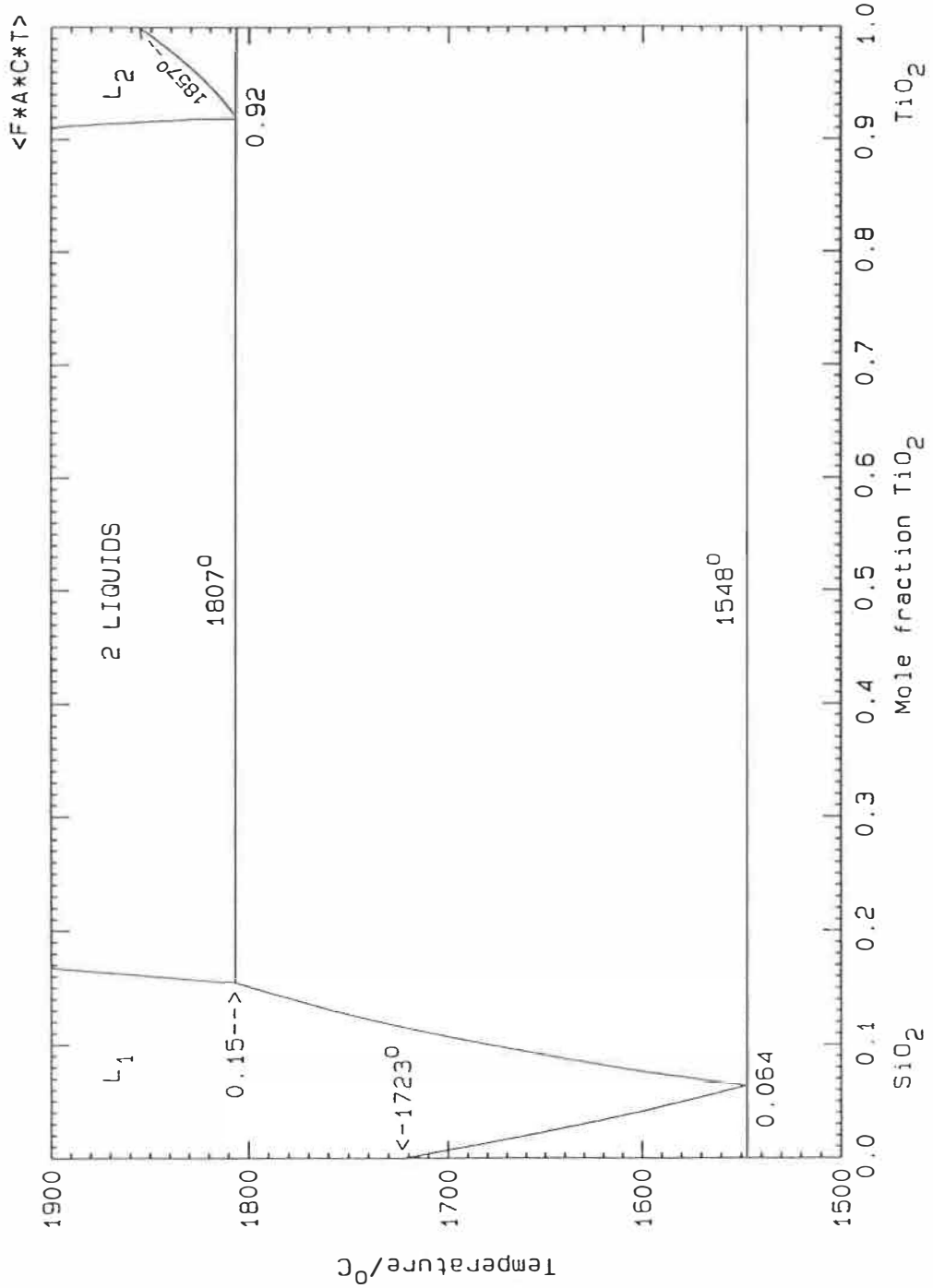


Fig. 2-17 Optimized SiO_2-TiO_2 Phase Diagram

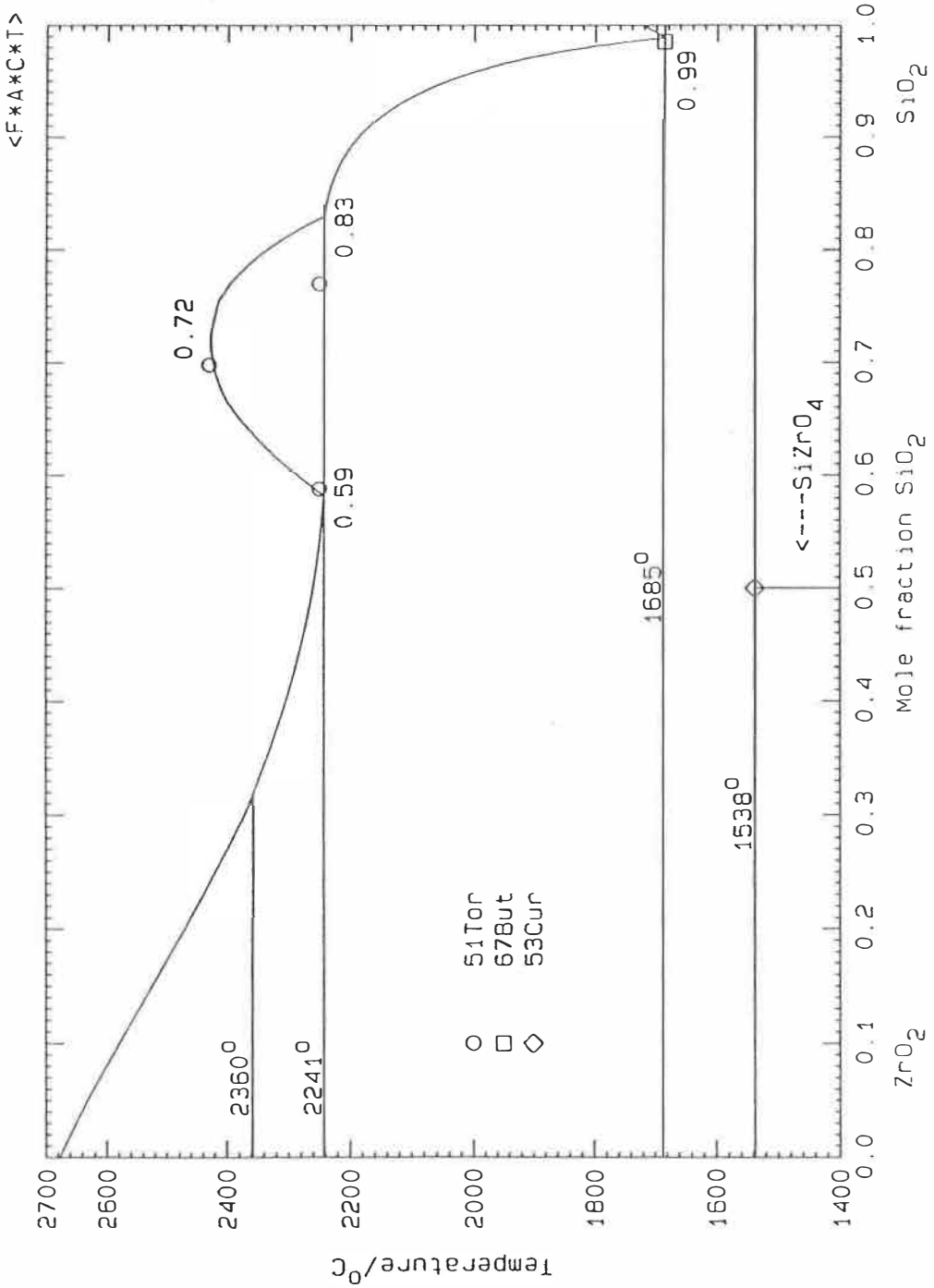


Fig. 2-18 Optimized ZrO_2-SiO_2 phase diagram showing data of [56Tor, 67But, 53Cur].

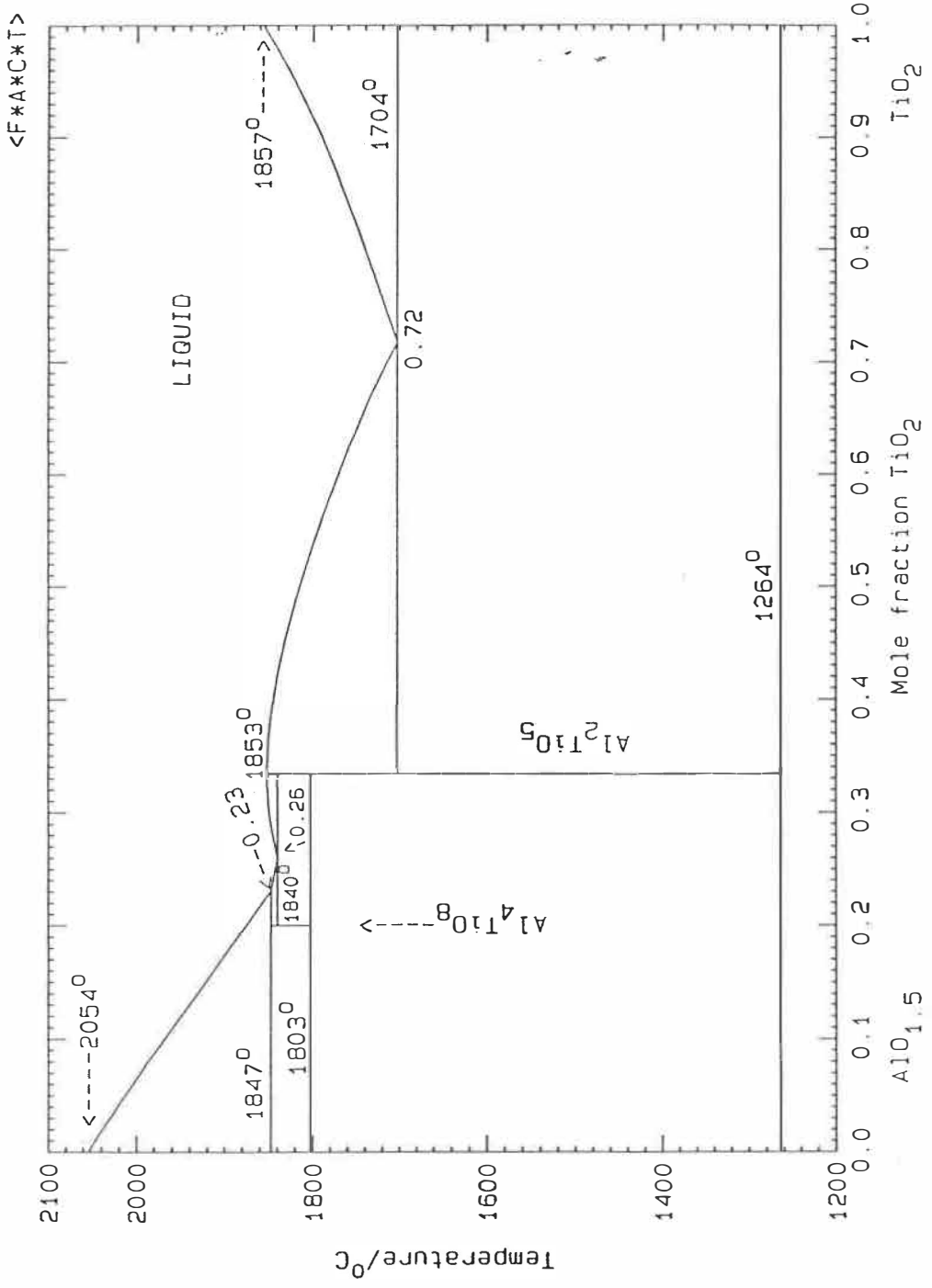


Fig. 2-19 Optimized Al_2O_3-TiO_2 Phase Diagram Compositions are in Terms of the Components $AlO_{1.5}$-TiO_2

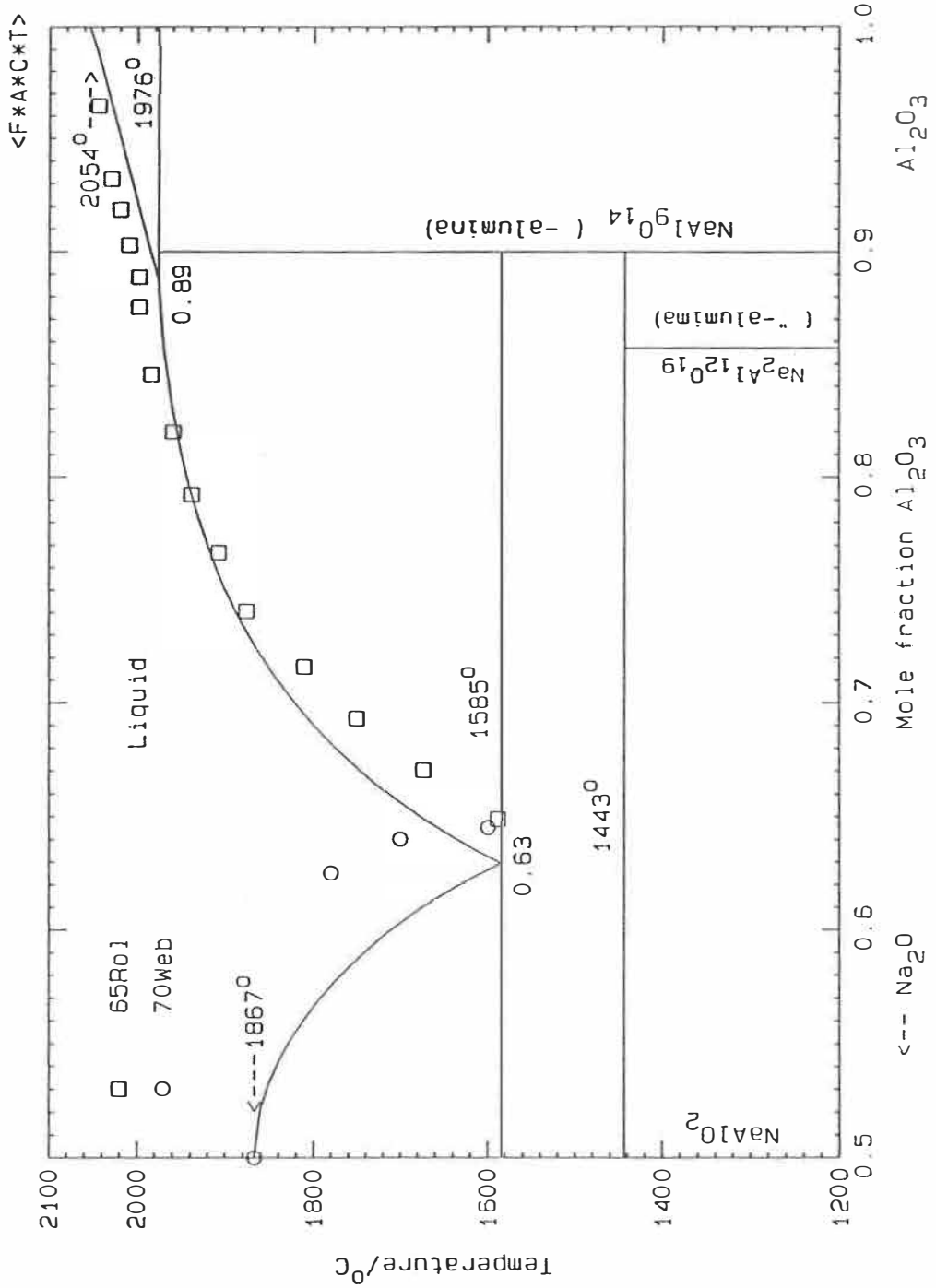


Fig. 2-20 Assessed Na_2O-Al_2O_3 Phase Diagram

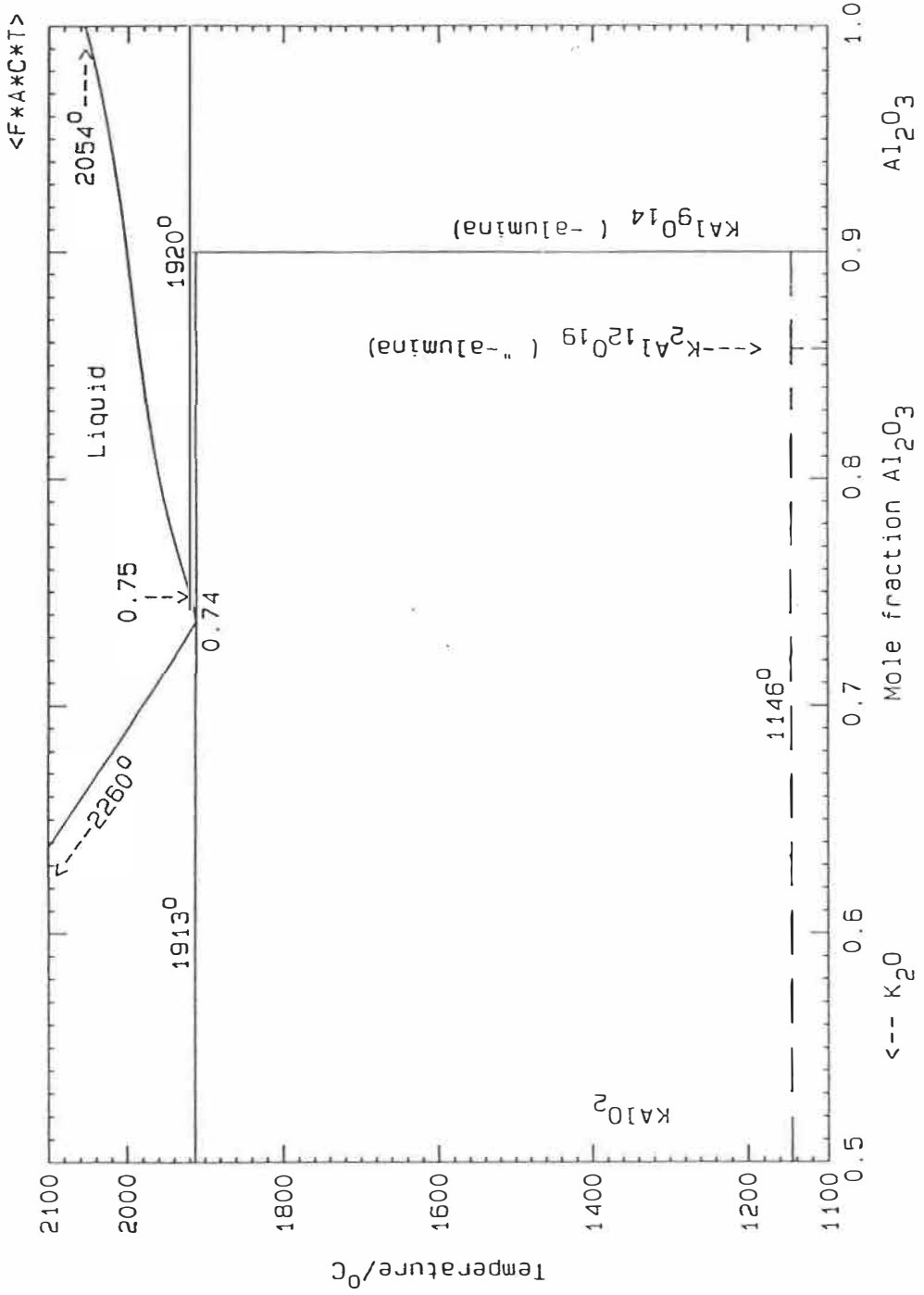


Fig. 2-21 Assessed K_2O-Al_2O_3 Phase Diagram

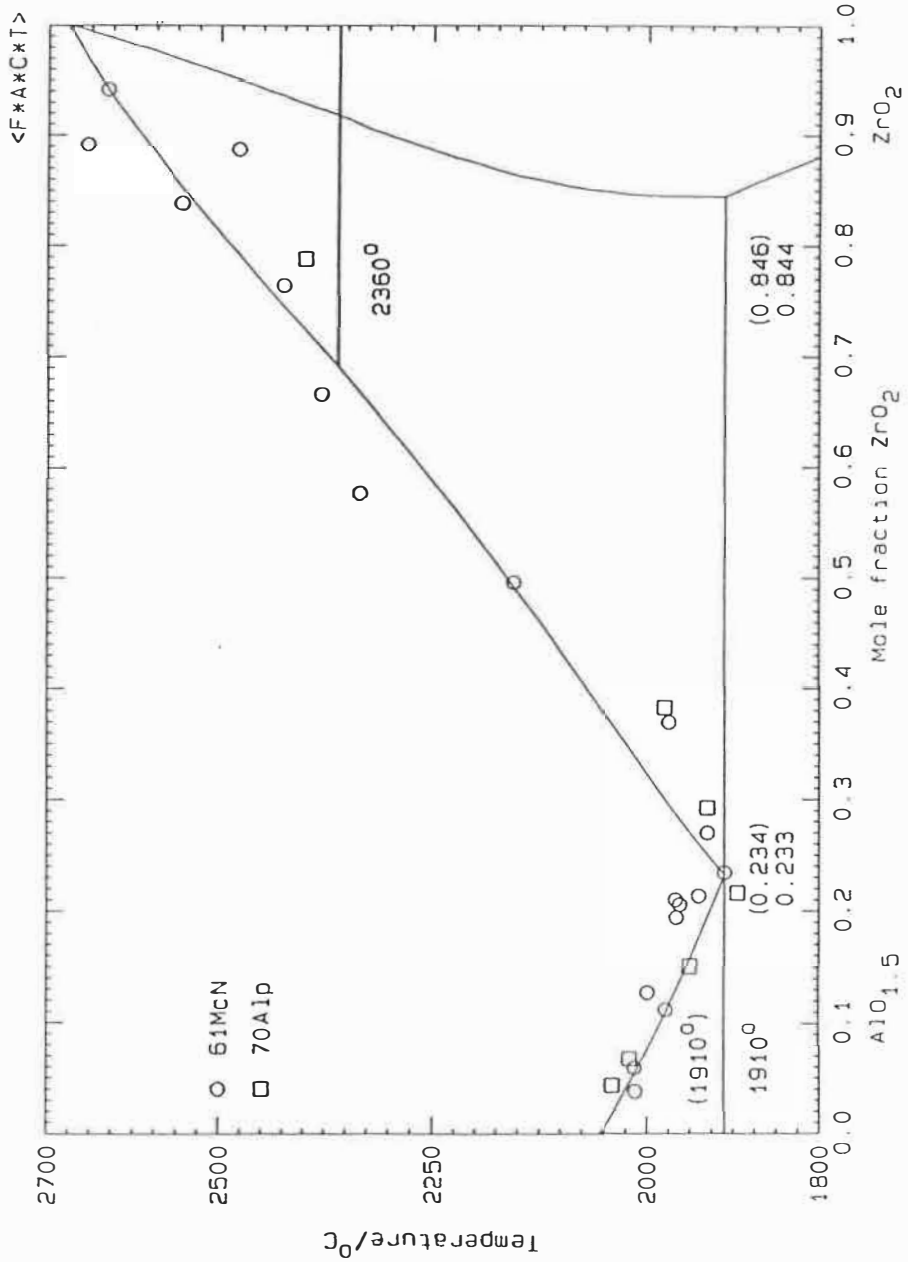


Fig. 2-22 Optimized $AlO_{1.5}$-ZrO_2 phase diagram with selected experimental points [70Alp, 61McN]. Values in parentheses are experimental from [81Fis, 64Alp].

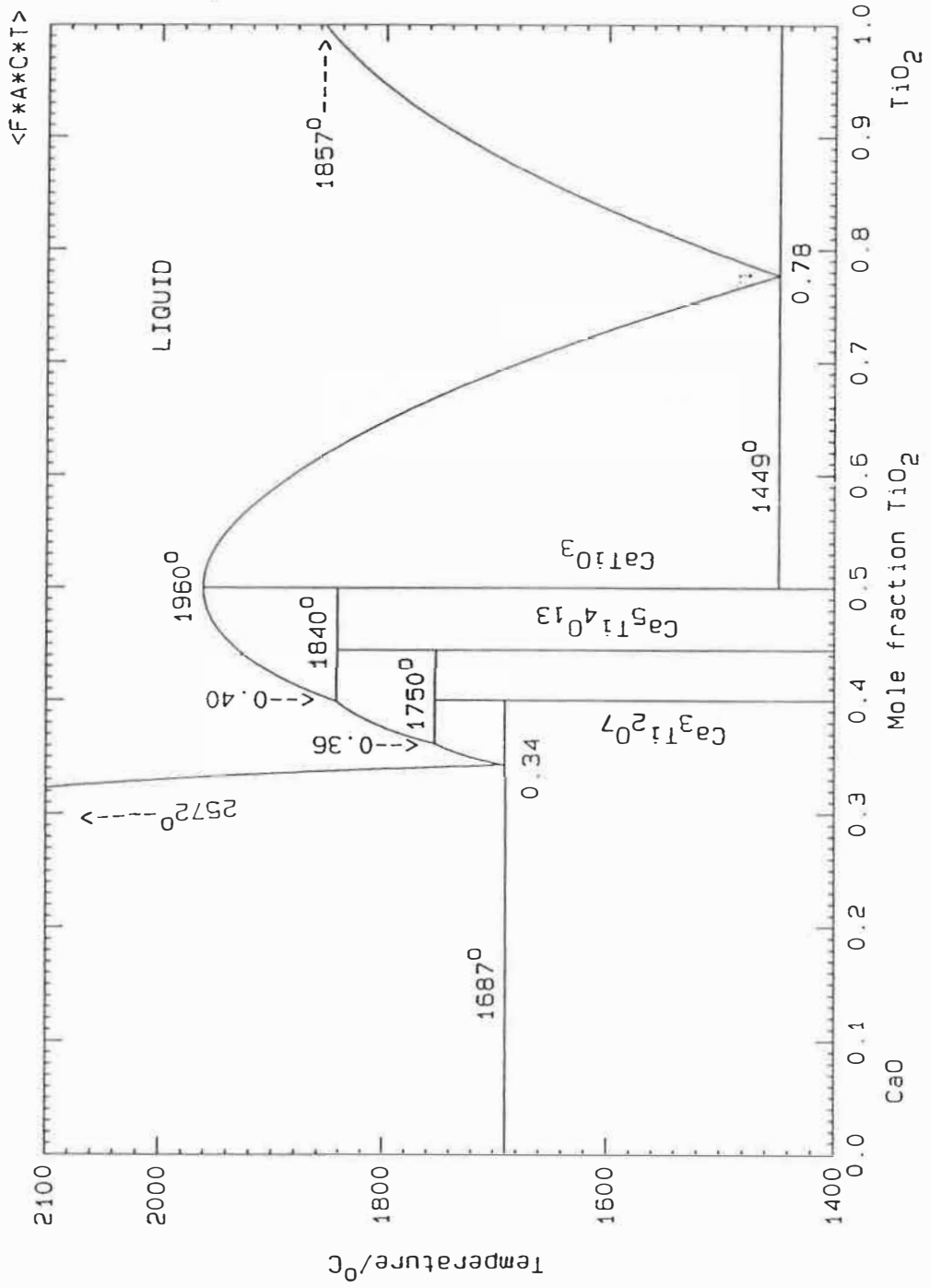


Fig. 2-23 Optimized $CaO-TiO_2$ Phase Diagram

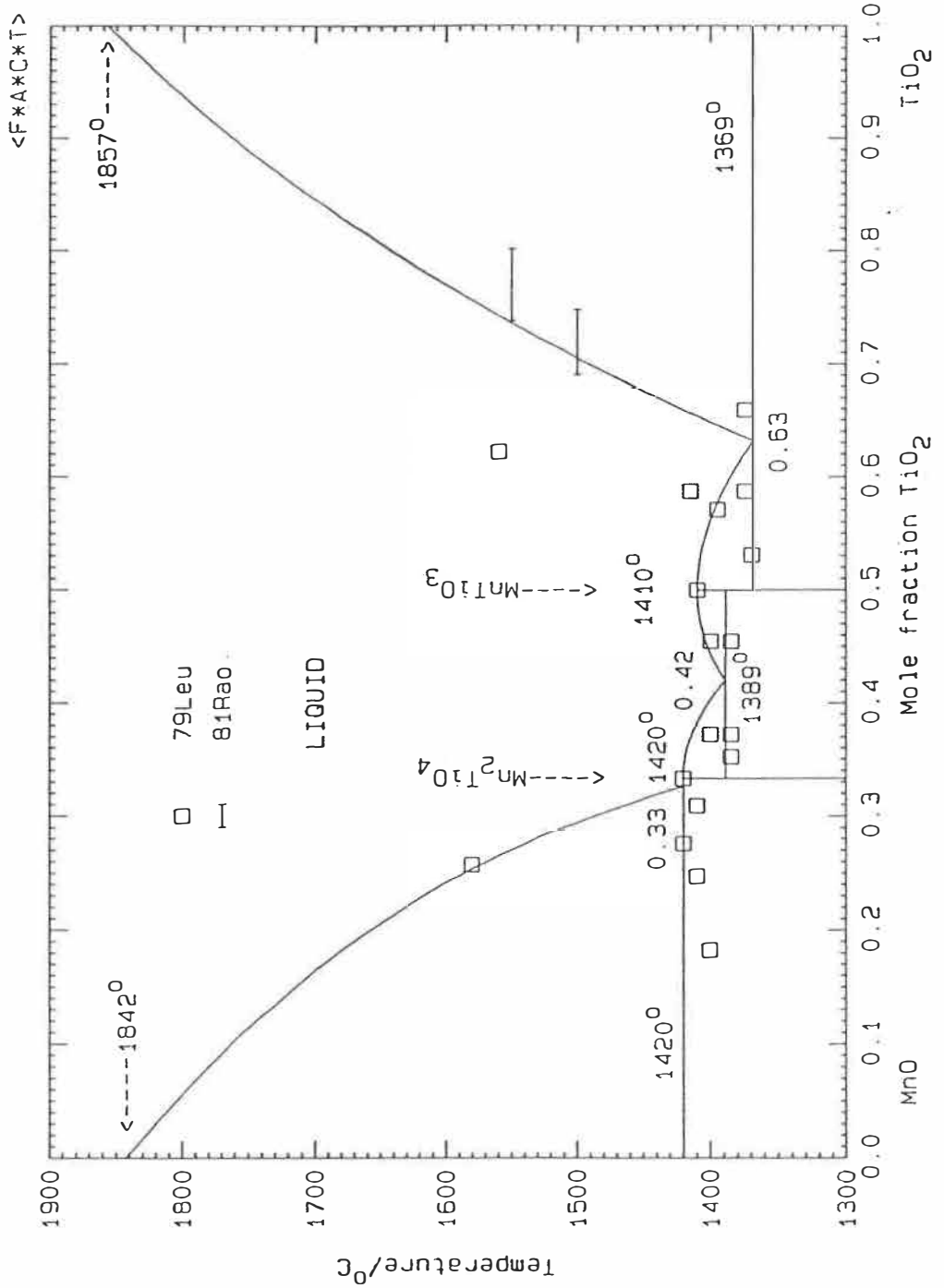


Fig. 2-24 Optimized MnO-TiO_2 Phase Diagram

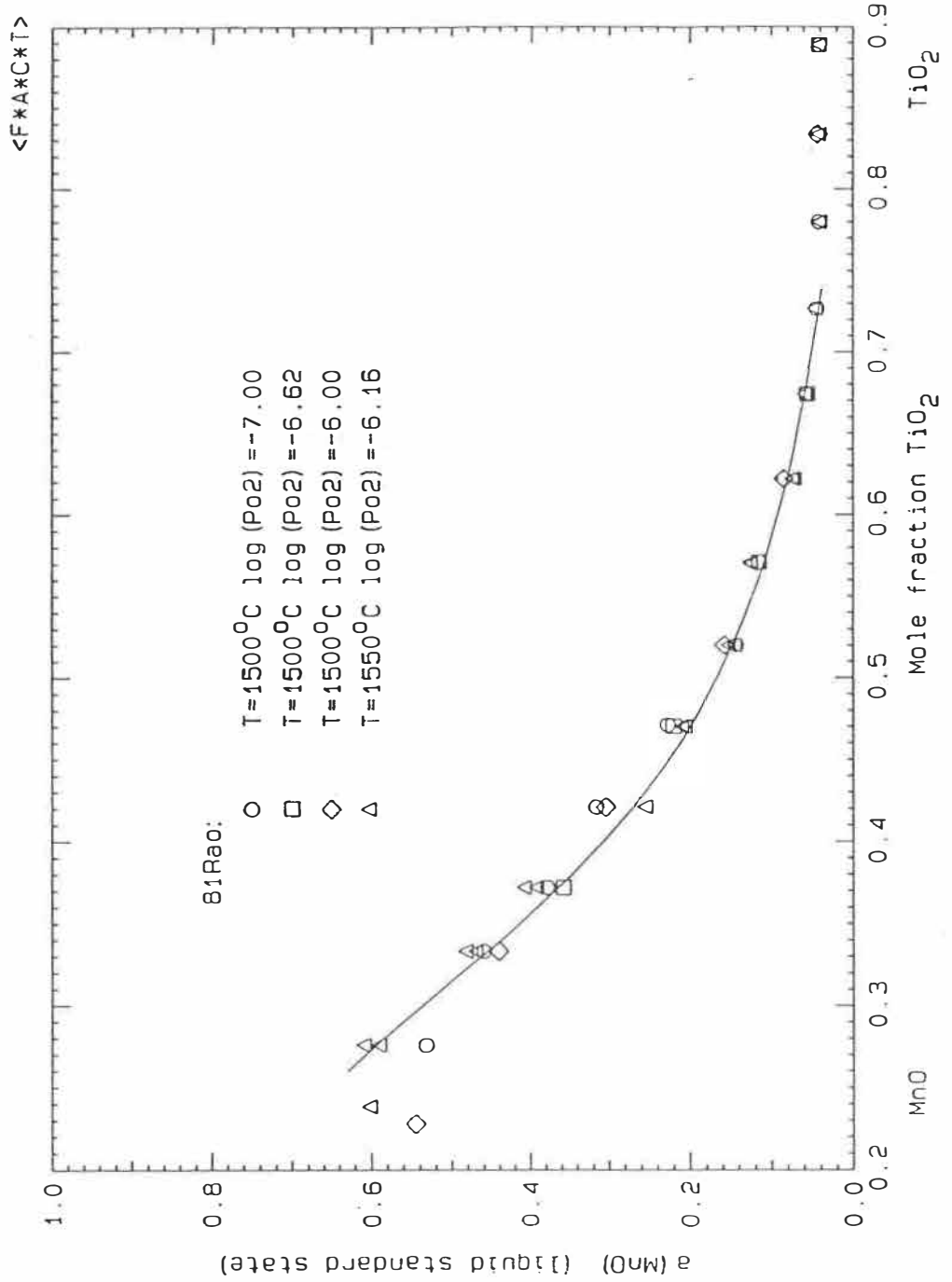


Fig. 2-25 Optimized activities of MnO in liquid $MnO-TiO_2$ solutions at 1500°C

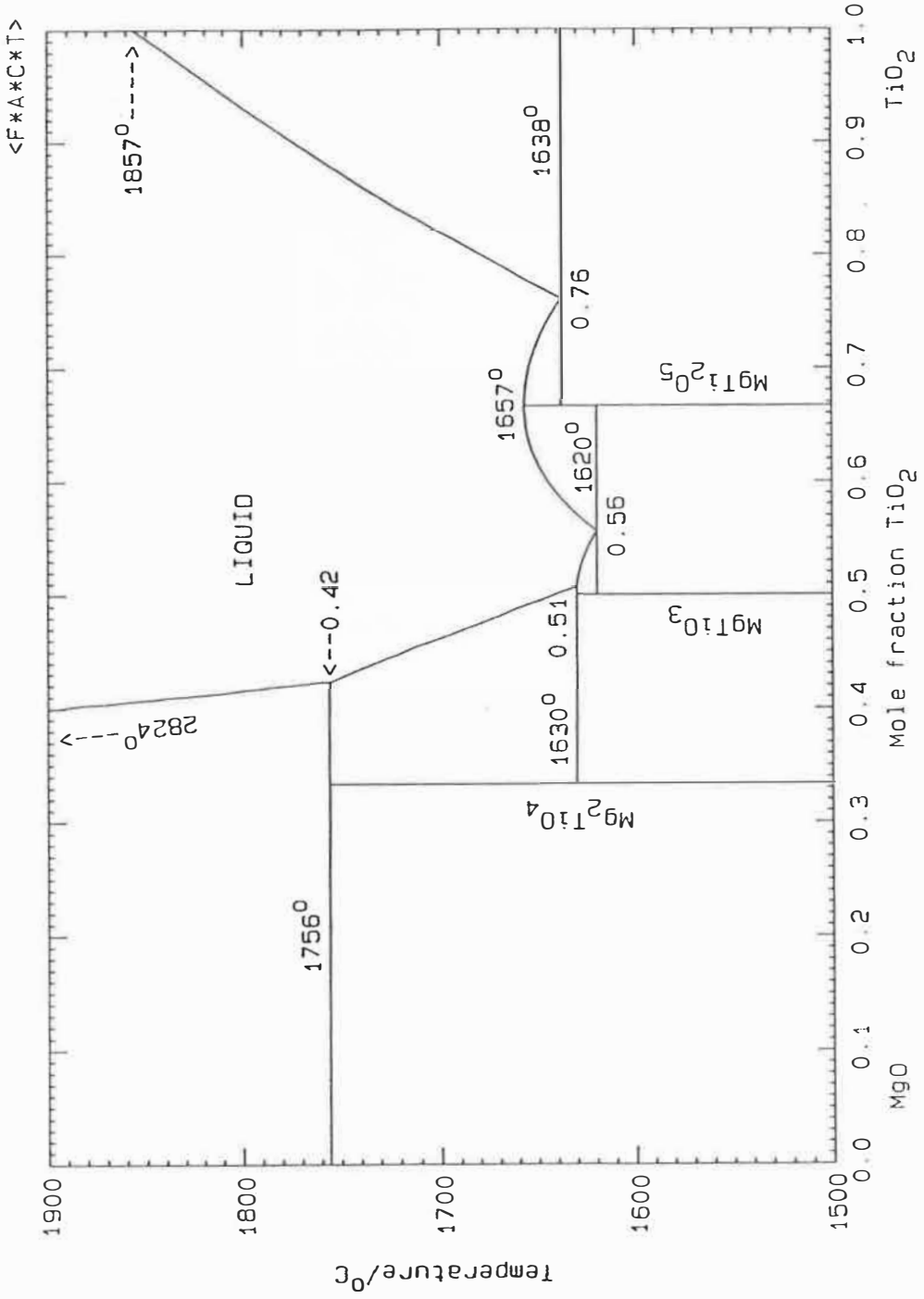


Fig. 2-26 Optimized $MgO-TiO_2$ Phase Diagram

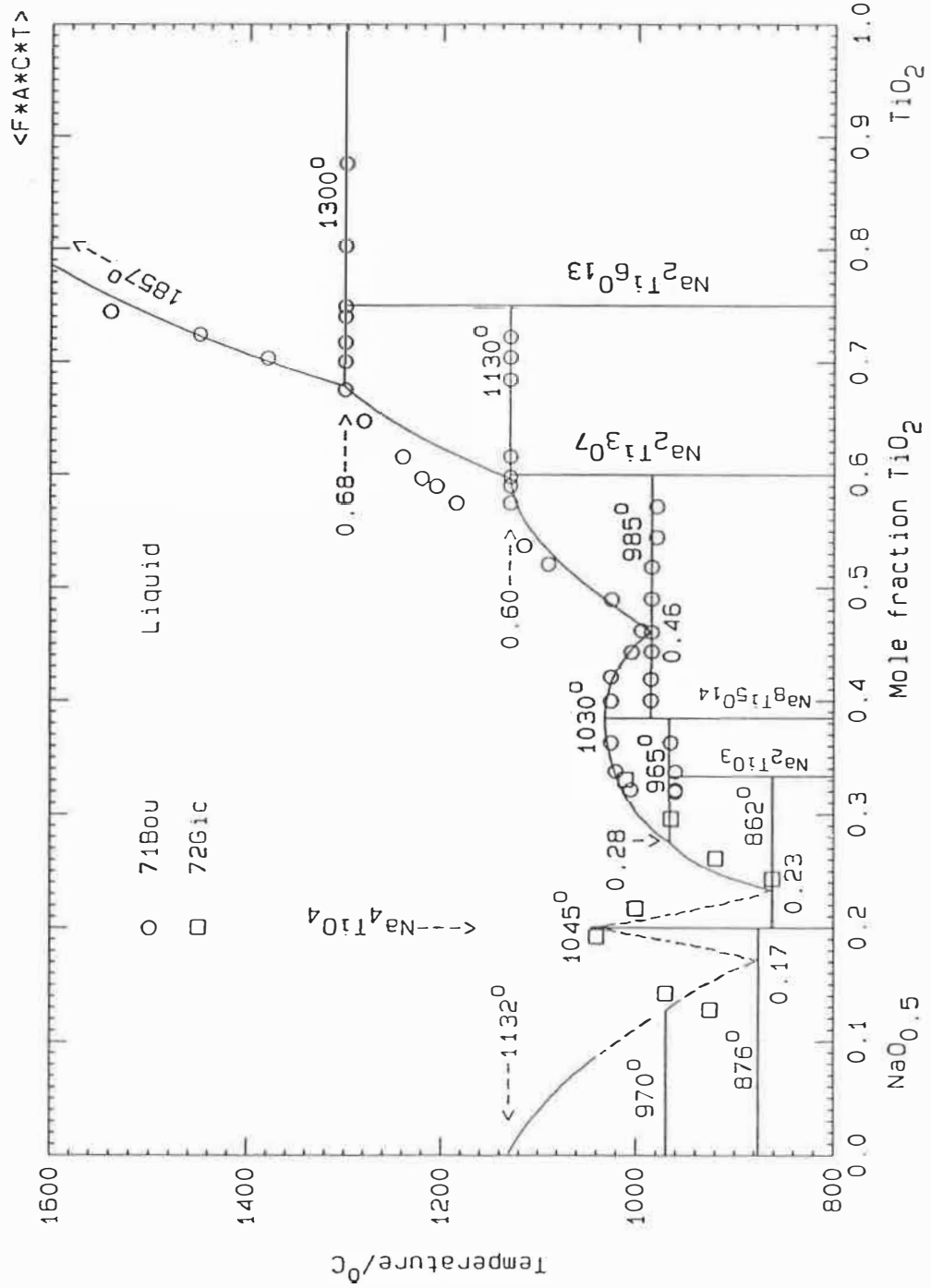


Fig. 2-27 Assessed Na_2O-TiO_2 Phase Diagram
Compositions in terms of components
$NaO_{0.5}$-TiO_2

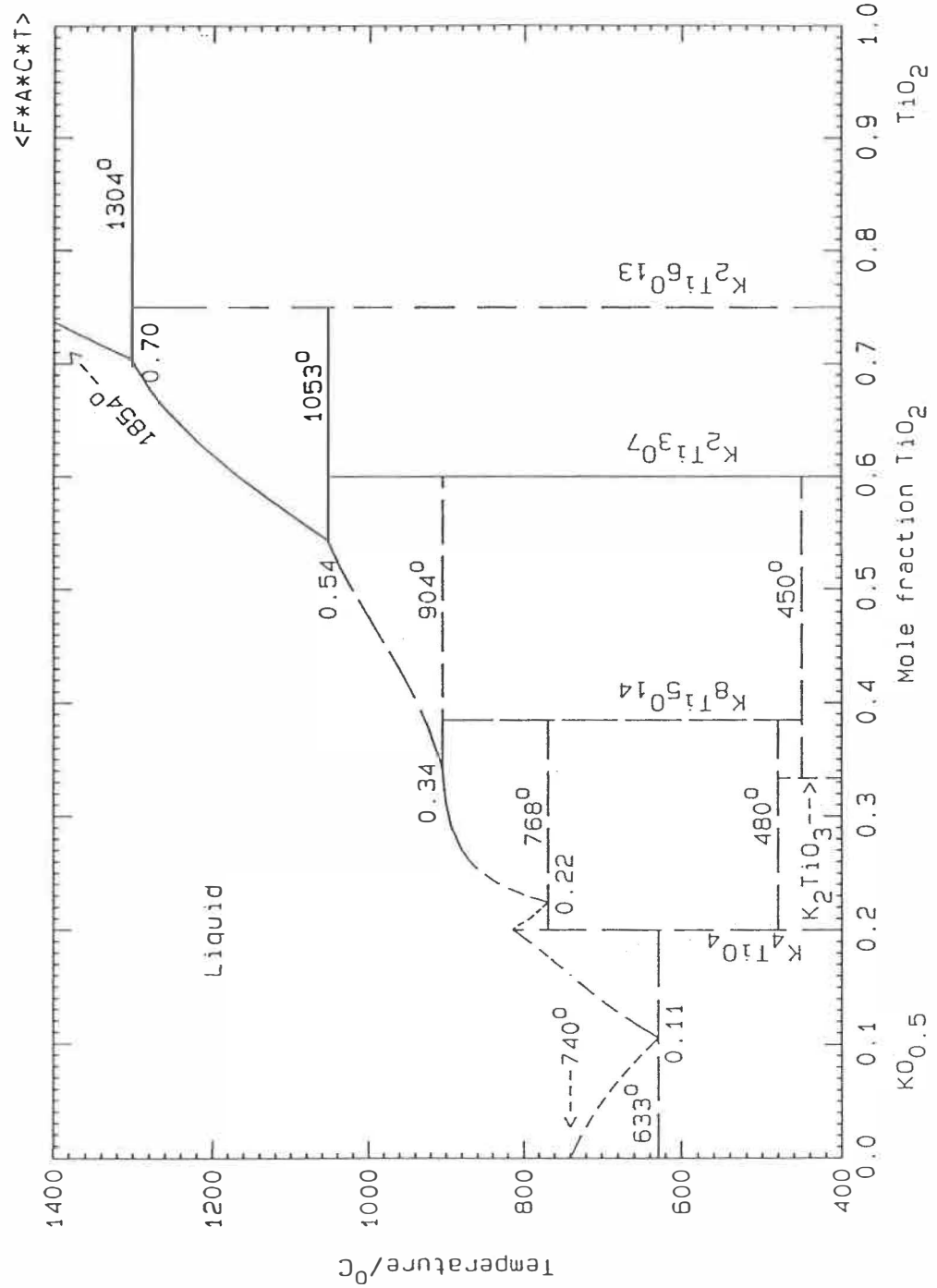


Fig. 2-28 Assessed K_2O-TiO_2 Phase Diagram Compositions in terms of components $KO_{0.5}$-TiO_2

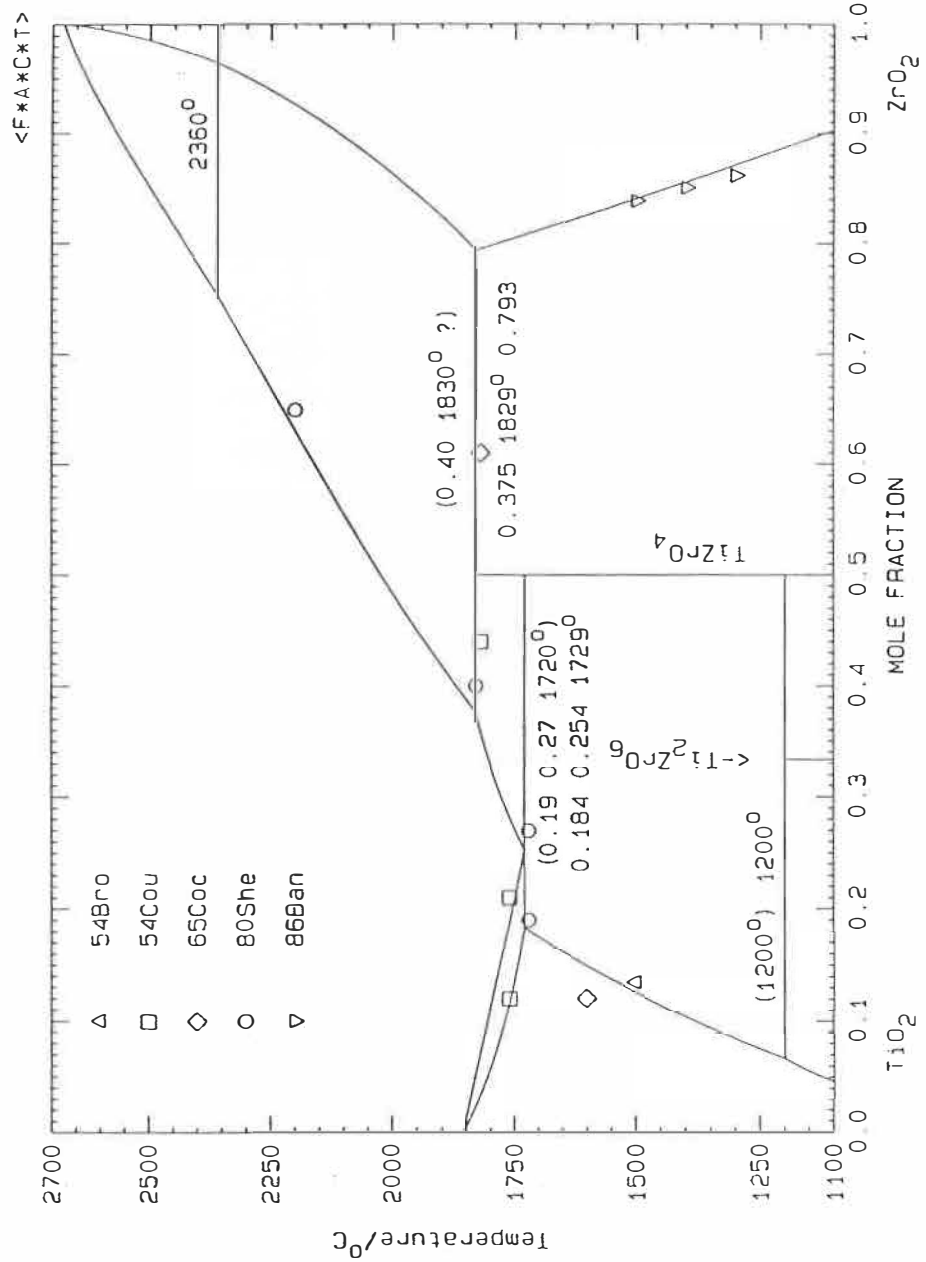


Fig. 2-29 Optimized TiO_2-ZrO_2 phase diagram with selected experimental points [54Bro, 54Cou, 65Coc, 80She, 86Ban, 86McH]. Values in parentheses are experimental (from [80She] except for 1200° peritectoid from [86McH]).

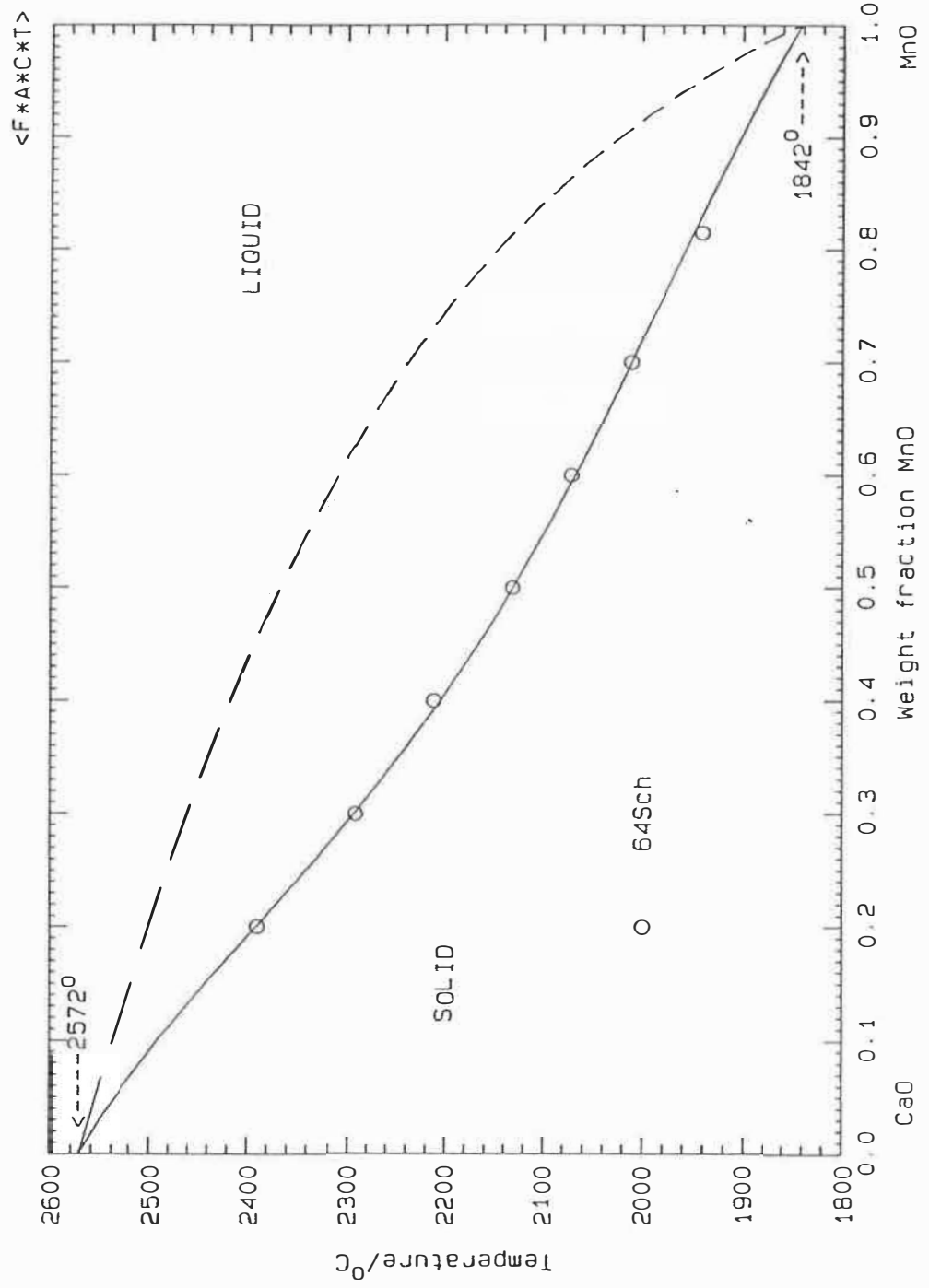


Fig. 2-30 Optimized CaO-MnO Phase Diagram

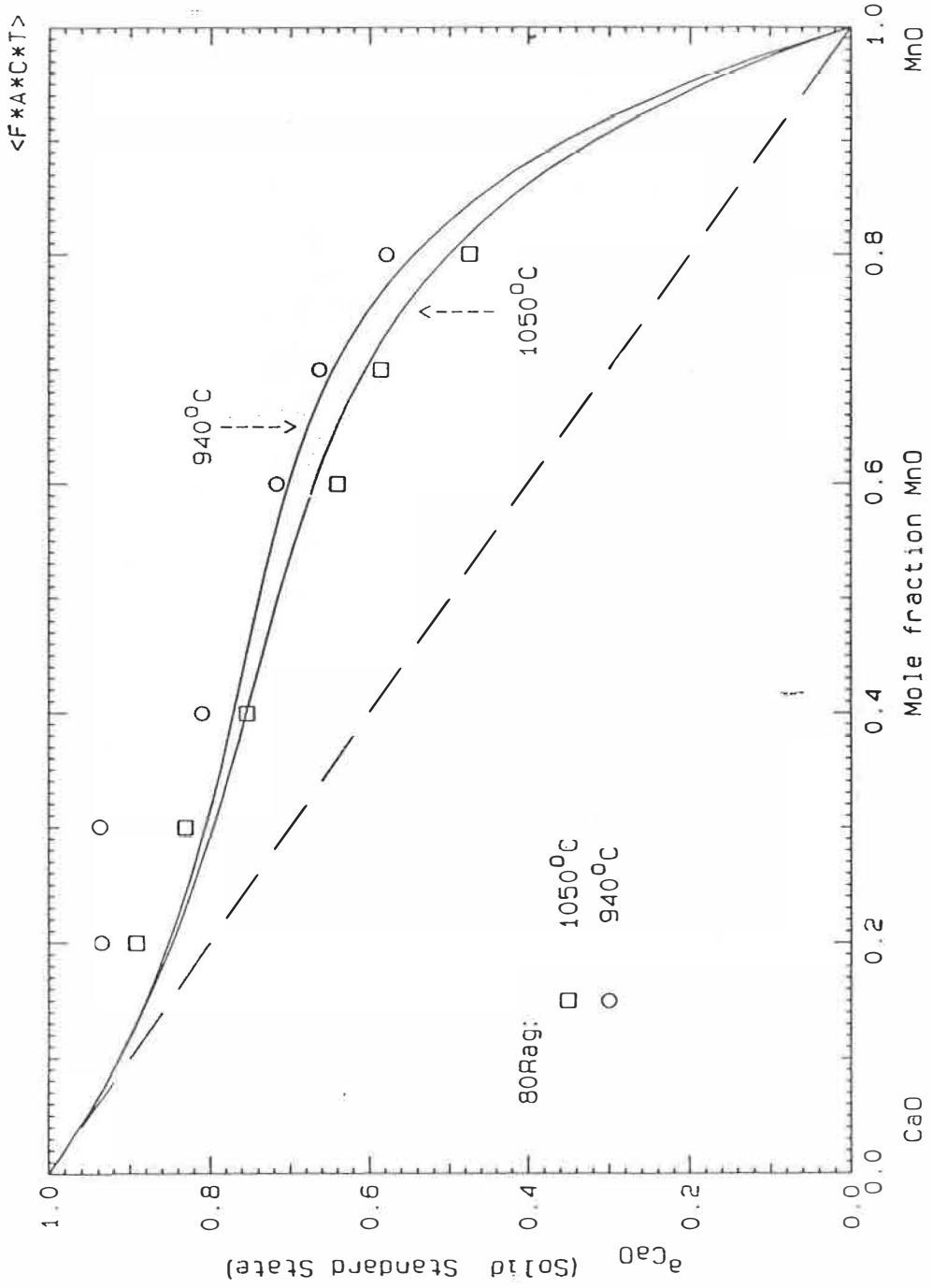


Fig. 2-31 Optimized activities of CaO in CaO-MnO solid solutions

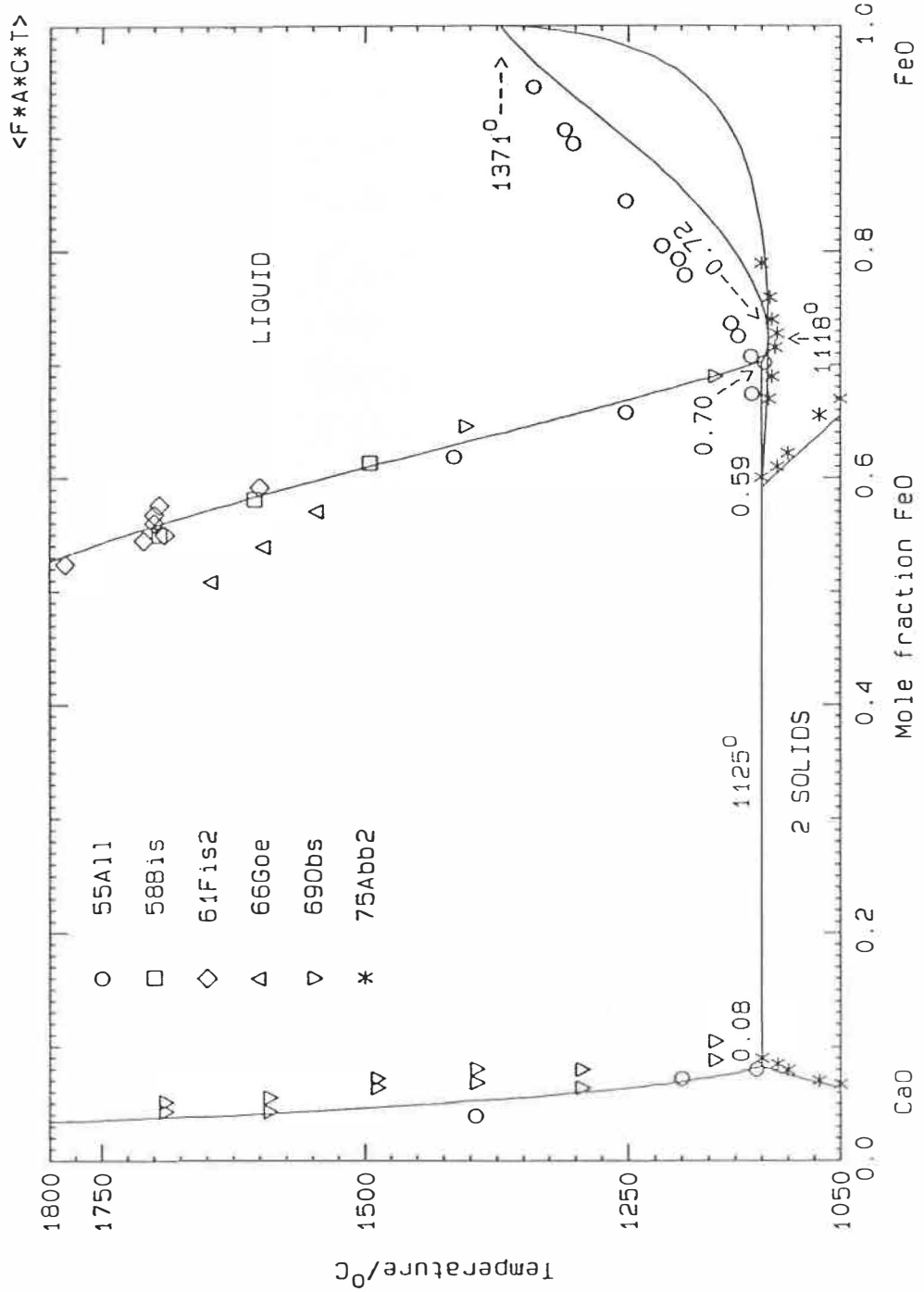


Fig. 2-32 Optimized CaO-FeO Phase Diagram for Equilibrium with Fe.

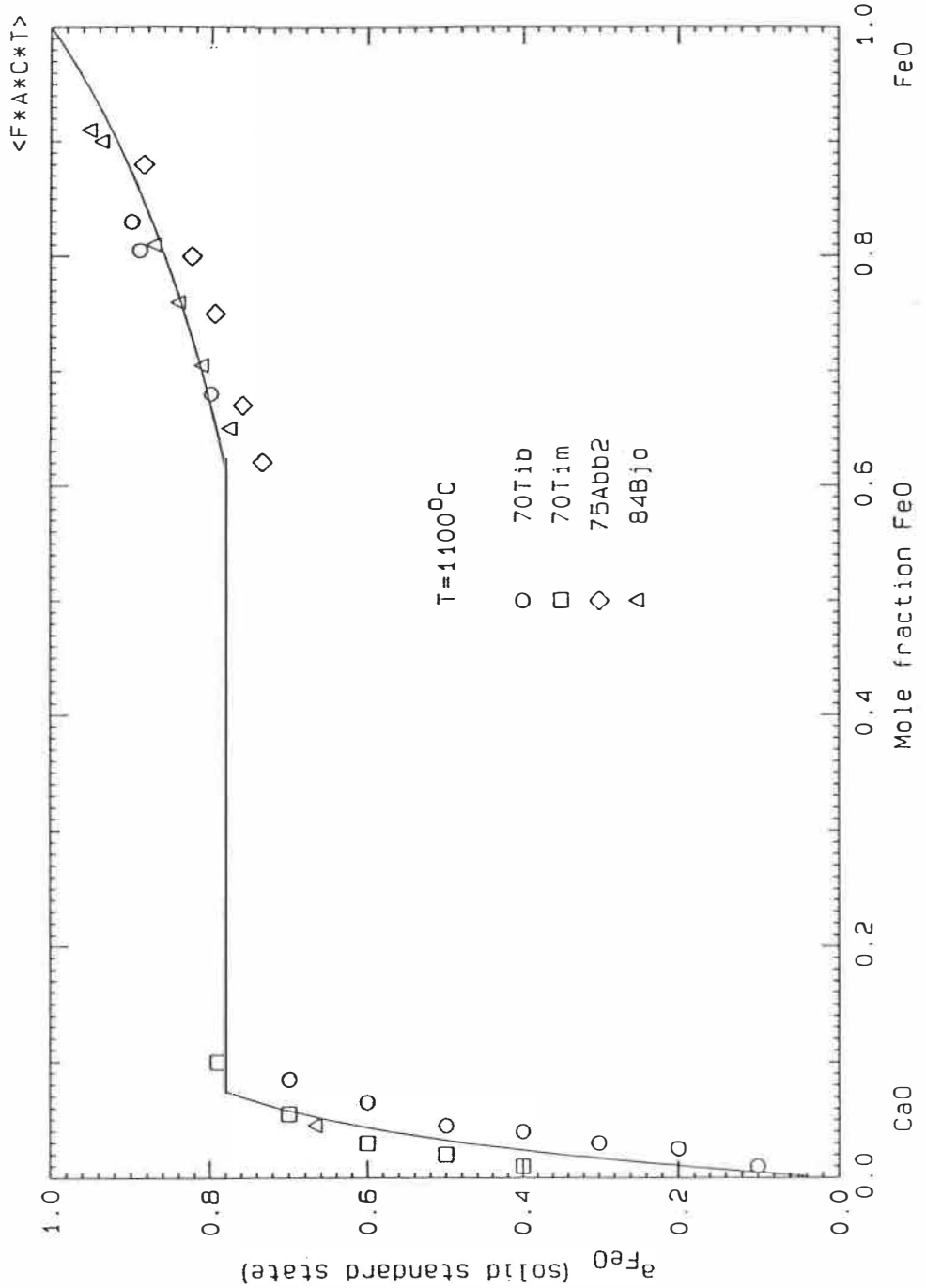


Fig. 2-33 Optimized FeO activities at 1100°C for CaO-FeO solid solutions in equilibrium with Fe.

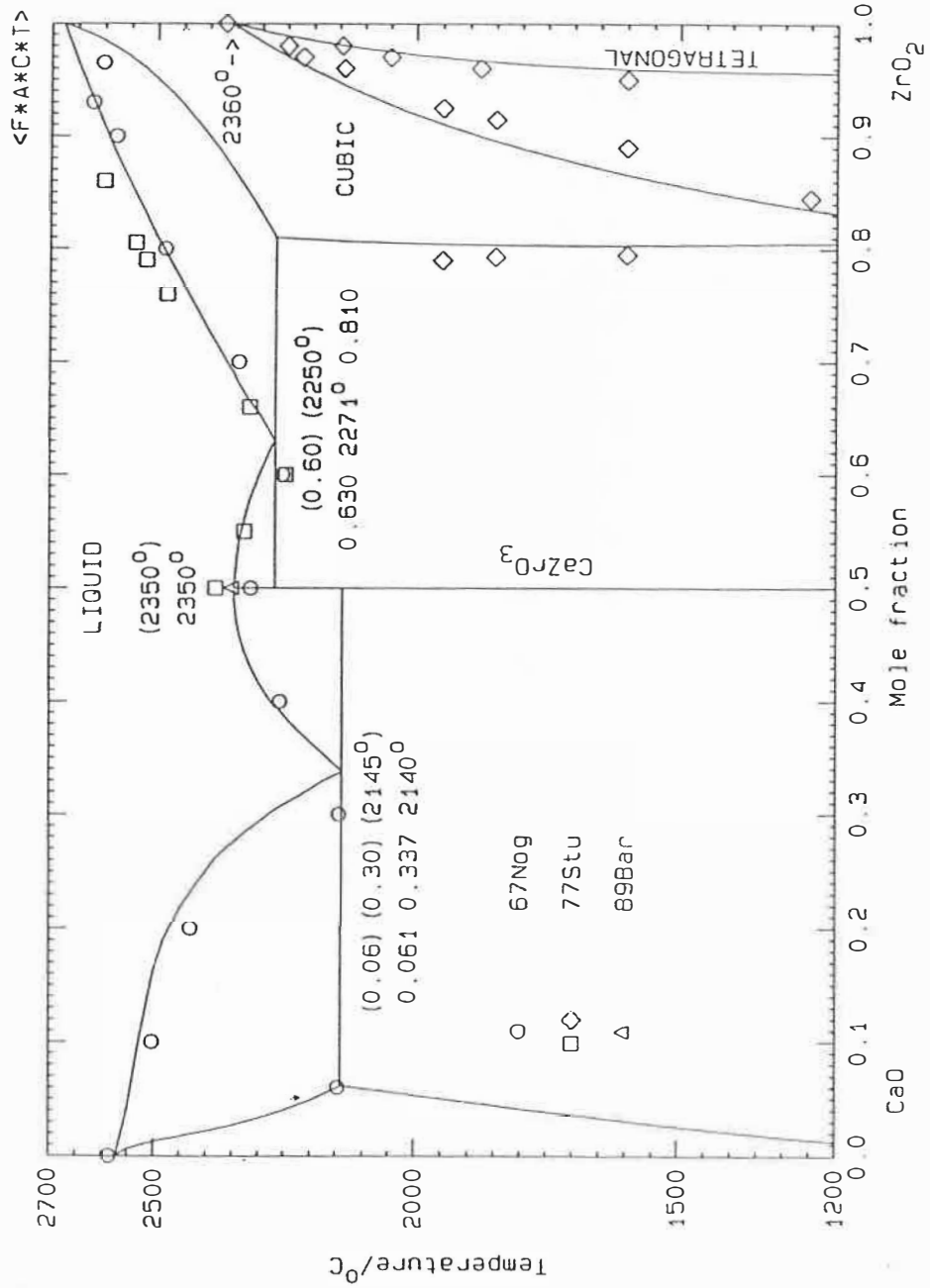


Fig. 2-34 Optimized $CaO-ZrO_2$ phase diagram with selected experimental points [89Bar, 77Stu, 67Nog]. Values in parentheses are experimental from [67Nog, 77Stu, 89Bar].

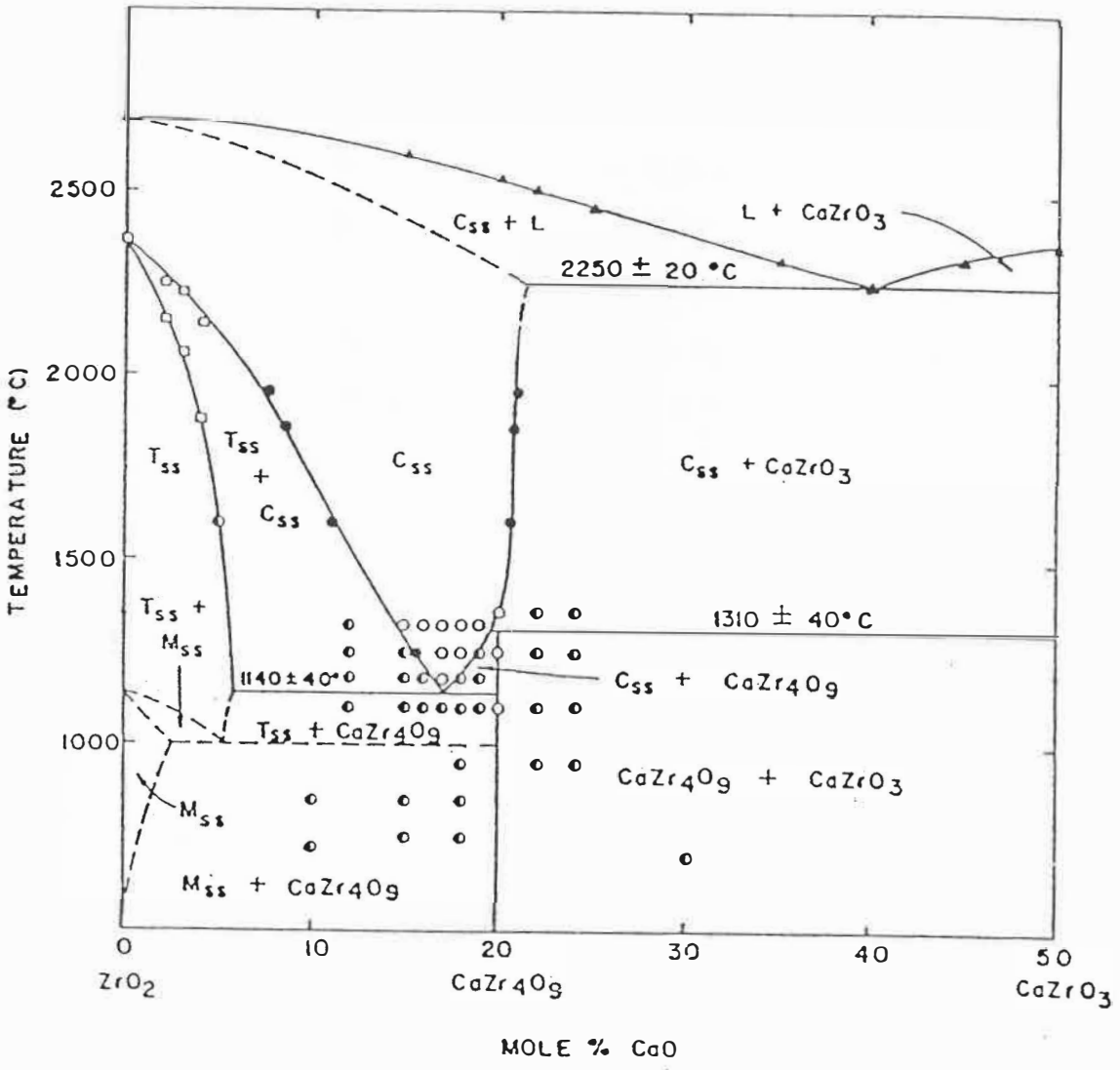


Fig. 2-35 Experimental ZrO_2-CaO phase diagram reported by [77Stu].

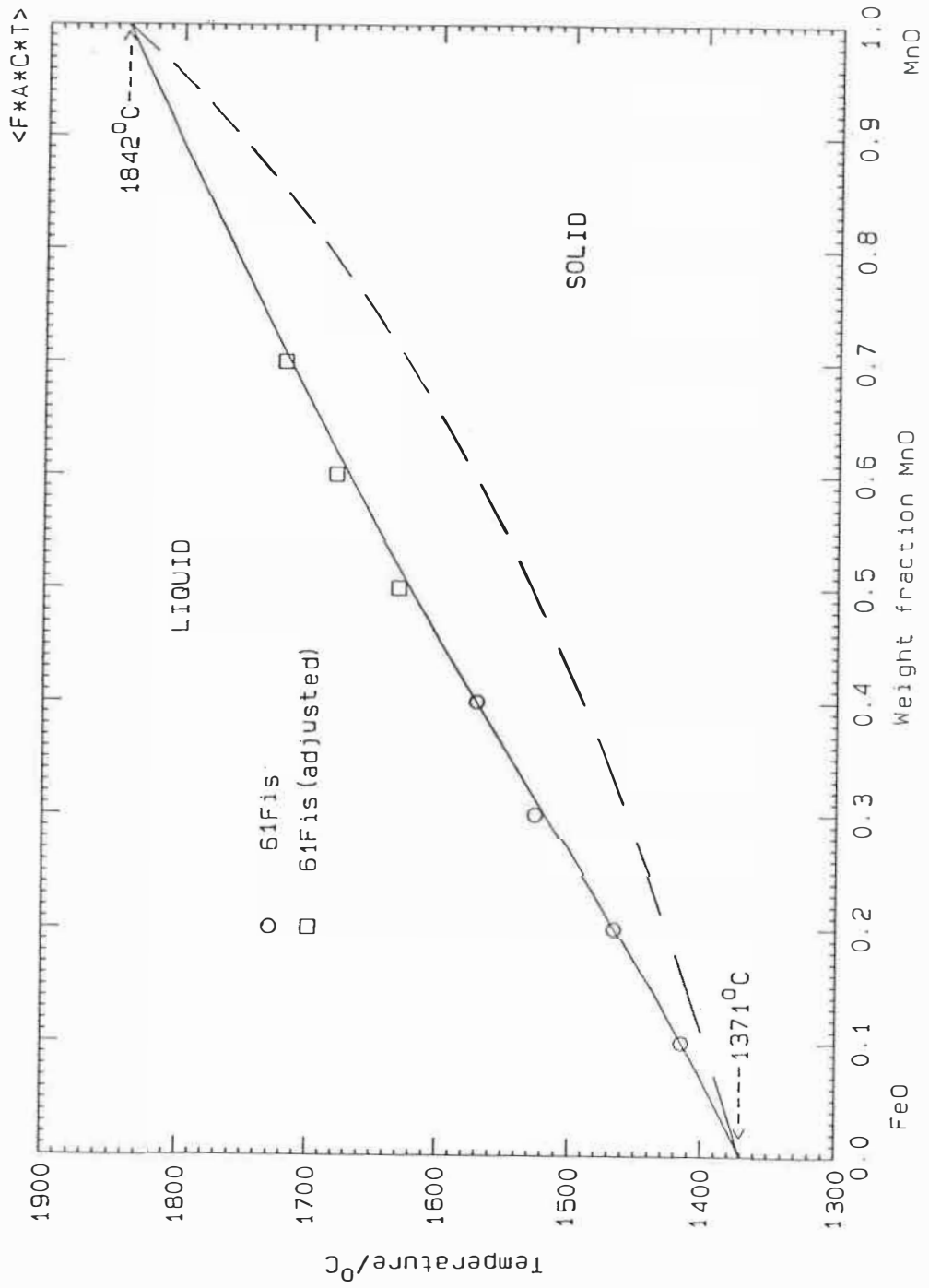


Fig. 2-36 Optimized FeO-MnO Phase Diagram for Equilibrium with Fe.

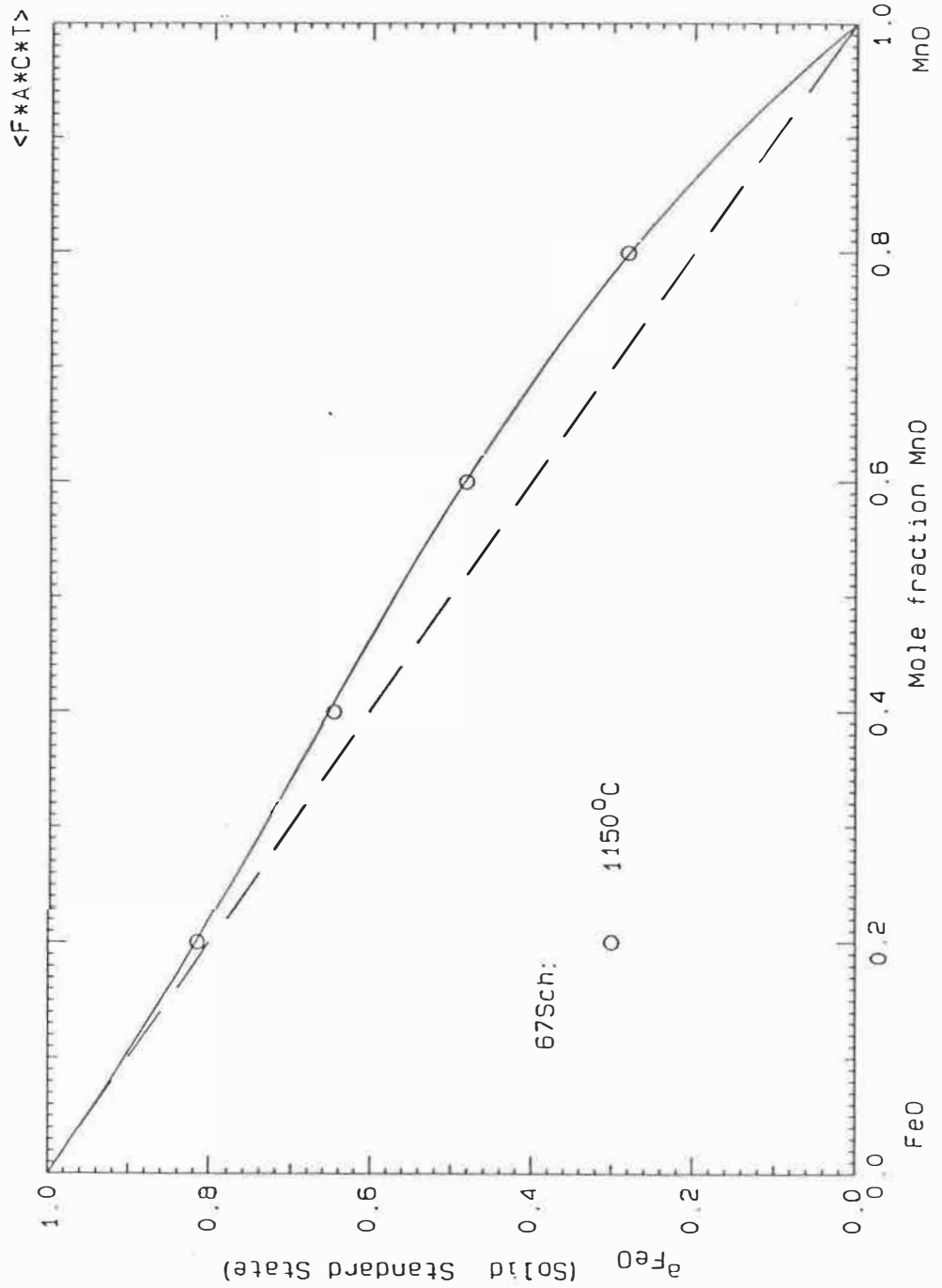


Fig. 2-37 Optimized activities of FeO in FeO-MnO solid solutions in equilibrium with Fe at 1150°C

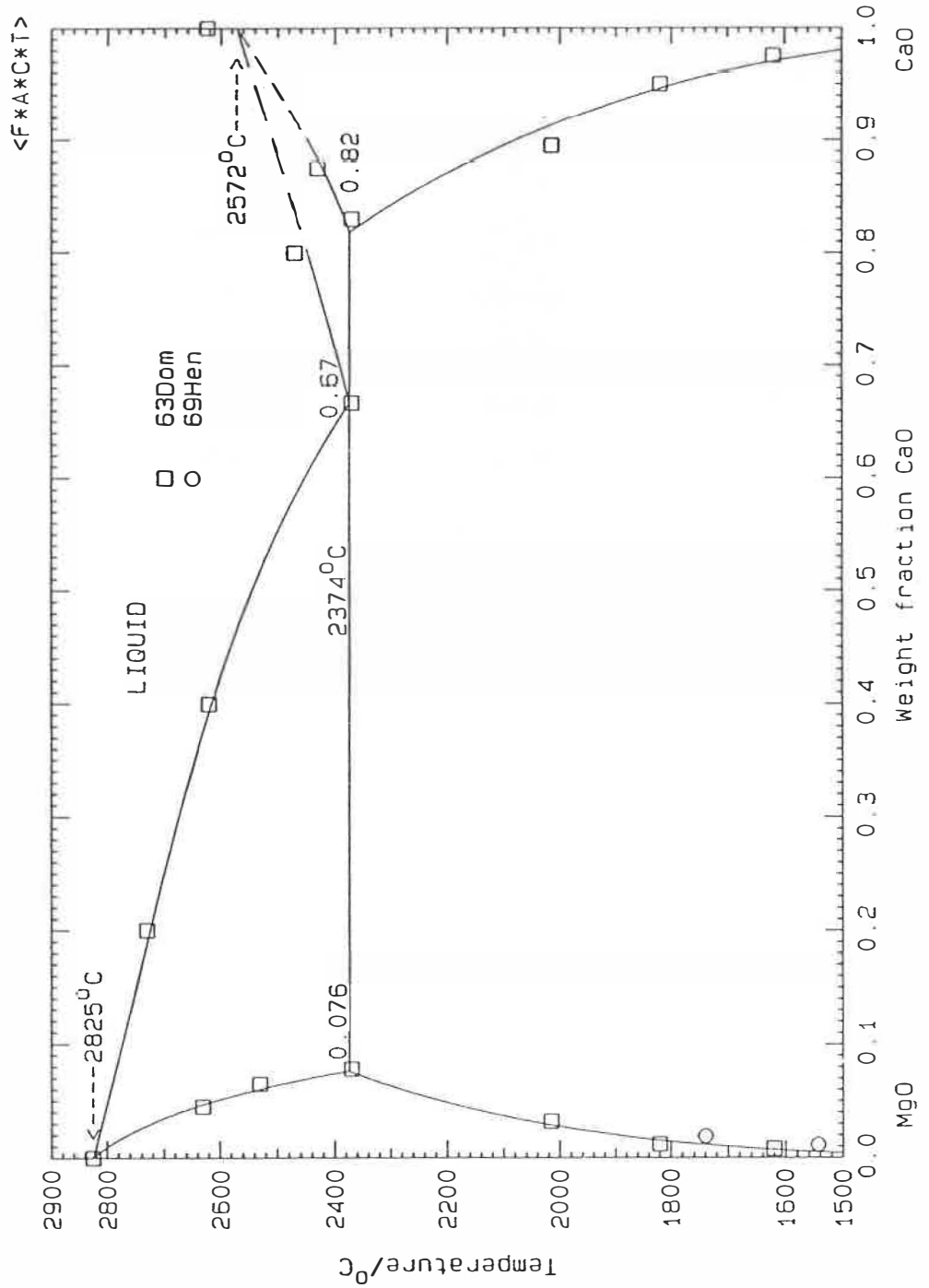


Fig. 2-38 Assessed MgO-CaO Phase Diagram.

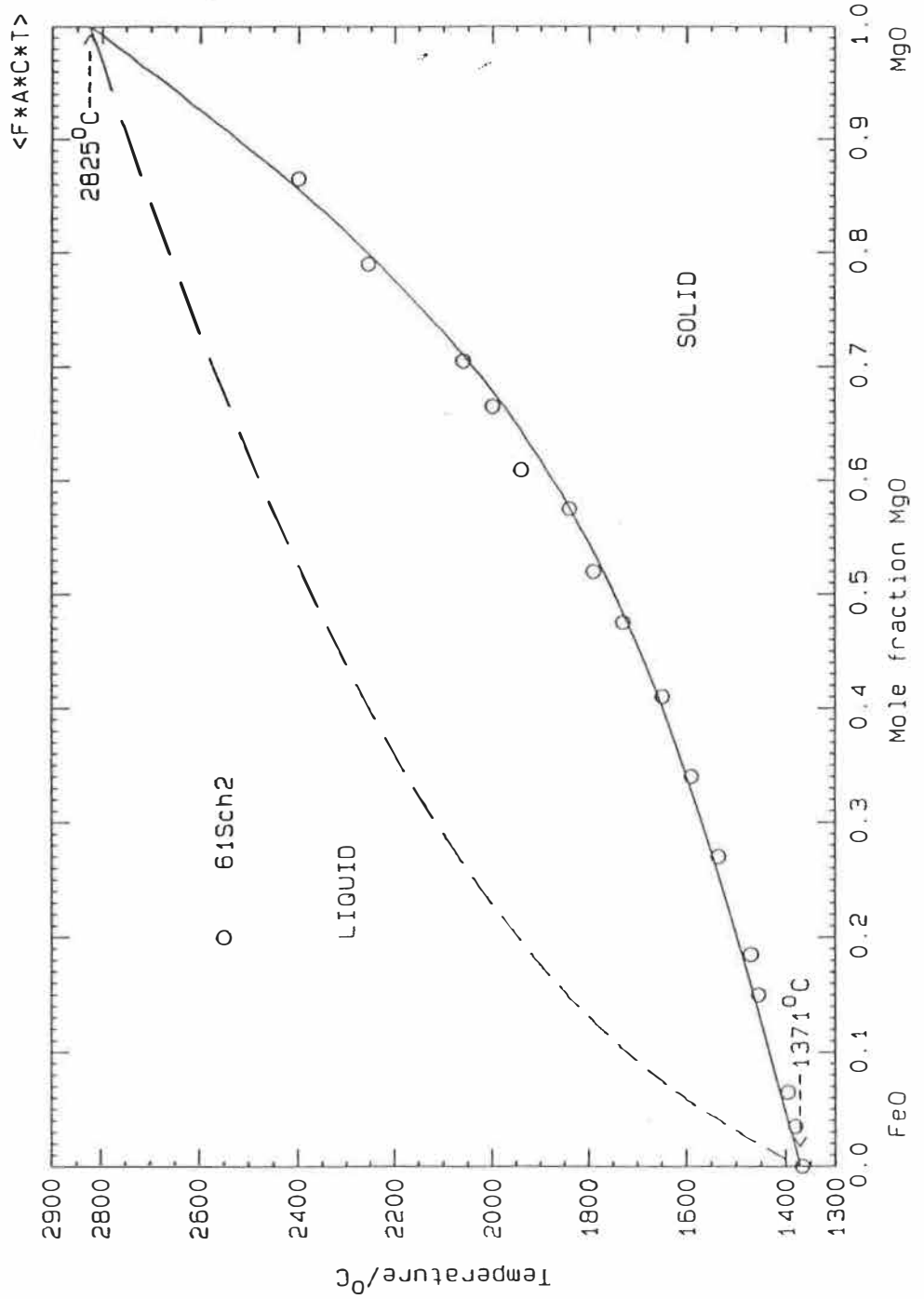


Fig. 2-39 Optimized FeO-MgO phase diagram for equilibrium with Fe

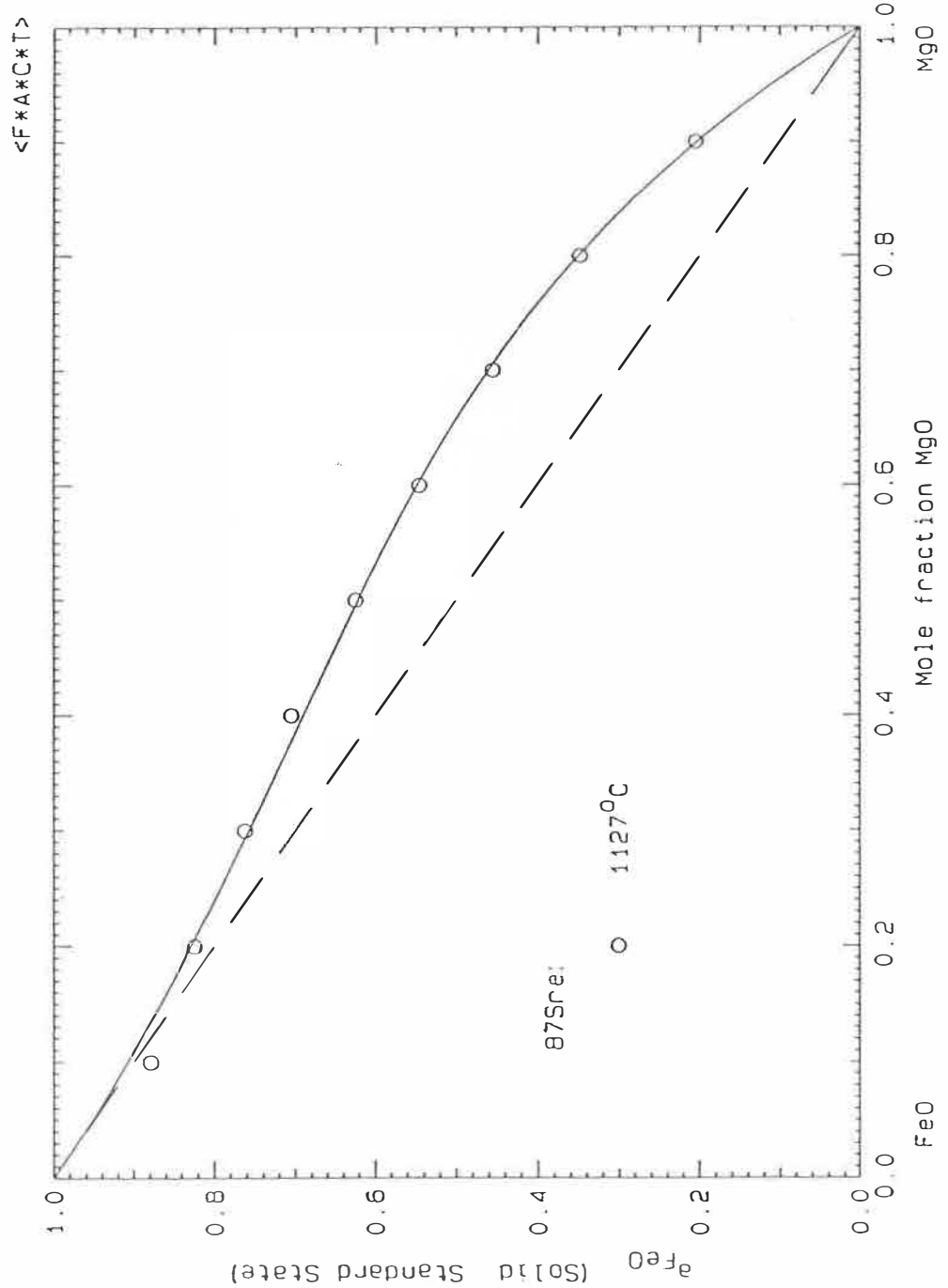


Fig. 2-40 Optimized FeO activities in FeO-MgO solid solutions at 1127°C in equilibrium with Fe

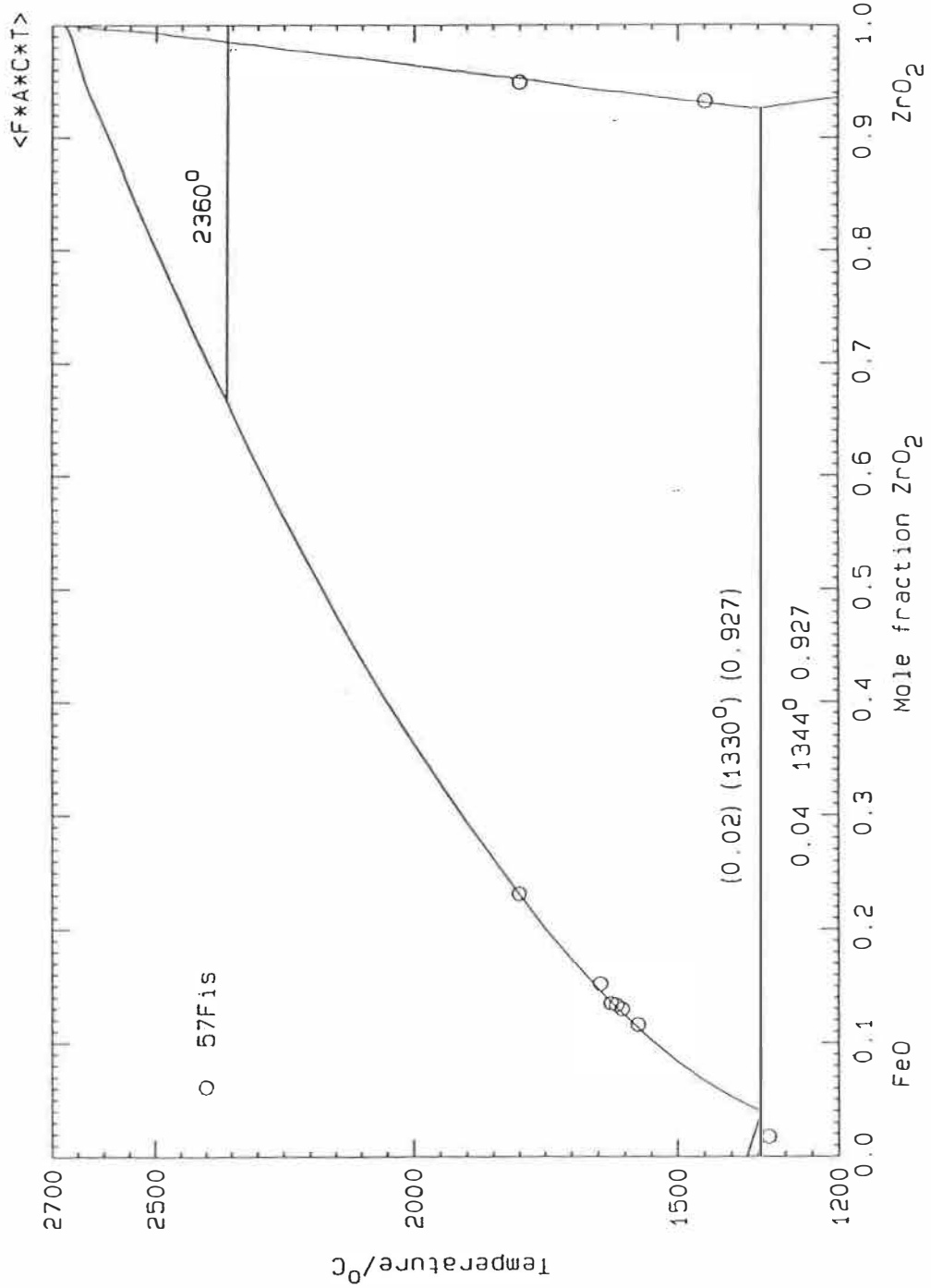


Fig. 2-41 Optimized $FeO-ZrO_2$ phase diagram with experimental points from [57Fis]. Values in parentheses are experimental from [57Fis].

Table 2-1 List of optimized binary systems

	Al_2O_3	TiO_2	MgO	CaO	MnO	FeO	Ti_2O_3	Na_2O	K_2O	ZrO_2	NiO	Fe_2O_3	PbO	ZnO
SiO_2	A	A	A	A	A	A	A	A	A	A	A	A$^-$	A$^-$	A$^-$
Al_2O_3		A	A	A	A	A	A	A	A	A				
TiO_2			A	A	A	A	A	A	A	A				
MgO				A	A	A	A	X	X	A	A			
CaO					A	A	A	X	X	A	A	A$^-$	A$^-$	X$^-$
MnO						A	A	X	X	A	A			
FeO							A	X	X	A		A$^-$	A$^-$	X$^-$
Ti_2O_3								A	A					
Na_2O									X					
K_2O														
ZrO_2														
NiO														
Fe_2O_3													A$^-$	X$^-$
PbO														A$^-$

A cell marked with an A in the above table indicates that the binary system of the oxides is available in the present database while X represents an assumed ideal liquid solution and "-" indicates that only the liquid phase has been optimized. Another 15 Al_2O_3-R_2O_3(R = La, Ce, Pr, Nd, Sm, Eu, Gd, Dy, Ho, Er, Yb, Lu, Tm, Tm, Pm) systems available in the database are not listed in the above table.

CHAPTER 3

THERMODYNAMIC AND PHASE DIAGRAM CALCULATION OF BINARY RARE EARTH OXIDE-Al_2O_3 SYSTEMS

3.1 INTRODUCTION

In Chapter 2, optimization of individual binary oxide systems, in which thermodynamic or phase diagram data are available, has been presented. This technique is, however, particularly important when evaluating a series of systems such as the R_2O_3-Al_2O_3 (R=rare earth) binary systems, because trends in the properties as one proceeds along the series can be exploited in order to refine the assessments and to predict properties by interpolation or extrapolation. In this chapter, a critical assessment of all 15 R_2O_3-Al_2O_3 systems will be performed and thermodynamic properties of all compounds will be predicted along with the thermodynamic properties of the liquid solutions, although for 3 of the 15 systems no phase diagrams have been previously reported.

This chapter is composed of a paper accepted by the Journal of Alloys and Compounds [92Wu]. A copy of the letter of acceptance follows.

3.2 COUPLED THERMODYNAMIC/PHASE DIAGRAM ASSESSMENT OF THE RARE EARTH OXIDE-ALUMINUM OXIDE BINARY SYSTEMS

I am pleased to inform you that your article

Date August 1991

Coupled Thermodynamic/Phase Diagram Assessment of the Rare Earth Oxide-Aluminum Oxide Binary Systems

has been accepted for publication in

JOURNAL OF THE LESS-COMMON METALS

Arthur D. Pelton
Centre for Research in Computational Thermochemistry
Ecole Polytechnique de Montréal
C.P. 6079, Succursale "A"
Montréal, Québec
CANADA

Copyright Transfer Notice

Formal written transfer of copyright from the author(s) to the publisher is required for each article. This transfer enables the p lisher to provide for the widest possible dissemination of the article through activities such as distribution of reprints; authoriza of reprints; translation or photocopies by others; production of microfilm editions and authorization of indexing and abstrac services in print and data base formats. Without this transfer of copyright, such activities on the part of the publisher and the cc sponding spread of information are limited.

We therefore ask that you complete and return the attached form promptly.
Your cooperation is essential and appreciated.

The Editor

ELSEVIER SEQUOIA S.A.
c/o Editorial Office (U.K.)
Mayfield House, 256 Banbury Road, OXFORD OX2 7DH, England.

ABSTRACT

A critical assessment of the binary R_2O_3-Al_2O_3 systems (R = La, Ce, Pr, Nd, Pm, Sm, Eu, Gd, Tb, Dy, Ho, Er, Tm, Yb, Lu) has been carried out through the technique of coupled thermodynamic/phase diagram analysis. Thermodynamic properties of the various compounds and of the liquid oxide solutions have been deduced, and optimized phase diagrams have been calculated.

1. INTRODUCTION

Recent years have seen the development of the field of coupled thermodynamic/phase diagram analysis, pioneered in large part by the international CALPHAD group. In this method of critical assessment, all available thermodynamic and phase equilibrium data for a system are evaluated simultaneously with a view to obtaining one set of consistent "optimized" equations for the Gibbs energies of all phases as functions of temperature and composition. The data are thus smoothed and evaluated in a thermodynamically correct manner in accordance with principles of solution behavior. The thermodynamic data can aid in the phase diagram assessment, and the phase diagram assessment permits the calculation of thermodynamic properties.

This approach is particularly well suited to the evaluation of a series of systems such as the R_2O_3-Al_2O_3 (R = rare earth) binary systems, because trends in the properties as one proceeds along the series can be exploited in order to refine the assessments and to predict properties by interpolation or extrapolation.

In the present case, a thorough literature survey has been made of phase equilibrium and thermodynamic data for the R_2O_3-Al_2O_3 systems. From the critical assessments and optimizations, thermodynamic properties of all compounds have been predicted along with the thermodynamic properties of the liquid solutions. A set of optimized "best" phase diagrams are proposed.

The optimized parameters for the binary systems can be used along with appropriate solution models to predict the thermodynamic properties of multicomponent systems and thus to calculate phase diagrams of ternary and higher order rare earth oxide-alumina systems. This will be the subject of future articles.

1.1 The Rare Earths

All the lanthanides form R^{3+} ions. The La^{3+} ion has the noble gas [Xe] electronic configuration. Ce^{3+} has a 4f configuration, Pr^{3+} has a $4f^2$ configuration, and so on up to Lu^{3+} with $4f^{14}$. The occurrence of the 2+ and 4+ oxidation states can be correlated with the electronic structure if it is assumed that there is a special stability associated with a filled or half-filled f shell (f^0, f^7 or f^{14}). Thus, the 2+ state is observed for Eu and Yb, while Ce, and to a lesser extent Tb, can exhibit the 4+ state. There is also some tendency for Pr^{4+} to occur. The oxide, when heated in air to moderate temperatures forms Pr_6O_{11}. In plots of properties of the lanthanides, anomalies can occur near filled and half-filled f-shell positions as shown in the plot of the melting points of the metals in Fig. 1 [1].

2. COUPLED THERMODYNAMIC/PHASE DIAGRAM ANALYSIS

The principles of coupled thermodynamic/phase diagram analysis have been the subject of numerous reviews and articles, many of which have appeared in the Calphad Journal (Pergamon Press) which is devoted to this type of work. The use of least-squares techniques in finding the optimum Gibbs energy parameters has been discussed by [2-4]. Computer programs to perform the least-squares optimizations and to calculate and plot the binary phase diagrams from the equations for the thermodynamic properties are available [5].

An R_2O_3-Al_2O_3 binary phase diagram is shown schematically in Fig. 2 along with a Gibbs-energy composition diagram at a constant temperature T'. A completely miscible liquid phase and three stoichiometric solids (R_2O_3, $RAlO_3$ and Al_2O_3) are shown. $G_i^{o(l)}$ and $G_i^{o(s)}$ are the standard Gibbs energies of the pure liquid and solid compounds. The Gibbs energy of fusion of R_2O_3 is shown on Fig. 2:

$$\Delta G^o_{fus(R_2O_3)} = \Delta H^o_{fus(R_2O_3)} - T\Delta S^o_{fus(R_2O_3)} \qquad (1)$$

Similarly for Al_2O_3:

$$\Delta G^o_{fus(Al_2O_3)} = \Delta H^o_{fus(Al_2O_3)} - T\Delta S^o_{fus(Al_2O_3)} \qquad (2)$$

The Gibbs energy of formation of $RAlO_3$ from solid R_2O_3 and Al_2O_3 and the Gibbs energy of fusion of $RAlO_3$ are also indicated on Fig. 2:

$$\Delta G^o_{f(RAlO_3)} = \Delta H^o_{f(RAlO_3)} - T\Delta S^o_{f(RAlO_3)} \qquad (3)$$

$$\Delta G^{o}_{fus(RAlO_3)} = \Delta H^{o}_{fus(RAlO_3)} - T\Delta S^{o}_{f(RAlO_3)} \quad (4)$$

The tangent intercepts at points **a, b** and **c** determine the liquidus compositions at T'.

The Gibbs energy of liquid mixing is also indicated on Fig. 2:

$$\Delta G_m = \Delta H_m - T\Delta S_m \quad (5)$$

In the present analysis, the various enthalpies and entropies of fusion and formation in Eqs (1-4) were assumed to be independent of temperature. Part of the task of the thermodynamic analysis is to obtain values of these enthalpies and entropies which are consistent with all the available data, which follow relatively simple trends proceeding from La to Lu, and which are thermodynamically reasonable.

For example, the entropies of fusion $\Delta S^{o}_{fus(RAlO_3)}$ of the compounds $RAlO_3$ would be expected to be very nearly constant or to vary only slightly and regularly proceeding along the series. In the analysis, care was taken to ensure that this criterion was respected.

A useful observation, resulting from the thermodynamic analysis, is that the liquidus of a compound must descend more or less symmetrically on either side of its melting point, unless there is some reason to believe that the shape of the $G^{(liquid)}$ curve should change abruptly at this composition.

A very useful equation is related to the limiting slopes of the liquidus curves at 100% R_2O_3 and 100% Al_2O_3 (see Fig. 2). If terminal solid solubility is negligible, then:

$$(dT/dX_i)_{X_i=1} = 2RT^o_{fus(i)}/\Delta S^o_{fus(i)} \quad (6)$$

where i = R_2O_3 or Al_2O_3, X_i is the mole fraction of i, and $T^o_{fus(i)}$ is the melting point (in kelvins) of i. This equation results from Raoult's Law. (See [6] for a derivation.)

In the analysis, parameters of model equations for ΔH_m and ΔS_m of the liquid phase were optimized. To this end, the modified quasichemical model, discussed in the following section was used.

2.1 Quasichemical Model for Liquid Oxides

In our laboratory we are systematically evaluating many oxide systems. For molten oxide phases showing a large degree of short-range ordering, such as molten silicates, we have developed the modified quasichemical model [7-9]. Accordingly, in order that all our evaluations can be incorporated into one database for multicomponent liquid oxides, we are using the quasichemical model for all molten oxide evaluations including those of the R_2O_3-Al_2O_3 systems.

As applied to binary R_2O_3-Al_2O_3 liquid solutions, the model supposes that R^{3+} and Al^{3+} ions mix on cation sites. We consider the formation of two R^{3+}-Al^{3+} second-nearest-neighbour pairs from R^{3+}-R^{3+} and Al^{3+}-Al^{3+} second-nearest-neighbour pairs:

$$[R\text{-}R] + [Al\text{-}Al] = 2[R\text{-}Al] \quad (7)$$

Let the Gibbs energy change for reaction (7) be ω, where in general ω can be expanded as a polynomial in $X_{Al_2O_3}$, the mole fraction of Al_2O_3:

$$\omega = \omega_0 + \omega_1 X_{Al_2O_3} + \omega_2 X_{Al_2O_3}^2 + \ldots \quad (8)$$

Let X_{11}, X_{22} and X_{12} be the fractions respectively of R-R, Al-Al and R-Al pairs in solution. A "quasichemical equilibrium constant" for reaction (7) can be written:

$$\frac{X_{12}^2}{X_{11}X_{22}} = 4e^{-\omega/RT} \quad (9)$$

From mass balance considerations:

$$2X_{R_2O_3} = 2X_{11} + X_{12} \quad (10)$$

$$2X_{Al_2O_3} = 2X_{22} + X_{12} \quad (11)$$

Given values of the parameters ω_i, Eqs. (9-11) can be solved to give X_{11}, X_{22} and X_{12}. The enthalpy and entropy of liquid mixing of R_2O_3 and Al_2O_3 can then be calculated as:

$$\Delta H_m = 2(X_{12}/2)\omega \quad (12)$$

$$\Delta S_m = -2R(X_1 \ln X_1 + X_2 \ln X_2) - (2.066)R\left(X_{11}\ln\frac{X_{11}}{X_1^2} + X_{22}\ln\frac{X_{22}}{X_2^2} + X_{12}\ln\frac{X_{12}}{2X_1X_2}\right) \quad (13)$$

where $X_1 = X_{R_2O_3}$ and $X_2 = X_{Al_2O_3}$. The factors 2 in Eqs. (12, 13) account for the fact that each mole of R_2O_3 or Al_2O_3 produces two moles of R^{3+} or Al^{3+} ions. The factor 2.066 in Eq. (13) is chosen to maintain consistency in the multicomponent database as has been explained previously [7-9].

Note that if ω is small, Eqs (9-11) give $X_{12} \approx 2X_1X_2$, $X_{11} \approx X_1^2$ and $X_{22} \approx X_2^2$. The entropy expression in Eq. (13) then becomes the ideal entropy expression, and ΔH_m in Eq. (12) becomes:

$$\Delta H_m \approx 2X_1X_2(\omega_0 + \omega_1 X_{Al_2O_3} + \omega_2 X_{Al_2O_3}^2 + ...) \quad \textbf{(14)}$$

That is, the model reduces to a simple polynomial model for ΔH_m with ideal mixing.

As ω becomes more negative, reaction (7) is displaced to the right and the number of [R-Al] pairs increases beyond that for random mixing.

The activity of R_2O_3 in solution is given by:

$$RT\ln a_{R_2O_3} = 2RT\ln X_1 + (2.066)RT\ln\frac{X_{11}}{X_1^2} - \frac{(2.066)}{2}X_{12}X_2(\partial\omega/\partial X_2) \quad \textbf{(15)}$$

with a similar expression for the activity of Al_2O_3.

It is the parameters ω_i of Eq. (8) which are the empirical constants of the optimizations. In general, these can be temperature dependent, but in the present case this was not necessary.

3. RESULTS - GENERAL

The evaluated high temperature phase diagrams, calculated from the optimized thermodynamic parameters, are shown in Figs. 3-17. Several selected experimental points are also shown on these figures. In Fig. 18 are shown the calculated diagrams at lower temperatures. (Polymorphic transformations have not been shown on Fig. 18 for the sake of clarity.) Table 1 lists the optimized parameters of Eq. (8) for the liquid solutions. In Fig. 19 are shown the evaluated or estimated melting points of the various compounds. In the case of compounds which do not melt congruently, these are the calculated metastable congruent melting points.

In Table 2 are listed the thermodynamic properties of the compounds resulting from the thermodynamic analysis. The enthalpies and entropies of formation in Table 2 are for the formation from solid R_2O_3 and Al_2O_3 and are assumed to be independent of temperature (that is, ΔC_p for the formation reaction is assumed to be zero) except for the case of $CeAlO_3$. This is the only compound for which thermodynamic data are available [1]. For the formation of $CeAlO_3$, ΔC_p = 0.455 cal/mol [1] which is, as expected, very small. The values of ΔH_f^o and ΔS_f^o for $CeAlO_3$ in Table 2 are those at the melting point as obtained by the present analysis. At 298 K, taking ΔC_p = 0.455, we calculate ΔH_f^o = -6649 cal/mol and ΔS_f^o = 3.031 cal/mol K. These compare within error limits with the values of -4197 cal/mol and 2.118 cal/mol K given by ref. [1] at 298 K.

T_{fus}^o in Table 2 is the congruent melting point as in Fig. 19, while ΔH_{fus}^o and ΔS_{fus}^o are the temperature independent enthalpy and entropy of (congruent) melting.

In this section, the optimized diagrams and thermodynamic properties will be discussed generally for all the systems together. The detailed evaluations for each individual system will be discussed in Section 4.

3.1 Solid solubility - Stoichiometry of compounds

In the present analysis, all compounds were assumed to be stoichiometric (i.e. to have very narrow ranges of homogeneity). In the case of the compounds $RAlO_3$ this stoichiometry has been confirmed in most systems by the X-ray studies of Mizuno and co-workers [10-18].

Some solubility of Al_2O_3 in the compounds $Yb_3Al_5O_{12}$ and $Lu_3Al_5O_{12}$ has been reported [19, 20]. The possible non-stoichiometry of all the other compounds has not been studied.

It has also been assumed in the present analysis that there is no terminal solid solubility of Al_2O_3 in R_2O_3 or of R_2O_3 in Al_2O_3. In the latter case, this is confirmed by limiting liquidus slope calculations as discussed in Section 3.2.

3.2 Al_2O_3-liquidus

The Gibbs energy of fusion of Al_2O_3 was taken from ref. [21] as:

$$\Delta G^{o}_{fus} = 21204 + 33.549T + 1.0985\ X\ 10^{-3}\ T^2 \qquad (16)$$

$$-5.8190\ T\ln T - 5.78\ X\ 10^{5}\ T^{-1}\ \ cal/mol$$

where T is in kelvins. The equilibrium melting point is 2054°C and the enthalpy and entropy of fusion at the melting point are 28300 cal/mol and 12.162 cal/mol.K. Under the assumption of negligible solid solubility of R_2O_3 in Al_2O_3 it can be seen from Figs 3-17 that the measured limiting slopes of the Al_2O_3-liquidus curves at 100% Al_2O_3 are reproduced well, thus showing that solid solubility is, in fact, small. In the few systems in which agreement is not good, the measured limiting liquidus slopes are steeper than the calculated.

This is not possible since solid solubility makes the liquidus less steep. Hence, in these cases the calculated liquidus is preferred.

3.3 The sesquioxides R_2O_3

Melting Points: The melting points of the sesquioxides R_2O_3 shown in Figs 3-17 were taken mainly from the work of Mizuno and co-workers [10-18] who employed a thermal analysis technique using an optical pyrometer. These authors did not study Ce_2O_3, Tb_2O_3, Tm_2O_3 and Lu_2O_3. In these cases, the melting points were taken from Shevthenko and Lopato [22] who employed thermal analysis in unspecified "controlled atmospheres". For the lighter rare earth oxides (La to Gd), the melting points reported by the two groups agree to within 14^o. From Dy to Yb, the values of Shevthenko and Lopato are from 18^o to 47^o higher than those of Mizuno et al. The melting point of Pm_2O_3 has not been reported, and was taken as the average of the selected melting points of Nd_2O_3 and Sm_2O_3.

The selected melting points are plotted in Fig. 19. The minima observed in the plot of the melting points of the metals (Fig. 1) at Ce, Eu and Yb may, perhaps, be mirrored as very shallow minima at Ce_2O_3 and Yb_2O_3, but not at Eu_2O_3. However, the minimum at Ce_2O_3 may be spurious due to the presence of tetravalent Ce, and the apparent minimum at Yb_2O_3 may result from the fact that the melting points of Tm_2O_3 and Lu_2O_3 were taken from Shevthenko and Lopato [22] while that of Yb_2O_3 was taken from Mizuno and Noguchi [18]. The melting point of Yb_2O_3 reported by the former authors is 47^o higher.

Polymorphism: Earlier studies of the polymorphism of the sesquioxides R_2O_3 are reviewed by Foex and Traverse [23]. In general, with increasing temperature the sequence C(cubic) ⇒ B(monoclinic) ⇒ A(hexagonal) is observed, with the transformation temperatures increasing along the series from La to Lu. For the heaviest rare earth oxide, Lu_2O_3, the cubic form appears stable up to the melting point.

Foex and Traverse [23] measured transformation temperatures above 1800°C by thermal analysis. Two new high temperature modifications were found, an hexagonal H structure and an unidentified X form, both becoming relatively less stable for the heavier rare earths. Similar studies were carried out by Shevthenko and Lopato [22] in unspecified "controlled atmospheres". The results of the two studies are in agreement within 80° in all cases, and generally within 30°. The transformation temperatures plotted on Figs 3-17 are generally those of Foex and Traverse. For Ho_2O_3 and Er_2O_3, the values reported by Mizuno [17] are shown (these are 15° to 25° lower than those of Foex and Traverse). For Ce_2O_3, the values are from Shevthenko and Lopato. For Pm_2O_3 and Tm_2O_3, the transformation temperatures shown are the averages of those of the neighbouring oxides. The C ⇒ B transformation temperature of Tb_2O_3 is from Boganov and Rudenko [24]. For the lighter R_2O_3 sesquioxides, the B ⇒ C (and A ⇒ B) transformations occur below 1600°C. These temperatures are generally not well known. High temperature polymorphs can exists metastably at room temperature.

Entropies of fusion and transformation: In Figs 3-12 for those systems from La to Dy for which data are available, the limiting slope of the R_2O_3-liquidus at 100% R_2O_3, when substituted into Eq (6), corresponds in all cases to nearly the same entropy of fusion of 6.0 cal/mol.K if it is assumed that solubility in the solid is negligible. The two exceptions are the systems with Ce_2O_3 and Pr_2O_3, but in these cases a limiting slope corresponding to this entropy of fusion is within experimental error limits. Accordingly, for all the sesquioxides from La_2O_3 to Dy_2O_3, a temperature-independent entropy of fusion of 6.0 cal/mol.K was assumed. That is:

$$\Delta G_{fus(R_2O_3)} = 6.0T^{o}_{fus} - 6.0T \quad cal/mol \tag{17}$$

where T is in kelvins and T^{o}_{fus} is the equilibrium melting point. It is interesting that this entropy of fusion of 6.0/2 = 3.0 cal/K per mole of cations is significantly lower than that of the majority of metal oxides.

In their DTA studies of polymorphism, Foex and Traverse [23] classified the peaks for the solid state transformations from "weak" to "very strong". For all oxides from La_2O_3 to Dy_2O_3, the X ⇒ H transformations were classified as either "fairly strong" or "strong", with all others being "weak" to "fairly strong". From an examination of Figs 3-12, no change in slope of the liquidus curves is evident at any transformation temperature. Accordingly, it was assumed that the enthalpy and entropy change of these transformations is zero.

The H ⇒ B transformation of Ho_2O_3 was found by Foex and Traverse to give a "strong" DTA peak, while the H ⇒ C transformations of Er_2O_3 and Yb_2O_3 were listed as "very strong". Mizuno [17] and Mizuno and Noguchi [18] observed liquidus slope changes for the Ho_2O_3 and Er_2O_3 transformations as can be seen on Figs 13, 14. In both cases, the limiting slope at 100% R_2O_3 and the slope change at the transformation temperature correspond closely to an entropy of fusion of 4.28 cal/mol.K and an entropy of transformation of 1.72 cal/mol.K. The sum of these two values, which is the entropy of fusion of the lower temperature form, is 6.0 cal/mol.K as in Eq (17). Accordingly, the entropies of the B ⇒ H transformation of Ho_2O_3 and of the C ⇒ H transformation of Er_2O_3, Tm_2O_3 and Yb_2O_3 were assumed to be temperature independent and equal to 1.72 cal/mol.K, while the entropies of fusion of the H polymorphs were assumed temperature independent and equal to 4.28 cal/mol.K. The entropy of fusion of cubic Lu_2O_3 was assumed to be given by Eq (17).

3.4 Liquid Solutions

The best fits to all the data were obtained when two temperature independent parameters, ω_0 and ω_3, of the quasichemical model, Eq (8), were used. These are listed in Table 1. In all systems, quite large negative deviations from ideality are observed, indicating that R_2O_3 and Al_2O_3 interact strongly in the liquid solutions even at these high temperatures. This is not surprising, however, in view of the existence of so many solid compounds which are stable to very high temperatures.

In all systems the analysis showed that deviations from ideality are somewhat more negative in Al_2O_3-rich than in R_2O_3-rich solutions. This was found to be best treated with a small negative ω_3 parameter, but nearly as good fits could be obtained with an ω_2 or an ω_4 parameter.

As expected, the values of ω_0 are nearly the same for all systems. Given the large error limits of the available data, it is not surprising that the optimized values of ω_3, obtained by least-squares regression and resulting mainly from fitting the Al_2O_3-liquidus curves, do not vary systematically. However, they are all negative and relatively small.

In order to show the extent of the negative deviations from ideality and of the asymmetry, it has been calculated from Eq. (18) with the parameters in Table 1 that at 2300°C in a liquid La_2O_3-Al_2O_3 solution containing 50 mol % Al_2O_3 the activity coefficients of the components are: $\gamma_{LaO_{1.5}} = 0.49$ and $\gamma_{AlO_{1.5}} = 0.43$. At 2300°C at infinite dilution in liquid La_2O_3, $\gamma_{AlO_{1.5}} = 0.10$, while $\gamma_{LaO_{1.5}} = 0.06$ at infinite dilution in Al_2O_3.

3.5 Compounds $RAlO_3$

The rare earth orthoaluminates have been the subject of numerous studies [19, 25-29]. These compounds have a trigonal distortion of the perovskite structure from La through Nd, and an orthorhombic distortion from Sm to Lu [29]. They have also been reported to undergo cubic to trigonal transformations at temperatures varying from 435°C for $LaAlO_3$ [26] to 1100°C for $NdAlO_3$ [13].

These compounds become generally less thermodynamically stable from La to Lu (not monotonically) as can be seen from the melting points, Fig. 19, and the enthalpies of formation, Table 2. As is discussed in more detail in the descriptions of the Yb_2O_3-Al_2O_3 and Lu_2O_3-Al_2O_3 systems in Section 4, it is not certain whether $YbAlO_3$ and $LuAlO_3$ actually exist as thermodynamically stable phases. The weight of evidence appears, however, to be in favour of their existence.

The melting points of $PmAlO_3$, $TbAlO_3$ and $TmAlO_3$, which have not been measured, were estimated by interpolation (Fig. 19) as were their entropies of fusion (Table 2). The remaining thermodynamic properties could then all be calculated.

As shown in Fig. 18, the calculations predict a lower (eutectoid) decomposition temperature for all the orthoaluminates from Eu to Lu, which increases as the compound becomes less stable from Eu to Lu. Garton and Wanklyn [28] produced the orthoaluminates from Dy to Yb by precipitation from a solution of the component oxides in PbO flux by slow cooling below 1260°C. This result would tend to contradict the existence of a lower decomposition temperature. However, it is not clear that such precipitation yields the equilibrium phases. Dernier and Maines [29] produced pure orthoaluminates for all rare earths including Lu by direct reaction of the component oxides at pressures above 30 kbar.

In Fig. 19, it can be seen that the minima in the melting points of the metals at Ce, Eu, and Yb are reflected by shallow minima in the melting points of the orthoaluminates at Ce, Eu and (speculatively) at Yb. Although a melting point not only reflects the solid properties but also the liquid properties. It is also true that the stronger the bonds between atoms in the solid phase the higher melting point the solid has, such as ice has lower melting point than carbon.

3.6 Compounds $R_4Al_2O_7$

The existence of the compounds $R_4Al_2O_7$, with monoclinic structure, were reported by Schneider et al [19]. They have subsequently been observed in all systems except the La, Ce and Pr systems. As can be seen from Fig. 19 and Table 2, these compounds become somewhat more stable proceeding from La to Lu. From extrapolation of the melting points in Fig. 19, it is predicted that $Pr_4Al_2O_7$ may be stable over a limited range of temperature as has been indicated tentatively on Figs 5 and 18.

Thermodynamic properties of metastable $La_4Al_2O_7$ and $Ce_4Al_2O_7$ are predicted by extrapolation of Fig. 19. These values will be useful in predicting solubilities in multicomponent systems.

3.7 Compounds $R_3Al_5O_{12}$

These compounds, of the garnet structure, were reported in early studies [19, 27]. They become increasingly more stable proceeding from La to Lu.

$Gd_3Al_5O_{12}$ has been observed [27], but not at liquidus temperatures. $Eu_3Al_5O_{12}$ has not been observed. However, extrapolation of the melting points in Fig. 19, as well as analysis of the phase diagrams as discussed in Section 4, suggest that these compounds may, in fact, be stable at high temperatures. Hence, they are tentatively shown in Figs. 9, 10.

The thermodynamic properties of the compounds from La to Sm, obtained by extrapolation, will be useful in predicting solubilities in multicomponent systems.

3.8 Compounds $RAl_{11}O_{18}$

The compound $LaAl_{11}O_{18}$ with the ß-alumina structure was identified by Roth and Hasko [30]. Subsequently, the Ce, Pr and Nd compounds have been observed. The compounds decrease in stability proceeding from La to Lu. The thermodynamic analysis predicts that these compounds all dissociate eutectoidally to $RAlO_3$ and Al_2O_3 at lower temperatures as shown tentatively in Fig. 18.

3.9 Compound $La_{33}Al_7O_{60}$

A compound of this approximate composition was reported by Mizuno et al [10]. It is shown tentatively on Fig. 3.

4. DETAILS OF EVALUATIONS

4.1 La_2O_3-Al_2O_3

The system was studied by X-ray and microscopic techniques over the entire composition range by Bondar and Vinogradova [31]. $LaAlO_3$ was reported to melt congruently at 2100 ± 20°C and $LaAl_{11}O_{18}$ was found to melt incongruently at 1930 ± 20°C with a peritectic liquid composition near 88 mol % Al_2O_3. Eutectics at 26 mol % Al_2O_3 at 1875 ± 20°C and 76 mol % Al_2O_3 at 1830 ± 20°C were found.

The liquidus was investigated by thermal analysis and X-ray techniques in the range from 65 to 100 mol % Al_2O_3 by Rolin and Thank [32] who reported the same two compounds with a eutectic at 78 mol % Al_2O_3 at 1760 ± 20°C. They show $LaAl_{11}O_{18}$ melting peritectically at 1855°C to give a peritectic liquid of 85 mol % Al_2O_3. However, their Al_2O_3 liquidus exhibits a sharp downward bend near 1930°C, and descends very steeply from 1930° to 1855°C. It seems most likely that the observed effect at 1930°C was actually the peritectic reaction, and that kinetic problems associated with the precipitation of $LaAl_{11}O_{18}$ were responsible for the anomalous effects.

Fritsche and Tensmeyer [33] reported $LaAl_{11}O_{18}$ to melt congruently at 1925°C.

Cooling curves were measured with an optical pyrometer over the range 0 to 50 mol% Al_2O_3 by Mizuno et al [10]. X-ray and micrographic studies of quenched specimens were also performed over the entire composition range. The data points shown on Fig. 3 were obtained in Ar atmospheres. In O_2 atmospheres, liquidus temperatures were identical near 0 and 50 mol % Al_2O_3, but were up to 90 K lower around 30 mol % Al_2O_3. (See the discussion below of the Nd_2O_3-Al_2O_3 system in which a similar phenomenon was observed.) Other authors did not report their experimental atmospheres.

Mizuno et al report a melting point of $LaAlO_3$ of 2110°C, and a peritectic involving $LaAl_{11}O_{18}$ at 1848 ± 20°C. Eutectics were reported at 27.5 mol % Al_2O_3 at 1840 ± 20°C and at 77.5 mol % Al_2O_3 at 1791 ± 20°C.

These authors also claim to have identified, by X-ray studies, a new orthorhombic phase of the approximate stoichiometry $La_{33}Al_7O_{60}$ which melts incongruently at 1890 ± 20°C and which decomposes eutectoidally to La_2O_3 and $LaAlO_3$ below 1810°C. As can be seen in Table 2, the optimization of these data yields reasonable enthalpies and entropies of formation and fusion of this compound. The calculated lower decomposition (eutectoid) temperature is 1067°C. Yamaguchi et al. [34] report the preparation of an orthorhombic compound $La_{10}Al_4O_{21}$ (28.6 mol % Al_2O_3) from an amorphous material by hydrolysis of the alkoxides. The phase appears to decompose above 1280°C. They did not report the compound $La_{33}Al_7O_{60}$. These two compounds are reported only in these two studies. No similar compounds are reported in other R_2O_3-Al_2O_3 systems with the exception of the Ce_2O_3-Al_2O_3 system in which the same authors [11] tentatively propose the existence of a compound with approximately 20 mol % Al_2O_3 with a narrow temperature range of existence. Hence, the existence of these compounds requires verification.

4.2 Ce_2O_3-Al_2O_3

Of all the rare earths, Ce exhibits the greatest stability of the tetravalent state.

The phase diagram was studied by Leonov et al [35] by quenching and X-ray techniques in H_2 and in air; and by Mizuno et al [11] by thermal analysis using an optical pyrometer in (Ar + 5% H_2) atmospheres and in air. It is the results in the hydrogen atmospheres which are discussed here. In air, the phase diagrams, which now correspond closely to the CeO_2-Al_2O_3 system, are very different.

Both sets of authors report the compound $CeAlO_3$, melting congruently at 2030°C [35] or 2075°C [11], and both report $CeAl_{11}O_{18}$, with a peritectic temperature and liquid

composition of 1950°C and 85 mol % Al_2O_3 [35] or 1890° and 88 mol % Al_2O_3 [11]. A eutectic between these two compounds is reported at 1810°C and 72 mol % Al_2O_3 [35] (as read from a very small published diagram) or at 1780°C at 79 mol % Al_2O_3 [11]. Hence, for Al_2O_3 contents above 50 mol % the phase diagram is reasonably well established.

In Ce_2O_3-rich solutions, however, the situation is less clear, possibly because of the stability of the Ce^{4+} valence state. The melting point of pure Ce_2O_3 was reported [22] from studies in (unspecified) "controlled atmospheres" as 2240°C, while Leonov et al [35] report a melting point of 2160°C in H_2, and Mizuno et al [11] indicate a value near 2200°C. A eutectic between Ce_2O_3 and $CeAlO_3$ at approximately 1870°C and 19 mol % Al_2O_3 is reported by Leonov et al [35], while Mizuno et al [11] report a eutectic at 1900°C and 30 mol % Al_2O_3. These latter authors tentatively propose the existence of a compound containing approximately 21 mol % Al_2O_3 with a peritectic at 1990°C and a lower (eutectoid) decomposition temperature of 1850°C. The same authors [10] propose a similar compound in the La_2O_3-Al_2O_3 system.

In both studies, [11, 35], the slope of the Ce_2O_3-liquidus is much less than is the case in all other R_2O_3-Al_2O_3 systems. This could be due to Ce_2O_3 having a much higher entropy of fusion than the other R_2O_3 oxides, or to an appreciable solubility of Al_2O_3 in solid Ce_2O_3 (which is not the case in the other R_2O_3 oxides), or to the presence of Ce^{4+} during the measurements. The latter explanation seems to be the most likely. The diagram in Fig. 4, calculated under the assumption of no solid solubility and an entropy of fusion of Ce_2O_3 of 6.0 cal/mol.K as for all the other R_2O_3 oxides, is thus tentatively proposed.

4.3 Pr_2O_3-Al_2O_3

An early study [36] showed the existence of the compounds $PrAlO_3$ and $PrAl_{11}O_{18}$. In a later study [12] involving thermal analysis and X-ray techniques, the existence of these compounds was confirmed and the liquidus was determined. $PrAlO_3$ was shown to be stoichiometric.

The starting material in the later study [12] was Pr_6O_{11}. The exact procedure of the experiments is not clear. Samples were prepared by annealing Al_2O_3 and Pr_6O_{11} in air at 1300° and 1600°C. The cooling curves were apparently carried out in an atmosphere of air. X-ray patterns were obtained for air-quenched samples and, apparently, high temperature X-ray studies at temperatures up to 1350°C were performed under He. Some Pr_6O_{11} was observed in specimens quenched in air. Presumably, however, only trivalent Pr^{3+} was present at the liquidus temperatures. The reported melting point of Pr_2O_3 was 2290°C which is close to the value of 2280° reported by Shevthenko and Lopato [22] who used "controlled atmospheres". Transformation temperatures of Pr_2O_3 were observed [12] at 2050° and 2102°C which are again close to the values of 2030° and 2130° reported by Shevthenko and Lopato [22].

Liquidus points of Mizuno et al [12] are shown on Fig. 5. These authors reported eutectics at 1819°C at 25 mol % Al_2O_3 and 1800°C at 79 mol% Al_2O_3, as well as a peritectic at 1855°C.

The reported [12] Al_2O_3-liquidus is much steeper than is thermodynamically possible and the reported limiting slope of the Pr_2O_3-liquidus is also steeper than in the other systems. However, the eutectic points [12] are reproduced well by the optimization with reasonable thermodynamic parameters.

From the optimization, $PrAl_{11}O_{18}$ is predicted to decompose eutectoidally below about 1580°C. This is consistent with the observations of Mizuno et al [12] who found no X-ray evidence for this compound in samples annealed in air at 1300°C, but did observe it in samples annealed at 1600°C.

As discussed in Section 3.6, extrapolation from the other systems predicts that the compound $Pr_4Al_2O_9$ may be stable over a limited temperature range. This is indicated tentatively on Fig. 5.

4.4 Nd_2O_3-Al_2O_3

An early study [37] reported one compound, $NdAlO_3$, melting at 2070°C, and two eutectics at 1800°C and 25 mol % Al_2O_3 and at 1750°C and 80 mol % Al_2O_3. In another study [36], the compound $NdAl_{11}O_{18}$ was reported to melt incongruently at 1920°C. No liquidus data were reported in either study.

The phase diagram was examined by Mizuno et al [13] by thermal analysis in air with an optical pyrometer and by X-ray studies on quenched specimens and at temperatures up to 1350°C in He atmospheres. They reported two compounds, $NdAlO_3$ melting at 2165°C and $NdAl_{11}O_{18}$ melting incongruently at 1795°C. Eutectics at 1850°C and 20 mol % Al_2O_3 and at 1720°C and 77 mol% Al_2O_3 were found.

The additional compound $Nd_4Al_2O_9$ was found in quenched specimens by Coutures et al [38]. The phase diagram was later re-examined by Coutures [39] using X-ray techniques and cooling curves under both Ar and O_2. His results in Ar atmospheres are shown on Fig. 6. Under O_2, he observed no changes in the melting points of Nd_2O_3, Al_2O_3 or $NdAlO_3$, but liquidus temperatures up to 90° lower were observed in the vicinities of the two eutectics. The author claims that the stability of the trivalent state of Nd precludes this being due to the presence of Nd^{4+}. Rather, he claims that it most likely results from a "spitting" phenomenon due to oxygen dissolution in the melt which is more pronounced at lower temperatures. In this regard, however, the liquidus temperatures of Mizuno et al [13], obtained in air, are not consistently higher or lower than those of Coutures.

Coutures [39] reports a melting temperature of $NdAlO_3$ of 2090°C and a peritectic melting of $NdAl_{11}O_{18}$ at 1900°C. The compound $Nd_4Al_2O_9$ was reported to melt incongruently at 1905°C. This temperature corresponds well with an apparent change in slope of the liquidus of Mizuno et al. $Nd_4Al_2O_9$ was reported by Coutures on the basis of the thermal analysis results, to decompose eutectoidally below 1780°C. However, this could

not be reproduced by the present thermodynamic analysis with reasonable entropies of formation of the compounds.

The liquidus curves of $NdAlO_3$ reported by both studies [13, 39] are asymmetric about the 50% composition, descending more steeply on one side than on the other. Mizuno et al report that there is no solid solubility on either side of the compound. Hence, the reported asymmetry is thermodynamically unlikely and is not reproduced in the calculated diagram.

4.5 System Pm_2O_3-Al_2O_3

Melting points of the compounds were interpolated from Fig. 19, and the entropies of fusion of the compounds were assumed to be equal (or as close as possible) to those of the corresponding Nd and Sm compounds. Enthalpies and entropies of formation of the compounds in Table 2, and values of ω in Table 1, were then chosen to be, simultaneously, as close as possible to the averages of the corresponding values for the Nd and Sm systems.

4.6 Sm_2O_3-Al_2O_3

An early study [40] reported one compound, $SmAlO_3$, with a melting point of 1920°C and a eutectic between $SmAlO_3$ and Al_2O_3 at 1720°C. In another study [41] involving micrographic and X-ray examination as well as thermal analysis, a second compound, $Sm_4Al_2O_9$, was observed to melt incongruently at 1920°C, while the compound $SmAlO_3$ was observed to melt at approximately 2060°C. Eutectics were observed at approximately 1860°C at 25 mol % Al_2O_3 and 1760°C at 77 mol % Al_2O_3. No appreciable range of stoichiometry of either compound was observed in X-ray studies.

No reaction between $SmAlO_3$ and Al_2O_3 was observed when the compounds were annealed together at 1700°C. In contradiction, however, Bondar and Toropov [20] reported

the existence of $SmAl_{11}O_{18}$, stable to at least 1900°C. No other authors report this compound. These authors report eutectics at 1925°C and 1825°C.

The phase diagram was measured by Mizuno et al [14] by thermal analysis in air with an optical pyrometer. Their points are shown on Fig. 8. Only the two compounds were observed, both melting congruently at 1977°C and 2104°C respectively. Three eutectic points were reported at 1880°C at 20 mol% Al_2O_3, at 1910°C at 39 mol% Al_2O_3, and at 1755°C at 76 mol % Al_2O_3.

The calculated optimized diagram agrees very well with the diagram of Mizuno et al except for the eutectic at 1948°C which is too high. This temperature could be lowered by making the calculated $SmAlO_3$ liquidus steeper by changing the entropy of fusion of $SmAlO_3$. However, this liquidus would then be too steep on the Al_2O_3-rich side of the compound. A tempting conclusion is that the compound $Sm_3Al_5O_{12}$, instead of decomposing near 1400°C as predicted by the calculations (Fig. 18), remains stable up to a peritectic temperature near 1900°C. This would permit the $SmAlO_3$ liquidus to be steeper, while still preserving the observed eutectic near 1746°C. The liquidus points [14] even suggest a possible change of slope near 1900°C. However, as noted above, no reaction between $SmAlO_3$ and Al_2O_3 was observed [41] at 1700°C.

4.7 Eu_2O_3-Al_2O_3

Timofeeva et al [42] examined the system by quenching techniques and observed the compounds $EuAlO_3$, melting at 1940°C, and $EuAl_{11}O_{18}$ melting incongruently at 1800°C. However, $EuAl_{11}O_{18}$ could not be obtained in pure form and its X-ray pattern was unindexed. It's existence is questionable. These authors report eutectics at 1630° and 1650°C, but their reported melting point of Al_2O_3 is 54° below the recommended value.

Mizuno et al [15] examined the system by thermal analysis in air, using an optical pyrometer, as well as by X-ray and micrographic techniques. The two compounds $Eu_4Al_2O_9$

and $EuAlO_3$ were reported with congruent melting points of 1950° and 2047°C respectively. Three eutectics were positioned at 1860 ± 20°C at 23 mol % Al_2O_3, at 1900 ± 20°C at 38 mol % Al_2O_3, and at 1710 ± 20°C at 76 mol % Al_2O_3.

In the optimized diagram, the calculated eutectics on either side of $Eu_4Al_2O_9$ are at higher temperatures that the reported [15] values because the steep $Eu_4Al_2O_9$-liquidus curves required to reproduce the measured values would require an unacceptably low entropy of fusion of this compound.

It was also not possible to reproduce the measured [15] eutectic at 1712°C without postulating the compound $Eu_3Al_5O_{12}$ melting peritectically near 1767°C as shown in Fig. 9. The alternative, raising the entropy of fusion of $EuAlO_3$ to make its liquidus less steep, would result in an unacceptably high entropy of fusion and, furthermore, would make the $EuAlO_3$-liquidus not steep enough on the Eu_2O_3-rich side.

The problem is that the compound $Eu_3Al_5O_{12}$ was not reported by Mizuno et al [15]. Furthermore, Budnikov et al [41], in studies on the Sm_2O_3-Al_2O_3 and Gd_2O_3-Al_2O_3 systems, observed no reaction when $SmAlO_3$ or $GdAlO_3$ were annealed with Al_2O_3 at 1700°C. If this compound does not, in fact, exist at these temperatures, then a lower eutectic temperature (near 1650°C as measured by Timofeeva et al [42]) is predicted by the calculations.

4.8 Gd_2O_3-Al_2O_3

The system was examined [41] by thermal analysis as well as by X-ray and micrographic examination. The compound $GdAlO_3$ was reported to melt congruently at 2050°C, while $Gd_4Al_2O_9$ was reported to melt incongruently at 1950°C. Eutectics were found at 1890°C at 27 mol % Al_2O_3 and 1755°C at 77 mol % Al_2O_3.

In another study [15], the phase diagram was determined by thermal analysis in air with an optical pyrometer as well as by X-ray and micrographic analysis. $Gd_4Al_2O_9$ and

$GdAlO_3$ were both reported to melt congruently, at 1951° and at 2069°C respectively. Eutectics were reported at 1930°, 1920° and 1720°C at 27, 35 and 75 mol % Al_2O_3 respectively.

In order to reproduce the measured temperature of the eutectic near 76 mol % Al_2O_3, the compound $Gd_3Al_5O_{12}$ has been tentatively proposed to melt peritectically near 1807°C. The problem with this hypothesis is that Budnikov et al [41] observed no reaction when $GdAlO_3$ and Al_2O_3 were annealed together at 1700°C, although the existence of $Gd_3Al_5O_{12}$ at lower temperatures has been reported [27]. If, in fact, this compound does not exist at liquidus temperatures, then a eutectic temperature below 1700°C is predicted by the calculations.

4.9 Tb_2O_3-Al_2O_3

Melting points of the compounds were interpolated from Fig. 19 and the entropies of fusion of the compounds were assumed to be equal to those of the corresponding Gd and Dy compounds. Enthalpies and entropies of formation of the compounds in Table 2 and values of ω in Table 1 were then chosen to be, simultaneously, as close as possible to the averages of the corresponding values for the Gd and Dy systems.

4.10 Dy_2O_3-Al_2O_3

The system was examined [16] by thermal analysis in air with an optical pyrometer as well as by X-ray and micrographic analysis. Three compounds, $Dy_4Al_2O_9$, $DyAlO_3$ and $Dy_3Al_5O_{12}$, were prepared by reaction of the component oxides at 1600°C. All three were reported to melt congruently, at 1954°, 2000° and 1920°C respectively. Eutectics were found at 1830°, 1920°, 1890° and 1760° at 21, 40, 58 and 82 mol % Al_2O_3 respectively.

The reported eutectic temperature of 1830°C between Dy_2O_3 and $DyAlO_3$ is not well reproduced by the optimization. However, this reported temperature is questionable in view

of the fact that in the R_2O_3-Al_2O_3 systems where R = Sm, Eu, Gd, Ho, Er or Yb, this eutectic temperature is significantly higher.

4.11 Ho_2O_3-Al_2O_3

The system was studied by Miuzuno [17] by thermal analysis in air and by X-ray and metallographic techniques. Three compounds, $Ho_4Al_2O_9$, $HoAlO_3$ and $Ho_3Al_5O_{12}$, were formed by reaction of the component oxides at 1600°C. They were all found to melt congruently at 1975°, 1980° and 1950°C respectively. Eutectics were found at 1885°, 1910°, 1930° and 1780° at 22, 40, 57.5 and 81 mol % Al_2O_3 respectively.

Transitions from the C to B and B to H structures of Ho_2O_3 were measured [17] at 2160° and 2225°C. These values compare well with the values of 2180° and 2240°C reported by Foex and Traverse [23] and 2190° and 2200° given by Shevthenko and Lopato [22].

4.12 Er_2O_3-Al_2O_3

The system was studied [17] by thermal analysis in air and by X-ray and metallographic techniques. Three compounds, $Er_4Al_2O_9$, $ErAlO_3$ and $Er_3Al_5O_{12}$, were formed by reaction of the component oxides at 1600°C. They were all found to melt congruently, at 1990°, 1963° and 1960°C respectively. Eutectics were found at 1885°, 1920°, 1930° and 1810°C at 20, 43, 57.5 and 82 mol % Al_2O_3 respectively.

The cubic to hexagonal transition of Er_2O_3 was found [17] by thermal analysis to occur at 2255°C, which may be compared with values of 2280° [23] and 2320°C [22] reported in other studies.

4.13 Tm_2O_3-Al_2O_3

The compound $TmAlO_3$ has been reported to exist at 1845°C [28]. Melting points of the compounds were interpolated from Fig. 19, and the entropies of fusion of the compounds were assumed to be equal to those of the corresponding Er and Yb compounds. Enthalpies and entropies of formation of the compounds in Table 2, and values of ω in Table 1 were then chosen to be, simultaneously, as close as possible to the average of the corresponding values for the Er and Yb systems.

4.14 Yb_2O_3-Al_2O_3

The system was studied [18] by thermal analysis in air with an optical pyrometer as well as by X-ray and micrographic techniques. Two compounds, $Yb_4Al_2O_9$ and $Yb_3Al_5O_{12}$ were reported to melt congruently at 2002° and 2000°C respectively. The $Yb_3Al_5O_{12}$ compound was prepared by reaction of the component oxides at 1600°C. Three eutectics were reported at 1890°, 1875° and 1845°C at 18, 52.5 and 82 mol % Al_2O_3 respectively.

The system was studied earlier by a quenching technique by Bondar and Toropov [20] who reported the same two compounds but whose liquidus temperatures differ by over 100° from those of the later work.

Some solubility of Al_2O_3 in $Yb_3Al_5O_{12}$ was found in two separate studies [19, 20]. In the present calculations, stoichiometry was assumed.

Although Mizuno and Noguchi [18] do not report the existence of the compound $YbAlO_3$, the same authors in an earlier study [43], report this compound as melting congruently and as decomposing below about 1800°C. They also give indexed X-ray patterns of this compound as does Roth [44]. The compounds $ErAlO_3$, $TmAlO_3$ and $LuAlO_3$ have all been reported. By assuming that $YbAlO_3$ melts incongruently as shown in Fig. 16, all data were well fitted with reasonable thermodynamic functions. The compound is calculated to have a narrow temperature range of existence which corresponds closely to that proposed in the earlier study [43].

4.15 Lu_2O_3-Al_2O_3

The system was studied by X-ray and metallographic analysis of quenched samples [45]. The compound $Lu_4Al_2O_9$, melting incongruently at 2000°C, and the compound $Lu_3Al_5O_{12}$, melting congruently at 2060°C, were reported. Eutectics were found at 1960° and 1860°C at 49 and 80 mol % Al_2O_3 respectively. Points shown on Fig. 17 were read off a small diagram given by the authors.

The melting point of Lu_2O_3 reported by these authors is over 100° lower than that of Shevthenko and Lopato [22]. The reported Lu_2O_3-liquidus has only half the slope of that found in all the other R_2O_3-Al_2O_3 systems. For these reasons, the data points [45] at higher Lu_2O_3 concentrations were largely discounted. It may be noted that the calculated eutectic temperature of 1981°C in Fig. 17 is close to the peritectic temperature of 2000°C proposed by Shrivinskaya and Popova [45].

Some solubility of Lu_2O_3 in $Lu_3Al_5O_{12}$ was reported in an early study [19]. In the present calculations, this compound was assumed to be stoichiometric.

The compound $Lu_4Al_2O_9$ was formed by annealing the component oxides at 1650°C [45]. It was subsequently found to be stable after 45 days of annealing in the temperature range 1000° to 1450°C.

The existence of the compound $LuAlO_3$ at 1900°C has been confirmed by X-ray studies [46]. The compound was found subsequently to decompose at 1600°C. Shirvinskaya and Popova [45] could not obtain this compound by annealing at 1650°C nor by slow cooling from the melt, but they did observe it in samples which had been quenched rapidly. Schneider et al [19] did not observe it after annealing at 1850°C. In the present analysis it is very tentatively proposed that the compound is stable at 1900°C as found by Petrosyan et al [46] and melts just above this temperature. With the same entropy of fusion as the other

heavy $RAlO_3$ compounds, $LuAlO_3$ is then predicted to have a very narrow temperature range of stability.

5. CONCLUSIONS

Available phase diagram data for the R_2O_3-Al_2O_3 systems have been critically assessed. Equations for the Gibbs energies of formation of all compounds and for the Gibbs energy of mixing of the liquid phase have been deduced. The parameters vary systematically along the series from La to Lu. These equations have been used to calculate optimized phase diagrams for all fifteen systems, including three for which no phase diagrams have been reported. The phase diagrams have thus been smoothed and evaluated in a thermodynamically correct manner in accordance with principles of solution behavior. The assessment of each system has been aided by virtue of evaluating all the systems together.

Gibbs energies of formation of metastable compounds have been predicted. These will be useful in predictions of multicomponent phase diagrams.

The binary R_2O_3-Al_2O_3 liquid solutions all exhibit approximately the same negative deviations from ideal solution behavior.

Depending on the system and the composition range, the liquidus curves of the optimized diagrams are estimated to be accurate to ± 25 to ± 50 K, while the Gibbs energies of formation of the compounds at high temperatures have an estimated accuracy of ± 2000 cal/mol.

ACKNOWLEDGEMENTS

This work was supported by the Natural Sciences and Engineering Research Council of Canada.

REFERENCES

[1] I. Barin, "Thermochemical Data of Pure Substances", VCH, Weinheim, Germany (1989).

[2] C.W. Bale and A.D. Pelton, Met. Trans., 14B, 77-84 (1983).

[3] H.L. Lukas, E.-Th. Henig and B. Zimmermann, Calphad J., 1, 225 (1977).

[4] A.D. Pelton and M. Blander, Calphad J., 12, 97-108 (1988).

[5] F*A*C*T (Facility for the Analysis of Chemical Thermodynamics), An On-line Thermodynamic Computing System, W.T. Thompson, C.W. Bale and A.D. Pelton, McGill University/Ecole Polytechnique, Montreal.

[6] A.D. Pelton, "Thermodynamics and Phase Diagrams of Materials", Ch. 1 in "Materials Science and Technology", vol. 5, ed. R.W. Cahn, P. Haasen and E.J. Kramer, VCH, Weinheim, Germany (1991).

[7] A.D. Pelton and M. Blander, Proc. Int'l Symp. Molten Salts and Slags, pp. 281-294, TMS-AIME, Warrendale, PA (1984).

[8] A.D. Pelton and M. Blander, Met. Trans., 17B, 805-815 (1986).

[9] M. Blander and A.D. Pelton, Geochim et Cosmochim. Acta, 51, 85-95 (1987).

[10] M. Mizuno, R. Berjoan, J.-P. Coutures and M. Foex, Yogyo-Kyokai-Shi, 82, 631-636 (1974).

[11] M. Mizuno, R. Berjoan, J.-P. Coutures and M. Foex, Yogyo-Kyokai-Shi, 83, 50-56 (1975).

[12] M. Mizuno, T. Yamada and T. Noguchi, Reports Govt. Ind. Res. Inst., Nagoya (Hirate-machi Kita-Ku Nagoya, Japan), 27(2), 47-52 (1978); Yogyo-Kyokai-Shi, 85, 24-29 (1977).

[13] M. Mizuno, T. Yamada and T. Noguchi, Yogyo-Kyokai-Shi, 85, 91-95 (1977).

[14] M. Mizuno, T. Yamada and T. Noguchi, Yogyo-Kyokai-Shi, 85, 374-379 (1977).

[15] M. Mizuno, T. Yamada and T. Noguchi, Yogyo-Kyokai-Shi, 85, 543-548 (1977).

[16] M. Mizuno, T. Yamada and T. Noguchi, Yogyo-Kyokai-Shi, 86, 360-364 (1978).

[17] M. Mizuno, Yogyo-Kyokai-Shi, 87, 405-412 (1979).

[18] M. Mizuno and T. Noguchi, Yogyo-Kyokai-Shi 88, 322-327 (1980).

[19] S.J. Schneider, R.S. Roth and J.L. Waring, J. Res. Natl. Bur. Stand. 65A, 345-374 (1961).

[20] I.A. Bondar and N.A. Toropov, Izv. Akad. Nauk SSSR, Ser. Khim., no. 2, 212-218 (1966); Bull. Acad. Sci. USSR, Div. Chem. Sci., no. 2, 195 (1966).

[21] I. Barin, O. Knacke and O. Kubaschewski, "Thermochemical Properties of Inorganic Substances", Springer-Verlag, N.Y. (1973).

[22] A.V. Shevthenko and L.M. Lopato, Thermochim. Acta, 93, 537-540 (1985).

[23] M. Foex and J.-P. Traverse, Bull. Soc. Franc., Minér. Crist., 89, 184-205 (1966).

[24] A.G. Boganov and V.S. Rudenko, Dokl. Akad. Nauk SSSR, 161, 590 (1965).

[25] A. Rugiero and R. Ferro, Gaz, Chim. Ital., 85, 892-897 (1955).

[26] S. Geller and V.B. Bala, Acta Cryst., 9, 1019-1025 (1956).

[27] F. Bertaut and F. Forrat, Compt. Rend., 243, 1219-1222 (1956).

[28] G. Garton and B.M. Wanklyn, J. Cryst. Growth, 1, 164-166 (1967).

[29] P.D. Dernier and R.G. Maines, Mat. Res. Bull., 6, 433-440 (1971).

[30] R.S. Roth and S. Hasko, J. Am. Cer. Soc., 41, 146 (1958).

[31] I.A. Bondar and N.V. Vinogradova, Izv. Akad. Nauk SSSR Ser. Khim., 5, 785 (1964).

[32] M. Rolin and P.H. Thanh, Rev. Hautes Temp. Réfract., 2, 182-185 (1965).

[33] E.T. Fritsche and L.G. Tensmeyer, J. Am. Ceram. Soc., 50, 167 (1967).

[34] O. Yamaguchi, K. Sugiura, A. Mitsui and K. Shimizu, J. Am. Ceram. Soc., 68, C44-45 (1985).

[35] A.I. Leonov, A.V. Andreeva, V.E. Shvaiko-Shvaikovskii and E.K. Keler, Izv Akad. Nauk SSSR, Neorg. Mater., 2, 517 (1966); Inorg. Mater. (USSR), 2, 446 (1966).

[36] N.A. Godina and E.K. Koehler, Izv. Akad. Nauk SSSR, 1, 24-31 (1966).

[37] N.A. Toropov and T.P. Kiseleva, Zhur. Neorg. Khim., 6, 2353-58 (1961); Russ. J. Inorg. Chem., 6, 1193-96 (1961).

[38] J.-P. Coutures, E. Antic and P. Caro, Mat. Res. Bull., 11, 699-706 (1976).

[39] J.-P. Coutures, J. Am. Ceram. Soc., 68, 105-107 (1985).

[40] F.H. Aldred and A.E. White, Trans. Brit. Ceram. Soc., 58, 199 (1959).

[41] P.P. Budnikov, V.I. Kushakovskii and V.S. Belevanstev, Dokl. Akad. Nauk SSSR, 165, 1075 (1965).

[42] N.I. Timofeeva, E.N. Timofeeva, L.N. Drozdova and O.A. Mordovin, Izv. Akad. Nauk SSSR, Neorg. Mater., 5, 1742-44 (1969).

[43] T. Noguchi and M. Mizuno, Kogyo-Kogakuza-Shi, 70, 839 (1967).

[44] R.S. Roth, J. Res. Nat. Bur. Stand., 58, 75 (1957).

[45] A.K. Shirvinskaya and V.F. Popova, Dokl. Akad. Nauk SSSR, 233, 1110-13, (1977).

[46] A.G. Petrosyan, G.O. Shirinyan and A.S. Kuzanyan, Dokl. Akad. Nauk Arm. SSR, 70, 175-178 (1980).

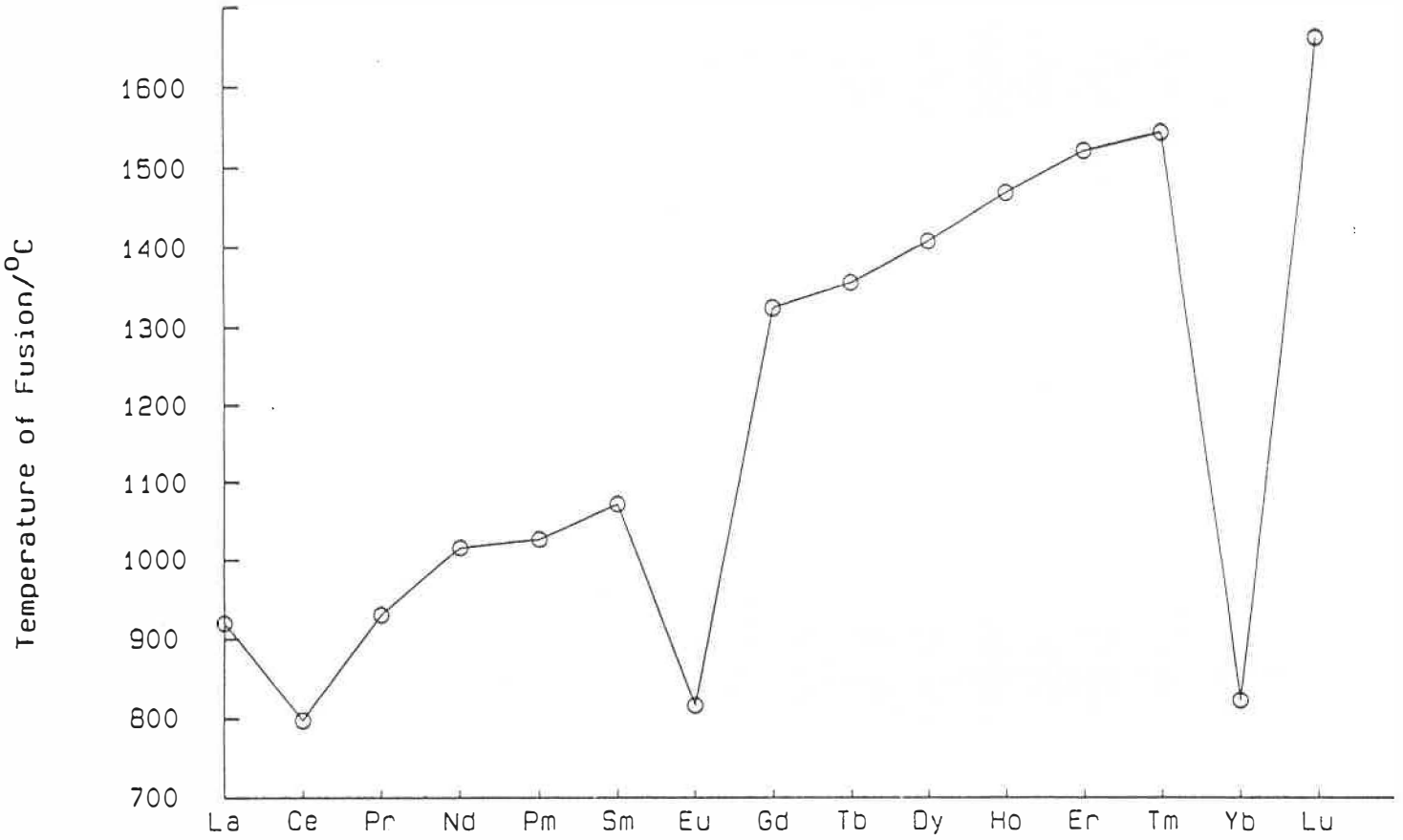


Fig. 3-1

Fig. 1 Melting points of the rare earth metals (1)

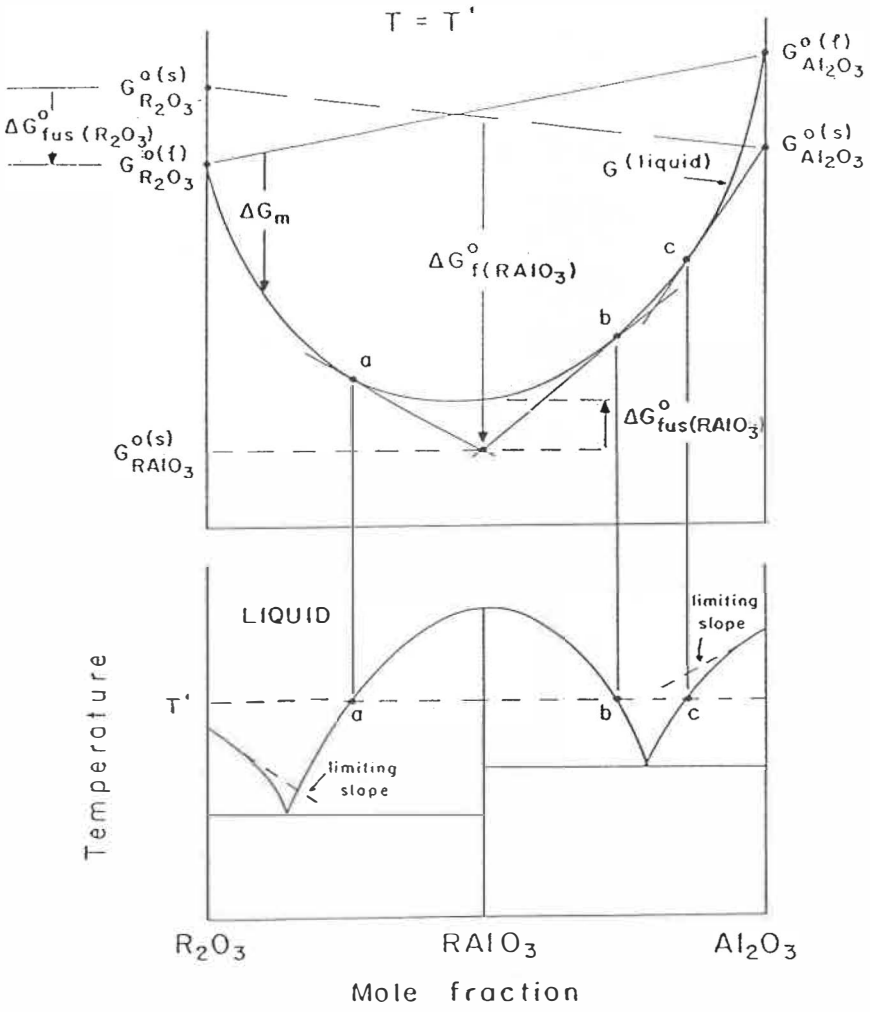


Fig. 3-2

Fig. 2 Schematic phase diagram of an R_2O_3-Al_2O_3 system and the corresponding Gibbs energy-composition diagram at a temperature T'

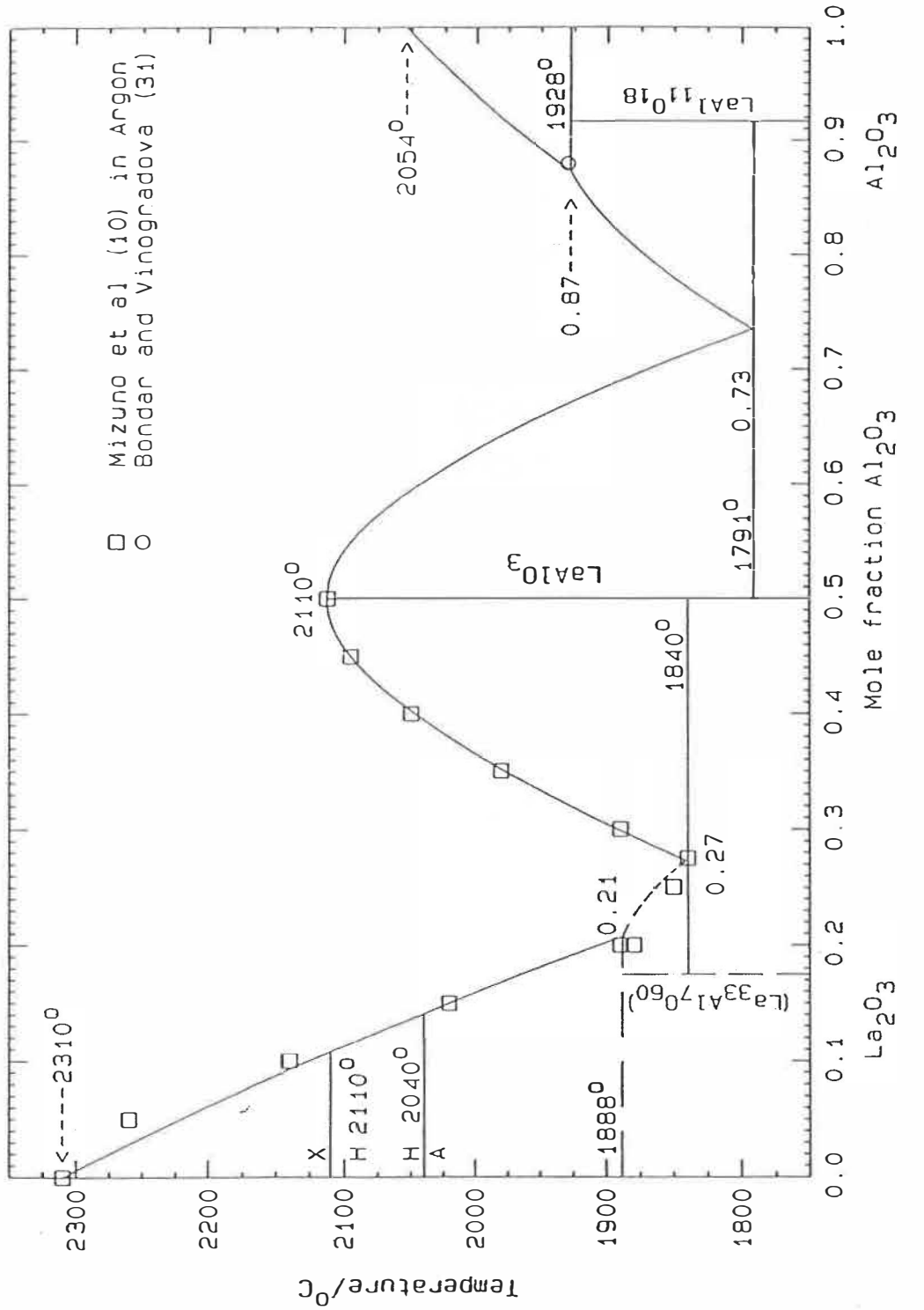


Fig. 3-3

Fig. 3 Assessed La_2O_3-Al_2O_3 phase diagram calculated thermodynamically

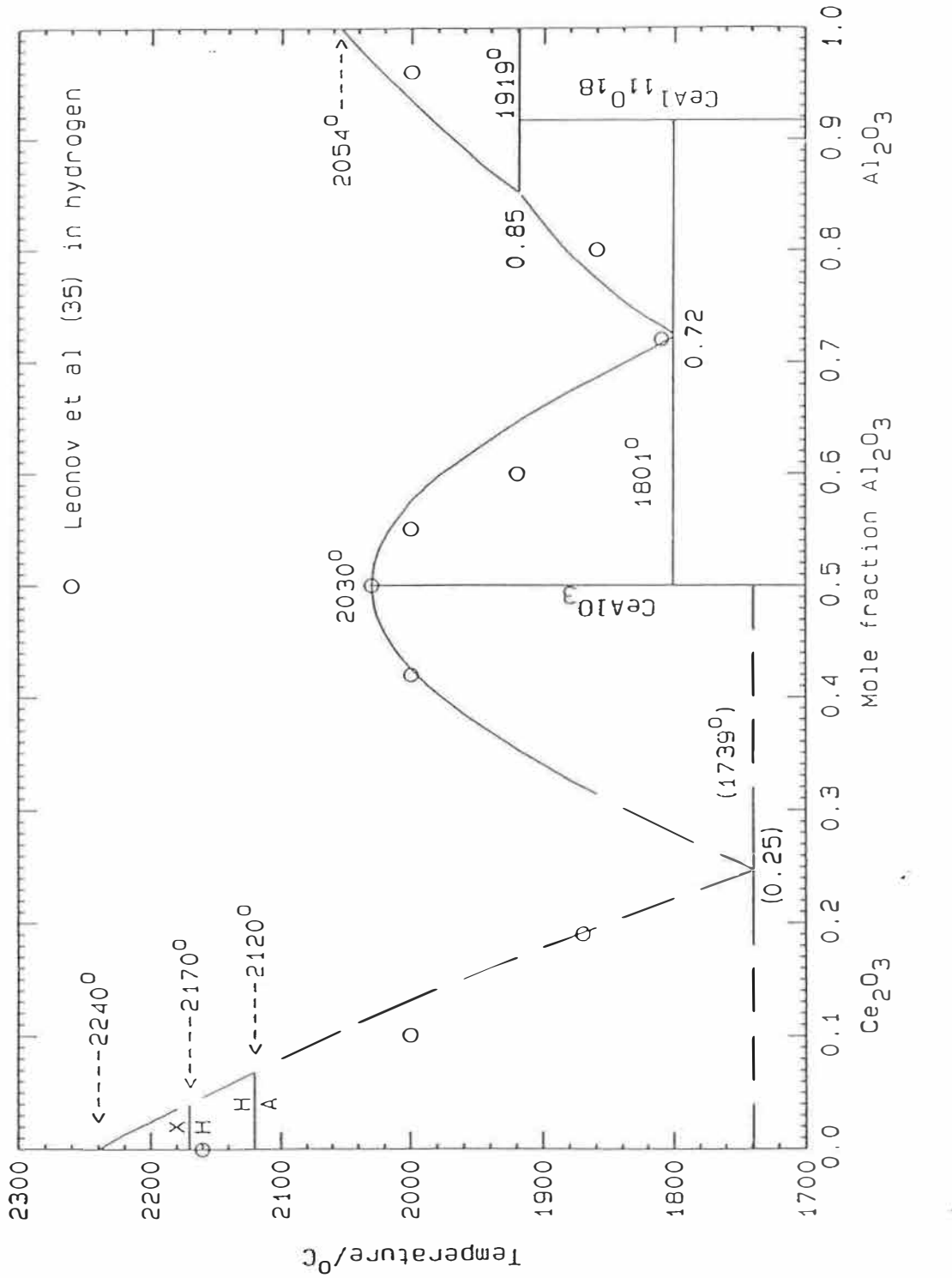


Fig. 3-4

Fig. 4 Assessed Ce_2O_3-Al_2O_3 phase diagram calculated thermodynamically

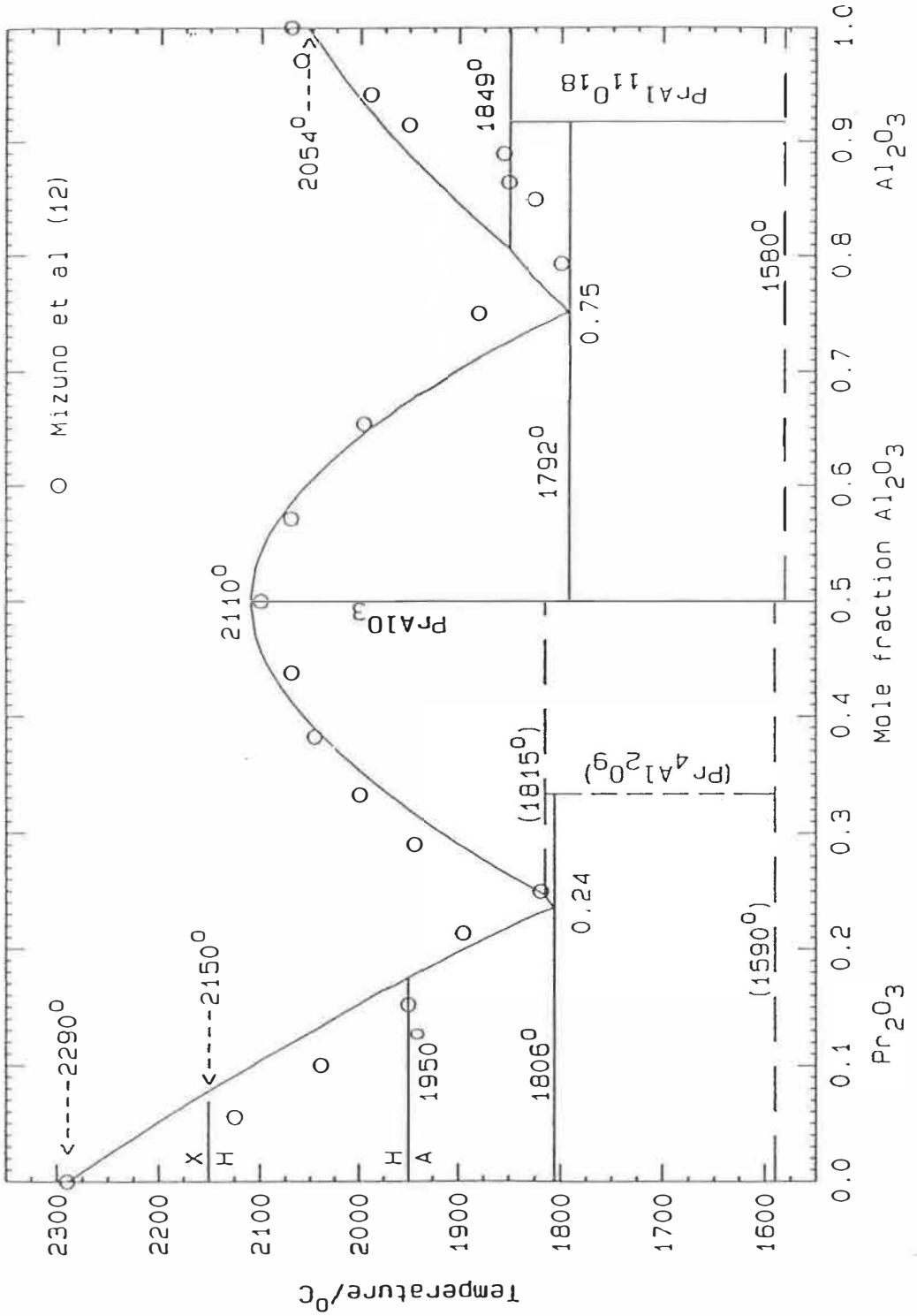


Fig. 3-5

Fig. 5 Assessed Pr_2O_3-Al_2O_3 phase diagram calculated thermodynamically

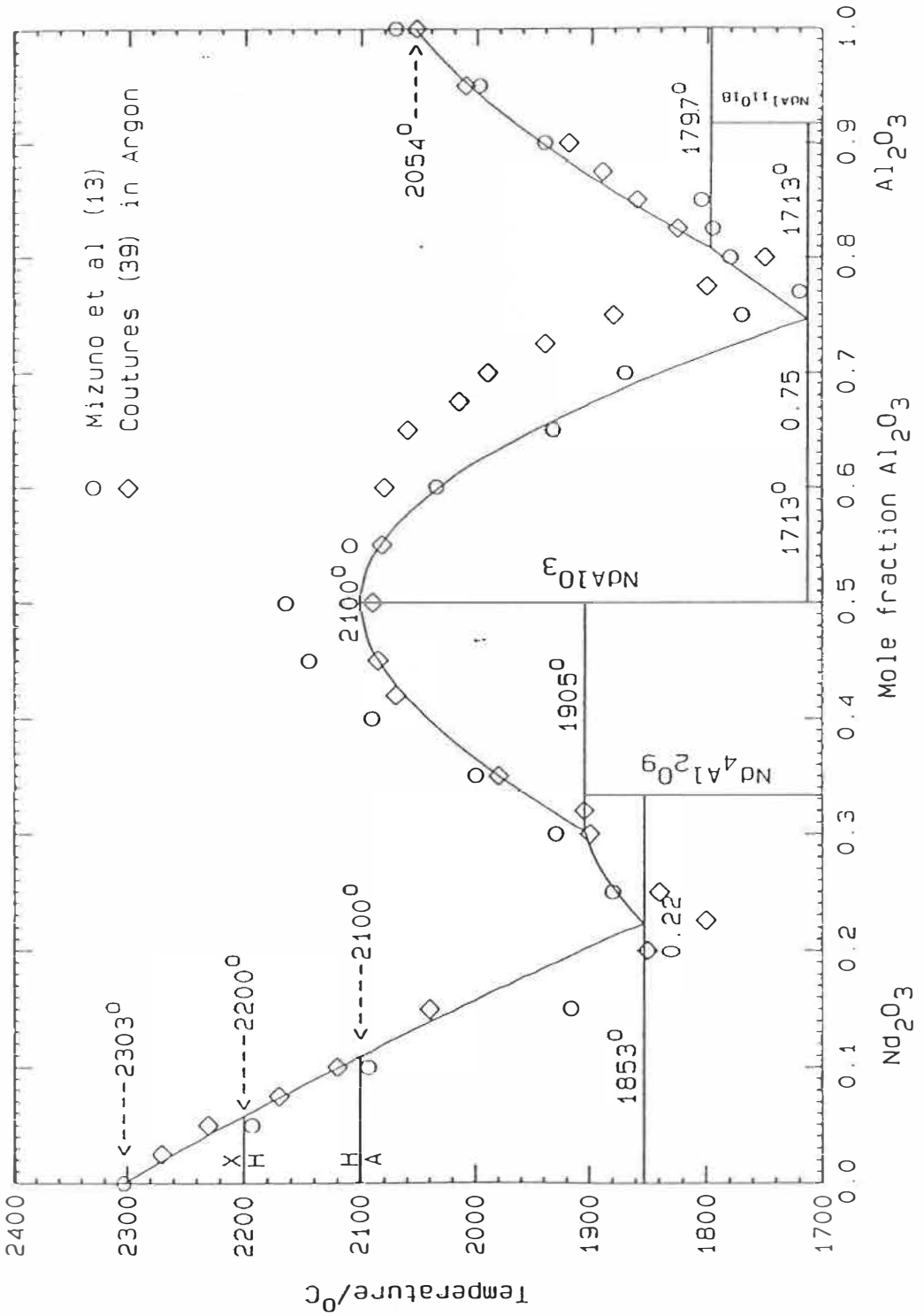


Fig. 3-6

Fig. 6 Assessed Nd_2O_3-Al_2O_3 phase diagram calculated thermodynamically

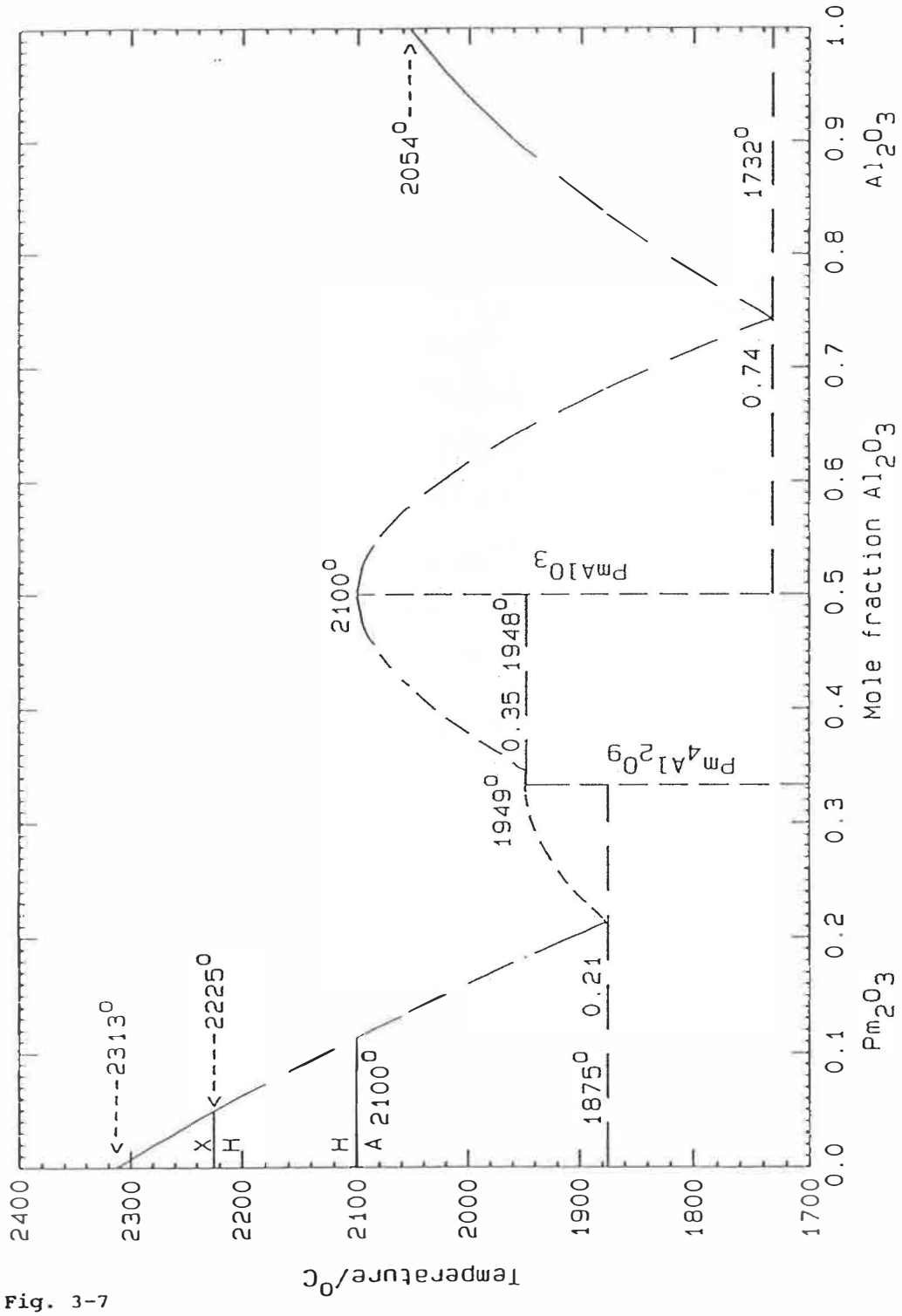


Fig. 3-7

Fig. 7 Assessed Pm_2O_3-Al_2O_3 phase diagram calculated thermodynamically

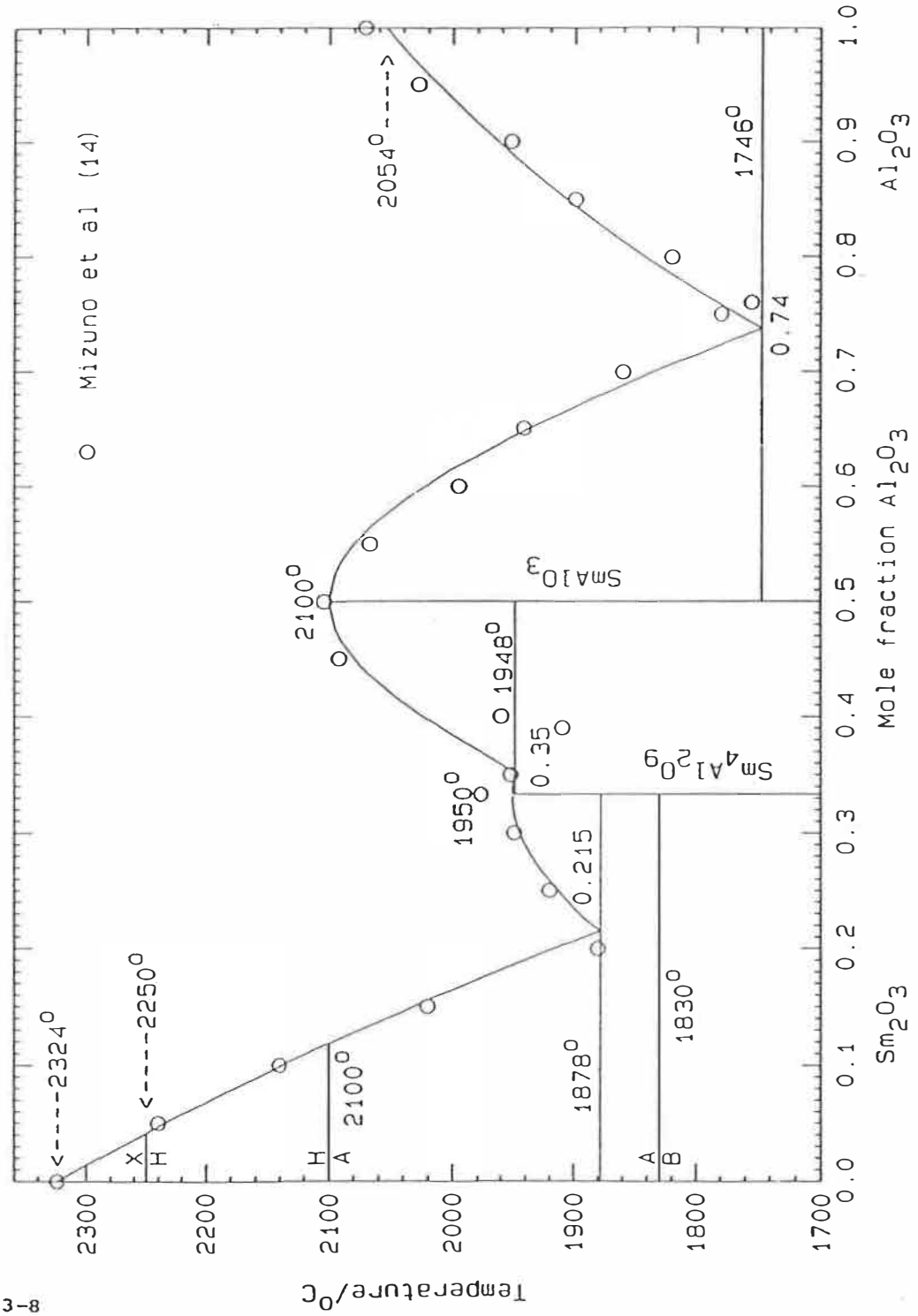


Fig. 3-8

Fig. 8 Assessed Sm_2O_3-Al_2O_3 phase diagram calculated thermodynamically

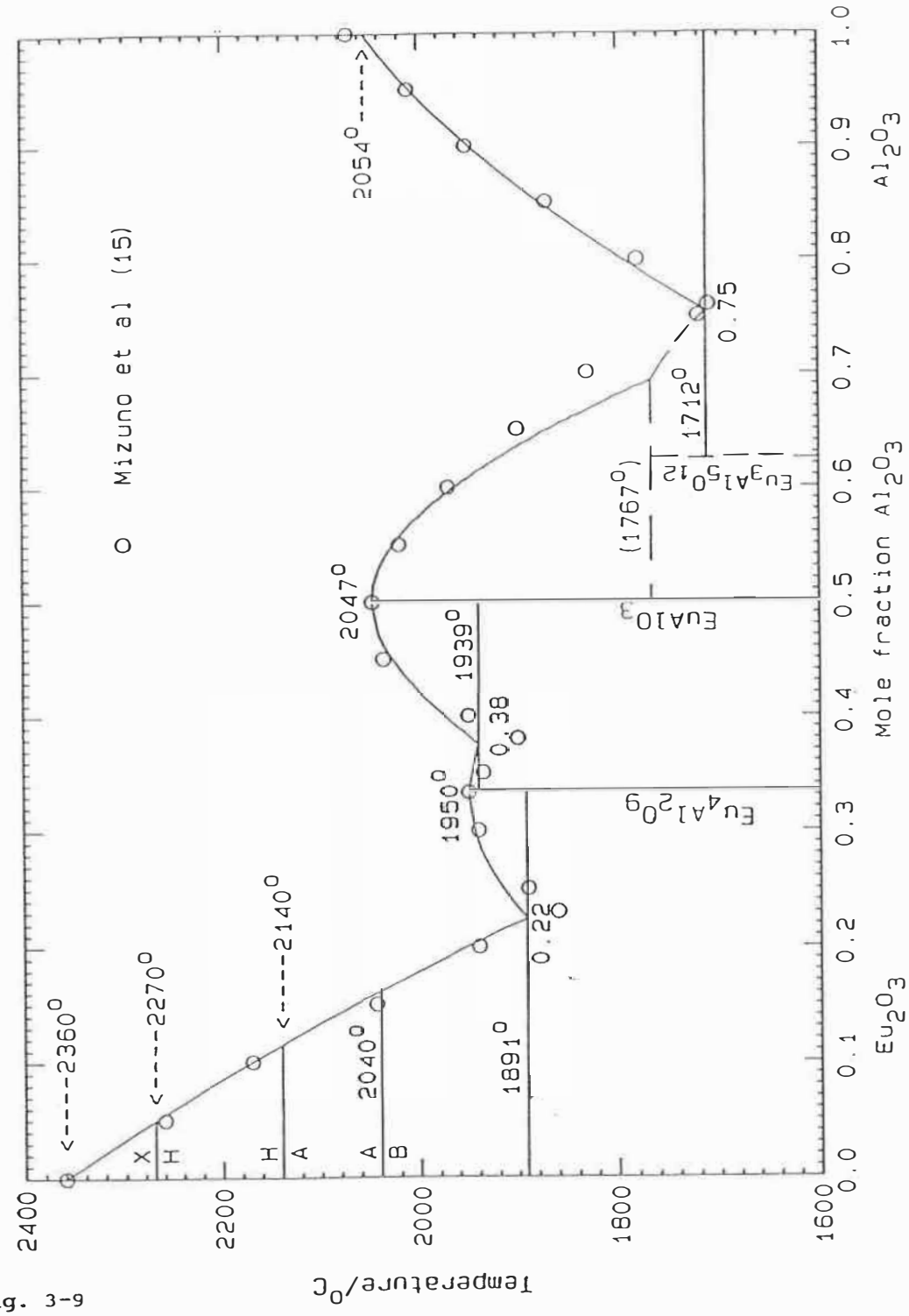


Fig. 3-9

Fig. 9 Assessed Eu_2O_3-Al_2O_3 phase diagram calculated thermodynamically

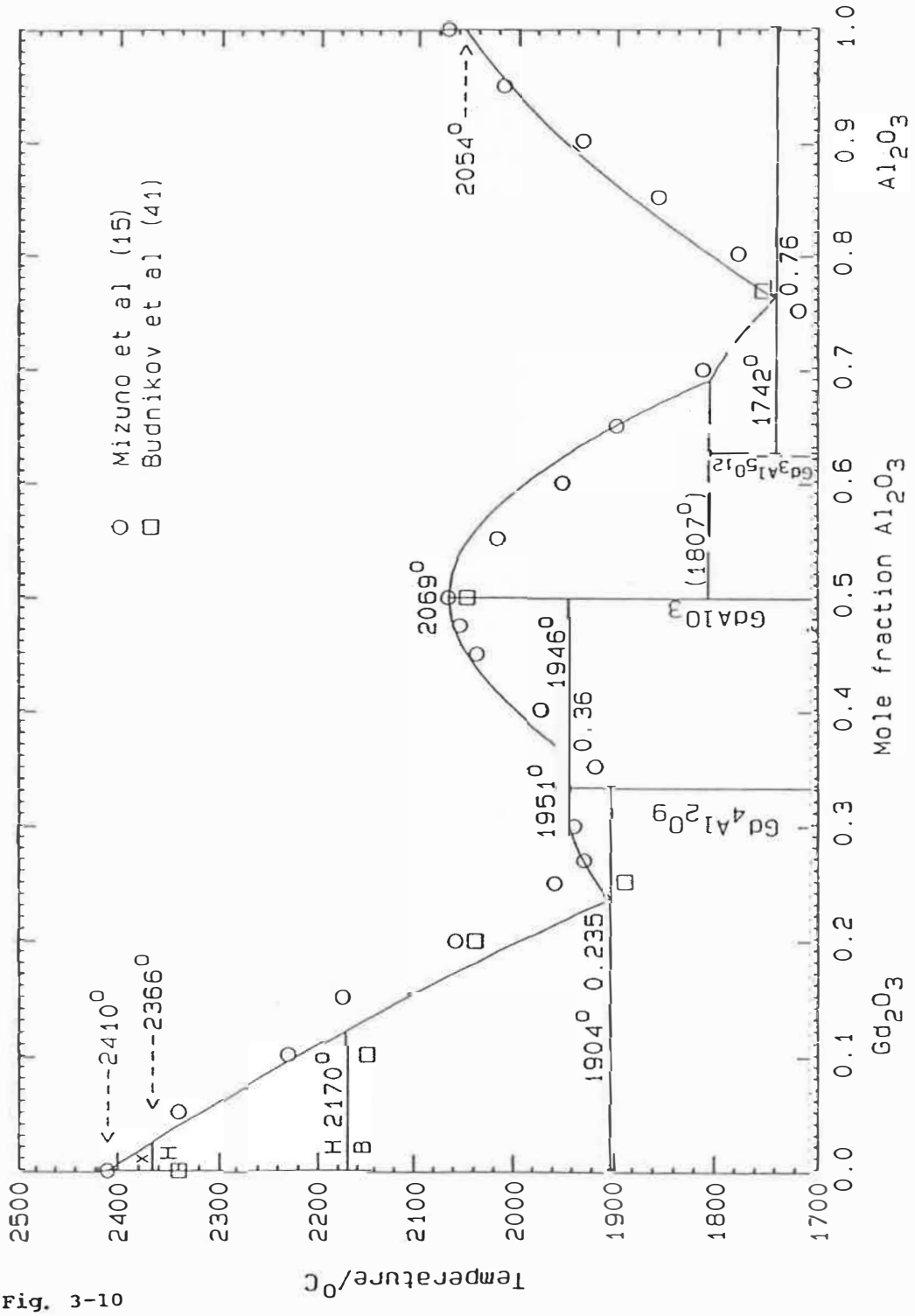


Fig. 3-10

Fig. 10 Assessed Gd_2O_3-Al_2O_3 phase diagram calculated thermodynamically

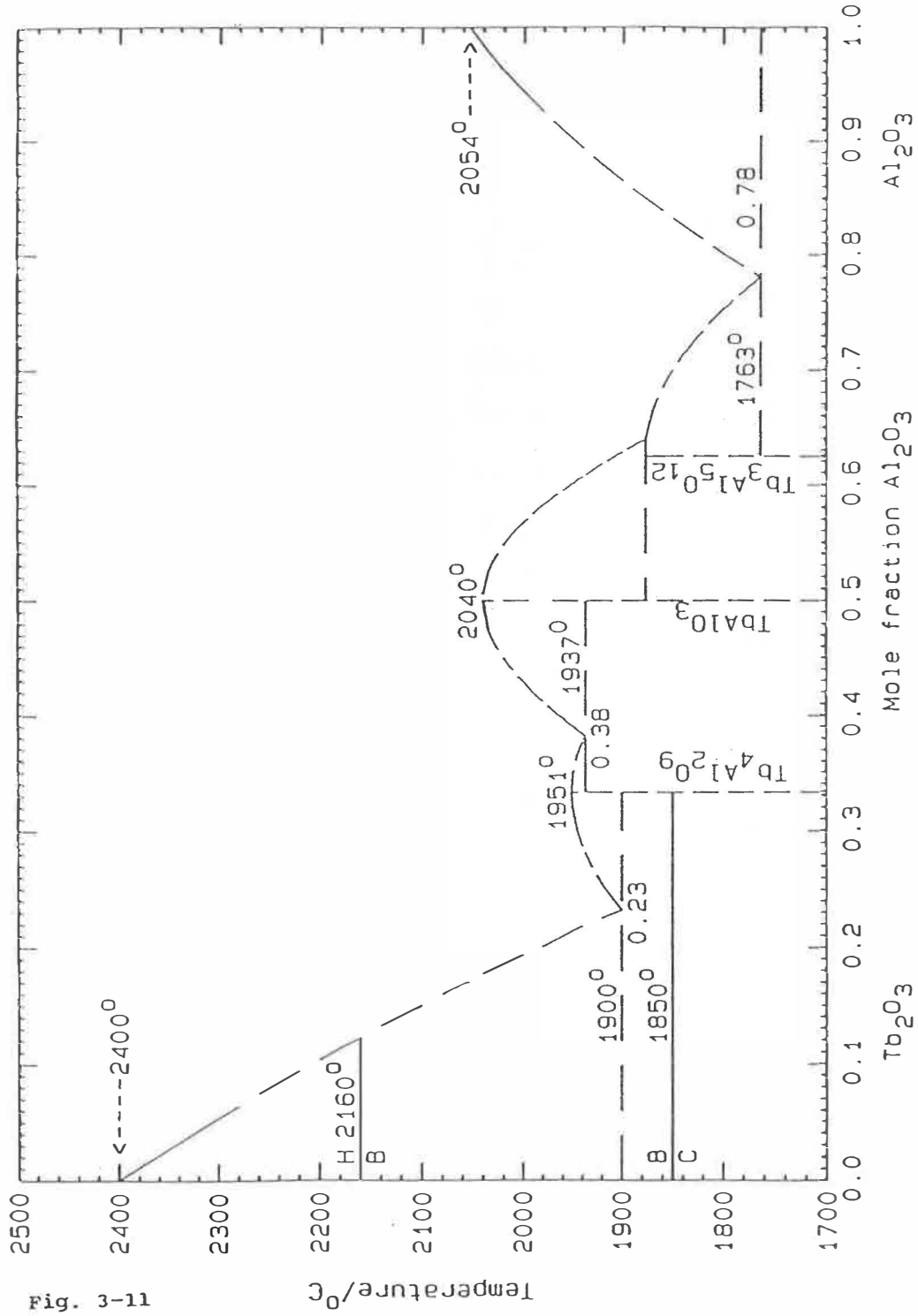


Fig. 3-11

Fig. 11 Assessed Tb_2O_3-Al_2O_3 phase diagram calculated thermodynamically

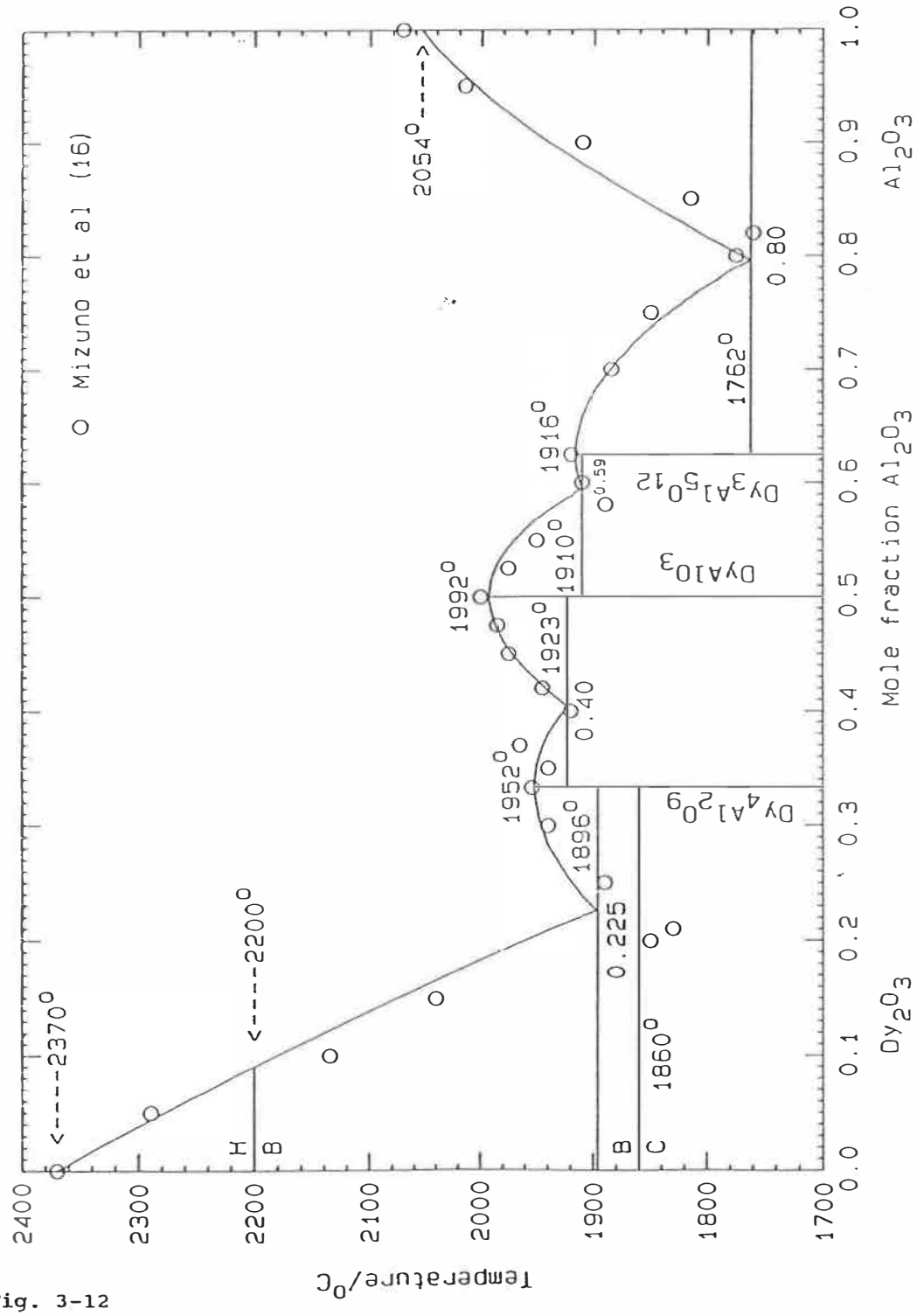


Fig. 3-12

Fig. 12 Assessed Dy_2O_3-Al_2O_3 phase diagram calculated thermodynamically

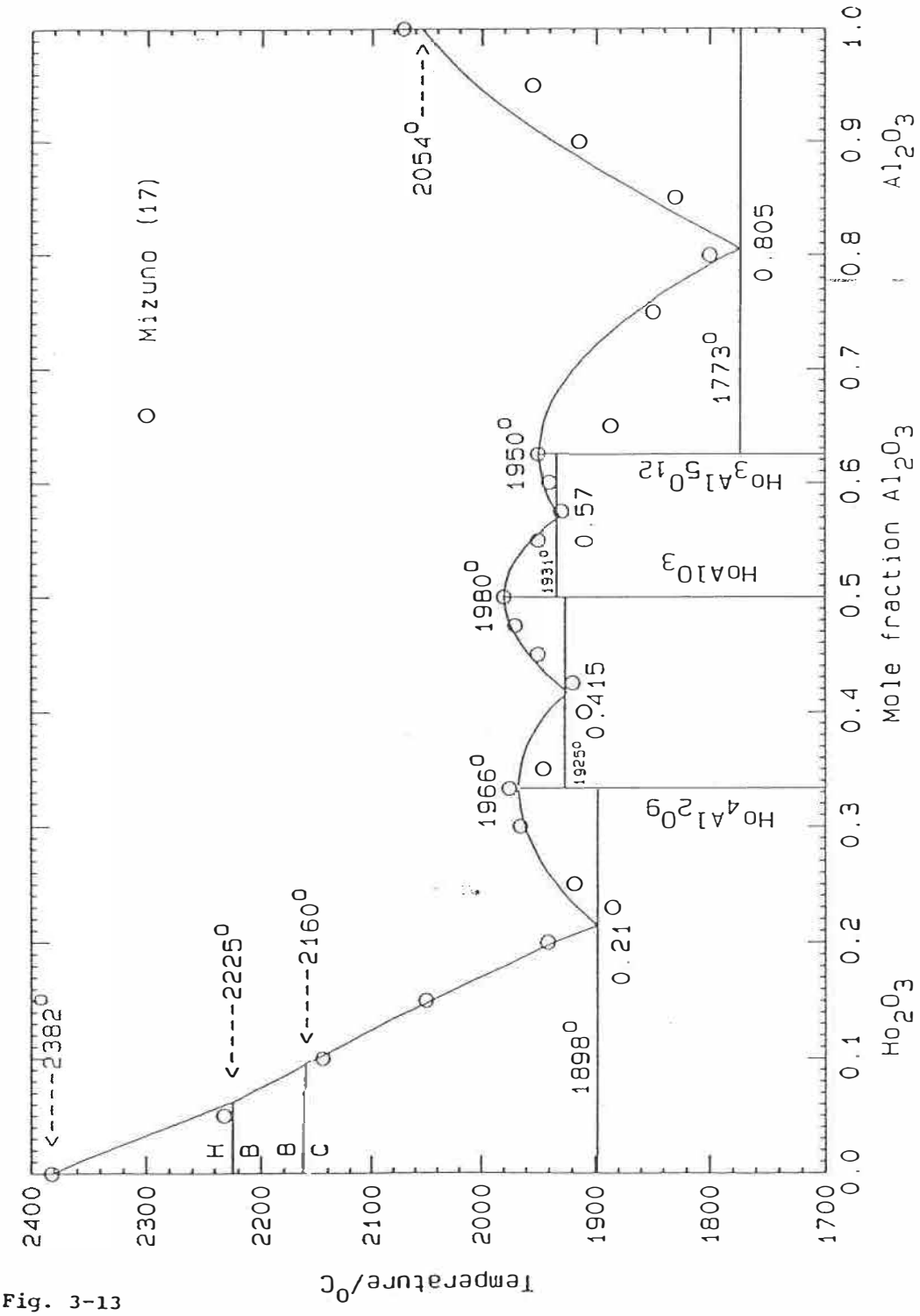


Fig. 3-13

Fig. 13 Assessed Ho_2O_3-Al_2O_3 phase diagram calculated thermodynamically

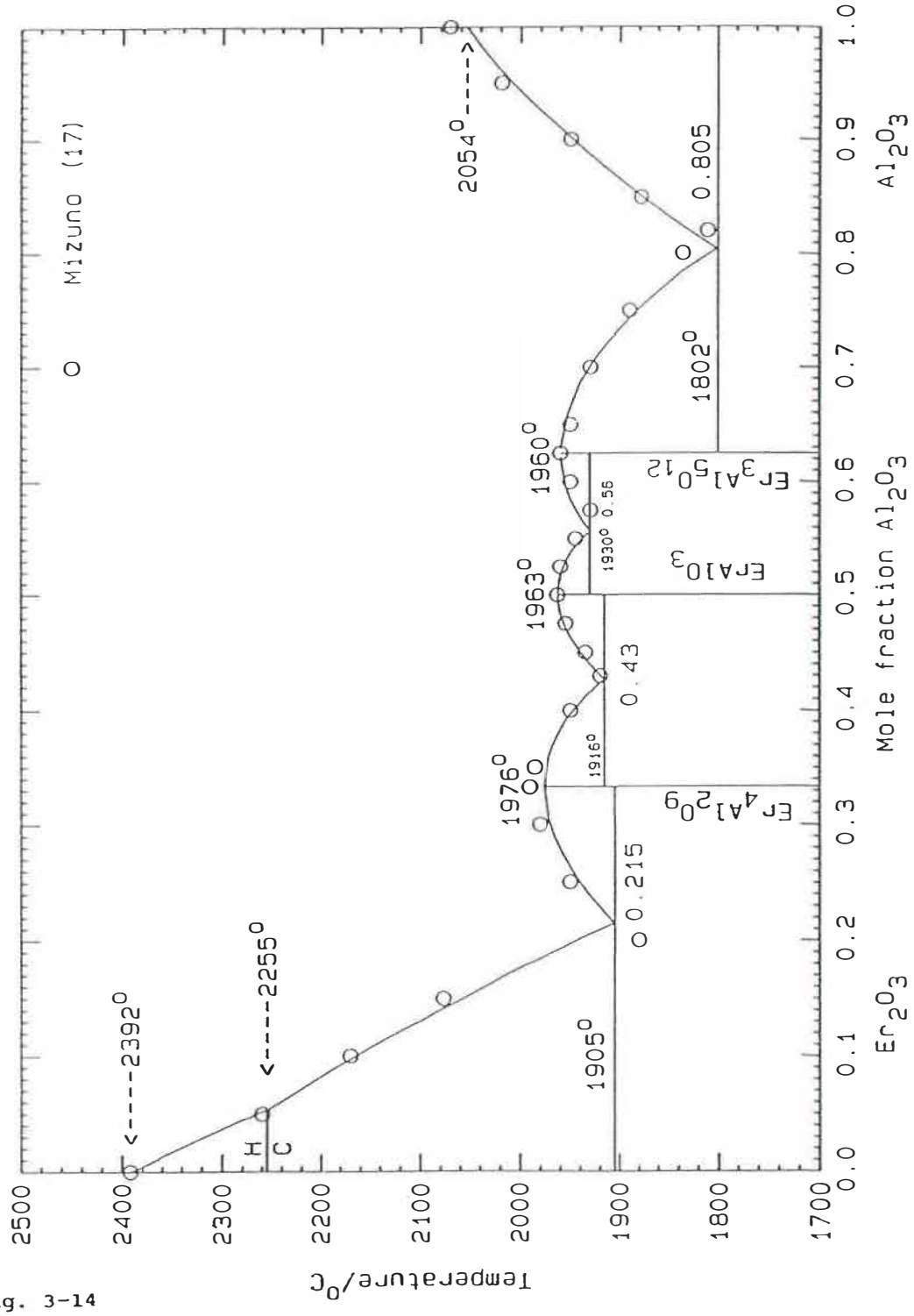


Fig. 3-14

Fig. 14 Assessed Er_2O_3-Al_2O_3 phase diagram calculated thermodynamically

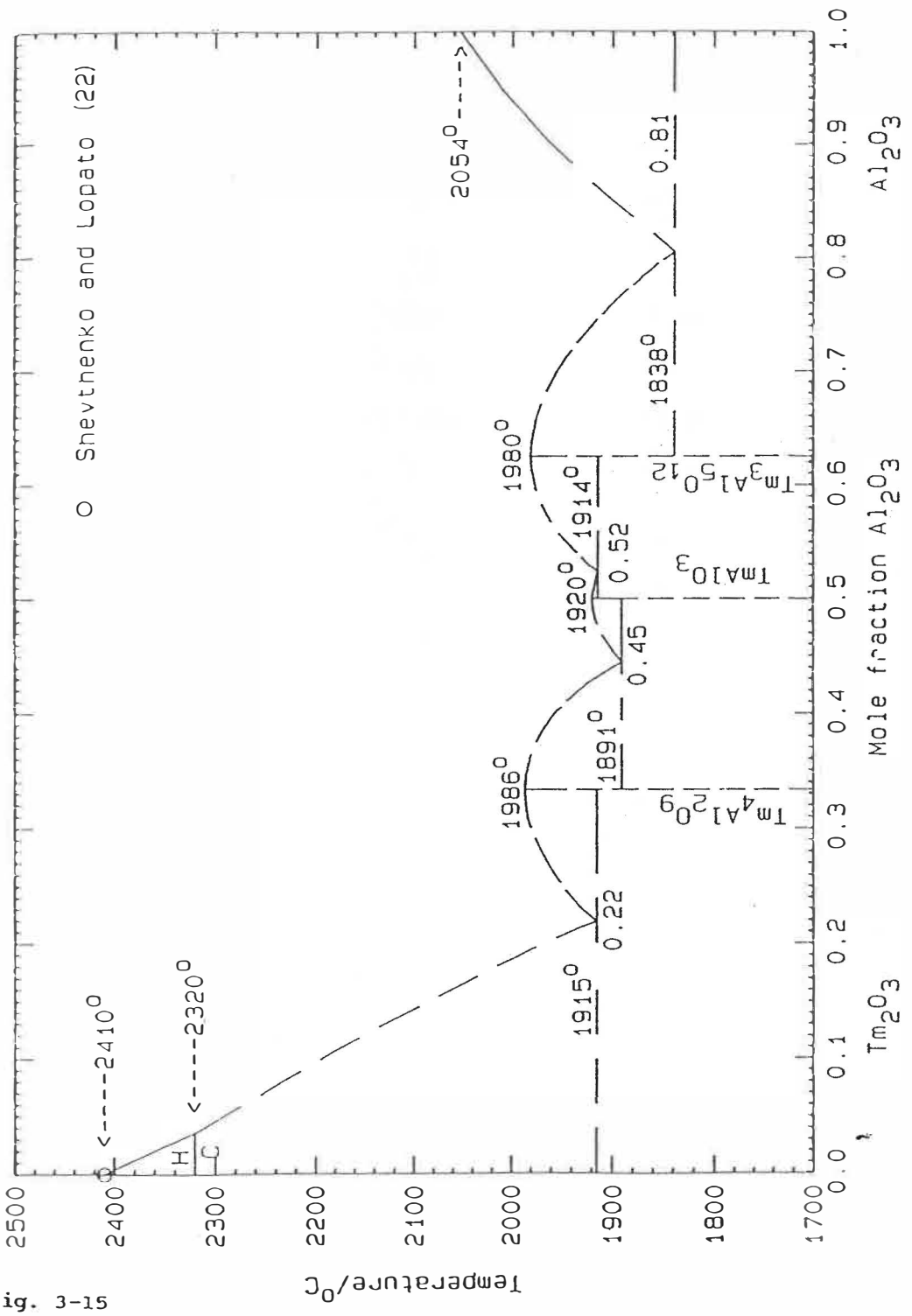


Fig. 3-15

Fig. 15 Assessed Tm_2O_3-Al_2O_3 phase diagram calculated thermodynamically

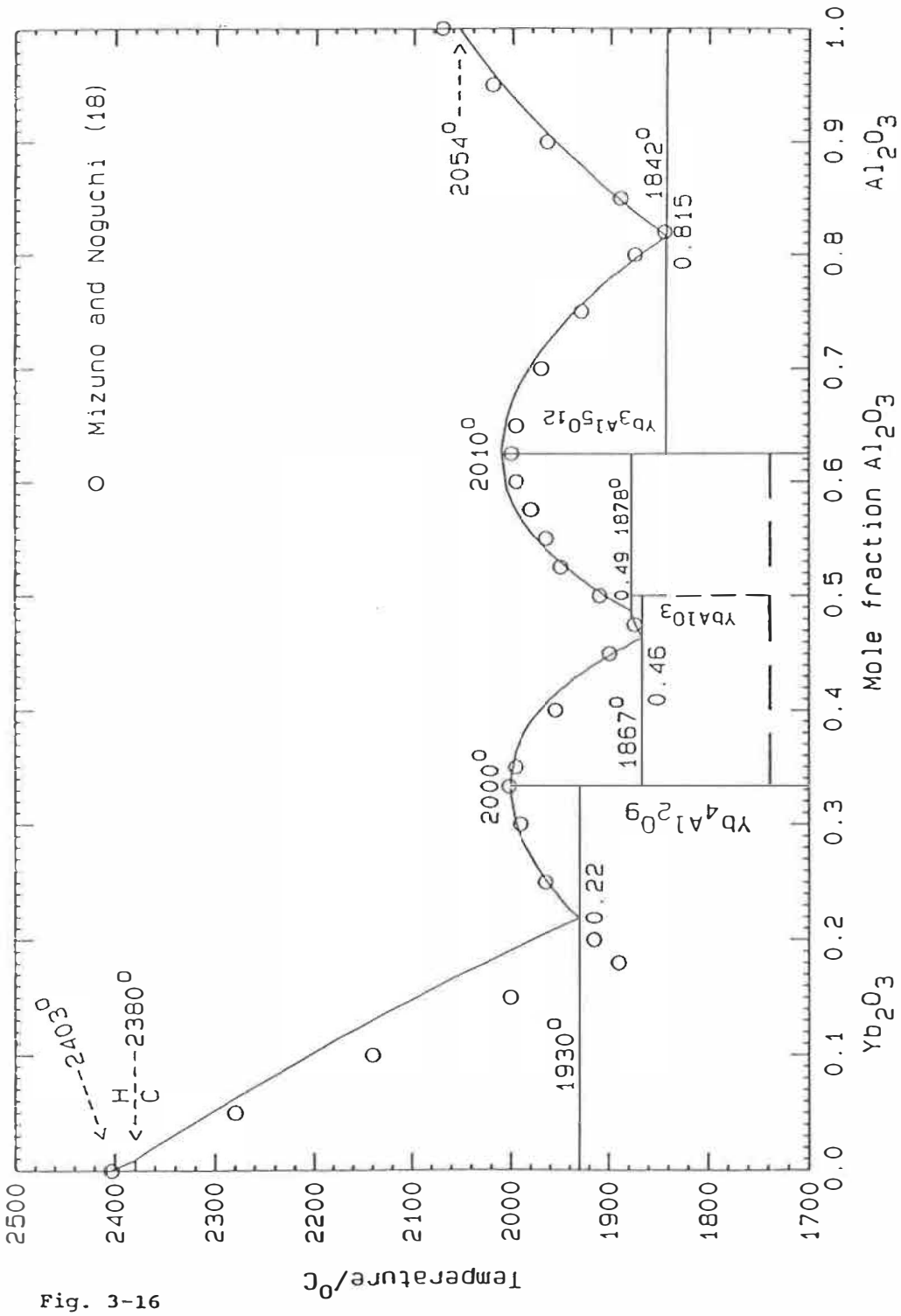


Fig. 3-16

Fig. 16 Assessed Yb_2O_3-Al_2O_3 phase diagram calculated thermodynamically

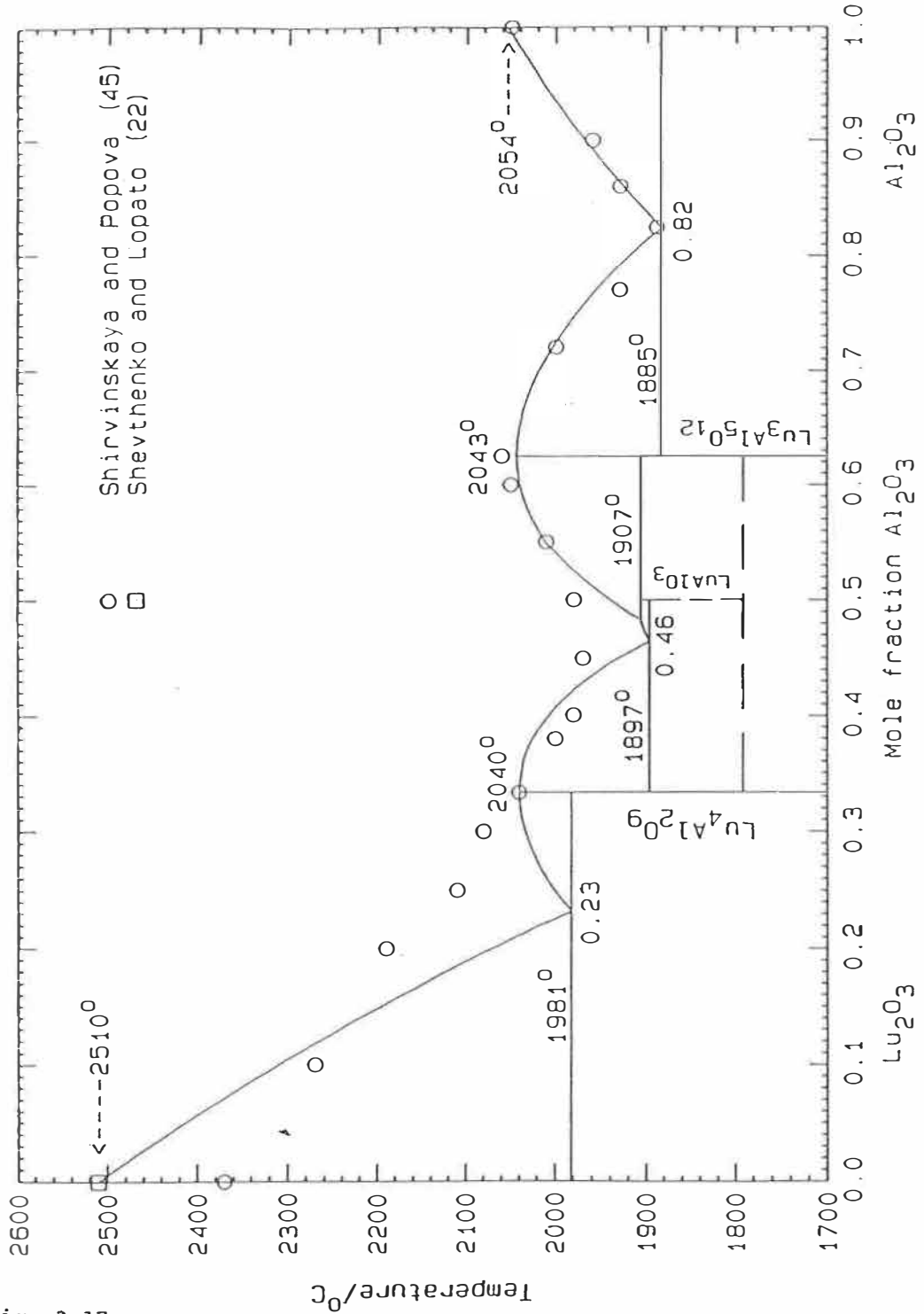


Fig. 3-17

Fig. 17 Assessed Lu_2O_3-Al_2O_3 phase diagram calculated thermodynamically

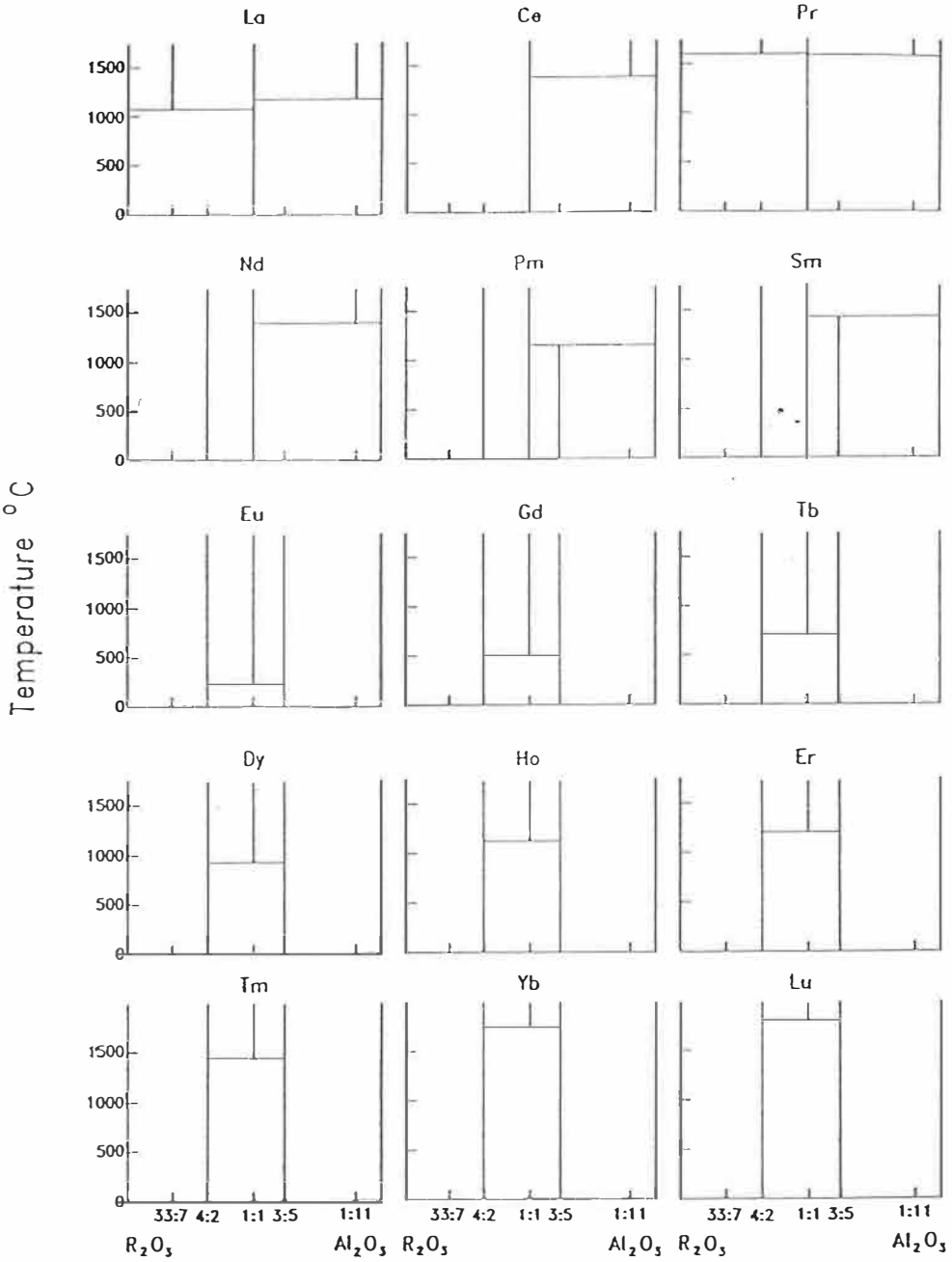


Fig. 18 Calculated R_2O_3-Al_2O_3 phase diagrams at lower temperatures. Tentative only.

Fig. 3-18

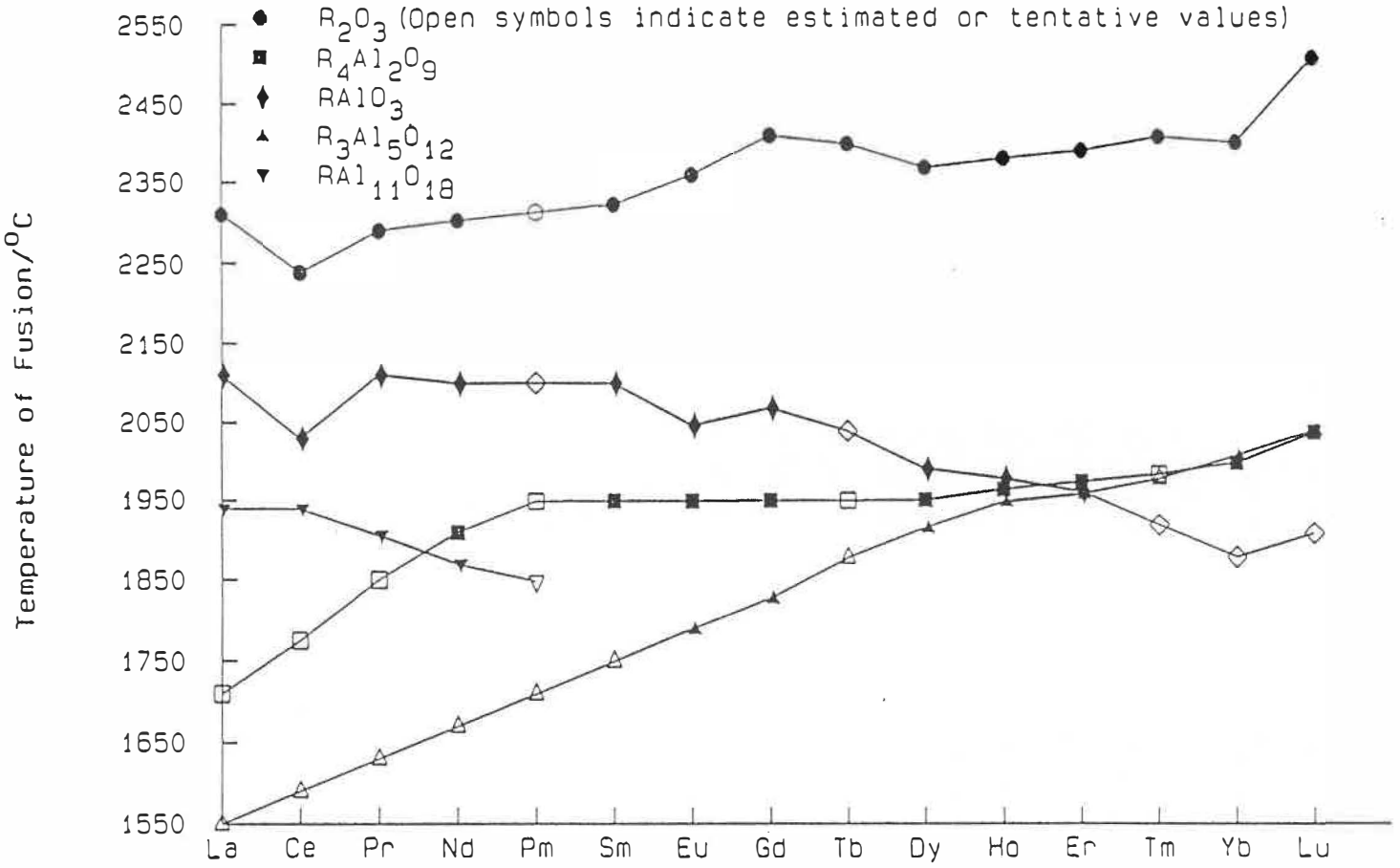


Fig. 3-19

Fig. 19 Assessed congruent melting points of oxides (congruent melting may be metastable).

Table 3-1

TABLE I

Optimized Parameters of Quasichemical Model for Liquid Oxides

SYSTEM	ω_o(cal)	ω_3(cal)
La_2O_3-Al_2O_3	-11700	-2279
Ce_2O_3-Al_2O_3	-10000	0
Pr_2O_3-Al_2O_3	-9000	-1500
Nd_2O_3-Al_2O_3	-10636	-5917
Pm_2O_3-Al_2O_3	-11580	-2488
Sm_2O_3-Al_2O_3	-11903	-1127
Eu_2O_3-Al_2O_3	-12046	-4938
Gd_2O_3-Al_2O_3	-11135	-4166
Tb_2O_3-Al_2O_3	-12248	-4747
Dy_2O_3-Al_2O_3	-12435	-7000
Ho_2O_3-Al_2O_3	-12704	-7568
Er_2O_3-Al_2O_3	-12968	-4931
Tm_2O_3-Al_2O_3	-13000	-2000
Yb_2O_3-Al_2O_3	-13000	-3005
Lu_2O_3-Al_2O_3	-13000	0

Table 3-2

TABLE 2

Calculated Thermodynamic Properties of Compounds

COMPOUND	FORMATION FROM SOLID OXIDES $\frac{x}{2} R_2O_3 + \frac{y}{2} Al_2O_3 = R_xAl_yO_{3(x+y)/2}$		FUSION PER MOLE OF $R_{x/(x+y)}Al_{y/(x+y)}O_{3/2}$		
* = values estimated	ΔH_f^o (cal/mol)	ΔS_f^o (cal/mol.K)	T_{fus}^o (°C)	ΔH_{fus}^o (cal/mol)	ΔS_{fus}^o (cal/mol.K)
$La_{33}Al_7O_{60}$	-45861	30.000	1894	7910	3.65
*$La_4Al_2O_9$	-12671	5.820	1710	8031	4.05
*$Ce_4Al_2O_9$	-8510	6.318	1775	8294	4.05
*$Pr_4Al_2O_9$	-9866	6.396	1850	8598	4.05
$Nd_4Al_2O_9$	-15004	6.211	1909	8837	4.05
*$Pm_4Al_2O_9$	-17776	6.054	1949	8999	4.05
$Sm_4Al_2O_9$	-18061	6.113	1950	9003	4.05
$Eu_4Al_2O_9$	-18118	6.113	1950	9003	4.05
$Gd_4Al_2O_9$	-15538	6.216	1951	9007	4.05
*$Tb_4Al_2O_9$	-18180	6.075	1951	9007	4.05
$Dy_4Al_2O_9$	-19135	6.055	1952	9011	4.05
$Ho_4Al_2O_9$	-20435	6.062	1966	9067	4.05
$Er_4Al_2O_9$	-18932	6.007	1976	9108	4.05
*$Tm_4Al_2O_9$	-20205	6.072	1986	9148	4.05
$Yb_4Al_2O_9$	-19513	6.096	2001	9209	4.05
$Lu_4Al_2O_9$	-20105	6.096	2040	9367	4.05

$LaAlO_3$	-9652	1.971	2110	10961	4.60
$CeAlO_3$	-5737[a]	2.396[a]	2030	10363	4.50
$PrAlO_3$	-6083	2.581	2110	10485	4.40
$NdAlO_3$	-7633	2.590	2100	10203	4.30
$^*PmAlO_3$	-7604	2.763	2100	9966	4.20
$SmAlO_3$	-7297	2.930	2100	9729	4.10
$EuAlO_3$	-7082	3.000	2047	9349	4.03
$GdAlO_3$	-5686	3.263	2069	9250	3.95
$^*TbAlO_3$	-6525	3.232	2040	9020	3.90
$DyAlO_3$	-7009	3.068	1992	8833	3.90
$HoAlO_3$	-7216	3.105	1980	8786	3.90
$ErAlO_3$	-6490	3.100	1963	8720	3.90
$^*TmAlO_3$	-6227	3.089	1920	8552	3.90
$^*YbAlO_3$	-5861	3.174	1880	8396	3.90
$^*LuAlO_3$	-5596	3.106	1910	8513	3.90
$^*La_3Al_5O_{12}$	-25966	1.412	1550	10208	5.60
$^*Ce_3Al_5O_{12}$	-16768	2.452	1590	10432	5.60
$^*Pr_3Al_5O_{12}$	-19373	2.482	1630	10656	5.60
$^*Nd_3Al_5O_{12}$	-29901	1.944	1670	10880	5.60
$^*Pm_3Al_5O_{12}$	-31669	2.068	1710	11104	5.60
$^*Sm_3Al_5O_{12}$	-33056	2.210	1750	11328	5.60
$Eu_3Al_5O_{12}$	-37811	2.120	1790	11552	5.60
$Gd_3Al_5O_{12}$	-35186	2.456	1828	11765	5.60
$^*Tb_3Al_5O_{12}$	-41413	2.345	1878	12045	5.60
$Dy_3Al_5O_{12}$	-45635	2.308	1916	12258	5.60
$Ho_3Al_5O_{12}$	-48649	2.312	1950	12448	5.60
$Er_3Al_5O_{12}$	-56090	2.415	1960	12504	5.60
$^*Tm_3Al_5O_{12}$	-45572	2.600	1980	12616	5.60
$Yb_3Al_5O_{12}$	-46681	3.071	2010	12784	5.60
$Lu_3Al_5O_{12}$	-45546	2.833	2043	12969	5.60

$LaAl_{11}O_{18}$	1340	9.592	1939	12298	5.56
$CeAl_{11}O_{18}$	5906	9.643	1939	12298	5.56
$PrAl_{11}O_{18}$	6707	9.487	1905	12109	5.56
$NdAl_{11}O_{18}$	3447	9.246	1869	11909	5.56
$^{*}PmAl_{11}O_{18}$	6742	9.300	1848	11792	5.56

(a) at melting point

CHAPTER 4

OPTIMIZATION AND CALCULATION OF TERNARY AND MULTI-COMPONENT SYSTEMS

4.1 INTRODUCTION

To build an oxide data base by employing the quasi-chemical model, it is very important that the model can be applied not only to binary (as shown in the previous chapters) but also to ternary and multi-component systems. Hence, in this chapter, the quasi-chemical model will be extrapolated to ternary and multi-component systems, and a ternary optimization program will also be introduced. Examples of ternary optimization and calculation for the $CaO-TiO_2-MgO$, $CaO-SiO_2-TiO_2$, $MgO-SiO_2-TiO_2$, $MnO-SiO_2-TiO_2$, $ZrO_2-SiO_2-TiO_2$, $ZrO_2-SiO_2-Al_2O_3$, $ZrO_2-TiO_2-Al_2O_3$ and $SiO_2-TiO_2-Al_2O_3$ systems will be discussed. We will use binary and ternary parameters to estimate the Gibbs energy of multi-component system. As an example predictions of multi-component and multiphase equilibria in the $ZrO_2-Al_2O_3-SiO_2-TiO_2$ system will be presented at the end.

4.1.1 Quasi-chemical model for ternary and multi-component systems

Consider a ternary system where X_1, X_2 and X_3 are mole fractions of the component 1, 2 and 3, y_1, y_2 and y_3 are "equivalent fractions" as follows

$$y_i = \frac{b_i X_i}{b_1 X_1 + b_2 X_2 + b_3 X_3} \qquad (i=1,2,3) \qquad (4\text{-}1\text{-}1)$$

where b_i (i=1,2,3) are numbers chosen to describe the ordering position as discussed in Section 1.4.2.1.

Pair-bond mole fractions are defined as;

$$X_{ij} = \frac{n_{ij}}{n_{11} + n_{12} + n_{31} + n_{22} + n_{23} + n_{33}} \qquad (i,j=1,2,3) \qquad (4\text{-}1\text{-}2)$$

By mass balance, we have:

$$\begin{aligned} 2y_1 &= 2X_{11} + X_{12} + X_{31} \\ 2y_2 &= 2X_{22} + X_{12} + X_{23} \\ 2y_3 &= 2X_{33} + X_{31} + X_{23} \end{aligned} \qquad (4\text{-}1\text{-}3)$$

Let the parameters ω_{12}, ω_{23}, ω_{31} and η_{12}, η_{23}, η_{31} be the molar enthalpy and non-configurational entropy changes for the three pair exchange reactions:

$$[i-i] + [j-j] = 2[i-j] \qquad (i,j=1,2,3) \qquad (4\text{-}1\text{-}4)$$

The ternary enthalpy of mixing and excess entropy are, then, given by extension of equations (1-4-9), (1-4-10) and (1-4-11) in Chapter 1:

$$\Delta H = \frac{b_1 X_1 + b_2 X_2 + b_3 X_3}{2} (X_{12}\omega_{12} + X_{23}\omega_{23} + X_{31}\omega_{31}) \qquad (4\text{-}1\text{-}5)$$

$$S^E = \frac{RZ}{2}(b_1X_1 + b_2X_2 + b_3X_3)$$
$$(X_{11}\ln\frac{X_{11}}{y_1^2} + X_{22}\ln\frac{X_{22}}{y_2^2} + X_{33}\ln\frac{X_{33}}{y_3^2} +$$
$$X_{12}\ln\frac{X_{12}}{2y_iy_2} + X_{23}\ln\frac{X_{23}}{2y_2y_3} + X_{31}\ln\frac{X_{31}}{2y_1y_3}) +$$
$$\frac{(b_1X_1 + b_2X_2 + b_3X_3)}{2}(X_{12}\eta_{12} + X_{23}\eta_{23} + X_{31}\eta_{31}) \qquad (4\text{-}1\text{-}6)$$

By minimizing the total Gibbs energy at constant composition, three equations are generated

$$\frac{X_{ij}^2}{X_{ii}X_{jj}} = 4\exp\frac{-2(\omega_{ij} - \eta_{ij}T)}{zRT} \qquad (i,j=1,2,3) \qquad (4\text{-}1\text{-}7)$$

If ω_{ij} and η_{ij} are known, the ternary Gibbs energy can then be calculated through equations (4-1-1), (4-1-2), (4-1-3), (4-1-5), (4-1-6) and (4-1-7). Therefore it is fundamental to estimate ω_{ij} and η_{ij} values from their values in the binary sub-systems in order to calculate the ternary equilibrium by the quasi-chemical model.

Models such as those of Kohler [60Koh], Muggianu [75Mug], Toop [65Too], Hillert [80Hil] and Colinet [67Col] have been frequently employed for predicting the ternary Gibbs energy from those of its sub-binaries. Two models, similar to the Kohler and Toop, have been proposed to predict ω_{ij} and η_{ij} values (not Gibbs energy) directly from those of the sub-binaries. In the "symmetric approximation" (Kohler-like model, illustrated in Fig. 4-1a), ω_{ij} and η_{ij} are assumed to

be constant along lines of constant molar ratio y_i/y_j, while in the "asymmetric approximation" (Toop-like model, illustrated in Fig. 4-1b), ω_{12} and ω_{31} (and η_{12} and η_{31}) are constant at constant y_1, while ω_{23} (and η_{23}) are constant at constant y_2/y_3, where component 1 was chosen as the asymmetric component. Thus, values of ω_{ij} and η_{ij} in the ternary can be obtained from the binary values by one of these approximation models.

Furthermore, if experimental ternary data are available, then the approximations may be refined by the addition of "ternary parameters"; $\omega^{nm}_{ij(k)}$

$$\omega_{12} = \underbrace{\sum\omega^{n0}_{12}\,(y_2+y_3)^n}_{(binary\ terms)} + \underbrace{\sum\omega^{nm}_{12(3)}\,(y_2+y_3)^n\left(\frac{y_3}{y_2+y_3}\right)^m}_{(ternary\ terms)}$$

$$\omega_{23} = \underbrace{\sum\omega^{n0}_{23}\left(\frac{y_3}{y_2+y_3}\right)^n}_{(binary\ terms)} + \underbrace{\sum\omega^{nm}_{23(1)}\left(\frac{y_3}{y_2+y_3}\right)^n y_1^m}_{(ternary\ terms)} \qquad (4\text{-}1\text{-}8a)$$

$$\omega_{31} = \underbrace{\sum\omega^{n0}_{31}\,(y_2+y_3)^n}_{(binary\ terms)} + \underbrace{\sum\omega^{nm}_{31(2)}\,(y_2+y_3)^n\left(\frac{y_2}{y_2+y_3}\right)^m}_{(ternary\ terms)}$$

where 1 was chosen as the asymmetric component (that is: Toop-like model), or

$$\omega_{ij} = \underbrace{\Sigma\omega_{ij}^{n0}\left(\frac{y_j}{y_i+y_j}\right)^n}_{(binary\ terms)} + \underbrace{\Sigma\omega_{ij(k)}^{nm}\left(\frac{y_j}{y_i+y_j}\right)^n y_k^m}_{(ternary\ terms)} \quad (4\text{-}1\text{-}8b)$$

where neither i, j or k was chosen as the asymmetric component (that is : Kohler-like model).

In both equation (4-1-8a) and equation (4-1-8b), ternary terms will become zero when compositions reduce from the ternary to a sub-binary. This is very important because it guarantees that the ternary terms do not change the optimized three sub-binary calculations. In the quasi-chemical model, reactions between pair bonds are considered, and the proposed "ternary parameters" do not postulate any kind of new bonds but only describe the influence of the third particle on the pair bonds.

Ideally, of course, the model should be good enough so that such ternary terms $\omega_{ij(k)}^{nm}$, if necessary at all, should be small compared to the binary ω_{ij}^{n0} terms. This requirement is well satisfied in many ternary systems as will be shown later. In this way the quasi-chemical model has been extrapolated to ternary systems.

For multi-component systems, equations consistent with equation (4-1-8a) and equation (4-1-8b) can be written if the

components are divided into groups A and B. In any ternary sub-system in which two components are from one group and one component is from the other, the equation reduces to the asymmetric approximation (equation (4-1-8a)), while if all three components are members of the same group, the equation reduces to the symmetric approximation (equation (4-1-8b)). Let λ_A and λ_B be the sums of the equivalent fractions in groups A and B, respectively. Then, for a multi-component solution:

$$\omega_{ij} = \sum\omega_{ij}^{n0}\lambda_B^n + \sum_{n,m,k}\omega_{ij(k)}^{nm}\ \lambda_B^n\left(\frac{y_k}{\lambda_B}\right)\left(1-\frac{y_j}{\lambda_B}\right)^{m-1} \qquad (4\text{-}1\text{-}8c)$$

when component i is from group A (or B), j and k are from group B (or A) and k is any component other than j in group B (or A); or:

$$\omega_{ij} = \sum\omega_{ij}^{n0}\left(\frac{y_j}{y_i+y_j}\right)^n + \sum_{n,m,k}\omega_{ij(k)}^{nm}\left(\frac{y_j}{y_i+y_j}\right)^n y_k(1-y_i-y_j)^{m-1} \qquad (4\text{-}1\text{-}8d)$$

when components i, j and k are from the same group.

In equation (4-1-8c) and equation (4-1-8d), only binary and ternary parameters are employed to approximate ω_{ij} and η_{ij} values of a multi-component solution. Therefore, by a similar procedure as developed for ternary systems, thermodynamic properties (such as Gibbs energy and enthalpy of mixing) of

a multi-component solution can be expressed as functions of its sub-binary and sub-ternary parameters, composition and temperature. Hence, the model has been extrapolated to multi-component systems.

4.1.2 Optimization and Calculation of ternary systems

Normally the number of additional parameters in a ternary system is less than that of a binary. For example, only one relatively small ternary term was required in optimizing the $CaO-TiO_2-MgO$ system. As a general introduction, ternary optimization procedures as well as a ternary optimization program will be discussed here.

Consider a hypothetical A-B-C ternary system, and let two congruent stoichiometric compounds (which could be unary, binary or ternary compounds), named n and m, be in equilibrium with e, a liquid (univariant) composition. Let n_i, m_i and e_i (i=A,B,C) be the component mole fractions of the compounds n, m and the point e, respectively. At the point e, the following equations are obtained;

$$\begin{aligned} G_A^L(e_A,e_B,e_C) &= G_A^n(n_A,n_B,n_C) = G_A^m(m_A,m_B,m_C) \\ G_B^L(e_A,e_B,e_C) &= G_B^n(n_A,n_B,n_C) = G_B^m(m_A,m_B,m_C) \\ G_C^L(e_A,e_B,e_C) &= G_C^n(n_A,n_B,n_C) = G_C^m(m_A,m_B,m_C) \end{aligned} \qquad (4\text{-}1\text{-}9)$$

where $G_i^n(n_A,n_B,n_C)$, $G_i^m(m_A,m_B,m_C)$ and $G_i^L(e_A,e_B,e_C)$ are chemical potentials of component i (i=A,B,C) in compounds n, m and the

liquid phase at the point e, respectively. Let G_n, G_m be the Gibbs energies of formation of compounds n and m from the three liquid components. Thus

$$G_n = n_A G_A^n + n_B G_B^n + n_C G_C^n$$
$$= n_A G_A^L(e_A, e_B, e_C) + n_B G_B^L(e_A, e_B, e_C) + n_C G_C^L(e_A, e_B, e_C) \quad (4\text{-}1\text{-}10)$$

$$G_m = m_A G_A^m + m_B G_B^m + m_C G_C^m$$
$$= m_A G_A^L(e_A, e_B, e_C) + m_B G_B^L(e_A, e_B, e_C) + m_C G_C^L(e_A, e_B, e_C) \quad (4\text{-}1\text{-}11)$$

By definition:

$$G_A^L(e_A, e_B, e_C) = G_A^{0(L)} + RT\ln e_A + G_A^{L(E)}$$
$$G_B^L(e_A, e_B, e_C) = G_B^{0(L)} + RT\ln e_B + G_B^{L(E)}$$
$$G_C^L(e_A, e_B, e_C) = G_C^{0(L)} + RT\ln e_C + G_C^{L(E)}$$

where $G_i^{o(L)}$ (i=A,B,C) is the Gibbs energy of pure component i at the equilibrium temperature, and $G_i^{L(E)}$ (i=A,B,C) is the partial excess chemical potential of component i which is determined by the quasi-chemical model. For convenience, let $G_i^{o(L)} = 0$ (i=A,B,C); then

$$G_A^L(e_A, e_B, e_C) = RT\ln e_A + G_A^{L(E)}$$
$$G_B^L(e_A, e_B, e_C) = RT\ln e_B + G_B^{L(E)}$$
$$G_C^L(e_A, e_B, e_C) = RT\ln e_C + G_C^{L(E)}$$

Substituting these equations into equations (4-1-10) and (4-1-11), we have

$$G_n = n_A RT\ln e_A + n_A G_A^{L(E)} + n_B RT\ln e_B + n_B G_B^{L(E)} + n_C RT\ln e_C + n_C G_C^{L(E)}$$

$$G_m = m_A RT\ln e_A + m_A G_A^{L(E)} + m_B RT\ln e_B + m_B G_B^{L(E)} + m_C RT\ln e_C + m_C G_C^{L(E)}$$

The so-called ternary optimization finds the values of the ternary parameters to satisfy the above equations. Rearranging these equations, we have:

$$G_n - n_A RT\ln e_A - n_B RT\ln e_B - n_C RT\ln e_C = n_A G_A^{L(E)} + n_B G_B^{L(E)} + n_C G_C^{L(E)} \qquad (4\text{-}1\text{-}12)$$

$$G_m - m_A RT\ln e_A - m_B RT\ln e_B - m_C RT\ln e_C = m_A G_A^{L(E)} + m_B G_B^{L(E)} + m_C G_C^{L(E)} \qquad (4\text{-}1\text{-}13)$$

where the left sides of the above equations are determined from experimental data, and the right sides are functions of binary and ternary parameters of the quasi-chemical model. Thus, experimental values such as univariant and invariant points and Gibbs energies of formation of compounds can be expressed directly as non-linear functions of binary and ternary parameters of the quasi-chemical model. In equations (4-1-12) and (4-1-13), n and m could be either pure components, or binary or even ternary compounds in the ternary system, and e could be any point on the ternary liquid surface. Thus, in principle all ternary liquid solution data can be employed to construct the above equations. As mentioned in Chapter 2, to solve these equations, a non-linear regression has to be adopted owing to the non-linear nature of the quasi-chemical model.

In principle, the same non-linear least squares regression which was applied to binary optimization in Chapter 2 can be employed in the ternary optimization. However, since differentiation of ternary thermodynamic functions (such as Gibbs energy) is much too tedious and complicated, a modified gradient method which uses the first derivative of the non-linear function is adopted in our ternary optimization.

Suppose we have a quadratic model,

$$\boldsymbol{Y} = \boldsymbol{A} + \boldsymbol{X}'\boldsymbol{B} + \frac{1}{2}\boldsymbol{B}'\boldsymbol{G}\boldsymbol{B} \qquad (4\text{-}1\text{-}14)$$

where **Y, X , A, G** and **B** are matrices and **A, X** and **G** are independent of the coefficient matrix **B**. Differentiating (4-1-14) with respect to **B**, we obtain a gradient vector

$$\boldsymbol{g}(\boldsymbol{B}) = \boldsymbol{X} + \boldsymbol{G}\boldsymbol{B} \qquad (4\text{-}1\text{-}15)$$

Differentiating (4-1-15), we obtain the so-called Hessian matrix

$$\boldsymbol{H}(\boldsymbol{B}) = \boldsymbol{G} \qquad (4\text{-}1\text{-}16)$$

Therefore, **G** can be determined by second derivatives of (4-1-14). When (4-1-14) reaches its minimum value at optimal $\mathbf{B}^*$, $\mathbf{g}(\mathbf{B}^*) = 0$, thus **GB=-X**. In addition, for a non-singular **G**,

$$\boldsymbol{B}^* = -\boldsymbol{G}^{-1}\boldsymbol{X} \qquad (4\text{-}1\text{-}17)$$

which is the basis of the so-called Newton method.

As discussed in Chapter 2, a linear Taylor expansion of a non-linear function resulted in a successful non-linear least squares regression. In the Newton method, a second-order truncated Taylor series approximation transforms the non-linear least squares function to a quadratic function which can be minimized according to equation (4-1-17). Iterations are introduced to guarantee the convergence of the method.

To avoid the complicated differentiating in the Newton method, a simple gradient method was employed in the non-linear least squares optimization. The finite differences of the non-linear function were taken as the approximations of the first derivative values. The computational procedure can be summarized below;

(1) at an initial point $\mathbf{B}^1$, calculate the ternary function $\mathbf{Z}$ (such as ternary Gibbs energy) at $\mathbf{B}^1+\mathbf{d}$ and $\mathbf{B}^1$ where $\mathbf{d}$ is a small deviation matrix.

(2) calculate finite-differences to estimate the gradient vector,

$$\mathbf{g}(\mathbf{B}^1) \approx (\mathbf{Z}(\mathbf{B}^1+\mathbf{d}) - \mathbf{Z}(\mathbf{B}^1))'\mathbf{d}^{-1}$$

(3) from

$$\mathbf{Z}(\mathbf{B}^*) \approx \mathbf{Z}(\mathbf{B}^1) + \mathbf{g}(\mathbf{B}^1)(\mathbf{B}^* - \mathbf{B}^1) \approx 0;$$ calculate

$$\mathbf{B}^* \approx -\mathbf{Z}(\mathbf{B}^1)(\mathbf{g}(\mathbf{B}^1))^{-1} + \mathbf{B}^1$$

(4) check the convergence criteria. If $\mathbf{B}^*$ is the optimal matrix, then stop. Otherwise, let $\mathbf{B}^1=\mathbf{B}^*$ and go to step 1.

A ternary optimization program had been written by Professor Pelton based on the above procedure. Two major improvements for the program were made in the present study, and these will be discussed below.

At step 1, one has to calculate thermodynamic properties of the solution at one given set of ternary parameters ($\mathbf{B}^1$). Equation (4-1-7) is, then, to be solved along with equations (4-1-2) and (4-1-3). In the previous program, this calculation was accomplished by rearranging equations (4-1-7), (4-1-2) and (4-1-3) and a successive iteration procedure. Only when the ternary parameters are relatively small does this procedure work. Otherwise it fails, because when the ternary parameters become considerably large some pair-bond fractions will reduce to very small values (such as 10^{-7}) and lose their significant digits. Hence, a new subroutine which was originally written by Professor Pelton is introduced to this end.

The new subroutine is written according to a simulation of a physical mechanism of the approach to equilibrium in the solution. Let N_{ij} be the number of i-j pairs. The initial

state is an ideal solution. To reach a real solution six steps are considered;

$$
\begin{aligned}
&[1\text{-}1] + [2\text{-}2] \rightleftharpoons [1\text{-}2] + [1\text{-}2] && (a)\\
&[1\text{-}1] + [2\text{-}3] \rightleftharpoons [1\text{-}3] + [1\text{-}2] && (b)\\
&[1\text{-}2] + [2\text{-}3] \rightleftharpoons [1\text{-}3] + [2\text{-}2] && (c)\\
&[1\text{-}1] + [3\text{-}3] \rightleftharpoons [1\text{-}3] + [1\text{-}3] && (d)\\
&[1\text{-}2] + [3\text{-}3] \rightleftharpoons [1\text{-}3] + [2\text{-}3] && (e)\\
&[2\text{-}2] + [3\text{-}3] \rightleftharpoons [2\text{-}3] + [2\text{-}3] && (f)
\end{aligned}
$$

These steps are permitted to occur one at a time. In each step, a certain number of bonds will be transferred between reactants and products in whatever direction decreases the Gibbs energy until equilibrium is attained. The procedure then continues with the next step. Iterations are continued until all N_{ij} values no longer change between two iterations. The equilibrium is then established. Because the real equilibrium in the solution is well simulated this way, the calculation is valid even at very large ternary parameters. The method must always converge. This subroutine was originally written by Professor Pelton, but did not accept ternary parameters. In the present study, ternary parameters were introduced.

Introducing an immiscibility gap in the ternary optimization is another improvement made in the present study. Ternary liquid immiscibility gaps are frequently observed in silicate slags, but could not be accepted into the previous program.

Consider a ternary miscibility gap as shown in Fig. 4-2, where points a and b are located at the two ends of a tie-line of the miscibility gap. The mole fractions at points a and b are denoted by a_1, a_2, a_3 and b_1, b_2, b_3, respectively. When liquid a and liquid b are in equilibrium, then;

$$\begin{aligned} G_A^a(a_1,a_2,a_3) &= G_A^b(b_1,b_2,b_3) \\ G_B^a(a_1,a_2,a_3) &= G_B^b(b_1,b_2,b_3) \\ G_C^a(a_1,a_2,a_3) &= G_C^b(b_1,b_2,b_3) \end{aligned} \qquad (4\text{-}1\text{-}18)$$

where $G_i^a(a_1,a_2,a_3)$ and $G_i^b(b_1,b_2,b_3)$ (i=A,B,C) are chemical potentials of component i in liquids a and b, respectively. Unlike equations (4-1-11) and (4-1-12), neither the left nor right sides of the above equations can be determined from the phase diagram. To directly group these equations along with all the other equations like equation (4-1-12) to optimize the ternary parameters, one can move the left sides of equations (4-1-18) to the right sides and let the left sides be zero. However, when this was done, many problems with convergence were encountered. On the other hand, ternary parameters usually have less influence on the total Gibbs energy of the liquid phase than binary parameters. It is possible, as a first approximation, to calculate all the left side expressions of equations (4-1-18) by assuming the ternary parameters equal zero , and then to take these calculated data as experimental values for the right sides to optimize ternary parameters along with other equations. In the next iteration,

the right sides are calculated with the optimized ternary parameters (from the last iteration) and these are taken as the experimental values for the left sides to optimize new ternary parameters. Progressive iterations converge to give the optimization.

4.1.3 Calculation of multi-component oxide systems

Since extension of the equations in Section 4.1.1 to systems with more than three components is straightforward, the model can be extrapolated in a similar way to multi-component systems.

Consider a 1-2-3-4 quaternary system, where 1, 2, 3 and 4 are components of the system. By equations (4-1-8a) and (4-1-8b), ω and η values in its sub-ternaries (1-2-3, 1-2-4, 1-3-4 and 2-3-4) are given. Similarly, by equation (4-1-8c) and equation (4-1-8d) ω and η values in the 1-2-3-4 system can be estimated from those in the 1-2-3, 1-2-4, 1-3-4 and 2-3-4 sub-ternaries. Unlike ternary systems (where ternary parameters have been introduced), no extra parameters are created in the calculation of a quaternary or higher order solution. Such direct prediction has proved to be very successful as shown in Section 4.3 and Chapter 5.

In this section, the quasi-chemical model has been extrapolated to a ternary system; the extension to multi-

component systems is straightforward. The general ternary optimization procedure (non-linear least squares regression) has been discussed and two improvements have been made for the ternary optimization program. Thus, next we will optimize real ternary systems to test both the quasi-chemical model and the ternary optimization program. Furthermore, as an example, predictions of multi-component and multiphase equilibria in the ZrO_2-TiO_2-Al_2O_3-SiO_2 system will be carried out. Thus the database can be used to calculate multi-component and multiphase equilibria involving oxide slags.

4.2 TERNARY SYSTEM EVALUATIONS

In this section, details of evaluations of 8 ternary oxide systems will be discussed. The liquid phase is optimized by our ternary optimization program based on the modified quasi-chemical model. Thermodynamic data for all solid stoichiometric compounds are listed in the Appendix.

4.2.1 The CaO-MgO-TiO_2 system

The first study of the system was made by Coughanour et al. [55Cou] who determined its compatibility relations. A partial phase diagram of the TiO_2-CaO.TiO_2-MgO.TiO_2 system which is shown as Fig. 4-3, was reported by Rouf et al. [69Rou] through several experimental techniques. The melting

points of the mixed oxides were determined by visual observation using a hot-stage microscope, and sub-liquidus changes were detected by means of micro-differential analysis or in some cases were checked with a Stanton D.T.A. apparatus. Extensive use was made of powder X-ray diffraction patterns to determine the phases present and to identify the primary phase for certain compositions. Therefore, the whole experimental work seems carefully done. In their investigation, no solid solution nor ternary compound but three invariant points (denoted as A,B,C, respectively in Fig. 4-3) were observed. The $CaTiO_3$-$MgTi_2O_5$ quasi-binary section reported by these authors is also shown in Fig. 4-3, which is a simple eutectic type binary with eutectic point at 50 mol% and 1450°C. Fig. 4-3 was accepted in the present optimization, because they are the most reliable phase diagrams of the system.

By means of the quasi-chemical model, all three binaries of CaO-MgO, CaO-TiO_2, MgO-TiO_2 systems were optimized in Section 2.3. Only one solid solution, in the CaO-MgO system, was considered in these optimization. The Toop-like model (equation (4-1-8a)) was employed to represent ω_{ij} and η_{ij} (i,j=1,2,3) values in the ternary while TiO_2 was considered as the "asymmetric" component.

As discussed earlier, data of these ternary invariant points (noted as A,B,C in Fig. 4-3) as well as of the eutectic

point in the $CaTiO_3$-$MgTi_2O_5$ quasi-binary (see Fig. 4-3), can be directly put into the ternary optimization program. In order to obtain the best fit for these data, a relatively small ternary parameter of

$$\omega^{01}_{CT(M)} = -43932 \qquad \text{J/mol}$$

(where C=CaO, T=TiO_2 and M=MgO) was evaluated by the program.

To calculate the ternary phase diagram, all the binary parameters along with the optimized ternary parameter were put into TERNFIG (a program for calculation of ternary phase diagrams in the F*A*C*T system [85Tho]).

Although the CaO-TiO_2 sub-system reported by Rouf et al. [69Rou] is rather different from what we accepted in the optimization and calculation of the ternary system, the calculation is, within the experimental error limits.

The calculated and experimental invariant points are listed in Table 4-1, and the calculated phase diagram is shown as Fig. 4-4. Furthermore, the calculated eutectic point in the $CaTiO_3$-$MgTi_2O_5$ quasi-binary is located at 51 mol% and 1446 °C while the observed value is 50 mol % at 1450 °C [69Rou].

In the optimization, only one relatively small ternary parameter was required to reproduce the phase diagram. Hence, the quasi-chemical model as well as the ternary optimization

program are very efficient in thermodynamic calculations of this relatively simple eutectic type ternary system. But if a ternary system contains ternary compounds (which indicates very strong interactions between component species in the liquid phase) or a large liquid immiscibility gap, do they still maintain their usefulness as they have in simple ternary systems? The answer will be found in the next section.

4.2.2 The TiO_2-SiO_2-CaO system

The first investigation of the system was reported by Smolensky [12Smo], who found extensive solid solution between $CaSiO_3$ and $CaTiO_3$. Fukusima [34Fuk] restudied the system by means of thermal analysis and micro-examination of quenched specimens under reflected light, and found a eutectic at 24 mol% $CaTiO_3$ and 1407°C measured along the $CaSiO_3$-$CaTiO_3$ join, with no solid solution. Fukusima also reported on the joins $CaSiO_3$-$CaTiSiO_5$, $CaTiSiO_5$-TiO_2, SiO_2-$CaTiSiO_5$ and $CaTiSiO_5$-$CaTiO_3$. All these were found to be binary and of the simple eutectic type in the regions studied.

Iwasè and Fukusima [37Iwa], following Fukusima's earlier work, reported the metastable crystallization of $CaTiO_3$, TiO_2, SiO_2, and $CaSiO_3$ in place of $CaTiSiO_5$ due to the supercooling of the latter and established metastable diagrams of the system for which Fukusima had reported equilibrium diagrams. They constructed a phase diagram of the system CaO-TiO_2-SiO_2 for purposes of discussing the metastable crystallization, although they apparently had no data for the interior of the system other than the joins which had been investigated. Houdremont [38Hou], using the data of Iwase and Fukusima [34Fuk], constructed a similar diagram for the ternary system for a discussion of certain metallurgical processes including titanium. A fusion diagram of the ternary system CaO-TiO_2-SiO_2, probably based on observations on melting of

cones, was presented by Berezhnoi [50Ber]. Agamawi and White [53Aga] presented data for part of the α-$CaSiO_3$-$CaTiSiO_5$-SiO_2 system. The two-liquid region in this system was not reported by Agamawi and White.

DeVries et al. [55Dev] studied the CaO-TiO_2-SiO_2 system by a heating and quenching method. Their reported phase diagram is shown in Fig. 4-5 in which both the ternary compound $CaTiSiO_5$ (sphene) and the large two-liquid region extending from the SiO_2-CaO side to the SiO_2-TiO_2 side of the triangle are very prominent features. Agreement with Fukusima's measurements is good. Their study shows that solid solution in the system is virtually non-existent except for the small-scale substitution of Ti^{+4} for Si^{+4} in wollastonite. Fig. 4-5 is accepted in the present study because it is the most reliable study of the system.

The three sub-binaries (CaO-TiO_2, CaO-SiO_2 and TiO_2-SiO_2) were previously optimized using the quasi-chemical model. $Ca_5Ti_4O_{13}$ which is missing in Fig. 4-5, has been added in the CaO-TiO_2 system as shown in Section 2.3. To calculate ω_{ij} and η_{ij} values for the ternary system, the Toop-like model was adopted while CaO was considered as the "asymmetric" component. All the invariant point and immiscibility data were put into the ternary optimization program.

In the phase diagram [55Dev], the liquidus surface is extremely flat in the two liquid phase region, and suddenly appears very steep at both the tridymite liquidus and the perovskite liquidus near sphene. In the earlier optimization of the $CaO-SiO_2$ system, η_7, which acts mostly on the composition region of the binary miscibility gap, was introduced to lower the congruent point of the binary miscibility gap. But the η_7 term also made the tridymite liquidus rather flat. Hence, to reproduce the steep tridymite liquid surface, a ternary entropy parameter ($\eta^{71}_{CS(T)}$=-133.888 J/K, C=CaO, S=SiO_2 and T=TiO_2) of the same order and equal value but reverse sign to η_7 of the $CaO-SiO_2$ binary system (see equation 2-3-8) was introduced in the optimization. In all, one fixed and four adjustable ternary parameters were required to obtain a quantitative optimization of the ternary phase diagram:

$$\omega^{71}_{CS(T)} = -89871 \text{ J}$$
$$\omega^{51}_{CS(T)} = -242433 \text{ J}$$
$$\omega^{01}_{ST(C)} = -100216 \text{ J}$$
$$\omega^{14}_{CT(S)} = 60211 \text{ J}$$
$$\eta^{71}_{CS(T)} = -133.888 \text{ J/K}$$

where C=CaO, S=SiO_2 and T=TiO_2.

The optimized diagram is shown in Fig. 4-6. Agreement with the reported diagram Fig. 4-5 is very good. A comparison

of the experimental and calculated invariant points is given in Table 4-2.

The temperatures of points A, B, C and D (Fig. 4-5) cannot be reproduced, although their calculated compositions are within the reported experimental uncertainties. The temperature of the invariant point D (where the equilibrium phases are: liquid, CaO, Ca_2SiO_4 and Ca_3SiO_5) is reported as 1900°C. However, according to the CaO-SiO_2 binary phase diagram (see Section 2.3), Ca_3SiO_5 will decompose to CaO and the non-stoichiometric compound Ca_2SiO_4 at 1800°C. Therefore, the calculated temperature for point D (1764°C) makes sense. On the other hand, only 6 experimental points determined the CaO-rich corner of the CaO-SiO_2-TiO_2 phase diagram where the CaO content is higher than 55 weight percent [55Dev]. At one experimental point located near point C in Fig. 4-6, the liquid phase was observed as low as 1600°C [55Dev] while the calculated temperature of point C is 1591°C which agrees well with experimental observation. Unfortunately, the lowest liquidus temperature of all the other 5 experimental points is reported as 1630° which is 130°C higher than the calculated temperature of point A. There are two possible explanations for this discrepancy. Since the value of the ternary term which presents the CaO stabilizing effect for the liquid phase is directly proportional to X_{CaO} according to the Toop-like model, the CaO liquidus where the CaO content is rather high

and may be possibly over-stabilized by the ternary term. On the other hand, let A', B' and C' be the points located on the $CaO-TiO_2$ binary system on the same univariant lines as the points A, B and C (see Fig. 4-6), respectively. According to the evaluated $CaO-TiO_2$ phase diagram (Section 2.3.), the temperatures of points A', B' and C' are 1687°, 1750° and 1840°C, respectively. Therefore, it would be very surprising if the temperatures of points A and B are as high as 1670° and 1650°C, respectively. This would mean that the temperature decrease from A' to A is only 18°, from B' to B is 100° and from C' to C is 249°C, respectively. Such uneven temperature decreases seem unlikely, and cannot be reproduced by calculations. To clarify this discrepancy more experimental study may be necessary.

The thermodynamic property data of sphene ($CaSiTiO_5$) reported by [85Ber1] were used in the present study (see Appendix).

The question posed at the end of the last section may be answered with a qualified "yes". Even in such a complicated ternary system where extremely negative (indicated by the formation of a ternary compound) and large positive (immiscibility gap was formed) coexisted in the liquid phase, the system is well evaluated by using the quasi-chemical model. Furthermore, the ternary optimization program is quite

powerful and efficient as has been shown in the present optimization.

4.2.3 The $MgO-SiO_2-TiO_2$ System

The optimized phase diagram is shown in Fig. 4-7.

Using a method of quenching and micrographic analysis, Massaza and Sirchia (58Mas) reported temperatures and compositions of the univariant points M, N, O, V, W, X, Y. Their results are shown in Table 4-3. The phase relationships in the vicinity of points "1, 2 and 3" on Fig. 4-7 were re-examined by Jansen (89Jan) who reported the invariant temperatures and compositions listed in Table 4-3. Massaza and Sirchia had shown the univariant line between the $MgTi_2O_5$ and TiO_2 fields as intersecting the line "2-3", with a resultant short univariant line between the TiO_2 and $MgSiO_3$ fields. That is, on their diagram the point "1" lay on the univariant line between points "2" and "3".

MacGregor (64Mac) reported liquidus measurements along the $MgSiO_3-TiO_2$ and $Mg_2SiO_4-TiO_2$ joins at pressures of 10 and 20 kbar. From the limiting slopes of the liquidus lines at pure $MgSiO_3$ and Mg_2SiO_4, thermodynamic calculations indicate that the solubility of TiO_2 in both solid $MgSiO_3$ and solid Mg_2SiO_4 is negligible. In the present calculations, all compounds were assumed to be stoichiometric.

The phase diagram in Fig. 4-7 was calculated with two optimized ternary parameters:

$$\omega^{71}_{ST(M)} = -239463 \quad J/mol$$

$$\omega^{11}_{ST} = -128971 \quad J/mol$$

where S=SiO_2, T=TiO_2 and M=MgO.

The calculated and reported invariant points are compared in Table 4-3. It is difficult to assess the experimental error limits on the compositions of the invariant points. However, the agreement in Table 4-3 is probably within these limits. The calculated invariant temperatures all agree with the reported values within 2° to 15°C except for point M. The phase relationships in the vicinity of points "1, 2 and 3" as reported by Jansen (89Jan) are confirmed.

4.2.4 The $MnO-SiO_2-TiO_2$ system

No phase diagram for the $MnO-SiO_2-TiO_2$ system has ever been published. However, the phase equilibria in this system are expected to be very similar to those of the $FeO-SiO_2-TiO_2$ system. In the present calculation, the same quasi-chemical ternary parameters of the $FeO-SiO_2-TiO_2$ system according to professor Eriksson [91Eri] were accepted for the $MnO-SiO_2-TiO_2$ system:

$$\omega^{01}_{ST(M)} = -46338 \text{ Joules}$$

$$\omega^{11}_{ST(M)} = -136557 \text{ Joules}$$

where $S=SiO_2$, $T=TiO_2$ and $M=MnO$.

Therefore, the calculated phase diagram is shown as Fig. 4-8 and the calculated invariant points are shown in Table 4-4. As observed in the $MgO-SiO_2-TiO_2$ system, our calculation predicts that the TiO_2 liquid surface does not touch the $MnSiO_3$ liquid surface.

4.2.5 The SiO_2-TiO_2-ZrO_2 system

The most recent reported diagram [76Pen, 57McT] is shown in Fig. 4-9. Primary phase fields of TiO_2, ZrO_2, SiO_2, $ZrTiO_4$ (ZT) and $ZrSiO_4$ (ZS) were reported by [76Pen]. The miscibility gap was measured by [57McT]. The calculated optimized diagram is shown in Fig. 4-10.

Earlier studies located a eutectic at 2 wt. % ZrO_2, 10 wt. % TiO_2 and 88 wt. % SiO_2 at 1500°C [51Sow, 54McK] and a peritectic involving TiO_2, ZrO_2 and $ZrTiO_4$ at 3 wt. % ZrO_2, 17 wt. % TiO_2 and 80 wt. % SiO_2 at 1615°C. A primary phase field of $ZrSiO_4$ was suspected by [51Sow] but was not confirmed by [54McK].

As discussed in Section 2.3.9 in conjunction with the ZrO_2-SiO_2 system, $ZrSiO_4$ may not be an equilibrium phase above 1538°C. In this case, there will be no primary phase field of $ZrSiO_4$ in the ternary system and none is shown on the calculated diagram in Fig. 4-10.

The very rapid drop in the TiO_2-SiO_2 monotectic temperature from 1780°C to 1680°C with 3 % ZrO_2 addition followed by virtually no temperature change with further ZrO_2 addition as shown in Fig. 4-9 is very unlikely and probably results from a misinterpretation of the data. The calculated

miscibility gap is slightly larger than the measured, but only one experimental point of [57McT] had to be discarded.

No experiments were performed near the ZrO_2-SiO_2 binary, and so the other miscibility gap shown in the calculated diagram does not appear in Fig. 4-9.

One small ternary parameter for the liquid was required in the optimization:

$$\omega^{01}_{ZS(T)} = -20920 \ Joules$$

where Z=ZrO_2, S=SiO_2 and T=TiO_2.

The calculated diagram, Fig. 4-10, exhibits a ternary peritectic and a ternary eutectic at 1553° and 1515°C respectively. These temperatures compare well with the temperatures of 1545° and 1500° in Fig. 4-9, although the calculated ZrO_2 contents (7 and 5.5 wt. % respectively) are higher than the reported [76Pen] values (2.5 and 2.0 wt. %).

The calculated diagram shows a ternary monotectic at 1659°C.

4.2.6 The TiO_2-ZrO_2-Al_2O_3 system

The only published phase diagram is that of [55Ber] shown in Fig. 4-11. Only points along the ZrO_2-Al_2TiO_5 quasi-binary join were actually measured. The rest of the diagram was "estimated" from this join and from the binaries. The eutectic (saddle point) in the quasi-binary was measured [55Ber] as 1620°C at an estimated composition of 51 mol % ZrO_2. The measurements were made by the method of fusion cones in which the temperature of initial melting of a pressed mixture of ZrO_2 and Al_2TiO_5 was observed. In order to reproduce this point, one small ternary coefficient was required in the quasi-chemical model for the liquid:

$$\omega^{01}_{TZ(A)} = 24476 \quad Joules$$

where T=TiO_2, Z=ZrO_2 and A=Al_2O_3.

This gives a quasi-binary eutectic temperature of 1641°C at 54 mol % ZrO_2. In this calculation, no solid solution in ZrO_2 was assumed because the method of fusion cones probably does not give enough time for a solid solution to form by solid state diffusion. That is, the experimental quasi-binary eutectic temperature is probably that formed when there is no solid solution in ZrO_2.

The parameter chosen for the liquid phase gives a eutectic temperature slightly higher than that measured (but still within the error limits). This was done in order to provide a somewhat better fit to the quaternary data discussed in Section 4.3.

Actually, TiO_2 and Al_2O_3 are both soluble in solid ZrO_2 as shown in Section 2.3. Hence, this solid solution was treated using a "Toop" model (which estimates the Gibbs energy of the ternary solid solution from those of its three sub-binary systems). The hypothetical solid Al_2O_3-TiO_2 solution in this model was given a regular solution parameter of:

$$G^E = -29288\ X_{TiO_2} X_{AlO_{1.5}} \quad J/mol$$

(29288 J = 7000 cal), chosen in order to give the best fit to the Al_2O_3-SiO_2-TiO_2-ZrO_2 data discussed in Section 4.3.

The calculated ternary phase diagram has the same form as the estimated diagram of Fig. 4-11. No comparison of invariant temperatures and compositions is made because, as stated above, the points on Fg. 4-11 were all simply estimated.

4.2.7 The SiO_2-ZrO_2-Al_2O_3 system

The diagram measured by [56Bud] is shown in Fig. 4-12. Measurements were performed only in Al_2O_3-rich solutions.

The ZrO_2-SiO_2 and Al_2O_3-ZrO_2 systems are evaluated in Section 2.3. The Al_2O_3-SiO_2 system was optimized by Professor Eriksson [91Eri1] who obtained:

$$\omega = -5921 + 40716 y_{AlO_{1.5}} - 18149 y^5_{AlO_{1.5}} + 25056 y^7_{AlO_{1.5}} \quad Joules$$

Based on these sub-binary parameters, phase equilibria calculations of the SiO_2-ZrO_2-Al_2O_3 system have been performed. In the calculation, the non-stoichiometric mullite phase ($Al_6Si_2O_{13}$) was approximated as a stoichiometric compound. The calculated univariant "valley" between the ZrO_2 and Al_2O_3 fields agrees well with that shown on Fig. 4-12. No ternary parameters were used for this system.

4.2.8 The TiO_2-SiO_2-Al_2O_3 system

The reported phase diagram [52Aga, 58Gal] is shown in Fig. 4-13. The two invariants, A and B, at high SiO_2 content were measured by [52Aga] who also examined much of the liquidus surface. Cone fusion as well as quenching techniques were employed. These authors were seemingly unaware of the existence of the miscibility gap extending from the SiO_2-TiO_2 binary. As discussed in Section 2.3 in conjunction with this binary system, this gap was not established until 2 years later [54DeV]. The third invariant, C, in Fig. 4-13 was reported by [58Gal].

Ternary liquid parameters $\omega^{k\,1}_{S\,T\,(A)}$ ($S=SiO_2$, $T=TiO_2$, $A=Al_2O_3$ and k =0, 1 and 3) were set equal to -1 times the three binary $\omega_{i\,j}$ (SiO_2, TiO_2) parameters. That is, effectively, one ternary adjustable parameter was introduced.

The calculated invariant points A and B are compared with the measured values [52Aga] in Table 4-5. Since point B is far from the mullite ($Al_6Si_2O_{13}$) composition, mullite could be approximated as being stoichiometric. However, as discussed in Section 4.2.7 in conjunction with the SiO_2-ZrO_2-Al_2O_3 system, we did not consider the non-stoichiometric behaviour of the mullite phase. The third invariant C was, thus, not calculated. However, the calculated univariant "valley"

between the primary phase fields of Al_2O_3 and $TiAl_2O_5$ agrees well with the reported line.

4.3 THE Al_2O_3-SiO_2-TiO_2-ZrO_2 SYSTEM

There are totally 6 sub-binary and 4 sub-ternary systems in the Al_2O_3-SiO_2-TiO_2-ZrO_2 system. In Section 2.3 and 4.2, these sub-binary and sub-ternary systems have been optimized except for the Al_2O_3-SiO_2 system which has been optimized by [91Eri1], based on the discussion of Chapter 2 and Section 4.1. Therefore, one can directly construct the Gibbs energy expression of the quaternary slag melt by means of the quasi-chemical model from the ω and η data of its 10 binary and ternary sub-systems. The calculation of phase equilibria in the quaternary system can be carried out by Gibbs energy minimization programs such as the program EQUILIB in the F*A*C*T system [85Tho]. In this section, phase equilibria have been calculated as shown below.

Invariant temperatures and some invariant liquid compositions were measured by Pena and DeAza [77Pen1, 77Pen2, 79Pen, 84Pen] by a quenching technique. A comparison of measured and calculated results is given in Table 4-6.

In these calculations, mullite ($A_6Si_2O_{13}$) was approximated as a stoichiometric compound. The point R could not be calculated since this involves zircon ($ZrSiO_4$) above the dissociation temperature of 1538°C assumed in the present

analysis (see discussion of the ZrO_2-SiO_2 binary in Section 2.3).

The agreement in Table 4-6 is quite good. No further adjustable parameters beyond those for the binary and ternary solutions were required except that the ZrO_2-rich ternary solid solution of TiO_2, Al_2O_3 and ZrO_2 was adjusted to be more positive (by giving the hypothetical solid Al_2O_3-TiO_2 solution a regular constant as -29288 J/mol as discussed in Section 4.2.6) in order to fit points P and Q as closely as possible. If only the TiO_2-ZrO_2-Al_2O_3 system was concerned, the above regular constant could be more negative in order to fit the eutectic (saddle point) in the ZrO_2-Al_2TiO_5 quasi-binary join better.

Therefore, as expected, in a multi-component system, multiphase equilibria may be reliably predicted by means of the quasi-chemical model from the ω and η values in its sub-binary and sub-ternary systems. This is the ultimate purpose of the present study.

4.4 CONCLUSIONS

In this chapter, the quasi-chemical model has been extrapolated to ternary systems; the extension to multi-component systems is straightforward. Discussions of ternary optimization as well as a ternary optimization program have been given. Two improvements of the ternary optimization program have been added by the present author to enhance the convergence of the program and to include liquid immiscibility data in the optimization procedure. Examples of optimization for several ternary systems are performed to test both the quasi-chemical model and the ternary optimization program. To demonstrate multi-component multiphase equilibria calculation using the present database, phase equilibria in the ZrO_2-Al_2O_3-TiO_2-SiO_2 system have been predicted. Agreement with experimental data is good. The quasi-chemical model has been therefore fully developed to build a thermodynamic slag database which may be used to predict multi-component multiphase equilibria involving oxide slags.

By means of the quasi-chemical model and the ternary optimization program as discussed above, some 28 ternary systems as listed in Table 4-7 and 4-8 have been optimized (in some systems only parts of their diagrams were evaluated). Some of these ternary optimizations are detailed in Section 4.2.

Multi-component phase equilibria calculation using the present database can be organized based on the confidence of estimation:

(1) Calculations for multi-component systems containing only oxides for which all sub-binary and sub-ternary systems have been optimized (as listed in Table 2-1, Table 4-7 and Table 4-8) are of high confidence.

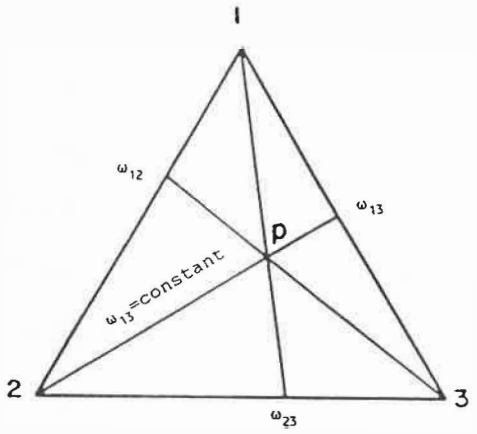
(2) Calculations for systems containing only oxides for which all sub-binary systems are optimized as listed in Table 2-1, and for which all sub-ternaries are either optimized or marked with "O" in Table 4-7, are of medium confidence.

(3) Calculations for systems for which all sub-binaries have been optimized but for which some sub-ternaries are marked with "N" in Table 4-7 are of low confidence.

(4) Calculations for systems for which some sub-binaries have not been optimized are of minimum confidence.

In the next chapter, an industrial application of the present database will be presented.

(a)



(b)

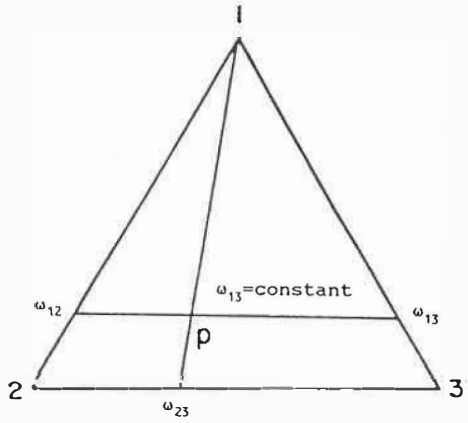


Fig. 4-1 The geometrical relationships involved in the Kohler-like (a) and the Toop-like (b) models.

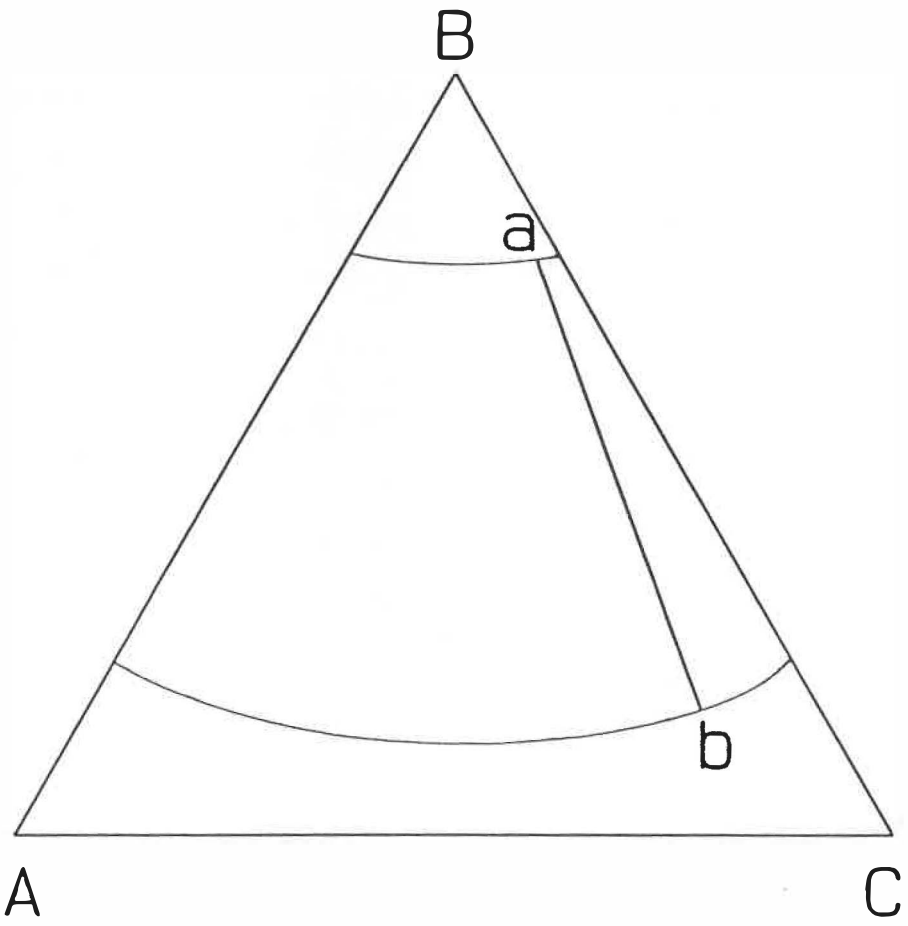


Fig. 4-2 A ternary miscibility gap.

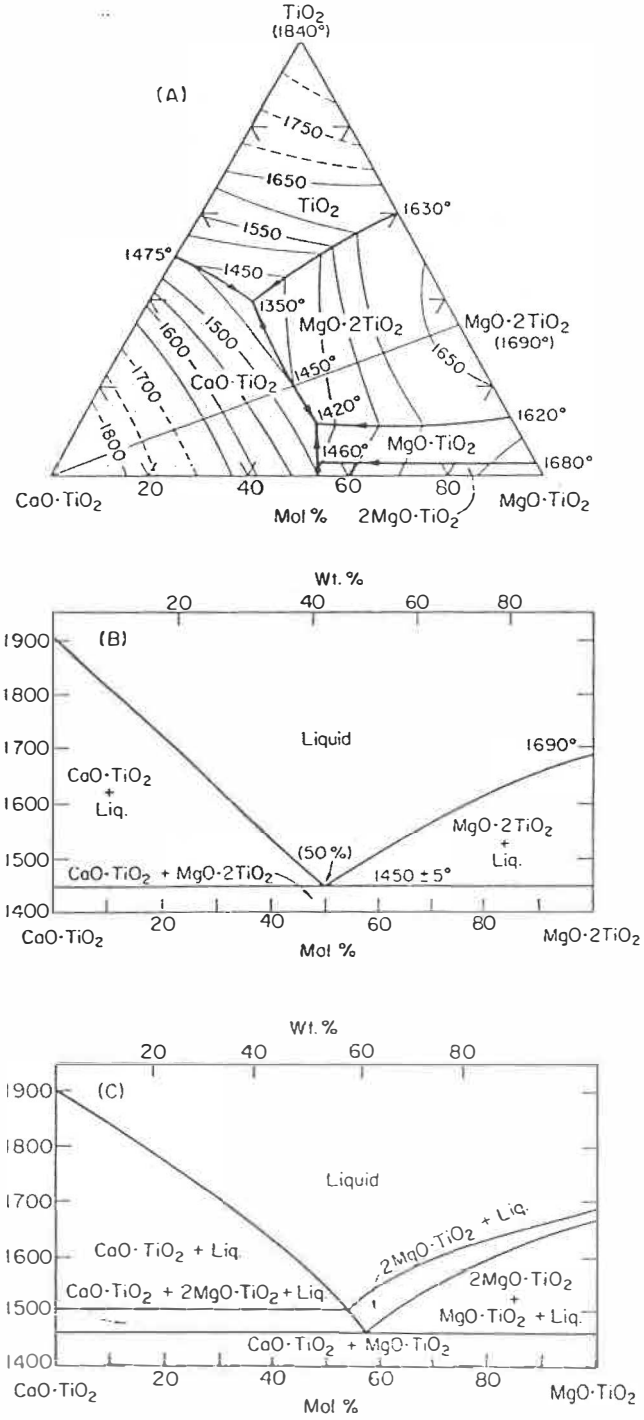


Fig. 4-3 Reported [69Rou] CaO-MgO-TiO_2 phase diagram (mol. %).

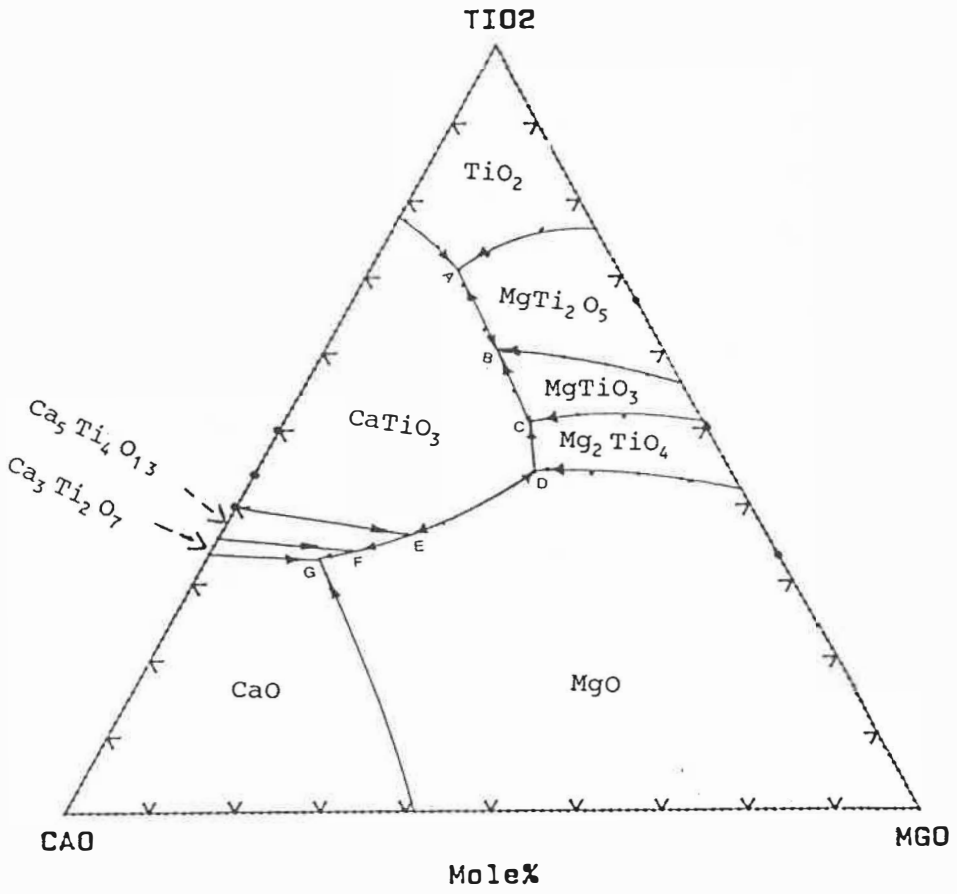


Fig. 4-4 Calculated $CaO-MgO-TiO_2$ phase diagram (mol. %).

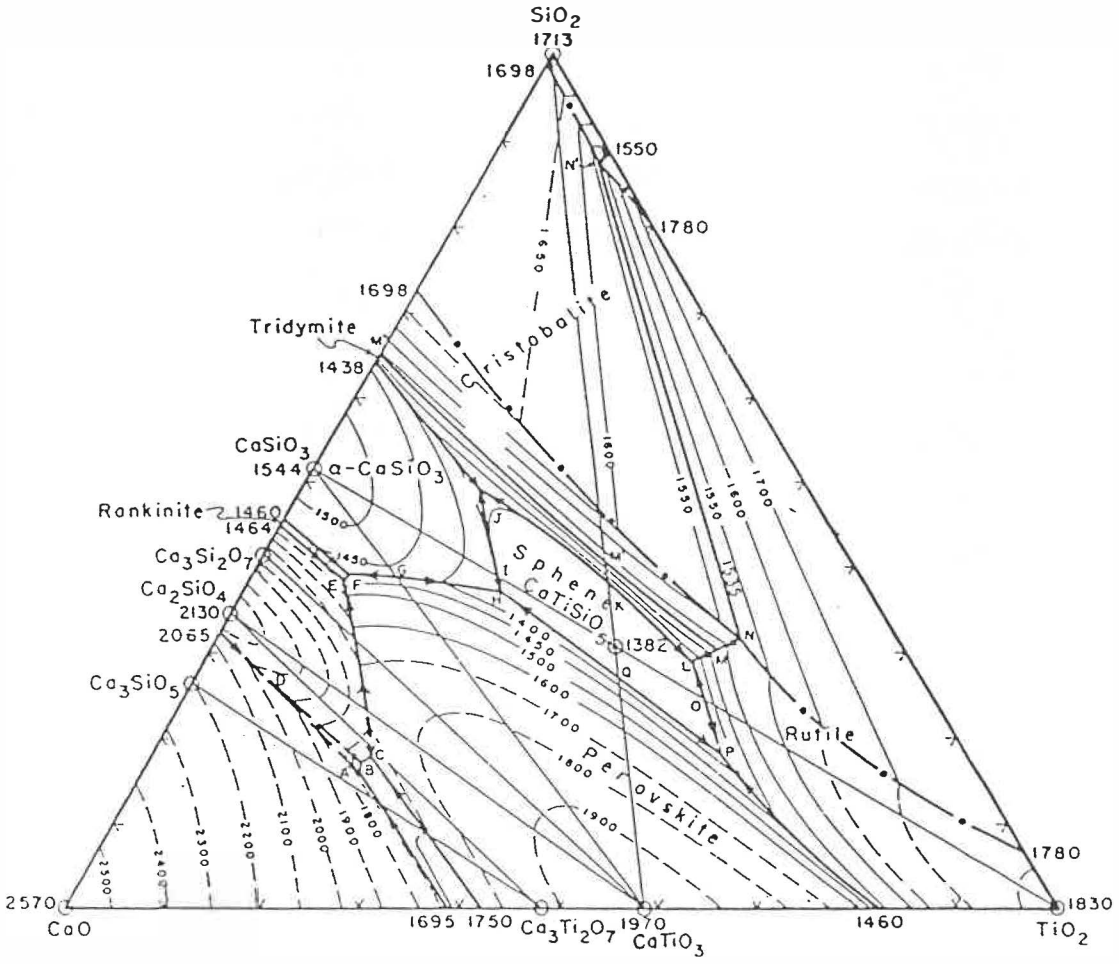


Fig. 4-5 Reported [55Dev] $CaO-SiO_2-TiO_2$ phase diagram (wt. %).

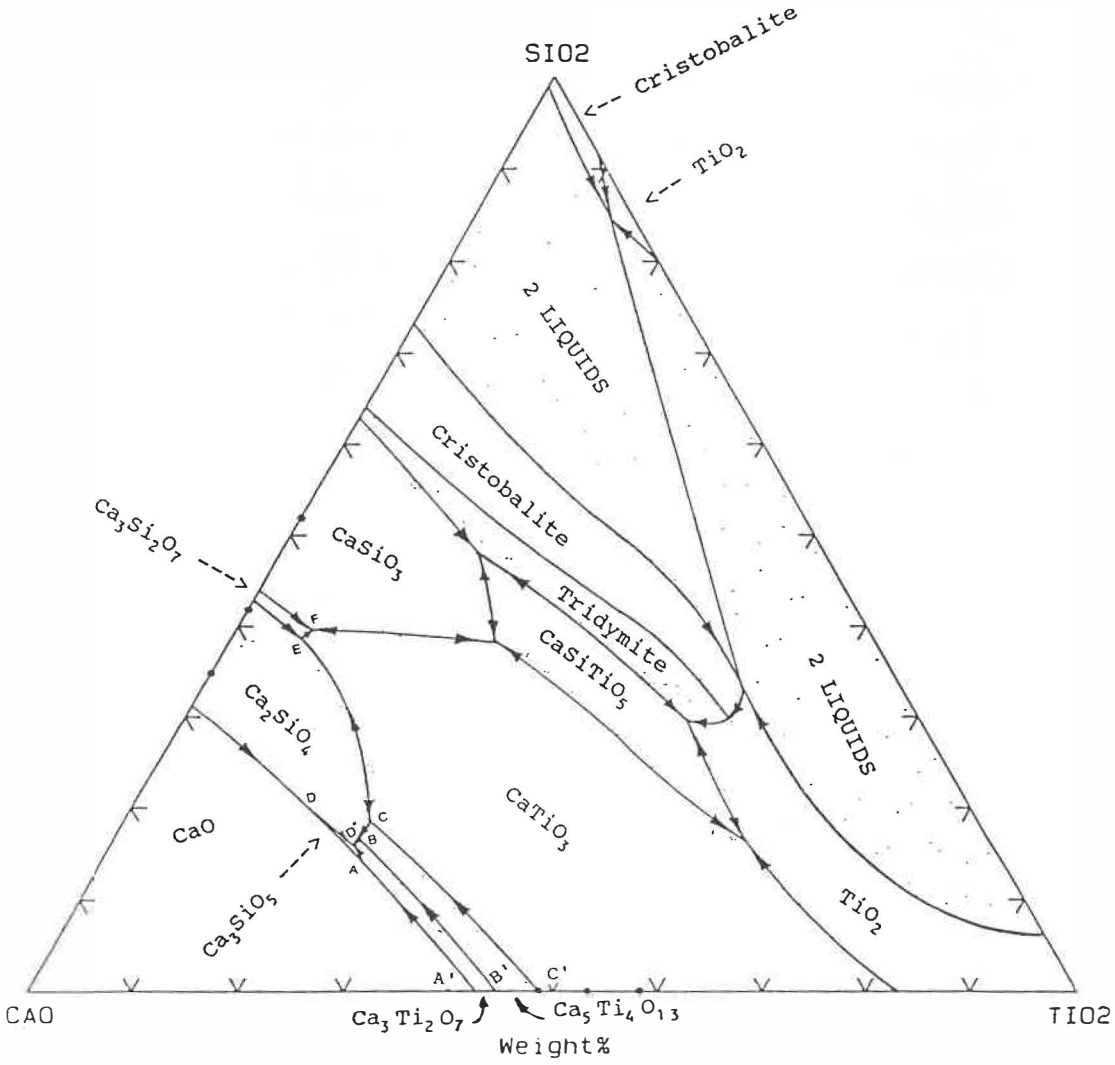


Fig. 4-6 Calculated $CaO-SiO_2-TiO_2$ phase diagram (wt. %).

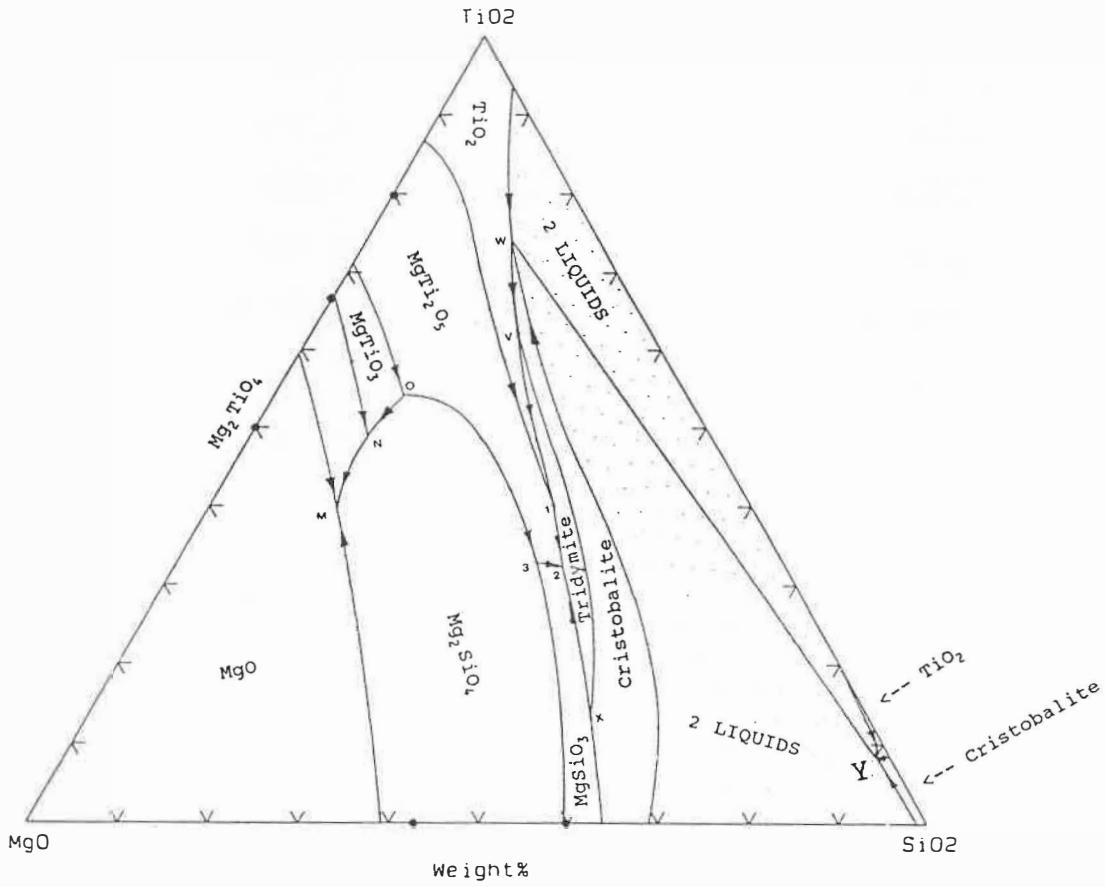


Fig. 4-7 Calculated $MgO-SiO_2-TiO_2$ phase diagram (wt. %).

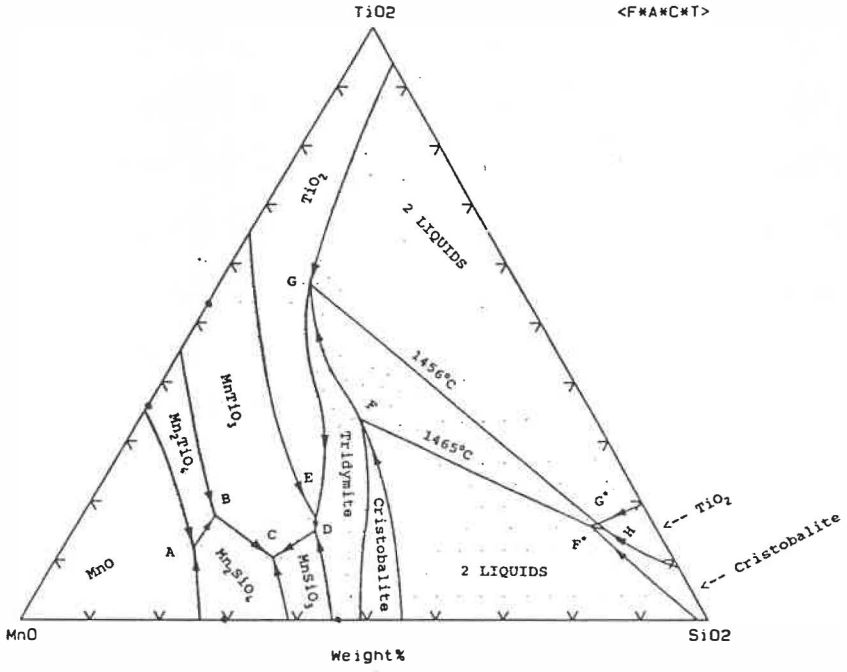


Fig. 4-8 Calculated $MnO-SiO_2-TiO_2$ phase diagram (wt. %).

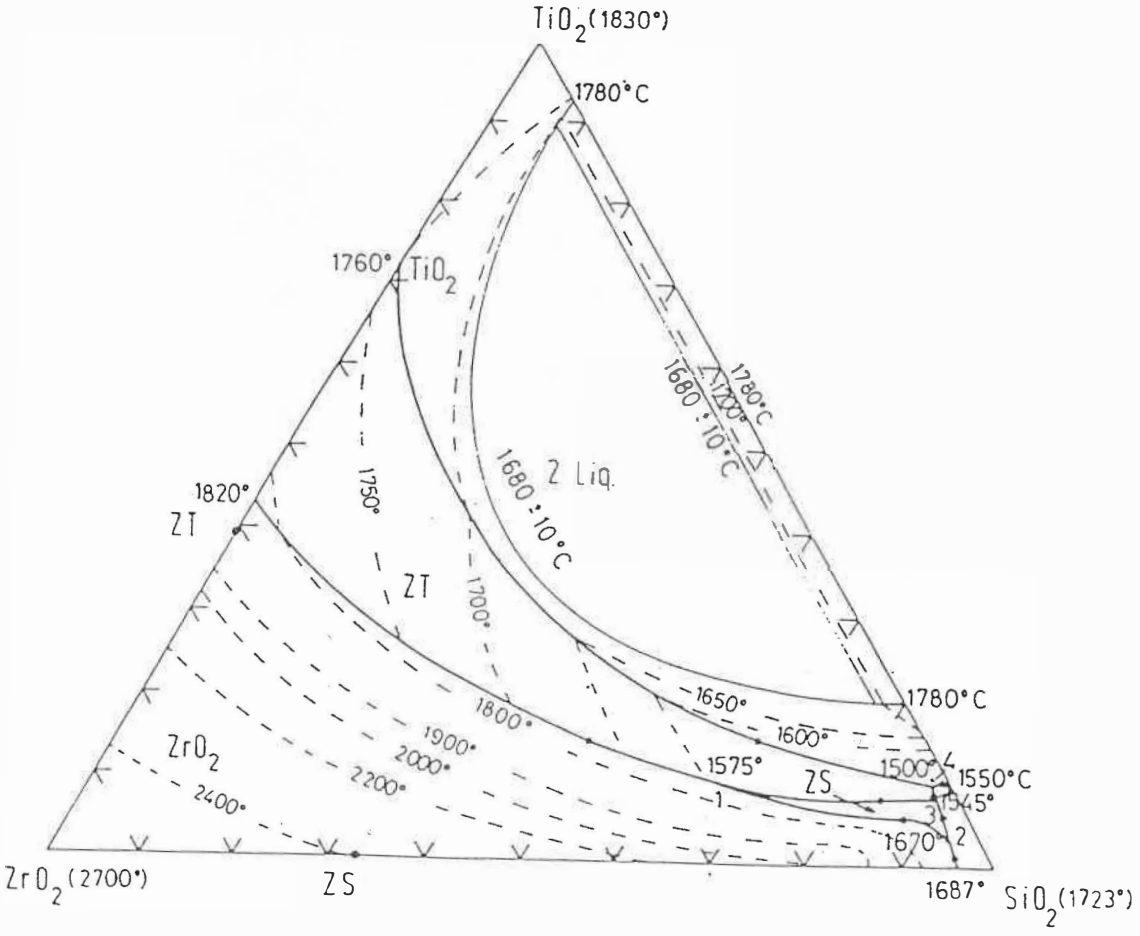


Fig. 4-9 Reported [76Pen, 57McT] SiO_2-TiO_2-ZrO_2 phase diagram (wt. %).

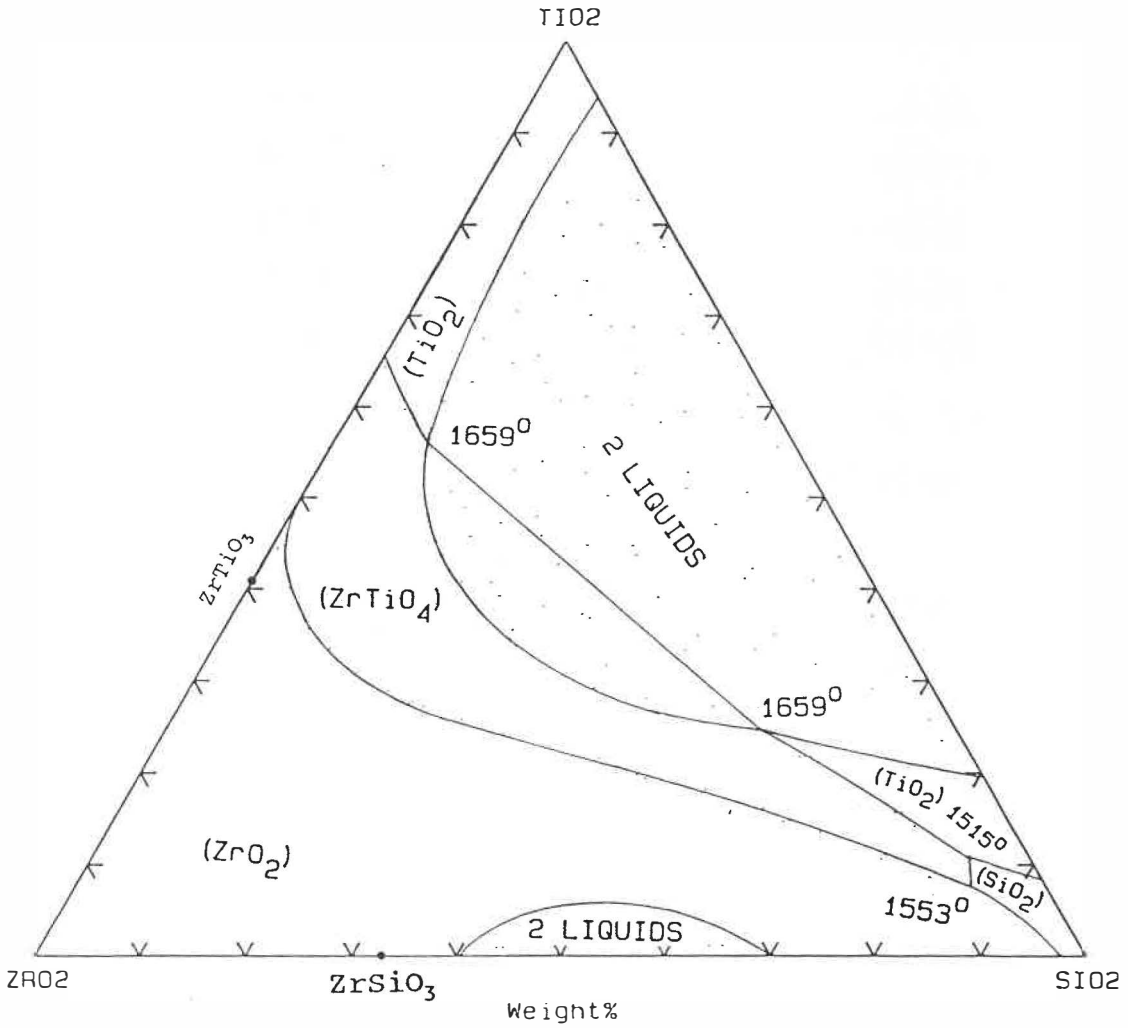


Fig. 4-10 Calculated SiO_2-TiO_2-ZrO_2 phase diagram (weight %, T in °C).

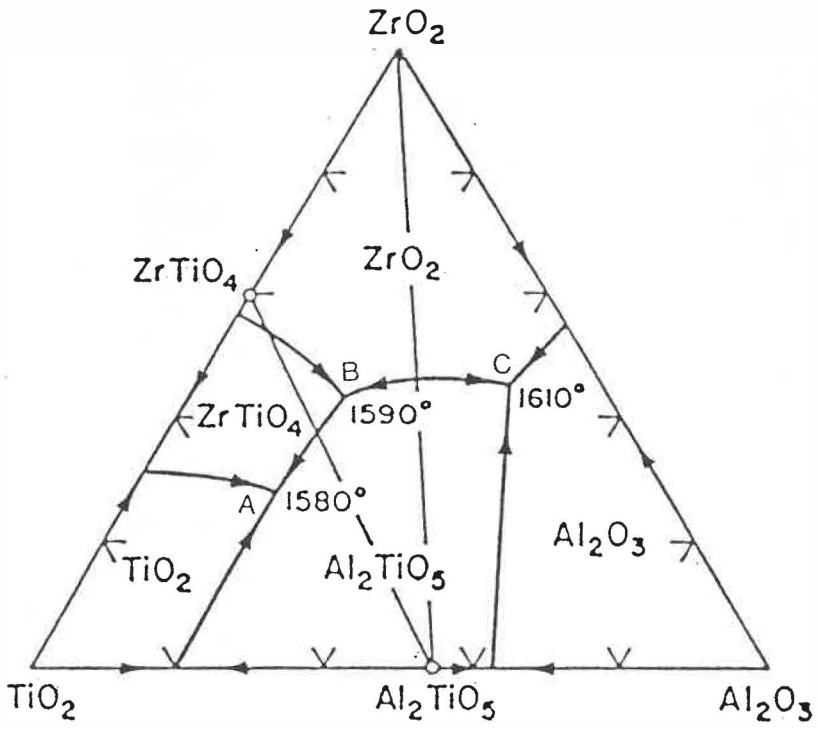


Fig. 4-11 TiO_2-ZrO_2-Al_2O_3 phase diagram as estimated by [55Ber].

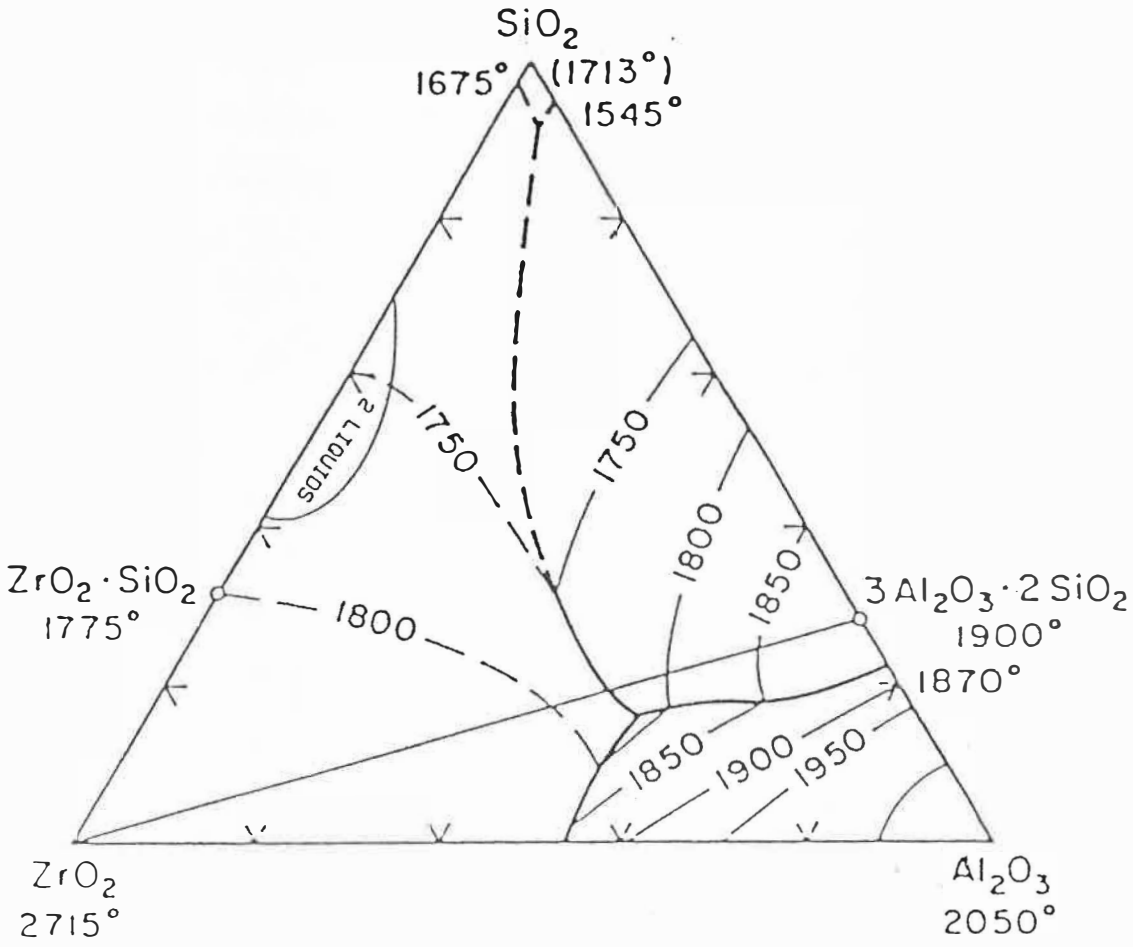


Fig. 4-12 SiO_2-ZrO_2-Al_2O_3 phase diagram reported by [56Bud].

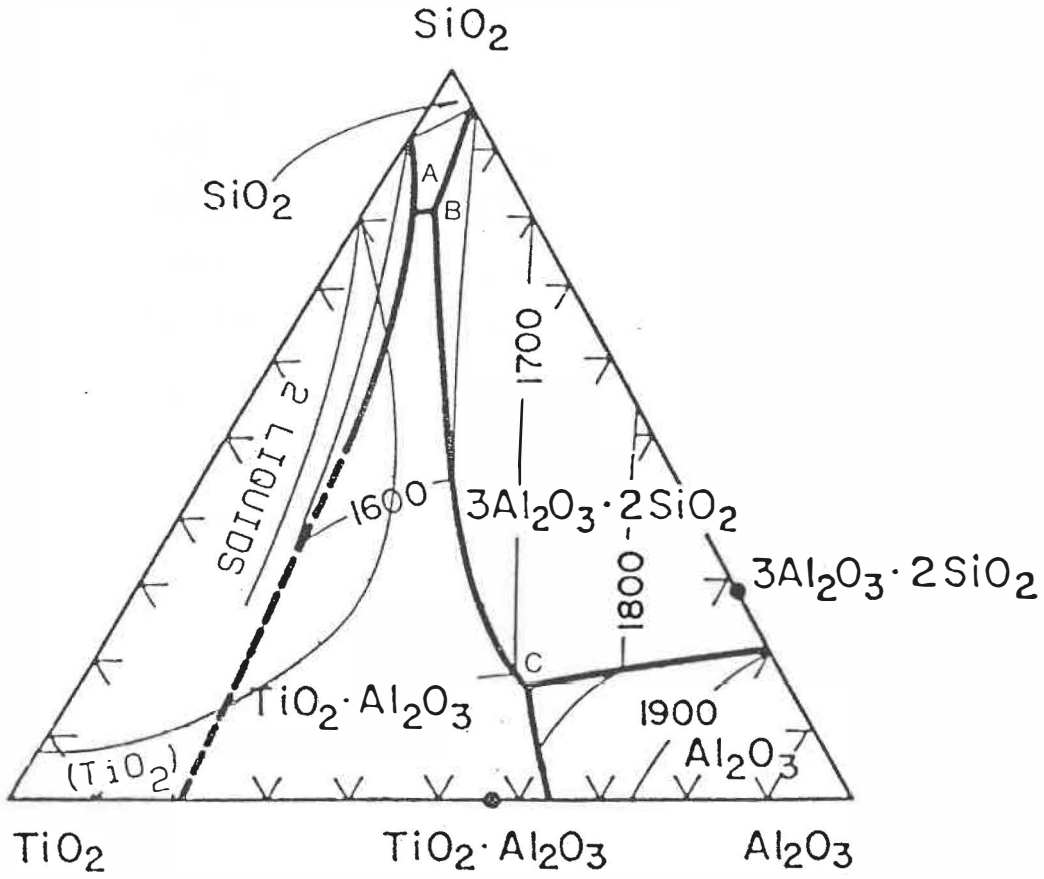


Fig. 4-13 TiO_2-SiO_2-Al_2O_3 phase diagram reported by [52Aga, 58Gal].

Table 4-1
Comparison of calculated and reported invariant points in the TiO_2-CaO-MgO system

Experimental values of Rouf et al. [69Rou]

point	T(°C)	X_{TiO2}	X_{CaO}	X_{MgO}
C	1460	0.515	0.225	0.26
B	1420	0.56	0.205	0.235
A	1350	0.70	0.20	0.10

Calculated

point	T(°C)	X_{TiO2}	X_{CaO}	X_{MgO}
C	1446	0.51	0.20	0.29
B	1410	0.60	0.19	0.20
A	1364	0.71	0.19	0.10
D	1492	0.45	0.22	0.33
E	1595	0.36	0.42	0.22
F	1584	0.34	0.50	0.16
G	1580	0.33	0.54	0.13

Table 4-2
Comparison of calculated and reported invariant points in the TiO_2-CaO-SiO_2 system

Experiment data of DeVries et al. [55Dev]

point	T(°C)	X_{TiO2}	X_{SiO2}	X_{CaO}
H	1352	0.205	0.385	0.410
G	1427	0.105	0.395	0.500
P	1367	0.490	0.210	0.300
Q	1377	0.353	0.294	0.353
J	1320	0.135	0.505	0.360
K	1375	0.295	0.410	0.295
L	1367	0.410	0.325	0.265
N	1537	0.455	0.360	0.190
E	1405	0.070	0.385	0.550
F	1400	0.070	0.393	0.545
A	1670	0.167	0.162	0.671
B	1650	0.163	0.177	0.660
C	1670	0.167	0.182	0.651
D	1900	0.059	0.258	0.683

Calculated

point	T(°C)	X_{TiO2}	X_{SiO2}	X_{CaO}
H	1360	0.200	0.397	0.403
G	1435	0.105	0.395	0.500
P	1356	0.550	0.162	0.288
Q	1382	0.347	0.306	0.347
J	1343	0.143	0.504	0.363
K	1377	0.296	0.408	0.296
L	1368	0.399	0.333	0.268
N	1519	0.438	0.376	0.186
E	1415	0.049	0.379	0.572
F	1403	0.054	0.388	0.557
A_*	1500	0.184	0.153	0.663
D	1486	0.175	0.162	0.663
B	1531	0.176	0.170	0.654
C	1591	0.177	0.190	0.633
D	1764	0.137	0.192	0.671

Table 4-3

Invariant Points in the $MgO-TiO_2-SiO_2$ System

Experimental data of [89Jan] for points 1-3, and of [58Mas] for all the other points

point	T(°C)	W_{TiO2}	W_{SiO2}	W_{MgO}
M	1630	0.363	0.169	0.468
N	1543	0.492	0.128	0.380
O	1508	0.542	0.142	0.316
V	1465	0.662	0.204	0.134
W	1528	0.742	0.162	0.096
X	1465	0.119	0.568	0.316
Y	1528	0.095	0.897	0.007
1	1398	0.396	0.382	0.222
2	1390	0.324	0.430	0.247
3	1405	0.315	0.409	0.276

Calculated

point	T(°C)	W_{TiO2}	W_{SiO2}	W_{MgO}
M	1580	0.436	0.126	0.438
N	1540	0.516	0.126	0.358
O	1520	0.526	0.130	0.344
V	1470	0.434	0.360	0.206
W	1530	0.474	0.358	0.160
X	1470	0.200	0.510	0.290
Y	1530	0.148	0.834	0.018
1	1425	0.394	0.406	0.200
2	1405	0.328	0.431	0.241
3	1415	0.328	0.386	0.286

Table 4-4

Calculated invariant points in the $MnO-SiO_2-TiO_2$ system

point	T(°C)	X_{TiO_2}	X_{SiO_2}	X_{MnO}
A	1243	0.108	0.217	0.675
B	1228	0.153	0.223	0.624
C	1182	0.089	0.354	0.557
D	1198	0.127	0.396	0.477
E	1209	0.145	0.386	0.469
F	1465	0.533	0.159	0.308
G_*	1456	0.524	0.161	0.315
G	1456	0.129	0.797	0.074

Table 4-5

Comparison of calculated and reported [52Aga] invariant points in the TiO_2-SiO_2-Al_2O_3 system (Fig. 4-13)

	T(°C)		Composition (wt. %) calc			Composition (wt. %) expt.		
Point	calc	expt.	TiO_2	SiO_2	Al_2O_3	TiO_2	SiO_2	Al_2O_3
A	1461	1470	10	82	8	14	79	8
B	1464	1480	9	82	9	12	79	8

Table 4-6
Comparison of Calculated and Experimental [77Pen1, 77Pen2, 79Pen, 84Pen] Invariant Points in the Al_2O_3-SiO_2-TiO_2-ZrO_2 System

Point	Solid equilibrium phases*	Temp(°C)	Liquid phase Composition (wt.%) ZrO_2	Al_2O_3	SiO_2	TiO_2
P expt.	Z+A+AT+A_3S_2	1595	28	31	12	29
calc	Z+A+AT+A_3S_2	1582	31	27	13	29
Q expt.	Z+AT+A_3S_2+ZT	1575	36	24	15	25
calc	Z+AT+A_3S_2+ZT	1565	31	24	15	30
R expt.	Z+A_3S_2+ZT+ZS	1540	--	--	--	--
S expt.	A_3S_2+ZT+ZS+S	1450	--	--	--	--
calc	A_3S_2+ZT+ZS+S	1452	10	10	72	8
T expt.	A_3S_2+ZT+AT+S	1440	--	--	--	--
calc	A_3S_2+ZT+AT+S	1419	7	8	72	13
U expt.	ZT+S+T+AT	1430	--	--	--	--
calc	ZT+S+T+A_3S_2	1427	7	9	72	12

* Z = ZrO_2 AT = $Al_2O_3.TiO_2$

A = Al_2O_3 A_3S_2 = $3Al_2O_3.2SiO_2$

T = TiO_2 ZT = $ZrTiO_4$

S = SiO_2 ZS = $ZrSiO_4$

Table 4-7. List of optimized ternary systems containing SiO_2.

	TiO_2	MgO	CaO	MnO	FeO	Ti_2O_3	Na_2O	K_2O	ZrO_2	NiO	Fe_2O_3	PbO	ZnO
Al_2O_3	W˙	N	E	N	N	N	N	N	W˙	N	N	N	N
TiO_2		W	W	W	E	E	N	N	W	N	N	N	N
MgO			O	E	O	E	N	N	N	O	O	O	O
CaO				O	W	E	N	N	N	O	O	W˙	W˙
MnO					O	E	N	N	W	O	O	O	O
FeO						E	N	N	W	O	W˙	W˙	W˙
Ti_2O_3							N	N	N	N	N	N	N
Na_2O								O	N	N	N	N	N
K_2O									N	N	N	N	N
ZrO_2										O	O	O	O
NiO											O	O	O
Fe_2O_3												W˙	O
PbO													W˙

A cell marked with a W or E in the above table indicates that the ternary system of the oxides on the row and column of the cell and SiO_2 has been evaluated by the author (W) or Professor Eriksson (E). A "-" means that the system has not been fully optimized. O and N indicate that the system has not been optimized at all while its ternary parameters most likely can (O) or most likely cannot (N) be well approximated as zero.

Table 4-8
List of optimized non-silicate ternary systems

$CaO-MgO-TiO_2$ (W)	$CaO-MgO-Ti_2O_3$ (E)
$FeO-Fe_2O_3-CaO$ (W)	$ZrO_2-TiO_2-Al_2O_3$ (W)

where W, E and "-" are explained in Table 4-7.

CHAPTER 5

PREDICTION OF PbO CONTENT AND $Fe^{+3}/(Fe^{+2}+Fe^{+3})$ RATIO IN LEAD SLAGS

5.1 INTRODUCTION

In lead smelting practice, the values of PbO content and $Fe^{+3}/(Fe^{+2}+Fe^{+3})$ ratio in the slag are very important indices which influence the losses of lead metal during the process. Therefore, some empirical relations [84Tas, 85Fon] have been proposed to predict PbO content and $Fe^{+3}/(Fe^{+2}+Fe^{+3})$ ratio from the temperature and initial composition of slags. These empirical equations are, however, normally limited to certain temperature and composition ranges. More reliable and accurate methods to predict these data over a considerable temperature and composition range are required.

In lead smelting operations if the bullion and slag are in thermodynamic equilibrium, then the following equilibrium is established:

$$Pb(liq) + \tfrac{1}{2}O_2 = PbO(liq) \qquad (5\text{-}2\text{-}1)$$

$$K_1 = a_{PbO}/a_{Pb}\ P_{O_2}^{1/2} \qquad (5\text{-}2\text{-}2)$$

where K_1 is the equilibrium constant of reaction (5-2-1), a_{PbO} is the activity of PbO in the slag, a_{Pb} is the activity of Pb in the bullion, and P_{O_2} is the equilibrium oxygen pressure.

The following equilibrium is also established in the slag:

$$2FeO(liq) + \tfrac{1}{2}O_2 = Fe_2O_3(liq) \qquad (5\text{-}2\text{-}3)$$

$$K_3 = a_{Fe_2O_3}/a^2_{FeO}\ p^{1/2}_{O_2} \qquad (5\text{-}2\text{-}4)$$

where K_3 is the equilibrium constant of reaction (5-2-3), and $a_{Fe_2O_3}$ and a_{FeO} are the activities of Fe_2O_3 and FeO in the slag.

The equilibrium constants K_1, and K_3 are known from literature data for the pure compounds. In the present study, K_1 is taken from a recent compilation [77Bar], K_3 is obtained by combining Gibbs energy data for the solid oxides from [85Ber] with the evaluation of the Gibbs energy of fusion of FeO [84Pel] and a Gibbs energy of fusion of Fe_2O_3 estimated by taking its entropy of fusion to be 37.1907 $J.K^{-1}\ mol^{-1}$ (8.8888 $cal.K^{-1}\ mol^{-1}$) and its melting point to be 1600°C [77Bar].

The resulting equations are:

$$-RT\ln K_1 = -51289 + 60.974\,T + 3.73 \times 10^{-4}\,T^2 - 5.464\,T\ln T - 1.000 \times 10^{4}\,T^{-1}\ cal. \qquad (5\text{-}3\text{-}3)$$

$$-RT\ln K_3 = -52765 + 376.252\,T + 7.566 \times 10^{-3}\,T^2 - 40.136\,T\ln T + 5.0976 \times 10^{4}\,T^{-1} - 2.09380 \times 10^{7}\,T^{-2} - 2869.8\,T^{1/2}\ cal. \qquad (5\text{-}3\text{-}4)$$

Typical compositions of lead blast furnace slags and lead bullion are shown in Table 5-1. In this study the Fe^{III} oxide component is taken as $FeO_{1.5}$ rather than Fe_2O_3 since the liquid dissociates into ions.

Since the bullion is very rich in lead, Raoult's Law applies to a very good approximation. That is, the activity of Pb in the bullion is equal to its atomic fraction. The major impurity in the bullion is Cu according to Table 5-1. The activity coefficient of Pb in a Pb-Cu liquid alloy containing 2.75 wt. % Cu is approximately 1.01 [73Hul]. Hence, an assumption of Raoultian behaviour is justified.

Therefore, if the composition of the bullion is known, and if P_{O_2} is fixed, then the PbO activity can be computed from equation (5-2-2) and the ratio of the Fe_2O_3 and FeO activities can be computed from equation (5-2-4).

If a model giving the component activities as functions of the composition of the slag were available, then the PbO content of the slag as well as the Fe^{3+}/Fe^{2+} ratio could be calculated from these activities. As shown in chapter 4, the quasi-chemical model can be used to calculate these activity functions. In the next section are given details of the optimizations of available thermodynamic and phase diagram data in the various slag sub-systems from which the parameters

of the model were deduced. Following this are found comparisons of the predictions with available data on lead blast furnace slags.

5.2 OPTIMIZATION OF SLAG SUB-SYSTEMS

In this section, the optimization of the various sub-systems containing PbO, ZnO and Fe_2O_3 of the PbO-ZnO-SiO_2-FeO-Fe_2O_3-CaO system will be detailed. Other binary systems were discussed in Section 2.3.

For the phase diagram analyses, thermodynamic data for the pure solid and liquid components were discussed in Section 2.2.

PbO-SiO_2

Activities in liquid PbO-SiO_2 slags at 1000°C have been measured by several authors [77Ouc, 68Cha, 70Koz, 73Oka, 82Tas]. These have been compiled by [82Tas] and plotted on Fig. 5-1 which is taken from [82Tas]. Over the range $0 < X_{SiO_2} < 0.5$, these data were optimized with the two parameters in Table 5-2. The line shown on Fig. 5-1 is calculated from the model. There are some data on the temperature dependence of the activity. At $X_{SiO_2} = 0.5$, Charette and Flengas [68Cha] show a_{PbO} increasing by 0.028 from 750° to 1000°C, while

[67Sri] show an increase of 0.041 over the same interval. The present model predicts an increase of 0.049.

Although the PbO-liquidus is also quite well reproduced by the present optimization, the liquidus temperatures are well below the range of interest of the present study.

ZnO-SiO_2

Reyes and Gaskell [83Rey] measured the activity of ZnO in liquid ZnO-SiO_2 solutions at 1560°C by a gas equilibration technique. Their results are shown in Table 5-3. The phase diagram, reproduced from [30Bun], is shown in Fig. 5-2.

The activity data and the ZnO-liquidus of the phase diagram were optimized simultaneously, resulting in the two binary parameters shown in Table 5-2. Calculated activities are shown in Table 5-3. The ZnO-liquidus is reproduced within 2 mol % at 1500°C and 0 mol % at 1610°C.

PbO-CaO

The PbO-CaO phase diagram of [74Kux] is reproduced in Fig. 5-3. The reported eutectic point is reproduced nearly exactly with the one binary parameter shown in Table 5-2.

PbO-ZnO

The phase diagram of [63Bau] is reproduced in Fig. 5-4. The eutectic point and reported solid solubility are reproduced nearly exactly with the one small parameter given in Table 5-2 and with the assumption of Henrian behaviour for the solid solution with $RT\ln\gamma_{ZnO}$ = 200 cal/mol in solid PbO.

PbO-Fe_2O_3

The phase diagram of Nevriva et al. [86Nev] is reproduced in Fig. 5-5, while an older version [62Mou] is shown in Fig. 5-6. The two diagrams are in reasonable agreement. The PbO-liquidus of the more recent study [86Nev] is fitted within 1 mol % and the Fe_2O_3-liquidus point at 1315°C (where the two experimental diagrams agree within 2 mol %) is fitted within 2 mol % by the one very small binary parameter given in Table 5-2.

PbO-FeO

No data are available for this system. It is expected to be close to ideal. The parameter $\omega_{oo}(PbO,FeO)$ was estimated to be equal to $\omega_{oo}(PbO,FeO_{1.5})$ for the PbO-$FeO_{1.5}$ system.

$CaO-Fe_2O_3$

The $CaO-Fe_2O_3$ diagram of [76Sch] is reproduced in Fig. 5-7. This diagram is not a true binary, but was measured in air (at constant P_{O_2}). Hence, at higher temperatures there will be a significant amount of Fe^{2+} in Fe_2O_3-rich solutions. This can be seen in Fig. 5-7 where magnetite is the equilibrium solid phase at higher temperatures.

Accordingly, optimization was performed in Fe_2O_3-rich solutions only at lower temperatures. With the two binary parameters given in Table 5-2, the Fe_2O_3 liquidus at 1300°C and the CaO liquidus from 1438°C to 1550°C were reproduced nearly exactly.

$FeO-Fe_2O_3$

The phase diagram is reproduced in Fig. 5-8. This diagram is based on studies by [45Dar, 60Phi, 58Mua]. Oxygen pressure isobars are shown on the diagram.

In the model, the liquid components are, formally, FeO and $FeO_{1.5}$ with Fe^{2+} and Fe^{3+} ions occupying cationic sites.

At points A,B and C in Fig 5-20 along the Fe_3O_4-liquidus, the following equilibria are established:

$$Fe_3O_4\,(solid) = 3\ FeO(liq) + 0.5O_2 \qquad (5\text{-}5\text{-}1)$$

$$0.5O_2 + 2\ Fe_3O_4\,(solid) = 6\ FeO_{1.5}\,(liq) \qquad (5\text{-}5\text{-}2)$$

Equilibrium constants for reactions (5-5-1) and (5-5-1) can be calculated from the compilation of [85Ber]. Along the liquidus line at points A,B and C, the activity of solid Fe_3O_4 is unity, and P_{O_2} is known. Hence, the activities of FeO and $FeO_{1.5}$ in the liquid at these three points can be computed. Also, at point D in Fig. 5-8 the oxygen pressure is known to be 10^{-10} atm. Since this composition is rich in FeO, Raoult's law is assumed to apply: $a_{FeO} = X_{FeO}$. The activity of $FeO_{1.5}$ at point D can thus be computed from the equilibrium constant K_3 of reaction (5-2-3) which was given previously in equation (5-3-4). (Note that $a_{Fe_2O_3} = a^2_{FeO_{1.5}}$).

The activities at the four points A,B,C,D were optimized to yield the two small binary parameters listed in Table 5-2. Oxygen pressure isobars calculated from these parameters are shown on Fig. 5-8.

ZnO-CaO, ZnO-FeO and ZnO-Fe_2O_3

No data are available for these systems. Ideal behaviour was assumed. This is probably a reasonable approximation.

$\underline{Fe_2O_3\text{-}SiO_2}$

No data have been reported for this system. However, the ternary $FeO\text{-}Fe_2O_3\text{-}SiO_2$ phase diagram has been reported. The diagram of [60Osb] is reproduced in Fig. 5-9. By extrapolation, the extent of the $Fe_2O_3\text{-}SiO_2$ binary two-liquid region as well as of the binary eutectic point were estimated. These were then optimized with the two parameters given in Table 5-2.

$\underline{FeO\text{-}Fe_2O_3\text{-}SiO_2}$

The ternary phase diagram compiled by [60Osb] is reproduced in Fig. 5-9. This diagram includes oxygen pressure isobars in the liquid region.

The quasi-chemical model was used to calculate compositions and temperatures on the isobars for $P_{O_2} = 10^{-11}$, 10^{-10}, 10^{-8} and 10^{-6} at the eight points indicated by the large dots on Fig. 5-9 which are in the range of Fe_2O_3/FeO ratios of interest in the present study. Results are shown in Table 5-4. Agreement with experimental values is well within error limits.

No ternary parameters were required.

FeO-CaO-Fe_2O_3

Phase diagrams at 1200° and 1300°C with oxygen isobars from [80Tak] are reproduced in Fig. 5-10. The eight composition points shown on Fig. 5-10 at $P_{O_2} = 10^{-10}$ and 10^{-11} were optimized to yield the one ternary parameter shown in Table 5-2. These points lie in the range of Fe_2O_3/FeO ratios of interest in the present study. With the one ternary parameter, the eight composition points at $P_{O_2} = 10^{-10}$ and 10^{-11} were reproduced to within 2 mol % and 10°C.

PbO-SiO_2-ZnO

The activity of PbO in PbO-rich ternary liquids at 1000°C was measured by [84Toi] by an emf technique. The measurements were all carried out at PbO/SiO_2 ratios above those of interest in the present study.

An optimization was performed on those data at the lowest PbO-SiO_2 ratios in order to obtain one ternary parameter which is listed in Table 5-2. The calculated and measured PbO activities are compared in Table 5-5.

PbO-SiO_2-CaO

The activity of PbO in PbO-rich ternary slags at 1000°C was measured by [82Tas] by an emf technique. The measurements

were all carried out at PbO/SiO_2 ratios above those of interest in the present study.

An optimization was performed on those data at the lowest $PbO-SiO_2$ ratios in order to obtain the one ternary parameter listed in Table 5-2. Calculated and measured PbO activities are compared in Table 5-6.

FeO-CaO-SiO_2 -Fe_2O_3

Oxygen isobars in the liquid slags at 1450°C were reported by Timucin and Morris [70Tim]. Their results are reproduced in Fig. 5-11. The isobars at $P_{O_2} = 10^{-9}$, 10^{-7} and 10^{-5} were optimized to give the one small ternary parameter ω^{01}_{CS} (where C=CaO and S=SiO_2) listed in Table 5-2.

Calculated isobars at $P_{O_2} = 10^{-9}$ and 10^{-7} agree with the experimental isobars to within 1.5 wt. % and 10°C. The isobar at $P_{O_2} = 10^{-5}$ is reproduced to within these limits at low CaO contents, but at the highest CaO content the agreement is within 5 wt. % and 15°C.

The slight curvature of the isobars is well reproduced by the model.

Another report on this quaternary system by Bodsworth [59Bod] gives data which do not agree closely with those of Timucin and Morris. The data of Timucin and Morris (Fig. 5-11) agree well with the results for the 5-component PbO-FeO-$CaO-SiO_2-Fe_2O_3$ system discussed earlier (Figs. 5-12 to 5-16). Hence, these data were chosen in the present case.

$\underline{FeO-CaO-ZnO-SiO_2}$

Activities of FeO and ZnO in Fe-saturated slags were measured by an emf technique at 1250°C [78Fil] at low ZnO contents. Most of the data were collected at SiO_2 and FeO contents above those of interest in the present study. However, two points were retained for optimization. Two ternary parameters, $\omega_{Z\,S}^{0\,1}$ (where Z=ZnO and S=SiO_2) and $\omega_{F\,S}^{0\,1}$ (where F=FeO and S=SiO_2), were obtained as shown in Table 5-2. A comparison of experimental [78Fil] and calculated activities is given in Table 5-7.

$\underline{PbO-FeO-CaO-SiO_2-Fe_2O_3}$

Measurements on this system by Taskinen et al. [84Tas] at 1300°C will be discussed later in Section 5.3 and were plotted in Figs. 5-12 to 5-16. In order to give the best fit to these data at higher PbO contents, one small ternary

parameter ω_{FS}^{03} (where F=FeO and S=SiO_2) was employed. This parameter has little effect at lower PbO contents.

5.3 COMPARISON OF MODEL PREDICTIONS WITH DATA ON LEAD SLAGS

Few systematic studies of lead slags have been made. The most extensive and best controlled is that of Taskinen et al. [84Tas]. These authors were concerned with slags used in direct lead smelting.

These authors equilibrated slags of various CaO/SiO_2 and Fe/SiO_2 ratios with pure Pb at 1300°C and measured P_{O_2} with an oxygen probe. They then analyzed the slags to determine the PbO content and the $Fe^{3+}/(Fe^{2+}+Fe^{3+})$ ratio.

In Figs. 5-12 to 5-14 are shown their smoothed results for the activity coefficient of PbO defined as $\gamma_{PbO} = a_{PbO}/X_{PbO}$ where X_{PbO} is the mole fraction of PbO in the slag. (For these purposes, a mole of Fe^{III} oxide is defined as $FeO_{1.5}$ rather than Fe_2O_3). They calculated a_{PbO} from the probe emf and equation (5-2-2). However, for the equilibrium constant K_1 they did not use equation (5-3-3). Rather, they used a value obtained by measuring the emf of a probe in pure PbO at 800 - 930°C and then extrapolating to 1300°C. As a result, their calculated activity coefficients at 1300°C are

lower by a factor of 1.09 than they would be had they used equation (5-3-3).

Values of activity coefficients calculated from the present model are also shown in Figs. 5-12 to 5-14. Agreement is within experimental error limits. Note that Taskinen et al. made no measurements for PbO contents below 20 wt. %.

Measured and calculated $Fe^{3+}/(Fe^{2+}+Fe^{3+})$ ratios are shown in Figs. 5-15 and 5-16. Again, note that in blast furnace slags the PbO content is always below 13 wt. %, whereas the measurements in Figs. 5-15 and 5-16 begin at 20%. The observed influence of CaO/SiO_2 ratio upon the $Fe^{3+}/(Fe^{2+}+Fe^{3+})$ ratio is well reproduced by the model as can be seen in Fig. 5-15. However, as seen in Fig. 5-16, the model predicts that the Fe/SiO_2 ratio has very little influence upon the $Fe^{3+}/(Fe^{2+}+Fe^{3+})$ ratio when the CaO/SiO_2 ratio is held constant, whereas the data in Fig. 5-16 suggest that there should actually be some dependence.

As shown in Figs. 5-15 and 5-16, when the PbO content increases from zero, the $Fe^{+3}/(Fe^{+2}+Fe^{+3})$ ratio rises very rapidly at first as the oxygen partial pressure value increases from zero. This rapid increase was actually observed by Jahanshahi and Player [89Jah] which indicated that the slag composition is changing rapidly in this concentration region.

As a result, γ_{PbO} in Figs. 5-12 to 5-14 changes quite rapidly at first as the PbO content increases from zero.

Fontainas et al. [85Fon] measured the Pb content of several slags in contact with lead bullion. They also measured P_{O_2} by using a solid electrolyte probe. Experiments were carried out in both a laboratory furnace and a blast furnace with good agreement between the two. Their results are shown in Fig. 5-17. These data were "normalized" to 1150°C and a CaO/SiO_2 weight ratio of 0.6 by means of an empirical correlation given by the authors.

Unfortunately, the authors do not give any other details of their slag composition. They do state that the atomic fraction of Pb in the bullion was about 0.85.

In order to compare the present calculations with the results of Fontainas et al., a slag composition corresponding approximately to that of Table 5-1, with a CaO/SiO_2 ratio of 0.6 was chosen. Specifically, a starting composition of 28.33 SiO_2 , 17.0 CaO, 10.0 ZnO and 38.4 total Fe as FeO was chosen, with the bullion composition given in Table 5-1 (which yields an atomic fraction of Pb of 0.856). Calculated results are compared with the experimental data in Fig. 5-17 (The calculated wt. % PbO is multiplied by the ratio of the molecular weights of Pb and PbO in order to convert to wt. %

Pb). Agreement is within the experimental error limits, particularly when it is considered that the slag composition of the experiments is not completely given.

In contrast to Taskinen et al. [84Tas], investigations at lower PbO contents (<0.6 wt.% Pb) region were reported by Meyer and Richardson [66Mey], Grant [80Gra], and Wright et al. [89Wri]. As shown in Fig. 5-18, their results are very scattered.

Meyer and Richardson [66Mey] employed a gas phase equilibrium method to determine γ_{PbO} data but their results are inconsistent with the extrapolated values of [84Tas]. For example, γ_{PbO} was reported as 0.81 in [66Mey] for a slag of CaO/SiO_2=0.448 and Fe/SiO_2=1.540, and could be extrapolated from [84Tas] to be about 0.48 for a similar slag. Furthermore, if γ_{PbO}=0.81 [66Mey] was considered correct at lower PbO content, when PbO content increases to about 20 wt.% γ_{PbO} will be about 0.53 according to [84Tas]. This decrease in γ_{PbO} with increasing PbO content is contrasted to that observed by [89Jah]. So it is impossible to reproduce simultaneously both the results of [84Tas] and [66Mey] (see Table 5-8).

Grant [80Gra] applied a computer model of the slag-fuming process to derive some thermodynamic properties of components

in Pb blast furnace slags. He rejected those of his points at very low PbO levels and placed more emphasis on values from higher lead contents when calculating the average γ_{PbO} as 0.657 at 1200°C.

Wright et al. [89Wri] measured γ_{PbO} in lead blast furnace slags in which hydrogen-nitrogen mixtures were adopted as reductant. The P_{O_2} [89Wri] was measured by an EMF method. In their experiment, a high-zinc slag was added at a constant rate to the bath of low-zinc slag at 1300°C, with reducing gas blowing at a known rate. Therefore, the compositions of slag, which were not reported [89Wri], were changing for all the experimental points. Consequently, we cannot predict their γ_{PbO} values.

As mentioned by [89Wri], the slags used by [66Mry, 80Gra, 89Wri] are apparently similar. Therefore, to be able to compare the present calculations with the results of [66Mry, 80Gra, 89Wri], a typical blast furnace slag, A, with a starting composition of 28.33 wt.% SiO_2, 17.0 wt.% CaO, 10.0 wt.% ZnO and 38.4 wt.% FeO, was chosen. In this way, at 1250°C the predicted γ_{PbO} is 0.62 at X_{PbO} = 0.0002 and 0.64 at X_{PbO} = 0.0015, which lie favourably among the points of [66Mry, 80Gra, 89Wri] in Fig 5-18.

A final study is that of Riley [79Ril] who measured Fe^{3+}/Fe^{2+} ratios versus wt. % Pb for several quenched industrial slags from Mount Isa Mines in Australia. His results are shown in Fig. 5-19. The range of composition of these slags is given in the article. Taking the average composition and a temperature of 1225°C, the curve shown in Fig. 5-19 was calculated. That agreement is not obtained with the data is not surprising since Riley estimates that from 50 to 100% of the Pb content which he analyzed was entrained bullion and not dissolved PbO. The percentage of total lead which was entrained lead would be highest at the lowest Pb contents.

5.4 CONCLUSIONS

By optimizing all the available thermodynamic and phase equilibrium data of all the sub-systems of $PbO-ZnO-SiO_2-FeO-Fe_2O_3-CaO$ slag, a thermodynamic database has been built using the modified quasi-chemical model. Furthermore, based on equations (5-2-2) and (5-2-4) the database can be used by the F*A*C*T system [85Tho] to calculate the equilibrium composition of lead blast furnace slag if P_{O_2} is known and if the composition of the bullion is known. Therefore, one can predict the PbO content and $Fe^{+3}/(Fe^{+2}+Fe^{+3})$ ratio of the blast furnace slags. Agreement of our predictions with the available experimental results is good over a wide composition

and temperature ranges. The database may thus provide a useful tool in simulations of actual and proposed lead smelting operations.

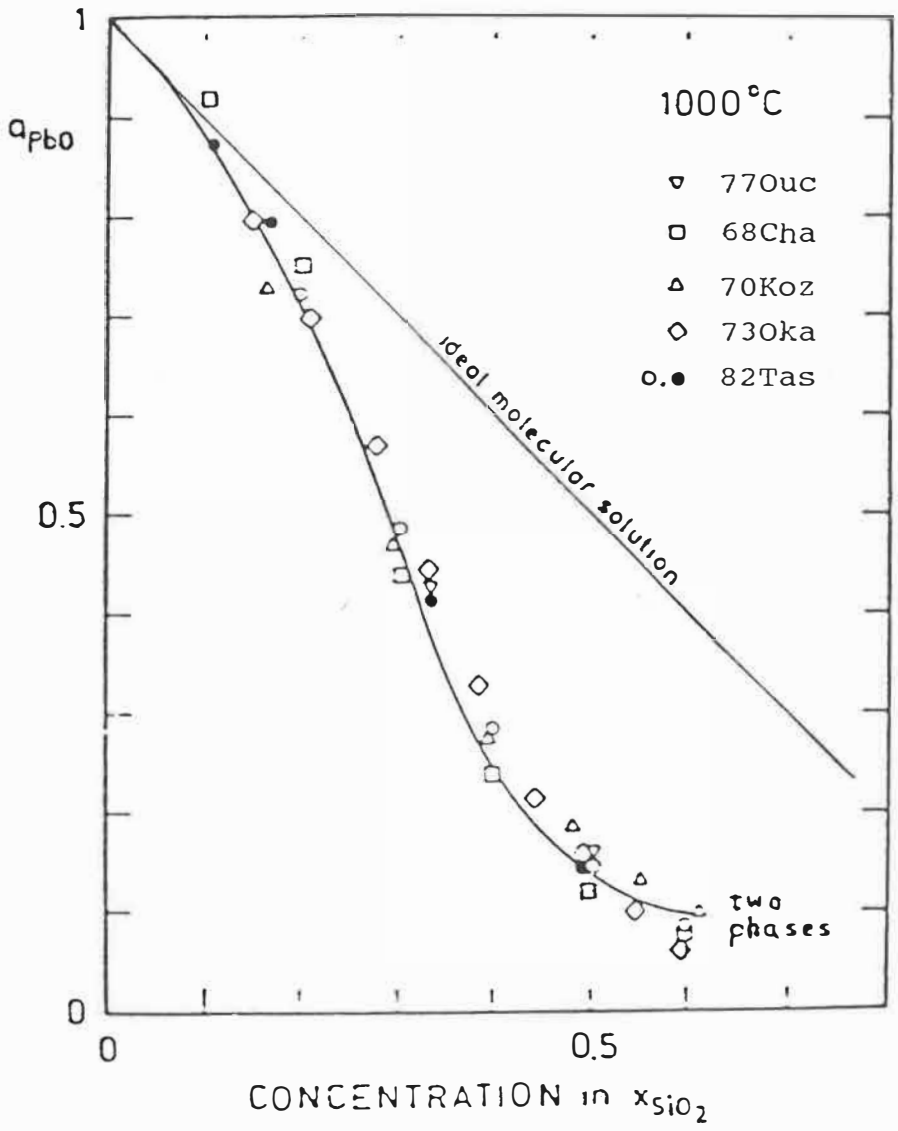


Fig. 5-1 PbO(liq) activities in PbO-SiO_2 slags at 1000°C as reported by several authors. Diagram taken from [82Tas]. Line is calculated from model.

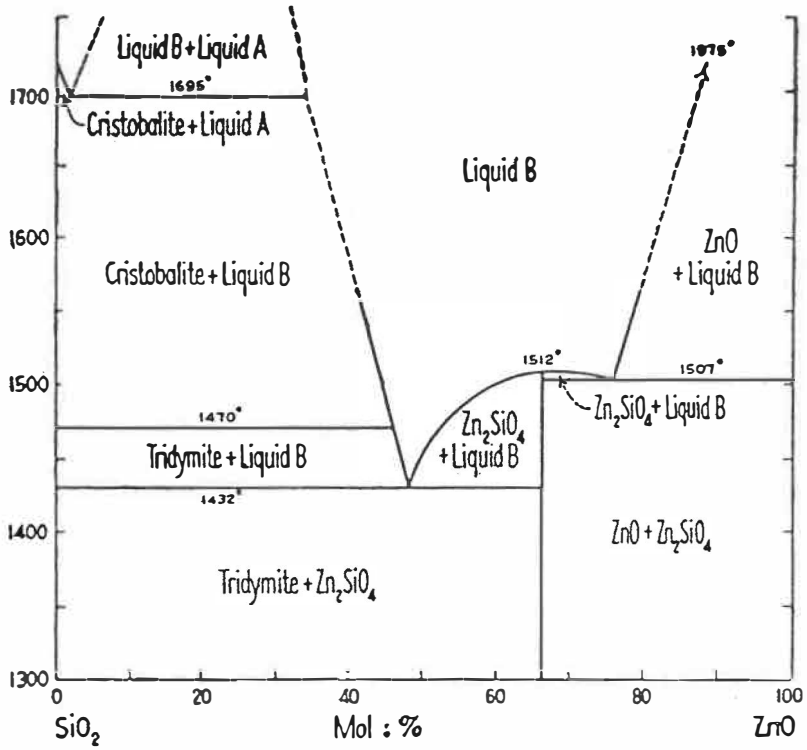


Fig. 5-2 SiO_2-ZnO phase diagram [30Bun]

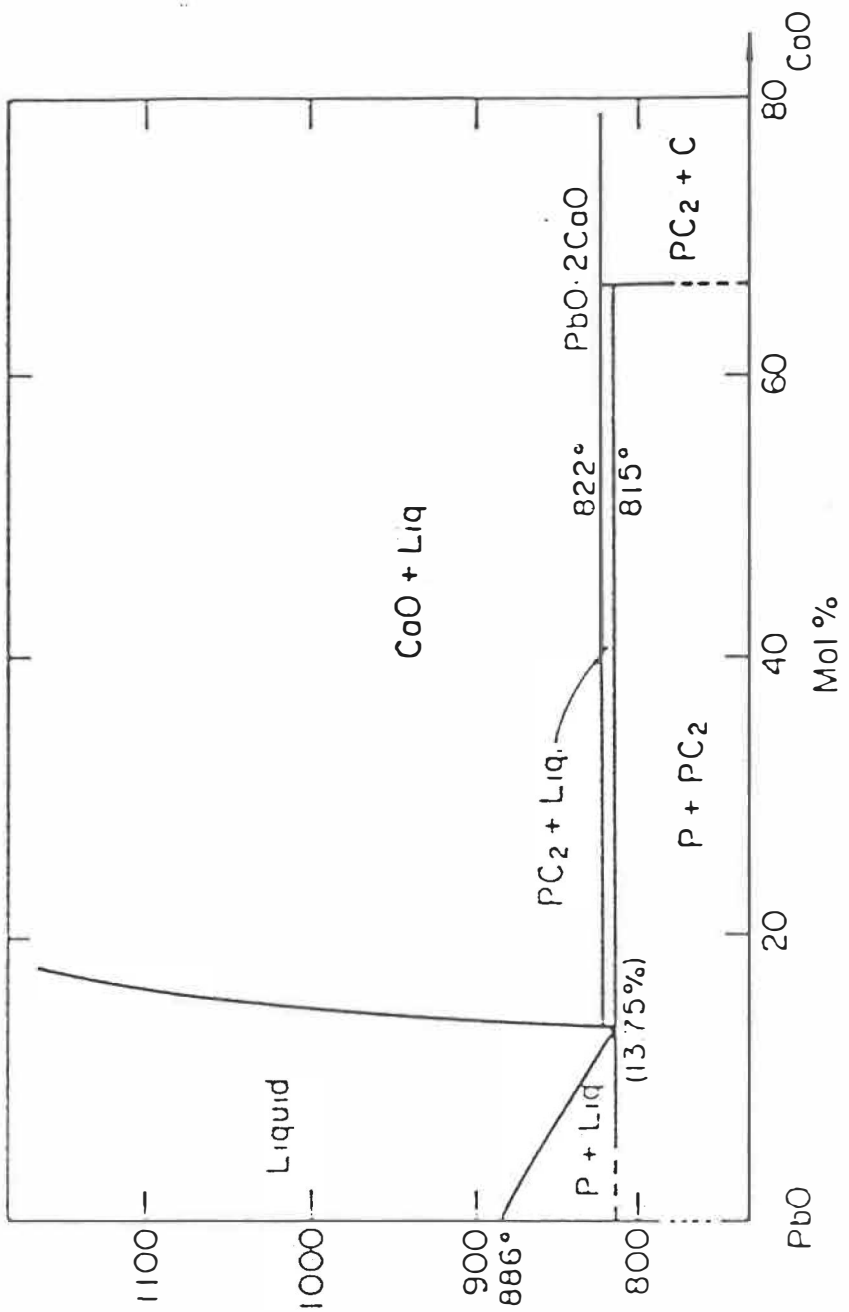


Fig. 5-3 PbO-CaO phase diagram [74Kux]

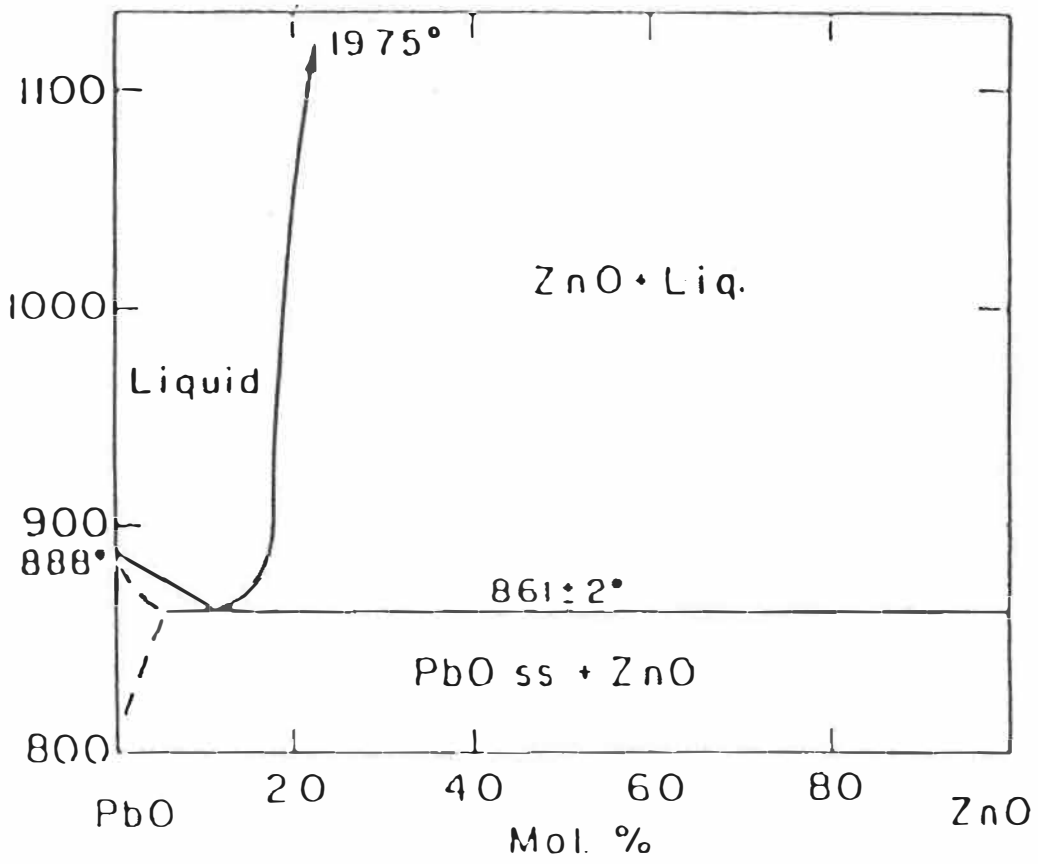


Fig. 5-4 PbO-ZnO phase diagram [63Bau]

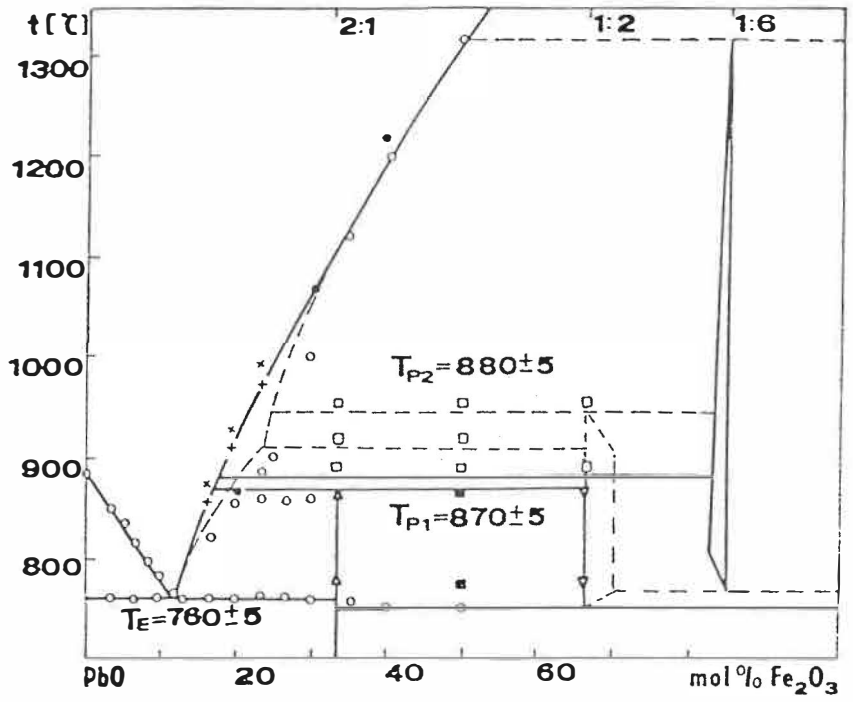


Fig. 5-5 PbO-Fe_2O_3 phase diagram [86Nev]

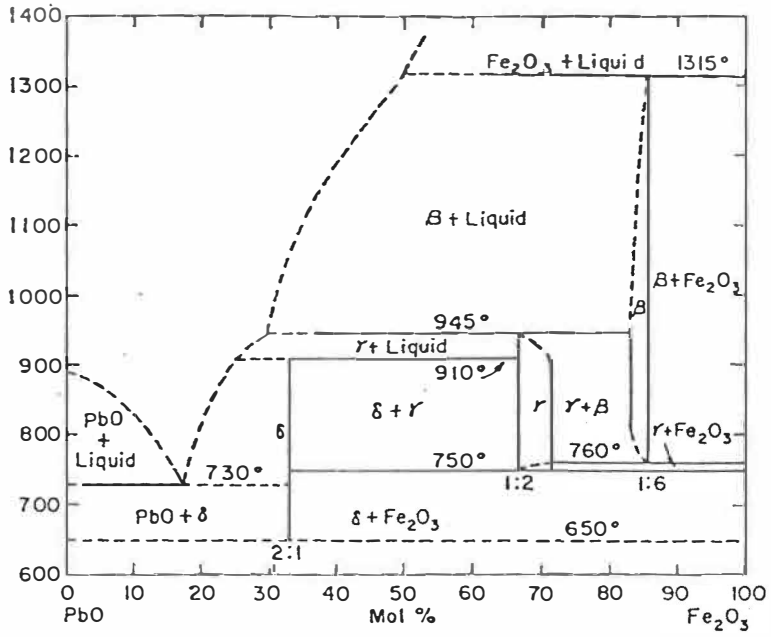


Fig. 5-6 PbO-Fe_2O_3 phase diagram [62Mou]

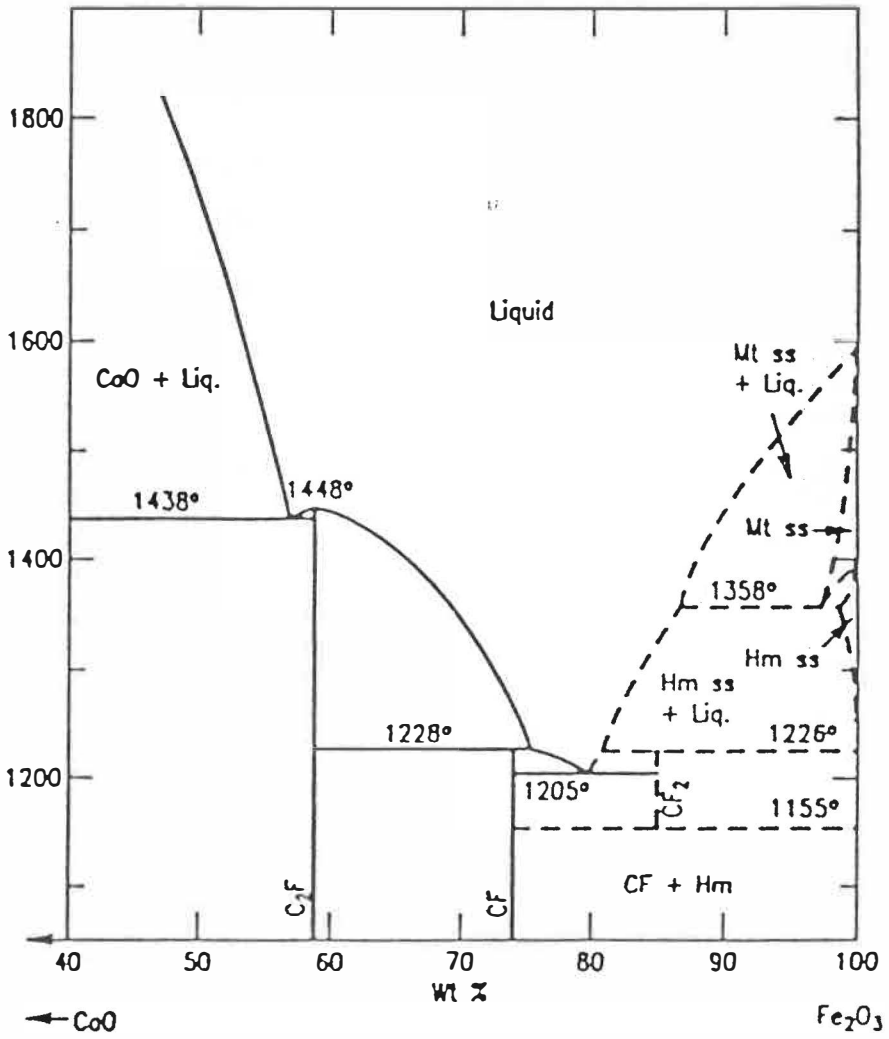


Fig. 5-7 $CaO-Fe_2O_3$ phase diagram in air [76Sch].

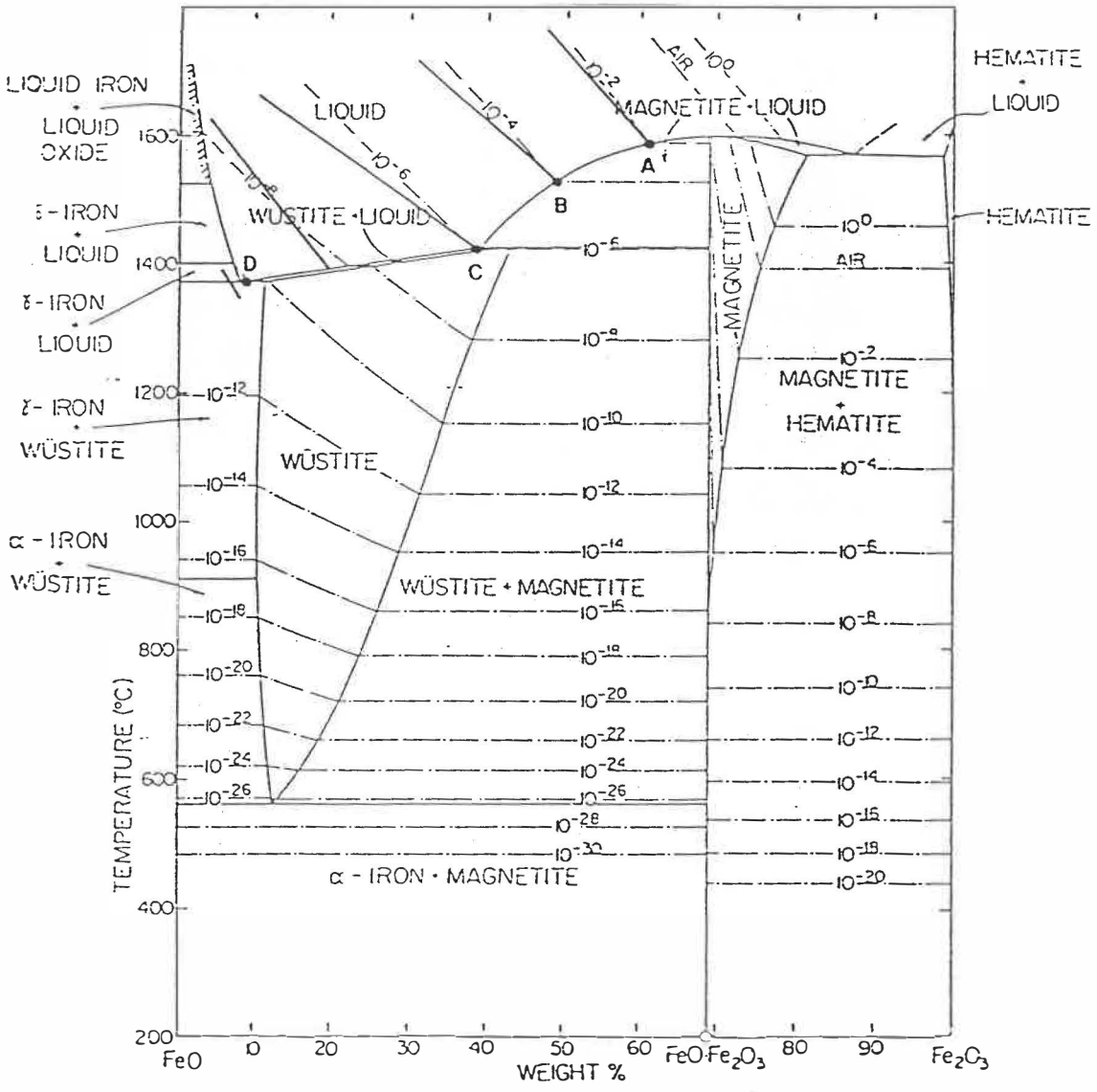


Fig. 5-8 $FeO-Fe_2O_3$ phase diagram showing oxygen isobars from work of [45Dar, 60Phi, 58Mua]. Calculated isobars in the liquid are shown as solid lines.

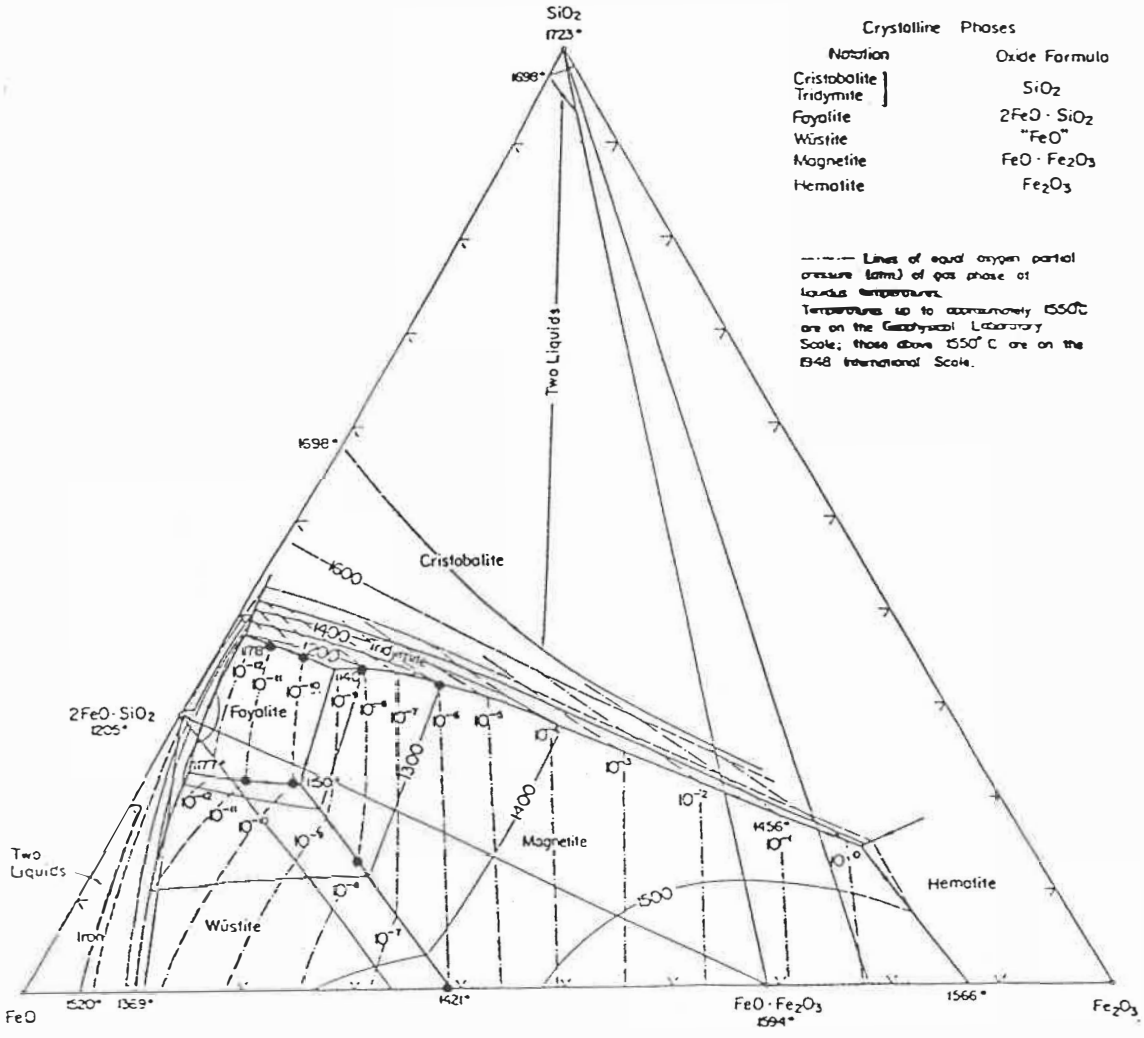


Fig. 5-9 $FeO-Fe_2O_3-SiO_2$ phase diagram [600sb] showing oxygen isobars in the liquid region.

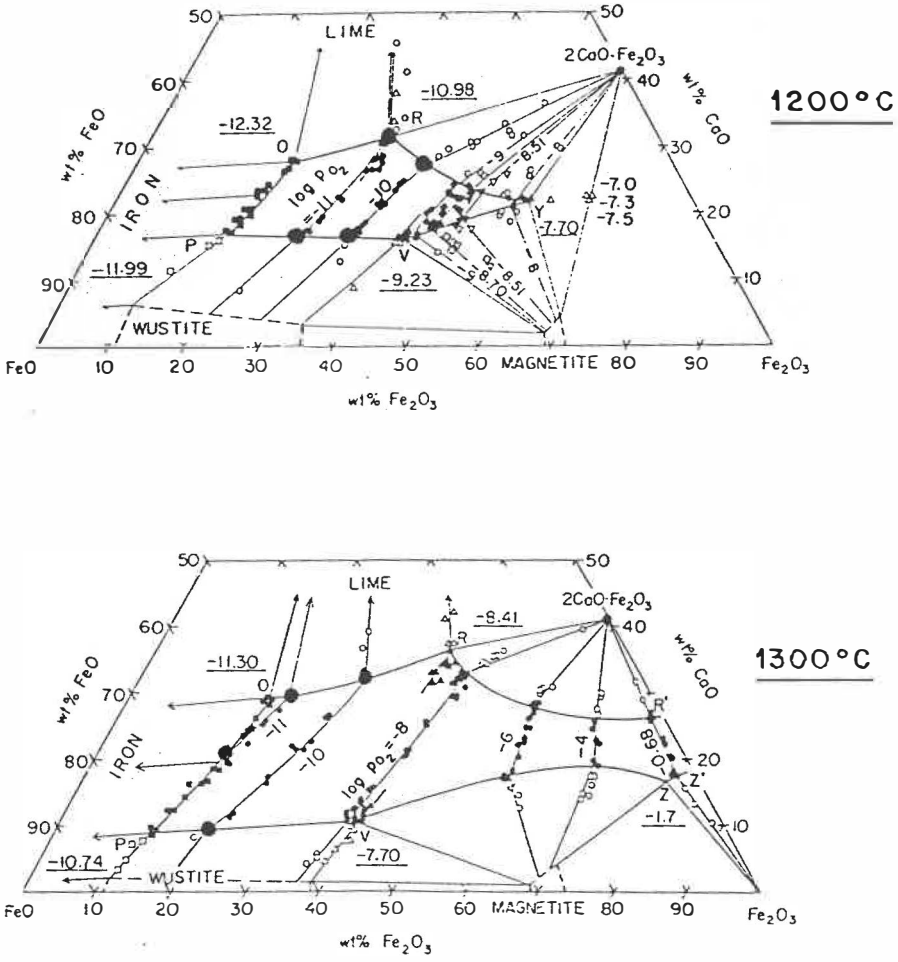
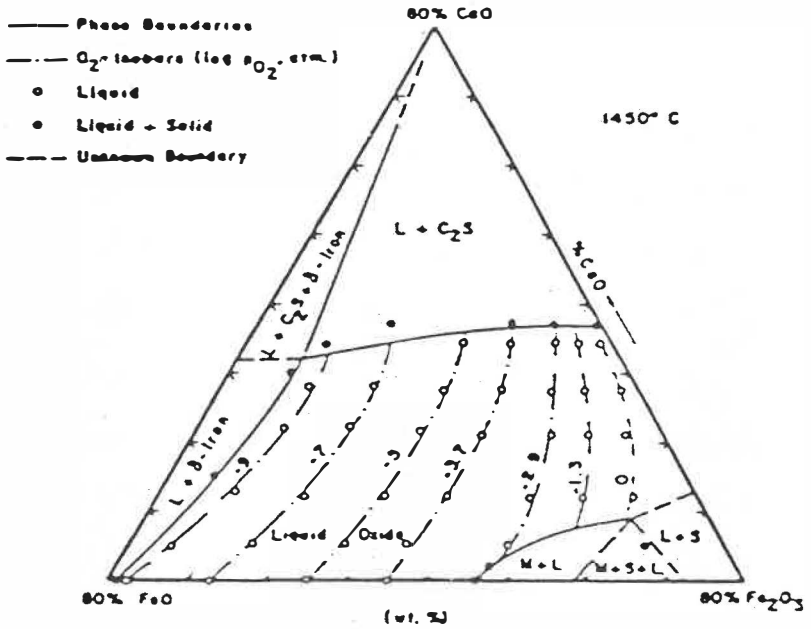
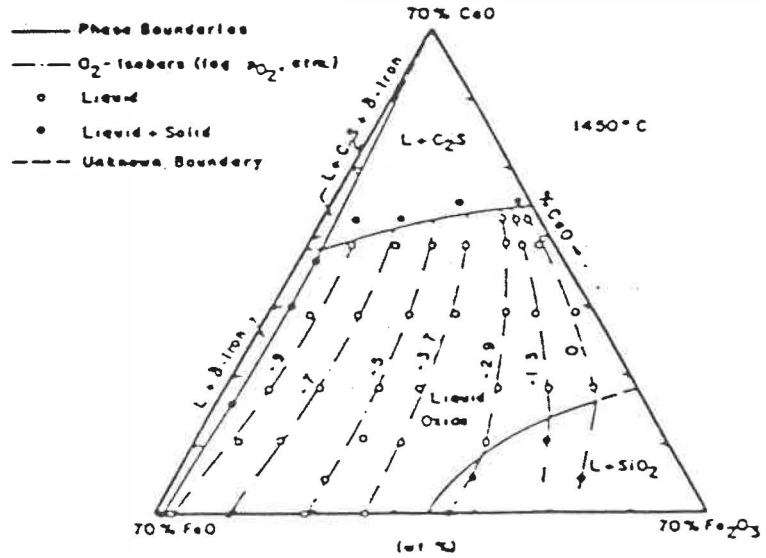


Fig. 5-10 $CaO-FeO-Fe_2O_3$ phase diagram at 1200° and 1300°C [80Tak] showing oxygen isobars. (In the article of [80Tak], the labels for 1200° and 1300°C were inverted).



The 20 pct SiO_2-isothermal phase diagram for the CaO-FeO-Fe_2O_3-SiO_2 system. Abbreviations: M = magnetite, S = silica, L = liquid oxide, C_2S = $2CaO \cdot SiO_2$.



The 30 pct SiO_2-isothermal phase diagram for the CaO-FeO-Fe_2O_3-SiO_2 system. Abbreviations: L = liquid oxide, C_2S = $2CaO \cdot SiO_2$.

Fig. 5-11 SiO_2-CaO-FeO-Fe_2O_3 system at 1450°C showing oxygen isobars in the liquid region [70Tim].

<F*A*C*T>

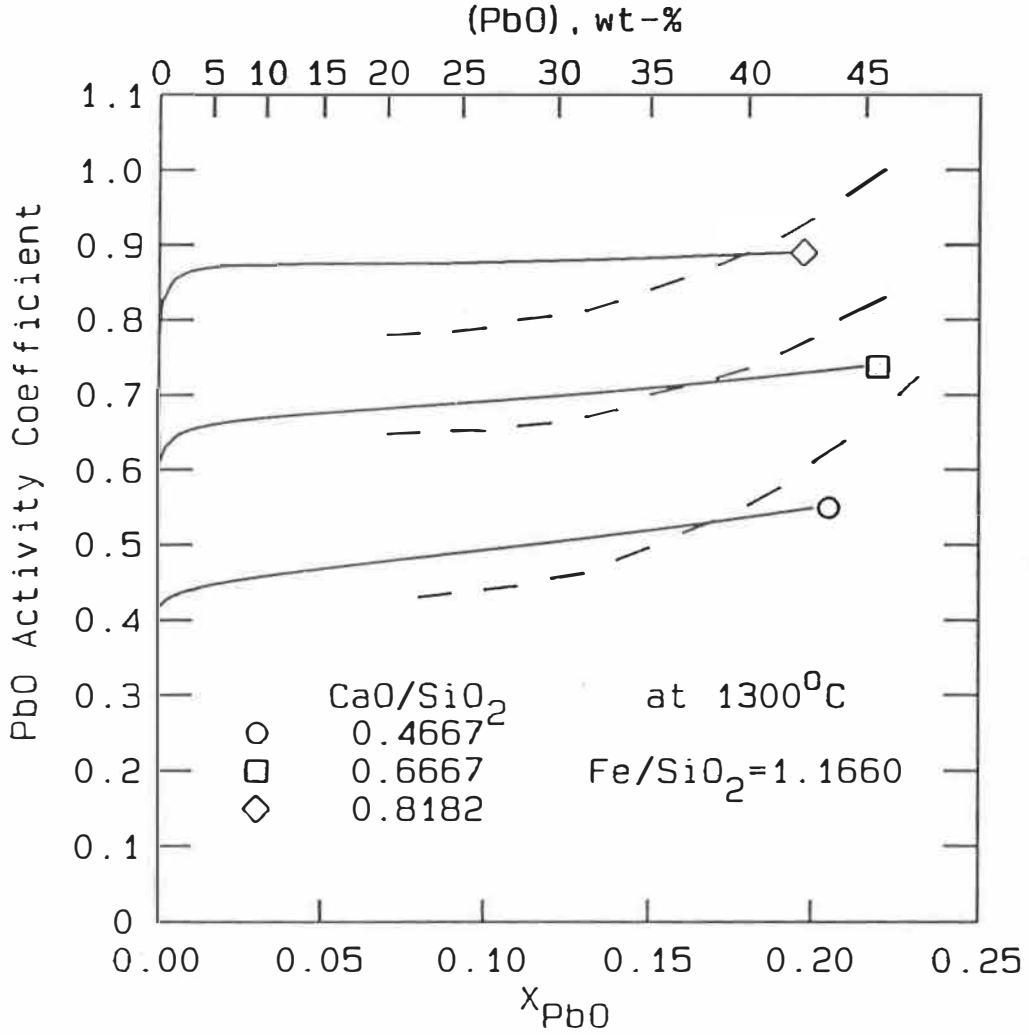


Fig. 5-12 Experimental [84Tas] and calculated PbO(liq) activity coefficients in PbO-FeO-CaO-SiO_2-Fe_2O_3 slags in equilibrium with liquid Pb.

<F*A*C*T>

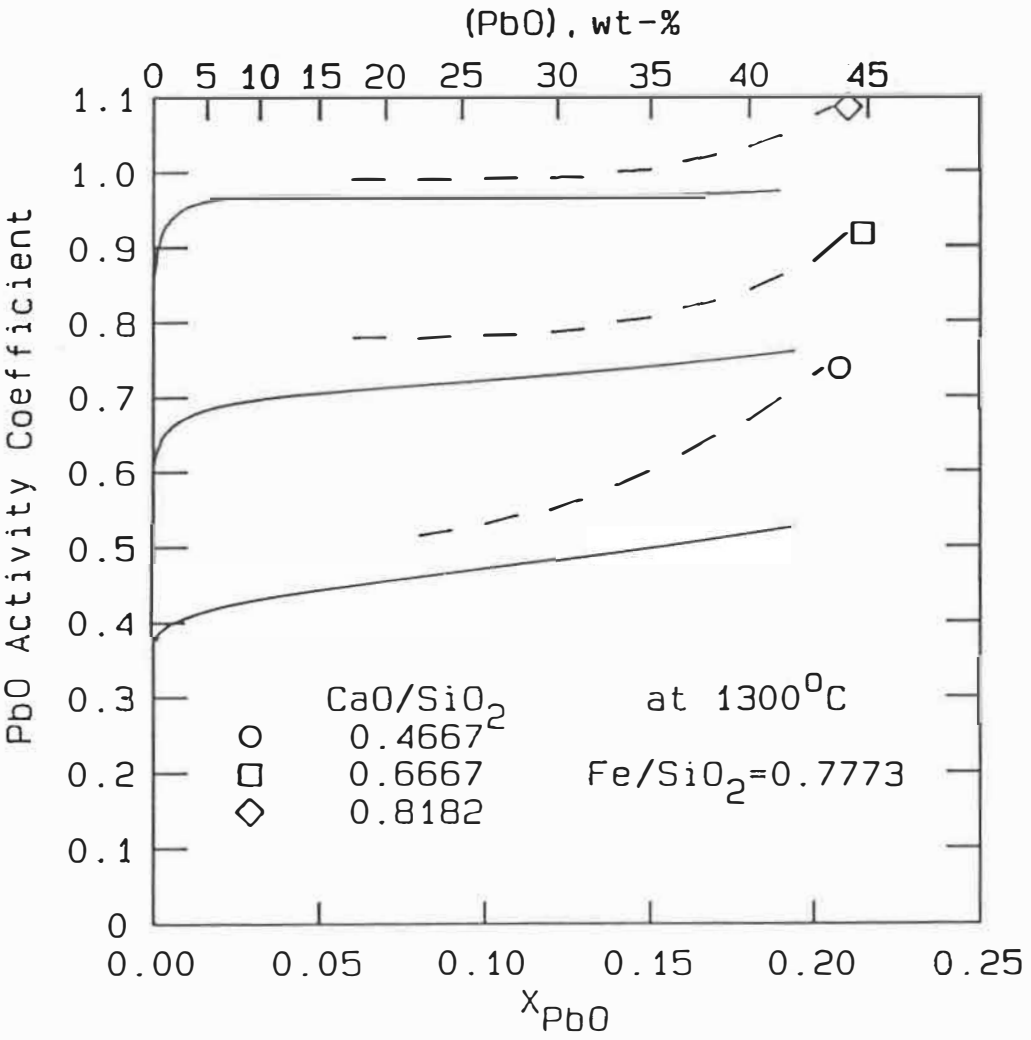


Fig. 5-13 Experimental [84Tas] and calculated PbO(liq) activity coefficients in $PbO-FeO-CaO-SiO_2-Fe_2O_3$ slags in equilibrium with liquid Pb.

<F*A*C*T>

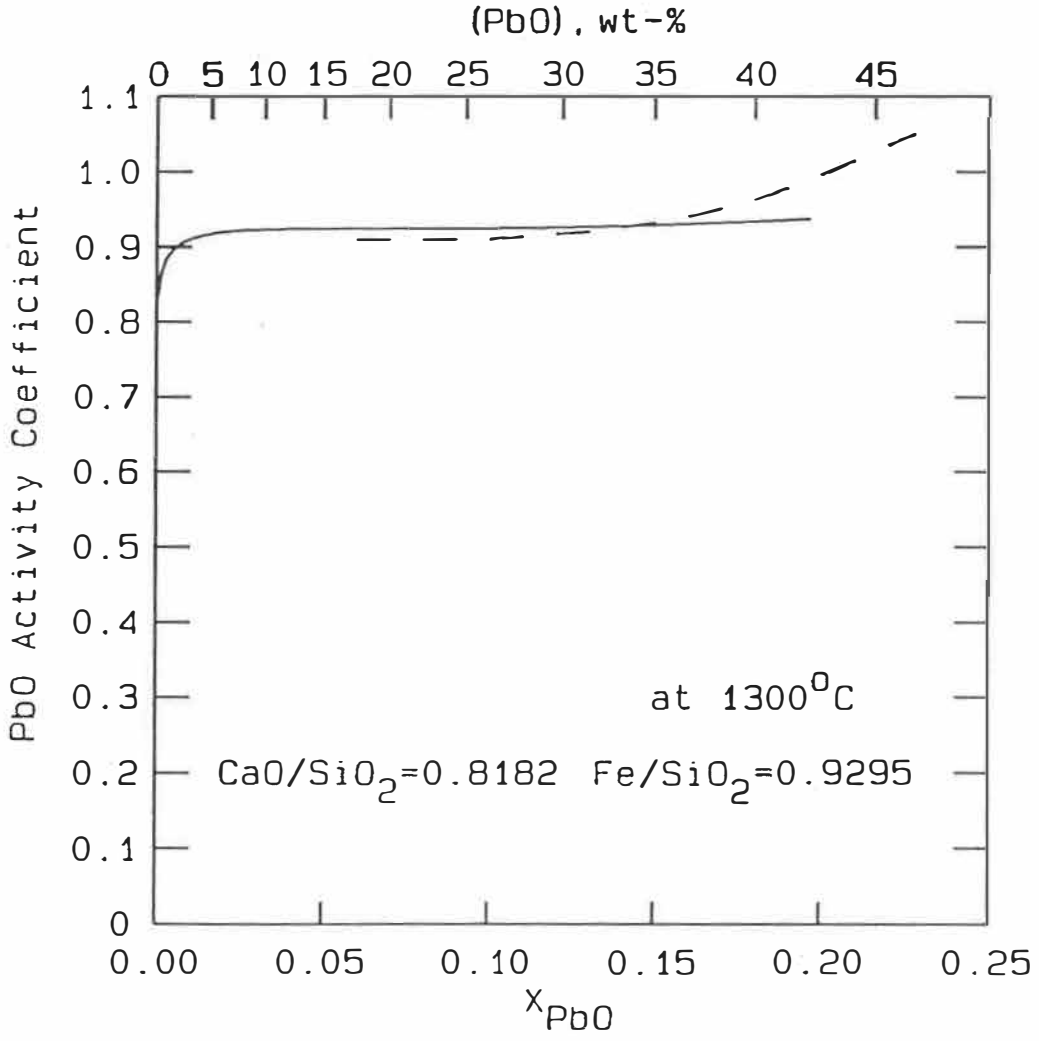


Fig. 5-14 Experimental [84Tas] and calculated PbO(liq) activity coefficients in PbO-FeO-CaO-SiO_2-Fe_2O_3 slags in equilibrium with liquid Pb.

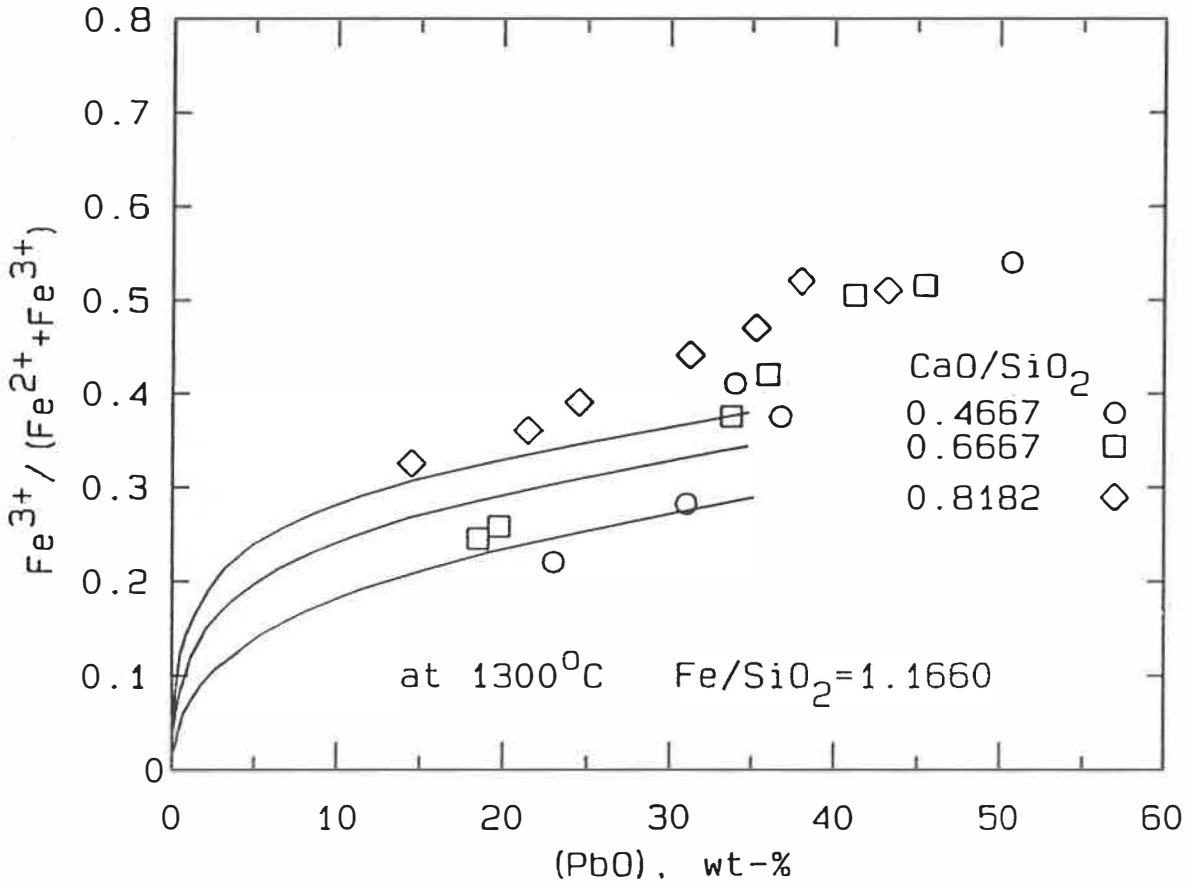


Fig. 5-15 Experimental [84Tas] and calculated $Fe^{3+}/(Fe^{2+}+Fe^{3+})$ ratios in PbO-FeO-CaO-SiO_2-Fe_2O_3 slags in equilibrium with liquid Pb.

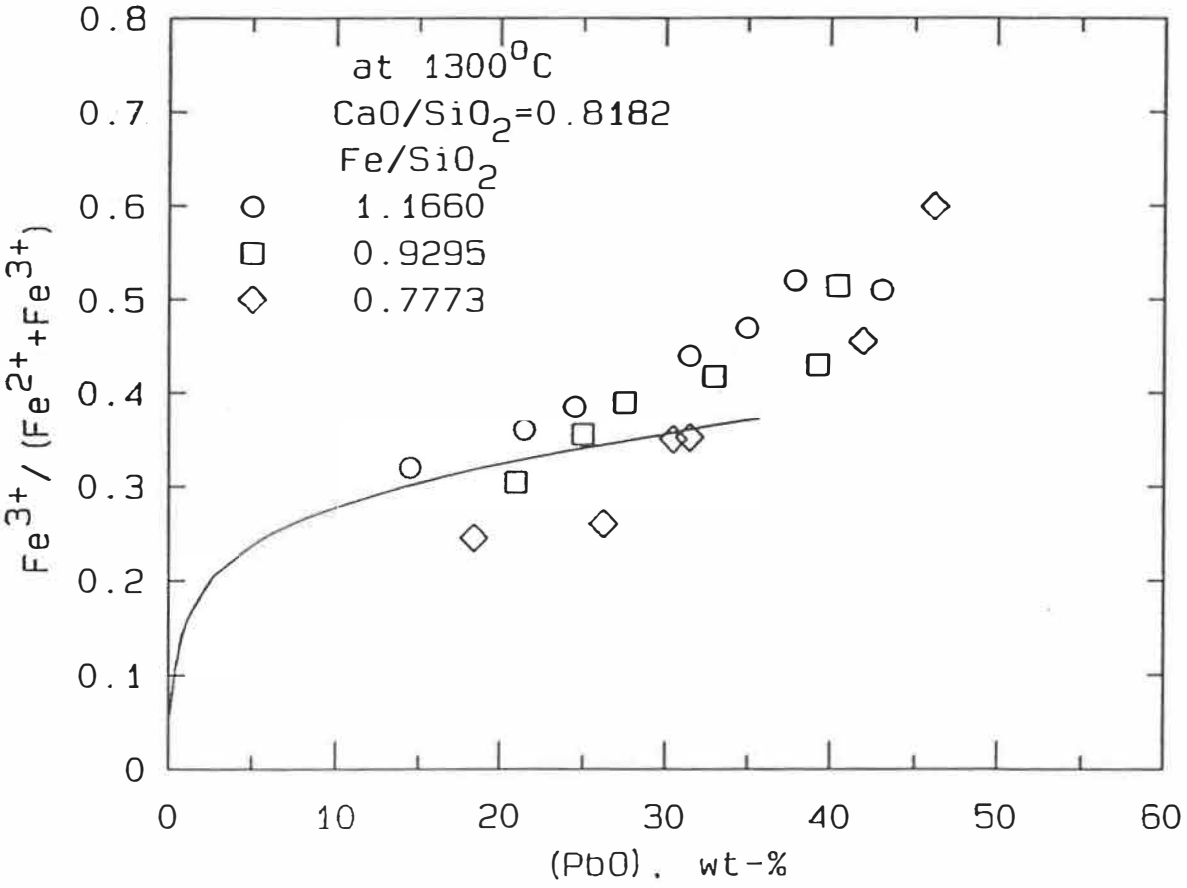


Fig. 5-16 Experimental [84Tas] and calculated $Fe^{3+}/(Fe^{2+}+Fe^{3+})$ ratios in PbO-FeO-CaO-SiO_2-Fe_2O_3 slags in equilibrium with liquid Pb.

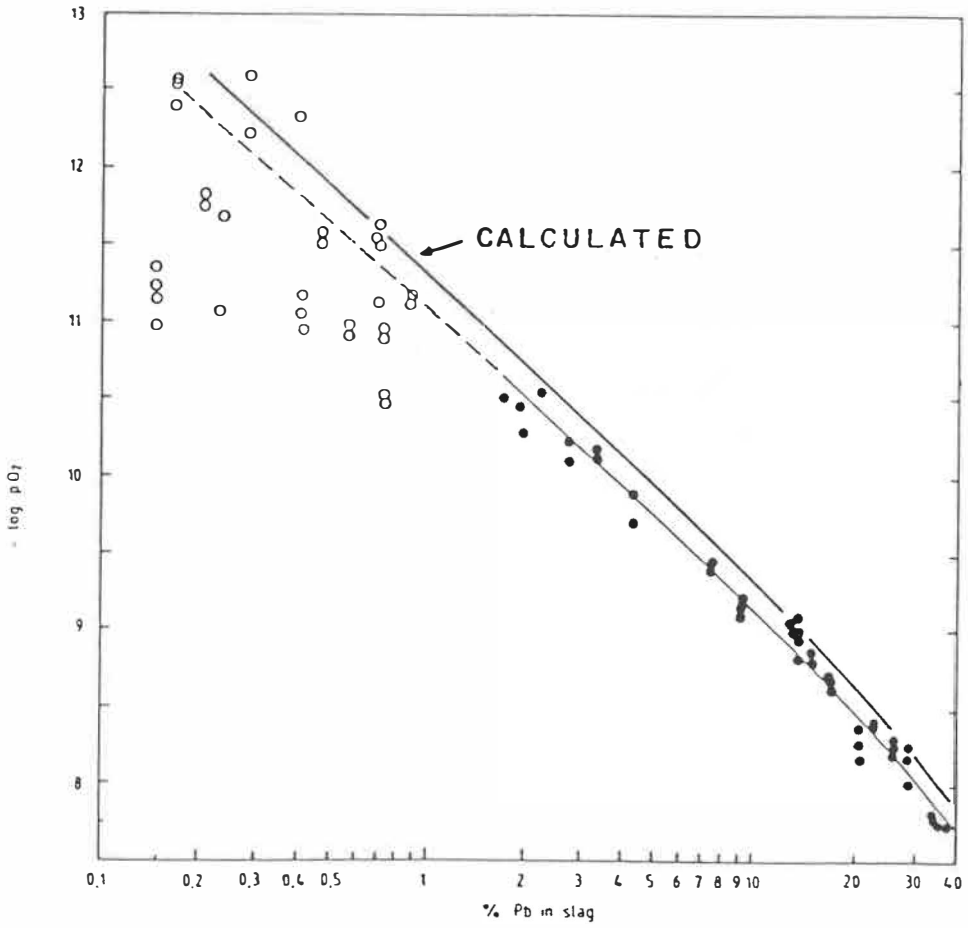


Fig. 5-17 Pb content versus oxygen pressure for lead blast furnace type slags "normalized" to 1150°C and a CaO/SiO_2 weight ratio of 0.6 as reported by [85Fon] and as calculated by assuming a typical slag composition.

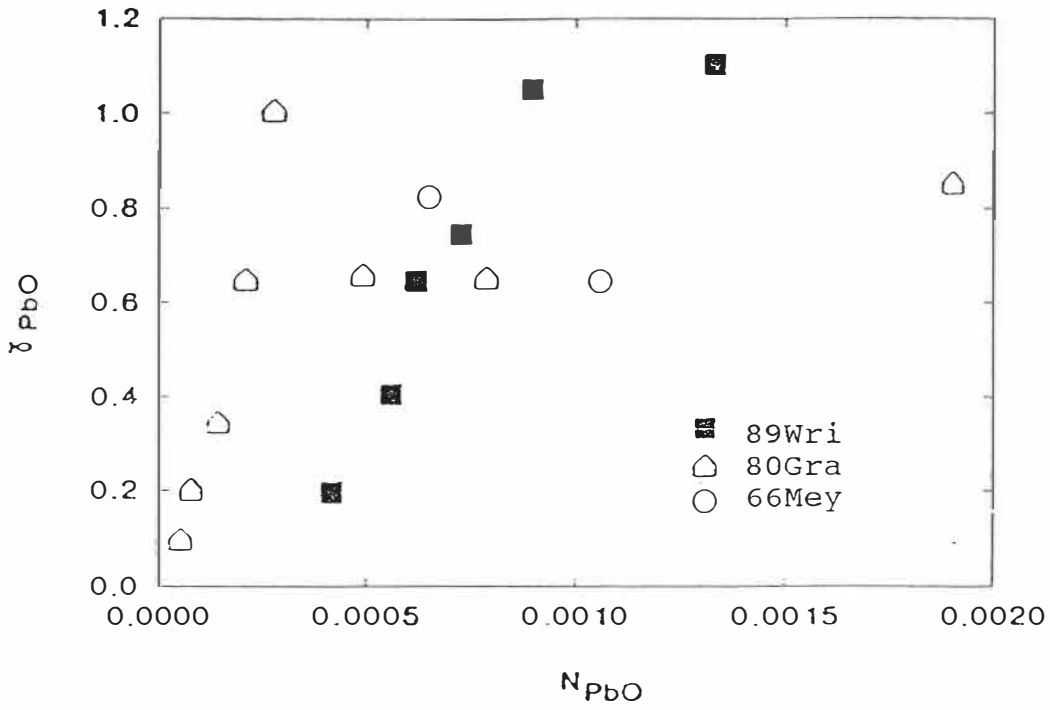


Fig. 5-18 Reported PbO activity coefficient data [66Mey, 80Gra, 89Wri] at low PbO content.

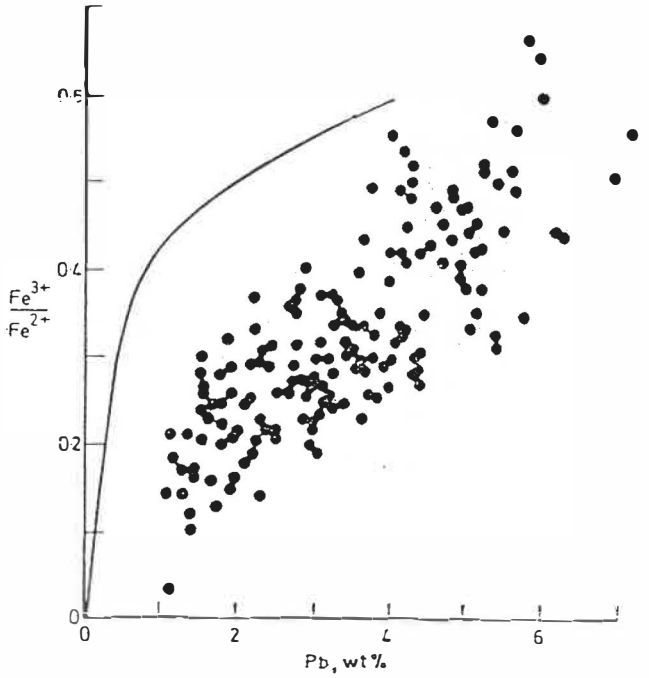


Fig. 5-19 Fe^{3+}/Fe^{2+} ratio versus Pb content of quenched blast furnace slags as reported by [79Ril]. Line shown is calculated dissolved Pb content calculated at 1225°C for the average slag composition given by [79Ril]. The experimental lead contents comprise from 50 to 100% entrained bullion.

TABLE 5-1

Typical compositions of lead blast furnace slags and bullion wt.% [91CAN]

	slag			bullion
	≥	≤	avg	
ZnO	6.5	13.9	10.0	
Pb	0.5	13.0	4.08	95.3
FeO*	30.8	43.5	38.4	
Cu	0.06	2.6	0.22	2.75
SiO_2	16.0	29.6	21.5	
CaO	13.0	21.5	17.8	
S	0.12	9.5	1.59	0.5
As			0.38	0.8
Cd			0.11	
Sb	-	-	-	0.7
Bi	-	-	-	0.4
mag coeff**	3	57	24	

* total iron calculated as FeO.
** magnetic coefficient of reagent grade Fe_3O_4 is considered to be 100.

TABLE 5-2

Optimized binary parameters ω_{A-B}^{j0} and ternary parameters $\omega_{AB(C)}^{jk}$ of the quasichemical model for molten PbO-ZnO-SiO_2-FeO-Fe_2O_3-CaO slags in cal/equivalent.

BINARY PARAMETERS

A	B	j	ω_{AB}^{j0}
$FeO_{1.5}$	SiO_2	0	4000
		1	12500
FeO	$FeO_{1.5}$	1	-3386
		7	7853
CaO	$FeO_{1.5}$	0	-7159
		1	-18404
PbO	ZnO	0	-2246
PbO	$FeO_{1.5}$	0	-1713
ZnO	SiO_2	0	-22467
		1	14643
PbO	SiO_2	0	-5919
		1	-2084
PbO	CaO	0	-11325
PbO	FeO	0	-1713

TABLE 5-2 - (Continued)

TERNARY PARAMETERS

A	B	C	j	k	$\omega^{jk}_{AB(C)}$
FeO	$FeO_{1.5}$	CaO	0	1	3700
CaO	SiO2	PbO	0	1	10000
PbO	SiO_2	ZnO	0	1	7700
ZnO	SiO_2	CaO	0	1	15270
FeO	SiO_2	ZnO	0	1	6500
FeO	SiO_2	PbO	0	3	-7000
CaO	SiO_2	FeO	0	1	7500

TABLE 5-3

Comparison of measured [83Rey] and calculated activities of ZnO (relative to the solid standard state) in molten $ZnO-SiO_2$ slags at 1560°C

X_{SiO_2}	a_{ZnO} (expt)	a_{ZnO} (calc)
0.640	0.033	0.078
0.600	0.035	0.082
0.520	0.051	0.093
0.450	0.10	0.11
0.330	0.27	0.26
0.280	0.39	0.48
0.250	0.62	0.64
0.230	0.89	0.76

TABLE 5-4

Comparison of calculated and reported [600sb] oxygen isobars at the eight points shown on Fig. 5-17 for the $FeO-Fe_2O_3-SiO_2$ system

Composition (wt.%)

P_{O_2} (atm)		SiO_2	FeO	Fe_2O_3	T(°C)
10^{-11}	expt	22.5	68.3	9.2	1164
	calc	22.5	68.3	9.2	1166
10^{-11}	expt	36.6	58.8	4.6	1168
	calc	36.6	57.8	5.6	1168
10^{-10}	expt	35.3	57.4	7.3	1155
	calc	35.3	57.4	7.3	1136
10^{-10}	expt	22.0	64.5	13.5	1155
	calc	22.0	66.5	11.5	1140
10^{-8}	expt	34.0	52.0	14.0	1200
	calc	34.0	52.0	14.0	1208
10^{-8}	expt	13.5	63.0	23.5	1255
	calc	13.5	63.0	23.5	1257
10^{-6}	expt	32.0	46.0	22.0	1300
	calc	32.0	46.0	22.0	1307
10^{-6}	expt	0.0	61.5	38.5	1423
	calc	0.0	61.5	38.5	1415

TABLE 5-5
Comparison of measured [84Toi] and calculated activities of PbO(liq) in $PbO-SiO_2-ZnO$ slags at 1000°C

Mole fractions				
X_{SiO_2}	X_{PbO}	X_{ZnO}	a_{PbO} (expt)	a_{PbO} (calc)
0.50	0.45	0.05	0.125	0.122
0.50	0.40	0.10	0.110	0.103
0.50	0.35	0.15	0.090	0.090
0.60	0.36	0.04	0.080	0.075
0.60	0.32	0.08	0.075	0.065
0.60	0.28	0.12	0.070	0.058

TABLE 5-6
Comparison of measured [82Tas] and calculated activities of PbO(liq) in $PbO-SiO_2-CaO$ slags at 1000°C

Mole fractions				
X_{SiO_2}	X_{PbO}	X_{CaO}	a_{PbO} (expt)	a_{PbO} (calc)
0.50	0.45	0.05	0.14	0.130
0.50	0.40	0.10	0.13	0.118
0.60	0.36	0.04	0.075	0.068
0.60	0.32	0.08	0.065	0.054
0.60	0.28	0.12	0.055	0.045

TABLE 5-7

Comparison of experimental [78Fil] and calculated activities of FeO (liq. standard state) and ZnO (solid standard state) in FeO-CaO-ZnO-SiO_2 slags at 1250°C.

Composition - weight %

FeO	SiO_2	CaO	ZnO	a_{FeO} (expt)	a_{FeO} (calc)	a_{ZnO} (expt)	a_{ZnO} (calc)
53.3	28.3	12.7	5.7	----	----	0.82	0.81
52.4	32.4	10.5	4.8	0.49	0.50	----	----

TABLE 5-8

Comparison of calculated activity coefficients of PbO(liq) in slags with those reported by Willis [80Wil, 66Mey].

Slag Composition (wt. %)

FeO	Fe_2O_3	CaO	SiO_2	ZnO	γ_{PbO} (expt)	γ_{PbO} (calc)
53	5	13	29	0	0.81	0.51
53	5	20	22	0	1.21	0.87
75	7	0	18	0	0.31	0.23
0	0	18	32	50	2.0	1.25

CONCLUSIONS

A thermodynamic database for oxide systems has been successfully developed. As a result, all thermodynamic as well as phase diagram data of an oxide system are represented and stored by means of a small set of coefficients. This greatly reduces the data needed to characterize fully the system. Moreover, because of the thermodynamic consistency in the whole process, interpolation and extrapolation using these coefficients are quite rational. The Gibbs energy equation of a multi-component oxide solution can be constructed from those of its sub-binary and sub-ternary systems. Consequently, multi-component multiphase equilibria involving oxides with other phases such as gas, metals etc. can be predicted by Gibbs energy minimization programs (such as EQUILIB) using the present database. These are the original motivations of the present study.

To build a database, proper thermodynamic models have first to be selected to supply the Gibbs energies expressions for all phases involved. Simple models such as the Raoultian, regular or polynomial solution models have been employed for solid oxide solutions. In oxide slags, however, wide variations from liquid ideality are observed. Hence, a general solution model which can be applied to both ordered and non-ordered systems is preferred for the liquid phase. As discussed in Chapter 1, although polynomial solution models

are the simplest, they cannot, however, correctly represent the ordering effects which commonly exist in silicate slags. Furthermore, thermodynamic properties of higher order systems cannot be properly approximated from their sub-systems by polynomial solutions models. Other models include the structure-based silicate models, which are successfully applied in silicate slags in spite of their complexity. If the database is to be built by means of only one model, most of the structure-based silicate models are not acceptable because of their complexity and they can be employed only in silicate slags. The cell model and two-sub-lattice silicate model have been applied successfully in studies of both silicate melts and non-silicate oxide systems. The cell model is appealing theoretically because it claims that no ternary but only binary parameters are needed to approximate thermodynamic properties of a multi-component oxide solution. However, in practice it is very difficult to precisely reproduce ternary oxide phase diagrams by means of the cell model. On the other hand, although many successful studies of oxide systems have been made by means of the sub-lattice model [90Hil1], the model is still under development to revise the assumption of charged vacancies in the liquid phase. Therefore, the modified quasi-chemical model has been chosen to build the present thermodynamic oxide database.

According to the modified quasi-chemical model, thermodynamic properties (such as ΔG and ΔH) are non-linear functions of the model coefficients ω_i and η_i (i=0,1,...7). Hence, non-linear least squares techniques have been developed. In the binary optimization practice, the first-order Taylor expansion at an estimated $(\omega^* - \eta^* T)$ point which is a linear function of $(\omega - \eta T)$, was accepted for this function formalism. By a linear least squares regression, $(\omega - \eta T)$ was calculated and was considered as the estimated $(\omega^* - \eta^* T)$ value for next iteration. As the iterations continue, a correct value of $(\omega - \eta T)$ will be reached. In certain oxide systems, reliable knowledge about the entropy or enthalpy in the solutions may be available. A binary optimization program called FITQUAS has been written with which all thermodynamic and phase diagram data of the liquid phase can be evaluated. Thermodynamic properties of intermediate compounds such as entropy or enthalpy of formation can be indirectly evaluated as well. Details of evaluation of 26 binary oxide systems have been discussed in Section 2.3. From the calculated quasi-chemical parameters and the quasi-chemical model one can calculate both thermodynamic properties and phase diagram of the system. In this way, all liquid and solid thermodynamic properties and phase diagram data are internally consistent with each other. The thermodynamic properties may then be reliably extrapolated or interpolated. They may be used for the construction of phase diagrams for higher order systems.

Thermodynamic internal consistency has been demonstrated in Chapter 3 when evaluating the series of rare earth oxide-Al_2O_3 binary systems. Trends in the properties as one proceeds along the series can be exploited in order to refine the assessments and to predict properties by interpolation or extrapolation. A critical assessment of all 15 R_2O_3-Al_2O_3 systems has been performed and thermodynamic properties of all compounds have been predicted along with the thermodynamic properties of the liquid solutions, although for 3 of the 15 systems no phase diagrams have been previously reported.

The modified quasi-chemical model has been successfully extrapolated to ternary and multi-component systems by Pelton and Blander [86Pel]. The non-linear ternary optimization may be performed based on a simple gradient method. In the present study, two improvements have been made to the ternary optimization program so that ternary immiscibility gap data can be optimized simultaneously with other thermodynamic and phase diagram data. The ternary optimization remains valid even for very large ternary terms. In Section 4.2, details of evaluations of 8 ternary oxide systems have been discussed. The liquid phase has been optimized by the ternary optimization program based on the modified quasi-chemical model. In the optimization, only relatively small ternary parameters were normally required to reproduce the phase

diagram. Even for some complicated ternary systems where extremely negative (indicated by the formation of a ternary compound) and large positive (immiscibility gap was formed) deviations coexisted in the liquid phase, the phase diagrams can also be well evaluated by using the quasi-chemical model. Hence, the quasi-chemical model as well as the ternary optimization program are very efficient in ternary thermodynamic calculations.

In Section 4.3, to demonstrate multi-component multiphase equilibria calculations using the present database, phase equilibria in the ZrO_2-Al_2O_3-TiO_2-SiO_2 system have been predicted. Agreement with experimental data is good.

In Chapter 5, by optimizing all the available thermodynamic and phase equilibrium data of all the sub-systems of the PbO-ZnO-SiO_2-FeO-Fe_2O_3-CaO slag, a thermodynamic database has been built using the modified quasi-chemical model. Furthermore, the database can be used by the F*A*C*T computer [85Tho] system to calculate the equilibrium composition of lead smelting slags, if P_{O_2} is known and if the composition of the bullion is known. Therefore, one can predict the PbO content and the $Fe^{+3}/(Fe^{+2}+Fe^{+3})$ ratio of the slags. Agreement of our prediction with the available experimental results is good over a wide composition and temperature range.

At present, all liquid phases and all solid compounds (except the solid compounds containing PbO) of 84 binary systems listed in Table 2-1 as well as 28 ternary slags shown in Table 4-7 and 4-8 have been evaluated. In addition, 3 quaternary systems ZrO_2-TiO_2-SiO_2-Al_2O_3, FeO-Fe_2O_3-CaO-SiO_2 and FeO-CaO-ZnO-SiO_2, and 1 quinary system PbO-SiO_2-CaO-Fe_2O_3-FeO have been successfully predicted.

In a multi-component multiphase system, as shown in Chapter 5, the present database can be used to provide the Gibbs energy expression of a multi-component slag phase, while other databases (Gas, Alloy etc.) in the F*A*C*T system can provide the Gibbs energy expressions for other phases. Therefore, by minimizing the total Gibbs energy of the multi-component multiphase system (through the free-energy minimization programs of the F*A*C*T system) complex equilibria involving slags containing SiO_2, TiO_2, Al_2O_3, FeO, Fe_2O_3, CaO, MgO, MnO, PbO, ZnO, Na_2O, K_2O, ZrO_2 NiO Ti_2O_3 and rare earth oxides can be calculated. Multi-component and multiphase equilibria can thus be reasonably predicted with the present database.

REFERENCES

1895Mar: M. Margules, Sizungsber. Akad, Wiss, Wien, Mathem. Naturwiss. KL., 11a, 104, 1243 (1895).

08Rie : R. Rieke, Sprechsaal, 41, 405-406 (1908).

08Van: J.J. Vanlaar, Z. Physik. Chem. 63, 216 (1908); 64, 257(1908)

09She : E.S. Shepherd, G.A. Rankin and F.E. Wright, Am. J. Sci., 28, 293-333 (1909).

11Doe : F. Doerinckel, Metallurgie,8, 201 - 209 (1911).

11Leb : P. Lebedev, Z. Anorg. Chem., 70, 301 - 324 (1911).

12Smo : S. Smolenskii, Z. Anorg. Chem., 73, 293 - 303 (1912).

14Bow : N.L. Bowen and O. Andersen, Am. J. Sci., 37, 487 - 500 (1914).

14Kal : S. Kallenberg, Z. Anorg. Chem., 88, 355 - 363 (1914).

15Ran : G.A. Rankin and F.E. Wright, Am. J. Sci., 39, 1-79 (1915).

16Jae : F.M. Jaeger and H.S. van Klooster, Proc. Akad. Wetenschappen, 18, 896-913 (1916).

16Ran : G.A. Rankin and H.E. Merwin, J. Am. Chem. Soc., 38, 568 - 588 (1916).

18Ran : G.A. Rankin and H.E. Merwin, Am. J. Sci., 45, 301-325 (1918).

20Was : E.W. Washburn and E.E. Libman, J. Amer. Ceram. Soc., 3, 634-40 (1920).

23Mat : C. Matignon, Compt. Rend., 177, 1290-1293 (1923).

24Bow : N.L. Bowen and J.W. Greig, J. Am. Ceram. Soc., 7, 238-254 (1924).

26Gla : O. Glaser, Centr. Miner. Goel., Abt. A, 81 - 96 (1926).

27Gre : J.W. Greig, Am. J. Sci., 13, 1-44, 133 - 154 (1927);Ibid, 14, 473 - 484 (1927).

28War : H.V. Wartenberg, H. Linde and R. Jung, Z. Anorg. Allg. Chemie. 176, 349 (1928).

29Sch : R. Schenck, H. Franz and H. Willeke, Z. Anorg. Allg. Chem., 184, 1 - 38 (1929).

30Bun: E.N. Bunting, Bur. Standards J. Research, 4, 131-136 (1930).

30Dan : J. D'Ans and J. Loeffler, Z. Anorg. Allg. Chem., 191, 1-34 (1969).

30Her : C. H. Herty Jr., Metals & Alloys, 1, 883 - 889 (1930).

30Kra1: F.C. Kracek, J. Am. Chem. Soc., 52, 1436 - 1442 (1930).

30Kra2: F.C. Kracek, J. Phys. Chem., 34, 1583-1598 (1930).

30Mey : S.L. Meyers, Rock Products, 33, 78-79 (1930).

30Ume : S. Umezu and F. Kakiuchi, Nippon Kogyo Kwaishi, 46, 866 - 877 (1930).

31Car : E.T. Carlson, Rock Products, 34, 52-56 (1931).

32Bar : H.B. Bartlett, J. Amer. Ceram. Soc., 14, 837-843 (1932).

32Bow : N.L. Bowen and J.F. Schairer, Am. J. Sci., 24, 177 - 213 (1932).

32Von1: H. von Wartenberg and H.J. Reusch, Z. Anorg. Allg. Chem., 207, 1 - 20 (1932).

32Von2: H. von Wartenberg and E. Prophet, Z. Anorg. Allg. Chem., 208, 369 - 379 (1932).

33Bun : E.N. Bunting, Bur. Standards J. Research, 11, 719 - 725 (1933).

33Ruf : O. Ruff, F. Ebert and U. Krawczynski, Z. Anorg. Allg. Chem., 213, 333 - 335 (1933).

34Bor : G. Borelius, Ann, Physik, series 5, 20, 57 (1934).

34Fuk: M. Fukusima, Kinzoku-no-Kenkyu, Tokyo, 11, 428-40, 377-95, 590-600 (1934).

34Whi : J. White, D. D. Howat and R. Hay, J. Roy. Tech. Coll. (Glasgow), 3, 231 - 240 (1934).

34Zhi : N. Zhirnowa, Z. Anorg. Allgem. Chem., 218, 193-200 (1934).

35Bow : N.L. Bowen and J.F. Schairer, Am. J. Sci., 29, 157-217 (1935).

35Hay : R. Hay, J. White and A.B. McIntosh, J. West Scot. Iron Steel Inst., 42, 99-104 (1935).

35Voo : E. Voos, Veroeffentl. Kaiser Wilhelm-Inst. Silikatforsch. Berlin - Dahlem, 7, 65 - 81 (1935).

36Bog : D. Bogatskii, Metallurgy (USSR), 1, 59-67 (1936).

36Hay : R. Hay, A.B. McIntosh, J.R. Rait and J. White, J. West Scot. Iron Steel Inst., 44, 85-92 (1936/37).

36Iwa: K. Iwase and M. Fukusima, Science Repts. Tohoku Imp. Univ., Series 1, Honda Anniv. Vol., pp. 454-64 (Oct. 1936); Ceram. Abstr., 16[5] 162 (1937).

36Jun : E. Junker, Z. Anorg. Allg. Chem., 228, 97-111 (1936).

37Kra : F.C. Kracek, N.L. Bowen and G.W. Morey, J. Phys. Chem., 41, 1183 - 1193 (1937).

37Lag : K. Lagerqvist, S. Wallmark and A. Westgren, Z. Anorg. Allg. Chem., 234, 1-16 (1937).

37Sko : V. Skola, Keram. Rundschau, 45, 188-190, 200-202, 212-213, 215 (1937).

37Von : H. von Wartenberg, H.J. Reusch and E. Saran, Z. Anorg. Allg. Chem, 230, 257 - 276 (1937).

38Hou : E. Houdremont, Stahl u. Eisen, 58, 1185-99 (1938)

39Ehr : P. Ehrlich, Z. Elektrochem., 45, 362-370 (1939).

39Gri : J. Grieve and J. White, J. Roy. Tech. Coll. (Glasgow), 4, 444 (1939).

39Gug: E.A. Guggenheim: Proc. Roy. Soc., 1035, A148, 304; R.H. Fowler and E.A. Guggenheim; Statistical Thermidynamics, Cambridge, 350-66 (1939).

39Kra : F.C. Kracek, J. Am. Chem. Soc., 61, 2863-2877 (1939).

40Gri : J. Grieve and J. White, J. Roy. Tech. Coll. (Glasgow), 4, 660 - 670 (1940).

41Oel : W. Oelsen, W. Middel and H. Maetz, Mitt. Kaiser Wilhelm-Inst. Eisenforsch., 23, 195-245 (1941).

43Osb : E.F. Osborn, J. Am. Ceram. Soc., 26, 321-332 (1943).

45Dar: L.S. Darken and R.W. Gurry, J. Am. Chem. Soc., 67, 1398-1412 (1945).

45Jay: A. H. Jay and K. W. Andrews, J. Iron Steel Inst., London, Cl II, 15 (1945).

45Tem: M. Temkin, Acta Physicochim., URSS, 20, 411-20 (1945).

48Red: O. Redlich and A.T. Kister, Ind. Engng. Chem. 40, 345 (1948)

48Zaw : J. Zawadski and J. Gotlieb, Bull. Intern. Acad. Polon. Sci., Classe Sci. Math. Nat., Ser. A, 1940-1946, 32-34 (1948).

49Fil : N.E. Filonenko and I.V. Lavrov, Dokl. Akad. Nauk S.S.S.R., 66, 673-676 (1949).

49For : W.F. Ford and J. White, Trans. Brit. Ceram. Soc., 48, 417 - 427 (1949).

49Gel : R.F. Geller and S.M. Lang, J. Amer. Ceram. Soc., 32, 157 (1949).

49Tro : F. Trojer and K. Konopicky, Radex-Rundschau, 4, 161 - 162 (1949).

50Ber: A. S. Berezhnoi,Ogneupory, 15 [8] 350-59; [10] 446-53 (1950); Ceram. Abstr., 1951, April, p. 66h.

50Fil : N.E. Filonenko and I.V. Lavrov, Zh. Priklad. Khim., 23, 1040-1046 (1950).

50Hil: J.H. Hildebrand and R.L. Scott, The solubility of Nonelectrolytes, 3rd. ed. Reinhold Publishing Corp., New York (1950)

51Cou : J.P. Coughlin, E.G. King and K.R. Bonnickson, J. Am. Chem. Soc., 73, 3891-3893 (1951).

51Ols : Ya. I. Ol'shanskii, Dokl. Akad. Nauk SSSR, 76, 93 - 96 (1951).

51Ric : R.W. Ricker and F.A. Hummer, J. Am. Ceram. Soc., 34, 271-279 (1951).

51Sch : R. Schuhmann Jr. and P.J. Ensio., J. Metals., 3, 401 - 411 (1951).

51Sow : H.G. Sowinan and A.I. Andrews, J. Am. Ceram. Soc., 34, 298-301 (1951).

51Tor : N.A. Toropov and F. Ya. Galakhov, Dokl. Akad. Nauk S.S.S.R., 78, 299-302 (1951).

52Aga : W.M. Agamawi and J. White, Trans. Brit. Ceram. Soc., 51, 293-325 (1952).

52Duw : P. Duwez, F. Odell and F.H. Brown, Jr., J. Am. Ceram. Soc., 35, 107-13 (1952).

52Lan : S.M. Lang, C.L. Fillmore and L.H. Maxwell, J. Research Natl. Bur. Standards, 48, 298 - 312 (1952).

53Aga : W. M. Agamawi and J. White, Trans. Brit. Ceram. Soc., 52 [6] 271-310 (1953).

53Cou : L.W. Coughanour and V.A. DeProsse, J. Research Natl. Bur. Standards, 51, 85 - 88 (1953).

53Cur : C.E. Curtis and H.G. Sowman, J. Amer. Ceram. Soc., 36, 190-98 (1953).

53Dar : L.S. Darken and R.W. Gurry, Physical Chemistry of Metals, p.340, McGraw-Hill Book Co., New York, 1953.

53Die : A. Dietzel and H. Tober, Ber. Dtsch. Keram. Ges., 30, 47 (1953); Ibid, 30, 71 (1953).

53Roy : D.M. Roy, R. Roy and E.F. Osborn, Am. J. Sci., 251, 337-361 (1953).

54Bro : F.H. Brown and P. Duwez, J. Am. Ceram. Soc. 37, 129-32 (1954).

54Bud : P.P. Budnikov and S.G. Tresvyats'kii, Dopovidi Akad. Nauk, Ukr. R.S.R., 371-376 (1954).

54Cou : L.W. Coughanour, R.S. Roth and V.A. DeProsse, J. Research Natl. Bur. Standards, 52, 37-42 (1954).

54Dev1: R.C. DeVries, R. Roy and E.F. Osborn, J. Phys. Chem., 58, 1069 - 1073 (1954).

54Dev2: R.C. DeVries, R. Roy and E.F. Osborn, Trans. Brit. Ceram. Soc., 53, 525-40 (1954).

54McK : I.J. McKeand, Ph.D. thesis, University of Illinois (1954).

54Pri : I. Prigogine and R. Defay, Chemical Thermodynamics, Longmans Green and Co. London (1954)

54Ric : F.D. Richardson and L.E. Webb, Trans. Inst. Min. Met., London, 65, 529 (1954-55).

54She : E.C. Shears and W.A. Archibald, Iron & Steel (London), 27, 26-30, 61-66 (1954).

55All : W.C. Allen and R.B. Snow, J. Am. Ceram. Soc., 38, 264 - 280 (1955).

55Ber : A.S. Berezhnoi and N.V. Gul'ko, Dopovidi Akad. Nauk Ukr. R.S.R., 1, 77-80 (1955).

55Cou : Coughanour, L. W., Roth, R. S., and Marzullo, S., J. Research Natl Bur. Stand., 54, 153 (1955).

55Dav : M. W. Davies, PhD. Thesis, Imperial College, London (1955).

55Dev : R.C. DeVries, R. Roy and E.F. Osborn, J. Am. Ceram. Soc., 38, 158-171 (1955).

55Ell : J.F. Elliott, J. Metals, 7, 485 (1955).

55Kin : E.G. King, J. Phys. Chem., 59, 218-219 (1955).

55Oel : W. Oelsen and G. Heynert, Arch. Eisenhuttenw., 26, 567-575 (1955).

55Sch : J.F. Schairer and N.L. Bowen, Am. J. Sci., 253, 681-746 (1955).

55Wis : L.G. Wisnyi, PhD. Thesis, Rutgers University, New Jersey (1955).

56Bud : P.P. Budnikov and A.A. Litvakovskii, Doklady Akad. Nauk S.S.S.R., 106, 267-70 (1956).

56Cou : J.P. Coughlin, J. Am. Chem. Soc., 78, 5479-5482 (1956).

56Fis : W.A. Fischer and A. Hoffmann, Arch. Eisenhuttenw., 27, 343-346 (1956).

56Fos : P.K. Foster and A.J.E. Welch, Trans. Faraday Soc., 52, 1636 - 1642 (1956).

56Kon : K. Konopicky, Bull. Soc. Franc. Ceram., 33, 33-36 (1956).

56Mat : M.A. Matveev, Proc. Acad. Sci. USSR Sect. Chem., 107, 177 (1956).

56Nis : H. Nishimura and H. Kimura, J. Jpn. Inst. Met., 20, 524-527 (1956).

56Sch : J.F. Schairer and N.L. Bowen, Am. J. Sci., 254, 129-195 (1956).

56Tor : N.A. Toropov and F.Y. Galakhov, Izv. Akad. Nauk SSSR, Otd. Khim. Nauk, No. 2, 153-56 (1956).

56Tor1: N.A. Toropov, F.Ya. Galakhov and I.A. Bondar, Izv. Akad. Nauk S.S.S.R., Otdel. Khim. Nauk, 641-648 (1956).

57And : S. Andersson, B. Collen, U. Kuylenstierna and A. Magneli, Acta Chem. Scand., 11, 1641-1652 (1957).

57Car : P.T. Carter and T.G. Macfarlane, J. Iron Steel Inst. (London), 185, 54-66 (1957).

57Fis : W.A. Fischer and A. Hoffmann, Arch. Eisenhuttenw., 28, 743 (1957).

57Kle : O.J. Kleppa, Thermodynamics and Properties of Liquid Solution, Liquid Metals and solidification, Am. Soc. Metals, Cleveland, 1957.

57McT : G.D. McTaggart and A.I. Andrews, J. Am. Ceram. Soc., 40, 167-70 (1957).

57Saa : H. Saalfeld and H. Jagodzinski, Z. Krist., 109, 87-109 (1957).

57Tro : G. Troemel, K.H. Obst, K. Konopicky, H. Baur and I. Patzsak, Ber. Deut. Keram. Ges, 34, 397-402 (1957).

58Bai : J.D. Baird and J. Taylor, Trans. Faraday Soc., 54, 526 - 539 (1958).

58Bis : H.L. Bishop Jr., N.J. Grant and J. Chipman, Trans.-AIME 212, 185-192 (1958).

58Coc : A. Cocco and A. Schromek, Ceramica, 12, 45-48 (1958).

58Gal : F.Ya. Galakhov, Izvest. Akad. Nauk S.S.S.R., Otdel. Khim. Nauk, 529-34 (1958).

58Gel : G. Gelsdorf, H. Mueller-Hesse and H.E. Schwiete, Arch. Eisenhuttenw., 29, 513-519 (1958).

58Gla : F.P. Glasser, Am. J. Sci., 256, 398-412 (1958).

58Mas : F. Massazza and E. Sirchia, Chim. Ind. (Milan), 40, 376 - 380 (1958).

58Mas1: F. Massazza and E. Sirchia, La Chimica e L'Industria, 40, 460-467 (1958).

58Mua : A. Muan, Am. J. Sci., 256, 171-207 (1958).

58Rot : R.S. Roth, J. Research Natl. Bur. Standards, 61, 437 - 440 (1958).

58Tur : E.T. Turkdogan and R.A. Hancock, Bull. Inst. Mining Met., 621, 573 - 600 (1958).

59Bod : C. Bodsworth, J. Iron Steel Inst. (London), 193, 13 - 24 (1959).

59Sch : O. Schmitz-DuMont and H. Reckhard, Monatsh., 90, 134-142 (1959).

59Wel : J.H. Welch and W. Gutt, J. Am. Ceram. Soc., 42, 11-15 (1959).

60Abr : K.P. Abraham, M.W. Davies and F.D. Richardson, J. Iron Steel Inst. (London), 196, 82 - 89 (1960).

60Bra : G. Brauer and W. Littke, J. Inorg. Nucl. Chem., 16, 67-76 (1960).

60Fre : A.S. Frenkel', K.M. Shmukler, B. Ya. Sukharevskii and N.V. Gul'ko, Dokl. Akad. Nauk S.S.S.R., 130, 1095-1098 (1960).

60Ell : J.F. Elliott and M. Gleiser, "Thermochemistry for Steelmaking", Addison-Wesley, Reading, Mass. (1960).

60Kay : D.A.R. Kay and J. Taylor, Trans. Faraday Soc., 56, 1372-1386 (1960).

60Koh: F. Kohler, Monatsh. Chemie, 91, 738 (1960)

60Osb : E.F. Osborn and A. Muan, "Phase Equilibrium Diagrams of Oxide Systems", Am. Ceram. Soc. and The E. Orton Jr. Ceramic Foundation (1960).

60Phi : B. Phillips and A. Muan, J. Phys. Chem., 64, 1451-2 (1960).

60Zol : T. Zoltai and M.J. Buerger, Zeitschrift fur Kristallographie, 114, 1-8 (1960).

61Fis1: W.A. Fischer and H.J. Fleischer, Arch. Eisenhuttenw., 32, 1 - 10 (1961).

61Fis2: W.A. Fischer and H.J. Fleischer, Arch. Eisenhuttenw., 32, 305-313 (1961).

61Kle : O.J. Kleppa and L.S. Hersh, J. Am. Chem. Soc., 34, 351-358 (1961).

61Mac : J.B. MacChesney and A. Muan, Amer. Miner., 46, 572-582 (1961).

61McN : R.N. McNally, F.I. Peters and P.H. Ribbe, J. Amer. Ceram. Soc. 44, 491 (1961).

61Sch1: H.Schenck, M.G. Frohberg and T. El Gammal, Arch. Eisenhuttenw., 8, 509 - 511 (1961).

61Sch2: H. Schenck and W. Pfaff, Arch. Eisenhuttenw., 32, 741 - 751 (1961).

61Sch3: N.G. Schmahl, B. Frisch and F. Stock, Arch. Eisenhuttenw., 32, 297 - 302 (1961).

61Sha : R.A. Sharma and F.D. Richardson, J. Iron Steel Inst. (London), 198, 386-390 (1961).

61Suz : H. Suzuki, S. Kumura, H. Yamada and T. Yamauchi, J. Ceram. Assoc. Japan 69, 52 (1961).

61Wol : R. Wollast, Silic. Ind., 26, 89-92 (1961).

62Alp : A.M. Alper, R.N. McNally, P.H. Ribbe and R.C. Doman, J. Am. Ceram. Soc., 45, 263-268 (1962).

62Ara : S. Aramaki and R. Roy, J.Am. Ceram. Soc., 45, 229-242 (1962).

62Eng1 : H.J. Engell and H.K. Kohl : Z. Elektrochem., 66, 684 - 689 (1962).

62Eng2 : H.J. Engell, Z. Physik. Chem. (Frankfurt), 35, 192 - 195 (1962).

62Gla : F.P. Glasser, J. Amer. Ceram. Soc. 45, 242 (1962).

62Hah : W.C. Hahn Jr. and A. Muan, Trans.-AIME, 224, 416 - 420 (1962).

62Lej : A.M. Lejus and R. Collongues, Compt. Rend., 254, 2780-2781 (1962).

62Mou: A.J. Mountvala and S.F. Ravitz, J. Am. Ceram. Soc., 45, 286 (1962).

62Sha : R.A. Sharma and F.D. Richardson, J. Iron Steel Inst. (London), 200, 373-379 (1962).

62Sin : E.L. Singleton, L. Carpenter and R.V. Lundquist, U.S. Bur. Mines, Rept. Invest., no. 5938, 31 pp. (1962).

62Too : G.W. Toop and C.S. Samis, Trans. TMS-AIME 224, 878 (1962).

62Wan: C. Wangner, Thermodynamics of Alloys, Addison-Wesley, Erading, MA, 51 (1962)

62Zur : H. zur Strassen and C.H. Schmitt, Tonind. Ztg. Keram. Rundschau, 86, 222-226 (1962).

63Bau : M.P. Bauleke and K.O. McDowell, J. Am. Ceram. Soc., 46, 243 (1963).

63Dom : R.C. Doman, J.B. Barr, R.N. McNally and A.M. Alper, J. Am. Ceram. Soc., 46, 313 - 316 (1963).

63Fer : S. Fernandes and L. Beaudin, "Sub-Solidus Equilibria in the CaO-ZrO_2 System"; presented at the 21st Annual Pittsburgh Diffraction Conference, Mellon Institute, Pittsburgh, Pa., (November 1963).

63Flo : H. Flood and W.J. Knapp, J. Am. Ceram. Soc., 1963, vol. 46, pp. 61-65.

63Gen : A.L. Gentile and W.R. Foster, J. Am. Ceram. Soc., 46, 74-76 (1963).

64Alp : A.M. Alper, R.N. McNally and R.C. Doman, Bull. Amer. Ceram. Soc., 43, 643 (1964).

64Bon : I.A. Bondar and N.V. Vinogradova, Izv. Akad. Nauk S.S.S.R. Ser. Khim., 5, 785 (1964).

64For : T. Forland, Fused Salts, B.R. Sundheim, ed., McGraw-Hill, New York, NY, 1964, ch.2.

64Fro : V. Frohberg, Arch. Eisenhuttenwes., 35, 269-77 (1964)

64Har : A. Hardy, A. Lecerf, M. Rault and G. Villers, Compt. Rend., 259, 3462 - 3465 (1964).

64Jou : J. C. Joubert and A. Durif, Bull. Soc. Franc. Miner.. Crist., 87, 517 - 519 (1964).

64Lej : A.M. Lejus, Rev. Hautes Temp. Réfractaires, 1, 53-95 (1964).

64Mac : I.D. MacGregor, Carnegie Inst. Washington, Yearbook, 64, 137 (1964-65).

64Sch : H. Schenck, M.G.Frohberg and R. N. Nünninghoff, Arch. Eisenhuttenw., 35, 269 - 277 (1964).

65Coc : A. Cocco and G. Torriano, Ann. Chim. (Italy), 55, 162 (1965).

65Her : L.S. Hersh and O.J. Kleppa, J. Am. Chem. Soc., 42, 1309-22 (1965).

65Joh : R.E. Johnson and A. Muan, J. Am. Ceram. Soc., 48, 359-364 (1965).

65Kra : A. Krauth and H. Meyer, Ber. Dtsch. Keram. Ges., 42, 61 (1965).

65Lan : S.M. Lang, E.W. Franklin and N.J. Tylutki, Air Force, Off. Aerospace Res., Rep. ARL 65-140, p. 1-22 (1965).

65Lin : D.H. Lindsley, Year Book, Carnegie Institution, 64, 144 (1965).

65Mas : C.R. Masson, Proc. R. Soc., A287, 201-21 (1965).

65Meh : S.R. Mehta and F.D. Richardson, J. Iron Steel Inst. (London), 203, 524 - 528 (1965).

65Nov : I.A. Novokhatskii, B.F. Belov, A.V. Gorokh and A.A. Savinskaya, Zh. Fiz. Khim., 39, 2806-2808 (1965).

65Nur1: R.W. Nurse, J.H. Welch and A.J. Majumdar, Trans. Brit. Ceram. Soc., 64, 323-332 (1965).

65Nur2: R.W. Nurse, J.H. Welch and A.J. Majumdar, Trans. Brit. Ceram. Soc., 64, 409-418 (1965).

65Rei : R.H. Rein and J. Chipman, Trans. - AIME, 233, 415 - 425 (1965).

65Rol : M. Rolin and H.T. Pham, Rev. Hautes Temp. Réfractaires, 2, 175 - 185 (1965).

65Sch : C.M. Schlaudt and D.M. Roy, J. Am. Ceram. Soc., 48, 248 - 251 (1965).

65Sha : R.A. Sharma and F.D. Richardson, Trans. AIME, 233, 1586-1592 (1965).

65Smi : D.K. Smith and C.F. Cline, cited by D. Viechnicki and V.S. Stubican, J. Am. Ceram. Soc., 48, 292-297 (1965).

65Stu : V.S. Stubican and R. Roy, J. Phys. Chem. Solids, 26, 1293-1297 (1965).

65Too : G.W. Toop, Trans. AIME, 233, 850 (1965).

65Wil : J. Williamson and F.P. Blasser, Science, 148, 1589-1591 (1965).

66Goe : E. Goerl, F. Oeters and R. Scheel, Arch. Eisenhuttenw., 37, 441-451 (1966).

66Lej : A.M. Lejus, D. Goldberg and A. Revcolevschi, C.R. Acad. Sci., Paris, Ser. C 263, 1223 - 1226 (1966).

66Leo : A.E. Leonov, A.V. Andreeva, V.E. Shvaiko - Shvaikovskii and E.K. Keler, Izv. Akad. Nauk S.S.S.R., Neorg. Mater., 2, 517 (1966); Inorg. Mater U.S.S.R., 2, 446 (1966).

66Mes : H. Meschkowsky, Mathematisches Begriffswoerter buch, Bibliogrephisches Institut, Mannheim, 1966.

66Mey : H.W. Meyer, J.B. Nolan, and F.D. Richardson, Trans. Ins. Min. Met. (Sect. C), 76, 121-2, (1966).

66Nov : I.A. Novokhatskii, L.M. Lenev, A.A. Savinskaya and A.V. Gorokh, Zh. Neorg. Khim., 11, 427-428 (1966).

66Tro : G. Troemel, K.H. Obst, E. Goerl and J. Stradtmann, Tonind. Ztg. Keram. Rundschau, 90, 193-209 (1966).

66Wah : P.G. Wahlbeck and P.W. Gilles, J. Am. Ceram. Soc., 49, 180-183 (1966).

67But : W.C. Butterman and W.R. Forster, Amer. Mineral., 52, 880 (1967).

67Col : C. Colinet, D.E.S., Fac. des Sci., Univ. Grenoble, France, (1967).

67Dar : L.S. Darken, TMS-AIME, 239, 90-6 (1967)

67Dzi : M.A. Dzieciuch and N. Weber; Fr. Pat. 1,491,673, July 3, 1967; assigned to Ford Motor Co.

67Fri : E.T. Fritsche and L.G. Tensmeyer, J. Am. Ceram. Soc., 50, 167 (1967).

67Gil : P.W. Gilles, K.D. Carlson, J.F. Franzen and P.G. Wahlbeck, J. Chem. Phys., 46, 2461-2465 (1967).

67Jon : T.S. Jones, S. Kimura and A. Muan, J. Am. Ceram. Soc., 50, 139 (1967).

67Kub : O. Kubaschewski, E.L. Evans and C.B. Alcock, "Metallurgical Thermochemistry", Pergamon, London (1967).

67Nog : T. Noguchi, M. Mizuno and W.M. Conn., Sol. Energy. 11, 151 (1967).

67Per : P. Perrot, Thesis, University of Nancy, France (1967).

67Sch : K. Schwerdtfeger and A. Muan, Trans. Met. Soc. AIME, 239, 1114 - 1119 (1967).

67Sri : R. Sridhar and J.H.E. Jeffes, Trans. I.M.M., 76, C44-C60 (1967).

68Bab : C.L. Babcock, J. Am. Ceram. Soc., 51, 163-169 (1968).

68Car : R.E. Carter and W.L. Roth; pp. 125-44 in "Electromotive Force Measurements in High Temperature Systems", Edited by C.B. Alcock, Institution of Mining and Metallurgy, London (1968).

68Cev : G. Cevales, Ber. Dtsch. Keram. Ges., 45, 216 (1968).

68Cha : G.G. Charette and S.N. Flengas, Can. Met. Quart., 7, 191 (1968).

68Gar : R.C. Garvie, J. Am. Ceram. Soc., 51, 553-56 (1968).

68Gol : D. Goldberg, Rev. Int. Hautes Temp. Refract., 5, 181 - 194 (1968).

68Nog : T. Noguchi and M. Mizuno, Bull. Chem. Soc. Japan, 41, 2895 (1968).

68Roy : S.K. Roy and R.L. Coble, J. Am. Ceram. Soc., 51, 1-6 (1968).

68Sta : A. Staronka, H. Pham and M. Rolin, Rev. Int. Hautes Temp. Refract., 5, 111-115 (1968).

69Bec : D. Becherescu and F. Winter, Silicates Ind., 34, 17-20 (1969).

69Dev : R.C. DeVries and W.L. Roth, J. Am. Ceram. Soc., 52, 364-369 (1969).

69Hen : J.W. Henney and J.W.S. Jones, Trans. Brit. Ceram. Soc., 68, 210 - 213 (1969).

69Loe : J. Loeffler, Glastech. Ber., 42, 92-96 (1969).

69Mac1: I.D. MacGregor, Am. J. Sci., 267-A, 342 - 363 (1969).

69Mac2: J.F. MacDowell and G.H. Beall, J.Am. Ceram. Soc., 52, 17-25 (1969).

69Obs : K.H. Obst and J. Stradtmann, Arch. Eisenhuttenw., 40, 615-617 (1969).

69Rob : H.A. Robinson, J. Am. Ceram. Soc., 53, 392-399 (1969).

69Rou : M.A. Rouf., A.H. Cooper and H. B. Bell, Trans. Brit. Ceram. Soc., 68, 263 - 267 (1969).

69Tra : J.P. Traverse and M. Foex, High Temp. - High Pressures, 1, 409-427 (1969).

69Tro1: G. Troemel, K. Koch and J. Geiseler, Arch. Eisenhuttenw., 40, 87-98 (1969).

69Tro2: G. Troemel, W. Fix and R. Heinke, Tonind. Ztg. Keram. Rundschau, 93, 1-8 (1969).

69Woe : E. Woermann, B. Brezny and A. Muan, Am. J. Sci., 267-A, 463 - 479 (1969).

69Wre : H.A. Wreidt, Trans. Met. Soc. AIME, 245, 2565 (1969)

69Yok : T. Yokokawa and K. Niwa, Trans. Jap. Inst. Metals, 10, 3 - 81 (1969).

70Alp : A.M. Alper, R.C. Doman, R.M. McNally and H.C. Yeh, in "Phase Diagrams", edited by A.M. Alper, Academic Press, London and New York, p. 117 (1970).

70Aub : J. Aubry, A. Berthet, R. Duchene, H. Etienne, O. Evrard, F. Jeannot, C. Gleitzer, C. Offroy and P. Perrot, Ann. Chim. (Paris), 5, 299-308 (1970).

70Ber : A. Berthet and P. Perrot, Mem. Sci. Rev. Met., 67, 747 - 753 (1970).

70Cha : M.W. Chase et al., JANAF Thermochemical Tables, 2nd ed., (1970).

70Jon : A. Jongejan and A.L. Wilkins, J. Less-Common Metals, 20, 273 - 279 (1970).

70Koz : Z. Kozuka and C.S. Samis, Met. Trans. 1, 871 (1970).

70Hah : W.C. Hahn Jr. and A. Muan, Mater. Res. Bull., 5, 955-964 (1970)

70Sch : F. Schmid and D. Viechnicki, J. Mater. Sci. 5, 470 (1970).

70Tib : N. Tiberg and A. Muan, Metall. Trans., 1, 435 - 439 (1970).

70Tim : M. Timucin and A.E. Morris, Amer. Soc. Test. Mater., Spec. Tech. Publ., 472, 25-31 (1970).

70Tim1: M. Timucin and A.E. Morris, Met. Trans., 1, 3193-3201 (1970).

70Web : N.Weber and A.F. Venero, paper 1-JV-70, 72nd Annual Meeting of Am. Ceramic Soc., May 1970, Philadelphia.

70Whi : S.G. Whiteway, I.B. Smith and C.R. Masson, Can. J. Chem. 48, 33 (1970).

70Whi1: S.G. Whiteway, I.B. Smith and C.R. Masson, Can. J. Chem., 48, 1456 (1970).

70Woe : E. Woermann and A. Muan, Mater. Res. Bull., 5, 879-888 (1970).

71Bou : R. Bouaziz and M. Mayer, C.R. Acad. Sci., Ser. C., 272, 1874-1877 (1971).

71Dis : P.A. Distin, S.G. Whiteway and C.R. Masson, Can. Metall. Q., 10, 73 - 78 (1971).

71Dis1: P.A. Distin, S.G. Whiteway and C.R. Masson, Can. Metall. Q., 10, 13-18 (1971).

71Eva : L.G. Evans and A. Muan, Thermochimica Acta, 2, 277 - 292 (1971).

71Ham : P.J. Hampson and P.W. Gilles, J. Chem. Phys., 55, 3712-3728 (1971).

71Jan : JANAF Thermochemical Tables, 2nd Ed. (1971).

71Kap : M.L. Kapoor and M.G. Frohberg, Symposium on Chemical Metallurgy of Iron and Steel, Sheffield, 1971.

71Sch : R. Scheel and F. Oeters, Arch. Eisenhuttenw., 42, 769-777 (1971).

71Shu : R.L. Shultz and A. Muan, J. Am. Ceram. Soc., 54, 504 (1971).

71Whi1: W.P. Whitney II and V.S. Stubican, J. Phys. Chem. Solids, 32, 305-312 (1971).

71Whi2: W.P. Whitney II and V.S. Stubican, J. Am. Ceram. Soc., 54, 349-352 (1971).

72Dav : R.F. Davis and J. A. Pask, J. Am. Ceram. Soc., 55, 525-531 (1972).

72Gic : C. Gicquel, M. Mayer and R. Bouaziz, C.R. Acad. Sci., Ser. C, 275, 1427-1430 (1972).

72Han : F. Hanic, J. Stracelsky and L. Sumichrast, Colloq. Int. Cent. Nat. Rech. Sci., No. 205, 347-349 (1972).

72Kub : O. Kubaschewski, High Temp. - High Pressures, 4, 1 - 12 (1972).

72Kum : J.T. Kummer, Prog. Solid State Chem., 7, 141-175 (1972).

72Nog : T. Noguchi, Colloq. Int. Cent. Nat. Rech. Sci., No. 205, 347-349 (1972).

72Suz : K. Suzuki and K. Sambongi, Tetsu to Hagane, 58, 1579 (1972).

73Abb : F. Abbattista, G. Borroni-Grassi and M. Maja, Metall. Ital., 65, 485 - 488 (1973).

73Ben : K.O. Bennington and R.R. Brown, Rep. Invest. U.S. Bur. Mines, RI 7778, 13 pp. (1973).

73Cho : N.S. Choudhury, J. Electrochem. Soc., 120, 1663-1667 (1973).

73Die : M. Dieter, Mater. Res. Bull., 8, 943-49 (1973).

73Eas : A.J. Easteal and D.J. Udy, J. Inorg. Nucl. Chem. 35, 3956-3959 (1973).

73Fro : M.G. Frohberg, E. Caune and M.L. Kapoor, Arch. Eisenhuttenw., 44, 585 - 588 (1973).

73Hul : R. Hultgren, P.D. Desai, D.T. Hawkins, M. Gleiser and K.K. Kelley "Selected Values of the Thermodynamic Properties of Binary Alloys", ASM, Metals Park, OH (1973).

73Oka : K. Okajima and H. Sakao, Trans. JIM, 14, 68 (1973).

73Sch : W. Schartau and R. Hoppe, Naturwissenschaften, 60, 105 (1973).

73Sly : N.P. Slyusar, A.D. Krivorotenko, E.N. Fomichev, A.A. Kalashnik and V.P. Bondarenko, Teplofiz. Vys. Temp., 11, 213-215 (1973); High Temp., 11, 190-192 (1973).

73Spe : P.J. Spencer, Nat. Phys. Lab. (U.K.), Div. Chem. Stand., Rep. No. 21, 36 pp. (1973).

74Bal : C.W. Bale and A.D. Pelton, Met. Trans., 5, 2323 (1974).

74Bel : E.K. Belyaev, N.M. Panasenko and V.M. Tomenko, Izv. Akad. Nauk SSSR, Neorg. Mater., 10, 460-464 (1974).

74Bha : A.B. Bhatia, W.H. Hargrove and D.E. Thornton, Phys. Rev., B9, 435 (1974).

74Hal : W. Haller, D.H. Blackburn and J.H. Simmons, J. Am. Ceram. Soc., 57, 120-126 (1974).

74Kap : M.L. Kapoor, G.M. Mehrotra and M.G. Frohberg, Archiv. Eisenhuttenw 45, 663 (1974).

74Kux : V. Kuxmann and P. Fischer, Erzmetall., 27, 533 (1974).

74Lin : D.H. Lindsley, S.E. Kesson, M.J. Hartzman and M.K. Cushman, Proc. Lunar Sci. Conf., 5th, 1, 521 - 534 (1974).

74Mer : R.R. Merritt and A.G. Turnbull, J. Solid State Chem., 10, 252-259 (1974).

74Miz : M. Mizuno, R. Berjoan, J.-P. Coutures and M. Foex, Yogyo-Kyokai-Shi, 82, 631 - 636 (1974).

74Ros : K. Rosenbach and J.A. Schmitz, Arch. Eisenhuttenw., 45, 843-847 (1974).

74Sah : P. Saha and G.M. Biggar, Indian J. Earth Sci., 1, 131 - 140 (1974).

74Sch : R. Scheel, Arch. Eisenhuttenw., 45, 751-756 (1974).

74Shi : K. Shirasuka and G. Yamaguchi, Yogyo-Kyokai-Shi, 82, 650-653 (1974).

74Vie : D. Viechnicki, F. Schmid and J.W. McCauley, J. Am. Ceram. Soc., 57, 47-48 (1974).

75Abb1: F. Abbattista and M. Maja, Atti Accad. Sci. Torino, Cl. Sci. Fis., Mat. Nat., 109, 157 - 163 (1975).

75Abb2: F. Abbattista, A. Burdese and M. Maja, Rev. Int. Hautes Temp. Refract., 12, 337-342 (1975).

75Aks : I.A. Aksay and J.A. Pask, J. Am. Ceram. Soc., 58, 507-512 (1975).

75All : J.G. Allpress and H.J. Rossell, J. Solid State Chem., 15, 68-78 (1975).

75Hil : M. Hillert and L.-I. Staffansson, Metall. Trans., 6B, 37-41 (1975).

75Kay : A.K. Kay and E.C. Subbarao, Mater. Res. Bull., 10, 583-590 (1975).

75Miz : M. Mizuno, R. Berjoan, J.-P. Coutures and M. Foex, Yogyo-Kyokai-Shi, 83, 50 - 56 (1975).

75Mug : Y.M. Muggianu, M. Gambino and J.P. Bros., J. Chimie Physique, 72, 83 (1975).

75Nav : A. Navrotsky, Am. Miner., 60, 249 - 256 (1975).

75Ola : R. Olazcuaga, J.M. Reau, M. Devalette, G. Le Flem and P. Hagenmuller, J. Solid State Chem., 13, 275-282 (1975).

75Rav : D. Ravaine, E. Azandegbe and J.L. Souquet, Silic. Ind., 40, 333 - 340 (1975).

75Spe : F.E. Spencer Jr., J.C. Hendrie Jr. and D. Bienstock, "Proceedings of 6th Internat. Conf. on MHD Elect. Power Gener., Vol. II, p. 181, Washington, D.C., June 1975.

76Ans : M.R. Anseau, J.P. Biloque and P. Fierens, J. Mater. Sci. Letters, 11, 578-82 (1976).

76Pen : P. Pena and S. DeAza, Bol. Soc. Esp. Ceram. Vidr., Vol. 15, no. 2 (1976).

76Sch : E. Schuermann and G. Kraume, Arch. Eisenhuttenwes., 47, 267-269 (1976).

76Sch1: E. Schuermann and G. Kraume, Arch. Eisenhuttenw., 47, 327-331 (1976).

76Tul : H.E. Tulgar, Instanbul Tek. Univ. Bul., 29, 111 - 129 (1976).

77Bar : I. Barin, O. Knacke and O. Kubaschewski, "Thermochemical Properties of Inorganic Substances, Springer Verlag, Berlin (1977).

77Bor : C. Borgianni and P. Granati, Metall. Trans. 8B, 147 (1977).

77Bor1: C. Borgianni and P. Granati, Metall. Trans. 10B, 21 (1977).

77Fra : D.J. Fray, Metall. Trans., 8B, 153-156 (1977).

77Ouc : Y. Ouchi and E. Kato, Nippon Kink. Gakk., 41, 855 (1977).

77Pen1: P.Pena and S.De Aza, La Ceramica, 30, 1-6 (1977).

77Pen2: P.Pena and S.De Aza, Science of Ceramics, Ed. K.J. de Vries, 9, 247-55 (1977).

77Sha : E.L. Shakhin, G.G. Mikhailov, A.A. Lykasov and V.I. Shishkov, Zh. Fiz. Khim., 51, 2519-2523 (1977).

77Stu : V.S. Stubican and J.R. Hellmann, Adv. Ceram., 3, 25-36 (1981); V.S. Stubican and S.P. Ray, J. Am. Ceram. Soc., 60, 534-7 (1977).

78Eli : I. Eliezer and R.A. Howald, High Temp. Sci., 10, 1-16 (1978).

78Eli1: I. Eliezer, R.A. Howald, M. Marinkovic, and I. Eliezer, J. Phy. Chem., 82, No.9, 1021-26 (1978)

78Fil : N.J. Filipovska and H.B. Bell, Trans. I.M.M., 87, C94-C98 (1978).

78Gri : H. Gripenberg, S. Seetharaman and L.I. Staffansson, Chem Scr., 13, 162-164 (1978-79).

78Rob : R.A. Robie, B.S. Hemingway and J.R. Fisher, "Thermodynamic Properties of Minerals and Related Substances at 298.15 K and 1 Bar (10^5 Pascals) Pressure and at Higher Temperatures", U.S. Government Printing Office, Washington, D.C., 456 pp. (1978).

79Gra : A.E. Grau, Can. Metall. Q., 18, 313-322 (1979).

79Hen : A.F. Henriksen and W.D. Kingery, Ceramurgia Int., 5, 11 - 17 (1979).

79Koh : S. Kohsaka, S. Sato and T. Yokokawa, J. Chem. Thermodyn., 11, 547-551 (1979).

79Kub : O. Kubaschewski and C.B. Alcock, "Metallurgical Thermochemistry", 5th ed. (1979).

79Leu : D. Leusmann, Neues Jahrb. Miner.. Monatsh., 6, 262 - 266 (1979).

79Pen : P.Pena, Ph.D. Thesis, University of Madrid (1979).

79Ril : J.F. Riley, Trans. I.M.M., 88, C19-C24 (1979).

79Tew : J.D. Tewhey and P.C. Hess, Phys. Chem. Glasses, 20, 41-53 (1979).

80Ban : S. Ban-ya, A. Chiba and A. Hikosaka, Tetsu to Hagane, 66, 1484 - 1493 (1980).

80Bey : R.P. Beyer, M.J. Ferrante and R.R. Brown, J. Chem. Thermodyn., 12, 985-991 (1980).

80Gas : P.H. Gaskell and I.D. Tallant, Phliosophical Magazine, B42, 265-286 (1980).

80Gra : R.M. Grant, Australia Japan Extractive Metallurgy Symposium, P. 75-92, (1980).

80Hil : M. Hillert, CALPHAD, 4, 1 (1980).

80Kat : E. Kato, K. Daimon and J. Takahashi, J. Am. Ceram. Soc., 63, 355 - 356 (1980).

80Mar : R. Marchand, L. Brohan and M. Tournoux, Mater. Res. Bull., 15, 1129-1133 (1980).

80Neu : D.A. Neudorf and J.F. Elliott, Metall. Trans. B, 11B, 607-614 (1980).

80Pel : A.D. Pelton, Ber. Bunsenges. Phys. Chem., 84, 212-217 (1980).

80Rag : S. Raghavan, G.N.K. Iyengar and K.P. Abraham, Trans. Indian Inst. Met., 33, 51 - 57 (1980).

80Rot : R.S. Roth, Adv. Chem. Ser., 186, 391-408 (1980); R.S. Roth, "Phase Diagrams for Ceramists", Eds. R.S. Roth, J.R. Dennis and H.F. McMurdie, vol. VI, p. 90, Am. Ceram. Soc., Westerville, OH (1987).

80Sha : B.A. Shakhmatkin and M.M. Shul'ts, Fiz. Khim. Stekla, 6, 129-135 (1980.

80She : A.V. Shevchenko, L.M. Lopato, I.M. Maister and O.S. Gorbunov, Russ. J. Inorg. Chem., 25, 1379-1381 (1980).

80Shi : I. Shindo, J. Cryst. Growth, 50, 839 - 851 (1980).

80Tak : Y. Takeda, S. Nakazawa and A. Yazawa, Can. Metall. Q. 19, 297-305 (1980).

80Vie : H.U. Viertel and F. Seifert, Neues Jahrb. Miner.., Abh., 140, 89-101 (1980).

80Wil : G.M. Willis, Proc. TMS-AIME Symp. on Metallurgy and Environmental Control, ed. J.M. Cigan, T.S. Mackey and T.J. O'Keefe, pp. 457-476, AIME (1980).

81All : M. Allibert, C. Chatillon, K.T. Jacob and R. Lourtau, J. Am. Ceram. Soc., 64, 307-314 (1981).

81Bor : K. Borowiec and T. Rosenqvist, Scand. J. Metall., 10, 217-224 (1981).

81Dub : A. Dubreuil, M. Malenfant and A.D. Pelton, J. Electrochem. Soc., 128, 2006-2008 (1981).

81Fer : A. Fernandes Guillermet, M. Hillert, B. Jansson, and B. Sundman, Metall. Trans., 12B, 745-54 (1981).

81Fis : G.R. Fischer, L.J. Manfredo, R.N. McNally and R.C. Doman, J. Mater. Sci. 16, 3447-51 (1981).

81Gas : D.R. Gaskell, Can. Metall. Q. 20, No. 1, 3-19 (1981).

81Jac : K.T. Jacob, Can. Metall. Q., 20, 89-92 (1981).

81Jan : C.M. Jantzen, D. Schwahn, J. Schelten and H. Herman, Phys. Chem. Glasses, 22, 122-137 (1981).

81Med : V.A. Medvedev, G.A. Bergman, L.V. Gurvich, V.S. Yungman, A.F. Vorobiev, V.P. Kolesov et al, Thermicheskie Konstanty, Veshchestv (Thermal Constants of Substances), V.P. Glushko (Editor), vol. 1 (1965), 2 (1966), 3 (1968), 4 (1970), 5 (1971), 6/1 (1973), 6/2 (1973), 7 (1974), 8 (1978), 9 (1979), 10 (1981), Akad. Nauk USSR, Viniti, Moscow.

81Rao1: B.K.D.P. Rao and D.R. Gaskell, Metall. Trans., 12B, 311 - 317 (1981).

81Rao2: B.K.D.P. Rao and D.R. Gaskell, Metall. Trans., 12B, 469 - 477 (1981).

82Ban1: S. Ban-ya, Y. Iguchi and H. Honda, Proc. Int. Symp. Phys. Chem. Iron Steelmaking, III/39 - III/44 (1982).

82Ban2: S. Banon, C. Chatillon and M. Allibert, High Temp. Sci., 15, 105-128 (1982).

82Hem : B.S. Hemingway, J. Phys. Chem., 82, 2802-2803 (1982).

82Moy : J.S. Moya, E. Criado and S. De Aza, J. Mater. Sci., 17, 2213-2217 (1982).

82Mys : B.O. Mysen, L.W. Finger, F.A. Seifert and D. Virgo, Am. Mineral., 67, 686-696 (1982).

82Rog : G. Rog and A.K. Rog, Solid State Ionics, 7, 291-294 (1982).

82Som : I.D. Sommerville and H.B. Bell, Can. Metall. Q., 21, 145-155 (1982).

82Ste : J.M. Steiler, Comm. Eur. Communities, [Rep.] EUR EUR 7820, Pt. 2, 21-1/21-36 (1982).

82Stu : J.M. Stuve, J. Chem. Eng. Data, 27, 391-392 (1982).

82Tas : P. Taskinen, A. Taskinen and L.E. Holappa, Can. Metall. Q., 21, 163-169 (1982).

82Wil : R.O. Williams and J. Brynestad, CALPHAD, 6, No. 1 25-38 (1982).

82Yam : S. Yamaguchi, A. Imai and K.S. Goto, Scand. J. Metall., 11, 263-264 (1982).

83Bri : R.J. Brisley and D.J. Fray, Metall. Trans., 14B, 435-440 (1983).

83Kam : S. Kambayashi and E. Kato, J. Chem. Thermodyn., 15, 701 - 707 (1983).

83Nit : N. Nityanand and H.A. Fine, Metall. Trans., 14B, 685-691 (1983).

83Rey : R.A. Reyes and D.R. Gaskell, Met. Trans., 14B, 725-731 (1983).

83Zad : S. Zador and C.B. Alcock, High Temp. Sci., 16, 187-207 (1983).

84Azi : S.A. Azimov, D.D. Gulamova, N.N. Mel'nik, M. Kh. Sarkisova, S. Kh. Suleimanov and L.M. Tsapenko, Izv. Akad. Nauk SSSR, Neorg. Mater., 20, 469 - 471 (1984).

84Bjo : B. Bjoerkman, Scand. J. Metall., 13, 193-200 (1984).

84Elr : F.A. Elrefaie and W.W. Smeltzer, Solid State Ionics, 12, 517-524 (1984).

84Gay : H. Gaye and J. Welfringer, 2nd International Conference on Molten Slags and Fluxes, Lake Tahoe, (1984).

84Hol: M.J. Hollitt, Aust. Inst. Min. and Met., Extractive Metallurgy Symp., pp. 70-78, Aust. Inst. Min. and Met., Victoria, Australia (1984).

84Kam : S. Kambayashi and E. Kato, J. Chem. Thermodyn., 16, 241 - 248 (1984).

84Pel: A.D. Pelton and M. Blander, Proc. Int'l. Symp. on Molten Slags and Fluxes, pp. 281-294, ed. H.A. Fine and D. Gaskell, TMS-AIME, Warrendale, PA (1984).

84Pen : P.Pena and S.De Aza, Sci. Ceram., 12, 201-8 (1984).

84Phi : J.C. Phillips, J. Non-Cryst. Solids, 63, 347-355 (1984).

84Tas : A.I. Taskinen, L.M. Toivonen and T.T. Talonen, Proc. Int'l. Symp. Metall. Slags and Fluxes, Ed. H.A. Fine and D.R. Gaskell, pp. 741-756, AIME, Warrendale, PA (1984).

84Toi : L. Toivonen and A. Taskinen, Scand. J. Metall., 13, 7-10 (1984).

84Wec : B.A. Wechsler and A. Navrotsky, J. Solid State Chem., 55, 165 - 180 (1984).

85Ber1: R.G. Berman and T.H. Brown, Contrib. Miner.. Petrol., 89, 168 - 183 (1985).

85Ber2: R.G. Berman, T.H. Brown and H.J. Greenwood, Atomic Energy of Canada Limited, TR-377, 62 pp. (1985).

85Fon : L. Fontainas, D. Verhulst and P. Bruwier, Can. Metall. Q. 24, 47-52 (1985).

85Hil : M. Hillert, B. Jansson, B. Sundman, and J. Agren, Metall. Trans. A, 16A, 261-66 (1985).

85Ito : M. Itoh, K. Kimura and Z. Kozuka, Trans. Jpr. Inst. Met., 26, 353-361 (1985).

85Jan : JANAF Thermochemical Tables, 3rd Ed., J. Phys. Chem. Ref. Data 14 (1985).

85Kum1: R.V. Kumar and D.A.R. Kay, Metall. Trans., 16B, 107-112 (1985).

85Kum2: R.V. Kumar and D.A.R. Kay, Metall. Trans., 16B, 295-301 (1985).

85Pel : A.D. Pelton, Computer Modeling of Phase Diagrams, L.H. Bennett, ed., National Bureau of Standards, 1985.

85Rag : S. Raghavan, G.N.K. Iyengar and K.P. Abraham, J. Chem. Thermodyn., 17, 585-591 (1985).

85She : A.V. Shevthenko and L.M. Lopato, Thermochim. Acta, 93, 537-540 (1985).

85Tho : W.T. Thompson, A.D. Pelton and C.W. Bale, "Facility for the Analysis of Chemical Thermodynamics", May, 1985.

85Tsu : F. Tsukihashi and N. Sano, Tetsu to Hagane, 71, 815-822 (1985).

85Yam : O. Yamaguchi, K.Sugiura, A. Mitsui and K. Shimizu, J. Am. Cram. Soc., 68, C 44 - 45 (1985).

86Ban : M.J. Bannister and J.M. Barnes, J. Am. Ceram. Soc., 69, C269-C271 (1986).

86Ber : R.G. Berman and T.H. Brown, Contrib. Miner.. Petrol.,94, 262 (1986).

86Cho : N.S. Choudhury, J. Electrochem. Soc., 133, 425-431 (1986).

86Dhi : A. Dhima, B. Stafa and M. Allibert, High Temp. Sci., 21, 143 - 159 (1986).

86Fer : M.J. Ferrante, Rep. Invest. U.S. Bur. Mines, RI 9018, 9 pp. (1986).

86Hag1: V.B.M. Hageman and H.A.J. Oonk;, Phys. Chem. Glasses, 27, 194 - 198 (1986).

86Hag2: V.B.M. Hageman, G.J.K. van den Berg, H.J. Janssen and H.A.J. Oonk, Phys. Chem. Glasses, 27, 100-106 (1986).

86Lin : P.L. Lin and A.D. Pelton, Metall. Tran. 10B 666-676 (1986).

86Mat : V.N. Matrosov, A.I. Alimpiev and T.A. Matrosova, Dokl. Akad. Nauk BSSR, 30, no 10, 933-34 (1986).

86McH : A.E. McHale and R.S. Roth, J. Am. Ceram. Soc., 69, 827-32 (1986).

86Nav : A. Navrotsky, B.A. Wechsler, K. Geisinger and F. Seifert, J. Am. Ceram. Soc., 69, 418-422 (1986).

86Nev : M. Nevriva and F. Fischer, Mat. Res. Bull., 21, 1285-1290 (1986).

86Pel : A.D. Pelton and M. Blander, Metall. Trans. 17B, 12, 805-15 (1986).

86Pel1: A.D. Pelton and C.W. Bale, Metall. Tran. 17A, 7, 1211-1215 (1986).

86Yam : T. Yamada, M. Yoshimura and S. Somiya, J. Am. Ceram. Soc., 69, C243-245 (1986).

87Bla : M. Blander and A.D. Pelton, Geochim. et Cosmochim. Acta, 51, 85-95 (1987).

87Cha : S.P. Chaudhuri, Ceram. Int., 13, 167-175 (1987).

87Klu : F.J. Klug, S. Prochazka and R.H. Doremus, J. Am. Ceram. Soc., 70, 750-759 (1987).

87Mur : J.L. Murray and H.A. Wriedt, Bull. Alloy Phase Diagrams., 8, 148-165 (1987).

87Rog : G. Rog and W. Pycior, J. Chem. Thermodyn., 19, 381 - 384 (1987).

87Shu : M.M. Shul'ts, .L. Stolyarova and G.G. Ivanov, Fiz. Khim. Stekla, 13, 168-172 (1987).

87Sre : I. Srecec, A. Ender, E. Woermann, W. Gans, E. Jacobsson, G. Eriksson and E. Rosen, Phys. Chem. Miner., 14, 492 - 498 (1987).

88Ber : B. Bergman and C. Song, J. Am. Ceram. Soc., 71, C121-C125 (1988).

88Gay : H. Gaye, P.V. Riboud and J. Welfringer, 3nd International Conference on Molten Slags and Fluxes, Glasgow, 1988.

88Ito : M. Itoh and Z. Kozuka, J. Am. Ceram. Soc., 71, C36-C39 (1988).

88Pel : A.D. Pelton, W.T. Thompson, C.W. Bale and N.G. Eriksson, from "Advances in Phase Transitions", Conf. Proc., ed. G. Purdy, pp. 52-67, Pergamon, N.Y. (1988).

88Pel1: A.D. Pelton, M. Blander, CALPHAD, 12, No. 1, 97-108 (1988).

88Win : W. Winter, Diplomarbeit, Institut fur Kristallographie der RWTH, Aachen, Germany, 118 pp. (1988).

89Bar : I. Barin, "Thermochemical Data of Pure Substances", VCH, Weinheim, Germany (1989).

89Bro : N.E. Brown and A. Navrotsky, Am. Miner., 74, 902 - 912 (1989).

89Chi : Y.-M. Chiang and W.D. Kingery, J. Am. Ceram. Soc., 72, 271-277 (1989).

89Hil : M. Hillert and X. Wang, CALPHAD, 13, No. 3, 253-266 (1989)

89Jah : S. Jahanshahi and R.L. Player, "Non-Ferrous Smelting Symposium", pp. 33-40, Port Pirie South Australia, (1989).

89Jan : H. Jansen, Studienarbeit, Rheinische-Westfalische Technische Hochschule, Aachen, Germany (1989).

89Kal : G.M. Kale and K.T. Jacob, Metall. Trans., 20B, 687-691, (1989).

89Ros : S.M. Ross, "Introduction To Probability Models", 4th. ed., Academic Press Limited, 26, (1989).

89Wri : S. Wright, W.T. Denholm and W.J. Rankin, "Non-Ferrous Smelting Symposium", pp. 79-85, Port Pirie South Australia, (1989).

90Hil1: M. Hillert, B. Jansson, and B. Sundman, Metall. Trans. B, 21B, 404-06 (1990).

90Hil2: M. Hillert and M. Selleby, Scand. J. Metall., 19, 23-25 (1990).

90Hil3: M. Hillert, M. Selleby, and B. Sundman, Metall. Trans. A, 21A, 2759-76 (1990).

90Hil4: M. Hillert, B. Sundman, and X.Z. Wang, Metall. Trans. B, 21B, 303-12 (1990).

90Mua : A. Muan, Private commmunication (1990).

90Woe : E. Woermann, Private communication (1990).

91CAN : CANMET, Private communication (1991).

91Eri : G. Eriksson, Private communication (1991).

91Eri1: G. Eriksson, Private communication (1991).

91Jac : K.T. Jacob, K. Swaminathan and O.M. Sreedharan, Electrochim. Acta, 36, 791-798 (1991).

92Rom : J.A. Romero and A.D. Pelton, "A Structure Model of Liquid Silicate Systems". Ph.D Thesis (1992).

92Wu : P. Wu and A.D. Pelton, J. Alloy and Compound., (1992).

APPENDIX - THERMODYNAMIC DATA OF PURE SUBSTANCES IN THE DATABASE

In this appendix, thermodynamic data of 100 pure substances in the present database will be listed. The following quantities will be tabled:

$\Delta H^{o}(298)$ Standard enthalpy of formation of the substance per formula weight from the elements in the reference state at 1 bar and 298.15 K.

This standard enthalpy of formation is zero for elements in reference phases.

$S^{o}(298)$ Standard entropy of substance per formula weight at 1 bar and 298.15 K.

Cp Heat capacity of the substance per formula weight.

$Cp = A + Bx10^{-3}T + Cx10^{-4}T^{-2} + Dx10^{-7}T^{2} + Ex10^{-11}T^{3} + FT^{-0.5} + Gx10^{6}T^{-3.0} + HT^{-1}$

Temperature range

The first and second values indicate the lowest and highest temperatures at which the data are considered valid. A high temperature given as 5000 K in the table simply denotes very high temperature.

In the following tables, G=gas, L=liquid, S=solid; 1, 2, 3 and 4 state for different phases.

Thermodynamic data of the rare earth oxides have been listed in Table 3-1 and Table 3-2.

Formula	phase	$\Delta H^{\circ}(298)$ (KJ)	$S^{\circ}(298)$ (J/K)	Temperature range (K)
O_2	G1	0.000	205.147	298.00---3001.00
$AlKO_2$	S1	-1144.444	85.550	298.00--- 810.00
$AlNaO_2$	S1	-1120.869	63.569	298.00--- 740.00
	S1	-1119.572	65.321	740.00---5000.00
$AlNaSi_3O_8$	S1	-3921.618	224.412	298.00---5000.00
	S2	-3935.100	207.443	298.00---5000.00
Al_2O_3	L1	-1596.353	43.569	298.00---2327.00
	L1	-1693.606	-53.070	2327.00---5000.00
	S1	-1675.700	50.820	298.00---2327.00
	S1	-1812.013	-103.954	2327.00---5000.00
Al_2CaO_4	S1	-2324.158	115.060	298.00---5000.00
$Al_2CaSi_2O_8$	S1	-4231.594	200.186	298.00---5000.00
Al_2FeO_4	S1	-1960.407	106.940	298.00---5000.00
Al_2MgO_4	S1	-2300.313	84.535	298.00---5000.00
Al_2MnO_4	S1	-2098.569	129.704	298.00---5000.00
Al_2TiO_5	S1	-2577.174	128.448	298.00---5000.00

Formula	phase	$\Delta H^{\circ}(298)$ (KJ)	$S^{\circ}(298)$ (J)	Temperature range (K)
$Al_2Ca_2SiO_7$	S1	-3985.858	198.600	298.00--- 698.00
	S1	-3988.652	189.215	698.00---1600.00
	S1	-3972.869	210.068	1600.00---5000.00
$Al_2Ca_3O_6$	S1	-3587.267	204.179	298.00---5000.00
$Al_2Ca_3Si_3O_{12}$	S1	-6632.859	255.150	298.00---5000.00
Al_4CaO_7	S1	-3999.689	177.820	298.00---5000.00
Al_4TiO_8	S1	-4194.883	211.576	298.00---5000.00
$Al_6Si_2O_{13}$	S1	-6806.610	274.900	298.00---5000.00
Al_9KO_{14}	S1	-7916.169	267.271	298.00---5000.00
$Al_{12}CaO_{19}$	S1	-10704.186	388.910	298.00---5000.00
$Al_{12}K_2O_{19}$	S1	-10788.496	374.908	298.00---5000.00
$Al_{12}Na_2O_{19}$	S1	-10702.896	358.119	298.00---5000.00
$Al_{18}Na_2O_{28}$	S1	-15746.738	517.752	298.00---5000.00

Formula	phase	$\Delta H^{o}(298)$ (KJ)	$S^{o}(298)$ (J)	Temperature range (K)
CaO	L1	-555.594	65.691	298.00---2845.16
	L1	-578.235	41.161	2845.16---5000.00
	S1	-635.090	37.750	298.00---2845.16
	S1	-657.731	13.220	2845.16---5000.00
$CaMgSiO_4$	S1	-2250.027	108.300	298.00---5000.00
$CaSiO_3$	S1	-1632.579	81.810	298.00---1404.00
	S1	-1628.506	85.279	1404.00---5000.00
$CaSiTiO_5$	S1	-2597.431	129.290	298.00---5000.00
$CaTiO_3$	S1	-1660.630	93.640	298.00---1530.00
	S2	-1667.508	76.525	1530.00---5000.00
$CaZrO_3$	S1	-1767.744	100.081	298.00---2623.00
$CaMgSi_2O_6$	S1	-3195.975	142.500	298.00---5000.00
$Ca_2MgSi_2O_7$	S1	-3861.625	214.092	298.00--- 358.00
	S2	-3861.173	215.355	358.00---5000.00
Ca_2SiO_4	S1	-2306.045	127.610	298.00--- 970.00
	S2	-2307.009	123.637	970.00---1710.00
	S3	-2281.887	143.248	1710.00---5000.00

Formula	phase	$\Delta H^{o}(298)$ (KJ)	$S^{o}(298)$ (J)	Temperature range (K)
$Ca_2Ti_2O_5$	S1	-3580.805	209.343	298.00--- 470.00
	S1	-3579.296	212.619	470.00---2115.00
	S1	-3602.655	173.178	2115.00---2130.00
	S1	-3513.091	279.353	2130.00---2845.00
	S1	-3518.751	273.220	2845.00---5000.00
$Ca_3MgSi_2O_8$	S1	-4549.010	251.777	298.00---5000.00
Ca_3SiO_5	S1	-2930.315	170.021	298.00---5000.00
$Ca_3Si_2O_7$	S1	-3942.846	210.874	298.00---5000.00
$Ca_3Ti_2O_6$	S1	-3579.296	212.619	298.00---5000.00
$Ca_3Ti_2O_7$	S1	-3963.480	234.722	298.00---5000.00
$Ca_3Si_3Ti_2O_{12}$	S1	-6405.731	355.487	298.00---5000.00
$Ca_5Ti_4O_{13}$	S1	-7281.596	431.580	298.00---5000.00
FeO	S1	-265.832	59.496	298.00---1644.00
	S1	-278.950	39.512	1644.00---5000.00
	L1	-234.643	78.466	298.00---1644.00
	L1	-247.761	58.482	1644.00---5000.00
$FeTiO_3$	S1	-1233.142	108.628	298.00---1650.00

Formula	phase	$\Delta H^{\circ}(298)$ (KJ)	$S^{\circ}(298)$ (J)	Temperature range (K)
$FeTi_2O_4$	S1	-1825.911	136.167	298.00--- 470.00
	S1	-1824.403	139.443	470.00---5000.00
$FeTi_2O_5$	S1	-2152.814	176.569	298.00---5000.00
Fe_2O_3	S1	-825.627	87.437	298.00--- 955.60
	S2	-817.641	97.340	955.60---1873.00
	L1	-747.990	134.527	298.00---1873.00
	L1	-839.442	18.088	1873.00---5000.00
Fe_2SiO_4	S1	-1479.917	150.930	298.00---1478.00
Fe_2TiO_4	S1	-1515.610	168.870	298.00---1668.00
Fe_3O_4	S1	-1117.403	146.114	298.00--- 848.10
	S2	-1102.702	166.309	848.10---1870.00
	L1	-964.630	240.144	1870.00---5000.00
K_2O	S1	-361.498	102.006	298.00---1013.00
	S1	-377.061	73.243	1013.00---5000.00
	L1	-334.298	128.857	298.00---1013.00
	L1	-349.861	100.094	1013.00---5000.00
K_2SiO_3	S1	-1560.362	146.147	298.00---5000.00
K_2TiO_3	S1	-1531.393	148.699	298.00---5000.00

Formula	phase	$\Delta H^{\circ}(298)$ (KJ)	$S^{\circ}(298)$ (J)	Temperature range (K)
$K_2Si_2O_5$	S1	-2522.542	182.004	298.00--- 510.00
	S2	-2521.609	183.833	510.00--- 867.00
	S2	-2518.865	186.998	867.00---5000.00
$K_2Ti_2O_5$	S1	-2483.204	200.581	298.00---5000.00
$K_2Ti_3O_7$	S1	-3433.990	260.831	298.00---5000.00
$K_2Si_4O_9$	S1	-4338.562	265.684	298.00--- 865.00
	S1	-4366.453	203.414	865.00---5000.00
$K_2Ti_6O_{13}$	S1	-6266.391	425.555	298.00---5000.00
K_4TiO_4	S1	-2102.950	251.154	298.00---5000.00
$K_8Ti_5O_{14}$	S1	-7050.248	687.697	298.00---5000.00
MgO	S1	-601.500	26.951	298.00---3097.00
	S1	-642.428	-13.759	3097.00---5000.00
	L1	-545.345	27.004	298.00---3097.00
	L1	-565.026	11.226	3097.00---5000.00
$MgSiO_3$	S1	-1545.474	66.325	298.00--- 886.00
	S2	-1545.100	66.170	886.00---1257.00
	S3	-1543.507	67.438	1257.00---5000.00
$MgTiO_3$	S1	-1571.552	74.560	298.00---5000.00

Formula	phase	$\Delta H^{o}(298)$ (KJ)	$S^{o}(298)$ (J)	Temperature range (K)
$MgTi_2O_4$	S1	-2131.422	114.943	298.00--- 470.00
	S1	-2129.914	118.220	470.00--- 933.00
	S1	-2128.914	119.291	933.00---5000.00
$MgTi_2O_5$	S1	-2504.887	137.343	298.00---5000.00
Mg_2SiO_4	S1	-2177.700	94.010	298.00---5000.00
Mg_2TiO_4	S1	-2156.788	115.102	298.00--- 933.00
	S1	-2155.788	116.174	933.00---5000.00
MnO	S1	-384.928	59.831	298.00---2115.00
	S1	-393.964	44.760	2115.00---5000.00
	L1	-330.536	85.547	298.00---2115.00
	L1	-339.572	70.475	2115.00---5000.00
$MnSiO_3$	S1	-1321.426	102.500	298.00---5000.00
$MnTiO_3$	S1	-1361.373	105.855	298.00---1683.00
$MnTi_2O_4$	S1	-1938.092	136.414	298.00--- 470.00
	S1	-1936.584	139.690	470.00---1043.00
	S1	-1935.584	140.649	1043.00---5000.00
Mn_2SiO_4	S1	-1724.564	163.200	298.00---5000.00
Mn_2TiO_4	S1	-1745.886	170.410	298.00---5000.00

Formula	phase	$\Delta H^{\circ}(298)$ (KJ)	$S^{\circ}(298)$ (J)	Temperature range (K)
Na_2O	S1	-417.982	75.061	298.00---1023.00
	S2	-416.225	76.779	1023.00---1243.00
	S3	-404.300	86.372	1243.00---1405.00
	L1	-356.603	120.320	298.00---1405.00
	L1	-372.791	91.722	1405.00---5000.00
Na_2SiO_3	S1	-1558.601	113.847	298.00---1363.00
$Na_2Si_2O_5$	S1	-2470.340	164.055	298.00--- 951.00
	S2	-2522.257	63.202	951.00--- 980.00
	S3	-2521.630	63.842	980.00---1148.00
$Na_2Ti_2O_5$	S1	-2539.688	173.636	298.00---5000.00
$Na_2Ti_3O_7$	S1	-3489.743	233.886	298.00---1403.00
$Na_2Ti_6O_{13}$	S1	-6321.205	398.610	298.00---1573.00
Na_4SiO_4	S1	-2101.297	195.811	298.00---1410.00
Na_4TiO_4	S1	-2267.505	163.639	298.00---1318.00
$Na_6Si_8O_{19}$	S1	-9167.917	652.863	298.00---1082.00
$Na_8Ti_5O_{14}$	S1	-7359.548	524.381	298.00---1303.00

Formula	phase	$\Delta H^{\circ}(298)$ (KJ)	$S^{\circ}(298)$ (J)	Temperature range (K)
NiO	S1	-239.743	37.991	289.15--- 525.00
	S1	-235.502	48.991	525.00--- 565.00
	S1	-239.912	36.787	565.00---2228.00
	S1	-232.847	41.159	2228.00---5000.00
	L1	-178.455	65.572	2228.00---5000.00
Ni_2SiO_4	S1	-1403.278	110.039	298.00---1818.00
PbO	S1	-218.062	68.699	298.00---1159.00
	S1	-227.770	51.355	1159.00---5000.00
	L1	-202.255	73.376	1159.00---5000.00
SiO_2	S1	-910.700	41.460	298.00---373.00
	S1	-910.703	41.451	373.00---848.00
	S1	-908.627	44.207	848.00---5000.00
	S2	-907.750	43.770	298.00---390.00
	S2	-907.045	45.524	390.00---5000.00
	S3	-907.753	43.394	298.00---535.00
	S3	-906.377	46.029	535.00---1996.00
	S3	-936.217	5.117	1996.00---5000.00
	L1	-896.796	50.829	298.00---1996.00
	L1	-926.636	9.917	1996.00---5000.00

Formula	phase	$\Delta H^{\circ}(298)$ (KJ)	$S^{\circ}(298)$ (J)	Temperature range (K)
$SiZrO_4$	S1	-2028.141	84.027	298.00---1400.00
	S1	-2041.620	55.451	1400.00---2000.00
TiO_2	S1	-944.750	50.460	298.00---2130.00
	S1	-993.603	-7.454	2130.00---5000.00
	L1	-898.726	72.068	298.00---2130.00
	L1	-947.579	14.154	2130.00---5000.00
$TiZrO_4$	S1	-2041.141	109.187	298.00---2143.00
Ti_2O_3	S1	-1520.884	77.253	298.00--- 470.00
	S2	-1519.375	80.529	470.00---2115.00
	S2	-1618.046	41.088	2115.00---5000.00
	L1	-1414.376	130.174	298.00---2115.00
	L1	-1437.734	90.733	2115.00---5000.00
Ti_2ZrO_6	S1	-2999.058	151.279	298.00---1573.00
Ti_3O_5	S1	-2452.465	157.617	298.00---5000.00
Ti_4O_7	S1	-3414.317	197.444	298.00---5000.00
Ti_5O_9	S1	-4360.918	248.954	298.00---5000.00
Ti_6O_{11}	S1	-5306.479	300.501	298.00---5000.00
Ti_7O_{13}	S1	-6251.589	351.911	298.00---5000.00
Ti_8O_{15}	S1	-7196.482	403.170	298.00---5000.00

Formula	phase	$\Delta H^{o}(298)$ (KJ)	$S^{o}(298)$ (J)	Temperature range (K)
Ti_9O_{17}	S1	-8141.242	454.365	298.00---5000.00
$Ti_{10}O_{19}$	S1	-9085.913	505.515	298.00---5000.00
$Ti_{20}O_{39}$	S1	-18533.039	1015.380	298.00---5000.00
ZnO	S1	-350.460	43.639	298.00---2248.00
	L1	-296.068	67.835	298.00---2248.00
	L1	-309.549	47.920	2248.00---5000.00
ZrO_2	S1	-1097.463	50.359	298.00---1478.00
	S2	-1093.146	47.836	1478.00---2633.00
	S3	-1082.561	51.856	2633.00---2950.00
	L1	-1031.019	50.670	2950.00---5000.00

Formula	Phase	A	B	C	D	E	F	G
O_2	G1	44.9	0.0	-1.3	0.0	0.0	-322.3	86.7
$AlKO_2$	S1	68.6	69.7	-97.2	-262.8	0.0	0.0	0.0
$AlNaO_2$	S1	89.1	15.3	-179.3	0.0	0.0	0.0	0.0
	S1	89.1	15.3	-179.3	0.0	0.0	0.0	0.0
$AlNaSi_3O_8$	S1	393.6	0.0	-789.3	0.0	0.0	-2415.5	1070.6
	S2	393.6	0.0	-789.3	0.0	0.0	-2415.5	1070.6
Al_2O_3	L1	179.4	-9.2	97.5	0.0	0.0	-828.4	409.1
	L1	192.5	0.0	0.0	0.0	0.0	0.0	0.0
	S1	155.0	0.0	-386.1	0.0	0.0	-828.4	409.1
	S1	192.5	0.0	0.0	0.0	0.0	0.0	0.0
Al_2CaO_4	S1	227.0	0.0	-56.1	0.0	0.0	-1669.1	-85.5
$Al_2CaSi_2O_8$	S1	439.4	0.0	0.0	0.0	0.0	-3734.1	-317.0
Al_2FeO_4	S1	204.3	0.0	-980.8	0.0	0.0	-258.3	1208.3
Al_2MgO_4	S1	235.9	0.0	-171.0	0.0	0.0	-1766.6	40.6

Formula	Phase	A	B	C	D	E	F	G
Al_2MnO_4	S1	154.9	25.9	-322.2	0.0	0.0	0.0	0.0
Al_2TiO_5	S1	249.3	0.0	-480.6	0.0	0.0	-1350.1	516.0
$Al_2Ca_2SiO_7$	S1	373.1	0.0	-477.9	0.0	0.0	-2276.8	477.9
	S1	151.3	369.5	1251.3	-1469.0	0.0	-2276.8	477.9
	S1	373.1	0.0	-477.9	0.0	0.0	-2276.8	477.9
$Al_2Ca_3O_6$	S1	321.6	0.0	-578.1	0.0	0.0	-1255.4	661.2
$Al_2Ca_3Si_3O_{12}$	S1	573.4	0.0	-1888.7	0.0	0.0	-2039.4	2319.3
Al_4CaO_7	S1	338.0	0.0	-1211.3	0.0	0.0	-1022.2	1510.6
Al_4TiO_8	S1	395.8	0.0	-1163.4	0.0	0.0	-1925.3	1505.1
$Al_6Si_2O_{13}$	S1	634.8	0.0	-1721.0	0.0	0.0	-3373.5	2122.7
Al_9KO_{14}	S1	751.8	0.0	-2111.1	0.0	0.0	-4124.0	2880.4
$Al_{12}CaO_{19}$	S1	992.7	0.0	-2814.8	0.0	0.0	-5350.0	3747.0

Formula	Phase	A	B	C	D	E	F	G
$Al_{12}K_2O_{19}$	S1	1037.5	0.0	-2814.8	0.0	0.0	-5691.1	3840.5
$Al_{12}Na_2O_{19}$	S1	1027.5	0.0	-3325.2	0.0	0.0	-5113.7	4674.2
$Al_{18}Na_2O_{28}$	S1	1493.7	0.0	-4732.6	0.0	0.0	-7670.6	6594.4
CaO	L1	58.8	0.0	-114.7	0.0	0.0	-133.9	103.0
	L1	62.8	0.0	0.0	0.0	0.0	0.0	0.0
	S1	58.8	0.0	-114.7	0.0	0.0	-133.9	103.0
	S1	62.8	0.0	0.0	0.0	0.0	0.0	0.0
$CaMgSiO_4$	S1	226.3	0.0	-118.0	0.0	0.0	-1542.7	-23.3
$CaSiO_3$	S1	149.1	0.0	-365.9	0.0	0.0	-690.3	484.3
	S1	141.2	0.0	-585.8	0.0	0.0	-417.2	940.7
$CaSiTiO_5$	S1	234.6	0.0	-511.8	0.0	0.0	-1040.3	591.5
$CaTiO_3$	S1	150.5	0.0	0.0	0.0	0.0	-621.3	-430.1
	S2	134.0	0.0	0.0	0.0	0.0	0.0	0.0
$CaZrO_3$	S1	129.6	9.1	0.0	0.0	0.0	-340.4	-429.3

Formula	Phase	A	B	C	D	E	F	G
$CaMgSi_2O_6$	S1	305.4	0.0	-716.6	0.0	0.0	-1604.9	921.8
$Ca_2MgSi_2O_7$	S1	387.1	0.0	0.0	0.0	0.0	-2938.8	-40.8
	S2	387.1	0.0	0.0	0.0	0.0	-2938.8	-40.8
Ca_2SiO_4	S1	209.7	0.0	-798.9	0.0	0.0	-701.9	1297.5
	S2	209.7	52.1	-798.9	-1058.4	5380.5	-701.9	1297.5
	S3	209.7	0.0	-798.9	0.0	0.0	-701.9	1297.5
$Ca_2Ti_2O_5$	S1	876.5	14.6	1944.9	0.0	0.0	-14638.3	-713.0
	S1	316.3	14.6	225.1	0.0	0.0	-783.7	-2278.5
	S1	303.2	14.6	64.1	0.0	0.0	-33.5	-713.0
	S1	261.8	14.6	-553.3	0.0	0.0	-33.5	25.7
$Ca_3MgSi_2O_8$	S1	453.6	0.0	0.0	0.0	0.0	-3250.0	-344.2
Ca_3SiO_5	S1	321.2	0.0	-99.5	0.0	0.0	-2450.2	97.5
$Ca_3Si_2O_7$	S1	339.9	0.0	-1066.0	0.0	0.0	-985.3	1373.6
$Ca_3Ti_2O_6$	S1	316.3	14.6	225.1	0.0	0.0	-783.7	-2278.5

Formula	Phase	A	B	C	D	E	F	G
$Ca_3Ti_2O_7$	S1	299.2	15.9	-572.4	0.0	0.0	0.0	0.0
$Ca_3Si_3Ti_2O_{12}$	S1	614.5	0.0	-597.6	0.0	0.0	-2966.9	-754.9
$Ca_5Ti_4O_{13}$	S1	642.2	0.0	-900.6	0.0	0.0	-2064.3	432.5
FeO	S1	-18.0	30.6	-253.3	0.0	0.0	1500.9	0.0
	S1	68.2	0.0	0.0	0.0	0.0	0.0	0.0
	L1	-18.0	30.6	-253.3	0.0	0.0	1500.9	0.0
	L1	68.2	0.0	0.0	0.0	0.0	0.0	0.0
$FeTiO_3$	S1	150.0	0.0	-332.4	0.0	0.0	-441.6	348.2
$FeTi_2O_4$	S1	920.0	-30.6	2470.9	0.0	0.0	-17923.1	-457.5
	S2	359.8	-30.6	751.1	0.0	0.0	-4068.5	-2023.0
$FeTi_2O_5$	S1	247.2	0.0	-450.3	0.0	0.0	-1026.1	455.5

Formula	Phase	A	B	C	D	E	F	G
Fe_2O_3								
	S1	146.9	5.5	-557.7	-413.4	7795.8	0.0	525.6
	S2	146.9	0.0	-557.7	0.0	0.0	0.0	525.6
	L1	146.9	0.0	-557.7	0.0	0.0	0.0	525.6
	L1	192.5	0.0	0.0	0.0	0.0	0.0	0.0
Fe_2SiO_4								
	S1	248.9	0.0	0.0	0.0	0.0	-1923.9	-139.1
Fe_2TiO_4								
	S1	249.6	0.0	0.0	0.0	0.0	-1817.4	-54.5
Fe_3O_4								
	S1	207.9	38.0	-724.3	-2380.7	37255.2	0.0	664.4
	S2	207.9	0.0	-724.3	0.0	0.0	0.0	664.4
	L1	207.9	0.0	-724.3	0.0	0.0	0.0	664.4
K_2O								
	S1	75.9	17.1	-59.2	0.0	0.0	0.0	0.0
	S1	107.0	0.0	0.0	0.0	0.0	0.0	0.0
	L1	75.9	17.1	-59.2	0.0	0.0	0.0	0.0
	L1	107.0	0.0	0.0	0.0	0.0	0.0	0.0
K_2SiO_3								
	S1	226.0	0.0	0.0	0.0	0.0	-1986.6	149.0
K_2TiO_3								
	S1	190.2	0.0	-225.1	0.0	0.0	-798.1	225.0

Formula	Phase	A	B	C	D	E	F	G
$K_2Si_2O_5$								
	S1	240.7	0.0	-1479.3	0.0	0.0	0.0	2289.2
	S2	240.7	0.0	-1479.3	0.0	0.0	0.0	2289.2
	S2	240.7	0.0	-1479.3	0.0	0.0	0.0	2289.2
$K_2Ti_2O_5$								
	S1	275.3	0.0	-450.3	0.0	0.0	-1018.8	450.0
$K_2Ti_3O_7$								
	S1	360.3	0.0	-675.4	0.0	0.0	-1239.5	674.9
$K_2Si_4O_9$								
	S1	253.2	159.4	0.0	0.0	0.0	0.0	0.0
	S2	391.4	16.2	0.0	0.0	0.0	0.0	0.0
$K_2Ti_6O_{13}$								
	S1	615.5	0.0	-1350.8	0.0	0.0	-1901.7	1349.9
K_4TiO_4								
	S1	295.3	0.0	-225.1	0.0	0.0	-1375.4	225.0
$K_8Ti_5O_{14}$								
	S1	845.9	0.0	-1125.7	0.0	0.0	-3413.0	1124.9
MgO								
	S1	61.1	0.0	-62.1	0.0	0.0	-296.2	5.8
	S1	66.9	0.0	0.0	0.0	0.0	0.0	0.0
	L1	72.8	-3.1	52.3	0.0	0.0	-296.2	5.8
	L1	66.9	0.0	0.0	0.0	0.0	0.0	0.0

Formula	Phase	A	B	C	D	E	F	G
$MgSiO_3$								
	S1	140.0	0.0	-440.0	0.0	0.0	-497.0	535.7
	S2	166.6	0.0	-227.1	0.0	0.0	-1200.6	279.1
	S2	166.6	0.0	-227.1	0.0	0.0	-1200.6	279.1
$MgTiO_3$								
	S1	146.2	0.0	-400.0	0.0	0.0	-416.0	402.3
$MgTi_2O_4$								
	S1	817.4	0.0	2109.6	0.0	0.0	-15688.8	-367.5
	S1	257.1	0.0	389.7	0.0	0.0	-1834.1	-1933.0
	S1	257.1	0.0	389.7	0.0	0.0	-1834.1	-1933.0
$MgTi_2O_5$								
	S1	232.6	0.0	-566.1	0.0	0.0	-755.5	582.1
Mg_2SiO_4								
	S1	238.6	0.0	0.0	0.0	0.0	-2001.2	-116.2
Mg_2TiO_4								
	S1	226.1	0.0	-170.1	0.0	0.0	-1380.1	41.3
	S1	226.1	0.0	-170.1	0.0	0.0	-1380.1	41.3
MnO								
	S1	46.5	8.1	-36.8	0.0	0.0	0.0	0.0
	S1	60.7	0.0	0.0	0.0	0.0	0.0	0.0
	L1	46.5	8.1	-36.8	0.0	0.0	0.0	0.0
	L1	60.7	0.0	0.0	0.0	0.0	0.0	0.0

Formula	Phase	A	B	C	D	E	F	G
$MnSiO_3$								
	S1	99.0	19.1	-304.1	0.0	0.0	274.5	0.0
$MnTiO_3$								
	S1	121.7	9.3	-218.8	0.0	0.0	0.0	0.0
$MnTi_2O_4$								
	S1	774.1	9.3	1998.8	0.0	0.0	-14604.9	-402.9
	S1	213.8	9.3	278.9	0.0	0.0	-750.2	-1968.5
	S1	213.8	9.3	278.9	0.0	0.0	-750.2	-1968.5
Mn_2SiO_4								
	S1	512.5	-182.7	460.2	520.6	0.0	-6640.4	0.0
Mn_2TiO_4								
	S1	168.2	17.4	-255.6	0.0	0.0	0.0	0.0
Na_2O								
	S1	66.2	43.9	-81.3	-140.9	0.0	0.0	0.0
	S2	66.2	43.9	-81.3	-140.9	0.0	0.0	0.0
	S3	66.2	43.9	-81.3	-140.9	0.0	0.0	0.0
	L1	66.2	43.9	-81.3	-140.9	0.0	0.0	0.0
	L1	104.6	0.0	0.0	0.0	0.0	0.0	0.0
Na_2SiO_3								
	S1	234.8	0.0	0.0	0.0	0.0	-2218.9	135.3
$Na_2Si_2O_5$								
	S1	250.7	0.0	-1565.1	0.0	0.0	0.0	2217.0
	S2	292.9	0.0	0.0	0.0	0.0	0.0	0.0
	S3	292.9	0.0	0.0	0.0	0.0	0.0	0.0

Formula	Phase	A	B	C	D	E	F	G
$Na_2Ti_2O_5$	S1	272.6	0.0	0.0	0.0	0.0	-1282.7	-157.6
$Na_2Ti_3O_7$	S1	367.2	0.0	0.0	0.0	0.0	-1940.3	-137.1
$Na_2Ti_6O_{13}$	S1	483.0	55.4	-909.6	0.0	0.0	0.0	0.0
Na_4SiO_4	S1	162.6	74.2	0.0	0.0	0.0	0.0	0.0
Na_4TiO_4	S1	275.4	0.0	-1246.0	0.0	0.0	-220.7	1892.3
$Na_6Si_8O_{19}$	S1	987.7	0.0	-3554.1	0.0	0.0	-4020.7	5410.6
$Na_8Ti_5O_{14}$	S1	805.9	0.0	-3167.3	0.0	0.0	-1103.6	4459.5
NiO	S1	420.7	-746.8	0.0	0.0	99962.3	0.0 H=-5374.6	0.0
	S1	-33.8	168.5	0.0	0.0	0.0	0.0	0.0
	S1	68.4	-45.1	0.0	404.4	-951.7	0.0	-24.9
	S1	54.4	0.0	0.0	0.0	0.0	0.0	0.0
	L1	54.4	0.0	0.0	0.0	0.0	0.0	0.0
Ni_2SiO_4	S1	163.2	19.8	-243.1	88.3	0.0	0.0	0.0

Formula	Phase	A	B	C	D	E	F	G
PbO								
	S1	47.6	12.3	0.0	0.0	0.0	-65.8	-45.5
	S1	65.0	0.0	0.0	0.0	0.0	0.0	0.0
	L1	65.0	0.0	0.0	0.0	0.0	0.0	0.0
SiO_2								
	S1	80.0	0.0	-354.7	0.0	0.0	-240.3	491.6
	S1	80.0	8.4	-354.7	-452.1	6055.1	-240.3	491.6
	S1	80.0	0.0	-354.7	0.0	0.0	-240.3	491.6
	S2	75.4	182.1	-595.8	-12338.2	209019.3	0.0	958.2
	S2	75.4	0.0	-595.8	0.0	0.0	0.0	958.2
	S3	83.5	20.2	-245.5	-1255.1	19485.2	-374.7	280.1
	S3	83.5	0.0	-245.5	0.0	0.0	-374.7	280.1
	S3	85.8	0.0	0.0	0.0	0.0	0.0	0.0
	L1	83.5	0.0	-245.5	0.0	0.0	-374.7	280.1
	L1	85.8	0.0	0.0	0.0	0.0	0.0	0.0
$SiZrO_4$								
	S1	257.7	-25.6	0.0	0.0	0.0	-2680.9	100.4
	S1	150.6	0.0	0.0	0.0	0.0	0.0	0.0
TiO_2								
	S1	77.8	0.0	-336.8	0.0	0.0	0.0	402.9
	S1	100.4	0.0	0.0	0.0	0.0	0.0	0.0
	L1	77.8	0.0	-336.8	0.0	0.0	0.0	402.9
	L1	100.4	0.0	0.0	0.0	0.0	0.0	0.0
$TiZrO_4$								
	S1	172.5	0.0	-336.8	0.0	0.0	-584.5	282.5

Formula	Phase	A	B	C	D	E	F	G
Ti_2O_3	S1	730.2	0.0	1880.8	0.0	0.0	-14604.9	0.0
	S2	170.0	0.0	161.0	0.0	0.0	-750.2	-1565.5
	S2	156.9	0.0	0.0	0.0	0.0	0.0	0.0
	L1	170.0	0.0	161.0	0.0	0.0	-750.2	-1565.5
	L1	156.9	0.0	0.0	0.0	0.0	0.0	0.0
Ti_2ZrO_6	S1	250.3	0.0	-673.5	0.0	0.0	-584.5	685.5
Ti_3O_5	S1	159.0	50.2	0.0	0.0	0.0	0.0	0.0
Ti_4O_7	S1	364.4	0.0	-252.0	0.0	0.0	-2110.9	-144.5
Ti_5O_9	S1	442.2	0.0	-588.7	0.0	0.0	-2110.9	258.4
Ti_6O_{11}	S1	520.0	0.0	-925.5	0.0	0.0	-2110.9	661.3
Ti_7O_{13}	S1	597.9	0.0	-1262.3	0.0	0.0	-2110.9	1064.3
Ti_8O_{15}	S1	675.7	0.0	-1599.1	0.0	0.0	-2110.9	1467.2
Ti_9O_{17}	S1	753.6	0.0	-1935.9	0.0	0.0	-2110.9	1870.2

Formula	Phase	A	B	C	D	E	F	G
$Ti_{10}O_{19}$	S1	831.4	0.0	-2272.7	0.0	0.0	-2110.9	2273.1
$Ti_{20}O_{39}$	S1	1609.8	0.0	-5640.5	0.0	0.0	-2110.9	6302.5
ZnO	S1	48.2	6.8	0.0	0.0	0.0	-91.5	-103.8
	L1	48.2	6.8	0.0	0.0	0.0	-91.5	-103.8
	L1	60.7	0.0	0.0	0.0	0.0	0.0	0.0
ZrO_2	S1	94.6	0.0	0.0	0.0	0.0	-584.5	-120.4
	S2	74.5	0.0	0.0	0.0	0.0	0.0	0.0
	S3	74.5	0.0	0.0	0.0	0.0	0.0	0.0
	L1	87.9	0.0	0.0	0.0	0.0	0.0	0.0

ÉCOLE POLYTECHNIQUE DE MONTRÉAL
3 9334 00233395 1